

AFFIDAVIT

I declare that I have authored this thesis independently, that I have not used other than the declared sources/resources, and that I have explicitly indicated all material which has been quoted either literally or by content from the sources used. The text document uploaded to TUGRAZonline is identical to the present doctoral thesis.

Date

Signature

Acknowledgements

I would like to very much thank my supervisor Prof. Dr. Peter Macheroux for giving me the opportunity to do my PhD in his working group. With all the ups and downs (definitely more ups, though ;-)) it was a great experience and I really enjoyed the time a lot. Starting with my work on EasE, which turned out to not be “EasE” to work with, continuing with *PpBBE1*, and finally studying different aspects of the mitochondrial electron transport, I was allowed to learn a great variety of biochemical and biophysical methods and could experience the exciting diversity of flavoenzymology. Thank you for giving me the chance to help with the cooperation projects on “ene-cyclases” and on “chorismate synthase”, which helped me to get in touch with more applied research like biocatalysis and inhibitor design. Thank you for giving me the opportunity to teach undergraduate students in various lab courses and for allowing me to supervise so many bachelor, master and project students and most importantly, thank you for your continuous support, the many great scientific discussions, and your help throughout the time.

I would also like to thank Dr. Andreas Winkler, especially for his help with crystallization of *PpBBE1* (and all the other proteins we failed to get crystals from ;-)), as well as for always taking time to discuss problems and findings in any of my projects - I really enjoyed working with you. You always tried to help me, whenever I did not know whom else to ask and our scientific discussions often encouraged me to even dig deeper into the literature to find an explanation for my observations.

Thank you to our cooperation partners Dr. Gertrud Wiedemann, Dr. Sebastian Hoernstein, Jennifer Kothe, and Prof. Dr. Ralf Reski from the University of Freiburg (Institute of Plant Biology) for the *in planta* characterization of *PpBBE1* as well as for the analysis of the *PpBBE1* knock-out strains. Thank you to Dr. Flavio Seixas and Dr. Erika Kioshima from the Universidade Estadual de Maringá (Brazil) for the interesting cooperation on “Inhibitors of the chorismate synthase from *P. brasiliensis*”, as well as to Dr. Kathrin Heckenbichler and Univ.-Prof. Dr. Rolf Breinbauer from the Institute of Organic chemistry (TU Graz) for the great cooperation on “ene-cyclases”.

Thank you to my numerous bachelor and project students (Pauline Macheroux, Nevena Cupara, Bettina Eggbauer, Katharina Fuchs, Samuele Suraci, Julia Schmidt, and Cornelia Böhm) for your enthusiasm and your willingness to learn new methods and techniques and to experience the ups and downs of scientific lab work with me.

I would especially like to thank my first project and bachelor student Jelena Ulićević and my bachelor and master student Julia Brunner for their great help with all the projects we were working on. Your enthusiasm and your interest in biochemical research were truly amazing and I really enjoyed the time we spent in the lab together.

Thank you to all the group members for the great working atmosphere and the nice time we had in and outside the lab together. I would especially like to thank my lab mates Eveline Brodl and Chaitanya Tabib for always assisting me, whenever I needed a helping hand.

Big thanks also to Julia Messenlehner for being such a motivated “StuMa” and managing the immunology lab course in such a great way, as well as for being a very special friend.

I would also like to thank our technicians Eva Frießer and Rosemarie Trenker-El-Toukhy for their support throughout the time – I am sure there are many things I could never have managed without your help! ;-)

Last but not least, I would like to thank my parents for their love and their tremendous support throughout my studies. Thank you for your encouragement, for always believing in me and for listening to all my problems, doubts, and worries I was dealing with during this time. Thank you to my brother for always helping me with IT stuff, as well as for your understanding and sometimes jolly comments that helped me to stay positive even when I was unhappy with my progress in the lab.

Abstract

Flavin-dependent proteins constitute one of the largest and most diverse protein families. Due to the redox activity of their vitamin B₂-derived cofactors, flavin mononucleotide (FMN) and flavin adenine dinucleotide (FAD), flavoproteins participate in one- and two-electron transfer reactions, and therefore play important roles in a great variety of metabolic pathways.

An especially interesting subfamily of flavoenzymes is the group of so-called berberine bridge enzyme- (BBE-) like proteins. They bind their FAD cofactor in a mono- or bivalent manner and thereby strongly enhance their reduction potential, which enables them to catalyze demanding oxidation reactions in various metabolic pathways ranging from carbohydrate catabolism to alkaloid biosynthesis. While BBE-like enzymes are only found in a few bacterial and fungal species, they are present in all land plants, with the number of homologs increasing from basal to higher plants.

To identify the primordial role of BBE-like proteins in plants, I heterologously produced the BBE-like protein from the most basal plant *Physcomitrella patens* (*PpBBE1*) and studied its biochemical and structural properties. Consistent with the results obtained from the *in planta* characterization of the protein, it was shown that *PpBBE1* is a cellobiose oxidase involved in carbohydrate metabolism.

In contrast to the function of flavoenzymes in carbohydrate metabolism, their role in mitochondrial electron transport of eukaryotic organisms has been studied rather extensively. Upon oxidizing their natural substrates, flavin-dependent dehydrogenases involved in fatty acid and amino acid degradation, take up electrons, which they deliver to electron transferring flavoproteins (ETFs). These important electron carriers, in turn, interact with the membrane protein ETF-ubiquinone oxidoreductase and thereby pass the electrons on to the respiratory chain. In order to guarantee efficient electron transfer along the cascade, the electrochemical properties of the protein-bound cofactors need to be very well-tuned, which is the reason why already small changes in the nature or environment of the cofactors can have adverse effects on the overall process. This phenomenon could nicely be observed in the course of my studies of the hETF and its electron donor human dimethylglycine dehydrogenase, which showed that the spontaneous modification of the FAD cofactor in hETF strongly affects the interaction as well as electron transfer efficiency between the two proteins.

While mitochondrial electron transport in humans is very well studied, hardly anything is known about the electron transfer reactions in yeast. It was speculated that a single enzyme, named D-lactate dehydrogenase 2 (Dld2), serves as electron donor of the yeast ETF (yETF), however, this interaction has never been confirmed experimentally. The detailed biochemical characterization of the two proteins, as well as the analysis of their possible interaction finally revealed Dld2 to be a much better D-2-hydroxyglutarate dehydrogenase than D-lactate dehydrogenase and confirmed Dld2 to be the natural electron donor of yETF.

The finding that humans suffering from defects in hETF or hETF-QO exhibit increased levels of D-2-hydroxyglutarate (D-2HG), prompted us to search the human genome for the presence of a Dld2

homolog. As a matter of fact, a human protein exhibiting more than 50% sequence identity with Dld2 (hD2HGDH) was identified and it could be shown that the recombinantly produced protein indeed transfers electrons to hETF. In the course of further biochemical characterizations of hD2HGDH, I also analyzed the effect of two pathogenic single amino acid exchanges on the properties of the enzyme, which helped to get a better understanding of the molecular basis of D2HGDH deficiency.

Zusammenfassung

Flavin- (Vitamin B₂-) abhängige Proteine stellen eine der vielfältigsten Proteinfamilien dar. Durch die chemischen Eigenschaften ihrer Kofaktoren können sie sowohl ein- als auch zwei-Elektronen Transferreaktionen katalysieren und sind daher in nahezu allen Stoffwechselwegen vertreten.

Eine besonders interessante Unterfamilie der Flavoenzyme bilden die sogenannten „Berberin-Brücken-Enzym“- (BBE-) ähnlichen Proteine. In dieser Familie ist der FAD Kofaktor über eine oder zwei kovalente Bindung(en) mit Aminosäureseitenketten des Proteins verknüpft, wodurch die Oxidationskraft des Kofaktors gesteigert wird, um anspruchsvolle Oxidationsreaktionen katalysieren zu können (u.a. Ringschlussreaktionen in der Alkaloid Biosynthese). Interessanterweise findet man BBE-ähnliche Enzyme nur in wenigen Bakterien und Pilzgattungen, aber in allen Landpflanzen, wobei in letzteren die Anzahl der Homologen von niedrig zu höher entwickelten Pflanzen zunimmt. Diese Beobachtung führte zur Frage, welche biochemische Rolle das ursprüngliche BBE-ähnliche Protein in Pflanzen innehatte. Dafür wurde das BBE-Homologe einer Pionierpflanze der Landbesiedelung, das BBE-ähnliche Enzym aus dem Moos *Physcomitrella patens* (*PpBBE1*), rekombinant hergestellt und biochemisch und strukturell untersucht. In Kombination mit der *in planta* Charakterisierung des Enzyms konnte gezeigt werden, dass *PpBBE1* eine Cellobioseoxidase ist und eine Funktion im Kohlenhydratstoffwechsel der Pflanze hat.

Im Gegensatz zur Rolle von Flavoproteinen im Kohlenhydratstoffwechsel von Pflanzen ist deren Aufgabe beim Elektronentransport in Mitochondrien besser erforscht. Um den Abbau von Fetten und Aminosäure für die Energiegewinnung einsetzen zu können, hat die Natur eine Kaskade entwickelt, über die Elektronen von Flavin-abhängigen Dehydrogenasen, zur Elektronentransportkette geleitet werden. Diese Dehydrogenasen geben die Elektronen, die sie durch die Oxidation verschiedener Substrate aufnehmen, an ein sogenanntes „Elektronen Transferierendes Flavoprotein“ (ETF) weiter, welches mit dem Membranprotein ETF-Ubiquinon Oxidoreduktase (ETF-QO) interagiert und so die Elektronen in die Atmungskette einspeist.

Um einen effizienten Elektronentransfer über mehrere Akzeptor- und Donorsysteme gewährleisten zu können, müssen die elektrochemischen Eigenschaften der beteiligten Kofaktoren sehr genau auf einander abgestimmt sein. Bereits minimale Änderungen in den chemischen Eigenschaften der Kofaktoren oder deren Umgebung, können negative Auswirkungen auf den gesamten Prozess haben. Dies konnte ich zum Beispiel bei Untersuchungen des menschlichen ETFs und dessen Elektronenlieferanten Dimethylglycinderhydrogenase dokumentieren.

Während die mitochondrialen Elektronentransportprozesse sind beim Menschen bereits eingehend studiert wurden, ist die Bedeutung dieser Prozesse im Modellorganismus *Saccharomyces cerevisiae* (Bäckerhefe) weitestgehend unerforscht. Bislang wurde davon ausgegangen, dass nur ein einziges Enzym, die sogenannte D-Lactatdehydrogenase 2 (*Dld2*), Elektronen an das ETF (*yETF*) liefern kann. Diese Vermutung wurde allerdings bisher nicht experimentell überprüft. Im Rahmen meiner Untersuchungen konnte gezeigt werden, dass *Dld2* die D-2-Hydroxyglutarsäure wesentlich effizienter

oxidiert als D-Lactat und auch der Elektronentransfer auf das yETF konnte experimentell bestätigt werden. Damit konnte ich in meiner Arbeit den Beweis erbringen, dass Dld2 und yETF einen funktionalen Teil der Elektronentransportprozesse in der Hefe darstellen. Im Anschluss daran habe ich mich der Frage zugewandt, ob ein orthologes Elektronentransportsystem beim Menschen existiert. Tatsächlich konnte eine D-2-Hydroxyglutarsäuredehydrogenase (D2HGDH) identifiziert werden und im Rahmen meiner Arbeit konnte gezeigt werden, dass diese in der Lage ist, Elektronen auf das ETF zu übertragen. Weiterführende Studien an Varianten der D2HGDH konnten darüber hinaus Aufschluss über die Entstehung der D-2-Hydroxyglutarsäure Azidämie geben.

Abbreviations

1,2-DME	1,2-dimethoxyethane
6HDNO	6-hydroxy-D-nicotine oxidase
8f-FAD	8-formyl-FAD
a.u.	atomic unit
A40926	teicoplanin homolog
AknOx	aclacinomycin-N/aclacinomycin-A oxidase
AldO	alditol oxidase
AmB	amphotericin B
<i>At</i>	<i>Arabidopsis thaliana</i>
<i>At</i> CKX	cytokinin dehydrogenase from <i>Arabidopsis thaliana</i>
ATP	adenosine triphosphate
BBE	berberine bridge enzyme
BG60	pollen allergen
<i>Ca</i> CS	chorismate synthase from <i>Candida albicans</i>
CBDAS	cannabidiolic acid synthase
CG	conjugate gradient
CFU	colony forming unit
ChitO	chito oligosaccharide oxidase
CholOx	cholesterol oxidase
CnsA	aurantioclavine synthase
CoQ	coenzyme Q (ubiquinone)
COSY	correlation spectroscopy
<i>Cp</i>	<i>Cavia porcellus</i>
<i>Cp</i> ADHAPS	alkyl dihydroxyacetonephosphate synthase from <i>C. porcellus</i>
CS	chorismate synthase
<i>Cv</i>	<i>Chlorella variabilis</i>
cyt c	cytochrome c
D-2HGA	D-2-hydroxyglutaric aciduria
D-2HG	D-2-hydroxyglutarate/D- α -hydroxyglutarate
D2HGDH	D-2-hydroxyglutarate dehydrogenase
DAD	diode array detector
DCPIP	2,6-dichlorophenylindophenol
<i>Dd</i>	<i>Dictyostelium discoideum</i>
<i>Dd</i> ADHAPS	alkyl dihydroxyacetonephosphate synthase from <i>D. discoideum</i>
de	diastereomeric excess
Dld2	D-lactate dehydrogenase 2 from <i>Saccharomyces cerevisiae</i>

DLDH	D-lactate dehydrogenase
DMF	<i>N,N</i> -dimethylformamide
DMGDH	dimethylglycine dehydrogenase
DMSO	dimethyl sulfoxide
DNA	deoxyribonucleic acid
DNS-assay	3,5-dinitrosalicylic acid-assay
DPPH	α,α' -diphenyl- β -picrylhydrazyl
DprE	decaprenylphosphoryl-beta-D-ribose oxidase
<i>e.e.</i>	enantiomeric excess
E22O	ecdysteroid-22-oxidase
EasE	chanoclavine synthase
<i>Ec</i>	<i>Eschscholzia californica</i>
<i>E. coli</i>	<i>Escherichia coli</i>
EDTA	ethylenediamine tetraacetic acid
EncM	FAD-dependent oxygenase
EPSP	5-enolpyruvylshikimate-3-phosphate
ETF	electron transferring flavoprotein
ETF-QO	electron transferring flavoprotein – ubiquinone oxidoreductase
EugO	eugenol oxidase
EWG	electron withdrawing group
FAD	flavin adenine dinucleotide
FF	force field
FIC	fractional inhibitory concentration
FMN	flavin mononucleotide
FOX	flavin-dependent oxidoreductase
FRET	fluorescence resonance energy transfer
FsqB	fructosyl amino acid oxidase
GAI	glutaric aciduria type II
GC-FID	gas chromatography - flame ionization detector
GilR	pregilvocarin V oxidase
GLDH	L-galactono-1,4-lactone dehydrogenase
GOOX	glucooligosaccharide oxidase
h	human
<i>Ha</i> -CHOX	<i>Helianthus annuus</i> carbohydrate oxidase
HEPES	4-(2-hydroxyethyl)-1-piperazineethanesulfonic acid
HMBC	heteronuclear multiple-bond correlation spectroscopy
HMM	hidden markov model

HOT	hydroxyacid-oxoacid transhydrogenase
HOX	hexose oxidase
HPLC	high performance liquid chromatography
HPM9	alcohol oxidase from <i>Hypomyces subiculosus</i>
HSQC	heteronuclear single-quantum correlation spectroscopy
IC ₅₀	50% inhibitory concentration
ICN	indole carbonyl nitrile
ITZ	itraconazole
k_{catapp}	turnover number
K_D	dissociation constant
K_{Mapp}	Michaelis-Menten constant
k_{obs}	observed rate constant
k_{ox}	oxidative rate
<i>K. phaffii</i>	<i>Komagataella phaffii</i>
k_{red}	reductive rate
LaO	carbohydrate oxidase
LB	lysogeny broth (also called Luria Bertani)
<i>Ls</i> -CHOX	<i>Lactuca sativa</i> carbohydrate oxidase
MADD	multiple acyl-CoA dehydrogenase deficiency
MCAD	medium chain acyl-CoA dehydrogenase
MD	molecular dynamics
MeCN	acetonitrile
MFC	minimal fungicidal concentration
MIC	minimal inhibitory concentration
MOPS	3-(<i>N</i> -morpholino)propanesulfonic acid
<i>Mp</i>	<i>Marchantia polymorpha</i>
MS	mass spectrometry
<i>Mt</i>	<i>Myceliophthora thermophile</i>
MTS	3-(4,5-dimethylthiazol-2-yl)-5-(3-carboxymethoxyphenyl)-2-(4-sulfophenyl)-2H-tetrazolium
MurB	UDP- <i>N</i> -acetylenolpyruvoyl glucosamine reductase
MWCO	molecular weight cut-off
<i>N. rileyi</i>	<i>Nomuraea rileyi</i>
NAD(P)	nicotinamide adenine dinucleotide (phosphate)
Nec5	nectarin 5
<i>Nf</i>	<i>Neosartorya fumigate</i>
Ni-NTA	nickel-nitrilotriacetic acid

NMR	nuclear magnetic resonance
<i>Nt</i>	<i>Nicotiana tabacum</i>
OMIM	online mendelian inheritance in man
OYE	old yellow enzyme
<i>PbCS</i>	chorismate synthase from <i>Paracoccidioides brasiliensis</i>
PCM	paracoccidioidomycosis
PCMH	<i>p</i> -cresol methylhydroxylase
PCR	polymerase chain reaction
PDB	protein data bank
PDI	protein disulfide isomerase
PFAM	protein family
Phl p 4	major pollen allergen (glucose dehydrogenase)
<i>Pi</i>	<i>Phytophthora infestans</i>
<i>Pp</i>	<i>Physcomitrella patens</i>
Q	ubiquinone
R _{gyr}	radius of gyration
RMSD	root mean square deviation
RMSF	root mean square fluctuation
RPA1076	oxidoreductase from <i>Rhodopseudomonas palustris</i>
SCOPe	structural classification of proteins – extended
SD	standard deviation
SDS-PAGE	sodium dodecyl sulfate-polyacrylamide gel electrophoresis
SEM	scanning electron microscopy
<i>Sm</i>	<i>Selaginella moellendorffii</i>
STOX	(<i>S</i>)-tetrahydroprotoberberine oxidase
TamL	tirandymycin oxidase
THCA	Δ^1 -tetrahydrocannabinolic acid
THCAS	tetrahydrocannabinolic acid synthase
UV-Vis	UV-visible
VAO	vanillyl-alcohol oxidase
<i>Vc</i>	<i>Volvox carteri f. nagariensis</i>
WT	wild type
XEG	xylan endoglucanase
XyIO	xylooligosaccharide oxidase
<i>y</i>	yeast (<i>Saccharomyces cerevisiae</i>)
ZmCKO2	cytokinin oxidase from <i>Zea mays</i>
ZmCKX1	cytokinin oxidase from <i>Zea mays</i>

Table of content

Acknowledgements	III
Abstract	V
Zusammenfassung	VII
Abbreviations	IX
Table of content	XIII
Introduction	1
Thesis outline	19
Chapter 1: The family of berberine bridge enzyme-like enzymes: a treasure-trove of oxidative reactions	
Abstract	24
Introduction	24
Structural characteristics of BBE-like proteins.....	25
Occurrence and development of the BBE-like protein family.....	32
Reactions catalyzed by BBE-like enzymes.....	34
Outlook.....	47
References	49
Supplementary information.....	57
Chapter 2: The single berberine bridge enzyme homolog of <i>Physcomitrella patens</i> is a cellobiose oxidase	
Abstract	64
Introduction	64
Results	65
Discussion	79
Experimental procedures.....	82
References	93
Supporting information	99

Chapter 3: Oxidation of the FAD cofactor to the 8-formyl-derivative in human electron transferring flavoprotein

Abstract	105
Introduction	105
Results	107
Discussion	115
Conclusions	120
Experimental procedures.....	121
References	127

Chapter 4: Toward understanding the reaction mechanism of 8-formyl FAD formation in human electron transferring flavoprotein

Introduction	133
Results	135
Discussion	141
Materials and methods	144
References	147

Chapter 5: Closing the gap: Yeast electron transferring flavoprotein links the oxidation of D-lactate and D- α -hydroxyglutarate to energy production via the respiratory chain

Abstract	150
Introduction	150
Results	152
Discussion	163
Experimental procedures.....	166
References	174

Chapter 6: Biochemical characterization of human D-2-hydroxyglutarate dehydrogenase and two disease-related variants reveal the molecular cause of D-2-hydroxyglutaric aciduria

Abstract	180
Introduction	180
Results	182
Discussion	190
Conclusions	193
Experimental procedures.....	194
References	201

Appendix A: Promising new antifungal treatment targeting chorismate synthase from *Paracoccidioides brasiliensis*

Abstract	207
Introduction	207
Results	209
Discussion	218
Conclusions	220
Materials and methods	220
References	227
Supplementary information.....	233

Appendix B: New inhibitors of chorismate synthase present antifungal activity against *P. brasiliensis*

Abstract	237
Introduction	237
Results and Discussion.....	238
Conclusion.....	245
Material and methods	245
References	251
Supplementary information.....	256

Appendix C: Asymmetric reductive carbocyclization using engineered ene reductases

Abstract	261
Main article	261
Conclusion.....	266
References	268
Supporting information	271

Author contributions 274**Curriculum vitae.....** 277

Introduction

History

The history of flavin research dates back to the early 20th century, when scientists from the University of Heidelberg (including Paul György, Richard Kuhn, and Theodore Wagner-Jauregg) isolated and purified vitamin B₂ from egg white (ovoflavin), from urine (uroflavin), from liver (hepatoflavin), and from whey (lactoflavin) for the first time (1). Initially, it was believed that all these flavins were structurally distinct, however, their crystallization and the subsequent determination of their chemical structure revealed that the four yellow compounds were all the same. They were shown to consist of an isoalloxazine and a ribityl moiety and were thus given the name riboflavin, which is still used today. In 1935, finally, also the first de novo synthesis of the compound was described (2, 3).

Flavoproteins

Flavoproteins are a diverse class of proteins, relying on the presence of the vitamin B₂- (riboflavin) derivatives flavin mononucleotide (FMN) or flavin adenine dinucleotide (FAD) for proper (catalytic) function. While yeasts, fungi as well as bacteria are able to synthesize vitamin B₂ on their own, mammals lack biosynthetic pathways leading to the formation of riboflavin and therefore depend on the uptake of the vitamin with their food (4, 5). In order to obtain the biologically active cofactors, the vitamin is then modified in two subsequent enzymatic reactions in all organisms (6). At first, riboflavin kinase phosphorylates the ribityl side chain bound to the N10 of the isoalloxazine ring to yield FMN as product. For the generation of FAD, a second enzyme, the so called

FAD-synthase is required, which is able to attach the adenylyl moiety to the FMN in an ATP dependent manner and is thus often referred to as FAD-adenylyl transferase (Figure 1) (6).

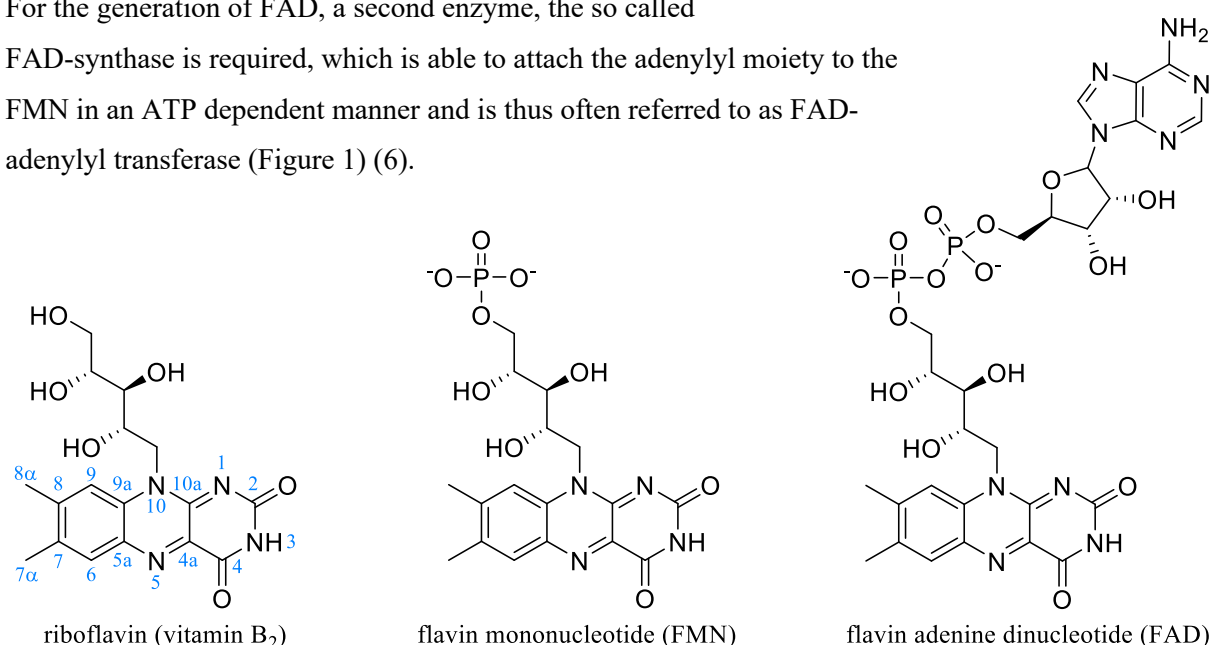


Figure 1: Structural representation of vitamin B₂ (riboflavin), including the correct atom numbering of the isoalloxazine ring (blue), and the two related biologically active cofactors flavin mononucleotide (FMN) and flavin adenine dinucleotide (FAD).

Flavin redox states

Owing to their chemical nature, flavins can adopt three different redox states; oxidized, radical (semiquinone) and reduced (hydroquinone), which can easily be distinguished based on their spectral characteristics (7).

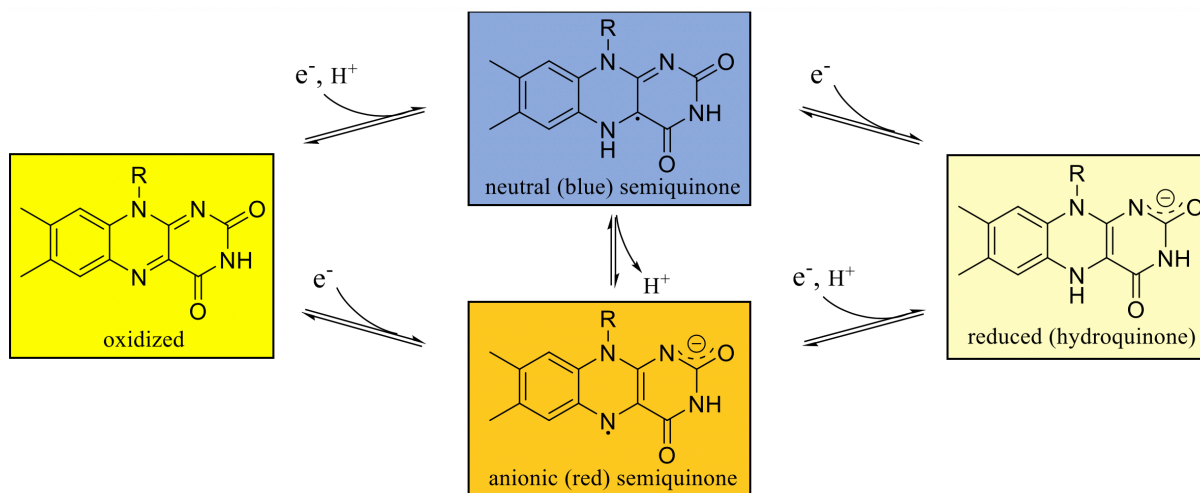


Figure 2: Structural representation of the important flavin redox states. Due to the chemical properties of their isoalloxazine moiety, flavins can adopt three different redox states; oxidized, radical (semiquinone), and reduced (hydroquinone). Upon single electron reduction, oxidized flavins are converted to their semiquinone state; either neutral or anionic, depending on the environment of the cofactor. The uptake of a second electron ultimately yields fully reduced flavin.

Oxidized flavins usually appear bright yellow and can be recognized from their typical “camel-like” absorption spectrum with maxima around 360/370 nm and 450 nm (Figure 2 and Figure 3A and B, *black* line) (7). Upon single electron reduction, oxidized flavins are converted to their semiquinone state, which coincides with major changes in their absorption characteristics. For some protein-bound flavins, a bathochromic shift and a strong increase in the intensity of the 360/370 nm peak, accompanied by a decrease of the absorbance at around 450 nm is observed (red semiquinone; Figure 2 and Figure 3A, *red* line), whereas others may be found to exhibit an additional peak in the 500 to 600 nm region (blue semiquinone) (Figure 2 and Figure 3B, *blue* line) (7, 8). Which of the two semiquinone states is formed, however, is determined by the nature of the flavin chromophore as well as by the chemical environment of the cofactor (7). Though some protein-bound flavins just adopt the two redox states discussed so far, most of them may take up a second electron, to finally end up in the hydroquinone/fully reduced state. In contrast to the oxidized and radical flavin species, the ring system of reduced flavins is no longer fully conjugated, which leads to the loss of their typical absorption characteristics and results in the bleaching of the protein sample (Figure 2 and Figure 3A, *pale yellow* line) (7).

This property, therefore, can nicely be utilized to study the biochemical characteristics of flavoproteins (7).

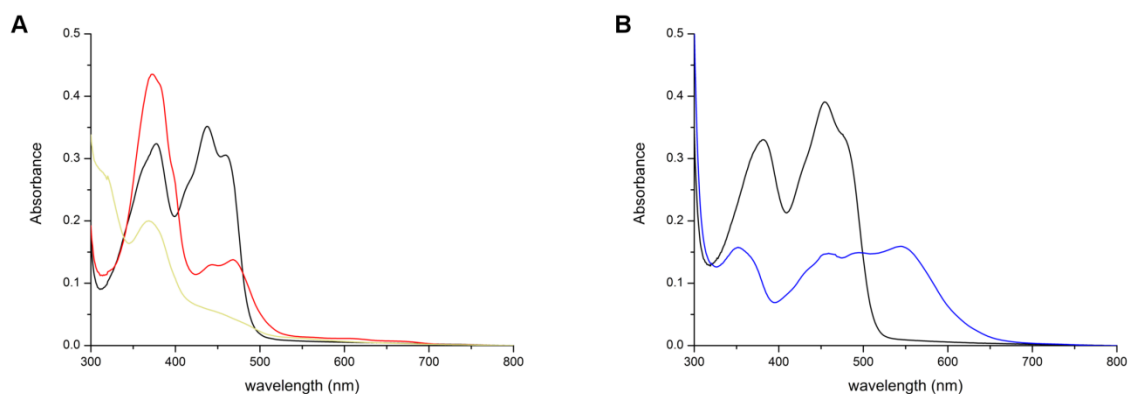


Figure 3: UV-visible absorption spectra representing the different redox states protein-bound flavins may adopt. A, The *black* line corresponds to a protein-bound flavin in its oxidized state, whereas the *red* line and the *pale yellow* line represent spectra of radical (red semiquinone) and reduced flavins, respectively. **B,** The UV-visible absorption spectrum shown in *black* also corresponds to a protein-bound flavin in its oxidized state, whereas the *blue* line represents the absorption characteristics of a protein-bound flavin in the blue semiquinone state.

Reactivity of flavoproteins

The fact that protein-bound flavins can adopt three different redox states, enables flavoproteins to not only catalyze two- but also one-electron transfer reactions (9), which strongly distinguishes them from the two-electron transferring NAD(P)-dependent enzymes (10). However, not all flavoenzymes are able to stabilize the radical state equally well, which is the reason why the transfer of single electrons cannot always be observed. In these proteins, electron transfer is accompanied by a simultaneous decrease of the 360 and 450 nm peaks, which is considered as a direct two-electron reduction process (7).

In addition to their involvement in electron transfer reactions, flavoproteins were also shown to participate in non-redox processes such as DNA-repair and circadian time keeping, where they act as lyases and play a role in signaling, respectively (11, 12).

Oxidative half reaction/oxygen reactivity

Once reduced, flavins need to be converted back to their oxidized state, in order to be able to undergo another catalytic cycle. While many flavoproteins transfer the electrons to dioxygen, yielding hydrogen peroxide as a side product (oxidases), others avoid the production of reactive oxygen species by transferring them to different electron acceptors, *i.e.*, metabolites or other proteins, (dehydrogenases) (9, 13–15). Mostly, oxygen reactivity is an intrinsic feature of the proteins, meaning that the active site of the proteins is organized in a way that they would either always or never react with oxygen (16, 17). However, there are few examples that may in the presence of substrate/product act as dehydrogenases,

whereas they exhibit strong oxidase activity when being reduced (photo)chemically (Chapter 5 and 6 and (18–20)).

Flavin modifications

As mentioned above, the electrochemical properties of flavins are determined by the nature of the flavin chromophore, as well as by the environment they are embedded in (21). While the reduction potential of free flavin is around -210 mV, it can range from about -370 to +160 mV in the protein-bound form (21). However, to cover such a wide range of reduction potentials, the adaption of the amino acid residues in the vicinity of the flavin chromophore and the variation of its solvent accessibility may be insufficient (21). Therefore, nature has developed the strategy of covalently modifying the flavin cofactor to its needs, which may for example result in the introduction of electron withdrawing groups at the 8(α)- or 6-position of the isoalloxazine ring (Figure 4), or in the mono- or bivalent attachment of the flavin cofactor to the proteins (Figure 5) (21).

Chemically modified protein-bound flavins

The first chemically modified protein-bound flavins (6- and 8-hydroxy flavins) were identified in the 1970s (Figure 4), in the course of the biochemical characterization of the electron transferring flavoprotein (ETF) from *Peptostreptococcus elsdenii* (22, 23). It was found that the cofactor modifications strongly affected the electrochemical properties of the ETF (see below for details), leading to an ~200 mV increase of the reduction potential of the protein-bound flavins. As a result, ETFs harboring these modified cofactors lose their ability of transferring electrons to their electron acceptors (in this case butyryl-CoA dehydrogenases), making it rather questionable, whether these modifications are of physiological significance (22). Interestingly, however, in our studies we were able to show that also the protein-bound flavin in human (h) ETF undergoes spontaneous modification under alkaline (physiological) conditions (Chapter 3). In contrast to the ETF from *Peptostreptococcus elsdenii*, the flavin cofactor of hETF gets oxidized at the 8 α -position, yielding 8-formyl FAD, a flavin derivative (Figure 4), which has previously been identified in formate oxidase from *Aspergillus oryzae* (24, 25). hETF bearing the formylated cofactor was found to more tightly interact with its client enzyme human dimethylglycine dehydrogenase (hDMGDH), whereas the electron transfer rates were shown to be significantly reduced (Chapter 3 and 4). Also, an increased reduction potential of the protein-bound flavin was observed, which indicates that like in *P. elsdenii* electron transfer to its natural electron acceptor (ETF-ubiquinone oxidoreductase) may be inhibited (Chapter 4).

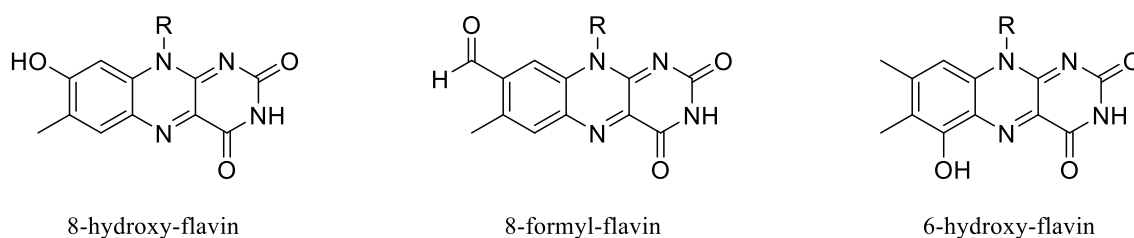


Figure 4: Chemical structure of three naturally occurring chemically modified flavin species; 8-hydroxy-flavin, 8-formyl-flavin, and 6-hydroxy-flavin.

Covalent flavin modifications

While it is rather doubtful that modifications of non-covalently bound flavins are of physiological importance, it could clearly be shown that some other proteins rely on the covalent linkage to their cofactor in order to be catalytically active (26–30). Studies performed within the last 70 years have identified seven different modes of covalent protein-flavin interaction that may either directly target the isoalloxazine ring or the ribityl side chain of the bound flavin cofactor; covalent interactions with the isoalloxazine ring were found to be formed between a histidine (via N^1 or N^3), a cysteine, or a tyrosine (via O) and the 8α -position of the cofactor and/or between a cysteine and the 6-position of the flavin ring (Figure 5), whereas the interaction with the ribityl side chain was shown to be formed by a threonine residue (21).

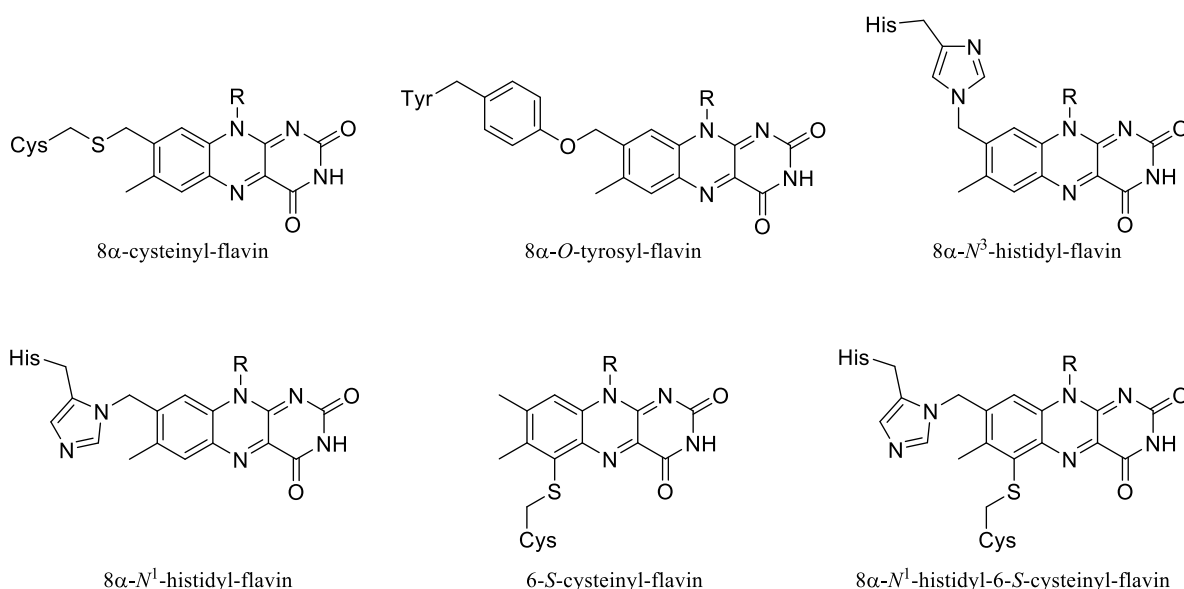


Figure 5: Naturally occurring covalent protein-flavin interactions involving the isoalloxazine ring. Mono-covalent linkage can either take place at the 6- or the 8α -position of the flavin ring and may be formed by a cysteine (to the 6-position) or a histidine, a cysteine, or a tyrosine (to the 8α -position), respectively. In bicovalent flavoproteins both a covalent linkage of a histidine to the 8α -position and of a cysteine to the 6-position is found.

Biochemical characterization of these proteins revealed that covalent linkage similar to the chemical modification of flavins strongly increases the reduction (midpoint) potential of the protein-bound cofactors, enabling the proteins to catalyze especially challenging oxidation reactions (21). This effect is even more pronounced in bivalent flavoenzymes that exhibit both a covalent linkage of a histidine to the 8 α - and of a cysteine to the 6-position of the isoalloxazine ring. As a result of this special flavin tethering, additionally, the space in the active site is strongly increased in these enzymes, which also allows them to catalyze the oxidation of sterically demanding substrates such as benzyloquinoline alkaloids or polysaccharides (31) (Chapter 1 and 2).

Modified flavin metabolites

However, modified flavin derivatives do not necessarily need to play a role in catalysis. The bacterial organisms *Streptomyces davawensis* and *Streptomyces cinabarinus*, for example, were found to harbor biosynthesis pathways for the formation of roseoflavin (8-demethyl-8-(dimethylamino)-riboflavin; Figure 6), a metabolite that exhibits antibiotic activity against gram-positive bacteria (32–34). Also bioluminescent bacteria were identified to accumulate a certain flavin derivative, which was shown to be formed as a side product in the course of the bioluminescence reaction (35). This 6-(3'-(*R*)-myristyl)-FMN exhibits an unusual C-C bond between the 6-position of the isoalloxazine ring and the C3 of myristic acid (Figure 6) and was found to have an inhibitory effect on the luciferase, the key enzyme involved in bacterial bioluminescence (36).

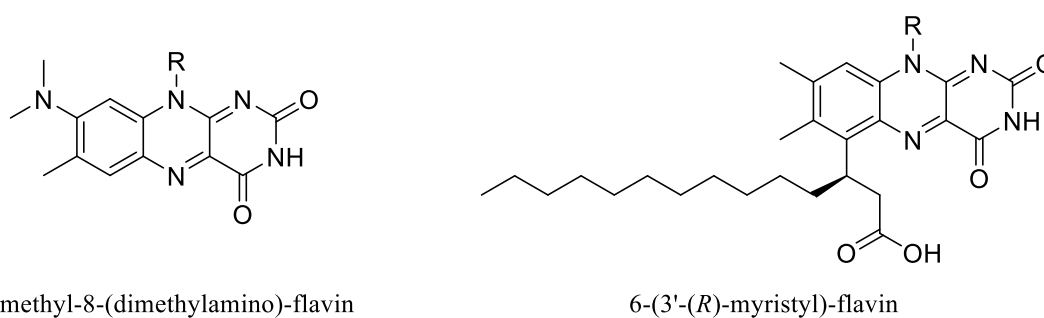


Figure 6: Chemical structures of two modified flavin metabolites; 8-demethyl-8-(dimethylamino)-flavin and 6-(3'-(*R*)-myristyl)-flavin.

Mitochondrial electron transport

Energy production/conversion is one of the most important cellular processes and mainly takes place in the intermembrane space of prokaryotes and in the mitochondrial membrane of eukaryotic cells. Though, being differently organized in prokaryotes as compared to eukaryotes, in both cases a proton gradient is formed across a membrane in order to drive ATP production by a complex called ATP-synthase (37, 38).

In prokaryotes, proton pumping is right away coupled to the oxidation of a great variety of metabolites by dehydrogenases, which transfer electrons to ubiquinone for cofactor recycling. Ubiquinone is then either directly oxidized by a heme-dependent quinol oxidase, coinciding with the reduction of dioxygen to water, or by a cytochrome complex. In the latter case, the electrons are further delivered to cytochrome *c* to finally be used by a terminal oxidase (cytochrome *c* oxidase), which catalyzes the reduction of dioxygen to water (38).

In eukaryotes, energy equivalents obtained in the form of NADH or FADH₂ in the course of the degradation of carbohydrates, fatty acids and/or amino acids are converted into the proton gradient in a more complex electron transfer process (Figure 7 and 8) (39). NADH, in a first step, is oxidized by NADH-ubiquinone oxidoreductase (complex I), a 44 subunit complex harboring one FMN molecule and eight to nine iron-sulfur clusters, which further mediates the transfer of the electrons to coenzyme Q (ubiquinone) and couples it with the translocation of four protons across the membrane (40). Reduced coenzyme Q later delivers these electrons to complex III (ubiquinone-cytochrome *c* oxidoreductase), which in turn passes them on to cytochrome *c* and further to complex IV (cytochrome *c* oxidase) (37). In this process, again four and two protons are pumped to the intermembrane space, respectively, finally yielding a total of ten protons that can drive ATP-synthesis by the ATP-synthase complex (Figure 7) (37, 41).

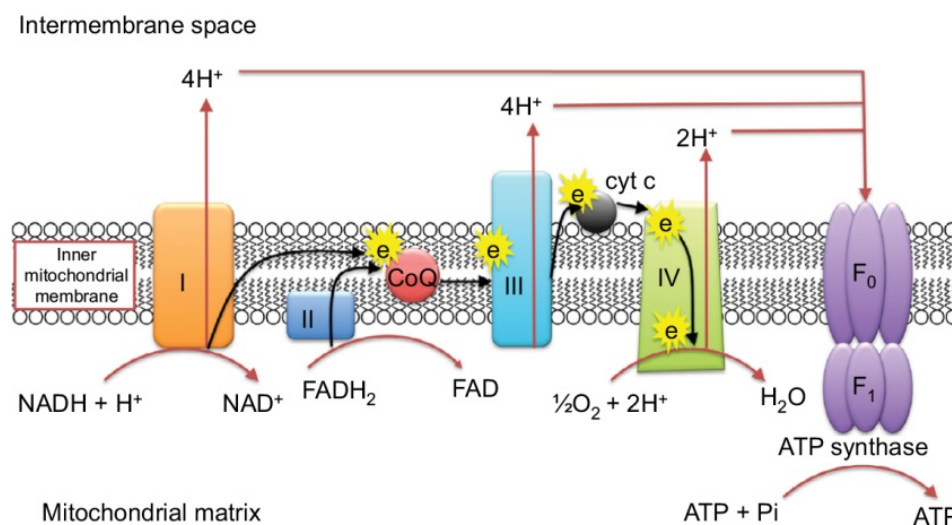


Figure 7: Overview of the mitochondrial electron transport chain. Electrons from NADH and FADH₂ are fed into the mitochondrial electron transport chain via complex I and complex II, respectively, and are further delivered to ubiquinone (*CoQ*). Subsequently, complex III passes the electrons on to cytochrome *c* (*cyt c*), which in the end is oxidized by complex IV. Electron transport is accompanied by the establishment of a proton gradient in the intermembrane space, which serves as the driving force for ATP production by the ATP-synthase complex (42).

The electrons derived from FADH₂, in general take the same overall path. However, they do not enter the electron transport chain via complex I, but via complex II (succinate-ubiquinone oxidoreductase) (37) or via ETF-ubiquinone oxidoreductase (43). Complex II is a homotrimeric protein, with each protomer consisting of four subunits; a flavoprotein (succinate dehydrogenase), an iron-sulfur subunit

(three iron-sulfur clusters and one cytochrome b), and two subunits acting as membrane anchors and binding both a heme and a ubiquinone (44). Electrons are initially taken up by the flavin cofactor bound to succinate dehydrogenase and passed on via the three iron-sulfur clusters to finally reduce coenzyme Q (44). In contrast to complex I, no protons are pumped in the course of the electron transfer through complex II (41).

Another option for electrons from flavoproteins to enter the electron transport chain is via ETF-ubiquinone oxidoreductase (43). The latter is also a membrane protein, which harbors an iron-sulfur cluster and an FAD cofactor. It can accept electrons from an important electron carrier localized in the mitochondrial matrix, the so called electron transferring flavoprotein (ETF; see below), which can receive electrons from a variety of flavin-dependent dehydrogenases itself (Figure 8) (45–47).

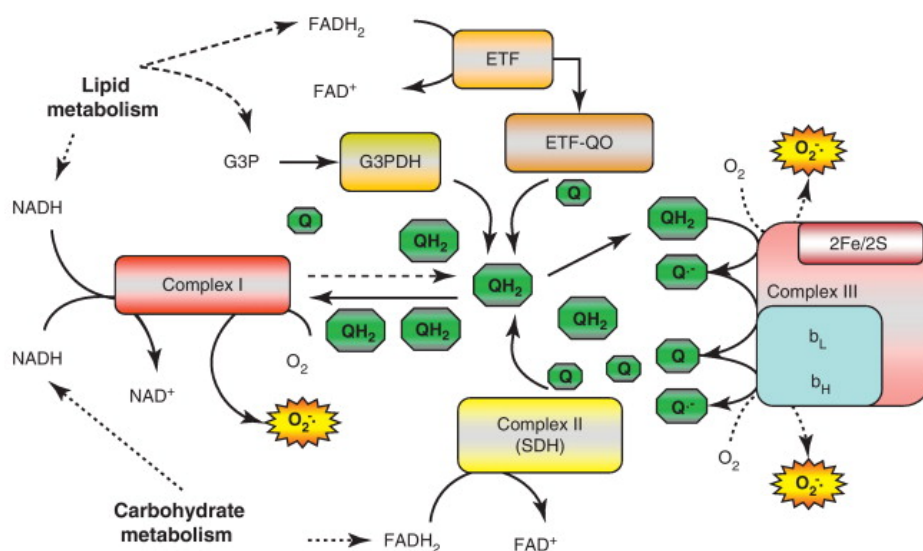


Figure 8: Schematic overview indicating the entry point of electrons to the respiratory chain. The degradation of carbohydrates, lipids, and amino acids yields in the formation of energy rich NADH and FADH₂, which use different entry points to deliver the electrons to the respiratory chain. Electrons from NADH (NAD⁺-dependent enzymes) enter the electron transport chain via complex I, whereas electrons from FADH₂ (FAD-dependent enzymes) are passed on either to complex II or to the ETF/ETF-QO system. In all cases, however, the electrons are further delivered to ubiquinone (Q), the key metabolite shuttling the electrons to complex III (48).

Which dehydrogenases may interact with the ETF, however strongly depends on the organization of the metabolic pathways in the various organisms. Since both the degradation of fatty acids and amino acids in humans mainly take place in mitochondria, a great number of enzymes involved in these catabolic pathways can transfer electrons to hETF, yielding a total of thirteen (fourteen) client enzymes for the human protein (47) (Chapter 3, 4 and 6). In yeast, in contrast, β -oxidation does not take place in the mitochondrial matrix but in the peroxisomes and amino acid degradation is organized very much differently as compared to other eukaryotic species (49–52). Therefore, just a single enzyme remains as electron donor for the ETF from *Saccharomyces cerevisiae* (Chapter 5).

Electron transferring flavoproteins

Electron transferring flavoproteins (ETFs) are important electron carriers found in species from all kingdoms of life. In most prokaryotic and eukaryotic organisms, they accept electrons from flavin-dependent dehydrogenases involved in β -oxidation and amino acid degradation (and in humans also choline degradation) and transfer them to membrane proteins named ETF-ubiquinone oxidoreductases (ETF-QOs) for subsequent ATP production via the respiratory chain. Sometimes, however, ETFs may also be part of a more specialized system, like it was shown for the proteins from *Methylophilus methylotrophus* (53) and from *Peptostreptococcus elsdenii* (23). These prokaryotic species lack the metabolic pathways mentioned above and obtain their electrons from reduced trimethylamine dehydrogenase and NADH, respectively, instead (23, 53).

Nevertheless, the overall structure of ETFs from various organisms is rather conserved. They are all heterodimeric flavoproteins, consisting of a larger α - and a smaller β -subunit of strong structural but no sequence similarity (54) and bind an FAD cofactor right at the interface of the two subunits (55). Interestingly, even the amino acid residues responsible for binding of the flavin at the subunit interface are very well-conserved among a broad range of organisms (47, 55), indicating most of them to be crucial for proper protein function (Figure 9).

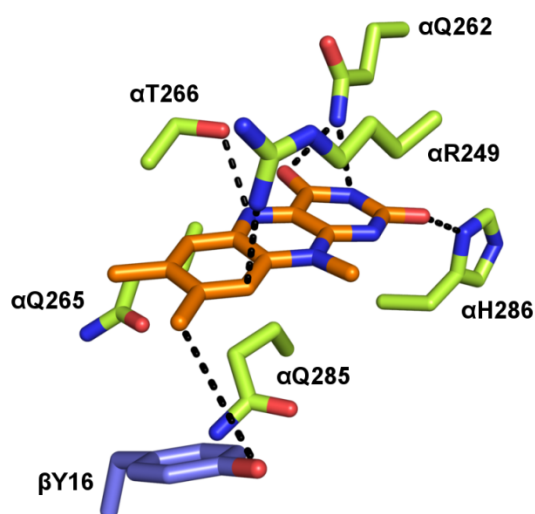


Figure 9: Amino acid residues near the isoalloxazine ring, which are most conserved among a broad range of organisms. Their possible interactions with the isoalloxazine ring are indicated by dashed lines (numbering of the amino acid residues according to hETF; PDB code, 1efv (54)).

By interacting with the N1-C2=O locus and the xylene moiety of the isoalloxazine, respectively, for example, α His286 and α Arg249 (numbering according to hETF) play an important role in stabilizing the catalytically important anionic flavin semiquinone (see later) (55, 56). Due to its partial positive charge, α His286 can contribute to the stabilization of a negative charge at the N1-C2=O locus, whereas α Arg249 stabilizes the aromatic character of the flavin ring system by cation- π -interaction. Interestingly, the amide-backbone of α Arg249 additionally interacts with the N1-C2=O locus and thereby may also assist in stabilizing the negative charge in this region (56).

Also, the threonine (or serine *M. methylotrophus* (57)) near the N5 of the flavin (α Thr266, numbering according to hETF) is very important for proper electron transfer. By forming a hydrogen-bond to the N5 position it is involved in modulating the reduction potential of the protein-bound flavin (55), which needs to be very fine-tuned for efficient electron transfer; while a lowered midpoint potential may inhibit electron transfer from the dehydrogenases to ETF, an increased reduction potential impedes electron delivery to ETF-QO.

Interaction of hETF with its client dehydrogenases

In order to be able to interact with such a wide range of dehydrogenases, ETFs need to be able to quickly accommodate their structure. It was found that in the presence of client enzymes, they do so by changing their overall conformation from a so-called closed (unproductive) to an open (productive) state (Figure 10A and B, respectively) (58). Thereby, the flavin cofactor, which in the closed conformation is embedded in the core of the protein, gets more surface-exposed, resulting in a facilitated electron transfer from the dehydrogenases to ETF (58).

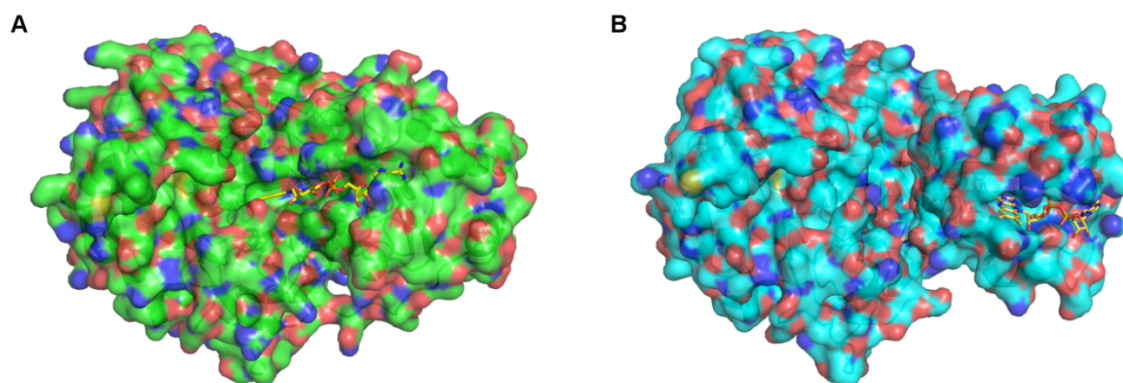


Figure 10: Surface representation of the closed (unproductive, green) and open (productive, blue) conformation of hETF. In the closed conformation (PDB code, 1EFV (54)), the FAD-cofactor is embedded in the core of the protein, whereas it is much more surface exposed in the productive state (PDB code, 2A1T (58)).

Studies by Toogood *et al.* have shown that two residues at the surface of the protein (in hETF: β E165 and α N259) are required to control this kind of protein motion (58). Once, one of them is replaced by an alanine (α N259A or β E165A), ETF preferentially adopts the open conformation, which goes along with a reduced rate of complex dissociation (dehydrogenase-ETF-complex) and a therefrom resulting decreased electron transfer rate to the natural electron acceptor ETF-QO (58).

Due to the increased stabilization of the open state, in addition, the FAD cofactor bound to the variants is much more solvent exposed than in the wild type ETF, which could nicely be made use of when studying 8-formyl formation in hETF (see above and Chapter 3). In both the variants (α N259A and β E165A), the FAD cofactor was found to get formylated a lot faster than in the wild type protein, which enabled the detailed characterization of the oxidation process and allowed studies on the effect of the

flavin modification on electron transfer from human dimethylglycine dehydrogenase (hDMGDH) to hETF (Chapter 3 and 4).

ETF-ubiquinone oxidoreductase

ETF-ubiquinone oxidoreductase is a mitochondrial membrane protein, which serves as an important entry point to the respiratory chain, as it takes electrons from ETF to pass them on to ubiquinone (43). For that purpose, the protein harbors two different cofactors, an iron-sulfur cluster and an FAD cofactor, with the iron-sulfur cluster being surface-exposed and the flavin moiety being embedded in the core of the protein (Figure 11, *orange* and *yellow sticks*, respectively) (46). As a result, electrons are initially transferred from ETFs to the iron-sulfur cluster, which passes them on to the flavin chromophore for subsequent ubiquinone reduction (45). To achieve full conversion of the FAD cofactor to the hydroquinone state, required for the reduction on ubiquinone, three electrons need to be transferred from ETFs to ETF-QO.

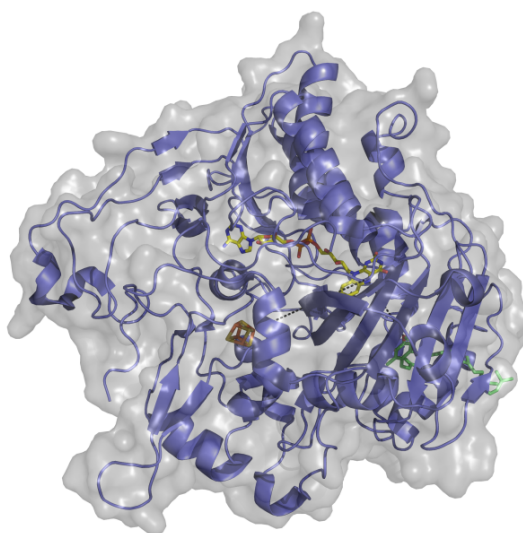


Figure 11: Overall structure of ETF-ubiquinone oxidoreductase with the secondary structure elements depicted in *blue* and the surface shown in *grey*. The two protein-bound cofactors, the iron-sulfur cluster and the FAD chromophore, are shown in *orange/brown* and *yellow* respectively, whereas the final electron acceptor ubiquinone is depicted in *green* (PDB code, 2GMH (59)).

Mechanism of electron transfer from flavin dependent dehydrogenases to ETF-QO

Electron transfer from the flavin-dependent dehydrogenases to ETF-ubiquinone oxidoreductase (ETF-QO) is a very well-studied but also highly complex process.

For most eukaryotic organisms it could be shown that a flavin-dependent dehydrogenase, in a first step, oxidizes its natural substrate, resulting in the two-electron reduction of its flavin chromophore (20, 60). In order to regenerate the cofactor for another catalytic cycle, the dehydrogenase passes these electrons on to ETFs. In contrast to the reductive half-reaction, however, reoxidation requires the transfer of two

single electrons, which are delivered to two different ETFs (20, 61). These ETFs (with their FAD cofactor in the semiquinone state) are then able to interact with the membrane protein ETF-QO, which triggers the disproportionation of two flavin radicals to yield reoxidized and fully reduced protein-bound cofactor (46). Subsequently, the fully reduced ETFs transfer single electrons to the iron-sulfur cluster of ETF-QO. Due to the very similar reduction potential of the iron-sulfur cluster ($[4\text{Fe}4\text{S}]^{2+/1+}$; +47 mV) and the oxidized semiquinone couple of FAD (+28 mV), the first electron accepted, however, will be “shared” between the two cofactors (62). Upon transfer of a second electron, both the iron-sulfur cluster and the flavin will “take” one electron, and only the uptake of three electrons will lead to the full reduction of the protein-bound flavin. Just then, ETF-QO is able to finally mediate the reduction of ubiquinone, thereby initiating energy production via the respiratory chain (46, 62).

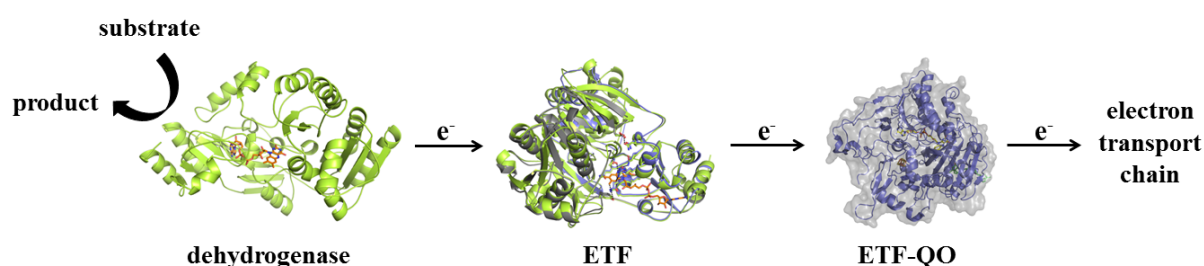


Figure 12: Schematic representation of the mitochondrial electron transport. In a first step, a flavin-dependent dehydrogenase oxidizes a substrate, leading to the reduction of its flavin cofactor. Then, electrons are passed on to ETF, which in turn delivers them to ETF-ubiquinone oxidoreductase, a membrane bound protein that is able to channel the electrons into the electron transport chain for subsequent ATP production (see text for exact mechanism).

Glutaric aciduria type II

Glutaric aciduria type II, also called multiple acyl-CoA dehydrogenase deficiency (MADD), is an inherited disorder resulting from defects in fatty acid degradation, branched-chain amino acid, choline, and/or lysine catabolism (63). It can either be caused by malfunction of flavoenzymes involved in the pathways themselves or by missense and nonsense mutations that lead to pathogenic amino acid replacements in the downstream electron acceptors ETF and/or ETF-QO, and results in the accumulation of organic acids and their CoA-derivatives as well as of marker metabolites of the deficient dehydrogenases (63, 64). Depending on the severity of the loss of enzyme function associated with the amino acid sequence variations, a broad range of phenotypes may be observed, ranging from hypertonia to facial dysmorphism and congenital abnormalities (63). While patients with milder forms can be treated rather well and thus have a rather normal life expectancy (65), humans suffering from more severe forms of the disease usually will not survive the first months/years of life (63).

References

1. Revuelta, J. L., Ledesma-Amaro, R., Lozano-Martinez, P., Díaz-Fernández, D., Buey, R. M., and Jiménez, A. (2017) Bioproduction of riboflavin: a bright yellow history. *J. Ind. Microbiol. Biotechnol.* **44**, 659–665
2. Kuhn, R., Reinemund, K., and Weygand, F. (1934) Synthesis of lumi-lactoflavin. *Eur. J. Inorg. Chem.* **67**, 1460–1462
3. Karrer, P., Becker, B., Benz, F., Frei, P., Salomon, H., and Schöpp, K. (1935) Synthesis of lactoflavin. *Helv. Chim. Acta.* **18**, 1435–1448
4. Bacher, A., Eberhardt, S., Fischer, M., Kis, K., and Richter, G. (2000) Biosynthesis of vitamin B₂ (riboflavin). *Annu Rev Nutr.* **20**, 153–167
5. Fischer, M., and Bacher, A. (2008) Biosynthesis of vitamin B₂: Structure and mechanism of riboflavin synthase. *Arch. Biochem. Biophys.* **474**, 252–265
6. Macheroux, P., Kappes, B., and Ealick, S. E. (2011) Flavogenomics - A genomic and structural view of flavin-dependent proteins. *FEBS J.* **278**, 2625–2634
7. Macheroux, P. (1999) UV-visible spectroscopy as a tool to study flavoproteins. in *Flavoprotein Protocols. Methods in Molecular Biology* (Chapman, S. K., and Reid, G. A. eds), pp. 1–7, Humana Press, Totowa, NJ, 10.1385/1-59259-266-X:1
8. Massey, V., and Palmer, G. (1966) On the existence of spectrally distinct classes of flavoprotein semiquinones. A new method for the quantitative production of flavoprotein semiquinones. *Biochemistry.* **5**, 3181–3189
9. Massey, V., and Ghisla, S. (1983) The mechanism of action of flavoprotein - catalyzed reactions. in *Biological Oxidations* (Sund, H., and Ullrich, V. eds), pp. 114–139, Springer, Berlin, **34**, 114–139
10. Sellés Vidal, L., Kelly, C. L., Mordaka, P. M., and Heap, J. T. (2018) Review of NAD(P)H-dependent oxidoreductases: Properties, engineering and application. *Biochim. Biophys. Acta - Proteins Proteomics.* **1866**, 327–347
11. Heelis, P. F., Hartman, R. F., and Rose, S. D. (1996) Energy and electron transfer processes in flavoprotein-mediated DNA repair. *J. Photochem. Photobiol. A Chem.* **95**, 89–98
12. Uchida, Y., Hirayama, J., and Nishina, H. (2010) A common origin: Signaling similarities in the regulation of the circadian clock and DNA damage responses. *Biol. Pharm. Bull.* **33**, 535–544
13. Ghisla, S., and Massey, V. (1989) Mechanisms of flavoprotein-catalyzed reactions. *Eur. J. Biochem.* **181**, 1–17
14. Mattevi, A. (2006) To be or not to be an oxidase: challenging the oxygen reactivity of flavoenzymes. *Trends Biochem. Sci.* **31**, 276–283
15. Chaiyen, P., Fraaije, M. W., and Mattevi, A. (2012) The enigmatic reaction of flavins with oxygen. *Trends Biochem. Sci.* **37**, 373–380

16. Lindqvist, Y., Branden, C. I., Mathews, F. S., and Lederer, F. (1991) Spinach glycolate oxidase and yeast flavocytochrome b2 are structurally homologous and evolutionarily related enzymes with distinctly different function and flavin mononucleotide binding. *J. Biol. Chem.* **266**, 3198–3207
17. Zafred, D., Steiner, B., Teufelberger, A. R., Hromic, A., Karplus, P. A., Schofield, C. J., Wallner, S., and Macheroux, P. (2015) Rationally engineered flavin-dependent oxidase reveals steric control of dioxygen reduction. *FEBS J.* **282**, 3060–3074
18. Wang, R., and Thorpe, C. (1991) Reactivity of medium-chain acyl-CoA dehydrogenase toward molecular oxygen. *Biochemistry.* **30**, 7895–7901
19. DuPlessis, E. R., Pellett, J., Stankovich, M. T., and Thorpe, C. (1998) Oxidase activity of the acyl-CoA dehydrogenases. *Biochemistry.* **37**, 10469–10477
20. Ghisla, S., and Thorpe, C. (2004) Acyl-CoA dehydrogenases: A mechanistic overview. *Eur. J. Biochem.* **271**, 494–508
21. Heuts, D. P. H. M., Scrutton, N. S., McIntire, W. S., and Fraaije, M. W. (2009) What's in a covalent bond? On the role and formation of covalently bound flavin cofactors. **276**, 3405–3427
22. Mayhew, S. G., Whitfield, C. D., Ghisla, S., and Schuman-Jörns, M. (1974) Identification and properties of new flavins in electron-transferring flavoprotein from *Peptostreptococcus elsdenii* and pig-liver glycolate oxidase. *Eur. J. Biochem.* **44**, 579–591
23. Whitfield, C. D., and Mayhew, S. G. (1974) Purification and properties of electron-transferring flavoprotein from *Peptostreptococcus elsdenii*. *J. Biol. Chem.* **249**, 2801–2810
24. Doubayashi, D., Ootake, T., Maeda, Y., Oki, M., Tokunaga, Y., Sakurai, A., Nagaosa, Y., Mikami, B., and Uchida, H. (2011) Formate oxidase, an enzyme of the glucose-methanol-choline oxidoreductase family, has a His-Arg pair and 8-formyl-FAD at the catalytic site. *Biosci. Biotechnol. Biochem.* **75**, 1662–1667
25. Robbins, J. M., Souffrant, M. G., Hamelberg, D., Gadda, G., and Bommarius, A. S. (2017) Enzyme-mediated conversion of flavin adenine dinucleotide (FAD) to 8-formyl FAD in formate oxidase results in a modified cofactor with enhanced catalytic properties. *Biochemistry.* **56**, 3800–3807
26. Fraaije, M. W., Van Den Heuvel, R. H. H., Van Berkel, W. J. H., and Mattevi, A. (1999) Covalent flavinylation is essential for efficient redox catalysis in vanillyl-alcohol oxidase. *J. Biol. Chem.* **274**, 35514–35520
27. Efimov, I., Cronin, C. N., and McIntire, W. S. (2001) Effects of noncovalent and covalent FAD binding on the redox and catalytic properties of *p*-cresol methylhydroxylase. *Biochemistry.* **40**, 2155–2166
28. Winkler, A., Kutchan, T. M., and Macheroux, P. (2007) 6-S-cysteinylolation of bi-covalently attached FAD in berberine bridge enzyme tunes the redox potential for optimal activity. *J. Biol. Chem.* **282**, 24437–24443

29. Huang, C. H., Winkler, A., Chen, C. L., Lai, W. L., Tsai, Y. C., Macheroux, P., and Liaw, S. H. (2008) Functional roles of the 6-S-cysteinyl, 8 α -N1-histidyl FAD in glucooligosaccharide oxidase from *Acremonium strictum*. *J. Biol. Chem.* **283**, 30990–30996
30. Winkler, A., Motz, K., Riedl, S., Puhl, M., Macheroux, P., and Gruber, K. (2009) Structural and mechanistic studies reveal the functional role of bicovalent flavinylation in berberine bridge enzyme. *J. Biol. Chem.* **284**, 19993–20001
31. Daniel, B., Konrad, B., Toplak, M., Lahham, M., Messenlehner, J., Winkler, A., and Macheroux, P. (2017) The family of berberine bridge enzyme-like enzymes: A treasure-trove of oxidative reactions. *Arch. Biochem. Biophys.* **632**, 88–103
32. Otani, S., Takatsu, M., Nakano, M., Kasai, S., Misra, R., and Matsui, K. (1974) Roseoflavin, a new antimicrobial pigment from *Streptomyces*. *J. Antibiot. (Tokyo)*. **27**, 88–89
33. Jhulki, I., Chanani, P. K., Abdelwahed, S. H., and Begley, T. P. (2016) A remarkable oxidative cascade that replaces the riboflavin C8 methyl with an amino group during roseoflavin biosynthesis. *J. Am. Chem. Soc.* **138**, 8324–8327
34. Konjik, V., Brünle, S., Demmer, U., Vanselow, A., Sandhoff, R., Ermler, U., and Mack, M. (2017) The crystal structure of RosB: Insights into the reaction mechanism of the first member of a family of flavodoxin-like enzymes. *Angew. Chemie - Int. Ed.* **56**, 1146–1151
35. Tabib, C. R., Brodl, E., and Macheroux, P. (2017) Evidence for the generation of myristylated FMN by bacterial luciferase. *Mol. Microbiol.* **104**, 1027–1036
36. Wei, C. J., Lei, B., and Tu, S. C. (2001) Characterization of the binding of *Photobacterium phosphoreum* P-flavin by *Vibrio harveyi* luciferase. *Arch. Biochem. Biophys.* **396**, 199–206
37. Hatefi, Y. (1985) The mitochondrial electron transport and oxidative phosphorylation system. *Annu. Rev. Biochem.* **54**, 1015–1069
38. Anraku, Y. (1988) Bacterial electron transport chains. *Annu. Rev. Biochem.* **57**, 101–132
39. Genova, M. L., and Lenaz, G. (2014) Functional role of mitochondrial respiratory supercomplexes. *Biochim. Biophys. Acta - Bioenerg.* **1837**, 427–443
40. Wirth, C., Brandt, U., Hunte, C., and Zickermann, V. (2016) Structure and function of mitochondrial complex I. *Biochim. Biophys. Acta - Bioenerg.* **1857**, 902–914
41. Chaban, Y., Boekema, E. J., and Dudkina, N. V. (2014) Structures of mitochondrial oxidative phosphorylation supercomplexes and mechanisms for their stabilisation. *Biochim. Biophys. Acta - Bioenerg.* **1837**, 418–426
42. Rodick, T. C., Seibels, D. R., Babu, J. R., Huggins, K. W., Ren, G., and Mathews, S. T. (2018) Potential role of coenzyme Q₁₀ in health and disease conditions. *Nutr. Diet. Suppl.* **Volume 10**, 1–11
43. Ruzicka, F. J., and Beinert, H. (1977) A new iron-sulfur flavoprotein of the respiratory chain. A component of the fatty acid beta oxidation pathway. *J. Biol. Chem.* **252**, 8440–8445

44. Sun, F., Huo, X., Zhai, Y., Wang, A., Xu, J., Su, D., Bartlam, M., and Rao, Z. (2005) Crystal structure of mitochondrial respiratory membrane protein Complex II. *Cell*. **121**, 1043–1057
45. Swanson, M. A., Usselman, R. J., Frerman, F. E., Eaton, G. R., and Eaton, S. S. (2008) The iron-sulfur cluster of electron transfer flavoprotein-ubiquinone oxidoreductase is the electron acceptor for electron transfer flavoprotein. *Biochemistry*. **47**, 8894–8901
46. Watmough, N. J., and Frerman, F. E. (2010) The electron transfer flavoprotein: Ubiquinone oxidoreductases. *Biochim. Biophys. Acta - Bioenerg.* **1797**, 1910–1916
47. Augustin, P., Toplak, M., Fuchs, K., Gerstmann, E. C., Prassl, R., Winkler, A., and Macheroux, P. (2018) Oxidation of the FAD cofactor to the 8-formyl-derivative in human electron-transferring flavoprotein. *J. Biol. Chem.* **293**, 2829–2840
48. Fisher-Wellman, K. H., and Neuffer, P. D. (2012) Linking mitochondrial bioenergetics to insulin resistance via redox biology. *Trends Endocrinol. Metab.* **23**, 142–153
49. Dickinson, J. R., Lanterman, M. M., Danner, D. J., Pearson, B. M., Sanz, P., Harrison, S. J., and Hewlins, M. J. E. (1997) A ¹³C nuclear magnetic resonance investigation of the metabolism of leucine to isoamyl alcohol in *Saccharomyces cerevisiae*. *J. Biol. Chem.* **272**, 26871–26878
50. Dickinson, J. R., Harrison, S. J., and Hewlins, M. J. E. (1998) An investigation of the metabolism of valine to isobutyl alcohol in *Saccharomyces cerevisiae*. *J. Biol. Chem.* **273**, 25751–25756
51. Dickinson, J. R., Harrison, S. J., Dickinson, J. A., and Hewlins, M. J. E. (2000) An investigation of the metabolism of isoleucine to active amyl alcohol in *Saccharomyces cerevisiae*. *J. Biol. Chem.* **275**, 10937–10942
52. Van Roermund, C. W. T., Waterham, H. R., Ijlst, L., and Wanders, R. J. A. (2003) Fatty acid metabolism in *Saccharomyces cerevisiae*. *Cell. Mol. Life Sci.* **60**, 1838–1851
53. Davidson, V. L., Husain, M., and Neher, J. W. (1986) Electron transfer flavoprotein from *Methylophilus methylotrophus*: Properties, comparison with other electron transfer flavoproteins, and regulation of expression by carbon source. *J. Bacteriol.* **166**, 812–817
54. Roberts, D. L., Frerman, F. E., and Kim, J. J. (1996) Three-dimensional structure of human electron transfer flavoprotein to 2.1-Å resolution. *Proc. Natl. Acad. Sci. U. S. A.* **93**, 14355–60
55. Roberts, D. L., Salazar, D., Fulmer, J. P., Frerman, F. E., and Kim, J. J. P. (1999) Crystal structure of *Paracoccus denitrificans* electron transfer flavoprotein: Structural and electrostatic analysis of a conserved flavin binding domain. *Biochemistry*. **38**, 1977–1989
56. Dwyer, T. M., Zhang, L., Muller, M., Marrugo, F., and Frerman, F. (1999) The functions of the flavin contact residues, α Arg249 and β Tyr16, in human electron transfer flavoprotein. *Biochim. Biophys. Acta - Protein Struct. Mol. Enzymol.* **1433**, 139–152
57. Chen, D., and Swenson, R. P. (1994) Cloning, sequence analysis, and expression of the genes encoding the two subunits of the methylotrophic bacterium W3A1 electron transfer flavoprotein. *J. Biol. Chem.* **269**, 32120–32130

58. Toogood, H. S., Van Thiel, A., Scrutton, N. S., and Leys, D. (2005) Stabilization of non-productive conformations underpins rapid electron transfer to electron-transferring flavoprotein. *J. Biol. Chem.* **280**, 30361–30366
59. Zhang, J., Frerman, F. E., and Kim, J.-J. P. (2006) Structure of electron transfer flavoprotein-ubiquinone oxidoreductase and electron transfer to the mitochondrial ubiquinone pool. *Proc. Natl. Acad. Sci.* **103**, 16212–16217
60. Augustin, P., Hromic, A., Pavkov-Keller, T., Gruber, K., and Macheroux, P. (2016) Structure and biochemical properties of recombinant human dimethylglycine dehydrogenase and comparison to the disease-related H109R variant. *FEBS J.* 10.1111/febs.13828
61. Gorelick, R. J., Schopfer, L. M., Ballou, D. P., Massey, V., and Thorpe, C. (1985) Interflavin oxidation-reduction reactions between pig kidney general acyl-CoA dehydrogenase and electron-transferring flavoprotein. *Biochemistry.* **24**, 6830–6839
62. Paulsen, K. E., Stankovich, M. T., Orville, A. M., Lipscomb, J. D., and Frerman, F. E. (1992) Redox properties of electron-transfer flavoprotein ubiquinone oxidoreductase as determined by EPR-spectroelectrochemistry. *Biochemistry.* **31**, 11755–11761
63. Schiff, M., Froissart, R., Olsen, R. K. J., Acquaviva, C., and Vianey-Saban, C. (2006) Electron transfer flavoprotein deficiency: Functional and molecular aspects. *Mol. Genet. Metab.* **88**, 153–158
64. Watanabe, H., Yamaguchi, S., Saiki, K., Shimizu, N., Fukao, T., Kondo, N., and Orii, T. (1995) Identification of the D-enantiomer of 2-hydroxyglutaric acid in glutaric aciduria type II. *Clin. Chim. Acta.* **238**, 115–124
65. Cornelius, N., Frerman, F. E., Corydon, T. J., Palmfeldt, J., Bross, P., Gregersen, N., and Olsen, R. K. J. (2012) Molecular mechanisms of riboflavin responsiveness in patients with ETF-QO variations and multiple acyl-CoA dehydrogenation deficiency. *Hum. Mol. Genet.* **21**, 3435–3448

Thesis outline

Flavoproteins are a diverse class of proteins, relying on the presence of the vitamin B₂-derivatives flavin mononucleotide (FMN) or flavin adenine dinucleotide (FAD) for proper (catalytic) function. While most enzymes bind them as non-modified cofactors in a non-covalent manner, a significant amount of flavoenzymes was found to adapt the nature of their cofactor to their need; either by introducing electron withdrawing groups at the 8 α - or 6-position of the isoalloxazine ring, or by mono- or bicovalently linking the flavin moiety to the protein.

Bicovalent flavin tethering, for instance, is the key feature of berberine bridge enzyme- (BBE-) like proteins. They are found in fungi, bacteria and plants and play important roles in a variety of metabolic pathways ranging from carbohydrate metabolism to alkaloid biosynthesis. Due to the bicovalent attachment of their FAD cofactor, enzymes of this class exhibit an extremely high redox potential as well as they harbor a large active site, which enables them to catalyze the oxidation of sterically demanding substrates such as benzyloquinoline alkaloids or polysaccharides. While BBE-like enzymes are only found in selected bacterial and fungal species, this class of proteins is represented in all land plants with the number of homologs increasing from basal to higher plants (Chapter 1).

In search of the primordial role of BBE-like enzymes in plants, we set out to investigate the biochemical and structural properties of the single BBE-like protein from the most basal plant, the moss *Physcomitrella patens* (*PpBBE1*). We could show that *PpBBE1* is an efficient cellobiose oxidase *in vitro*, suggesting it to be involved in primary carbohydrate metabolism *in planta*. This idea was further supported by the results obtained from the *in planta* characterization of a wild type moss as well as of a *PpBBE1* knock-out strain, as it was found that *PpBBE1* expression levels are highest in chloronema, the earliest stage of the plant's life cycle, where carbohydrate metabolism is strongly upregulated (Chapter 2).

How greatly the nature of the flavin cofactor can influence the biochemical properties of proteins can also be seen in non-covalent flavoproteins, such as the electron transferring flavoproteins (ETFs). ETFs from eukaryotic organisms are important electron carriers located in the mitochondrial matrix. They can accept electrons from a variety of dehydrogenases involved in fatty acid, amino acid, and choline degradation and deliver them to membrane bound ETF-ubiquinone oxidoreductases for subsequent energy production via the respiratory chain. Proper electron flux in this process is tightly controlled by the electrochemical properties of the protein-bound cofactors, which are determined by their nature and environment.

In the course of investigations of the interaction between hETF and one of its client dehydrogenases human dimethylglycine dehydrogenase (hDMGDH) we found that under alkaline (physiological) conditions the FAD cofactor bound to hETF is undergoing spontaneous oxidation to its 8-formyl derivative. Thereby, the spectral as well as electrochemical properties of the protein-bound cofactor

are significantly altered, leading to a tighter interaction between the two proteins, but to a lower rate of electron transfer from hDMGDH to hETF (Chapter 3).

Trying to resolve the mechanism of 8-formyl formation, we could show that several amino acid residues in the active site may be involved in the oxidation process (Chapter 3 and 4). Nevertheless, we identified one particular tyrosine residue close to the 8 α -position of the flavin cofactor to be especially important and therefore wanted to study 8-formyl formation in another naturally occurring ETF, where this tyrosine should ideally be replaced by a phenylalanine residue.

As we found this to be the case in the ETF from yeast (yETF), we recombinantly produced the protein and analyzed its tendency to form the 8f-FAD derivative; in line with our hypothesis, hardly any formylated cofactor was detected in yETF. Along with the detailed biochemical characterization of yETF, we were also aiming to study the interaction with its putative electron donor D-lactate dehydrogenase 2 (Dld2). Kinetic characterization of Dld2 revealed the enzyme to be a better D-2-hydroxyglutarate dehydrogenase (D2HGDH) than D-lactate dehydrogenase and showed that tight product binding to the dehydrogenase is used to prevent reoxidation of reduced Dld2 by molecular oxygen. The substrate-reduced enzyme, however, was found to efficiently transfer electrons to yETF, proving it to be the natural electron donor of yETF (Chapter 5).

Having confirmed the interaction between Dld2 and yETF, we wanted to know, whether humans would encode a Dld2 homolog that is able to transfer electrons to hETF. Since BLAST searches revealed a mitochondrial matrix protein exhibiting about 53% sequence identity, which interestingly was annotated as D2HGDH, we decided to take a closer look at this enzyme. In a detailed biochemical characterization of the protein we could show that hD2HGDH behaves rather similarly as compared to Dld2 and that also hD2HGDH is involved in mitochondrial electron transport, which provides an explanation for the strong accumulation of D-2-hydroxyglutarate (D-2HG) in patients suffering from the malfunction of hETF and/or hETF-QO.

However, increased levels of D-2HG are also detected in humans with defects in hD2HGDH itself. Previous studies have shown that point mutations in position 440 (T \rightarrow G) and 1331 (T \rightarrow C) of the *hd2hgdh* gene cause single amino acid exchanges in the mature protein (I147S and V444A, respectively), leading to severely reduced catalytic activity of the enzyme. The molecular causes of this dramatic loss in activity, nevertheless, were not investigated thus far. Therefore, we heterologously produced the two variants and realized that both of them were no longer able to bind the catalytically important FAD cofactor. This finding was rather surprising but could be explained with the help of CD-spectroscopy and limited proteolysis experiments as well as size exclusion chromatography, which revealed that the single amino acid replacements affected protein folding, causing the aggregation of the variants (Chapter 6).

Altogether, the studies summarized in this thesis underline the incredible enzymatic diversity of flavoproteins, as well as they provide deeper insights into the protein family of berberine bridge enzymes and the mechanisms of mitochondrial electron transport in humans and in yeast.

Chapter 1

BBE-like proteins

The family of berberine bridge enzyme-like enzymes: a treasure-trove of oxidative reactions

Bastian Daniel, Barbara Konrad, Marina Toplak, Majd Lahham, Julia Messenlehner,
Andreas Winkler and Peter Macheroux *

Institute of Biochemistry, Graz University of Technology, Petersgasse 12/2, 8010 Graz, Austria

*To whom correspondence should be addressed:

Prof. Dr. Peter Macheroux
Graz University of Technology
Institute of Biochemistry
Petersgasse 12/2
A-8010 Graz, Austria
Tel.: +43-316-873 6450
Fax: +43-316-873 6952
Email: peter.macheroux@tugraz.at

Keywords: FAD-linked oxidases; alkaloids; antibiotics; covalent FAD; flavoproteins

Abbreviations

6HDNO, 6-hydroxy-D-nicotine oxidase; A40926, teicoplanin homolog; CpADHAPS, alkyldihydroxyacetonephosphate synthase from *Cavia porcellus*; DdADHAPS, alkyldihydroxyacetonephosphate synthase from *Dictyostelium discoideum*; AknOx, aclacinomycin-N/aclacinomycin-A oxidase; AldO, alditol oxidase; *At*, *Arabidopsis thaliana*; AtCKX, cytokinin dehydrogenase from *Arabidopsis thaliana*; BBE, berberine bridge enzyme; BG60, pollen allergen; CBDAS, cannabidiolic acid synthase; ChitO, chitoooligosaccharide oxidase; CholOx, cholesterol oxidase; cnsA, aurantioclavine synthase; *Cv*, *Chlorella variabilis*; DLDH, D-lactate dehydrogenase; DprE, decaprenylphosphoryl-beta-D-ribose oxidase; E22O, Ecdysteroid-22-oxidase; EasE, chanoclavine synthase; *Ec*, *Eschscholzia californica*; EncM, FAD-dependent oxygenase; EugO, eugenol oxidase; FOX, flavin-dependent oxidoreductase; FsqB, fructosyl amino acid oxidase; GilR, pregilvocarcin V oxidase; GLDH, L-galactono-1,4-lactone dehydrogenase; GOOX, glucooligosaccharide oxidase; *Ha*-CHOX, *Helianthus annuus* carbohydrate oxidase;

HMM, hidden markov model; HOX, hexose oxidase; HPM9, alcohol oxidase from *Hypomyces subiculosus*; ICN, indole carbonyl nitrile; LaO, carbohydrate oxidase; *Ls*-CHOX, *Lactuca sativa* carbohydrate oxidase; *Mp*, *Marchantia polymorpha*; *Mt*, *Myceliophthora thermophila*; MurB, UDP-N-acetylenolpyruvoylglucosamine reductase; *N. rileyi*, *Nomuraea rileyi*; Nec5, nectarin 5; *Nf*, *Neosartorya fumigata*; *Nt*, *Nicotiana tabacum*; PCMH, *p*-cresol methylhydroxylase; PFAM, protein family; Phl p 4, major pollen allergen (glucose dehydrogenase); *Pi*, *Phytophthora infestans*; *Pp*, *Physcomitrella patens*; RPA1076, oxidoreductase from *Rhodopseudomonas palustris*; SCOPE, structural classification of proteins – extended; *Sm*, *Selaginella moellendorffii*; STOX, (S)-tetrahydroprotoberberine oxidase; TamL, tirandymycin oxidase; THCAS, tetrahydrocannabinolic acid synthase; VAO, vanillyl-alcohol oxidase; *Vc*, *Volvox carteri f. nagariensis*; XEG, xylanendoglucanase; XylO, xylooligosaccharide oxidase; *Zm*CKO2, cytokinin oxidase from *Zea mays*; *Zm*CKX1, cytokinin oxidase from *Zea mays*.

The chapter was published as “The family of berberine bridge enzyme-like enzymes: a treasure-trove of oxidative reactions“ in Archives of Biochemistry and Biophysics 2017, Vol. 632, p. 88-103.

Abstract

Biological oxidations form the basis of life on earth by utilizing organic compounds as electron donors to drive the generation of metabolic energy carriers, such as ATP. Oxidative reactions are also important for the biosynthesis of complex compounds, *i.e.* natural products such as alkaloids that provide vital benefits for organisms in all kingdoms of life. The vitamin B₂-derived cofactors flavin mononucleotide (FMN) and flavin adenine dinucleotide (FAD) enable an astonishingly diverse array of oxidative reactions that is based on the versatility of the redox-active isoalloxazine ring. The family of FAD-linked oxidases can be divided into subgroups depending on specific sequence features in an otherwise very similar structural context. The sub-family of berberine bridge enzyme (BBE)-like enzymes has recently attracted a lot of attention due to the challenging chemistry catalyzed by its members and the unique and unusual bi-covalent attachment of the FAD cofactor. This family is the focus of the present review highlighting recent advancements into the structural and functional aspects of members from bacteria, fungi and plants. In view of the unprecedented reaction catalyzed by the family's namesake, BBE from the California poppy, recent studies have provided further insights into nature's treasure chest of oxidative reactions.

Introduction

BBE-like enzymes form a subgroup of the superfamily of FAD-linked oxidases (SCOPe d.58.32) that is structurally characterized by a typical fold observed initially for vanillyl-alcohol oxidase (VAO) (1). Therefore, the structural architecture has been described initially as the VAO-fold (2) and all members of this superfamily share a common architecture that can be divided into a FAD-binding domain and a substrate binding domain, which is also referred to as the cap domain (1). A comprehensive review on the first identified members of this family was published by Leferink *et al.* (3). In recent years, however, the rapidly growing number of member proteins has revealed a relatively low sequence conservation and an astonishing diversity of catalyzed chemical reactions. To account for these observations the superfamily of FAD-linked oxidases can be divided into subfamilies that better reflect structural, functional and evolutionary aspects of individual group members. The family of BBE-like enzymes forms a relatively large subgroup featuring a characteristic C-terminal structural element following the substrate binding region (see below). Considering the differences in chemical reactivities observed for the relatively few enzymes that are characterized in detail, additional sub-classifications are helpful and will be introduced in this review.

The namesake of this family is the (*S*)-reticuline oxidase or berberine bridge enzyme from California poppy (*Eschscholzia californica*) that catalyzes the conversion of (*S*)-reticuline to (*S*)-scoulerine by mediating an oxidative ring closure reaction. The C-C bond that is formed in this reaction is referred to as the berberine bridge and marks a branch point in the biosynthesis of benzyloquinoline alkaloids (4) (Figure 1).

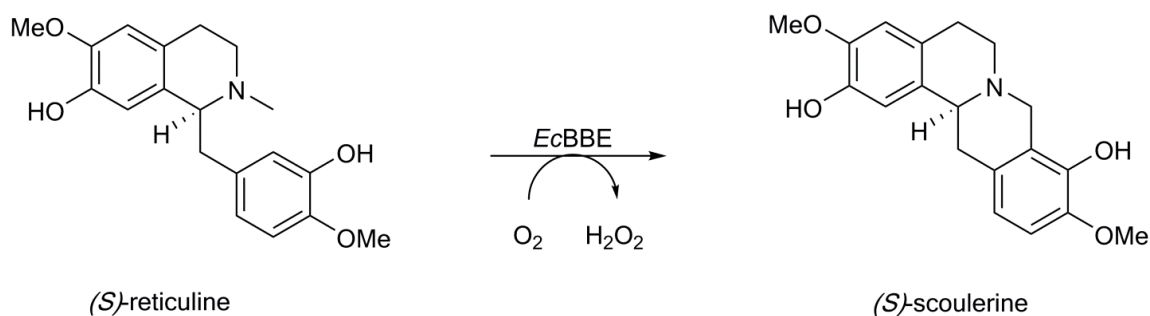


Figure 1: Reaction catalyzed by the berberine bridge enzyme. *EcBBE* catalyzes the oxidative ring closure reaction from (*S*)-reticuline to (*S*)-scoulerine.

Together with glucooligosaccharide oxidase (GOOX) from *Acremonium strictum* (5, 6), the characterization of BBE (7–9) revealed one interesting hallmark of the family of BBE-like proteins: a bi-covalently attached FAD cofactor. The characteristic 6-*S*-cysteinyl-, 8 α -*N*1-histidyl-FAD linkage is only found in the BBE-subfamily of the FAD-linked oxidases and has been shown to increase the redox potential of the cofactor by more than 300 mV compared to free flavin (10). How exactly this is linked to the individual reactions catalyzed is still not very well understood, especially since some family members appear to have lost the cysteinyl linkage. Additional highlights of BBE-like family members are the recently identified flavin N5-oxides observed in *EncM* (11) and challenging carbon-carbon bond formation reactions involving complex biomolecules in natural product biosynthesis (12, 13). In comparison to the rapidly growing number of group members identified in various sequencing projects, the functional characterization of individual proteins is severely lagging behind also due to the challenge of identifying the true *in vivo* substrates, as exemplified in reference (14). Considering the stunning reactions catalyzed by members of the BBE-like enzyme family that have been analyzed in detail so far, it will be interesting to witness which new surprising functional details of yet uncharacterized family members will be discovered in the future.

Structural characteristics of BBE-like proteins

Differentiation from other families of FAD-linked oxidases

As mentioned in the introduction, BBE-like enzymes are a sub-family of the large superfamily of FAD-linked oxidases (SCOPe d.58.32). Characteristic structural features of this family are a FAD binding module that is formed by the *N*- and *C*-terminal parts of the protein, and a substrate binding module that, together with the isoalloxazine ring of FAD, provides the environment for efficient substrate binding and oxidation (Figure 2). While the overall fold of BBE-like proteins is similar to that of other prototypic members of this superfamily, a specific structural feature in the vicinity of the FAD-binding site distinguishes the BBE family from other FAD-linked oxidases such as vanillyl

alcohol oxidase (VAO)-like enzymes (SCOPE d.58.32.1), the D-lactate dehydrogenase family (SCOPE d.58.32.2), cholesterol oxidase-like enzymes (SCOPE d.58.32.3), cytokinin dehydrogenases (SCOPE d.58.32.4) and alditol oxidase-like enzymes (SCOPE d.58.32.6).

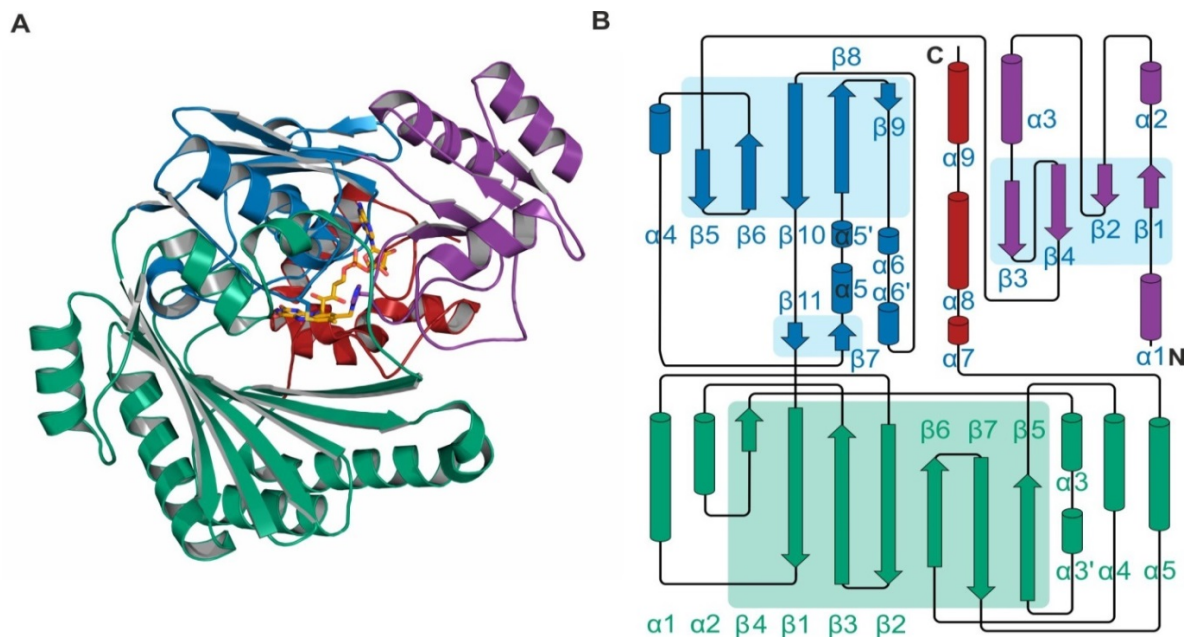


Figure 2: Overview of structural properties of the BBE-like family. **A**, The overall structure of a representative member (*EcBBE*; pdb 3d2j) is shown in *cartoon* representation. Individual sub-domains of the upper flavin-binding module are colored in *purple*, *blue* and *red*. The FAD cofactor (shown as *orange stick model*) is bound in an extended conformation with the ribityl chain and the adenyl moiety sandwiched between all three subdomains. The isoalloxazine ring projects towards the active site that is formed by residues from the substrate binding module (*green*) and the initial part of the BBE-like specific C-terminus (*red*, cf. Figure 3). **B**, Topology plot of the structure shown in *panel A*. Secondary structure elements are numbered consecutively for α -helices and β -strands in the flavin- and substrate-binding modules and are labeled in *green* and *blue*, respectively.

The *N*-terminal part of the hidden Markov model (HMM) specific for the BBE and BBE-like enzymes (pfam entry: PF08031, (15)) highlights a characteristic Y/FxN motif (Figure 3A). This element contains a highly conserved aromatic residue (Tyr or Phe), which in case of a Tyr interacts with the N1-C2=O locus of the isoalloxazine ring and a strictly conserved Asn residue that hydrogen bonds with the before mentioned Tyr side chain. This arrangement sterically influences the positioning of the ribityl side chain of the cofactor as well as a structural element (residues 169-179 – *EcBBE* numbering) involved in forming part of the oxygen binding pocket on the *re* side of the isoalloxazine ring (Figure 3C) (16). Additionally, Asn458 is important for the positioning of His174 that stabilizes the negative charge N1-C2=O locus of the reduced flavin and has been shown to be involved in the formation of the C6-cysteinyll linkage (20).

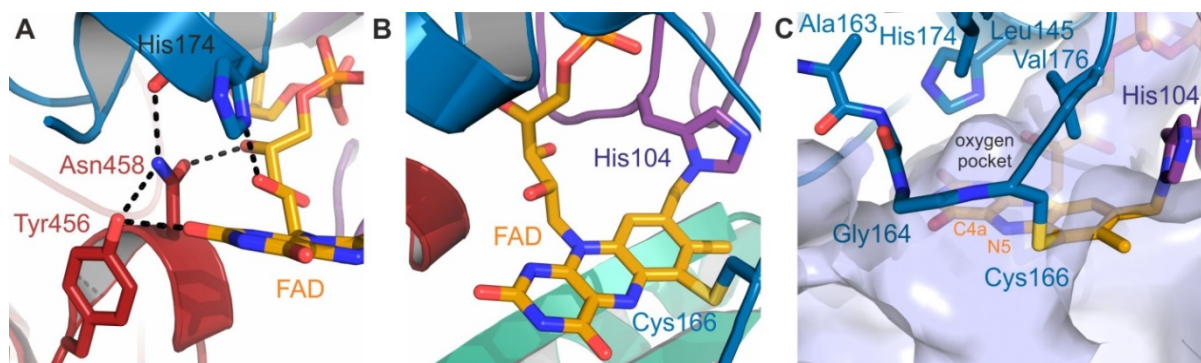


Figure 3: Close-up of the flavin binding site. **A**, The conserved Y/FxN motif of BBE-like enzymes establishes a defined hydrogen bonding network near the N1-C2=O locus of the isoalloxazine ring. His174, Tyr456, Asn458, and FAD are shown as *stick models*. **B**, The bi-covalent 6-*S*-cysteinyl-8 α -N1-histidyl-FAD attachment of the cofactor via residues His104 and Cys166 is shown. The *stick models* of His174, Tyr456, and Asn458 from panel A are omitted for clarity and the view is modified. Coloration of individual regions corresponds to Figure 2. Numbering reflects residues of *EcBBE* and the structural details correspond to pdb 3d2j. **C**, Environment of the characteristic oxygen binding pocket in BBE-like enzymes. The active site cavity and the oxygen binding pocket around the flavin cofactor are contoured as *transparent surface structures* in light blue. Residues surrounding the oxygen binding pocket on the *re*-side of the flavin are shown as *stick models* (pdb 3d2j).

The remaining conserved features of the HMM logo of the BBE-like protein pfam entry correspond to structurally relevant residues of the C-terminal FAD-binding region and are therefore also present in other groups of the superfamily. However, an additional important structural element that is directly coupled to the Y/FxN motif features another highly conserved element of the BBE-like protein family. In fact, the region closing the active site cavity at its rear part features a conserved salt bridge between Asp192 and Arg409. The structural integrity of this region with its glycine-rich elements (*EcBBE* residues 170-188) is important for accurately positioning both the FAD cofactor (via Tyr456) and the Cys residue involved in the covalent attachment of the cofactor (*EcBBE* Cys166, see *below*). The characteristic loop region between $\beta 6$ and $\beta 7$ of the substrate binding module (*EcBBE* residues 390-410) is structurally different to other families in the superfamily and apparently plays an important structural role in establishing the C-terminal connection between the substrate binding region and the FAD-binding module. Interestingly, this region has also been shown to play a role for access to the oxygen binding pocket and tuning of the reactivity of the substrate-reduced FAD cofactor towards molecular oxygen (17). Additional structural and functional insights into the oxygen reactivity of BBE-like proteins are summarized below.

Bi-covalent attachment of the flavin cofactor via His and Cys residues

The linkage of FAD to the protein is maybe the most significant peculiarity of the BBE-like protein family since it features an unusual bi-covalent attachment of FAD that has not been seen in any other

family of flavoproteins (Figure 3B). The formation of this bi-covalent attachment and other covalent modifications of the flavin cofactor has recently been reviewed by Heuts *et al.* (21). The characteristic dual 6-*S*-cysteinyl-, 8 α -N1-histidyl-FAD linkage was observed for the first time in the crystal structure of GOOX (5, 6) and initially characterized biochemically in detail for BBE (7–9). Since then it has been observed in many other proteins and can be safely predicted based on two characteristic motifs, *i.e.* the fingerprint motifs R/KxxGH and CxxV/L/IG for covalent attachment of residues His and Cys to the 8 α and 6-position of the isoalloxazine ring, respectively. While most of the members of the BBE-like protein family contain a bi-covalently attached FAD cofactor, there are also members with solved crystal structures that feature only a single 8 α -N1-histidyl attachment and at least for one of those it has been proposed that the second covalent linkage can be created by introduction of the Cys residue along with additional substitutions (11, 18–20). Mutagenesis studies have shown that both types of covalent attachment can be formed independently, however, so far no naturally occurring single 6-*S*-cysteinyl-FAD linkage within this family of flavoproteins has been described in detail (3, 6, 8, 21). Based on more extensive sequence alignments, several members of the BBE-like protein family were identified that are missing the residues required for the 6-*S*-cysteinyl-linkage and, in the case of the BBE homolog found in *Chlorella variabilis*, even the 8 α -N1-histidyl-FAD attachment appears to be missing. This of course raises the question of the functional and/or structural importance of this unusual type of cofactor attachment. Since bi-covalent attachment is not a prerequisite for proper folding, the divergence of enzymatic reactions and the evolutionary adaptation of BBE-like proteins might be responsible for the absence of a bi-covalent linkage in some family members; nevertheless, there appears to be a general positive effect of this type of attachment as it was observed that the rate of substrate oxidation is generally affected by the redox potential of the attached flavin cofactor, *i.e.* removal of a covalent linkage decreased the redox potential and the rate of flavin reduction in the pertinent protein variants. Equally important appears to be the role of bicovalent flavin attachment for the correct positioning of the substrate in proximity to the isoalloxazine ring (6, 9, 22). In addition to the functional relevance of boosting the oxidative power by a substantial increase of the redox potential, there is also the structural importance of bi-covalent cofactor attachment for maintaining active site architecture and preventing cofactor dissociation for enzymes accepting bulky substrates (6, 8, 9, 16, 19, 21). As shown in the detailed descriptions below, members of the BBE-like family generally accept large substrates and have therefore evolved wide open active sites. In order to facilitate precise orientation of the flavin cofactor in such an open active site environment, the bi-covalent attachment provides a mechanism for appropriately positioning the cofactor relative to bulky substrates (9, 11, 23, 24). Importantly, comparing different structures of BBE-like proteins it becomes obvious that access to the active site and properties of the active site cavity are modulated extensively by a mobile loop region connecting β 4 and β 5 of the β -sheet of the substrate-binding module (Figure 2B). Together with the variation of β -sheet residues projecting into the active site, this structural element enables the evolutionary adaption of family members to a variety of catalytic functions.

The reactivity of BBE-like enzymes with oxygen

Independent of the nature and size of the organic molecules accepted by various BBE-like members, the oxidation of the corresponding substrates results in reduction of the flavin cofactor. In order to regenerate the cofactor for the next round of enzymatic turnover it needs to be reoxidized. Classical oxidases allow a rapid reoxidation of the reduced FAD by molecular oxygen accompanied by the formation and release of hydrogen peroxide. The bimolecular reaction rate constants for the regeneration of the oxidized flavin cofactor in oxidases range from 1×10^4 to $1 \times 10^6 \text{ M}^{-1} \text{ s}^{-1}$. Therefore, the protein environment substantially accelerates the rate of cofactor reoxidation relative to free flavin in solution ($\sim 2.5 \times 10^2 \text{ M}^{-1} \text{ s}^{-1}$) (25, 26). Subtle changes around the flavin C4a-N5 region, which is involved in the initial one electron reduction of molecular oxygen to form a caged radical pair of the flavin semiquinone and a superoxide anion, can result in pronounced changes in the reactivity towards oxygen. Flavoprotein dehydrogenases typically exhibit bimolecular reaction rate constants for the oxidation of the reduced flavin by oxygen below $1 \times 10^4 \text{ M}^{-1} \text{ s}^{-1}$. It should be pointed out, however, that even the same protein can be converted from its dehydrogenase form to an oxidase by subtle conformational changes, as, for example, induced by thiol oxidation in xanthine dehydrogenase (27, 28).

As far as molecular determinants of oxygen reactivity within the family of BBE-like proteins are concerned, a specific oxygen binding pocket was identified on the *re* side of the flavin cofactor opposite the substrate binding region. This feature is shared by all members of the FAD-linked oxidase superfamily (SCOPe d.58.32) and was initially suggested by chloride binding to this region in VAO (1). This has later been confirmed by biochemical studies of the closely related L-galactono- γ -lactone dehydrogenase as well as by computational and experimental analysis of alditol oxidase, which is more closely related to BBE-like enzymes than to the members of the VAO family (17, 29). Even though the position of the oxygen binding pocket appears to be conserved also in BBE-like enzymes, the bi-covalent attachment of the flavin cofactor and the properties of the Y/FxN element slightly alter the architecture of this region and thereby cause other elements to function as gatekeeper residues for oxygen access and reactivity (Figure 3C). The most comprehensive analysis of how to convert an oxidase of the BBE-like enzyme family to a dehydrogenase and *vice versa* was performed by Zafred *et al.* with *EcBBE* and the plant allergen Phl p 4 (16). Substitution of a gatekeeper residue (Ile) in the dehydrogenase Phl p 4 with Val results in an increase of oxygen reactivity by almost 5 orders of magnitude whereas the inverse exchange of Val by Ile in *EcBBE* leads to a drop in O₂ reactivity by a factor of 500. Neighboring residues such as the partially conserved His174 in *EcBBE* also influence the rate of cofactor reoxidation and correlate to some extent with the dehydrogenase vs oxidase annotation. While oxidases preferentially have a His at this position, dehydrogenases feature either Asn (Phl p 4) or Gln (*AtBBE*-like 28 with intermediate oxygen reactivity) residues or even hydrophobic side chains (GilR) at this position to further modulate the general dehydrogenase feature of a bulky Leu or Ile gatekeeper residue at the position corresponding to Val176 of *EcBBE* (16, 19, 30,

31). Therefore, formation of a specific oxygen binding pocket enables flavoproteins to tune the reactivity toward oxygen and to channel the reducing equivalents generated during enzymatic conversion into either the formation of reactive oxygen species or reduction of electron carriers such as for example NAD(P)⁺ or coenzyme Q.

Protein-substrate interactions in BBE-like proteins

Since the catalytic turnover of a reduction-oxidation process comprises two half reactions, *i.e.* a reductive and an oxidative, it is important to define on which side of the isoalloxazine system, *i.e.* the *re-* or *si-* side the half reactions occur. In the case of BBE-like enzymes the most prominent interactions of the protein matrix and the isoalloxazine ring are established on the *re-* side and thus activation of oxygen in the course of the oxidative half reaction is orchestrated by these amino acids. On the other hand, the amino acids on the *si-* side of the isoalloxazine ring are involved in substrate binding and thus enable substrate oxidation and concomitant reduction of the isoalloxazine ring. This interaction includes the activation of a putative substrate by base-catalyzed proton abstraction and the stabilization of the transition state. In recent studies, we have shown that by variation of these residues very different active site types can be created in the same overall topology (19, 32). For example, in the plant family of Brassicaceae, we have recently identified four different frequently occurring active site types that were confirmed by X-ray crystallography (19, 33, 34). In Figure 4, a representative for the active site types I, II, III and IV is shown. The residues are colored according to the subdomain they belong to.

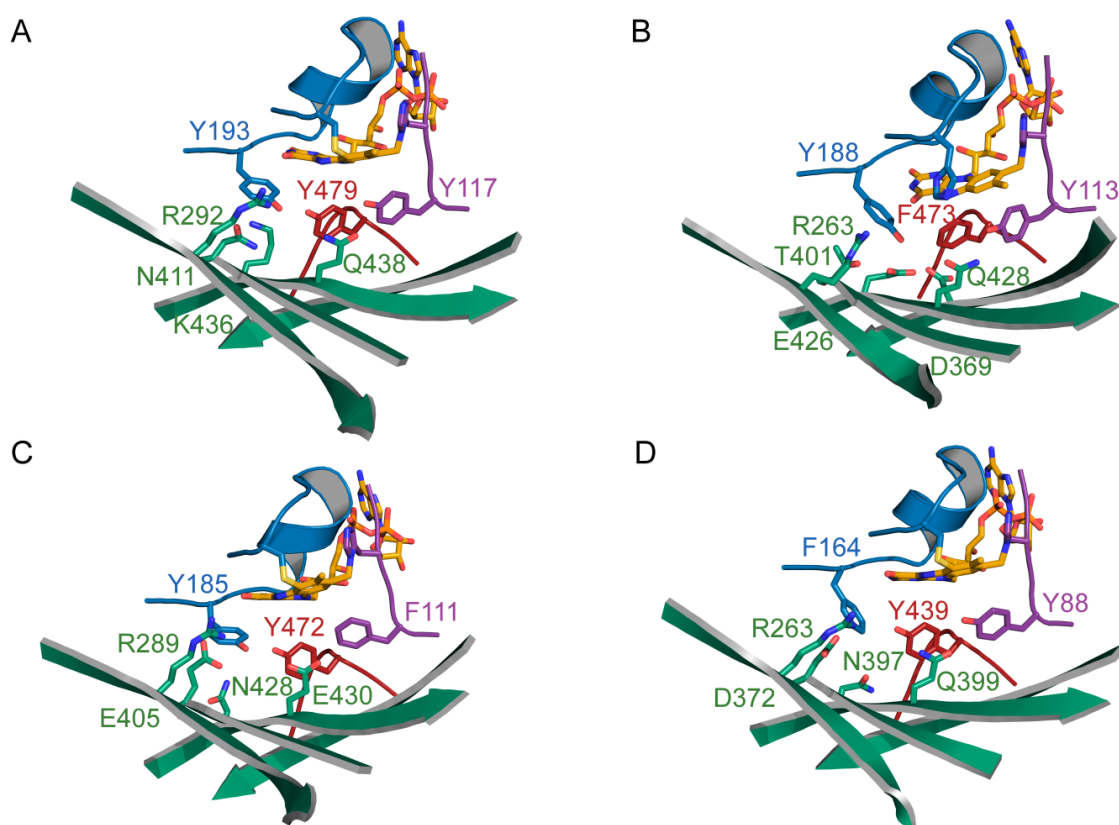


Figure 4: Frequently occurring active site types: **A**, Type I from *AtBBE*-like protein 15 (pdb code 4UD8); **B**, Type II from *AtBBE*-like protein 28 (pdb code 5D79); **C**, Type III from a homology model of *AtBBE*-like 22 (Q9SUC6) based on *AtBBE*-like protein 15 (4UD8); **D**, Type IV from Phl p 4 (pdb code 4PWC).

Active site type I has been described for monolignol dehydrogenases from *Arabidopsis thaliana* (32, 33). It is predominantly found in BBE-like enzymes from higher plants, for example 13 out of 27 BBE-like enzymes from *Arabidopsis thaliana*. Other well characterized enzymes harboring the active site type I are carbohydrate oxidases from sunflower and lettuce as well as *AtBBE*-like 3 (FOX1) that were reported to oxidize “gluco-oligomers” and 4-hydroxy indole-3-carbonyl nitrile, respectively (14, 35). Thus, all of these enzymes act on primary or secondary hydroxyl groups with an active site base initiating the reaction by proton abstraction. In the case of *AtBBE*-like enzyme 15, Tyr193 was identified as the catalytic base, which is activated by a close contact to Tyr479 and a π -cation-interaction with Lys436. Subsequently, the activated alcoholate substrate transfers a hydride to the N5 position of the flavin. The transition state is proposed to be stabilized by Gln438, which is in close contact to Tyr117 (33).

The active site type II was first described for *AtBBE*-like 28 and is associated with mono- or bi-covalent flavin linkage (19). The nature and position of the residues that stabilize the transition state is unchanged (compare Figure 4, *panel A*, amino acids Y117 and N438 to *panel B*, amino acids Y113 and Q428) with the position of the aromatic amino acids Tyr117, Tyr193 and Tyr479 corresponding to Tyr113, Tyr188 and Phe473 in the active site type I. However, Tyr479 and Lys436 in the active site type I (*e.g.* *AtBBE*-like protein 15) are replaced by Phe473 and Glu426 (*e.g.* *AtBBE*-like 28) enabling a completely new set of interactions, *e.g.* Glu426 forms a hydrogen bond to the hydroxyl group of Tyr188. The mechanism deduced from this arrangement involves deprotonation of Tyr188 by Glu426 and thus a similar role of Tyr188 as an active site base can be envisaged.

Active site type III is a mixture of type I and II. Similar to active site type I, it features two Tyr residues in the center of the active site but is missing the Lys residue that engages in a π -cation-interaction with one of the Tyr residues. Instead, active site type III possesses a Glu residue (Glu405) that extends into the active site. This active site type is rare and apparently confined to Brassicaceae. The enzymatic activity of BBE-like enzymes with this particular composition is currently unknown.

Active site type IV has been first described for GOOX from *Acremonium strictum* (5). It was found in BBE-like proteins from fungi and, predominantly, in basal plants (Figure 5). Important examples of this active site type are fungal BBE-like enzymes such as XylO, ChitO and LaO as well as the pollen allergens Phl p 4 and BG60 (34, 36–39). Characteristic for this active site type is the deprotonation of Tyr439 by Asp372, which is mediated by a water molecule (5). The phenolate species of Tyr439 was postulated to act as catalytic base to initiate the hydride transfer by proton abstraction at the anomeric center of the carbohydrate substrate. Similarly, Tyr88 and Gln399 are conserved and play a similar role in the stabilization of the transition state as suggested for the respective residues in active site type I.

Occurrence and development of the BBE-like protein family

Currently, the BBE-like protein family (Pfam 08031) encompasses 6382 sequences found in fungi (3712 sequences in 233 species), plants (1372 sequences in 60 species), bacteria (1156 sequences in 520 species) and archaea (20 sequences in 11 species). A phylogenetic tree of the proteins covered in this article is displayed in Figure 5.

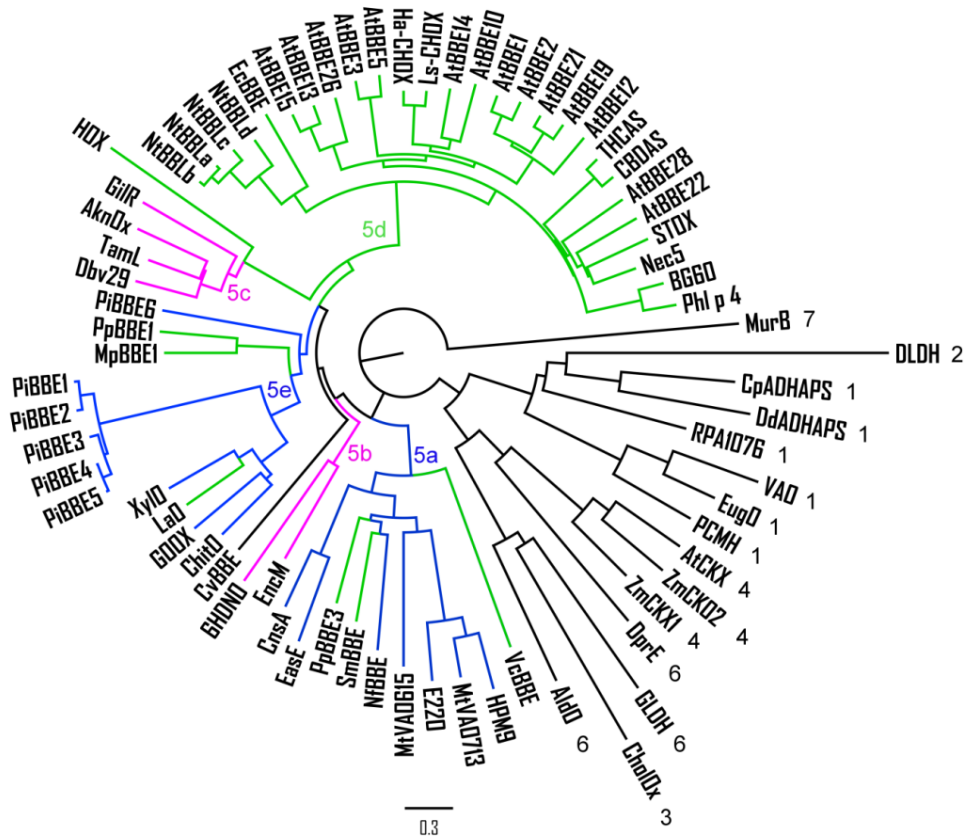


Figure 5: Phylogenetic tree of the superfamily of FAD-like oxidases (SCOPE d.58.32). The numbering of the subfamilies is according to the SCOPE database and indicated at the branch tips except for BBE-like proteins (subfamily 5). The latter are colored according to their origin; BBE-like proteins from fungi, plants and bacteria are depicted in *blue*, *green* and *violet*, respectively. Subfamily 5 has been subdivided into clades 5a-d. The tree was created employing the sequences compiled in Supplemental Table S1 as previously described (19) and visualized using Figtree (40). A bootstrap analysis was performed and the respective tree is shown in Supplemental Figure S1.

BBE-like proteins in bacteria

The PFAM entry of the BBE-like protein family currently harbors 1156 sequences of BBE-like proteins from bacteria, in average two per species. They do not appear in all species but only in selected strains. The majority of known BBE-like proteins in bacteria can be assigned to the phyla Actinobacteria, Proteobacteria and Firmicutes with 715, 170 and 102 sequences, respectively. A genus

that is exceptionally rich in BBE-like proteins is *Streptomyces* with in average of four BBE-like proteins per species. Well known BBE-like proteins from *Streptomyces* are GilR, TamL, Dbv29 and AknOx (23, 31, 41, 42). All of them are involved in the biosynthesis of antibiotics as described below and their genes are located in the respective gene clusters responsible for the whole biosynthesis of the pertinent antibiotic.

BBE-like proteins in fungi

In fungi, BBE-like proteins are restricted to the subkingdom of the “higher fungi”, Basidiomycota and Ascomycota, which have arisen approx. 600 million years ago (43). Despite their average occurrence of 16 BBE-homologs per species the vast majority of these proteins is still uncharacterized and they possess unknown functions. According to our analysis, BBE-like proteins from fungi can be found in clades 5a and 5e (Figure 5).

BBE-like proteins in plants

In plants, BBE-like proteins represent, like in fungi, a multigene family. Here, we present an analysis of the evolution of the BBE-like protein family in land plants. In Figure 6, a phylogenetic tree of plants, the occurrence of BBE-like proteins and the distribution of the previously categorized active site types is depicted.

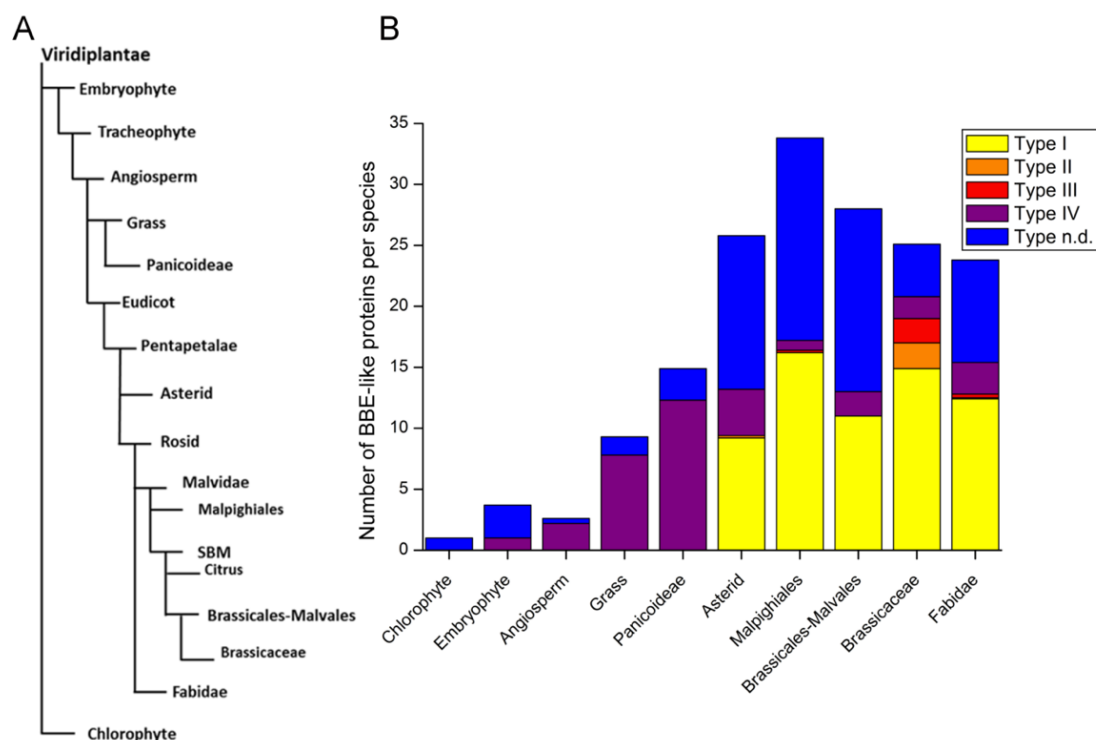


Figure 6: A, Phylogenetic tree of plants (note that the length of the lines does not reflect evolutionary distances); **B**, Graphical representation of the number of BBE-like proteins per species and the distribution of active site types using the following color code: *yellow*, type I; *orange*, type II; *red*, type III, and *violet*, type IV. In lower plants, active site type IV is predominant, for example Panicoideae have on average twelve BBE-like proteins per species with this active site type. The first appearance of the active site type I occurs in Asterids. In the course of evolution, the abundance of active site type IV is reduced to less than four BBE-like enzymes per species, while the abundance of the active site type I increased to up to sixteen on average per species in Malpighiales.

The most basal division in the kingdom of Viridiplantae are the chlorophytes. These comprise unicellular and multicellular organisms including most of the green algae (44). Not all chlorophytes harbor genes encoding BBE-like enzymes and the number of genes per species does not exceed two. In embryophytes, which are formally known as “land plants”, the number of BBE-like proteins has increased to four in *Marchantia polymorpha*, three in *Sphagnum fallax* and two in the moss *Physcomitrella patens*. This is the most basal species currently known to have a BBE-like protein with an active site type IV. During the evolution of monocotyledons, the number of genes encoding BBE-like enzymes has increased from three in angiosperms to eight and fifteen in grasses and Panicoideae, respectively. Predominantly, they contain BBE-like enzymes with the active site type IV. The first appearance of BBE-like enzymes with an active site type I is in eudicots, where the lowest developed species harboring the active site type I is *Aquilegia coerulea* (Colorado blue columbine). In eudicots, active site type I was replaced by the active site type IV as the most prominent active site type. The average occurrence of BBE-like enzymes in Asterids, Malpighiales, Brassicales-Malvales, Brassicaceae and Fabidae is 26, 34, 28, 25 and 24, respectively. Approximately half of them harbor the active site type I with type IV being present in one quarter of the BBE-homologs. Interestingly, the occurrence of the active site type II and III appears to be restricted to Brassicaceae. While enzymes harboring this active site types have been found in seven Brassicaceae species previously analyzed, they are absent in all other plants (19). It is noteworthy that in higher plants various BBE-like proteins with yet undefined (n.d.) active site types are present. These are typically not completely new active site types but variations predominantly of type I.

Reactions catalyzed by BBE-like enzymes

BBE-like enzymes catalyze diverse chemical reactions. In the following section these reactions will be discussed grouped according to their origin (plants, bacteria and fungi) and their appearance in the phylogenetic tree (clades 5a-e in Figure 5).

Reactions catalyzed by BBE-like enzymes from plants: alkaloid and cannabinoid biosynthesis

The majority of BBE-like enzymes from plants are found in clade 5d (Figure 5), with the two BBE-like enzymes from basal plants (*PpBBE1* and *MpBBE*) clustering with fungal carbohydrate oxidases (Figure 5). In the plant kingdom, BBE-like enzymes catalyze a broad variety of reactions. Very prominent is the oxidation of alcohols typically catalyzed by enzymes employing an active site type I or IV. From this pool of alcohol oxidases different BBE-like enzymes have been adapted to catalyze more complex reactions like oxidative ring closure reactions as exemplified by *EcBBE*, Δ^1 -tetrahydrocannabinolic acid (THCA) synthase and cannabidiolic-acid (CBDA) synthase (13, 45, 46). Figure 7 summarizes the currently known reactions catalyzed by BBE-like enzymes in alkaloid and cannabinoid biosynthesis.

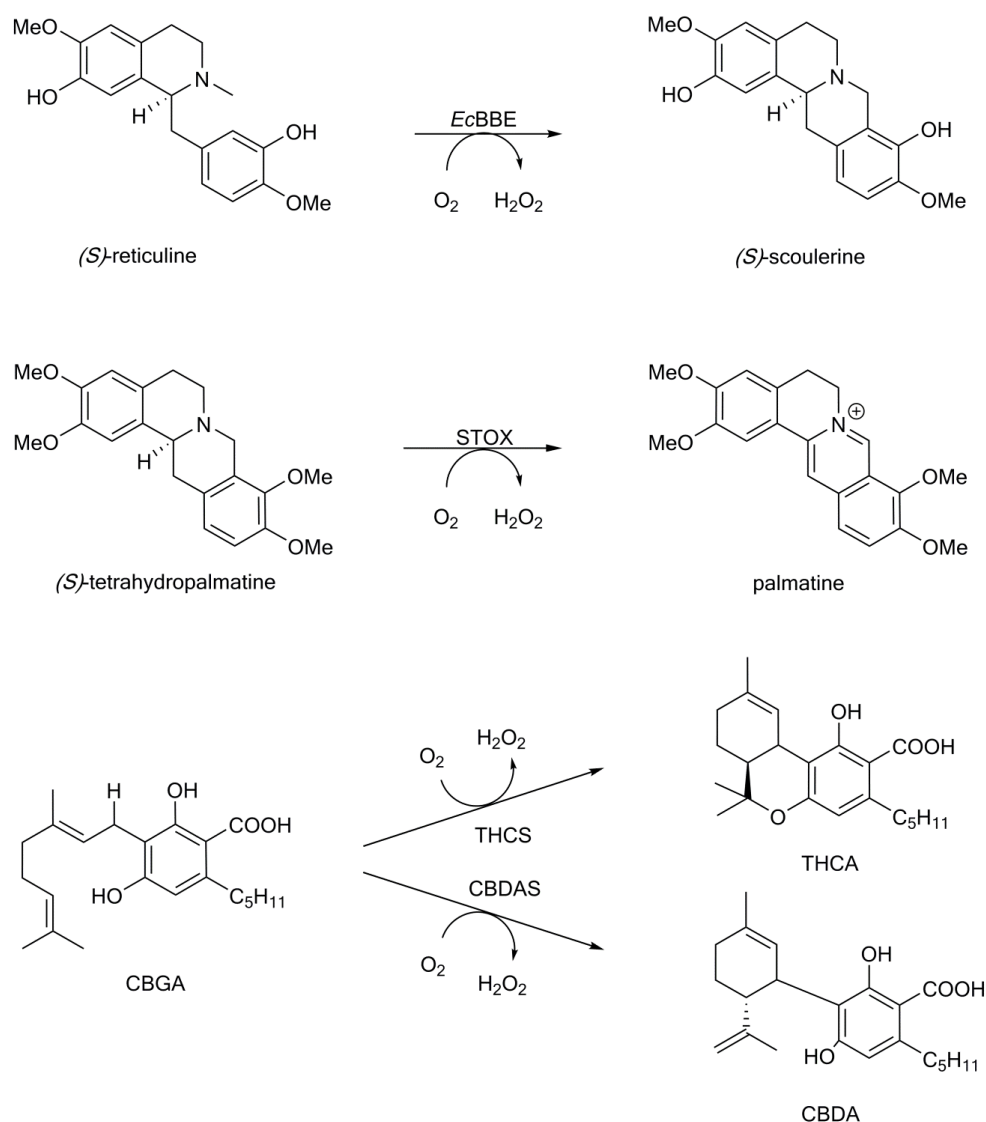


Figure 7: Reactions catalyzed by BBE-like enzymes in alkaloid and cannabinoid biosynthesis from plants. *EcBBE* catalyzes the oxidative ring closure reaction from *(S)*-reticuline to *(S)*-scoulerine (47). *STOX* catalyzes the oxidation of *(S)*-tetrahydropalmatine to palmatine (48). Cannabigerolic-acid (CBGA) is converted by tetrahydro-cannabinolic-acid (THCA) synthase to THCA and by cannabidiolic-acid (CBDA) synthase to CBDA (46, 49).

BBE is a branch point enzyme in the benzyloquinoline alkaloid biosynthesis (4). The enzyme was first isolated in 1975 from *Macleaya microcarpa* cell cultures (50). Subsequently, BBE activity was found in 66 differentiated plant and cell cultures mainly from *Papaveraceae* and *Fumariaceae* species (47). Kutchan *et al.* expressed the gene heterologously in insect cells and demonstrated that the FAD cofactor is covalently attached to the produced protein via a histidine residue at the 8 α -position of the isoalloxazine ring (45, 51). Larger quantities of the enzyme became available from expression in the methylotrophic yeast *Komagataella phaffii* (previously known as *Pichia pastoris*) by Winkler *et al.* enabling the identification of an additional cysteine residue that covalently binds to the flavin cofactor at the C6 position (7–9, 12). In addition, Winkler *et al.* solved the crystal structure and conducted site directed mutagenesis studies to probe the catalytic mechanism of the enzyme (12). The mutagenesis program was later extended by Wallner *et al.* and Zafred *et al.* to provide a better understanding of key features of the enzyme, such as the stabilization of a negative charge at the N(1)C(2)=O locus that occurs in the course of the reaction and the reactivity of the reduced enzyme towards oxygen (16, 30). BBE catalyzes the oxidative conversion of (*S*)-reticuline to (*S*)-scoulerine, which is subsequently converted to protoberberine, protobine or benzophenanthridine alkaloids (52). A concerted mechanism for this enzyme was proposed, following the initiation of the reaction by deprotonation of the C3' hydroxyl group of (*S*)-reticuline. The subsequent nucleophilic attack of the C2' atom at the N-methyl group of the substrate forms the so called berberine bridge and leads to the (concerted) transfer of a hydride from the N-methyl group to the N5-position of the isoalloxazine ring (12). Later studies, based on the measurement of kinetic isotope effects, have challenged the concerted mechanism and suggested that a previously proposed stepwise mechanism (45) might be more likely (53). According to this mechanism, the reaction is initiated by hydride transfer from the N-methyl group to the flavin to form an iminium intermediate, which is then nucleophilically attacked by the C2' carbon to close the berberine bridge, however, this study could not provide any evidence for the intermediate species required by this mechanism. Similar to BBE, (*S*)-tetrahydroprotoberberine oxidase (STOX) from *Argemone mexicana* and *Berberis wilsoniae* is involved in benzyloquinoline alkaloid biosynthesis (48, 54, 55). STOX was reported to oxidize tetrahydroprotoberberine to palmatine. Additionally, (*S*)-scoulerine and (*S*)-canadine were accepted as substrates by STOX from *B. wilsoniae*, whereas STOX from *A. mexicana* also oxidizes (*S*)-coreximine (56). Interestingly, *EcBBE* also features STOX like activity albeit with much lower efficiency (57). STOX and *EcBBE* share to some extent the same activity and are employed in the same biosynthetic pathway. Still, according to our phylogenetic analysis STOX is more closely related to carbohydrate oxidases such as Nec5 or Phl p 4 than to *EcBBE*. Two other BBE-like enzymes employed in the biosynthetic pathway leading to cannabinoids were found in *Cannabis sativa*. Tetrahydrocannabinolic acid (THCA) synthase and cannabidiolic-acid (CBDA) synthase convert cannabigerolic-acid (CBGA) into THCA and CBDA, respectively (13, 58, 59). Both enzymes catalyze the stereospecific oxidative cyclization of the geranyl group of CBGA. For both enzymes the same initial hydride transfer was postulated, followed by the cyclization that is

initiated by the deprotonation of a hydroxyl group to form THCA whereas CBGA synthase abstracts a proton from the terminal methyl group of CBGA (49, 53). Another plant that employs BBE-like enzymes for alkaloid biosynthesis is tobacco (*Nicotiana tabacum*), which features four BBE-like enzymes closely related to *EcBBE* (Figure 5, BBLa-d). They were assigned a role in the final reaction steps of the biosynthesis of pyridine alkaloids and thus affect the levels of nicotine and anabasine (60). The formal reactions and a hypothetical reaction mechanism for these enzymes are shown in Figure 8.

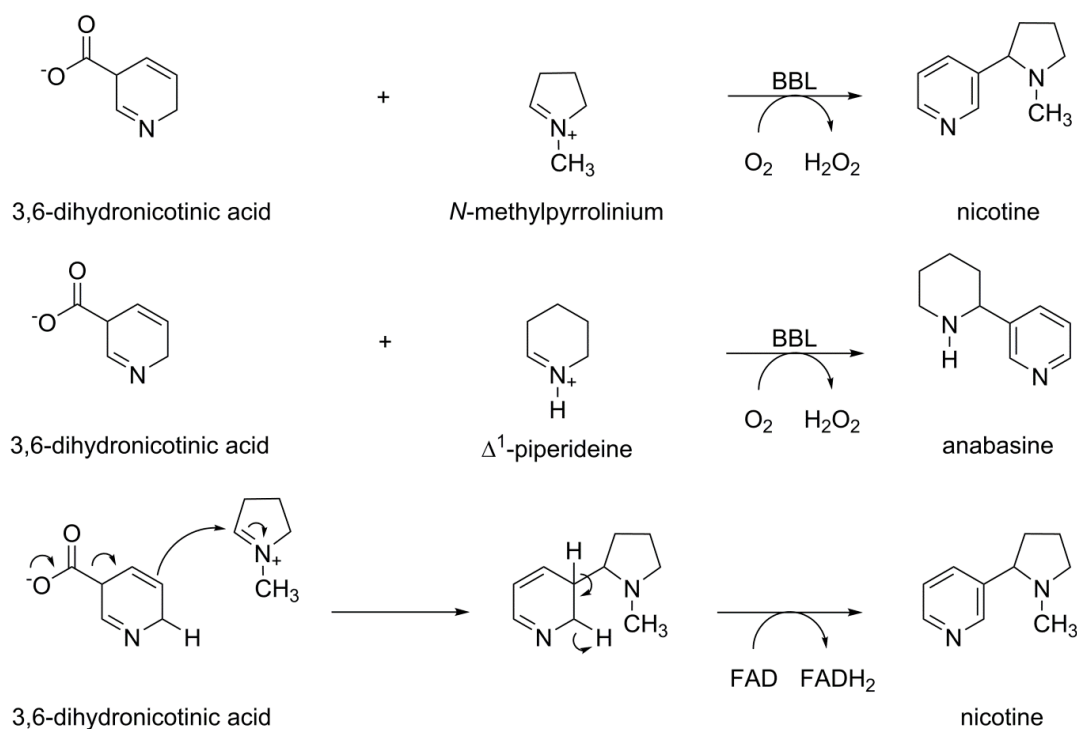


Figure 8: Reactions catalyzed by BBE-like enzymes involved in nicotine and anabasine biosynthesis (top and middle). A hypothetical reaction mechanism for this type of intermolecular C-C bond formation is shown at the bottom for the final biosynthetic step to nicotine. BBLa-d apparently catalyze the decarboxylation to 3,6-dihydronicotinic acid and the subsequent intermolecular C-C-bond to form a non-aromatic intermediate that re-aromatizes via a hydride transfer to the flavin and the concomitant formation of the corresponding alkaloid.

Briefly, they catalyze the C-C bond formation between 3,6-dihydronicotinic acid and *N*-methylpyrrolinium or Δ^1 -piperideine to yield either nicotine or anabasine (61). In contrast to BBE, which catalyzes an intramolecular C-C bond formation, these BBE-homologs carry out an intermolecular coupling of the two building blocks. These hypothetical reactions receive support from the finding that field grown tobacco plants possess reduced levels of pyridine alkaloids when the expression of BBLa-d is suppressed by RNA interference (61).

Reactions catalyzed by BBE-like enzymes from plants: alcohol oxidation

As the genes of the BBE-like enzymes form a multigene family in all land plants with the majority of them not carrying out alkaloid biosynthesis, it appears that BBE-like enzymes must play a more general role in plant physiology that would explain their ubiquitous presence in plants. In evolutionary terms, enzymes catalyzing reactions in secondary metabolism, *e.g.* alkaloid and terpene biosynthesis, have evolved by duplication of genes encoding enzymes operating in primary metabolism with subsequent neofunctionalization (62). Thus the question of the general function(s) of the BBE-like enzymes in plant physiology is connected to the search of reactions in primary metabolism that are potentially catalyzed by members of this family. In this context, the oxidation of various alcohol groups, as summarized in Figure 9, provides a first lead toward an understanding of the evolutionary origin of the BBE-like enzyme family as some of the reactions (*e.g.* oxidation of mono- and polysaccharides) appear to be present in most, if not all, plants.

A frequently observed reactivity of BBE-like enzymes from plants is the oxidation of carbohydrates at the anomeric center to the corresponding lactone. A representative of these enzymes is hexose oxidase (HOX) from the red algae *Chondrus crispus* that belongs to the division of Rhodophyta (63). It is more closely related to various bacterial BBE-like enzymes than to members present in plants (compare Figure 5). Initially, a stoichiometric copper ion but no spectroscopic evidence for a FAD cofactor was reported and thus it was postulated that HOX is a copper-dependent enzyme. However, more recently, a bicovalently attached FAD cofactor was confirmed for this enzyme as catalytic active species (64–66). HOX has a broad substrate specificity accepting glucose and galactose and a variety of oligomeric sugars derived from these building blocks. Another carbohydrate oxidizing BBE-like enzyme is nectarin V (Nec5) from ornamental tobacco, which converts glucose to gluconolactone (67). Nec5 was postulated to be part of the pathogen defense system of plants by protecting reproductive organelles (68). Interestingly, nectarine IV (Nec4) becomes part of the defense strategy by forming an inhibitory protein complex with xylan-specific endoglucanase (XEG), which is released by the pathogen to digest the xyloglucan present in the nectar. This Nec4:XEG-complex induces the enzymatic activity of Nec5 and thus glucose is oxidized to gluconolactone, followed by rapid hydrolysis to gluconic acid (68). Additionally, hydrogen peroxide is generated by the reaction of the reduced FAD cofactor with molecular oxygen. Both products, *i.e.* gluconic acid and hydrogen peroxide, are effective antimicrobial agents (69, 70).

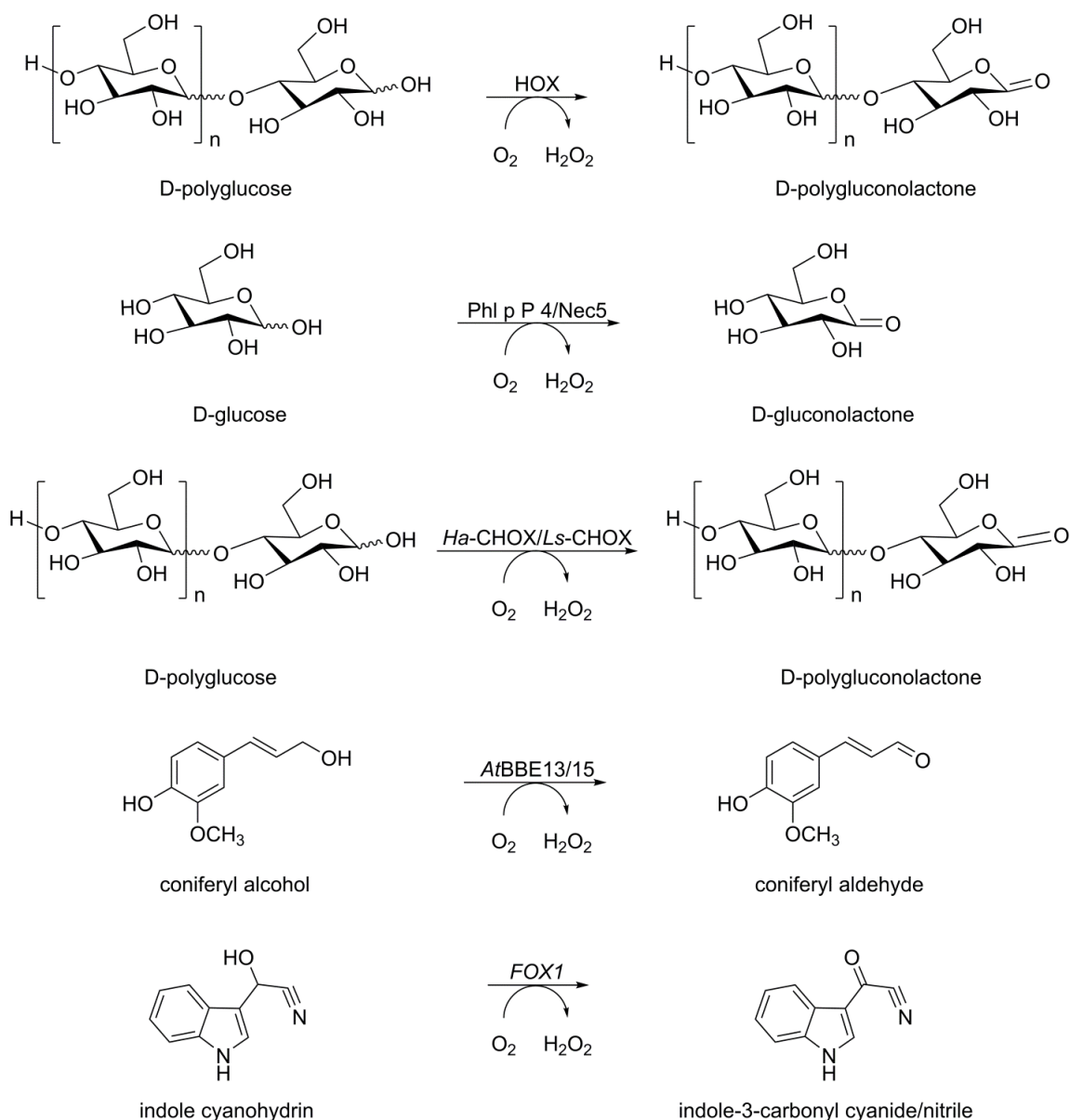


Figure 9: Reactions catalyzed by BBE-like enzymes from plants. HOX oxidizes various carbohydrates and oligomers of glucose to the corresponding lactones (63). Phl p 4 and Nec5 oxidize glucose (34, 67). *Ha*-CHOX and *Ls*-CHOX oxidize carbohydrates and oligomers of glucose to the corresponding lactones (35). The monolignol oxidoreductases *At*BBE-like enzyme 13 and 15 oxidize the monolignols *p*-coumaryl, coniferyl and sinapyl alcohol to the corresponding aldehydes (32). FOX1 (*At*BBE-like enzyme 3) oxidizes indole cyanohydrin to indole-3-carbonyl cyanide/nitrile.

Similar to Nec5 the pollen allergen Phl p 4 from timothy grass is a BBE-like enzyme that oxidizes glucose and plays a role in plant reproduction (34). Phl p 4 was identified to be a glucose dehydrogenase and subsequently similar pollen allergens like BG60 from the BBE-like enzyme family were identified (39) (71). Interestingly, BG60 was isolated in two isoforms that can be distinguished by the presence or absence of a small *N*-terminal domain. According to their spectral properties both

isoforms are isolated in the semiquinone state, stabilizing either the neutral or the anionic semiquinone (39).

Two carbohydrate oxidases from the BBE-like enzyme family were identified to play a role in the plant immune response (35). Custers *et al.* isolated two enzymes, *i.e.* *Ha*-CHOX and *Ls*-CHOX from sunflower (*Heliantus annuus*) and lettuce (*Lativa sativa*), respectively. Both enzymes were found to be highly upregulated after the treatment of the plants with elicitors or during infection. In other closely related BBE-like enzymes from *A. thaliana* such as *At*BBE-like 10 and 20, a similar expression pattern was observed (see Figure 5) (32). *Ha*-CHOX was expressed in *E. coli* to further characterize the catalytic properties of the enzyme. It oxidizes glucose to gluconolactone and the subsequent reoxidation of the reduced FAD cofactor produces hydrogen peroxide. In addition, it oxidizes the reducing end of glucose oligomers. In the case of a pathogen attack, oligosaccharides are released due to the degradation of the plant cell wall by the pathogen. These oligosaccharides act as potential elicitors to the plant immune system. The spatial and temporal expression pattern of *Ha*-CHOX near the lesion depends on the nature of the pathogen indicating that this enzyme has a very distinct role in the plant immune response (35). While hydrogen peroxide has antimicrobial properties the role of the oxidation of oligosaccharides in the plant immune response still requires further investigations. More recently, another BBE-like enzyme involved in the plant immune response was discovered by Rajniak and coworkers (14). They identified a biosynthetic pathway that leads from tryptophan to 4-hydroxyindole-3-carbonyl nitrile (4-OH-ICN) with one of the steps, *i.e.* the oxidation of indole cyanohydrin to indol-3-carbonyl nitrile, being catalyzed by *At*BBE-like enzyme 3 (also referred to as flavin dependent oxidase 1, FOX1, Figure 9). The gene encoding for *At*BBE-like protein 3 is located in a gene cluster with *At*BBE-like enzymes 4, 5, 6 and 7, and the enzymes share a similar expression pattern indicating a similar role in plant metabolism (14, 72). They are strongly upregulated under osmotic stress and after the exposure to pathogens (32). However, no significant change in the levels of ICN metabolites for *At*BBE-like 4, 5, 6 and 7 knock down lines was observed suggesting that they might play a role in the biosynthesis of alternative plant products or the creation of multiple knock out lines might be necessary to observe an effect due to a redundant activity of *At*BBE-like 3, 4, 5, 6 and 7 (14).

Recently, we have discovered yet another oxidation reaction carried out by BBE-like enzymes that suggests an involvement in lignification (32). *At*BBE-like protein 13 and 15 were identified as monolignol oxidoreductases catalyzing the oxidation of sinapyl-, coniferyl- and *p*-coumaryl alcohol to their corresponding aldehydes. These so-called monolignols as well as their corresponding aldehydes are utilized as building blocks for lignin biosynthesis and thus it is conceivable that *At*BBE13 and 15 (and other monolignol oxidoreductases) shift the extracellular pool of building blocks toward the aldehydes and thus may directly affect the composition of lignin in the plant cell wall.

The natural electron acceptor of the monolignol oxidoreductases is not known yet. For cytokinin dehydrogenases, members of the FAD-linked oxidase superfamily subfamily 4 (SCOPE d.58.32:4),

benzoxazinones were identified as electron acceptors that subsequently shuttle the electrons to laccases and peroxidases (73). As peroxidases and laccases are responsible for the conversion of monolignols to their radical state prior to polymerization via free radical combination a similar mechanism is conceivable for monolignol oxidoreductases (74).

In the case of *AtBBE15*, replacement of the gate keeper residue controlling access to the oxygen pocket, *i.e.* leucine to valine significantly accelerated the rate of reaction of the reduced FAD cofactor with molecular oxygen (Figure 3) (33). This variant was shown to be a useful biocatalyst for the oxidation of a broad spectrum of allylic and benzylic alcohols to the corresponding aldehydes (33).

Reactions of BBE-like proteins from bacteria

Not only plants and fungi possess genes encoding BBE-like proteins but also certain bacteria possess enzymes of that family (23, 31, 41). According to our analysis, they appear in the clades 5b and 5c (see Figure 5). Studies of gene clusters related to the biosynthesis of antibiotics revealed that in many of these pathways BBE-like enzymes are employed mostly in one of the last steps of these processes (23, 41). By oxidizing alcohol or aldehyde groups or by desaturating the carbon skeleton these enzymes contribute to the potency of the antibiotics in terms of their defensive function (23, 41).

So far, six bacterial BBE-like enzymes from various species of *Streptomyces* (GilR, TamL and AknOx), *Nonomuraea* (EncM and Dbv29) and *Arthrobacter* (6HDNO) have been studied in detail (11, 18, 23, 24, 31, 41, 42, 75, 76). The reactions catalyzed by BBE-like enzymes from clade 5c and 5b (see Figure 5) are summarized in Figure 10 and 11, respectively.

Similar to carbohydrate oxidases found in fungi, GilR catalyzes the oxidation of a hemiacetal to its corresponding lactone (Figure 10). This reaction found in gilvocarcin V biosynthesis is of great importance as the resulting lactone moiety carries structural features that are crucial for the stability of the resulting antibiotic. By introducing the lactone function the naphthyl and benzene ring get “fixed” in the same plane and opening of the pyran ring is inhibited, which increases the stability and hence the potency of the synthesized metabolite (31, 41).

TamL from *Streptomyces* was also shown to be involved in antibiotic metabolism (tirandamycin biosynthesis), where it catalyzes the conversion of tirandamycin E to tirandamycin D. In this two-electron transfer reaction the C10 hydroxyl group is converted to a keto function (Figure 10), which can then be recognized by TamI, a cytochrome P450 monooxygenase that is required in the final step of tirandamycin biosynthesis. Like GilR, TamL is also part of antibiotic metabolism and enhances the potency of the pathway products, which was found to be determined by the number of oxidative modifications (23). In contrast to the reactions catalyzed by GilR and TamL, the conversion catalyzed by AknOx requires two subsequent oxidation steps. Since four electrons are extracted from the substrate(s) during the reactions, recycling of the flavin cofactor by molecular oxygen in between the two reaction steps is required. Whereas Dbv29 catalyzes the last two steps in A40926 (a teicoplanin

homolog) biosynthesis, *i.e.* the conversion of *N*-acyl glucosamine to *N*-acyl aminoglucuronic acid (Figure 10), and thereby oxidizes the same functional group twice, AknOx is involved in the oxidation of two different carbon atoms (31, 41). In the first reaction, the alcohol group in the C4 position of the rhodiose found in aclacinomycin N is oxidized to a keto function yielding the pathway intermediate aclacinomycin A. The resulting cinerulose A ring system (Figure 10) is then further oxidized by introducing a double bond between C2 and C3 of the ring system to give the final product aclacinomycin Y (Figure 10). The fact that two different loci of the substrate are subject to oxidation by AknOx also rationalizes the finding that two sets of catalytic residues are present in the active site of the enzyme, which is a unique and unprecedented architecture in the BBE-like enzyme family (42).

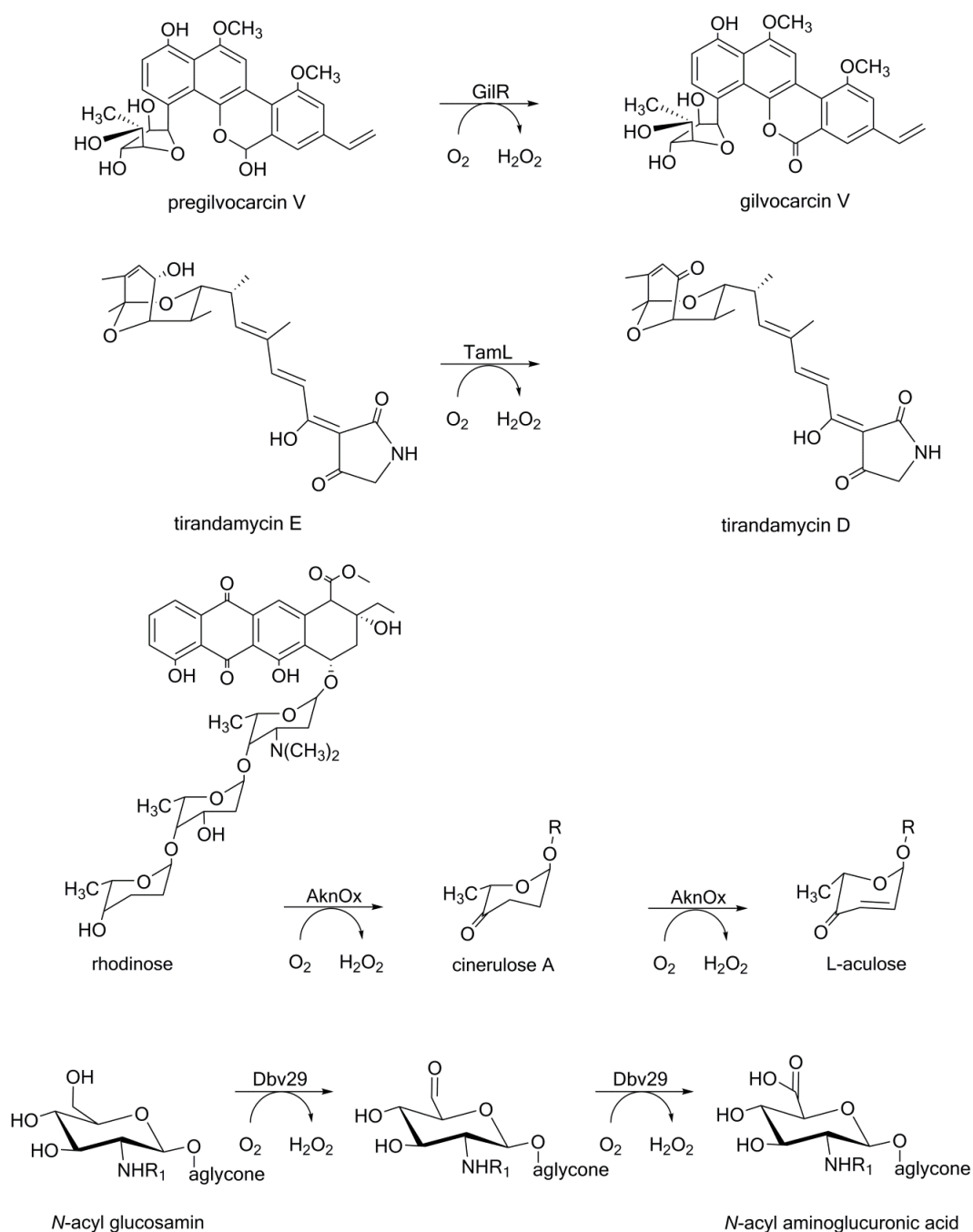


Figure 10: Reactions catalyzed by BBE-like enzymes from clade 5c. GilR catalyzes the conversion of pre-gilvocarcin V to gilvocarcin V. TamL converts tirandamycin E to tirandamycin D. AknOx catalyzes the four electron oxidation from rhodiose to cinerulose A to L-aculose. Dbv29 catalyzes a four electron oxidation that are the two last steps in the biosynthesis of A40926 (teicoplanin homolog) (24, 75). The enzyme converts an *N*-acyl glucosamine to an *N*-acyl aminoglucuronic acid.

While the bacterial BBE-like enzymes from clade 5c (Figure 5) bind the flavin cofactor in a bicovalent manner, 6HDNO and EncM were shown to attach the FAD via a single 8α -histidyl linkage. This change in cofactor binding does not only affect the oxidative power of these flavoproteins, but also influences the space in the active site and therefore strongly determines the structural features of the accepted substrate(s). In contrast to the bacterial BBE-like enzymes discussed so far, 6HDNO is not involved in an anabolic pathway, but is required for nicotine degradation. By oxidizing the C2 and C3 position of the pyrrolidine ring of 6-hydroxy-D-nicotine (Figure 11) the resulting product becomes destabilized and spontaneously hydrolyses to a ring open product. The resulting pseudooxynicotine is further metabolized yielding the TCA intermediate fumarate as the final product (76, 77).

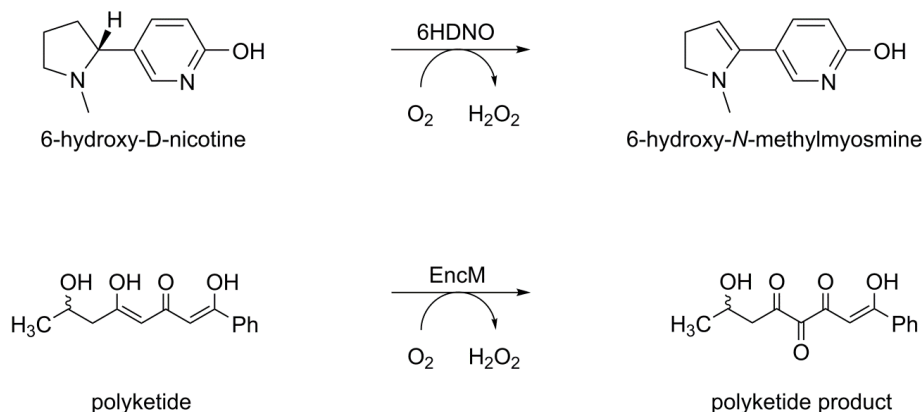


Figure 11: Reactions that are catalyzed by BBE-like enzymes belonging to clade 5b (Figure 5). 6HDNO oxidizes the C2 and C3 position of the pyrrolidine ring of 6-hydroxy-D-nicotine, the reaction product hydrolyses spontaneously (18). EncM is involved in the generation of enterocin. The enzyme catalyzes a Favorskii-type rearrangement as shown in more mechanistic detail in Figure 12 (11).

On the other hand, EncM participates again in antibiotic biosynthesis (enterocin formation), but the catalytic mechanism, shown in Figure 12, radically diverges from the previously discussed oxidation reactions.

As shown in Figure 12, the reduced flavin cofactor of EncM (**1**) is oxygenated to a rather unusual N-oxide intermediate (**2**) which deprotonates the bound substrate to yield intermediate **3** (11). Next, tautomer **4**, forms a covalent adduct with the deprotonated substrate **5**, which subsequently decays to the oxidized flavin (**6**) and a hydroxylated substrate-derived intermediate (**P_I**). Finally, the flavin oxidizes the newly introduced alcohol group to give the final product (**P_{II}**). Thus the final oxidation of the hydroxyl group regenerates the reduced state of the FAD cofactor priming the enzyme for the

turnover of another polyketide substrate (11). In other words, the enzyme does not require external electron delivery by a reducing agent such as NADH or NADPH, as is typically the case for internal monooxygenases because it has invented an ingenious self-feeding process to maintain the active (reduced) state of its FAD cofactor (78).

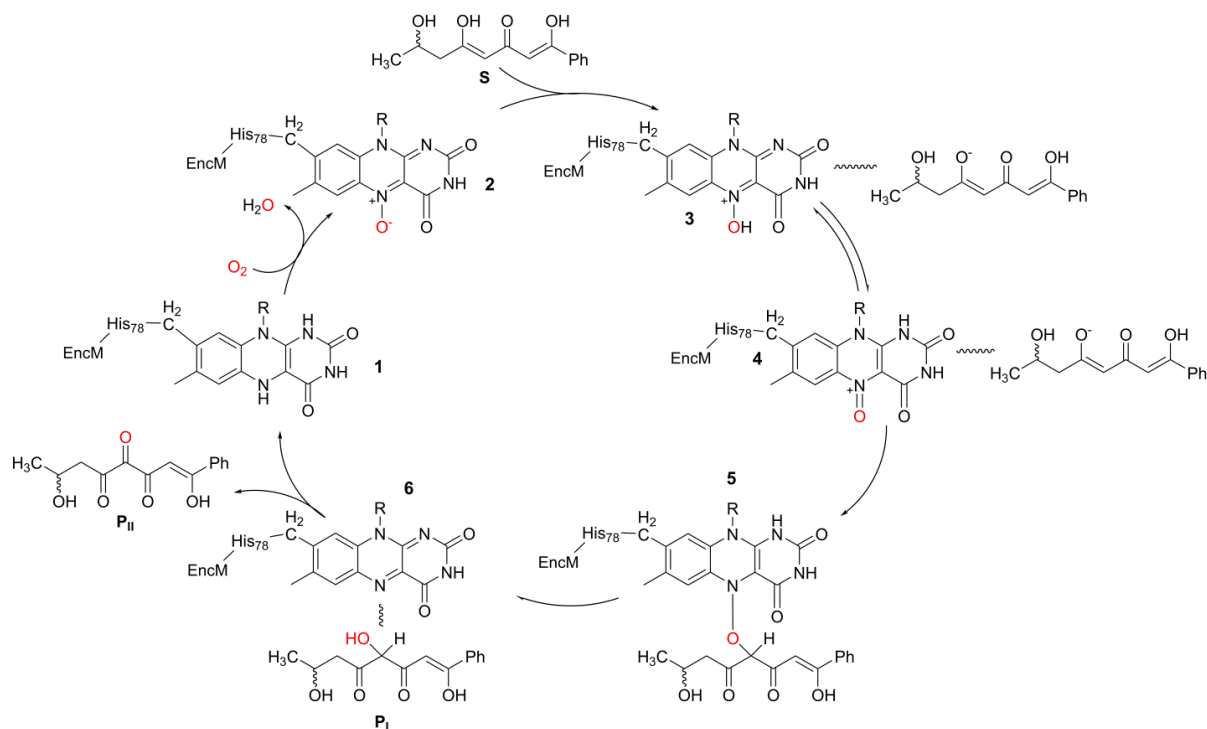


Figure 12: Proposed mechanism of EncM, adapted from (11). A detailed description of the reaction is given in the text.

Although the diversity of reactions catalyzed by bacterial BBE-like enzymes can already be glimpsed from the few reactions discussed here, it can be expected that the scope of reactions will be further expanded by future studies into the biosynthesis of natural products and in particular into the plethora of antibiotics generated in bacteria.

BBE-like enzymes from fungi

BBE-like enzymes from fungi can be divided into clades 5a and 5e (Figure 5). The latter clade appears to be associated with oligosaccharide oxidation, such as GOOX, XyLO, ChitO and LaO (Figure 13). A similar BBE-like enzyme activity was detected in the plant pathogen *Phytophthora infestans*. Apparently, this enzyme belongs to the predicted secretome that is required for the invasion of host plants (*PiBBE1-6*, Figure 5) (5, 36, 37, 79).

In these carbohydrate oxidases the active site type IV is highly conserved. GOOX and LaO are secreted enzymes that oxidize glucose-oligomers (*e.g.* cellotriose) at the reducing end to the

corresponding lactone, which subsequently spontaneously hydrolyzes (80) (38). Also, ChitO and XylO oxidize oligosaccharides that originate from the breakdown of the cell wall components chitin and xylan. Interestingly, GOOX and LaO share the same catalytic activity as *Ha*-CHOX that has been assigned a role in plant immune response, *i.e.* GOOX, LaO and *Pi*BBE1-6 might have a similar effect on the plant immune system, *i.e.* the down regulation of the plant immune system through deactivation of the elicitor function of the oligosaccharides.

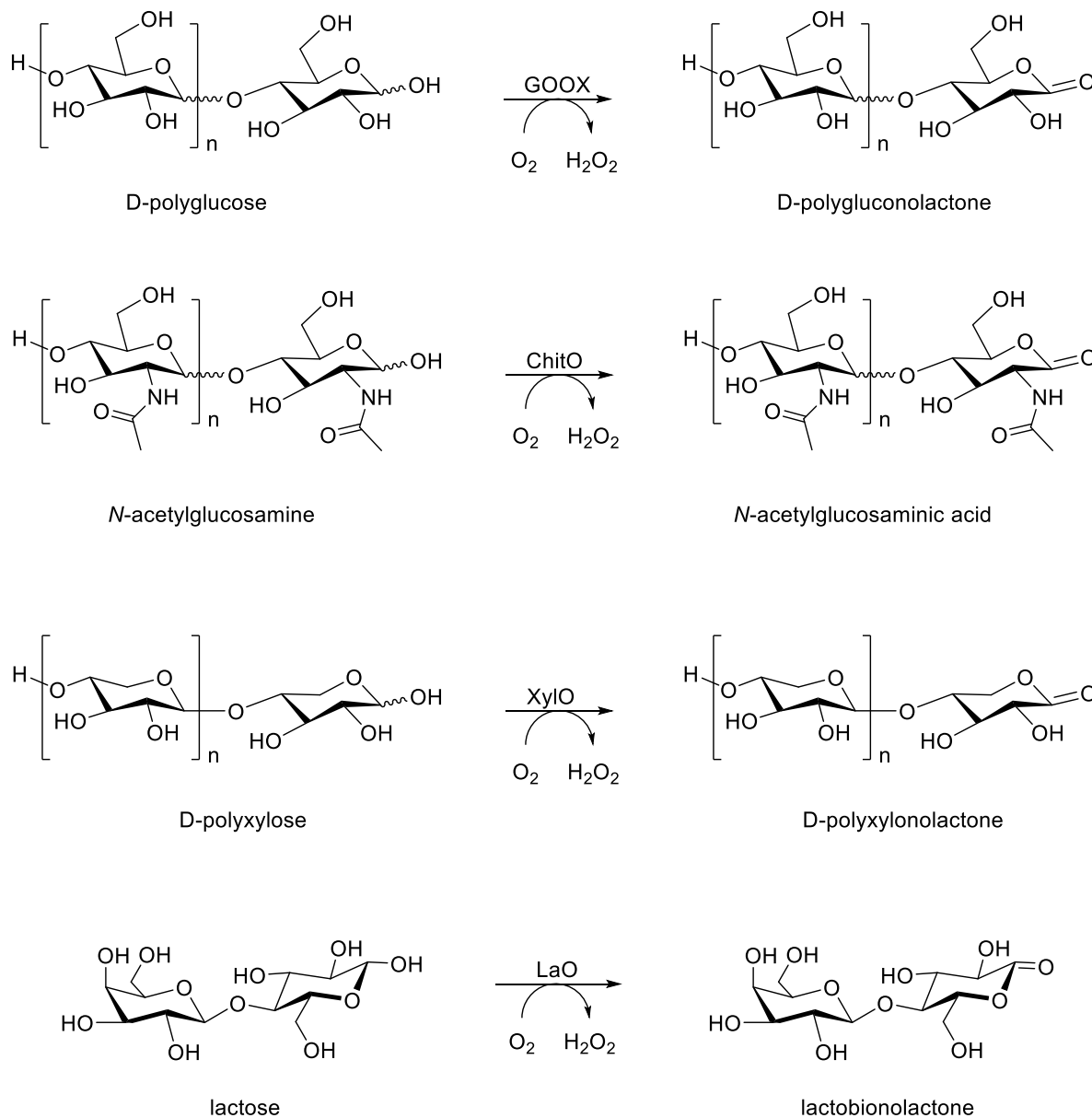


Figure 13: Reactions catalyzed by BBE-like proteins from fungi found in clade 5e (Figure 5). GOOX oxidizes various carbohydrates and oligomers of glucose to the corresponding lactones, which spontaneously hydrolyze (80). ChitO and XylO oxidize various carbohydrates with the highest specificity for the break down products of the cell wall polymers chitin and xylan, respectively (36, 37). LaO was found to be a secreted enzyme oxidizing various carbohydrates and oligomers of carbohydrates with the highest specificity for lactose (38).

In the clade 5a (Figure 5), enzymes catalyzing more complex reactions are found. Structural characterization of *MtVAO615* and *MtVAO713* from *Myceliophthora thermophila* was carried out by Ferrari and coworkers (81). In contrast to the oligosaccharide oxidases discussed in the previous paragraph, enzymes in this clade do not possess the active site type IV, but rather a histidine and glutamic acid in the corresponding positions of the two tyrosines in *AtBBE*-like enzyme 15, e.g. Tyr188 and Tyr479, respectively (Figure 4) (32). As shown in Figure 14, enzymes from clade 5a can be associated with more complex oxidations (ecdysteroid-22-oxidase, E22O and HPM9 from hypothemycin biosynthesis) and ring closure reactions catalyzed by *CnsA* and *EasE* in the biosynthesis of the indole alkaloid communesin and the ergot alkaloids, respectively (82, 83).

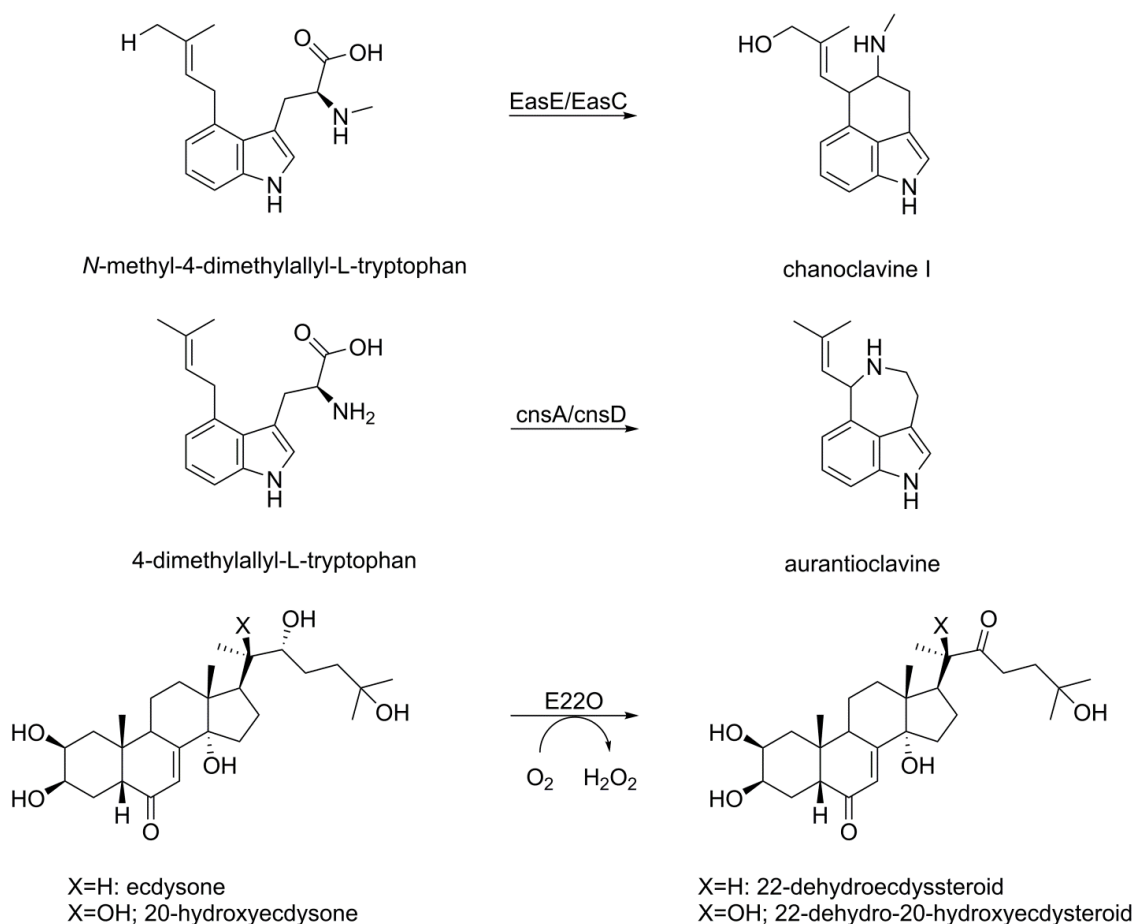


Figure 14: Reactions catalyzed by BBE-like enzymes from fungi belonging to clade 5a (Figure 4). *EasE* converts, presumably in cooperation with the catalase homolog *EasC*, the conversion of *N*-methyl-4-dimethylallyl-L-tryptophan to chanoclavine I. The reaction includes hydride transfer, decarboxylation and C-C bond formation (83). *CnsA* catalyzes the ring closure reaction from 4-dimethylallyl-L-tryptophan to auroantioclavine. Similar to *EasE*, *CnsA* was proposed to catalyze the reaction in cooperation with the catalase homolog *CnsD* (82). *E22O* from *N. rileyi* oxidizes and thereby deactivates the biological function of ecdysteroid from insects during fungal infection.

E22O is an ecdysteroid deactivating enzyme from the entomopathogenic fungus *Nomuraea rileyi* and catalyzes the oxidation of ecdysteroid-22 to the corresponding aldehyde. With this enzyme *N. rileyi*

manipulates the insect's hormone system in the course of the infection and thereby inhibits their molting, presumably to maintain appropriate growth conditions for the fungus (84). Other members of this clade are involved in alkaloid biosynthesis and, accordingly, the corresponding genes are located in gene clusters responsible for the biosynthesis of the respective alkaloids similar to the BBE-like enzymes from bacteria that are involved in antibiotic metabolism.

CnsA was found to be employed in the biosynthesis of communesins (82). It catalyzes the ring closure reaction from 4-dimethylallyl-L-tryptophane to aurantioclavine. The reaction involves decarboxylation and a hydride transfer step. Presumably, the reaction requires the action of both CnsA and the catalase homolog CnsD. Similarly, the BBE-like enzyme EasE was proposed to catalyze the ring closure reaction from *N*-methyl-4-dimethylallyl-L-tryptophan to chanoclavine I together with the catalase homolog EasC (85, 86). Again, this reaction involves a decarboxylation and a hydride transfer step, however the details of this proposed reaction remain to be elucidated. Interestingly, not only oxidoreductases from the BBE-like enzyme family are involved in ring closure reactions. Recently, an enzyme from *Aspergillus fumigatus* (termed fructosyl amine oxidase, FsqB) was shown to catalyze the oxidative ring closure reaction from *N*-methyl DOPA to isoquinoline in a reaction mechanism that was postulated to be analogous to the mechanism proposed for BBE (12, 87). Similar to many BBE-like proteins involved in alkaloid synthesis, *fsqb* is located in a cluster responsible for the expression of functionalities necessary for the production of fumisoquins (87).

Outlook

BBE-like enzymes share a common domain organization comprising a typical FAD-binding domain (FAD_binding_domain 4), a substrate binding domain ("BBE-domain"), which defines the family and sets it apart from other sub-families of the superfamily of FAD-linked oxidases. A remarkable feature of the BBE-like enzymes is the frequently occurring bi-covalent attachment to the protein backbone via a histidine and cysteine residue to positions 8 α and 6 of the isoalloxazine ring, respectively. This has significant electronic (redox potential) and structural implications enabling a plethora of oxidative reactions and accommodating an astonishing diverse range of complex substrates. This versatility results to a large extent from the inherent plasticity of the structural architecture that facilitates the redesign of the active site by adjusting the amino acid residues required for catalysis and/or substrate binding (Figure 4). The proliferation of the enzyme family in bacteria, fungi and particularly in plants clearly testifies to the evolutionary success of this concept. In view of the large number of uncharacterized BBE-like enzymes and the current efforts to understand the biosynthesis of natural products, it will be exciting to witness the future expansion of reactions and substrates catalyzed by members of the family as well as the physiological functions that BBE-like enzymes are involved in.

Acknowledgements

This work was supported by grants from the Austrian Science Fund (FWF) Doctoral program “Molecular Enzymology” W901 and P28678 to PM. ML has received a fellowship in the Erasmus Mundus Action 2 project (Avempace+ grant # 2014-0659).

References

1. Mattevi, A., Fraaije, M. W., Mozzarelli, A., Olivi, L., Coda, A., and van Berkel, W. J. (1997) Crystal structures and inhibitor binding in the octameric flavoenzyme vanillyl-alcohol oxidase: the shape of the active-site cavity controls substrate specificity. *Structure*. **5**, 907–20
2. Fraaije, M. W., van Berkel, W. J. H., Benen, J. A. E., Visser, J., and Mattevi, A. (1998) A novel oxidoreductase family sharing a conserved FAD-binding domain. *Trends Biochem. Sci.* **23**, 206–207
3. Leferink, N. G. H., Heuts, D. P. H. M., Fraaije, M. W., and van Berkel, W. J. H. (2008) The growing VAO flavoprotein family. *Arch. Biochem. Biophys.* **474**, 292–301
4. Kutchan, T. M. (1998) Chapter 7 Molecular genetics of plant alkaloid biosynthesis. *Alkaloids Chem. Biol.* **50**, 257–316
5. Huang, C.-H., Lai, W.-L., Lee, M.-H., Chen, C.-J., Vasella, A., Tsai, Y.-C., and Liaw, S.-H. (2005) Crystal structure of glucooligosaccharide oxidase from *Acremonium strictum*: a novel flavinylation of 6-*S*-cysteinyl, 8 α -*N1*-histidyl FAD. *J. Biol. Chem.* **280**, 38831–38838
6. Huang, C. H., Winkler, A., Chen, C. L., Lai, W. L., Tsai, Y. C., Macheroux, P., and Liaw, S. H. (2008) Functional roles of the 6-*S*-cysteinyl, 8 α -*N1*-histidyl FAD in glucooligosaccharide oxidase from *Acremonium strictum*. *J. Biol. Chem.* **283**, 30990–30996
7. Winkler, A., Hartner, F., Kutchan, T. M., Glieder, A., and Macheroux, P. (2006) Biochemical evidence that berberine bridge enzyme belongs to a novel family of flavoproteins containing a bi-covalently attached FAD cofactor *. *J. Biol. Chem.* **281**, 21276–21285
8. Winkler, A., Kutchan, T. M., and Macheroux, P. (2007) 6-*S*-cysteinyl-ation of bi-covalently attached FAD in berberine bridge enzyme tunes the redox potential for optimal activity. *J. Biol. Chem.* **282**, 24437–24443
9. Winkler, A., Motz, K., Riedl, S., Puhl, M., Macheroux, P., and Gruber, K. (2009) Structural and mechanistic studies reveal the functional role of bicovalent flavinylation in berberine bridge enzyme. *J. Biol. Chem.* **284**, 19993–20001
10. Massey, V. (1994) Activation of molecular oxygen by flavins and flavoproteins. *J. Biol. Chem.* **269**, 22459–22462
11. Teufel, R., Miyanaga, A., Michaudel, Q., Stull, F., Louie, G., Noel, J. P., Baran, P. S., Palfey, B., and Moore, B. S. (2013) Flavin-mediated dual oxidation controls an enzymatic Favorskii-type rearrangement. *Nature*. **503**, 552–556
12. Winkler, A., Łyskowski, A., Riedl, S., Puhl, M., Kutchan, T. M., Macheroux, P., and Gruber, K. (2008) A concerted mechanism for berberine bridge enzyme. *Nat. Chem. Biol.* **4**, 739–741
13. Taura, F., Morimoto, S., and Shoyama, Y. (1996) Purification and characterization of cannabidiolic-acid synthase from *Cannabis sativa L.* Biochemical analysis of a novel enzyme that catalyzes the oxidocyclization of cannabigerolic acid to cannabidiolic acid. *J. Biol. Chem.* **271**, 17411–17416

14. Rajniak, J., Barco, B., Clay, N. K., and Sattely, E. S. (2015) A new cyanogenic metabolite in *Arabidopsis* required for inducible pathogen defence. *Nature*. **525**, 375–379
15. Finn, R. D., Coghill, P., Eberhardt, R. Y., Eddy, S. R., Mistry, J., Mitchell, A. L., Potter, S. C., Punta, M., Qureshi, M., Sangrador-Vegas, A., Salazar, G. A., Tate, J., and Bateman, A. (2016) The Pfam protein families database: Towards a more sustainable future. *Nucleic Acids Res.* **44**, D279–D285
16. Zafred, D., Steiner, B., Teufelberger, A. R., Hromic, A., Karplus, P. A., Schofield, C. J., Wallner, S., and Macheroux, P. (2015) Rationally engineered flavin-dependent oxidase reveals steric control of dioxygen reduction. *FEBS J.* **282**, 3060–3074
17. Baron, R., Riley, C., Chenprakhon, P., Thotsaporn, K., Winter, R. T., Alfieri, A., Forneris, F., van Berkel, W. J., Chaiyen, P., Fraaije, M. W., Mattevi, A., and McCammon, J. A. (2009) Multiple pathways guide oxygen diffusion into flavoenzyme active sites. *Proc Natl Acad Sci U S A.* **106**, 10603–10608
18. Mauch, L., Bichler, V., and Brandsch, R. (1989) Site-directed mutagenesis of the FAD-binding histidine of 6-hydroxy-D-nicotine oxidase. Consequences on flavinylation and enzyme activity. *FEBS Lett.* **257**, 86–88
19. Daniel, B., Wallner, S., Steiner, B., Oberdorfer, G., Kumar, P., van der Graaff, E., Roitsch, T., Sensen, C. W., Gruber, K., and Macheroux, P. (2016) Structure of a berberine bridge enzyme-like enzyme with an active site specific to the plant family Brassicaceae. *PLoS One.* **11**, e0156892
20. Kopacz, M. M., and Fraaije, M. W. (2014) Turning a monocovalent flavoprotein into a bicovalent flavoprotein by structure-inspired mutagenesis. *Bioorganic Med. Chem.* **22**, 5621–5627
21. Heuts, D. P. H. M., Scrutton, N. S., Mcintire, W. S., and Fraaije, M. W. (2009) What's in a covalent bond? On the role and formation of covalently bound flavin cofactors. **276**, 3405–3427
22. Heuts, D. P. H. M., Winter, R. T., Damsma, G. E., Janssen, D. B., and Fraaije, M. W. (2008) The role of double covalent flavin binding in chito-oligosaccharide oxidase from *Fusarium graminearum*. *Biochem. J.* **413**, 175–183
23. Carlson, J. C., Li, S., Gunatilleke, S. S., Anzai, Y., Burr, D. A., Podust, L. M., and Sherman, D. H. (2011) Tirandamycin biosynthesis is mediated by co-dependent oxidative enzymes. *Nat. Chem.* **3**, 628–633
24. Liu, Y.-C., Li, Y.-S., Lyu, S.-Y., Hsu, L.-J., Chen, Y.-H., Huang, Y.-T., Chan, H.-C., Huang, C.-J., Chen, G.-H., Chou, C.-C., Tsai, M.-D., and Li, T.-L. (2011) Interception of teicoplanin oxidation intermediates yields new antimicrobial scaffolds. *Nat. Chem. Biol.* **7**, 304–309
25. Mattevi, A. (2006) To be or not to be an oxidase: challenging the oxygen reactivity of flavoenzymes. *Trends Biochem. Sci.* **31**, 276–283

26. Chaiyen, P., Fraaije, M. W., and Mattevi, A. (2012) The enigmatic reaction of flavins with oxygen. *Trends Biochem. Sci.* **37**, 373–380
27. McManaman, J. L., and Bain, D. L. (2002) Structural and conformational analysis of the oxidase to dehydrogenase conversion of xanthine oxidoreductase. *J. Biol. Chem.* **277**, 21261–21268
28. Nishino, T., Okamoto, K., Kawaguchi, Y., Hori, H., Matsumura, T., Eger, B. T., Pai, E. F., and Nishino, T. (2005) Mechanism of the conversion of xanthine dehydrogenase to xanthine oxidase: Identification of the two cysteine disulfide bonds and crystal structure of a non-convertible rat liver xanthine dehydrogenase mutant. *J. Biol. Chem.* **280**, 24888–24894
29. Leferink, N. G. H., Fraaije, M. W., Joosten, H. J., Schaap, P. J., Mattevi, A., and van Berkel, W. J. H. (2009) Identification of a gatekeeper residue that prevents dehydrogenases from acting as oxidases. *J. Biol. Chem.* **284**, 4392–4397
30. Wallner, S., Winkler, A., Riedl, S., Dully, C., Horvath, S., Gruber, K., and Macheroux, P. (2012) Catalytic and structural role of a conserved active site histidine in berberine bridge enzyme. *Biochemistry.* **51**, 6139–6147
31. Noinaj, N., Bosserman, M. a., Schickli, M. A., Piszczek, G., Kharel, M. K., Pahari, P., Buchanan, S. K., and Rohr, J. (2011) The crystal structure and mechanism of an unusual oxidoreductase, GilR, involved in gilvocarcin V biosynthesis. *J. Biol. Chem.* **286**, 23533–23543
32. Daniel, B., Pavkov-Keller, T., Steiner, B., Dordic, A., Gutmann, A., Nidetzky, B., Sensen, C. W., Van Der Graaff, E., Wallner, S., Gruber, K., and Macheroux, P. (2015) Oxidation of monolignols by members of the berberine bridge enzyme family suggests a role in plant cell wall metabolism. *J. Biol. Chem.* **290**, 18770–18781
33. Pils, S., Schnabl, K., Wallner, S., Kljajic, M., Kupresanin, N., Breinbauer, R., Fuchs, M., Rocha, R., Schrittwieser, J. H., Kroutil, W., Daniel, B., and Macheroux, P. (2016) Characterization of the monolignol oxidoreductase *AtBBE*-like protein 15 L182V for biocatalytic applications. *Journal Mol. Catal. B, Enzym.* **133**, S6–S14
34. Zafred, D., Nandy, A., Pump, L., Kahlert, H., and Keller, W. (2013) Crystal structure and immunologic characterization of the major grass pollen allergen Phl p 4. *J. Allergy Clin. Immunol.* 10.1016/j.jaci.2013.03.021
35. Custers, J. H. H. V, Harrison, S. J., Sela-Buurlage, M. B., Van Deventer, E., Lageweg, W., Howe, P. W., Van Der Meijs, P. J., Ponstein, A. S., Simons, B. H., Melchers, L. S., and Stuiver, M. H. (2004) Isolation and characterisation of a class of carbohydrate oxidases from higher plants, with a role in active defence. *Plant J.* **39**, 147–160

36. Ferrari, A. R., Rozeboom, H. J., Dobruchowska, J. M., Van Leeuwen, S. S., Vugts, A. S. C., Koetsier, M. J., Visser, J., Fraaije, M. W., and Hart, G. (2016) Discovery of a xylooligosaccharide oxidase from *Myceliophthora thermophila* C1. *J. Biol. Chem.* **291**, 23709–23718
37. Heuts, D. P. H. M., Janssen, D. B., and Fraaije, M. W. (2007) Changing the substrate specificity of a chitoooligosaccharide oxidase from *Fusarium graminearum* by model-inspired site-directed mutagenesis. *FEBS Lett.* **581**, 4905–4909
38. Ahmad, S. K., Brinch, D. S., Friis, E. P., and Pedersen, P. B. (2004) Toxicological studies on lactose oxidase from *Microdochium nivale* expressed in *Fusarium venenatum*. **39**, 256–270
39. Liaw, S., Lee, D. Y., Chow, L. P., Lau, G. X., and Su, S. N. (2001) Structural characterization of the 60-kDa bermuda grass pollen isoallergens, a covalent flavoprotein. *Biochem. Biophys. Res. Commun.* **280**, 738–743
40. Letunic, I., and Bork, P. (2016) Interactive tree of life (iTOL) v3: an online tool for the display and annotation of phylogenetic and other trees. *Nucleic Acids Res.* 10.1093/nar/gkw290
41. Kharel, M. K., Pahari, P., Lian, H., and Rohr, J. (2009) GilR, an unusual lactone-forming enzyme involved in gilvocarcin biosynthesis. *ChemBioChem.* **10**, 1305–1308
42. Alexeev, I., Sultana, A., Mäntsälä, P., Niemi, J., and Schneider, G. (2007) Aclacinomycin oxidoreductase (AknOx) from the biosynthetic pathway of the antibiotic aclacinomycin is an unusual flavoenzyme with a dual active site. *Proc. Natl. Acad. Sci. U. S. A.* **104**, 6170–5
43. Lutzoni, F., Kauff, F., Cox, C. J., McLaughlin, D., Celio, G., Dentinger, C., Padamsee, M., Hibbett, D., James, T. Y., Baloch, E., Grube, M., Reeb, V., Hofstetter, V., Schoch, C., Arnold, A. E., Miadlikowska, J., Spatafora, J., Johnson, D., Hambleton, S., Crockett, M., Shoemaker, R., Sung, G. H., Lücking, R., Lumbsch, T., O'Donnell, K., Binder, M., Diederich, P., Ertz, D., Gueidan, C., Hansen, K., Harris, R. C., Hosaka, K., Lim, Y. W., Matheny, B., Nishida, H., Pfister, D., Rogers, J., Rossman, A., Schmitt, I., Sipman, H., Stone, J., Sugiyama, J., Yahr, R., and Vilgalys, R. (2004) Assembling the fungal tree of life: Progress, classification, and evolution of subcellular traits. *Am. J. Bot.* **91**, 1446–1480
44. Adl, S. M., Simpson, A. G. B., Lane, C. E., Luke, J. D., Bass, D., Bowser, S. S., Brown, M. W., Burki, F., Dunthorn, M., Hampl, V., Heiss, A., Hoppenrath, M., Lara, E., Gall, L. Le, Lynn, D. H., McManus, H., Mitchell, E. A. D., Mozley-Stanridge, S. E., Parfrey, L. W., Pawlowski, J., Rueckert, S., Shadwick, L., Schoch, C. L., Smirnov, A., and Spiegel, F. W. (2012) The revised classification of eukaryotes. *J. Eukaryot. Microbiol.* **59**, 429–493
45. Kutchan, T. M., and Dittrich, H. (1995) Characterization and mechanism of the berberine bridge enzyme, a covalently flavinylated oxidase of benzophenanthridine alkaloid biosynthesis in plants. *J. Biol. Chem.* **270**, 24475–24481

46. Sirikantaramas, S., Morimoto, S., Shoyama, Y., Ishikawa, Y., Wada, Y., Shoyama, Y., and Taura, F. (2004) The gene controlling marijuana psychoactivity: molecular cloning and heterologous expression of $\Delta 1$ -tetrahydrocannabinolic acid synthase from *Cannabis sativa* L. *J. Biol. Chem.* **279**, 39767–39774
47. Steffens, P., Nagakura, N., and Zenk, M. H. (1985) Purification and characterization of the berberine bridge enzyme from berberis beaniana cell cultures. *Phytochemistry.* **24**, 2577–2583
48. Amann, M., and H. Zenk, M. (1987) Preparation of dehydrobenzylisoquinolines by immobilized (S)-tetrahydroprotoberberine oxidase from plant cell cultures. *Phytochemistry.* **26**, 3235–3240
49. Taura, F., Sirikantaramas, S., Shoyama, Y., Yoshikai, K., Shoyama, Y., and Morimoto, S. (2007) Cannabidiolic-acid synthase, the chemotype-determining enzyme in the fiber-type *Cannabis sativa*. *FEBS Lett.* **581**, 2929–2934
50. Rink, E., and Böhm, H. (1975) Conversion of reticuline into scoulerine by a cell free preparation from *Macleaya microcarpa* cell suspension cultures. *FEBS Lett.* **49**, 396–399
51. Kutchan, T. M., Bock, A., and Dittrich, H. (1994) Heterologous expression of the plant proteins strictosidine synthase and berberine bridge enzyme in insect cell culture. *Phytochemistry.* **35**, 353–360
52. Liscombe, D. K., and Facchini, P. J. (2008) Evolutionary and cellular webs in benzylisoquinoline alkaloid biosynthesis. *Curr. Opin. Biotechnol.* **19**, 173–180
53. Gaweska, H. M., Roberts, K. M., and Fitzpatrick, P. F. (2012) Isotope effects suggest a stepwise mechanism for berberine bridge enzyme. *Biochemistry.* **51**, 7342–7347
54. Chou, W. M., and Kutchan, T. M. (1998) Enzymatic oxidations in the biosynthesis of complex alkaloids. *Plant J.* **15**, 289–300
55. Amann, M., Nagakura, N., and Zenk, M. H. (1988) Purification and properties of (S)-tetrahydroprotoberberine oxidase from suspension-cultured cells of *Berberis wilsoniae*. *Eur. J. Biochem.* **175**, 17–25
56. Gesell, A., Chávez, M. L. D., Kramell, R., Piotrowski, M., Macheroux, P., and Kutchan, T. M. (2011) Heterologous expression of two FAD-dependent oxidases with (S)-tetrahydroprotoberberine oxidase activity from *Argemone mexicana* and *Berberis wilsoniae* in insect cells. *Planta.* **233**, 1185–1197
57. Winkler, A., Puhl, M., Weber, H., Kutchan, T. M., Gruber, K., and Macheroux, P. (2009) Berberine bridge enzyme catalyzes the six electron oxidation of (S)-reticuline to dehydroscoulerine. *Phytochemistry.* **70**, 1092–1097
58. Shoyama, Y., Takeuchi, A., Taura, F., Tamada, T., Adachi, M., Kuroki, R., Shoyama, Y., and Morimoto, S. (2005) Crystallization of $\Delta 1$ -tetrahydrocannabinolic acid (THCA) synthase from *Cannabis sativa*. *Acta Crystallogr. Sect. F Struct. Biol. Cryst. Commun.* **61**, 799–801

59. Shoyama, Y., Tamada, T., Kurihara, K., Takeuchi, A., Taura, F., Arai, S., Blaber, M., Shoyama, Y., Morimoto, S., and Kuroki, R. (2012) Structure and function of Δ 1-tetrahydrocannabinolic acid (THCA) synthase, the enzyme controlling the psychoactivity of *Cannabis sativa*. *J. Mol. Biol.* **423**, 96–105
60. Kajikawa, M., Shoji, T., Kato, A., and Hashimoto, T. (2011) Vacuole-localized berberine bridge enzyme-like proteins are required for a late step of nicotine biosynthesis in tobacco. *Plant Physiol.* **155**, 2010–2022
61. Lewis, R. S., Lopez, H. O., Bowen, S. W., Andres, K. R., Steede, W. T., and Dewey, R. E. (2015) Transgenic and mutation-based suppression of a berberine bridge enzyme-like (BBL) gene family reduces alkaloid content in field-grown tobacco. *PLoS One*. 10.1371/journal.pone.0117273
62. Ober, D., and Kaltenecker, E. (2009) Pyrrolizidine alkaloid biosynthesis, evolution of a pathway in plant secondary metabolism. *Phytochemistry*. **70**, 1687–1695
63. Hansen, O. C., and Stougaard, P. (1997) Hexose oxidase from the red alga *Chondrus crispus* - Purification, molecular cloning, and expression in *Pichia pastoris*. *J. Biol. Chem.* **272**, 11581–11587
64. Van der Lugt, J. P. (1998) Evaluation of methods for chemical and biological carbohydrate oxidation
65. Poulsen, C., and Hostrup, P. B. (1998) Purification and characterization of a hexose oxidase with excellent strengthening effects in bread. *Cereal Chem.* **75**, 51–57
66. Wolff, a M., Hansen, O. C., Poulsen, U., Madrid, S., and Stougaard, P. (2001) Optimization of the production of *Chondrus crispus* hexose oxidase in *Pichia pastoris*. *Protein Expr. Purif.* **22**, 189–199
67. Carter, C. J., and Thornburg, R. W. (2004) Tobacco nectarin V is a flavin-containing berberine bridge enzyme-like protein with glucose oxidase activity. *Plant Physiol.* **134**, 460–469
68. Harper, A. D., Stalnaker, S. H., Wells, L., Darvill, A., Thornburg, R., and York, W. S. (2010) Interaction of Nectarin 4 with a fungal protein triggers a microbial surveillance and defense mechanism in nectar. *Phytochemistry*. **71**, 1963–1969
69. Kaur, R., Macleod, J., Foley, W., and Nayudu, M. (2006) Gluconic acid: An antifungal agent produced by *Pseudomonas* species in biological control of take-all. *Phytochemistry*. **67**, 595–604
70. Wojtaszek, P. (1997) Oxidative burst: an early plant response to pathogen infection. *Biochem. J.* **322 (Pt 3)**, 681–692

71. Stumvoll, S., Lidholm, J., Thunberg, R., DeWitt, A. M., Eibesteiner, P., Swoboda, I., Bugajska-Schretter, A., Spitzauer, S., Vangelista, L., Kazemi-Shirazi, L., Sperr, W. R., Valent, P., Kraft, D., and Valenta, R. (2002) Purification, structural and immunological characterization of a timothy grass (*Phleum pratense*) pollen allergen, Phl p 4, with cross-reactive potential. *Biol. Chem.* **383**, 1383–1396
72. Chae, L., Kim, T., Nilo-Poyanco, R., and Rhee, S. Y. (2014) Genomic signatures of specialized metabolism in plants. *Science*. **344**, 510–3
73. Frébortová, J., Novák, O., Frébort, I., and Jorda, R. (2010) Degradation of cytokinins by maize cytokinin dehydrogenase is mediated by free radicals generated by enzymatic oxidation of natural benzoxazinones. *Plant J.* **61**, 467–481
74. Vanholme, R., Demedts, B., Morreel, K., Ralph, J., and Boerjan, W. (2010) Lignin biosynthesis and structure. *Plant Physiol.* **153**, 895–905
75. Li, Y.-S., Ho, J.-Y., Huang, C.-C., Lyu, S.-Y., Lee, C.-Y., Huang, Y.-T., Wu, C.-J., Chan, H.-C., Huang, C.-J., Hsu, N.-S., Tsai, M.-D., and Li, T.-L. (2007) A unique flavin mononucleotide-linked primary alcohol oxidase for glycopeptide A40926 maturation. *J. Am. Chem. Soc.* **129**, 13384–13385
76. Koetter, J. W. A., and Schulz, G. E. (2005) Crystal structure of 6-hydroxy-D-nicotine oxidase from *Arthrobacter nicotinovorans*. *J. Mol. Biol.* **352**, 418–428
77. Yu, H., Tang, H., Li, Y., and Xu, P. (2015) Molybdenum-containing nicotine hydroxylase genes in a nicotine degradation pathway that is a variant of the pyridine and pyrrolidine pathways. *Appl. Environ. Microbiol.* **81**, 8330–8338
78. Huijbers, M. M. E., Montersino, S., Westphal, A. H., Tischler, D., and Van Berkel, W. J. H. (2014) Flavin dependent monooxygenases. *Arch. Biochem. Biophys.* **544**, 2–17
79. Raffaele, S., Win, J., Cano, L. M., and Kamoun, S. (2010) Analyses of genome architecture and gene expression reveal novel candidate virulence factors in the secretome of *Phytophthora infestans*. *BMC Genomics.* **11**, 637
80. Lin, S.-F., Yang, T.-Y., Inukai, T., Yamasaki, M., and Tsai, Y.-C. (1991) Purification and characterization of a novel glucooligosaccharide oxidase from *Acremonium strictum* T1. *Biochim. Biophys. Acta - Protein Struct. Mol. Enzymol.* **1118**, 41–47
81. Ferrari, A. R. (2017) *Exploring flavin-containing carbohydrate oxidases*. Ph.D. thesis, University of Groningen
82. Lin, H. C., Chiou, G., Chooi, Y. H., McMahon, T. C., Xu, W., Garg, N. K., and Tang, Y. (2015) Elucidation of the concise biosynthetic pathway of the communesin indole alkaloids. *Angew. Chemie - Int. Ed.* **54**, 3004–3007

83. Nielsen, C. A. F., Folly, C., Hatsch, A., Molt, A., Schröder, H., O'Connor, S. E., and Naesby, M. (2014) The important ergot alkaloid intermediate chanoclavine-I produced in the yeast *Saccharomyces cerevisiae* by the combined action of EasC and EasE from *Aspergillus japonicus*. *Microb. Cell Fact.* **13**, 95
84. Kiuchi, M., Yasui, H., Hayasaka, S., and Kamimura, M. (2003) Entomogenous fungus *Nomuraea rileyi* inhibits host insect molting by C22-oxidizing inactivation of hemolymph ecdysteroids. *Arch. Insect Biochem. Physiol.* **52**, 35–44
85. Nielsen, C., Folly, C., Hatsch, A., Molt, A., Schröder, H., O Connor, S. E., and Naesby, M. (2014) The important ergot alkaloid intermediate chanoclavine-I produced in the yeast. *Microb. Cell Fact.* **13**, 95
86. Lorenz, N., Olšovská, J., Šulc, M., and Tudzynski, P. (2010) Alkaloid cluster gene *ccsA* of the ergot fungus *Claviceps purpurea* encodes chanoclavine I synthase, a flavin adenine dinucleotide-containing oxidoreductase mediating the transformation of *N*-methyl-dimethylallyltryptophan to chanoclavine I. *Appl. Environ. Microbiol.* **76**, 1822–1830
87. Baccile, J. A., Spraker, J. E., Le, H. H., Brandenburger, E., Gomez, C., Bok, J. W., Macheleidt, J., Brakhage, A. A., Hoffmeister, D., Keller, N. P., and Schroeder, F. C. (2016) Plant-like biosynthesis of isoquinoline alkaloids in *Aspergillus fumigatus*. *Nat. Chem. Biol.* **12**, 1–9

Supplementary information

Supplementary Table S1: Sequences used for the phylogenetic analysis of the FAD linked oxidase superfamily.

BBE-like proteins				
Abbreviation	Uniprot	PDB	Organism	Kingdom
HOX	P93762		<i>Chondrus crispus</i>	Algae
GilR	Q7X2G7	3POP	<i>Streptomyces griseoflavus</i>	Bacteria
AknOx	Q0PCD7	2IPI	<i>Streptomyces galilaeus</i>	Bacteria
Dbv29	Q7WZ62	2WDW	<i>Nonomuraea sp. ATCC 39727</i>	Bacteria
TamL	D3Y1I2	2Y08	<i>Streptomyces sp. 307-9</i>	Bacteria
6HDNO	P08159		<i>Arthrobacter oxydans</i>	Bacteria
EncM	Q9KHK2	4XLO	<i>Streptomyces maritimus</i>	Bacteria
EasE	Q4WZ61		<i>Neosartorya fumigata</i>	Fungi
NfBBE	B0XPK7		<i>Neosartorya fumigata</i>	Fungi
MtVAO615	G2QDQ9		<i>Myceliophthora thermophila</i>	Fungi
E22O	I0J0L0		<i>Metarhizium rileyi</i>	Fungi
MtVAO713	G2QMS8		<i>Myceliophthora thermophila</i>	Fungi
HPM9	B3FWS5		<i>Hypomyces subiculosus</i>	Fungi
PiBBE4	D0MXI8		<i>Phytophthora infestans</i>	Fungi
PiBBE5	D0MXJ2		<i>Phytophthora infestans</i>	Fungi
PiBBE3	D0MXI7		<i>Phytophthora infestans</i>	Fungi
PiBBE2	D0N574		<i>Phytophthora infestans</i>	Fungi
PiBBE1	D0N569		<i>Phytophthora infestans</i>	Fungi
LaO	I1SB12	3RJA	<i>Microdochium nivale</i>	Fungi
XyIO	G2QG48	5K8E	<i>Myceliophthora thermophila</i>	Fungi
GOOX	Q6PW77	2AXR	<i>Sarocladium strictum</i>	Fungi
ChitO	I1S2K2		<i>Gibberella zeae</i>	Fungi
PiBBE6	D0P2Y8		<i>Phytophthora infestans</i>	Fungi
VcBBE	D8TI34		<i>Volvox carteri f. nagariensis</i>	Viridiplantae
SmBBE	D8SFA1		<i>Selaginella moellendorffii</i>	Viridiplantae
PpBBE3	A9T8D8		<i>Physcomitrella patens subsp. patens</i>	Viridiplantae
Nec5	Q84N20		<i>Nicotiana langsdorffii x Nicotiana sanderae</i>	Viridiplantae
AtBBE12	Q9SA89		<i>Arabidopsis thaliana</i>	Viridiplantae
Ls-CHOX	Q8SA60		<i>Lactuca sativa</i>	Viridiplantae
Ha-CHOX	Q8SA59		<i>Helianthus annuus</i>	Viridiplantae
AtBBE14	F4HV09		<i>Arabidopsis thaliana</i>	Viridiplantae
AtBBE10	Q9SA87		<i>Arabidopsis thaliana</i>	Viridiplantae
AtBBE3	Q9FZC4		<i>Arabidopsis thaliana</i>	Viridiplantae

AtBBE5	Q9FZC6		<i>Arabidopsis thaliana</i>	Viridiplantae
AtBBE22	Q9SUC6		<i>Arabidopsis thaliana</i>	Viridiplantae
AtBBE26	Q9FKU8		<i>Arabidopsis thaliana</i>	Viridiplantae
AtBBE15	O64743	4UD8	<i>Arabidopsis thaliana</i>	Viridiplantae
AtBBE13			<i>Arabidopsis thaliana</i>	Viridiplantae
AtBBE28	Q9FI21	5D79	<i>Arabidopsis thaliana</i>	Viridiplantae
THCAS	Q8GTB6	3VTE	<i>Cannabis sativa</i>	Viridiplantae
CBDAS	A0A0E3TJM8		<i>Cannabis sativa</i>	Viridiplantae
Phl p 4	Q2I6V7	3TSH	<i>Phleum pratense</i>	Viridiplantae
BG60	Q5QJ60	4DNS	<i>Cynodon dactylon</i>	Viridiplantae
BBLd	F1T162		<i>Nicotiana Tabacum</i>	Viridiplantae
BBLc	F1T161		<i>Nicotiana Tabacum</i>	Viridiplantae
BBLb	A7WPL6		<i>Nicotiana Tabacum</i>	Viridiplantae
BBLa	F1T160		<i>Nicotiana Tabacum</i>	Viridiplantae
EcBBE	P30986	3D2D	<i>Eschscholzia californica</i>	Viridiplantae
CvBBE	E1ZHF1		<i>Chlorella variabilis</i>	Viridiplantae
MpBB1	A0A176WJ71		<i>Marchantia polymorpha subsp. polym.</i>	Viridiplantae
PpBBE1	A9SWH5		<i>Physcomitrella patens subsp. patens</i>	Viridiplantae
STOX	F1BVB7		<i>Argemone mexicana</i>	Viridiplantae
AtBBE19	Q9SVG4		<i>Arabidopsis thaliana</i>	Viridiplantae
AtBBE21	Q9SVG3		<i>Arabidopsis thaliana</i>	Viridiplantae
AtBBE2	Q9SA99		<i>Arabidopsis thaliana</i>	Viridiplantae
AtBBE1	Q9LPC3		<i>Arabidopsis thaliana</i>	Viridiplantae
CnsA	none		<i>Penicillium expansum</i>	Fungi

FAD-linked oxidases

DdADHAPS	O96759	2UUU	<i>Dictyostelium discoideum</i>	Amoebozoa
AldO	Q9ZBU1	2VFR	<i>Streptomyces coelicolor</i>	Bacteria
RPA1076	Q6NAV4	3PM9	<i>Rhodopseudomonas palustris</i>	Bacteria
EugO	Q0SBK1	5FXD	<i>Rhodococcus jostii</i>	Bacteria
PCMH	P09788	1DII	<i>Pseudomonas putida</i>	Bacteria
MurB	Q9HZM7	4JAY	<i>Pseudomonas aeruginosa</i>	Bacteria
DprE	P9WJF1	4FDN	<i>Mycobacterium tuberculosis</i>	Bacteria
CholOx	Q7SID9	1I19	<i>Brevibacterium sterolicum</i>	Bacteria
VAO	P56216	1VAO	<i>Penicillium simplicissimum</i>	Fungi
CpADHAPS	P97275	4BBY	<i>Cavia porcellus</i>	Mammalia
ZmCK02	Q709Q5	4ML8	<i>Zea mays</i>	Viridiplantae
ZmCKX1	Q9T0N8	1W1O	<i>Zea mays</i>	Viridiplantae
AtCKX	Q9FUJ1	2EXR	<i>Arabidopsis thaliana</i>	Viridiplantae
GLDH	Q9SU56		<i>Arabidopsis thaliana</i>	Viridiplantae
DLDH	P06149		<i>Escherichia coli</i>	Bacteria

Chapter 2

PpBBE1

The single berberine bridge enzyme homolog of *Physcomitrella patens* is a cellobiose oxidase

Marina Toplak,¹ Gertrud Wiedemann,² Jelena Ulićević,¹ Bastian Daniel,¹
Sebastian N. W. Hoernstein,² Jennifer Kothe,² Johannes Niederhauser,¹ Ralf Reski,^{2,3}
Andreas Winkler¹ and Peter Macheroux^{1*}

¹Institute of Biochemistry, Graz University of Technology, Petersgasse 12/2, A-8010 Graz, Austria

² Plant Biotechnology, Faculty of Biology, University of Freiburg, Schaezlestraße 1, D-79104
Freiburg, Germany

³BIOSS Centre for Biological Signalling Studies, University of Freiburg, Schaezlestraße 18, D-79104
Freiburg, Germany

*To whom correspondence should be addressed:

Prof. Dr. Peter Macheroux
Graz University of Technology
Institute of Biochemistry
Petersgasse 12/2
A-8010 Graz, Austria
Tel.: +43-316-873 6450
Fax: +43-316-873 6952
Email: peter.macheroux@tugraz.at

Running title: Cellobiose oxidase from *Physcomitrella patens*

Database: Structural data are available in the PDB under the accession numbers 6EO4 and 6EO5.

Keywords: enzyme catalysis, enzyme mechanism, flavin adenine dinucleotide (FAD), plant biochemistry, protein structure

Abbreviations

BBE, berberine bridge enzyme; GOOX, glucooligosaccharide oxidase; *PpBBE1*, berberine bridge enzyme homolog from *Physcomitrella patens* (gene #1); THCA, Δ^1 -tetrahydrocannabinolic acid;

This chapter was published as “The single berberine bridge enzyme homolog of *Physcomitrella patens* is a cellobiose oxidase” in FEBS Journal 2018, Vol. 285, p. 1923-1943.

Abstract

The berberine bridge enzyme from the California poppy *Eschscholzia californica* (*EcBBE*) catalyzes the oxidative cyclization of (*S*)-reticuline to (*S*)-scoulerine, that is, the formation of the berberine bridge in the biosynthesis of benzyloquinoline alkaloids. Interestingly, a large number of *BBE-like* genes have been identified in plants that lack alkaloid biosynthesis. This finding raised the question of the primordial role of *BBE* in the plant kingdom, which prompted us to investigate the closest relative of *EcBBE* in *Physcomitrella patens* (*PpBBE1*), the most basal plant harboring a *BBE-like* gene. Here, we report the biochemical, structural and *in vivo* characterization of *PpBBE1*. Our studies revealed that *PpBBE1* is structurally and biochemically very similar to *EcBBE*. In contrast to *EcBBE*, we found that *PpBBE1* catalyzes the oxidation of the disaccharide cellobiose to the corresponding lactone, that is, *PpBBE1* is a cellobiose oxidase. The enzymatic reaction mechanism was characterized by a structure-guided mutagenesis approach that enabled us to assign a catalytic role to amino acid residues in the active site of *PpBBE1*. *In vivo* experiments revealed the highest level of *PpBBE1* expression in chloronema, the earliest stage of the plant's life cycle, where carbon metabolism is strongly up-regulated. It was also shown that the enzyme is secreted to the extracellular space, where it may be involved in later steps of cellulose degradation, thereby allowing the moss to make use of cellulose for energy production. Overall, our results suggest that the primordial role of *BBE-like* enzymes in plants revolved around primary metabolic reactions in carbohydrate utilization.

Introduction

The berberine bridge enzyme (*BBE*)-like protein family is a large enzyme family found in bacteria, fungi and plants, named after its best characterized member, the *BBE* from *Eschscholzia californica* (*EcBBE*, EC 1.21.3.3). In Californian poppy (*E. californica*) *BBE* participates in the biosynthesis of benzyloquinoline alkaloids, where it catalyzes the oxidative formation of the berberine bridge resulting in the conversion of (*S*)-reticuline to (*S*)-scoulerine (1). Whole genome sequencing efforts have revealed the occurrence of many *BBE-like* genes in virtually all plants even those that lack alkaloid biosynthesis (2). In the model plant *Arabidopsis thaliana*, for example, 27 genes were identified to encode *BBE-like* enzymes, with an even higher number found in *Citrus clementina* (41 genes), *Glycine max* (43 genes) and *Populus trichocarpa* (65 genes). Despite the ubiquitous and abundant presence of *BBE-like* proteins in the plant kingdom the biochemical and physiological function of the enzymes remain largely unknown. Based on multiple sequence alignments, the 27 *BBE-homologs* of *A. thaliana* were classified into seven sub-families (3). Recent studies have successfully assigned a function to two of these sub-families, demonstrating oxidation of indole cyanohydrins and monolignols to the corresponding keto and aldehyde products, respectively (3, 4). Besides, earlier reports on enzymes involved in plant defense have implicated *BBE-like* proteins in the

oxidation of mono- and polysaccharides derived from glucose as well as from galactose (5). A similar activity was also assigned to the pollen allergen Phl p 4 (6) and to nectarin 5, a BBE-like protein from ornamental tobacco (7).

Unlike most other plants, the genome of the moss *Physcomitrella patens* harbors only two genes that can be assigned to the BBE-like family (8). Gene #1 (*Pp3c12_2640V3.1*) shares the highest sequence identity with fungal carbohydrate oxidases (ca. 30% identity on the amino acid sequence level) and is closely related to *EcBBE* and other plant enzymes from the BBE-like family (25-28% identity on the amino acid sequence level). In contrast, gene #2 (*Pp3c2_12420V3.1*) has a much lower similarity to *EcBBE* (< 20% sequence identity) and is more closely related to the ecdysteroid-22-oxidase from *Metarhizium rileyi* (29.3%; Uniprot: I0J0L0).

Because of the role of *P. patens* as a paradigm for the conquest of land by plants (9), we reasoned that unraveling the function of the moss BBE-like protein would provide insight into the evolutionary origin of this ubiquitous multigene family in plants. Toward this goal, we have produced the BBE-homolog, termed *PpBBE1* and encoded by gene #1 (*Pp3c12_2640V3.1*), in the methylotrophic yeast *Komagataella phaffii* and subsequently characterized the purified enzyme biochemically and structurally. In addition, expression and secretion of the wild type protein as well as the phenotypical characteristics of a knock-out strain were studied in order to reveal the *in vivo* function of the enzyme. Here, we report that *PpBBE1* is an efficient cellobiose oxidase that is very similar to fungal BBE-like oxidases, such as glucooligosaccharide oxidase (GOOX), in terms of the active site composition as well as the enzymatic reaction mechanism. Our *in vitro* findings are further supported by the data obtained from *in vivo* experiments, since the highest level of expression could be detected in chloronema, an early stage of the plant's life cycle, where carbohydrate metabolism is strongly up-regulated (10, 11). Thus, our results suggest that the diversity of enzymatic reactions found in the BBE-like protein family in the plant kingdom originated from this "primordial" carbohydrate oxidase.

Results

Gene organization, expression and secretion of Physcomitrella patens BBEs

According to the latest release of the genome V3.3 available on cosmos.org, *PpBBE1* is located on chromosome 12 and represented by the gene model *Pp3c12_2640V3.1* encoding a protein of 501 amino acids. The full length gene comprises 3243 bp, of which 2808 bp belong to the coding sequence. The latter consists of a 5'-UTR of 498 bp, a transcript of 1506 bp and a 3'-UTR of 804 bp, with the transcript being formed by 3 exons (99, 256 and 1151 bp for exon 1, 2 and 3, respectively) and two introns. *PpBBE3* (note that *PpBBE2* was identified as a pseudogene) is located on chromosome 2 and represented by *Pp3c2_12420V3.1*, consisting of two exons and an intron, encoding a protein of 586 amino acids (Figure 1A).

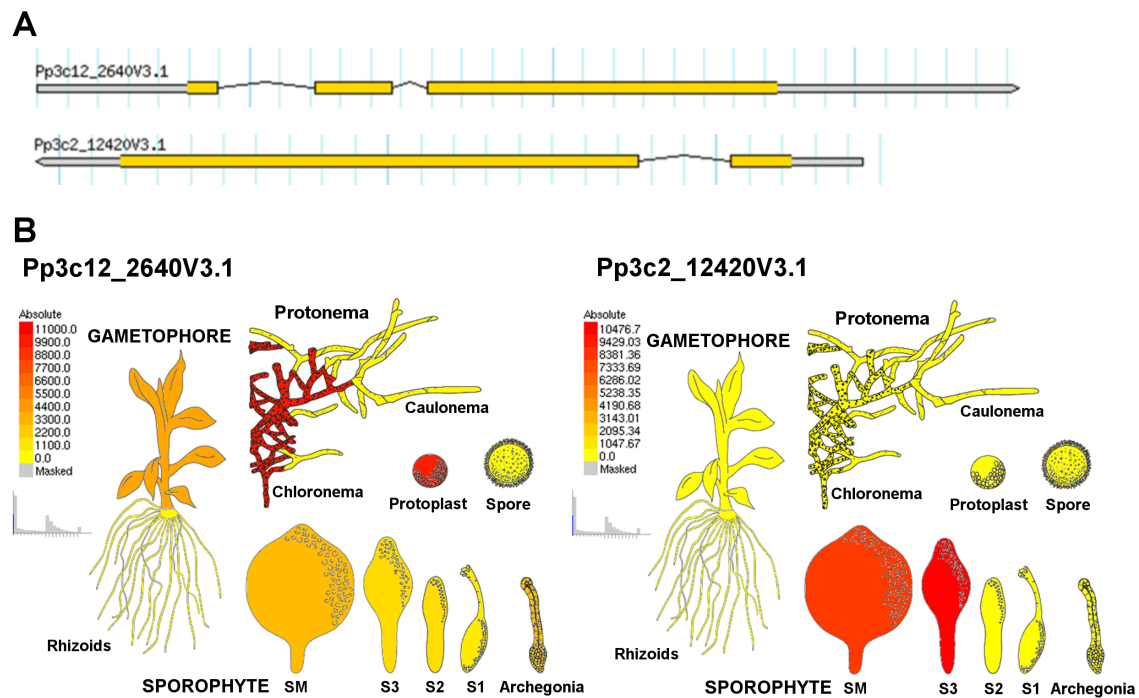


Figure 1: Genomic organization and expression of *PpBBE1* and *PpBBE3* throughout the life cycle. A, *PpBBE1* is represented by the model Pp3c12_2640V3.1 and *PpBBE3* by the model Pp3c2_12420V3.1 in the latest release of the genome V3.3 available on cosmos.org. B, *PpBBE1* (left) and *PpBBE3* (right) expression throughout the whole life cycle of *Physcomitrella patens* visualized using the *Physcomitrella* eFP Browser available on http://bar.utoronto.ca/efp_physcomitrella/cgi-bin/efpWeb.cgi (12).

The expression of *PpBBE1* throughout the whole life cycle and upon different growth conditions was analyzed *in silico* using publicly available transcriptomic data based on microarray experiments (12, 13). *PpBBE1* is highly expressed in protoplasts and chloronema cells, which both harbor large and numerous chloroplasts. Analysis of the caulonema, the fast growing cell type of protonema from which buds arise and which is characterized by fewer chloroplasts and slimmer cells with oblique cell walls, in contrast, did not reveal any expression. In the gametophore, expression of *PpBBE1* was restricted to the green parts, whereas in rhizoids no expression was detected. During sporophyte development *PpBBE1* expression was only detectable in unfertilized archegonia, the female sexual organs, and the mature spore capsule while *PpBBE3* expression was restricted to the late stages of sporophyte development ((12); Figure 1B). On dedifferentiation of leaves to chloronema as well as after incubation in darkness *PpBBE1* expression was upregulated (13).

PpBBE1 is about 54 kDa and harbors a predicted *N*-terminal signal peptide (1-30) according to SignalP (14) as well as an internal FAD-binding domain (78-216, PF01565) and a C-terminal BBE-domain (457-499, PF08031) according to the PFAM protein domain annotation (15). Furthermore, the *PpBBE1* was identified in the supernatant of *P. patens* liquid cultures by mass spectrometry whereas *PpBBE3* was not detected.

Production and purification of PpBBE1 & basic characterization

The gene of the *P. patens* BBE-like protein encoded by locus *Pp3c12_2640V3.1* (gene #1) was expressed in the methylotrophic yeast *Komagataella phaffii* as described in Experimental Procedures. The protein (molecular mass 54 kDa) was secreted into the culture medium and purified by Ni-NTA affinity chromatography using the C-terminal octahistidine tag. Typical yields of pure protein varied between 5-7 mg L⁻¹ of culture. The UV-Vis absorption spectrum of purified *PpBBE1* exhibited two peaks at 375 and 443 nm indicating the presence of a flavin chromophore (Figure 2, *black line*). Denaturation of the protein resulted in a single peak at 440 nm (Figure 2, *red line*).

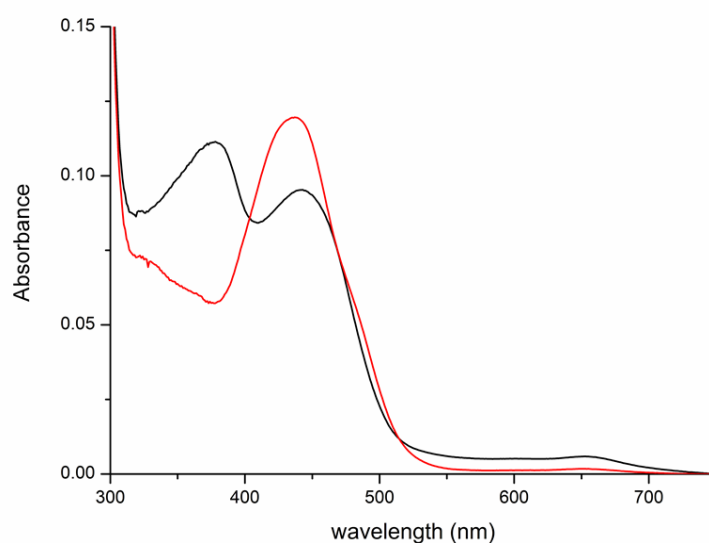


Figure 2: UV-Vis absorption spectrum of native (*black line*) and denatured (*red line*) *PpBBE1*. *PpBBE1* was diluted to a final concentration of about 10 μ M with 50 mM HEPES buffer pH 6, before recording the spectra at 25 $^{\circ}$ C.

Similar spectral changes were reported for other members of the BBE-family and reflect the bicovalent linkage of the isoalloxazine ring via the C6- and 8 α -position to a cysteine and histidine residue, respectively (2, 16–18). As both residues are conserved in the sequence of *PpBBE1* (H111 and C172), the observed spectral properties are in accordance with the formation of both covalent linkages. To further substantiate the presence of two covalent linkages, the protein was photoreduced under anoxic conditions. As shown in Figure 3, reduction initially yielded the anionic flavin semiquinone, which was then further reduced to the flavin hydroquinone (Figure 3A, B). Reoxidation of the fully reduced sample yielded absorption characteristics typical for a 6-thio-flavin with a sharp peak at 425 nm and a broad absorption centered at 750 nm (Figure 3B, C). The underlying cleavage of the carbon-sulfur bond in the covalently linked cysteine residue was previously observed for *EcBBE* (16) and appears to occur in all bicovalently linked flavins found in the BBE-family.

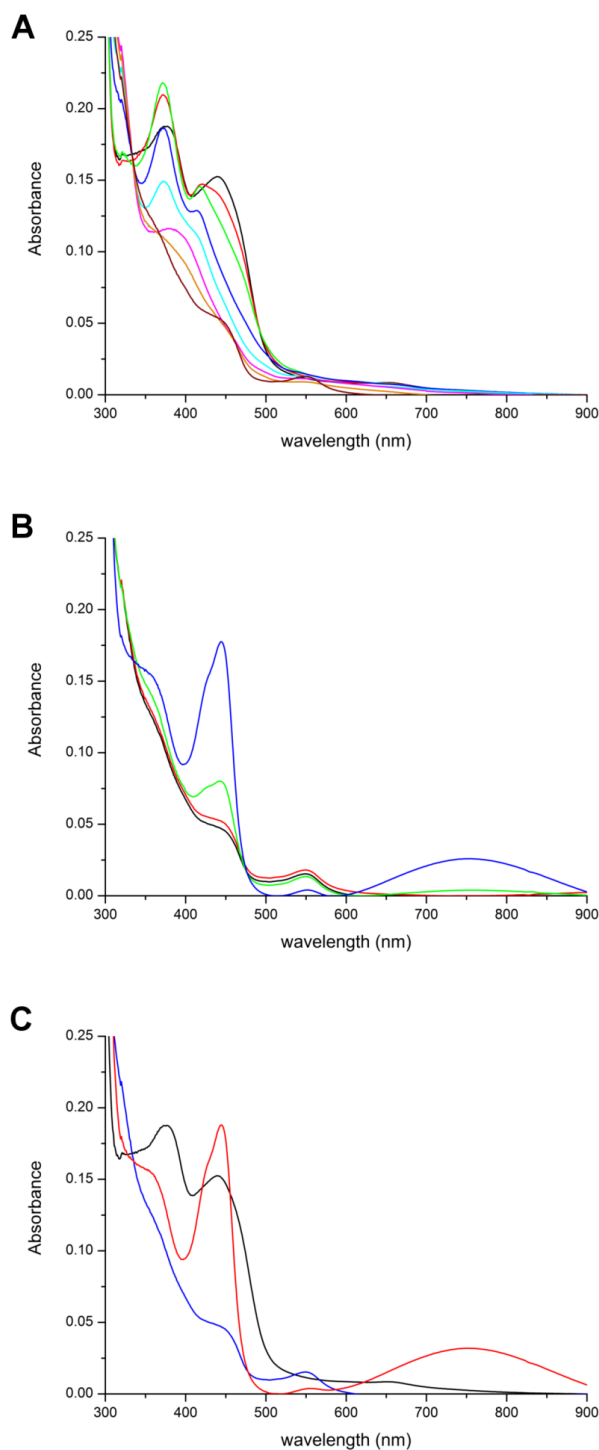


Figure 3: Photoreduction in *PpBBE1* under anoxic conditions. **A**, UV-Vis absorption spectra of *PpBBE1*, diluted to a final concentration of about 15 μM with 50 mM HEPES pH 7, were recorded during anaerobic photoreduction. The strong increase in absorption at 371 nm within the first minutes indicates the formation of an anionic flavin semiquinone [compare start spectrum (*black*) with spectrum recorded after 4 min (*green line*)], which was subsequently reduced to the flavin hydroquinone (*brown line*); **B**, Reoxidation of *PpBBE1* following photoreduction. The broad peak observed in the spectrum after full reoxidation (blue line) between 600 and 900 nm indicates the formation of 6-thio-FAD; **C**, Comparison of the UV-Vis absorption spectra of native (*black*), fully reduced (*blue*) and fully reoxidized (*red*) *PpBBE1*.

Yet, another hallmark of bicovalently linked flavins is their unusually high redox potential, which is typically more positive than +100 mV, for example, $+132 \pm 4$ mV for *EcBBE* (17). Thus, we also determined the redox potential for *PpBBE1* using the dye-equilibration method (19).

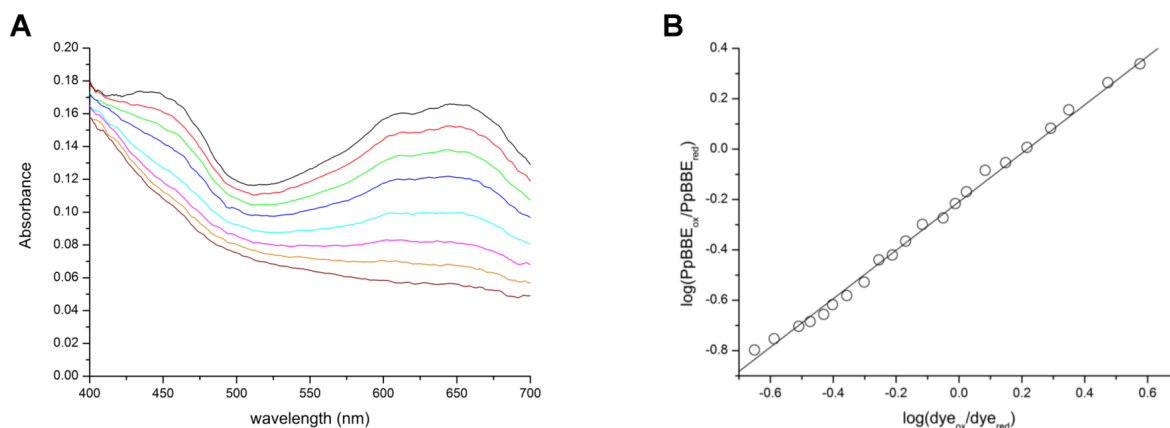


Figure 4: Determination of the redox potential of *PpBBE1* (in 50 mM HEPES pH 7). **A**, The UV-Vis absorption spectra recorded during the reduction reaction. **B**, Nernst plot obtained from the experimental data, that is, $\log(PpBBE1_{ox}/PpBBE1_{red})$ vs the $\log(dye_{ox}/dye_{red})$. The slope of near unity (0.96) is in keeping with a two-electron transfer process for both enzyme and the dye; the intercept was used to calculate the redox potential of *PpBBE1* ($+121 \pm 1$ mV from three determinations).

As shown in Figure 4, the reporting dye and the flavin were reduced synchronously allowing to plot the log of the ratio of oxidized versus reduced dye against the log of the ratio of oxidized versus reduced enzyme-linked FAD (Figure 4A, B). From this Nernst-plot a redox potential of $+121 \pm 1$ mV was obtained, which is comparable with other BBE-like enzymes (2, 17, 20).

Identification of substrates

Based on the fact that the majority of BBE-like enzymes in bacteria and fungi oxidize alcohol groups of a variety of complex saccharide structures, an initial screening for enzymatic activity focused on mono-, di- and polysaccharides (for a complete list of compounds see Experimental Procedures). This promptly revealed that *PpBBE1* oxidizes the two 1,4- β -linked disaccharides cellobiose and lactose. A more detailed kinetic analysis by steady-state kinetics yielded a higher apparent k_{cat} and lower apparent K_M for cellobiose, that is, 48 s^{-1} vs. 28 s^{-1} and 0.6 mM vs. 4.2 mM , respectively, indicating that the catalytic efficiency with cellobiose is 10-times higher than with lactose ($k_{cat}/K_M = 8 \times 10^4 \text{ M}^{-1} \text{ s}^{-1}$ and $7 \times 10^3 \text{ M}^{-1} \text{ s}^{-1}$ for cellobiose and lactose, respectively; Figure 5).

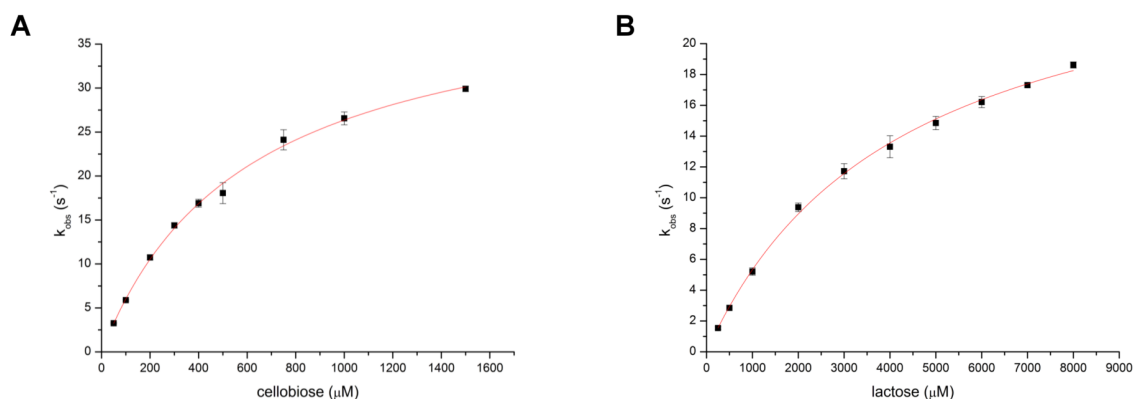


Figure 5: Steady state kinetics performed with *PpBBE1* using cellobiose (A) and lactose (B) as substrates. Reaction rates were determined at pH 6, near the pH-optimum of *PpBBE1* wild type, keeping the enzyme concentration constant (10 nM) and varying the substrate concentration (cellobiose: 50 μM to 1500 μM ; lactose: 250 μM to 8000 μM). From these data, it can be concluded that *PpBBE1* shows an about 10-fold higher catalytic efficiency with cellobiose than with lactose (apparent $k_{cat}/K_M = 8 \times 10^4 \pm 7 \times 10^3$ and $7 \times 10^3 \pm 1 \times 10^3 \text{ M}^{-1} \text{ s}^{-1}$ from three determinations, respectively; the standard deviations are displayed as error bars).

In order to identify the oxidation product, cellobiose was used in a scale-up experiment to obtain sufficient amounts of product, which was subsequently analysed by NMR-spectroscopy (see Experimental Procedures for details). The NMR-spectra clearly demonstrate the formation of cellobionolactone, that is, the free anomeric centre of cellobiose is oxidized to the corresponding lactone, which spontaneously hydrolyses to the ring-open acid form (see Supplementary Figure S1). Finally, we determined the pH-dependence of the reaction under steady-state conditions. As shown in Figure 6, the activity of *PpBBE1* reached a maximum at pH 5.8 (*black squares*).

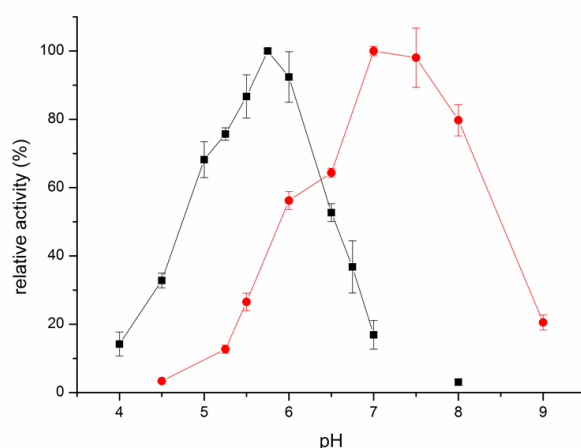


Figure 6: Comparison of the pH-profile of wild-type *PpBBE1* (*black*) and the D396A variant (*red*). Reaction rates were determined in the pH-range from 4-8, using cellobiose (500 μM) as substrate and DCPIP (100 μM) as final electron acceptor. All reactions were started upon addition of the enzyme (wild type: 10 nM; D396A: 200 nM) and the decrease in absorption at 600 nm was monitored for 120 s. The wild-type enzyme showed highest activity at pH 5.8, whereas the pH-optimum of the variant was shifted by more than one pH-unit to pH ~ 7.2 (turnover rates at the different pH-values were determined in triplicates; the standard deviations are displayed as error bars).

Pre-steady state experiments with cellobiose

To further evaluate the reductive and oxidative half-reaction of the enzyme, we conducted pre-steady state experiments in the stopped-flow apparatus (see *Experimental Procedures*). First, the rate of reduction in *PpBBE1* was measured as a function of cellobiose concentration. The rate of reduction increased linearly with the cellobiose concentration and saturation was not observed up to 1 mM. At higher concentrations, the observed rate constants could not be extracted reliably due to the dead time restrictions of the instrument. Due to this limitation, we were unable to determine or fit a limiting rate of reduction and a dissociation constant for cellobiose. Therefore, we have used the determined bimolecular rate constant of $1.7 \times 10^5 \text{ M}^{-1} \text{ s}^{-1}$ for further comparison and discussion. The rate of reoxidation of the reduced flavin by dioxygen was determined at a final oxygen concentration of $140 \mu\text{M}$ to $0.5 \times 10^5 \text{ M}^{-1} \text{ s}^{-1}$ and is thus ca. 3-times slower than the rate of reduction.

X-ray crystallographic structure of PpBBE1

In order to gain further insights into the structure-function relationships in the active site of *PpBBE1* and to develop a more detailed enzymatic reaction mechanism, we solved the three-dimensional structure by X-ray crystallography. Hanging drop vapour-diffusion crystallization setups was used to obtain light yellow, tetragonal bipyramidal crystals of wild-type protein as well as of a protein variant (D396N) that was generated in the course of our site-directed mutagenesis study (see site-directed mutagenesis of putative active site residues). Crystals of the D396N variant generally diffracted to higher resolution and data generated from these crystals was, therefore, used for phasing of the structure. Including data up to a resolution of 2.6 \AA , the structure was solved by molecular replacement using a homology model based on *AtBBE*-like 15 (PDB: 4UD8; (3)) as template, confirming a protein fold that had previously been shown for BBE-like enzymes (Figure 7) (2).

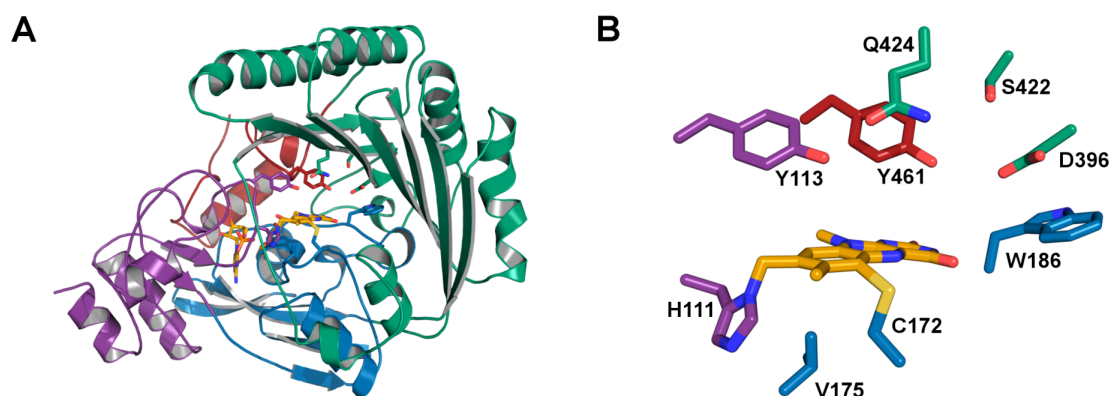


Figure 7: Overall crystal structure (A) and close-up view of the active site (B) of *PpBBE1*. A, Structure of the *PpBBE1* as determined by X-ray crystallography shown in cartoon representation, with the subdomain involved in substrate binding highlighted in green and the FAD-binding domain in purple, blue, and red. The FAD cofactor (yellow) and the two amino acids responsible for its bicovalent attachment are shown as sticks (H111, purple and C172, blue). B, Close-up of the active site of *PpBBE1*. The function of the amino acid residues shown were probed by site-directed mutagenesis (see text for details).

An identical structure was then confirmed for the wild-type data refined to 2.9 Å after phasing with the initial model of the variant. *PpBBE1* crystallized as a loose dimer in the asymmetric unit with a dimerization interface of no biological significance according to PISA analysis (21). In line with gel filtration experiments, *PpBBE1* is, therefore, expected to be functional as a monomer. Individual protomers also showed no substantial structural differences with a root-mean-square-deviation of 0.15 Å for 404 aligned backbone C α residues. A closer inspection of the active site revealed a relatively large active site with clear interpretable electron density of all active site residues. In addition, continuous electron density between the 8 α - and C6-positions of the flavin cofactor and residues H111 and C172, respectively, confirmed the bicovalent linkage of the flavin cofactor. Both wild-type and the D396N structure featured a pronounced density at the expected site of substrate binding that could not be interpreted at the current resolution limits. Interestingly, the density projects toward the C4a atom of the flavin cofactor and might thereby explain the unexpectedly weak yellow coloration of the crystals. Further studies are needed to identify the source of this copurified ligand species.

The closer inspection of the active site revealed six residues with a potential role in substrate binding and activation (Figure 8). Among these residues, two are likely to be required for substrate activation. D396 forms a hydrogen bond with Y461 and thereby may assist in the deprotonation of the tyrosine residue, which, in turn, could serve as catalytic base. Q424, which is in close vicinity to Y461 and D396, might also contribute to the activation of Y461, but could also play a role in substrate coordination or activation. The role of W186 and S422 is less obvious. Being able to interact with peptide backbone of L397 and the side chain of Y398, respectively, these two residues might be responsible for the correct positioning of D396 relative to Y461, but from the crystal structure, their importance is difficult to predict.

Site-directed mutagenesis of putative active site residues

In order to obtain more detailed information on the role of various active site residues, we initiated a site-directed mutagenesis program. Thus, all six amino acid residues found in close vicinity of the flavin cofactor were replaced, that is, tyrosine 113 and 461 to phenylalanine (Y113F and Y461F), aspartic acid 396 to alanine and asparagine (D396A and D396N), glutamine 424 to alanine (Q424A), tryptophan 186 to phenylalanine (W186F), and serine 422 to alanine (S422A). In addition, the residue held responsible for controlling the oxygen reactivity on the *si*-side of the isoalloxazine ring, that is, valine 175, was replaced by leucine (V175L; Figure 8).

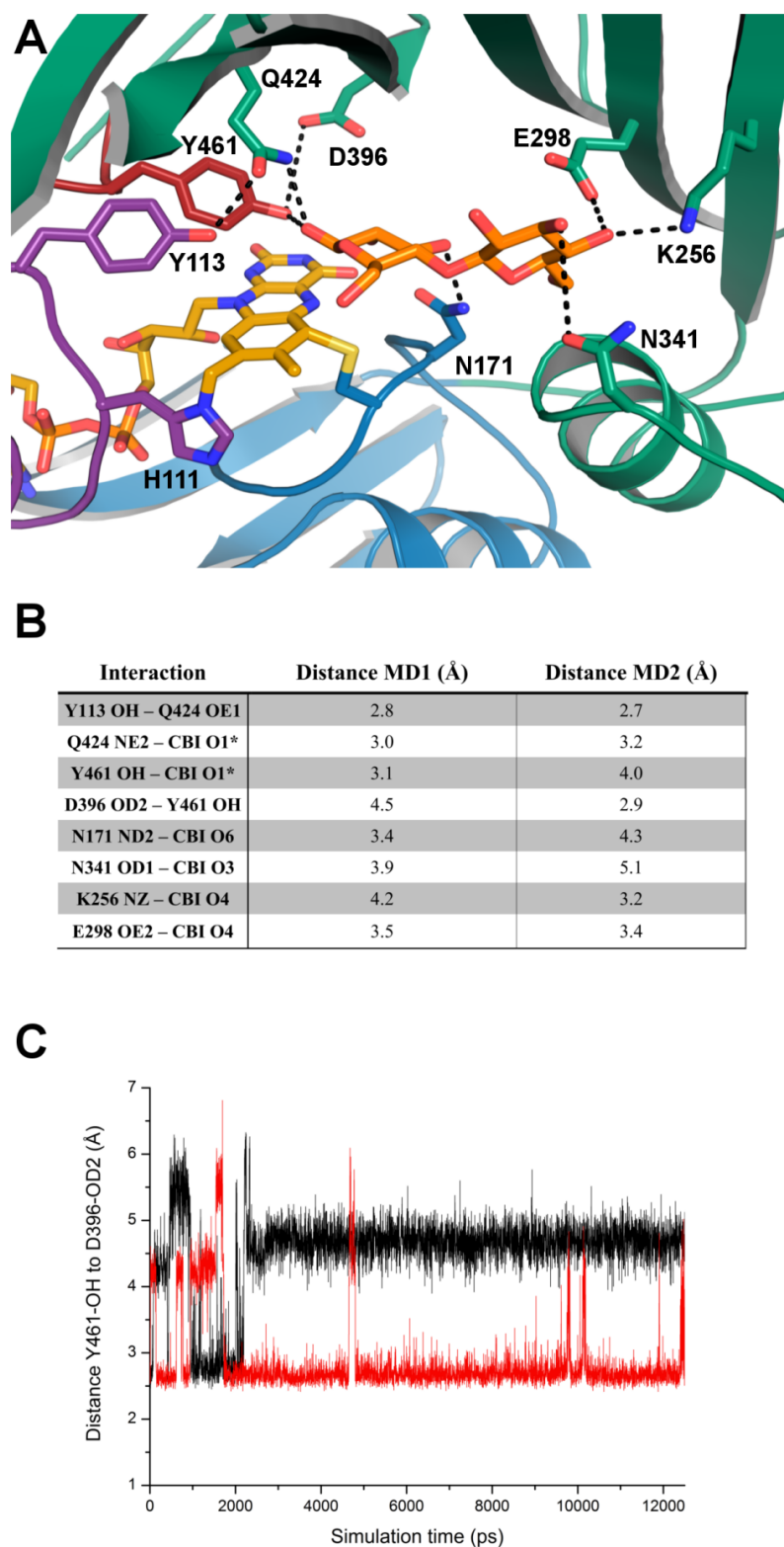


Figure 8: Results from molecular dynamic simulations performed after docking of cellobiose to the crystal structure of *PpBBE1*. **A**, Cellobiose-binding mode, including hydrogen-bonding interactions predicted by MD-simulations (for color coding, see Figure 6; cellobiose is shown as *orange sticks*). **B**, Distances between possible interaction partners as predicted in two independent MD-simulation runs (see *black dashed lines* in panel **A**). **C**, Time-dependent change in the distance between the two catalytic residues Y461 and D396 monitored for 12.5 ns.

As shown in the summary of kinetic parameters in Table 1, the replacement of Y461, D396, W186, S422, and Q424 significantly affected the catalytic rates whereas replacement of Y113 caused only marginal changes compared to the wild-type enzyme.

Table 1: Presteady-state and steady-state parameters determined for wild-type *PpBBE1* and the protein variants. All measurements were performed in 50 mM HEPES buffer, pH 6, that is, near the pH optimum found for wild-type *PpBBE1*. In the presteady-state experiments, no saturation could be observed up to 1 mM cellobiose, where the reaction was complete within the dead time of the instrument. Thus, a linear fit was applied in the range from 100 to 800/1000 μM in order to allow comparison with the variants. The slope obtained from this fit is presented as a bimolecular rate constant k_{red} ($\text{M}^{-1}\text{s}^{-1}$). The turnover rate (k_{obs}) refers to the reaction rates determined under steady-state conditions, using 1 mM cellobiose as substrate and 100 μM DCPIP as final electron acceptor.

	k_{red} ($\text{M}^{-1}\text{s}^{-1}$)	k_{red} (%)	k_{obs} (s^{-1})	k_{obs} (%)
WT	$1.7 \cdot 10^5$	100	27 ± 0.70	100 ± 8
Y113F	$9.7 \cdot 10^4$	57	25 ± 0.50	91 ± 6
Y461F	n.d.	-	0.13 ± 0.20	0.50 ± 0.1
D396A	$4.3 \cdot 10^3$	2.5	0.91 ± 0.07	3.4 ± 0.2
D396N	$1.4 \cdot 10^3$	0.8	0.65 ± 0.05	2.4 ± 0.2
Q424A	n.d.	-	0.17 ± 0.02	0.60 ± 0.02
W186F	$1.2 \cdot 10^3$	0.7	0.47 ± 0.05	1.7 ± 0.1
S422A	$7.0 \cdot 10^3$	4.1	3.3 ± 0.05	13 ± 0.1

These results further support the hypothesis that D396 acts as an active site base and therefore determines the pH-profile of the enzyme. This concept is also in agreement with the observation that replacement of D396 by an alanine resulted in a substantial shift of the pH-optimum from ~ 5.8 to ~ 7.2 (Figure 6, *red spheres*).

Previously, we established that the oxygen reactivity of the reduced flavin in the BBE-like enzyme family is controlled by a single “gate keeper” residue on the *si*-side of the isoalloxazine ring. In the case of *PpBBE1*, V175 is found in the pertinent “gate keeper” position, and thus, the reduced enzyme is expected to rapidly react with dioxygen, as confirmed by the high rate of reoxidation, that is, $0.5 \times 10^5 \text{ M}^{-1} \text{ s}^{-1}$. In accordance with our “gate keeper” model, replacement of this valine by leucine diminished the rate of reoxidation to $25 \text{ M}^{-1} \text{ s}^{-1}$, thus basically suppressing the reaction of the reduced flavin with dioxygen as previously found for other members of this enzyme family (3, 20, 22).

Molecular docking and molecular dynamics simulations

As the substantial decrease in enzymatic activity of some variants could not be fully explained based on the crystal structure alone, molecular docking and subsequent molecular dynamics simulations with *PpBBE1* and cellobiose were performed. The docking experiment resulted in a reasonable binding of cellobiose to the active site of *PpBBE1*, though some distances between the ligand and interacting residues were not in a favourable range. Therefore, two independent molecular dynamics simulations based on the previously obtained docking results were conducted (Figure 8A).

The resulting average structures demonstrated a high flexibility of Y461, as the distance between D396 and the tyrosine as well as between the tyrosine and the anomeric hydroxyl group of cellobiose strongly differed in the two simulations (Figure 8B, C). In one simulation, Y461 is in hydrogen-bonding distance with D396, thus indicating the activation of tyrosine for catalysis, whereas the second simulation better represents the deprotonation of the anomeric hydroxyl group of the substrate molecule.

Furthermore, the significant decrease in enzymatic activity resulting from the exchange of Q424 by alanine can be better explained based on our *in silico* data. The amide nitrogen of Q424 directly points toward the C1* hydroxyl group of cellobiose and thus may have a role in stabilization of the catalytic transition state. In addition, the simulations indicated the involvement of several other amino acid residues in substrate binding: Q298 and K256 are both in hydrogen-bonding distance to the C4 hydroxyl group of bound cellobiose (Figure 8B) suggesting that they are involved in substrate recognition. Their suggested role in substrate binding also explains the higher K_M of lactose compared to cellobiose, as the C4 hydroxyl of lactose is in an axial position and thus points away from these two amino acids.

Generation and analysis of BBE-deficient moss mutants

To analyze the function of *PpBBE1* *in vivo*, we generated moss $\Delta PpBBE1$ knockout mutants deleting the coding sequence almost completely. A 3.6 kb long fragment was amplified from genomic DNA and the central part of this fragment, comprising nearly the whole coding sequence leaving only 38 bp of exon 1 and 37 bp of exon 3, was replaced by the *nptII* selection cassette (Figure 9A). After poly(ethylene glycol)-mediated protoplast transformation (done in six independent approaches), antibiotic selection, and regeneration (23), 915 surviving colonies were picked. In an initial screening of 28 colonies by leaflet PCR (24), 12 putative $\Delta PpBBE1$ lines were identified and validated by RT-PCR (Figure 9B). Flow cytometry analysis (25) confirmed that these lines were haploid. Subsequently, the copy number of the targeting construct was analyzed with a qPCR-based method on genomic DNA (Figure 9C; (26)). For all further experiments three $\Delta PpBBE1$ single integration lines (#80, #83 and #100) were used.

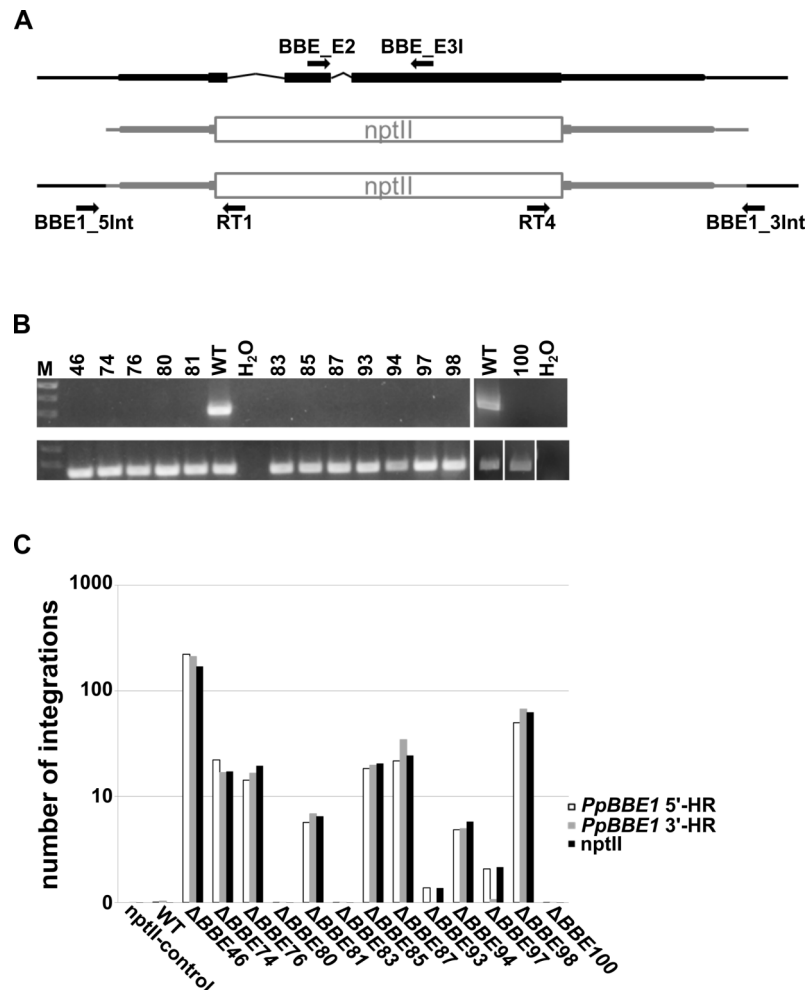


Figure 9: Molecular validation of $\Delta PpBBE1$ lines. **A**, Schematic representation of the genomic locus (*top*), the *PpBBE1*-targeting construct in which most parts of the *PpBBE1*-coding sequence is replaced by the nptII selection marker (*middle*) and the genomic locus in $\Delta PpBBE1$ (*bottom*). The targeting construct is depicted in grey color, the native genomic locus in black color. Exons are represented by boxes, UTRs as slim boxes and introns or the intergenic region 5' and 3' of *PpBBE1* as lines. Primers used for screening of correct 5'- and 3'-integration of the targeting construct into the genome are BBE_5Int and RT1 or RT4 and BBE_3Int, respectively, for RT-PCR BBE_E1 and BBE_E2I; **B**, Loss of *PpBBE1* transcript is validated via RT-PCR in 13 $\Delta PpBBE1$ lines ($\Delta PpBBE1-46$, 74, 76, 80, 81, 83, 85, 87, 93, 94, 97, 98, 100), in WT the product size using BBE_E1 and BBE_E2I is 546 bp, as negative control water (H₂O) was included (*top*). Control for successful cDNA synthesis is shown for all lines (*bottom*). **C**, Quantification of targeting construct integration numbers in the validated $\Delta PpBBE1$ lines with qPCR using three different primer pairs, amplifying a part of the 5'- and 3'-homologous region (*PpBBE1* 5'HR or *PpBBE1* 3'HR) or the coding sequence of the nptII selection marker (nptII). As controls a line with a single integration of the nptII selection marker (nptII-control) and WT were used.

Growth and morphology of $\Delta PpBBE1$ plants were unchanged compared to WT throughout the whole life cycle from protoplast regeneration to sporophyte development. Also, upon salt stress neither gametophores on solid plates nor protonema in liquid culture showed a phenotype differing from WT.

In order to study the effect of $\Delta PpBBE1$ on the degradation of the carbohydrate cellobiose, the plants were grown on media supplemented with either 0.5% cellobiose or 0.5% glucose, which is known to delay differentiation by prolongation of juvenile stages (27) and also promotes growth of *Physcomitrella* cultures in low light conditions (28). Growth and development of $\Delta PpBBE1$ lines were studied with and without supplementation of carbohydrates in standard growth conditions (16 h light, 8 h darkness) or darkness. Therefore, protonema cultures were grown in liquid medium (Figure 10A) and protonema spot inocula (Figure 11A) or single gametophores (Figure 11B) were used as starting material on solid medium.

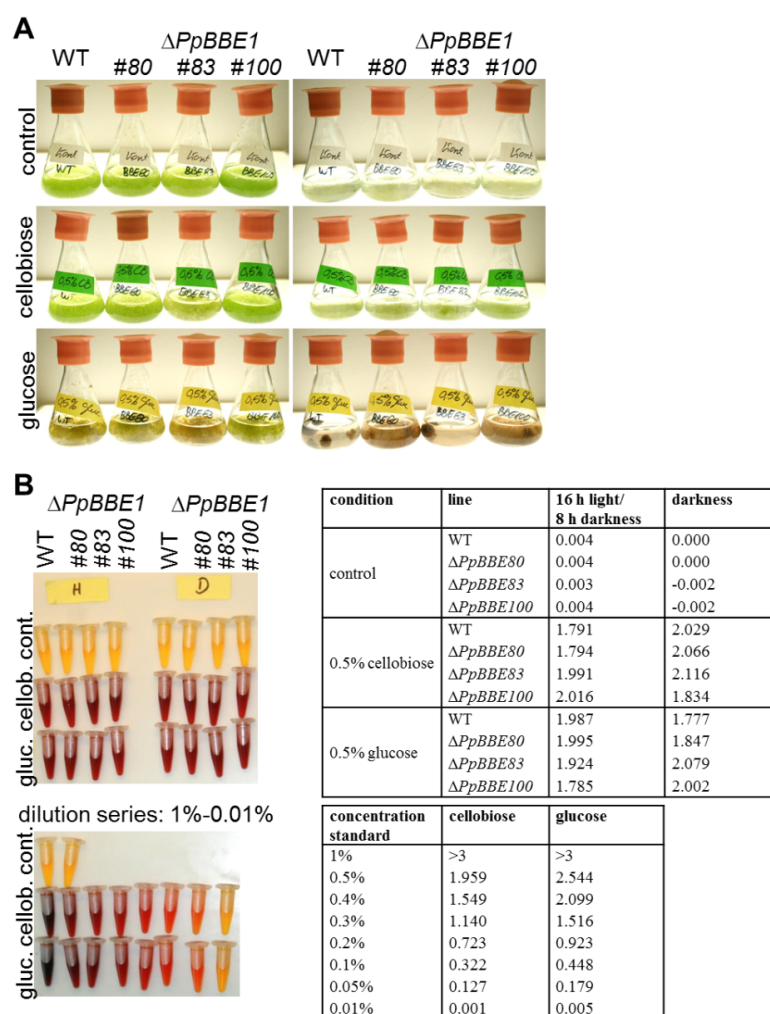


Figure 10: Protonema cultures of WT and $\Delta PpBBE1$ plants grown in liquid medium without or with 0.5% cellobiose or 0.5% glucose as a source of carbohydrates and assay of sugars in the media after 21 days of growth. **A**, Flasks with protonema cultures of WT or $\Delta PpBBE1$ lines grown under standard growth conditions with a 16 h light and 8 h darkness regime (*left panel*) or in complete darkness (*right panel*). **B**, Determination of glucose and cellobiose in the culture media compared with a dilution series of the sugars in the control growth medium with the DNS assay resulting in a concentration-dependent coloring from *dark red* (high concentration of reducing sugars) to *yellow* (no reducing sugars detected) in the *left panel*. The absorbance of the samples and dilution series shown in the *left panels* measured at 575 nm is shown in the tables.

In all conditions, no difference between $\Delta PpBBE1$ and WT was detected regarding growth rate and development. The addition of cellobiose to cultures grown in the dark led to an intermediate phenotype between the control without a carbohydrate source and media supplemented with glucose, but again no significant difference between the WT and the knockout strain could be observed.

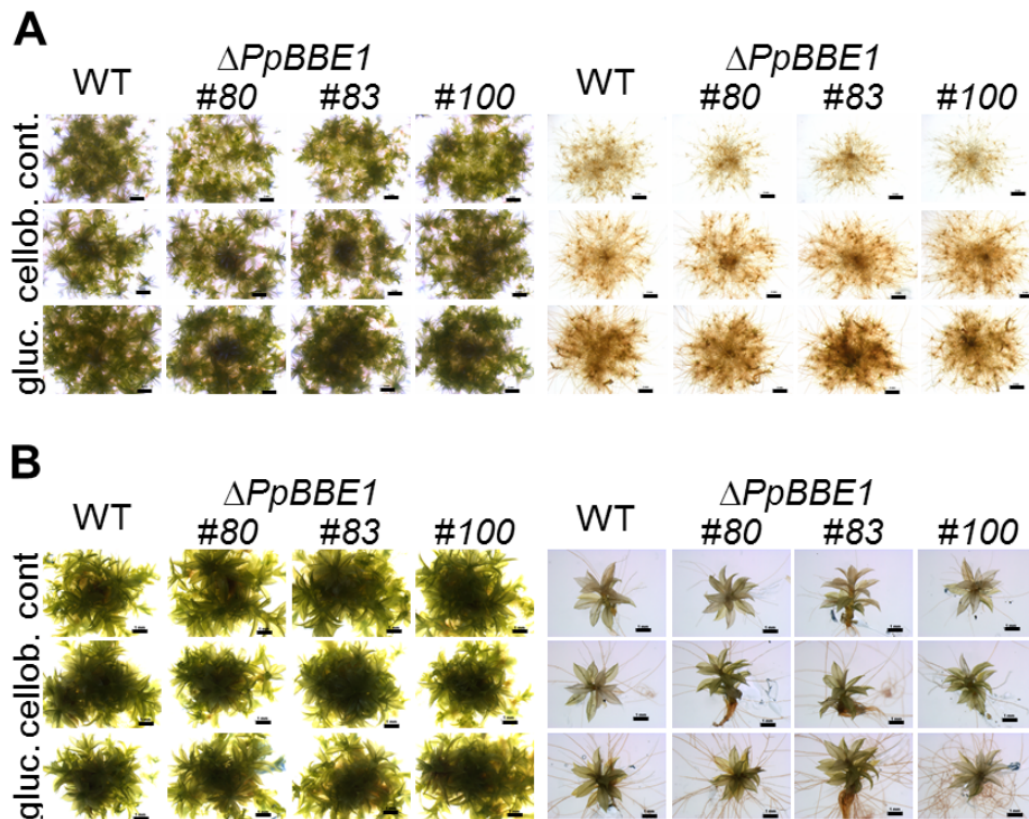


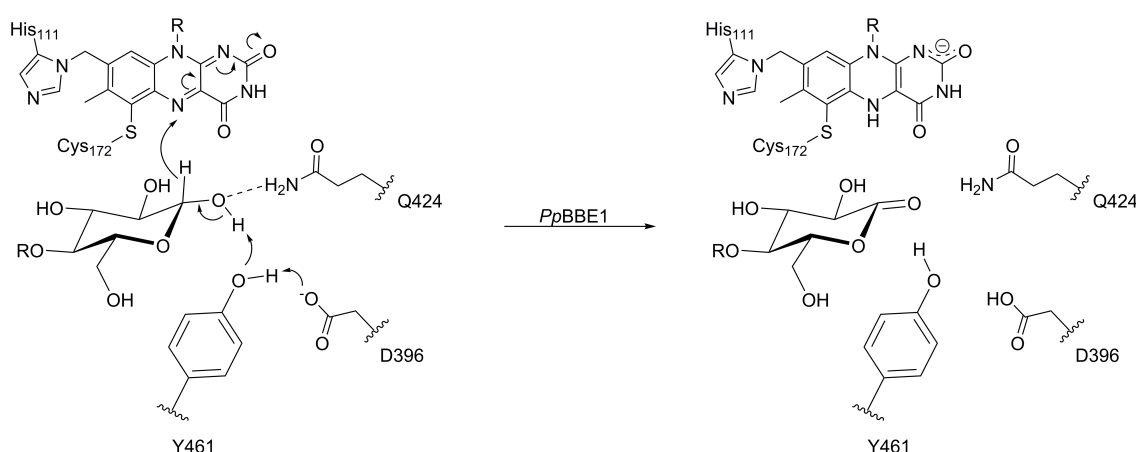
Figure 11: Growth of WT and $\Delta PpBBE1$ plants on solid media without or with 0.5% cellobiose or 0.5% glucose as a source of carbohydrates. **A**, Protonema spot inocula grown on solid media for six weeks. *Left panel*: 16 h light and 8 h dark regime, *right panel*: 2 weeks of growth in a 16 h light and 8 h dark regime before transfer to darkness for 4 weeks. Size bars: 1 mm; **B**, Single gametophores grown for four weeks. *Left panel*: 16 h light and 8 h dark regime, *right panel*: darkness. Size bars: 2 mm. Cont.: control (medium without supplements); cellob.: medium containing 0.5% cellobiose; gluc.: media containing 0.5% glucose.

In addition to the phenotypical analysis, qualitative and quantitative analysis of the glucose and cellobiose content in the supernatant of the liquid cultures was performed. After three weeks of incubation, the presence of reducing sugars was assayed with the Benedict's test, before conducting a quantitative analysis using the 3,5-dinitrosalicylic acid (DNS) assay (Figure 10B) and glucose test strips (for details the *Experimental Procedures*). As before, no differences between $\Delta PpBBE1$ and WT cultures were observed. Similarly, cultures that were grown on plates for four to six weeks were analyzed in terms of the carbohydrate content in the solid media using congo red staining. Again, this analysis did not reveal any difference between $\Delta PpBBE1$ and WT.

Discussion

The successful expression of gene #1 (*Pp3c12_2640V3.1*) in *Komagataella phaffii* led to the production of suitable amounts of *PpBBE1* and enabled us to carry out the biochemical and structural characterisation of the enzyme. In the course of our studies, we identified the disaccharide cellobiose as the best substrate, which is oxidized at the free anomeric centre to the corresponding cellobionolactone and spontaneously hydrolyses to cellobionate. The rate of cellobiose oxidation is very fast and exceeds the rate observed for many other flavin-dependent oxidases (29–32). In fact, the observed bimolecular rate constant already at rather low substrate concentrations is greater than the rate of reoxidation of the reduced flavin by dioxygen, which was also observed for other enzymes belonging to the BBE-like protein family. Thus, *PpBBE1* clearly harbours a very efficient active site for the oxidation of cellobiose. In order to understand the catalytic contributions of the amino acids in the active site, we have generated a set of seven variants and determined the relevant kinetic parameters (Table 1). In conjunction with the crystal structure of *PpBBE1*, we are now in a position to propose an enzymatic reaction mechanism for the oxidation of cellobiose. As shown in Scheme 1, we propose that the side chain carboxylate group of D396 deprotonates the neighbouring side chain of Y461, which in turn abstracts a proton from the anomeric hydroxyl group of the substrate leading to the transfer of a hydride to the N5-position of the flavin.

Scheme 1: Proposed reaction mechanism for the oxidation of cellobiose to the corresponding cellobionolactone catalysed by *PpBBE1*. D396 is expected to deprotonate the side chain -OH of Tyr461, which thereby gets activated to act as catalytic base. By abstracting the proton from the anomeric hydroxyl group (reducing end), lactone formation is triggered and a hydride is transferred from the anomeric carbon to the N5-position of the FAD cofactor. The latter thereby gets reduced and is regenerated upon reoxidation by molecular oxygen.



The relevance of this catalytic diade is in accordance with the observed effects on the rate of substrate oxidation (Table 1) and the changes in the pH-profile found for the D396A variant (Figure 6). The positioning of the anomeric centre in the vicinity of the side chain of Y461 and the N5-position of the flavin was confirmed by substrate docking to our crystallographic structure of the protein. In addition, the characterization of the W186F and the S422A variant also revealed that these residues play an

important role in organising the active site, probably by ensuring the correct positioning of the catalytic base D396. This view is supported by the structural network established by these residues, which apparently stabilize the structural topology by interacting with the backbone carbonyl of L397 (W186) and the hydroxyl group of Y398 (S422 via a water molecule), respectively. Q424, on the other hand, may form a hydrogen bond with Y113, but in view of the total loss of enzymatic activity in the Q424A variant, direct stabilisation of the transition state seems to be the primary function of this amino acid side chain. This finding is in line with the observation that according to the crystal structure Q424 forms only one hydrogen bond, whereas a possible second interaction with the hydroxyl group at the anomeric centre of cellobiose is revealed in our docking simulations.

As mentioned in the introduction, we were particularly curious to identify a substrate (or a group of substrates) for *PpBBE1* because this would provide information on the “primordial” function of the BBE-like enzyme family in plants. In this context, the identification of cellobiose and lactose as substrates of *PpBBE1* is very intriguing since most members of the BBE-like enzyme family in bacteria and fungi oxidize hydroxyl groups of various carbohydrate substrates, for example, aelacinomycin oxidoreductase from *Streptomyces* species (33) and GOOX from the rot fungus *Acremonium strictum* (18). Thus, it is apparent that this activity was already present in early land plants represented by mosses and constituted the starting point for the evolution of BBE-like enzymes in vascular plants, where members of the family are engaged in the oxidation of cyanohydrines and monolignols, as described for *A. thaliana* (3, 4). The unusual oxidative formation of the berberine bridge in benzyloisoquinoline biosynthesis and the cyclisation of the monoterpene moiety of cannabigerolic acid to Δ^1 -tetrahydrocannabinolic acid (THCA), catalysed by *EcBBE* and THCA synthase from *Cannabis sativa*, respectively, have clearly taken this enzyme family to an unprecedented new level of catalytic sophistication and reflect the diverse array of secondary metabolites found in several plant lineages. On the other hand, the observation that some plants possess BBE-like enzymes with glucose oxidase activity, such as nectarin V from tobacco (7), indicates that the ability to oxidize carbohydrates was also conserved in plants. These observations are in tune with the current concept that biosynthetic pathways have evolved in part by gene duplication and subsequent neo-functionalization of one of the genes to support novel enzymatic modifications of metabolites leading to the enormous variety of compounds found in plants (9, 34). The increasing number of genes encoding members of the BBE-like enzyme family during plant evolution as well as distinct changes in the active site composition suggests that this process was relevant for the evolutionary diversification of this enzyme family in the plant kingdom (2, 3).

Our *in vitro* findings are also in good accordance with the *in vivo* data obtained from the characterization of a WT and a *PpBBE1*-knockout strain. The expression of *PpBBE1* was high in defined developmental stages, namely chloronema and protoplasts, which originate from protonema tissue. The chloronema harbors high photosynthetic activity characterized by a high number of chloroplasts of large size. On the other hand, caulonema cells possess fewer and smaller chloroplasts

that are induced later by auxin and allow spreading of the colony by fast, radial growth relying on the availability of energy and carbon supply (28). The expression pattern of *PpBBE1* reflects the differences in the two protonema tissue types, being highly expressed in chloronema, but not detectable in caulonema. This finding nicely correlates with the recently performed transcriptome analysis of protoplasts (35) as well as of chloronema cells (10, 11) that have shown a significant up-regulation of carbohydrate and energy metabolism in these early stages of the plant's life cycle. Our hypothesis that *PpBBE1* is involved in carbohydrate degradation is further supported by the fact that also fungi use cellobiose for energy production, which is initially metabolized extracellularly to cellobionic acid and then further degraded by cellobionic acid phosphorylases after transport into the cytoplasm. The resulting products, gluconate and glucose-1-phosphate, are then converted to 6-phosphogluconate and glucose-6-phosphate before entering the pentose phosphate pathway and glycolysis, respectively (36). Even though this catabolic pathway has never been reported for plants, it is possible that *P. patens* has a similar set of enzymes allowing it to most efficiently use cellulose for energy production (37).

Similarly, *PpBBE1* expression was detected in the green parts of the gametophore but not the rhizoids, root-like structures with a similar morphology as caulonema filaments. On transition of the gametophyte to the sporophyte, a transcriptomic switch occurs regarding carbohydrate metabolism and photosynthesis, as the gametophyte has a primary role in photosynthesis, resource acquisition, and long-term maintenance of the plant, while the sporophyte predominantly relies on the gametophyte for both carbon and energy (10, 38, 39). This switch is also reflected by the expression of *PpBBE1*, which is very low or not detectable throughout the sporophyte development to the mature spore.

Interestingly, the knockout of *PpBBE1* showed no apparent impact on plant morphology and development throughout the whole life cycle in all conditions tested in this study. Even upon growth in darkness, when assimilation via photosynthesis does not take place and supplementation of the media with cellobiose or glucose as carbohydrate source is required for heterotrophic growth, no differences were detected comparing $\Delta PpBBE1$ and WT plants. The effect of glucose and sucrose on *Physcomitrella* grown in the dark leading to increased caulonema formation has been well studied (28, 40). In our study, the phenotype of cultures grown in cellobiose containing growth media is an intermediate between controls without a carbohydrate source and glucose supplemented cultures although, also here, no difference between the WT and the knockout strains was detected. These findings indicate that cellobiose is metabolized like other carbohydrates such as glucose, used as positive control, or sucrose. As upon heterotrophic growth not only the phenotype and development of $\Delta PpBBE1$ compared to WT plants but also the concentration of cellobiose or glucose in culture supernatants was unchanged, we conclude that *PpBBE1*, for which we identified cellobiose as best substrate, is not the only enzyme active in cellobiose metabolism in *Physcomitrella*. Therefore, we propose that the deletion of *PpBBE1* is compensated by the action of other enzymes involved in cellobiose turnover.

Experimental procedures

Materials

All chemicals and media ingredients were purchased from Sigma-Aldrich (St. Louis, MO, USA), Roth (Karlsruhe, Germany), Merck (Darmstadt, Germany), Fluka (Buchs, Switzerland) or Becton, Dickinson and Company (Franklin, Lakes, NJ, USA) and were of the highest grade commercially available. All restriction enzymes used were ordered from Thermo Scientific/Fermentas (St. Leon-Rot, Germany) or New England Biolabs (Ipswich, MA, USA), while the Ni-sepharose column material was obtained from GE Healthcare (Chalfont St. Giles, UK).

Cloning and expression

For heterologous expression of the *PpBBE*-gene in *K. phaffii* the respective gene was purchased from Thermo Scientific. On ordering, the native sequence was codon optimized for *K. phaffii* and nucleotides coding for an octahistidine tag were fused to the 3'-end of the gene.

After subcloning into the *Escherichia coli* pJET vector, PCR amplification was performed in order to remove the native signal sequence identified using SignalP. This PCR product was then cloned into the *K. phaffii* vector pPICZ α , to enable secretion of *PpBBE1* in the non-native host. Having linearized the DNA using SacI, electroporation following the instructions provided by the EasySelect™ ExpressionKit (Invitrogen, Waltham, MA, USA) was applied to transform KM71H cells with the gene of interest. These cells were also transformed with pPICK-PDI plasmid DNA to be able to coexpress of the protein disulfide isomerase from *Saccharomyces cerevisiae*.

Having identified stable and well-expressing clones in small-scale screenings, following the instructions given by (41), large-scale expression in a BBI CT5-2 fermenter (Sartorius, Göttingen, Germany) was performed as described by (42). After 96 h of MeOH feed (induction time), the pH was set to 8, and cells and medium were separated by centrifugation (3500 g for 20 min). The cells were discarded and the supernatant was incubated with 30 mL of Ni-Sepharose™ (GE Healthcare) Fast Flow column material, which had been equilibrated with binding buffer (50 mM NaH₂PO₄, 150 mM NaCl pH 8) prior to use. To ensure binding of all tagged protein, 1 h of stirring at 4°C was required, before the column material was filtered and packed into an empty column (XK 26). Having washed with approximately 150 mL of wash buffer (50 mM NaH₂PO₄, 150 mM NaCl, 20 mM imidazole pH 8) to remove all the unspecifically bound proteins, *PpBBE1* was eluted with elution buffer (50 mM NaH₂PO₄, 150 mM NaCl, 300 mM imidazole pH 8). SDS-PAGE analysis was then used to determine the quality of the purification, before pooling the fractions with the highest protein content and lowest amount of impurities (typical yields: 5-7 mg·L⁻¹ of culture; ~ 98 % purity). Subsequently, the protein solution was concentrated and the buffer was exchanged to 50 mM HEPES buffer pH 6 using Centripreps® 30 kDa MWCO (Millipore Merck, Burlington, MA, USA).

Protein denaturation

To be able to determine the protein concentration based on the characteristic absorption of FAD at about 450 nm, a spectrum of the native as well as of denatured *PpBBE1* was recorded. Assuming that the extinction coefficient of the flavin species found in denatured *PpBBE1* is equal to the one of 6-*S*-cysteinyl FMN, an extinction coefficient of $9800 \text{ M}^{-1} \cdot \text{cm}^{-1}$ could be calculated for native *PpBBE1* at 443 nm.

Photoreduction

Photoreduction was performed as described by Massey *et al.* (43). Under anaerobic conditions, quartz cuvettes were filled with 20 μM enzyme solution, which also contained 5 mM EDTA as photosubstrate as well as 5 μM 5-deaza-FMN. Having recorded a UV/VIS spectrum of the native, oxidized enzyme, the sample was irradiated and further spectra were recorded at different time points. In order to avoid heat denaturation of the protein, the cuvettes were constantly cooled to 15 °C.

Determination of the redox potential

The redox potential of the flavin cofactor was determined using the dye-equilibrium method based on the xanthine/xanthine oxidase system first reported by Massey (19). Two separate solutions, one containing 500 μM xanthine, 5 μM methyl viologen, and 30 μM *PpBBE1* and a second one with xanthine oxidase (about 5 ng) and toluyene blue ($A_{647} = 0.3$; $E^\circ: +115 \text{ mV}$) were prepared in 50 mM HEPES buffer pH 7. By mixing these solutions in a stopped flow device (SF-61DX2; Hi-Tech, TgK Scientific Limited, Bradford-on-Avon, UK), placed in an anaerobic glove box, the reaction was started. To monitor the reduction in the enzyme and the dye, 300 absorption spectra (350-700 nm) were recorded with a KinetaScanT diode array detector (MG-6560) from Hi-Tech, within 50 min. The $\log([\text{ox}]/[\text{red}])$ of the enzyme was plotted against the $\log([\text{ox}]/[\text{red}])$ of the dye allowing calculation of the redox potential as described by Minnaert (44).

Substrate screening

Since the physiological role of *PpBBE1* was not known, we performed a screening in 96-well plates using 1.5 mM 2,6-dichloroindophenol in 50 mM HEPES buffer pH 8, containing 1 mM of the following substrate, and 1 μM of purified enzyme: D-saccharose, D-fructose, D-glucose, D-galactose, D-mannose, L-arabinose, D-arabinose, D-sorbitol, D-mannitol, starch, D-maltose, D-lyxose, L-fucose, D-lactulose, D-ribose, D-xylose, D-trehalose, cellulose, hydroxyethylcellulose, lignin, amylose, ribitol

(adonitol), D-lactose, D-cellobiose, and cellotriase. The plates were incubated at room temperature and decolorization of the DCPIP solution was analysed as a function of time.

pH-optimium

Having identified two well-accepted substrates for *PpBBE1*, the pH-optimium was determined in order to be able to study the enzyme characteristic kinetic properties at the optimal pH. Therefore, different buffers in the pH-range of 4-9 were prepared and substrate conversion was analysed for the wild-type as well as for the variant enzymes. Since both substrate and product do not have any characteristic spectral properties, a coupled assay with DCPIP (100 μM final concentration) was established. By recording the change in absorption at 600 nm, substrate conversion could be monitored and the pH-optimium could be determined. All measurements were performed with constant substrate concentration (1 mM cellobiose) and an enzyme concentration of 10 nM for the wild-type and 200 nM for the variant enzymes, respectively.

Steady-state kinetics

Steady-state kinetics of *PpBBE1* were measured with cellobiose and lactose for the wild-type enzyme and all active site variants were subsequently only measured with the more efficiently converted cellobiose substrate. A coupled assay with DCPIP (100 μM final concentration in 50 mM HEPES pH 6) was used to determine the initial rates observed upon altering the substrate concentration (cellobiose: 50-1500 μM ; lactose: 250-8000 μM), while keeping the enzyme concentration constant. As for the analysis of the pH-optimium, final enzyme concentrations of 10 nM for the wild-type and the Y113F variant and of 200 nM for the remaining variants were used. All reactions were monitored at 600 nm for 120 s and were performed in triplicates.

By plotting the extracted initial velocities versus the respective substrate concentration, v_{max} as well as apparent K_M values could be determined. Due to the low reactivity of protein variants, no full Michaelis-Menten curve was recorded. Instead, conversion rates at 1 mM cellobiose were used for an internal comparison and measured in triplicates.

Presteady-state analysis

For analysis of the reductive and the oxidative half-reaction, a stopped-flow device from Hi-Tech (SF-61DX2) installed in a glove box (Belle Technology, Cambridge, UK) was used. In both cases, time dependent spectral changes of the flavin absorption were monitored either with a KinetaScanT diode array detector (MG-6560) or a photomultiplier (PM-61s). Data analysis was then performed with the Kinetic Studio Software (TgK Scientific Limited) by fitting the data points recorded at 443 nm.

To study the reductive half-reaction, observed rate constants for flavin reduction at six different substrate concentrations (100-1000 μM) were determined in 50 mM HEPES pH 6 (at higher substrate concentrations, the reaction was too fast to reliably fit the data to extract rate constants). By plotting k_{obs} vs the corresponding substrate concentration, a linear increase in reaction rate constants could be observed, making it impossible to fit a limiting reductive rate. In order to allow comparison with the active site variants, a linear fit was applied and the slopes were used for data interpretation.

The oxidative half-reaction was studied by following the reoxidation of the flavin upon mixing enzyme, reduced with 1.2 eq of substrate, with air-saturated buffer (20°C). To obtain bimolecular rate constants, the rates determined in this experiment were divided by the amount of oxygen dissolved in the buffer (final concentration: 140 μM).

Site-directed mutagenesis

In order to study the reaction mechanism in more detail, active site variants were produced. All constructs were generated from pPICZ α -*PpBBE1* wild-type expression strain applying polymerase chain reaction-based mutagenesis. The amino acid exchanges were introduced with the forward and reverse primers that both carried the desired mutations in the nucleotide sequence (for primer sequences see Table 2).

Table 2: Sequences of the primers used for site-directed mutagenesis, with the codon triplet carrying the mutation shown in bold.

Variant	Type	Sequence
Y113F	fwd.	5'-GTGGTCACTCT TTTC GAGGATTA CTC -3'
	rev.	5'-GAGTAATCCTCG AA AAGAGTGACCAC-3'
V175L	fwd.	5'-CTGTCCA ACTCT GGGTATTGCTGGTCATG-3'
	rev.	5'-CAATACCCAGAGTTGGACAGTTACCAGCTG-3'
W186F	fwd.	5'-GGAGGTGG TTTT CGGTTTTTCATC-3'
	rev.	5'-GATGAAAAACCG AA ACCACCTCC-3'
D396N	fwd.	5'-GCTTACTTCATCTACA ACT TGTACGG-3'
	rev.	5'-CCGTACA AGTT GTAGATGAAGTAAGC-3'
D396A	fwd.	5'-GCTTACTTCATCTAC GCT TTGTACGG-3'
	rev.	5'-CCGTACA AGCG TAGATGAAGTAAGC-3'
S422A	fwd.	5'-CTTGTAC GCT ATCCAGATGGTTGCTTCCTG-3'
	rev.	5'-CCTGGAT AGCG TACAAGGAATTTCTGTGGATG-3'
Q424A	fwd.	5'-GTA CTCT ATCGCTATGGTTGCTTC-3'
	rev.	5'-GAAGCAACCAT AGCG ATAGAGTAC-3'
Y461F	fwd.	5'-GTCAGGCT TTCC AGA ACT TACATCG-3'
	rev.	5'-CGATGTAGTTCTG AA AGCCTGAC-3'

After successful cloning and transformation of the mutant strains, expression and purification of the *PpBBE1* variants were performed as described for the wild-type protein.

NMR analysis of the oxidation product

For NMR product analysis, medium-scale turnover reactions were performed, using 3 mL of 10 mM cellobiose solution (in ddH₂O) and 200 nM enzyme. After 3 h of incubation at 25 °C, full conversion of the substrate was confirmed by thin layer chromatography [MeCN:H₂O (85:15)]. The samples were then dried in an ISS110 SpeedVac® System (Thermo Scientific, Waltham, MA, USA) and subsequently redissolved in 750 µL of D₂O. The last two steps were repeated twice, before NMR analysis was conducted. A Varian (Agilent, Santa Clara, California, USA) INOVA 500-MHz NMR spectrometer (Agilent Technologies) and the VNMRJ 2.2D software were used for all measurements. ¹H-NMR spectra (499.98 MHz) were measured on a 5 mm indirect detection PFG-probe, while a 5 mm dual direct detection probe with z-gradients was used for ¹³C-NMR spectra (125.71 MHz). HSQC and HMBC spectra were measured with 16 scans per increment and adiabatic carbon 180° pulses.

Crystallization and data collection

Protein crystals were grown in hanging drop vapour diffusion setups using EasyXtal® 15-Well Tools (Qiagen, Hilden, Germany) and the corresponding crystallization supports (Qiagen). Protein solution (200 µM in 50 mM HEPES buffer pH 6) and crystallization reagent (0.1 M Mg(OOCH)₂, 13/14% poly(ethylene glycol) 3350 for wild-type and variant, respectively) were mixed in 2:1 or 1.5:1 ratio and incubated at 20 °C. After overnight equilibration, streak seeding with crystals from the initial hit was performed. Ten to 14 days later, bipyramidal crystals appeared, which reached their final size after 3 weeks. For cryoprotecting crystals when flash freezing them in liquid nitrogen, 3 µL of 0.1 M Mg(OOCH)₂, 13/14% poly(ethylene glycol) 3350, and 40% glycerol were added to the drop containing the *PpBBE1* crystals a few minutes prior to freezing. Crystals were stored in liquid nitrogen and data were collected at 100 K at beamline P11 of the German Electron Synchrotron (DESY, Hamburg, Germany).

Data processing and structure elucidation

Data from the tetragonal bipyramidal crystals were processed with the XDS package (45). A unique molecular replacement solution was obtained in space group P4₁2₁2 in Phenix Phaser (46), using a homology model generated on the SWISS-MODEL server (47–49) based on the crystal structure of

AtBBE-like 15 (pdb code: 4UD8; (3)) as template. The initial solution was refined in cycles of maximum-likelihood least-squares refinement of models modified with Coot (50) using σ_A -weighted $2mF_o - DF_c$ and $F_o - F_c$ electron density maps and including an initial simulated annealing (torsion) step. Details of data collection, processing and refinement are summarized in Table 3.

Table 3: Data collection and refinement statistics.

	Wild-type <i>PpBBE1</i> (pdb: 6EO4)	<i>PpBBE1</i> D396N (pdb: 6EO5)
Data collection		
Space group	$P4_12_12$	$P4_12_12$
Cell dimensions		
<i>a</i> , <i>b</i> , <i>c</i> (Å)	149.2 / 149.2 / 205.6	148.7 / 148.7 / 204.8
α , β , γ (°)	90 / 90 / 90	90 / 90 / 90
Wavelength (Å)	1.009	1.009
Resolution (Å)	48.6 – 2.9 (3.0 – 2.9) ^a	48.4 – 2.6 (2.7 – 2.6)
R_{meas}	0.27 (2.45)	0.173 (2.16)
$I / \sigma I$	13.4 (1.6)	12.1 (1.2)
CC(1/2) (%)	99.8 (66.2)	99.7 (65.8)
Completeness (%)	99.9 (100)	99.9 (99.8)
Redundancy	25.9 (26.5)	14.7 (14.8)
Refinement		
Resolution (Å)	48.6 – 2.9	48.4 – 2.6
No. reflections	52,047	70,960
$R_{\text{work}} / R_{\text{free}}$	18.2 / 20.9	18.3 / 21.0
No. atoms		
Protein	7158	7158
Ligands	134	134
Solvent	10	131
B-factors		
Protein	61.0	63.4
Ligand/ion	66.5	68.6
Solvent	50.6	58.6
R.m.s. deviation		
Bond lengths (Å)	0.009	0.006
Bond angles (°)	1.053	0.884

^aValues in parentheses are for highest-resolution shell.

Molecular docking

The crystal structure of *PpBBE1* wild-type (WT; PDB: 6EO4) in complex with the bicovalently linked FAD cofactor was used as a basis for substrate-docking experiments. All molecular docking

experiments and subsequent MD simulations were performed with the YASARA Structure suite (YASARA structure version 17.3.30; YASARA Biosciences (51)). Crystal waters were removed from the structure prior to the docking experiment. Molecular docking was conducted utilizing the Autodock Vina Plugin (52) of the YASARA Structure suite. Docking was performed with the rigid receptor while the ligand was flexible with a docking cell lining the active site cavity of *PpBBE1*. The ligand chosen for the docking experiments was the previously identified substrate of *PpBBE1*, cellobiose. 250 docking runs were performed with an RMSD cutoff of 1 Å. The resulting docking poses were inspected visually.

Molecular dynamics simulation

The enzyme complex consisting of *PpBBE1*, the bicovalently linked FAD cofactor and the previously docked substrate cellobiose were used as the starting structure for molecular dynamics (MD) simulations. MD simulations and analyses were performed using the YASARA Structure suite, version 17.3.30 (YASARA Biosciences (51)). A periodic simulation cell that enveloped the whole enzyme with an additional 5 Å margin in each dimension was used with explicit solvent. The AMBER14 force field (53) was applied and long-range electrostatic potentials were calculated using the Particle Mesh Ewald (PME) method and a cutoff of 7.864 Å (54, 55). AutoSMILES utility was used to attribute force field parameters to *PpBBE1* and FAD (56). The hydrogen-bonding network optimization was carried out using the method of Hooft and coworkers (57), and pK_a values at pH 6 were assigned (58). The simulation cell was filled with water containing 0.9% of NaCl (density of 0.993 g mL⁻¹). Solvent was relaxed and the system was subsequently energy minimized using steepest descent minimization to remove conformational stress, followed by a simulated annealing minimization to convergence (< 0.05 kJ·mol⁻¹ per 200 steps). Integration time steps were 1.33 and 4 fs for intra- and intermolecular forces, respectively. Subsequently, MD simulations at 310 K were performed, whereby integration time steps for intramolecular and intermolecular forces of 1.25 fs and 2.5 fs were applied, respectively. MD simulations were carried out over a time span of 12.5 ns. A restrain was added to the force field to maintain a catalytically competent complex at the active site. A restraining spring with a force of 100 SFC was applied combined with a distance restrain of 3 Å between the catalytically relevant hydrogen (H1*) of the substrate and the N5 of FAD. Additionally, an angle of 105° was set between N10-N5 and the previously mentioned hydrogen atom (H1*) of the substrate. The restraints were set following the findings of defining general distances and angles for catalysis-competent complexes of flavoenzymes and their respective substrates (59). Analysis of MD simulation results included measuring general distance traces and hydrogen-bonding events of cellobiose with predefined amino acid side chains of *PpBBE1* that determine the structure of the active site.

Secretome analysis

For secretome analysis, the liquid culture supernatant of a *P. patens* line secreting human recombinant Erythropoietin (IMSC40216, www.moss-stock-center.org) (60, 61) was precipitated with TCA as described in (61). Sample preparation and subsequent SDS-PAGE, as well as mass spectrometry were performed as described in (62). Raw data processing and database search were performed against the V1.6 protein models (www.cosmoss.org) using Mascot software (Matrix Science, Boston, MA, USA).

***Physcomitrella patens* moss material and growth conditions**

For all experiments, *P. patens* (Hedw.) B.S. ecotype ‘Gransden 2004’ was used. This is the same strain that was used for genome sequencing (63) and was deposited at the International Moss Stock Centre (IMSC, <http://www.moss-stock-center.org>) under accession number 40001. The $\Delta PpBBE1$ lines described in this study were cryopreserved according to (64) and are available from the International Moss Stock Center (IMSC) with the following accessions: 40829 for $\Delta PpBBE1\#80$, 40830 for $\Delta PpBBE1\#83$ and 40831 for $\Delta PpBBE1\#100$.

The material was axenically cultured in Knop medium (250 mg·L⁻¹ KH₂PO₄, 250 mg·L⁻¹ KCl, 250 mg·L⁻¹ MgSO₄ x 7 H₂O, 1 g·L⁻¹ Ca(NO₃)₂ x 4 H₂O, and 12.5 mg·L⁻¹ FeSO₄ x 7H₂O, pH 5.8; (65)) supplemented with microelements (66) cultivated in a growth chamber under controlled conditions (25°C) with a 16 h : 8 h, light:dark regime at a light intensity of 70 μmol·m⁻²·s⁻¹ as described in (67). For supplementation of media with carbohydrates, cellobiose and glucose were added to a final concentration of 0.5% (w/v). For salt stress experiments, NaCl was added to the solid culture media in concentrations of 500 mM, 750 mM and 1 M. For the adjustment of dry weight in *P. patens*, 10 mL of liquid culture was removed prior to subculturing and filtered through gauze (Miracloth, Calbiochem, Schwalbach, Germany). The dry weight was determined after drying the sample at 105°C for 2 h. For the induction of sporophytes, the Petri dishes were transferred to inducing conditions according to (68). For dark treatment, protonema in liquid medium were grown for 3 weeks, whereas gametophores on solid medium were incubated in a light-tight box in a growth chamber for 4 to 6 weeks. Additionally, spot inocula of protonema were grown in darkness for 4 weeks either directly after inoculation or after preculture under standard light conditions for 2 weeks.

Generation and validation of $\Delta PpBBE$ lines

For construction of the *PpBBE1*-knockout construct, genomic DNA was isolated according to (69) and used as template in an overlap extension PCR. Fragments of exon 1 and exon 3, together with the respective ~850 bp flanking regions, were amplified in separate PCR reactions, with the reverse primer for exon 1 (first 38 bp) and the forward primer for exon 3 (last 37 bp) carrying an overlapping

sequence with the flanking regions of the *nptII* selection cassette, which should replace the missing gene fragment (Figure 9A, Table 4). In a second PCR reaction, all three fragments were fused, before subcloning the newly generated DNA to pJET and transforming the recombinant plasmid with *E. coli* Top 10 cells for further amplification. Since sequencing of the subcloned DNA revealed a mutation, the error was removed in an additional mutagenesis PCR reaction (Primers see Table 4).

Table 4: Primers used for the generation of the $\Delta PpBBE1$ strain.

Primer	Sequence
PpE1_fwd	5'-CGTGGCATGCATGCCTAAG-3'
PpE1_rev	5'-CGTGCTCCACCATGTTGACCGCCGCGAGTAACCCTAAGCACTG-3'
Pp_neo_fwd	5'-CAGTGCTTAGGGTTACTGCGGCGGTCAACATGGTGGAGCACG-3'
Pp_neo_rev	5'-CTTTGGGGGAAGTTGAAGACGTGCAGGTCACTGGATTTTGGTTTTAG-3'
PpE3_fwd	5'-CTAAAACCAAAATCCAGTGACCTGCACGTCTTCAACTTCCCCCAAAG-3'
PpE3_rev	5'-CACCTGTTGAAAATTAATTAATATTATTAATCCTAG-3'
Pp_mut_fwd	5'-CAGGCTCAAGGCGCGTATGCCCGACGGCG-3'
Pp_mut_rev	5'-CGCCGTCGGGCATACGCGCCTTGAGCCTG-3'

Prior to the transformation procedure, the *PpBBE1*-knockout construct was cut from the pJET vector using *SphI* and *PacI*. Protoplast isolation, transformation, and regeneration to obtain stable knockout plants were performed as previously described (23) using 40-50 μg of DNA. Selection was done in two successive cycles by transferring the cultures to solid media complemented with 25 $\text{mg}\cdot\text{L}^{-1}$ G418 (Promega, Mannheim, Germany) - release period of two weeks between the two selections as described in (23). Plants were screened for correct 5'- and 3'- integration of the knockout construct via direct PCR (24) using the primer combinations BBE_5'Int_f and RT1 or RT4 and BBE_3'Int_r, respectively. As a positive control for successful extraction of DNA, the primers EF1 α _fw and EF1 α _rev were used. The loss of transcript in the putative $\Delta PpBBE1$ lines was verified by direct PCR, using the primer couple BBE_E2_f and BBE_E3I_r, which generates a transcript of 546 bp length in WT. As control for successful cDNA synthesis, C45_fwd and C45_rev were used, amplifying a part of the constitutively expressed mRNA of the ribosomal protein L21.

To estimate the number of integrations of *PpBBE1*-targeting constructs, a qPCR-based method (26) was used. The 5'-HR region and the 3'-HR region were amplified using the primer couples qPCR_BBE_5HR_fw and qPCR_BBE_5HR_rev and qPCR_BBE_3HR_fw, and qPCR_BBE_3HR_rev, respectively, whereas transcripts of the *nptII* selection cassette and the single copy gene pCLF (internal control) were generated using the primer couples q_npt_fw and q_npt_rev and pCLF_5915_qf and pCLF_5981_qr or pCLF_7739_qf and pCLF_7804_qr, respectively. From these results, the copy number of *PpBBE1*-knockout genes could be determined.

As control lines, a WT strain and a line with a confirmed single integration of the *nptII* selection cassette were used. The complete list of primers used for the cloning of the *PpBBE1*-targeting construct and molecular validation of the transgenic plants is shown in Table 5.

Table 5: Primers used for the cloning of the *PpBBE1*-targeting construct and the subsequent molecular validation of the transgenic plants.

Purpose	Name	Sequence
5'- integration direct PCR	BBE_5'Int_f	5'-TCGACTACCAGCTTCTTGTGC-3'
	RT1	5'-TGTCGTGCTCCACCATGTTG-3'
3'- integration direct PCR	RT4	5'-GTTGAGCATATAAGAAACCC-3'
	BBE_3'Int_r	5'-ACCTTGTCAAGGAGTGATG -3'
control for DNA direct PCR	EF1 α _fw	5'-AGCGTGGTATCACAATTGAC-3'
	EF1 α _rev	5'-GATCGCTCGATCATGTTATC-3'
loss of transcript RT-PCR	BBE_E2_f	5'-TGTCGCTCAAGTGCAGAATG-3'
	BBE_E3I_r	5'-TCTTGAACAACACCGCCTTG-3'
cDNA control RT-PCR	C45_fwd.	5'-GGCTGGTCATGGGTTGCG-3'
	C45_rev.	5'-GAGGTCAACTGTCTCGCC-3'
qPCR copy number nptII	q-nptfw	5'-GGCTATTCGGCTATGACTGG-3'
	q-nptrev	5'-CAGGTCGGTCTTGACAAAAAG-3'
qPCR copy number 5'HR	qPCR_BBE_5HR_fw	5'-CAGTATTCTATTTGTTGCAGTTTCTCA-3'
	qPCR_BBE_5HR_rev	5'-GCTTCACGTTAGGCTGATTGA-3'
qPCR copy number 3'HR	qPCR_BBE_3HR_fw	5'-GGATGAACTGTAGAGAAATACTTCGAC-3'
	qPCR_BBE_3HR_rev	5'-AGTAGTGACCGTTTCTTAATGAAGTTT-3'
qPCR copy number control	PpCLF_5915_qf	5'-AGCAATGTCCGTGCTACTT-3'
	PpCLF_5981_qr	5'-TTGTAAGAATCACTCACCCACAG-3'
qPCR copy number control	PpCLF_7739_qf	5'-GTATTGGCGATCCCACTCTT-3'
	PpCLF_7804_qr	5'-GCATAAAATAGGTCACAGATTGAGG-3'

As the DNA content of *Physcomitrella* is known, haploidy of the $\Delta PpBBE1$ lines could be confirmed in a fluorescence-based assay. Nuclei prepared from 10 to 30 mg freshly chopped protonema material were stained with a 4',6-diamidino-2-phenylindole (DAPI)-containing buffer (25) and analysed using a Cyflow® Space flow cytometry system (Partec, Münster, Germany) as described in (70).

Qualitative and quantitative determination of cellobiose and glucose

In order to qualitatively assay the cellobiose and glucose content of solid media, plates were stained with a solution of 0.1% (w/v) congo red. After washing with a 0.5 M NaCl solution for five times, for better visualization of lighter stained zones, the pH was adjusted to 2. Benedict's test, using 1 mL of the sample and 200 μ L of Benedict's reagent, performed according to (71), was used to qualitatively analyze the liquid culture supernatants. Here, a color change from blue to red, caused by the precipitation of copper sulfate, indicates the presence of reducing sugars in the solution. For quantification of cellobiose and glucose in the liquid media, a DNS assay was performed as described (72) - 250 μ L of sample was mixed with 250 μ L of 0.005 M sodium acetate buffer pH 4.8 and 750 μ L of DNS reagent. Photometric quantification was done at 575 nm for all samples and appropriate

standard dilution series for each sugar. Additionally, sugars were quantified using the glucose test strips of the Reflectoquant system (Merck).

Image acquisition

Images were acquired with an ICc1 or Mrc5 CCD camera (Zeiss, Oberkochen, Germany) at an Olympus SZX7 binocular microscope (Olympus, Tokyo, Japan) or an Axiovert S100 (Zeiss). AXIOVISION Software Version 4.8 (Zeiss) was used for imaging.

Author contributions

P.M. initiated the project; M.T., R.R., G.W., B.D. and P.M. designed the experiments and interpreted the data. M.T. expressed and purified *PpBBE1* and performed analytical, biochemical and kinetic experiments. M.T. and A.W. crystallized proteins and determined the 3D-structure of *PpBBE1*. G.W. analyzed organization and expression of the *PpBBEs* and generated knock-out moss mutants. G.W. and J.K. analyzed the moss mutants. S.N.W.H. analyzed the secretion of *PpBBE1* into the moss culture medium. J.N. performed docking; M.T., A.W. and P.M. wrote the manuscript with the help of R.R. and G.W.

Conflict of interest

The authors declare no conflict of interest.

Acknowledgements

This work was supported by a grant from the Austrian Science Fund (FWF) through grants W901 (Doctoral Program “Molecular Enzymology”) and P28678 and by the Excellence Initiative of the German Federal and State Governments (EXC 294 to R.R.). The authors are also grateful for the support by the interuniversity program in natural sciences (NAWI Graz). We are very grateful to Prof. Hansjörg Weber (TU Graz) for his assistance in recording NMR-spectra, Richard Haas for his excellent technical assistance, *Greenovation* GmbH for providing the EPO strain, Dr. Juliana Parsons for preparation of the protein samples, Prof. Dr. Andreas Schlosser for MS measurements and Anne Katrin Prowse for proof-reading of the manuscript.

References

1. Kutchan, T. M., and Dittrich, H. (1995) Characterization and mechanism of the berberine bridge enzyme, a covalently flavinylated oxidase of benzophenanthridine alkaloid biosynthesis in plants. *J. Biol. Chem.* **270**, 24475–24481
2. Daniel, B., Konrad, B., Toplak, M., Lahham, M., Messenlehner, J., Winkler, A., and Macheroux, P. (2017) The family of berberine bridge enzyme-like enzymes: A treasure-trove of oxidative reactions. *Arch. Biochem. Biophys.* **632**, 88–103
3. Daniel, B., Pavkov-Keller, T., Steiner, B., Dordic, A., Gutmann, A., Nidetzky, B., Sensen, C. W., Van Der Graaff, E., Wallner, S., Gruber, K., and Macheroux, P. (2015) Oxidation of monolignols by members of the berberine bridge enzyme family suggests a role in plant cell wall metabolism. *J. Biol. Chem.* **290**, 18770–18781
4. Rajniak, J., Barco, B., Clay, N. K., and Sattely, E. S. (2015) A new cyanogenic metabolite in *Arabidopsis* required for inducible pathogen defence. *Nature*. **525**, 375–379
5. Custers, J. H. H. V., Harrison, S. J., Sela-Buurlage, M. B., Van Deventer, E., Lageweg, W., Howe, P. W., Van Der Meijs, P. J., Ponstein, A. S., Simons, B. H., Melchers, L. S., and Stuiver, M. H. (2004) Isolation and characterisation of a class of carbohydrate oxidases from higher plants, with a role in active defence. *Plant J.* **39**, 147–160
6. Zafred, D., Nandy, A., Pump, L., Kahlert, H., and Keller, W. (2013) Crystal structure and immunologic characterization of the major grass pollen allergen Phl p 4. *J. Allergy Clin. Immunol.* 10.1016/j.jaci.2013.03.021
7. Carter, C. J., and Thornburg, R. W. (2004) Tobacco nectarin V is a flavin-containing berberine bridge enzyme-like protein with glucose oxidase activity. *Plant Physiol.* **134**, 460–469
8. Zimmer, A. D., Lang, D., Buchta, K., Rombauts, S., Nishiyama, T., Hasebe, M., Van de Peer, Y., Rensing, S. A., and Reski, R. (2013) Reannotation and extended community resources for the genome of the non-seed plant *Physcomitrella patens* provide insights into the evolution of plant gene structures and functions. *BMC Genomics.* **14**, 498
9. Rensing, S. A., Ick, J., Fawcett, J. A., Lang, D., Zimmer, A., Van de Peer, Y., and Reski, R. (2007) An ancient genome duplication contributed to the abundance of metabolic genes in the moss *Physcomitrella patens*. *BMC Evol. Biol.* **7**, 130
10. O'Donoghue, M. T., Chater, C., Wallace, S., Gray, J. E., Beerling, D. J., and Fleming, A. J. (2013) Genome-wide transcriptomic analysis of the sporophyte of the moss *Physcomitrella patens*. *J. Exp. Bot.* **64**, 3567–3581
11. Xiao, L., Wang, H., Wan, P., Kuang, T., and He, Y. (2011) Genome-wide transcriptome analysis of gametophyte development in *Physcomitrella patens*. *BMC Plant Biol.* **11**, 177
12. Ortiz-Ramírez, C., Hernandez-Coronado, M., Thamm, A., Catarino, B., Wang, M., Dolan, L., Feijó, J. A. A., and Becker, J. D. D. (2016) A transcriptome atlas of *Physcomitrella patens* provides insights into the evolution and development of land plants. *Mol. Plant.* **9**, 205–220

13. Hiss, M., Laule, O., Meskauskiene, R. M., Arif, M. A., Decker, E. L., Erxleben, A., Frank, W., Hanke, S. T., Lang, D., Martin, A., Neu, C., Reski, R., Richardt, S., Schallenberg-Rüdinger, M., Szövényi, P., Tiko, T., Wiedemann, G., Wolf, L., Zimmermann, P., and Rensing, S. A. (2014) Large-scale gene expression profiling data for the model moss *Physcomitrella patens* aid understanding of developmental progression, culture and stress conditions. *Plant J.* **79**, 530–539
14. Petersen, T. N., Brunak, S., von Heijne, G., and Nielsen, H. (2011) SignalP 4.0: discriminating signal peptides from transmembrane regions. *Nat. Methods.* **8**, 785–786
15. Finn, R. D., Coghill, P., Eberhardt, R. Y., Eddy, S. R., Mistry, J., Mitchell, A. L., Potter, S. C., Punta, M., Qureshi, M., Sangrador-Vegas, A., Salazar, G. A., Tate, J., and Bateman, A. (2016) The Pfam protein families database: Towards a more sustainable future. *Nucleic Acids Res.* **44**, D279–D285
16. Winkler, A., Hartner, F., Kutchan, T. M., Glieder, A., and Macheroux, P. (2006) Biochemical evidence that berberine bridge enzyme belongs to a novel family of flavoproteins containing a bi-covalently attached FAD cofactor *. *J. Biol. Chem.* **281**, 21276–21285
17. Winkler, A., Kutchan, T. M., and Macheroux, P. (2007) 6-S-cysteinylation of bi-covalently attached FAD in berberine bridge enzyme tunes the redox potential for optimal activity. *J. Biol. Chem.* **282**, 24437–24443
18. Huang, C. H., Lai, W. L., Lee, M. H., Chen, C. J., Vasella, A., Tsai, Y. C., and Liaw, S. H. (2005) Crystal structure of glucooligosaccharide oxidase from *Acremonium strictum*: A novel flavinylation of 6-S-cysteinyl, 8 α -N1-histidyl FAD. *J. Biol. Chem.* **280**, 38831–38838
19. Massey, V. (1991) A simple method for the determination of redox potentials. in *Flavins and Flavoproteins* (Curti, B., Zanetti, G., and Ronchi, S. eds), pp. 59–66, Walter de Gruyter, Como, Italy
20. Zafred, D., Steiner, B., Teufelberger, A. R., Hromic, A., Karplus, P. A., Schofield, C. J., Wallner, S., and Macheroux, P. (2015) Rationally engineered flavin-dependent oxidase reveals steric control of dioxygen reduction. *FEBS J.* **282**, 3060–3074
21. Krissinel, E., and Henrick, K. (2007) Inference of macromolecular assemblies from crystalline state. *J. Mol. Biol.* **372**, 774–797
22. Pils, S., Schnabl, K., Wallner, S., Kljajic, M., Kupresanin, N., Breinbauer, R., Fuchs, M., Rocha, R., Schrittwieser, J. H., Kroutil, W., Daniel, B., and Macheroux, P. (2016) Characterization of the monolignol oxidoreductase AtBBE-like protein 15 L182V for biocatalytic applications. *Journal Mol. Catal. B, Enzym.* **133**, S6–S14
23. Hohe, A., Egener, T., Lucht, J. M., Holtorf, H., Reinhard, C., Schween, G., and Reski, R. (2004) An improved and highly standardised transformation procedure allows efficient production of single and multiple targeted gene-knockouts in a moss, *Physcomitrella patens*. *Curr. Genet.* **44**, 339–347

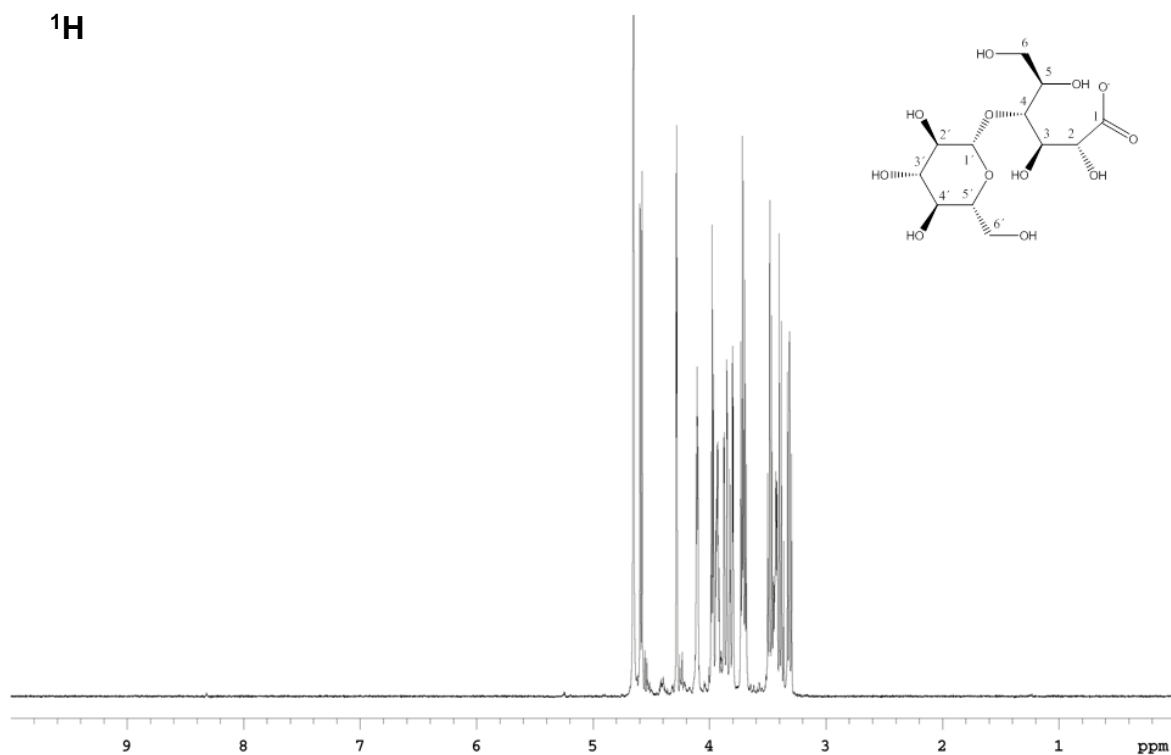
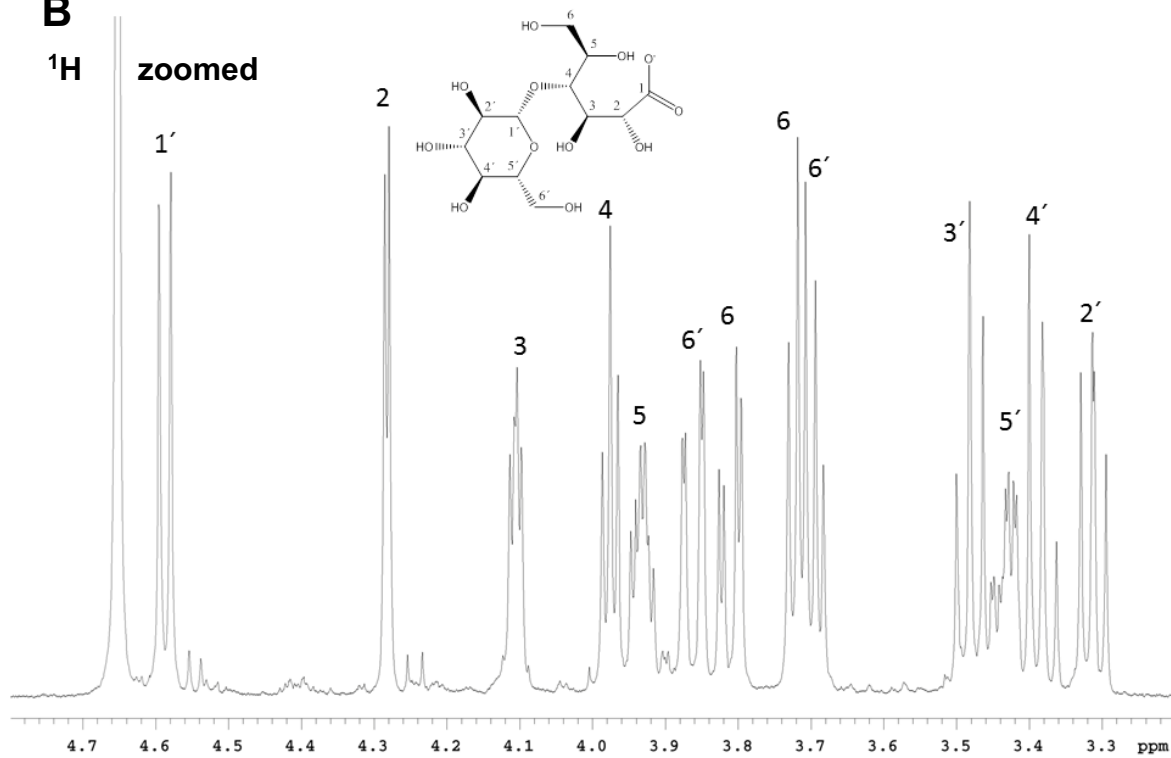
24. Schween, G., Fleig, S., and Reski, R. (2002) High-throughput-PCR screen of 15,000 transgenic *Physcomitrella* plants. *Plant Mol. Biol. Report.* **20**, 43–47
25. Schween, G., Gorr, G., Hohe, A., and Reski, R. (2003) Unique tissue-specific cell cycle in *Physcomitrella*. *Plant Biol.* **5**, 50–58
26. Noy-Malka, C., Yaari, R., Itzhaki, R., Mosquna, A., Auerbach Gershovitz, N., Katz, A., and Ohad, N. (2014) A single CMT methyltransferase homolog is involved in CHG DNA methylation and development of *Physcomitrella patens*. *Plant Mol. Biol.* **84**, 719–735
27. Lorenz, S., Tintelnot, S., Reski, R., and Decker, E. L. (2003) Cyclin D-knockout uncouples developmental progression from sugar availability. *Plant Mol. Biol.* **53**, 227–236
28. Thelander, M., Olsson, T., and Ronne, H. (2005) Effect of the energy supply on filamentous growth and development in *Physcomitrella patens*. *J. Exp. Bot.* **56**, 653–662
29. Winkler, A., Łyskowski, A., Riedl, S., Puhl, M., Kutchan, T. M., Macheroux, P., and Gruber, K. (2008) A concerted mechanism for berberine bridge enzyme. *Nat. Chem. Biol.* **4**, 739–741
30. Fan, F., and Gadda, G. (2005) On the catalytic mechanism of choline oxidase. *J. Am. Chem. Soc.* **127**, 2067–2074
31. Macheroux, P., Massey, V., Thiele, D. J., and Volokita, M. (1991) Expression of spinach glycolate oxidase in *Saccharomyces cerevisiae*: Purification and characterization. *Biochemistry.* **30**, 4612–4619
32. Harris, C. M., Molla, G., Pilone, M. S., and Pollegioni, L. (1999) Studies on the reaction mechanism of *Rhodotorula gracilis* D-amino-acid oxidase. Role of the highly conserved Tyr-223 on substrate binding and catalysis. *J. Biol. Chem.* **274**, 36233–36240
33. Alexeev, I., Sultana, A., Mäntsälä, P., Niemi, J., and Schneider, G. (2007) Aclacinomycin oxidoreductase (AknOx) from the biosynthetic pathway of the antibiotic aclacinomycin is an unusual flavoenzyme with a dual active site. *Proc. Natl. Acad. Sci. U. S. A.* **104**, 6170–5
34. Ober, D., and Kaltenecker, E. (2009) Pyrrolizidine alkaloid biosynthesis, evolution of a pathway in plant secondary metabolism. *Phytochemistry.* **70**, 1687–1695
35. Wang, X., Chen, L., Yang, A., Bu, C., and He, Y. (2017) Quantitative proteomics analysis of developmental reprogramming in protoplasts of the moss *Physcomitrella patens*. *Plant Cell Physiol.* **58**, 946–961
36. Nihira, T., Saito, Y., Nishimoto, M., Kitaoka, M., Igarashi, K., Ohtsubo, K., and Nakai, H. (2013) Discovery of cellobionic acid phosphorylase in cellulolytic bacteria and fungi. *FEBS Lett.* **587**, 3556–3561
37. Hildebrand, A., Bennett Addison, J., Kasuga, T., and Fan, Z. (2016) Cellobionic acid inhibition of cellobiohydrolase I and cellobiose dehydrogenase. *Biochem. Eng. J.* **109**, 236–242
38. Reski, R. (1998) Development, genetics and molecular biology of mosses. *Bot. Acta.* **111**, 1–15
39. Regmi, K. C., Li, L., and Gaxiola, R. A. (2017) Alternate modes of photosynthate transport in the alternating generations of *Physcomitrella patens*. *Front. Plant Sci.* 10.3389/fpls.2017.01956

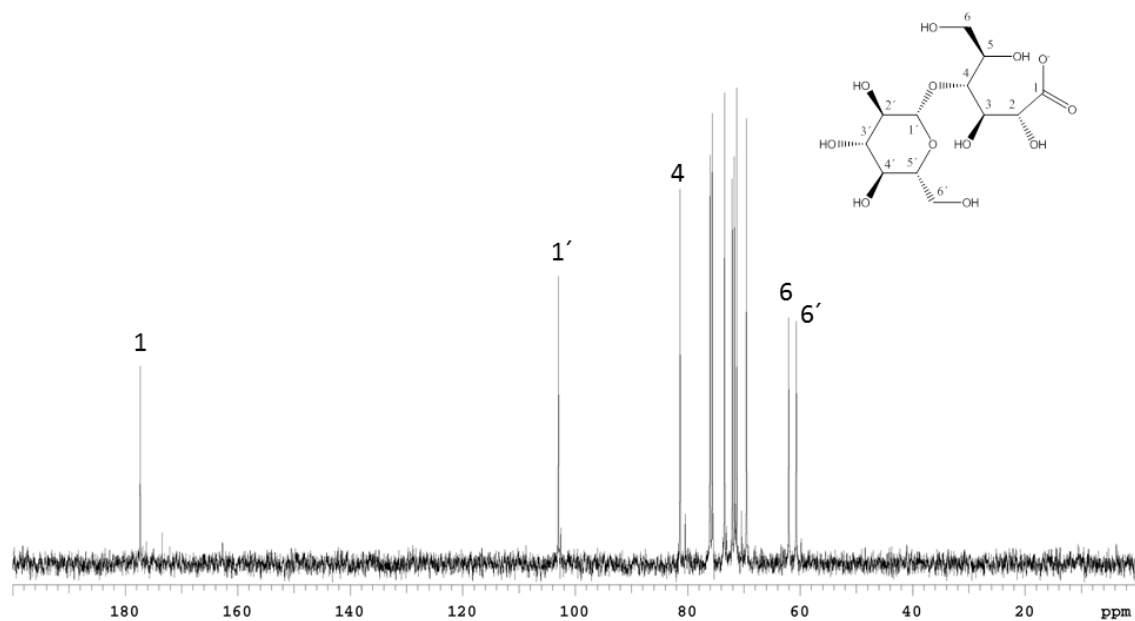
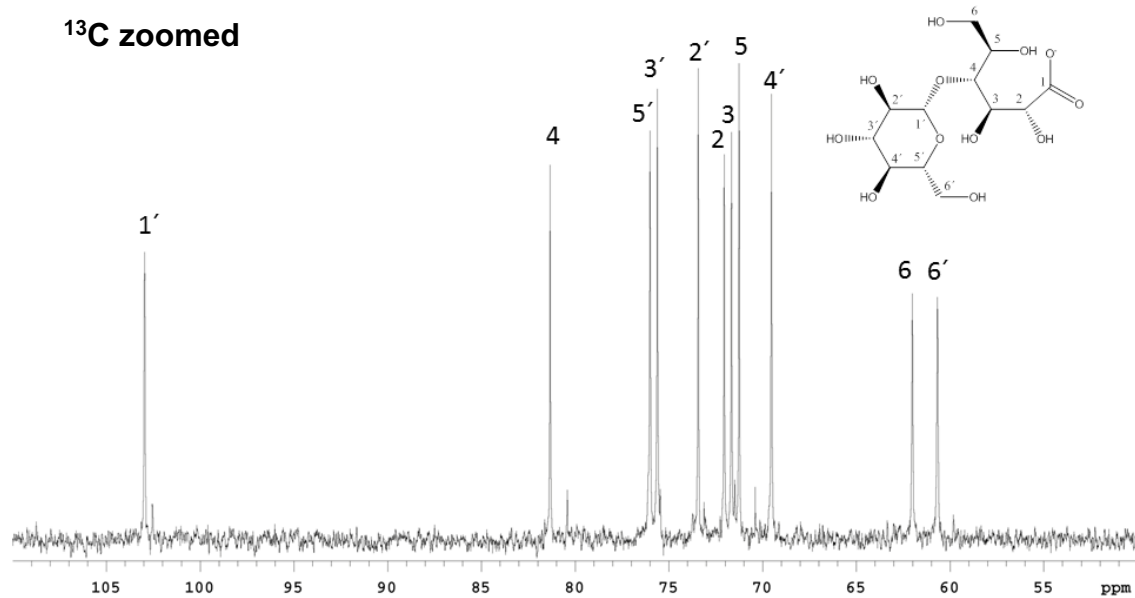
40. Olsson, T., Thelander, M., and Ronne, H. (2003) A novel type of chloroplast stromal hexokinase is the major glucose-phosphorylating enzyme in the moss *Physcomitrella patens*. *J. Biol. Chem.* **278**, 44439–44447
41. Weis, R., Luiten, R., Skranc, W., Schwab, H., Wubbolts, M., and Glieder, A. (2004) Reliable high-throughput screening with *Pichia pastoris* by limiting yeast cell death phenomena. *FEMS Yeast Res.* **5**, 179–189
42. Schrittwieser, J. H., Resch, V., Wallner, S., Lienhart, W. D., Sattler, J. H., Resch, J., Macheroux, P., and Kroutil, W. (2011) Biocatalytic organic synthesis of optically pure (*S*)-scoulerine and berbine and benzyloisoquinoline alkaloids. *J. Org. Chem.* **76**, 6703–6714
43. Massey, V., and Hemmerich, P. (1978) Photoreduction of flavoproteins and other biological compounds catalyzed by deazaflavins. *Biochemistry.* **17**, 9–16
44. Minnaert, K. (1965) Measurement of the equilibrium constant of the reaction between cytochrome c and cytochrome a. *Biochim. Biophys. Acta.* **110**, 42–56
45. Kabsch, W. (2010) XDS. *Acta Cryst (2010).* **D66**, 125–132 [[doi10.1107/S0907444909047337](https://doi.org/10.1107/S0907444909047337)]. 10.1107/S0907444909047337
46. McCoy, A. J., Grosse-Kunstleve, R. W., Adams, P. D., Winn, M. D., Storoni, L. C., and Read, R. J. (2007) Phaser crystallographic software. *J. Appl. Crystallogr.* **40**, 658–674
47. Biasini, M., Bienert, S., Waterhouse, A., Arnold, K., Studer, G., Schmidt, T., Kiefer, F., Cassarino, T. G., Bertoni, M., Bordoli, L., and Schwede, T. (2014) SWISS-MODEL: Modelling protein tertiary and quaternary structure using evolutionary information. *Nucleic Acids Res.* 10.1093/nar/gku340
48. Arnold, K., Bordoli, L., Kopp, J., and Schwede, T. (2006) The SWISS-MODEL workspace: A web-based environment for protein structure homology modelling. *Bioinformatics.* **22**, 195–201
49. Benkert, P., Biasini, M., and Schwede, T. (2011) Toward the estimation of the absolute quality of individual protein structure models. *Bioinformatics.* **27**, 343–350
50. Emsley, P., Lohkamp, B., Scott, W. G., and Cowtan, K. (2010) Features and development of Coot. *Acta Crystallogr. Sect. D Biol. Crystallogr.* **66**, 486–501
51. Krieger, E., and Vriend, G. (2014) YASARA View - molecular graphics for all devices - from smartphones to workstations. *Bioinformatics.* **30**, 2981–2982
52. Trott, O., and Olson, A. (2010) AutoDock Vina: improving the speed and accuracy of docking with a new scoring function, efficient optimization and multithreading. *J. Comput. Chem.* **31**, 455–461
53. Wang, J., Cieplak, P., and Kollman, P. A. (2000) How well does a restrained electrostatic potential (RESP) model perform in calculating conformational energies of organic and biological molecules? *J. Comput. Chem.* **21**, 1049–1074

54. Cornell, W. D., Cieplak, P., Bayly, C. I., Gould, I. R., Merz, K. M., Ferguson, D. M., Spellmeyer, D. C., Fox, T., Caldwell, J. W., and Kollman, P. A. (1995) A second generation force field for the simulation of proteins, nucleic acids, and organic molecules. *J. Am. Chem. Soc.* **117**, 5179–5197
55. Essmann, U., Perera, L., Berkowitz, M. L., Darden, T., Lee, H., and Pedersen, L. G. (1995) A smooth particle mesh Ewald method. *J. Chem. Phys.* **103**, 8577–8593
56. Jakalian, A., Jack, D. B., and Bayly, C. I. (2002) Fast, efficient generation of high-quality atomic charges. AM1-BCC model: II. Parameterization and validation. *J. Comput. Chem.* **23**, 1623–1641
57. Hooft, R. W. W., Vriend, G., Sander, C., and Abola, E. E. (1996) Errors in protein structures. *Nature.* **381**, 272–272
58. Krieger, E., Nielsen, J. E., Spronk, C. A. E. M., and Vriend, G. (2006) Fast empirical pKa prediction by Ewald summation. *J. Mol. Graph. Model.* **25**, 481–486
59. Fraaije, M. W., and Mattevi, A. (2000) Flavoenzymes: Diverse catalysts with recurrent features. *Trends Biochem. Sci.* **25**, 126–132
60. Weise, A., Altmann, F., Rodriguez-Franco, M., Sjoberg, E. R., Bäumer, W., Launhardt, H., Kietzmann, M., and Gorr, G. (2007) High-level expression of secreted complex glycosylated recombinant human erythropoietin in the *Physcomitrella* Delta-fuc-t Delta-xyl-t mutant. *Plant Biotechnol. J.* **5**, 389–401
61. Parsons, J., Altmann, F., Arrenberg, C. K., Koprivova, A., Beike, A. K., Stemmer, C., Gorr, G., Reski, R., and Decker, E. L. (2012) Moss-based production of asialo-erythropoietin devoid of Lewis A and other plant-typical carbohydrate determinants. *Plant Biotechnol. J.* **10**, 851–861
62. Hoernstein, S. N. W., Mueller, S. J., Fiedler, K., Schuelke, M., Vanselow, J. T., Schuessele, C., Lang, D., Nitschke, R., Igloi, G. L., Schlosser, A., and Reski, R. (2016) Identification of targets and interaction partners of arginyl-tRNA protein transferase in the moss *Physcomitrella patens*. *Mol. Cell. Proteomics.* 10.1074/mcp.M115.057190
63. Rensing, S. A., Lang, D., Zimmer, A. D., Terry, A., Salamov, A., Shapiro, H., Nishiyama, T., Perroud, P.-F., Lindquist, E. A., Kamisugi, Y., Tanahashi, T., Sakakibara, K., Fujita, T., Oishi, K., Shin-I, T., Kuroki, Y., Toyoda, A., Suzuki, Y., Hashimoto, S.-I., Yamaguchi, K., Sugano, S., Kohara, Y., Fujiyama, A., Anterola, A., Aoki, S., Ashton, N., Barbazuk, W. B., Barker, E., Bennetzen, J. L., Blankenship, R., Cho, S. H., Dutcher, S. K., Estelle, M., Fawcett, J. A., Gundlach, H., Hanada, K., Heyl, A., Hicks, K. A., Hughes, J., Lohr, M., Mayer, K., Melkozernov, A., Murata, T., Nelson, D. R., Pils, B., Prigge, M., Reiss, B., Renner, T., Rombauts, S., Rushton, P. J., Sanderfoot, A., Schween, G., Shiu, S.-H., Stueber, K., Theodoulou, F. L., Tu, H., Van de Peer, Y., Verrier, P. J., Waters, E., Wood, A., Yang, L., Cove, D., Cuming, A. C., Hasebe, M., Lucas, S., Mishler, B. D., Reski, R., Grigoriev, I. V., Quatrano, R. S., and Boore, J. L. (2008) The *Physcomitrella* genome reveals evolutionary

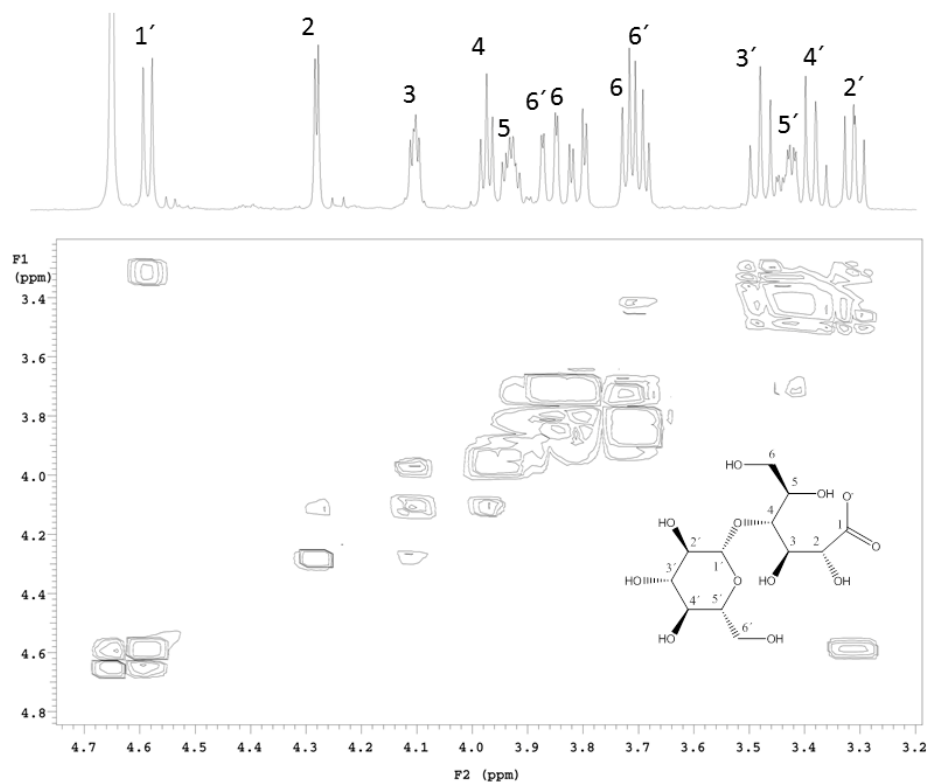
- insights into the conquest of land by plants. *Science*. **319**, 64–9
64. Schulte, J., and Reski, R. (2004) High throughput cryopreservation of 140,000 *Physcomitrella patens* mutants. *Plant Biol. (Stuttg)*. **6**, 119–27
 65. Reski, R., and Abel, W. O. (1985) Induction of budding on chloronemata and caulonemata of the moss, *Physcomitrella patens*, using isopentenyladenine. *Planta*. **165**, 354–358
 66. Schween, G., Hohe, A., Koprivova, A., and Reski, R. (2003) Effects of nutrients, cell density and culture techniques on protoplast regeneration and early protonema development in a moss, *Physcomitrella patens*. *J. Plant Physiol.* **160**, 209–12
 67. Decker, E. L., Wiedemann, G., and Reski, R. (2015) Gene targeting for precision glyco-engineering: Production of biopharmaceuticals devoid of plant-typical glycosylation in moss bioreactors. in *Glyco-Engineering: Methods and Protocols*, pp. 213–224, 10.1007/978-1-4939-2760-9_15
 68. Hohe, A., Rensing, S. A., Mildner, M., Lang, D., and Reski, R. (2002) Day length and temperature strongly influence sexual reproduction and expression of a novel MADS-box gene in the moss *Physcomitrella patens*. *Plant Biol.* **4**, 595–602
 69. Edwards, K., Johnstone, C., and Thompson, C. (1991) A simple and rapid method for the preparation of plant genomic DNA for PCR analysis. *Nucleic Acids Res.* **19**, 1349
 70. Schuessele, C., Hoernstein, S. N. W., Mueller, S. J., Rodriguez-Franco, M., Lorenz, T., Lang, D., Igloi, G. L., and Reski, R. (2016) Spatio-temporal patterning of arginyl-tRNA protein transferase (ATE) contributes to gametophytic development in a moss. *New Phytol.* **209**, 1014–1027
 71. Simoni, R., Hill, R., and Vaughan, M. (2002) Benedict's solution a reagent for measuring reducing sugars the clinical chemistry of Stanley R Benedict. *J. Biol. Chem.* **277**, 10–11
 72. Moretti, R., and Thorson, J. S. (2008) A comparison of sugar indicators enables a universal high-throughput sugar-1-phosphate nucleotidyltransferase assay. *Anal. Biochem.* **377**, 251–258

Supporting information

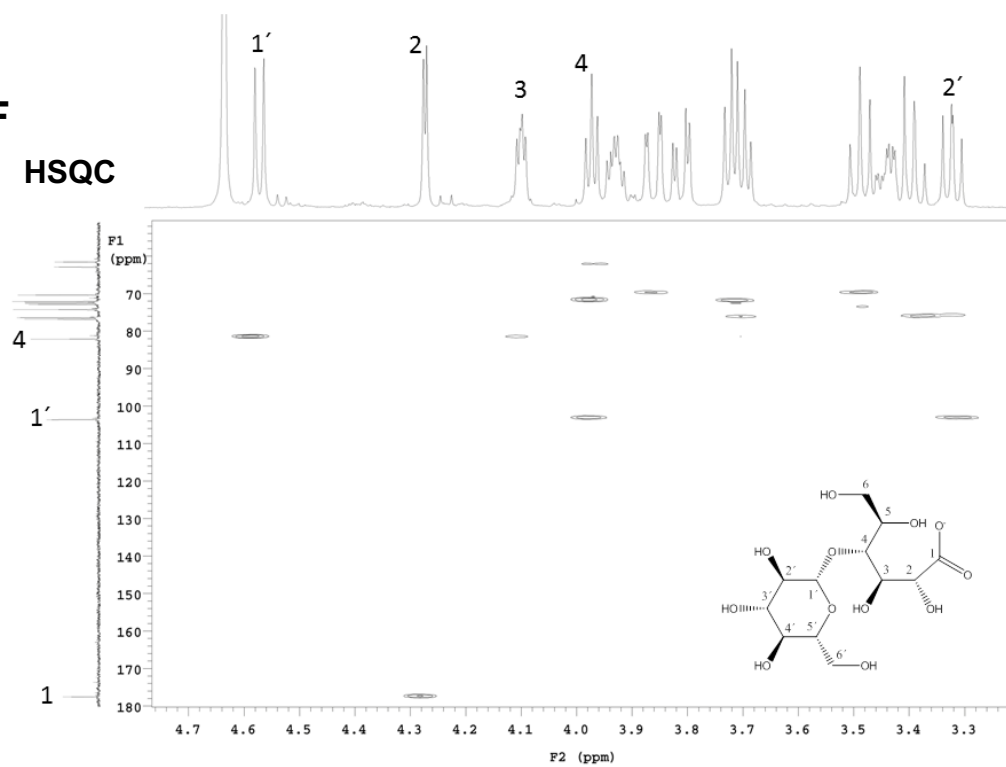
A
 ^1H **B**
 ^1H 

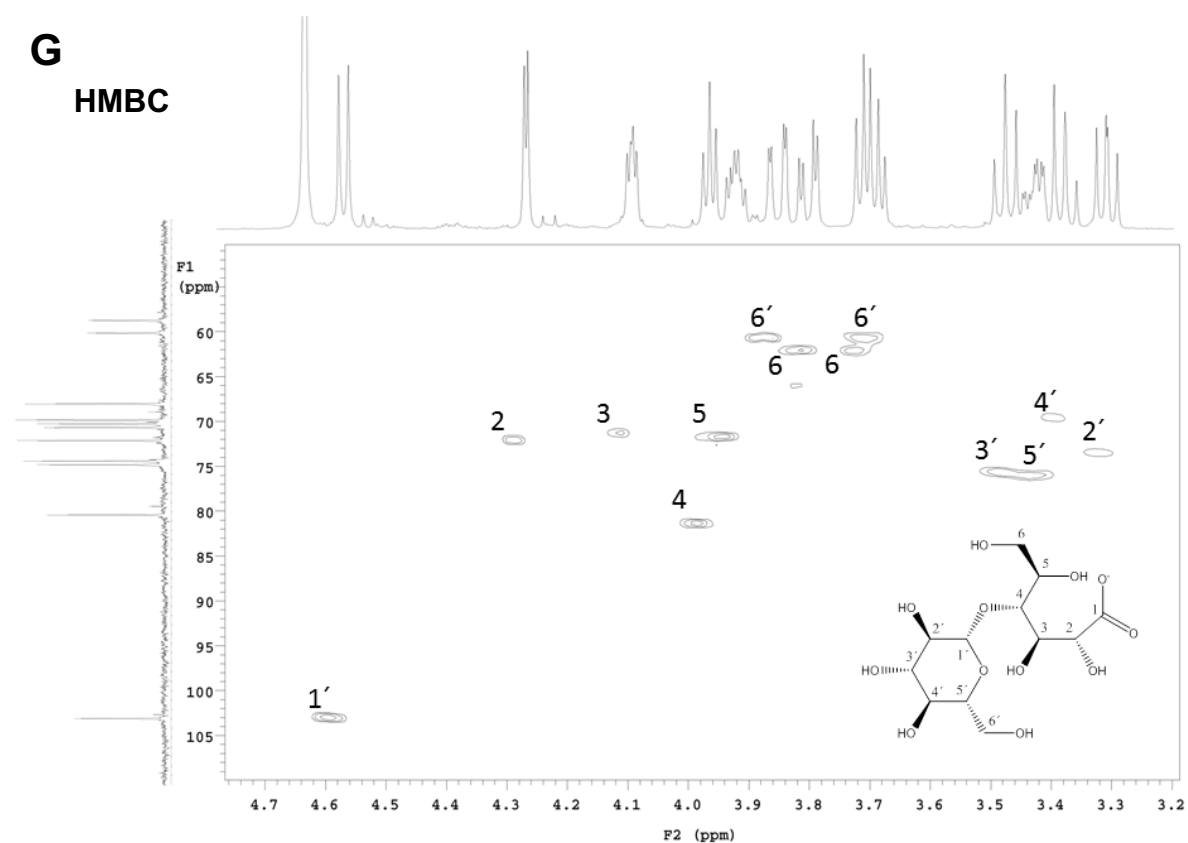
C
 ^{13}C **D**
 ^{13}C zoomed

E
COSY



F
HSQC





Supplementary Figure S1: NMR-analyses of the product formed in the enzymatic reaction of *PpBBE1* with cellobiose: ^1H - (panel A: full spectrum, panel B: zoomed), ^{13}C - (panel C: full spectrum; panel D: zoomed), COSY (panel E), HSQC (panel F) and HMBC (panel G) spectra were recorded in D_2O to clearly identify the product of the enzymatic turnover of cellobiose by *PpBBE1*.

Chapter 3

8f-FAD formation in hETF

Oxidation of the FAD cofactor to the 8-formyl-derivative in human electron transferring flavoprotein

Peter Augustin^{S*}, Marina Toplak^{S*}, Katharina Fuchs^S, Eva Christine Gerstmann^S, Ruth Prassl^S,
Andreas Winkler^S and Peter Macheroux^{S*}

^SInstitute of Biochemistry, Graz University of Technology, Petersgasse 12/II, 8010 Graz, Austria

^SInstitute of Biophysics, Medical University of Graz, Neue Stiftingtalstraße 6/IV, 8010 Graz, Austria

*These authors have contributed equally to this work

*To whom correspondence should be addressed:

Prof. Dr. Peter Macheroux

Graz University of Technology

Institute of Biochemistry

Petersgasse 12/II, A-8010 Graz

Telephone: +43-(0)316-873 6450;

FAX: +43 (0)316-873 6952;

E-mail: peter.macheroux@tugraz.at

Running title: 8-formyl-FAD formation in hETF

Keywords: 8-formyl-FAD, electron transfer, flavin semiquinone, mitochondrial matrix, dehydrogenases.

Abbreviations

8f-FAD, 8-formyl-FAD; (h)DMGDH, (human) dimethylglycine dehydrogenase; DPPH, α,α' -diphenyl- β -picryl hydrazyl; (h)ETF, (human) electron-transferring flavoprotein; (h)ETF-QO, (human) ETF-ubiquinone oxidoreductase; GAIL, glutaric aciduria type II; (h)MCAD, (human) medium chain acyl-CoA dehydrogenase.

This chapter was published as “Oxidation of the FAD cofactor to the 8-formyl-derivative in human electron transferring flavoprotein” in the *Journal of Biological Chemistry (JBC)* 2018, Vol. 283, p. 2829-2840.

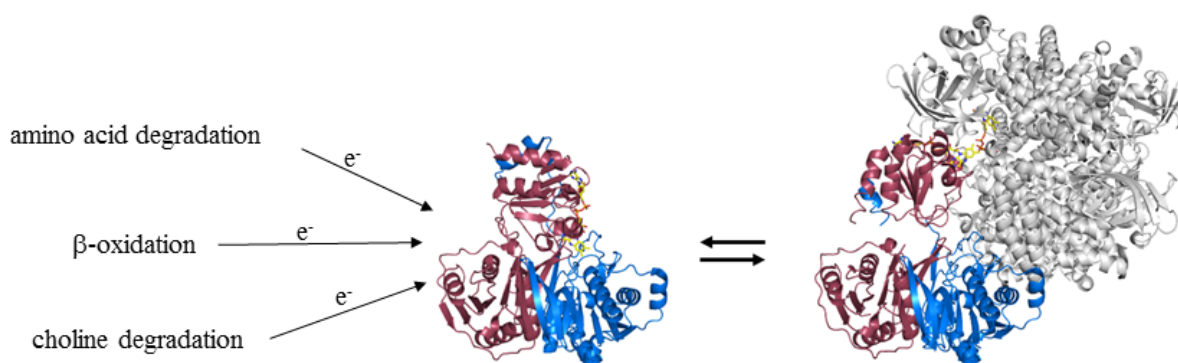
Abstract

The heterodimeric human (h) electron-transferring flavoprotein (ETF) transfers electrons from at least 13 different flavin dehydrogenases to the mitochondrial respiratory chain through a non-covalently bound FAD cofactor. Here, we describe the discovery of an irreversible and pH-dependent oxidation of the 8 α -methyl group to 8-formyl-FAD (8f-FAD), which represents a unique chemical modification of a flavin cofactor in the human flavoproteome. Furthermore, a set of hETF variants revealed that several conserved amino acid residues in the FAD-binding pocket of electron-transferring flavoproteins are required for the conversion to the formyl group. Two of the variants generated in our study, namely α R249C and α T266M, cause glutaric aciduria type II (GAI), a severe inherited disease. Both of the variants showed impaired formation of 8f-FAD shedding new light on the potential molecular cause of disease development. Interestingly, the conversion of FAD to 8f-FAD yields a very stable flavin semiquinone that exhibited slightly lower rates of electron transfer in an artificial assay system than hETF containing FAD. In contrast, the formation of 8f-FAD enhanced the affinity to human dimethylglycine dehydrogenase 5-fold, indicating that formation of 8f-FAD modulates the interaction of hETF with client enzymes in the mitochondrial matrix. Thus, we hypothesize that the FAD cofactor bound to hETF is subject to oxidation in the alkaline (pH 8) environment of the mitochondrial matrix, which may modulate electron transport between client dehydrogenases and the respiratory chain. This discovery challenges current concepts of electron transfer processes in mitochondria.

Introduction

In 1956, Crane *et al.* (1) identified the electron-transferring ability of an unknown flavoprotein from the pig liver, which they named electron-transferring flavoprotein (ETF). Since then, numerous studies on ETF have been reported and orthologs have been described in all kingdoms of life (2). The heterodimeric human (h) ETF serves as a central electron carrier in the mitochondrial matrix. hETF accepts electrons from 13 flavin dehydrogenases and transfers them to the human ETF-ubiquinone oxidoreductase (hETF-QO), an iron-sulfur cluster containing flavoprotein bound to the inner mitochondrial membrane that feeds these electrons into the mitochondrial respiratory chain (2, 3). The flavin dehydrogenases are either part of β -oxidation, amino acid or choline degradation, as shown in Scheme 1.

Scheme 1: Interaction of human flavin dehydrogenases with hETF. So far, 13 flavin dehydrogenases, involved in β -oxidation (short chain acyl-CoA dehydrogenase; medium chain acyl-CoA dehydrogenase; long chain acyl-CoA dehydrogenase; very long chain acyl-CoA dehydrogenase; and acyl-CoA dehydrogenase family member 9-11), amino-acid (short branched chain acyl-CoA, iso-valeryl-CoA, iso-butyryl-CoA and glutaryl-CoA dehydrogenase), and choline degradation (dimethylglycine and sarcosine dehydrogenase) were identified to interact with hETF. hETF exhibits a flexible interaction mechanism and adopts a closed non-productive form (PDB code 1EFV) and an open productive conformation, here shown bound to human medium chain acyl-CoA dehydrogenase (PDB code 2A1T). The α - and β -subunits of hETF are shown in *raspberry* and in *marine* cartoon view, respectively. hETF bound hMCAD is displayed in *grey*. hETF bound FAD is presented in *yellow sticks*, hMCAD bound FAD in *pink stick* representation.



Interestingly, these dehydrogenases are structurally distinct with dehydrogenases operating either in the degradation of fatty or amino acids adopting the “acyl-CoA dehydrogenase”-fold, whereas both dimethylglycine dehydrogenase (hDMGDH) and sarcosine dehydrogenase are part of the amine oxidase protein family. Apparently, hETF has evolved a flexible mechanism to interact with various dehydrogenases as well as with hETF-QO (2). The protein exists in a closed non-productive and in an open productive conformation with a highly flexible upper protein domain (Scheme 1). The interaction with client dehydrogenases is initiated by a recognition peptide of the β -subunit leading to the exposure of the FAD and concomitant electron transfer (4).

Recently, Toogood *et al.* have shown that a single amino acid replacement in the β -subunit (β E165A) favors the open conformation by removing a side-chain interaction with α Asn259 in the α -subunit (4). As a consequence, variant β E165A displayed higher affinity to the human medium-chain acyl-CoA dehydrogenase (hMCAD) (and to rat DMGDH) enabling co-crystallisation (Scheme 1). In the course of our attempts to co-crystallize hETF with hDMGDH, we have reproduced the β E165A variant as well as generated the corresponding α N259A variant. However, characterization of the variants by UV-visible absorption spectroscopy indicated that the FAD cofactor undergoes a slow conversion affecting the isoalloxazine ring. A detailed analysis of the isolated flavin moiety showed that the observed conversion entails the oxidation of the $\delta\alpha$ -methyl to the formyl group, *i.e.* 8-formyl-FAD (8f-FAD) is the product of the spontaneous conversion observed in these two variants. This prompted us to extend the study to include wildtype hETF and several variants with amino acid replacements in the

binding pocket of the isoalloxazine ring. In this study, we document that (i) conversion of FAD to 8f-FAD also occurs in wildtype hETF at alkaline pH, (ii) the 8f-FAD stabilizes an oxygen-insensitive semiquinone radical, and (iii) several highly conserved amino acid residues in the FAD binding pocket are essential for the formation of 8f-FAD. In addition, we demonstrate that wildtype hETF bearing 8f-FAD as cofactor exhibits increased affinity to reduced hDMGDH under steady-state conditions suggesting a potential role *in vivo*. Taken together, our results report entirely novel properties of hETF that may have important implications for our understanding of electron handling in the mitochondrial matrix.

Results

Time-dependent absorption changes of purified recombinant hETF

hETF produced in *Escherichia coli* host cells was purified by means of Ni-NTA affinity chromatography and yielded 2 mg of homogeneous protein per g of wet cell pellet (Figure 1).

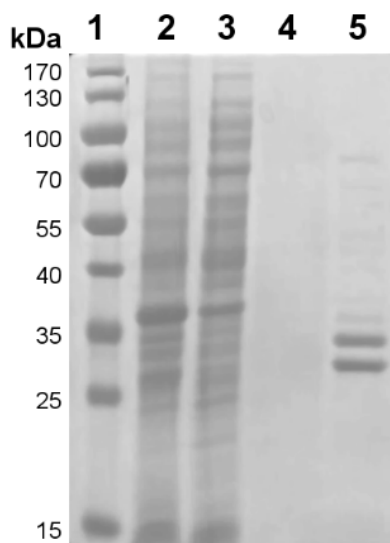


Figure 1: Purification of hETF-WT. The SDS-PAGE of hETF Ni-NTA affinity chromatography is shown as follows: *lane 1*, PageRuler[®] prestained protein ladder (Thermo Fisher Scientific); *lane 2*, cell lysate; *lane 3*, column flow-through; *lane 4*, washing fraction; and *lane 5*, elution fraction.

To explore the effect of the pH on protein yield and stability, purifications were performed at pH 7, 7.8, and 8.5. This gave rise to different UV-visible absorption spectra as shown in Figure 2A.

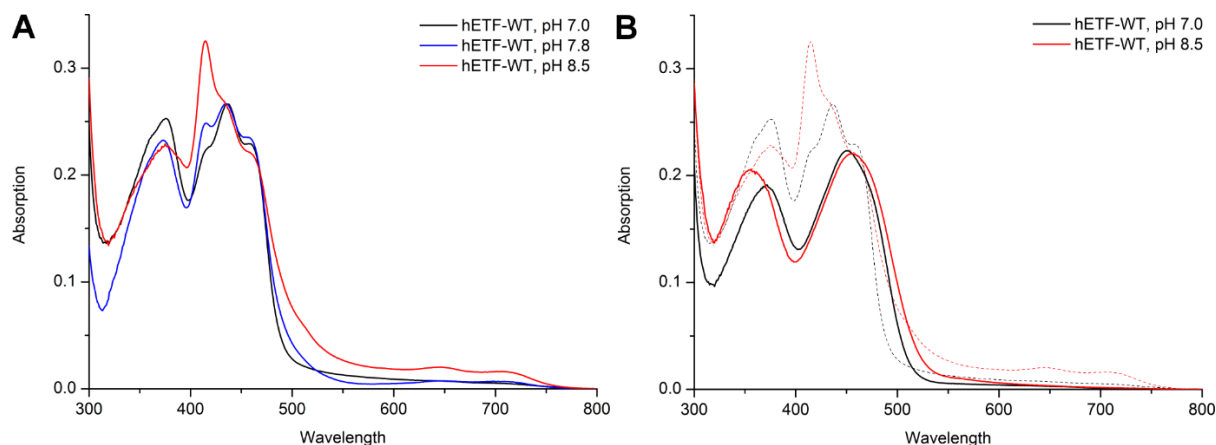


Figure 2: UV-visible absorption spectra of native (A) and denatured hETF-WT (B) purified at pH 7, (7.8), and 8.5. A, The pH conditions used in the purification of hETF-WT, pH 7 (*black line*), 7.8 (*blue line*), and 8.5 (*red line*), strongly affected the absorption spectra of the isolated protein. B, Denaturation of hETF purified at pH 7 (*black*) and 8.5 (*red*) with 20% SDS also resulted in different absorption spectra (*dotted and solid lines* represent spectra recorded before and after denaturation, respectively).

At neutral pH, the absorption spectrum featured two maxima at 375 and 436 nm, which were very similar to spectral properties reported for hETF and pig liver ETF, respectively (5, 6). However, pronounced changes were observed when hETF was purified at pH 7.8 or 8.5. These spectra were characterized by a bathochromic shift of the maximum at 436 nm to 415 nm accompanied by an increase in absorption at longer wavelength (Figure 2A). To check whether the observed spectral changes were caused by a chemical modification of the FAD cofactor, hETF purified at pH 7 and pH 8.5 was denatured and absorption spectra were recorded. As shown in Figure 2B, hETF purified at pH 7 yielded the typical absorption spectrum of free FAD with maxima at 370 and 450 nm, whereas the flavin moiety released from hETF purified at pH 8.5 featured spectral shifts to 354 and 456 nm, respectively.

Isolation and identification of the modified FAD generated at alkaline pH

To identify the nature of the chemical modification in the flavin chromophore, we extracted the cofactor(s) from hETF purified and kept at pH 8.5. After extraction and purification by HPLC (Figure 3, A and B), the two main fractions were analyzed by mass spectrometry and NMR spectroscopy (Figure 3, C and D, respectively).

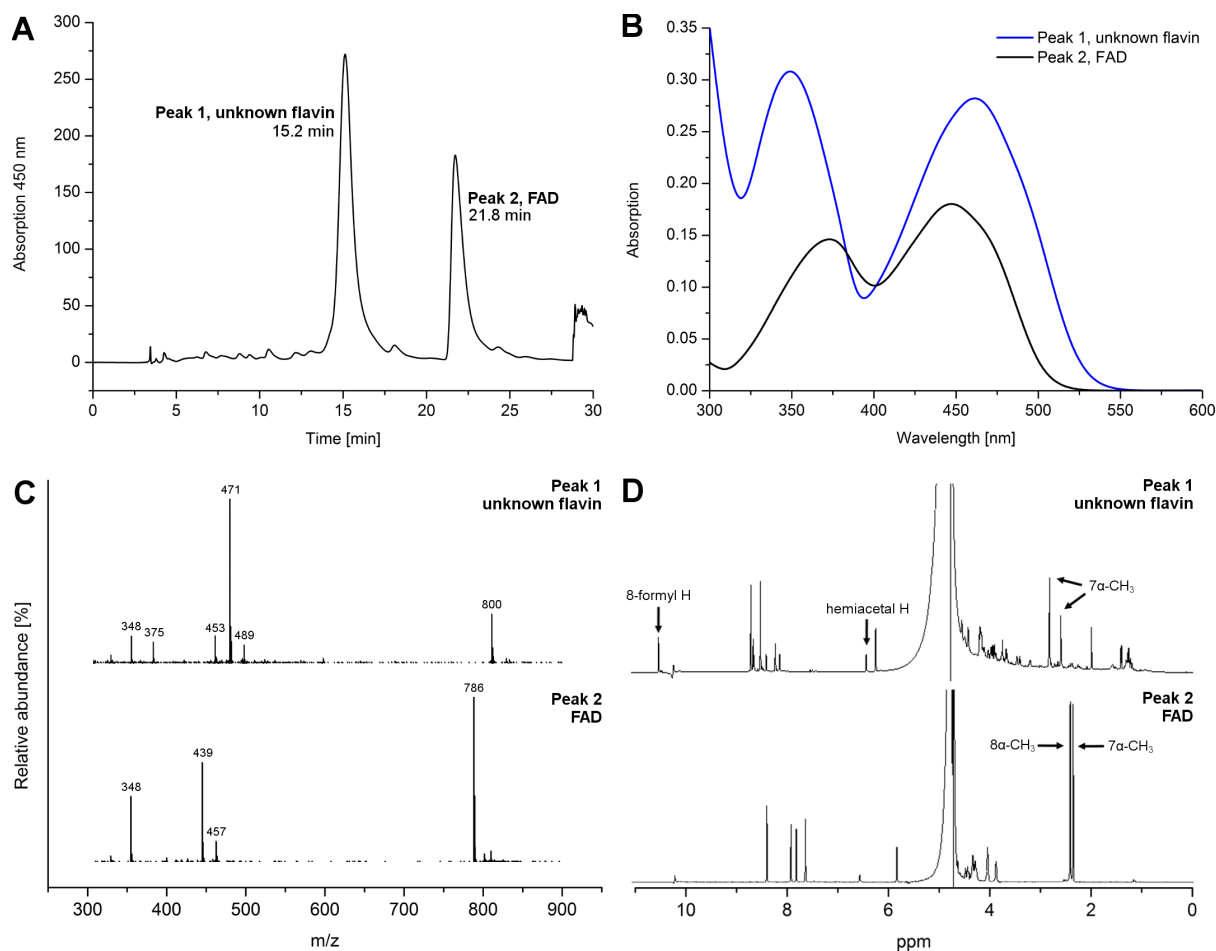


Figure 3: Analysis and comparison of the two main flavin-containing fractions isolated from hETF. **A**, HPLC reversed phase purification of the extracted cofactor(s) gave two major fractions, which were further analyzed by MS and NMR. **B**, Spectra of the two peaks of HPLC purification featured the same shifts as seen in Figure 2B. **C**, Mass spectra of the two main fractions as separated by HPLC. The spectrum shown at the *bottom* exhibits the typical fragmentation and mass peaks of FAD. The mass spectrum at the *top* shows a mass shift of 14 a.u. **D**, In agreement with the mass analysis, the ^1H -NMR spectrum at the *bottom* can be assigned to FAD, whereas the additional resonance at 10.4 ppm and the shifts observed for the methyl groups in position 7α and 8α indicate chemical changes in the dimethylbenzene ring moiety of the isoalloxazine ring. Both methods indicate that a small amount of a closed, hemiacetal form of 8f-FAD is present, as observed previously (12).

Mass spectrometric analysis of one of the major fractions (peak 2) clearly showed the typical fragmentation pattern (AMP: $m/z = 348$; FMN: $m/z = 439$ and 457) and mass of FAD ($m/z = 786$; MassBank accession number KNA00248, (7)), whereas the other fraction (peak 1) exhibited a shift of 14 a.u. of all major peaks, except that for AMP. In agreement with the observed differences in the absorption properties, this result confirmed that the chemical modification has most likely occurred in the isoalloxazine ring of the FAD cofactor. Further analysis of the two flavin-containing fractions by NMR-spectroscopy revealed the presence of a resonance at ~ 10.4 ppm in the unknown flavin species that is absent in FAD. Additional differences were observed in the resonances of the methyl groups at the 7α and 8α positions (see *arrows* in Figure 3D). Overall, the ^1H -NMR-spectrum possesses the same

features as previously reported for 8-formyl-FAD isolated from formate oxidase (8). Taken together with the observed mass difference, we therefore conclude that the 8 α -methyl group of FAD was oxidized to a formyl group to yield 8f-FAD.

Time-dependent formation of 8f-FAD in hETF

To obtain further insights into the formation of 8f-FAD in hETF, a sample purified at pH 7 was diluted into buffer at pH 8.5, and the spectral changes were observed over time. As shown in Figure 4A, the formation of 8f-FAD is a slow process with an approximate half time of 20 hours for hETF-WT and 4 hours for hETF- α N259A, respectively.

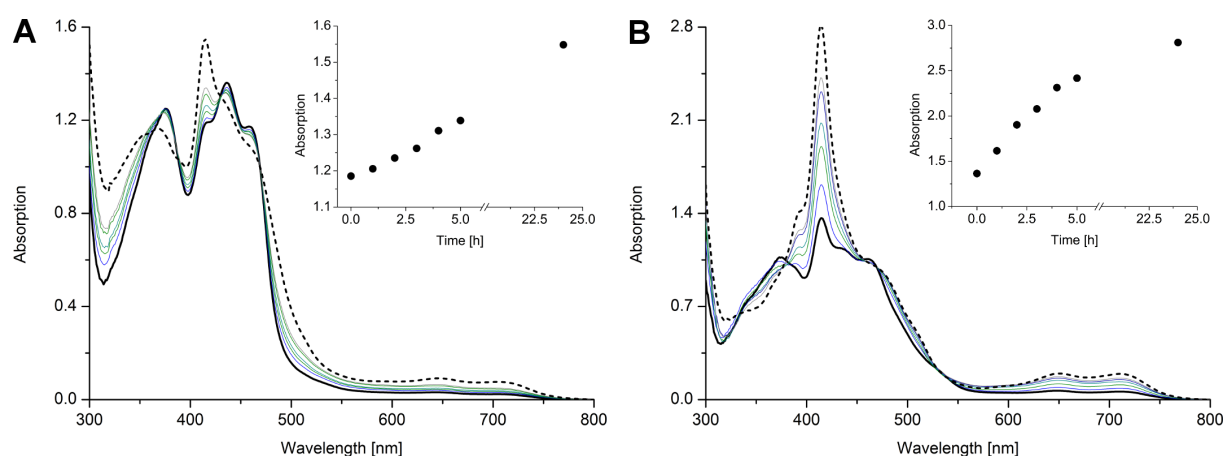


Figure 4: Formation of 8f-FAD radical in wildtype hETF and the α N259A variant. **A**, \sim 400 μ M wildtype hETF purified in 50 mM HEPES, pH 7.0, was diluted 1:20 with HEPES buffer, pH 8.5, and was incubated at 25 $^{\circ}$ C for 24 h. **B**, \sim 400 μ M hETF- α N259A purified in 50 mM HEPES, pH 7.0, was diluted 1:20 with HEPES buffer, pH 8.5, and was incubated at 25 $^{\circ}$ C for 24 h. The *dotted line* in both panels represents the spectrum measured after 24 h. The spectra were normalized to an absorption of 1 at the isosbestic point at 469 nm to simplify comparison. The *insets* show the time-dependent absorption changes recorded at the indicated times at 415 nm.

The spectral changes are marked by a single set of isosbestic points at 340, 375, 420 and 469 nm and the appearance of a sharp absorption maximum at 415 nm as well as much less pronounced maxima at 650 and 710 nm (Figure 4). The reverse reaction, the formation of FAD from 8f-FAD at neutral or acidic pH, was not observed. The formation of 8f-FAD was independent from the buffer used (HEPES, TRIS and phosphate buffer). Similarly, removal of the hexa-histidine tag using tobacco etch virus protease had no effect on the oxidation of the 8 α -methyl group.

Because the formation of 8f-FAD does not occur free in solution, we assumed that the oxidation is promoted by amino acid residues in the isoalloxazine-binding pocket. Therefore, we generated four

variants of hETF featuring single amino acid replacements: α R249C, α T266M, α H286A and β Y16F (Figure 5).

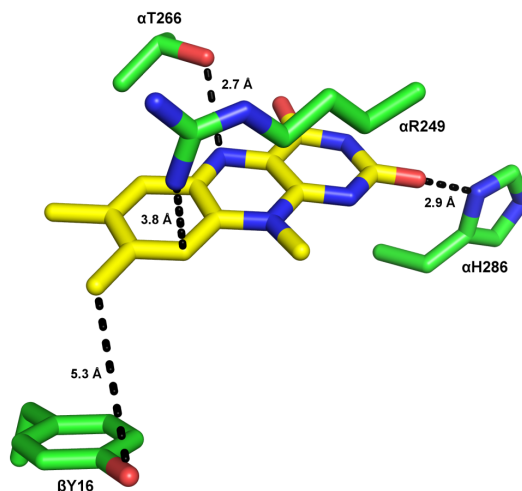


Figure 5: Amino acid residues near the isoalloxazine ring system that have been targeted by site-directed mutagenesis: α Thr-266 was replaced by a methionine, α Arg-249 by a cysteine, α His-286 by an alanine, and β Tyr-16 by a phenylalanine to study their influence on 8f-FAD formation. Possible interactions of these residues with the isoalloxazine ring are indicated by the *dashed lines*.

Interestingly, the formation of 8f-FAD was substantially affected in all variants and decreased in the order β Y16F > α T266M > α R249C (Table 1).

Table 1: Formation of 8f-FAD in wildtype hETF and the variants α R249C, α T266M, and β Y16F: Proteins were purified at pH 7.0 and diluted to a final concentration of 40 μ M using HEPES buffer, pH 8.5. Aliquots were taken and analyzed with HPLC after 0, 2, 4, 6, 8, and 24 h of incubation at 25 $^{\circ}$ C. Because the FAD cofactor was bound weakly to the α H286A variant, time-dependent formylation could not be measured reliably.

Protein	% 8f-FAD					
	0 h	2 h	4 h	6 h	8 h	24 h
WT	< 2.5	15	17	21	23	47
α R249C	< 2.5	< 2.5	< 2.5	< 2.5	< 2.5	< 2.5
α T266M	< 2.5	< 2.5	< 2.5	< 2.5	< 2.5	6
β Y16F	< 2.5	< 2.5	< 2.5	5	6	22

For the α H286A-variant, 8f-FAD formation could not be monitored reliably since the FAD-binding was apparently compromised by the amino acid replacement. Hence, we conclude that amino acid residues directly participate in the oxidation of the 8 α -methyl to the formyl group. In addition, we investigated two variants, α N259A and β E165A, that presumably increase the flexibility of the FAD-binding domain to favor the formation of a productive open conformation for electron transfer (9).

Both of the variants showed a much more rapid formation of 8f-FAD, which already occurred at neutral pH (Figure 4B, data for α N259A as an example). This observation strongly suggests that the conformational dynamics of hETF affect the rate of conversion of FAD to the 8f-FAD.

Generation of 8f-FAD leads to the flavin semiquinone

Although our analysis has clearly shown the oxidation of the 8 α -methyl to the formyl group, the spectral characteristics observed for the generated 8f-FAD are vastly different to those seen after release of the flavin from hETF (Figure 2B). As a matter of fact, the sharp peak at 415 nm as well as the long wavelength absorption is reminiscent of a flavin semiquinone species suggesting that the 8f-FAD is present as a semiquinone radical instead of the oxidized form. The presence of a flavin radical was confirmed by EPR spectroscopy of the hETF variant α N259A, which rapidly forms the 8f-FAD at pH 8.5. A g-factor of 2.0048 was calculated after calibration with DPPH (g-factor of 2.0036) and a peak-to-peak line width of 11-13 G was measured. This line width is rather narrow for a flavin radical and suggests the stabilization of the red anionic semiquinone (10). Expectedly, hETF variant β Y16F and wildtype hETF purified at pH 7.0 (no 8f-FAD formation) did not yield an EPR-signal.

Redox behavior of wild-type hETF and the α N259A variant

The stabilization of the anionic (red) FAD semiquinone in hETF is a well-established phenomenon (5, 6). As shown in Figure 6A (main panel), photoreduction of wild-type hETF purified at neutral pH yielded the FAD semiquinone before full reduction to the hydroquinone was achieved with sodium dithionite (Figure 6A, insert).

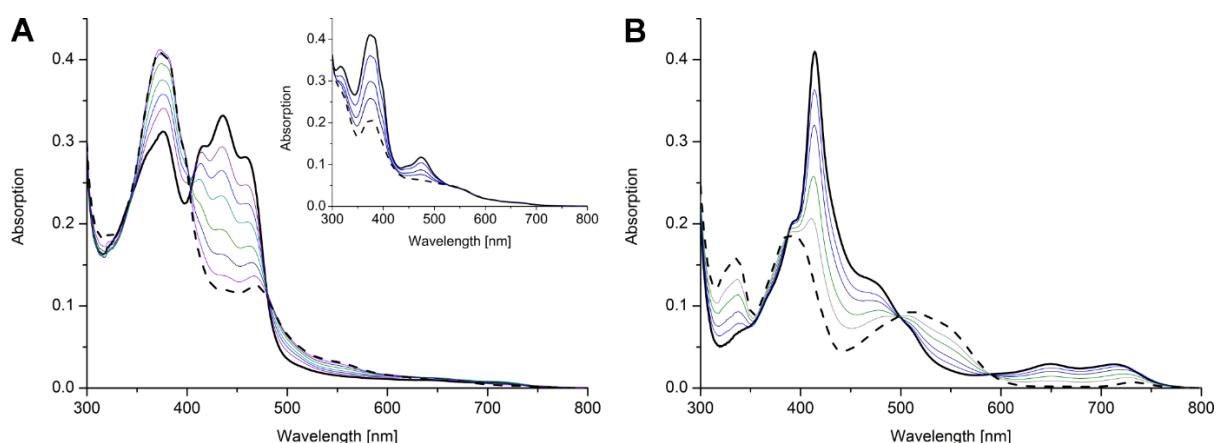


Figure 6: Photoreduction of wildtype hETF and variant α N259A. **A**, Photoreduction of wildtype hETF purified at pH 7.0 proceeded to the anionic (red) FAD semiquinone. The semiquinone resisted further photoreduction and was completely reduced to the hydroquinone upon addition of sodium dithionite (*inset*). **B**, In contrast to wildtype hETF, photoreduction of the hETF- α N259A variant purified at pH 8.5 occurred from the radical to the hydroquinone form.

In contrast to wildtype hETF, the α N259A variant purified at pH 8.5 was already present in the semiquinone form, and photoreduction yielded the fully reduced hydroquinone species featuring characteristic absorption maxima at 390 and 510 nm (11, 12). The hydroquinone form of 8f-FAD is sensitive to oxygen and is reoxidized to the semiquinone but not to the oxidized form. Thus, hETF not only stabilizes the semiquinone form of 8f-FAD but also prevents its oxidation by molecular oxygen. This differential behavior of FAD *versus* 8f-FAD has important implications for the one-electron transfer processes between hETF, the serviced dehydrogenases, as well as the electron acceptor hETF-QO.

Physiological relevance of 8f-FAD, effects on stability, and protein-protein interaction

In order to evaluate the potential impact of FAD cofactor formylation on the electron transfer reaction, we investigated the steady-state kinetics of hETF with hDMGDH, which is one of its client dehydrogenases. For that purpose, wildtype and variant α N259A were both purified in 50 mM HEPES pH 7.0 and pH 8.5, and afterward, the steady-state kinetic parameters were determined at pH 7.0. As shown in Figure 7 and summarized in Table 2, we observed moderate changes in the velocity of electron transfer (k_{cat} was reduced by ca. 50%) and a 5-fold decrease in the K_M values in the proteins harboring 8f-FAD.

Table 2: Steady-state kinetic parameters of hETF-WT and variants α N259A and β E165A. To obtain protein with a high FAD content, purification was carried out at pH 7, whereas pH 8.5 was used to maximize the 8f-FAD content. All kinetic parameters were determined at pH 7.

Protein	K_M	k_{cat}	k_I
	μM	min^{-1}	$\mu\text{M}^{-1} \text{min}^{-1}$
WT-FAD	71 ± 5	116 ± 5	1.6 ± 0.2
WT-8f-FAD	15 ± 2	44 ± 1	2.9 ± 0.5
α N259A-FAD	30 ± 2	114 ± 2	3.8 ± 0.3
α N259A-8f-FAD	16 ± 2	63 ± 3	3.9 ± 0.8
β E165A-FAD	74 ± 9	122 ± 8	1.6 ± 0.4
β E165A-8f-FAD	16 ± 1	43 ± 2	2.7 ± 0.3

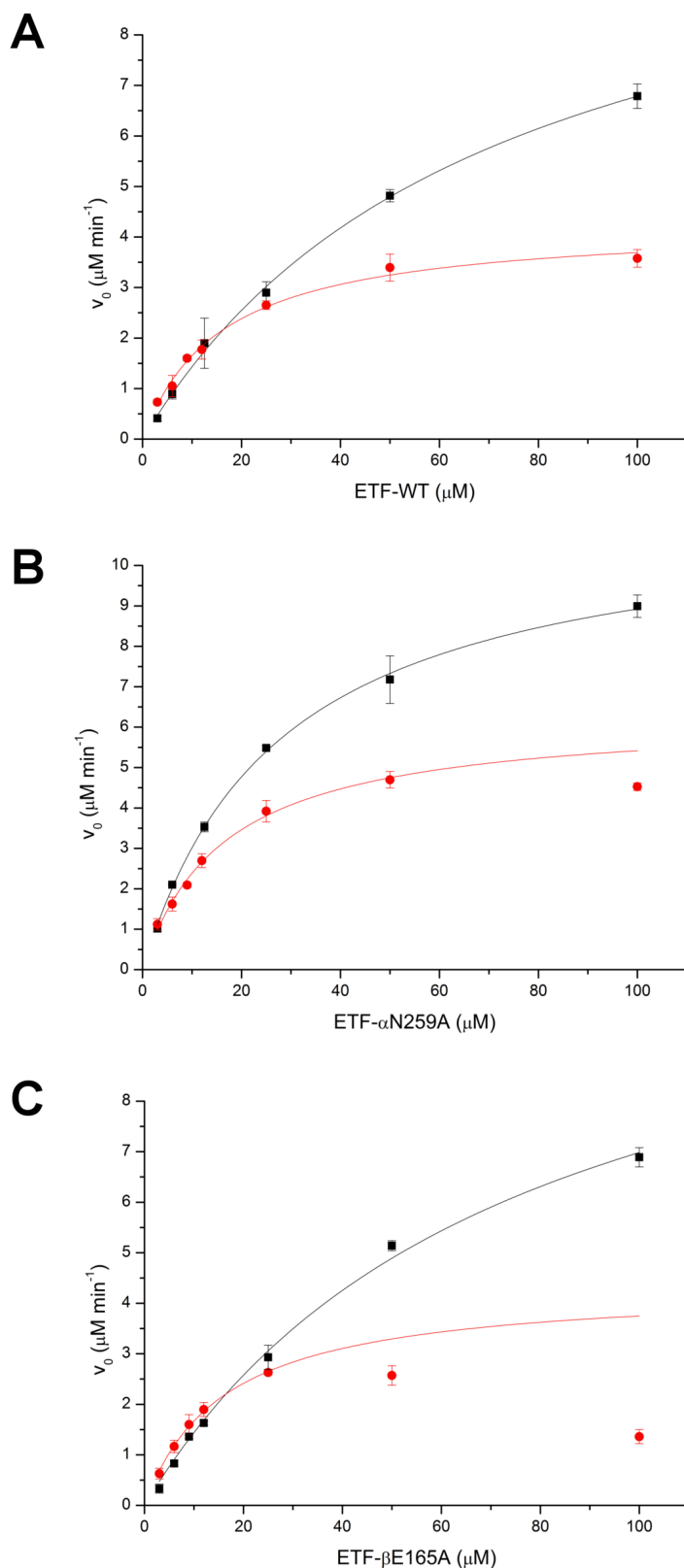


Figure 7: Steady-state kinetics of wildtype hETF and the variants α N259A and β E165A purified at pH 7 (black squares) and pH 8.5 (red dots). The measurements were performed at pH 7 with varying hETF concentrations, using hDMGDH as client dehydrogenase and DCPIP as the final electron acceptor.

It should be noted in this context that hETF- α N259A purified at pH 7.0 already contains ca. ~15-30% of 8f-FAD, which may contribute to the lower K_M value compared with the wildtype hETF (Table 2). In contrast, wildtype hETF purified at pH 8.5 contains only ~30-40% 8f-FAD, and thus the obtained K_M value reflects a mixed population of wildtype hETF, *i.e.* with the FAD cofactor in its methylated (native) and formylated structure, respectively. This may also contribute to the differences found between wildtype hETF and the hETF- α N259A variant (Table 2). The steady-state kinetics of protein variant β E165A purified at pH 7.0 resembled the values obtained for wildtype hETF purified at pH 7.0. In contrast to the corresponding variant α N259A, FAD formylation was absent in the freshly purified variant β E165A and was only observed during long-time storage at pH 7.

Discussion

Discovery of an unusual FAD derivative in an old protein

In the present investigation, we have unambiguously demonstrated the formation of 8f-FAD in hETF by means of various spectroscopies such as HPLC/MS, UV-visible absorption, and NMR- and EPR-spectroscopy. Furthermore, it was shown that the formation of 8f-FAD strongly depended on the pH such that wildtype hETF is resistant to the formation of 8f-FAD at acidic and neutral pH, whereas at alkaline pH the slow oxidation of the 8α -methyl to the formyl group is observable ($t_{1/2} = 20$ h, Figures 2A and 4A). Interestingly, 8f-FAD was not present in the oxidized but in the semiquinone state, which was stable toward oxidation by dioxygen. The UV-visible absorption spectrum featured a sharp peak at 415 nm and two minor absorption maxima at longer wavelengths (650 and 720 nm, Figure 2A). The latter spectral features are clearly indicative of the (blue) neutral semiquinone, although the peak-to-peak linewidth measured by EPR-spectroscopy suggested that the major fraction is the (red) anionic semiquinone. Thus, we conclude that a mixture of the blue and red semiquinone is present in hETF suggesting that our measurements were conducted near the pertinent pK_a of the flavin radical, as was also found earlier for a lysine to arginine replacement in the FMN binding pocket of lactate oxidase (13). Overall, the spectral characteristics are very similar to those reported earlier by Yorita *et al.* (13) and by Maeda *et al.* (14) for formate oxidase from *Aspergillus oryzae*. In the latter case, it was shown that oxidation of the 8α -methyl group significantly enhances enzyme activity, and thus it was argued that the 8f-FAD derivative is the cognate cofactor of the enzyme.

Since detailed studies on ETF date back to the 1950s, we were very surprised that our findings were apparently not observed previously. However, closer inspection of the literature revealed that isolation of ETF from pig liver yielded two forms (designated ETF_R and ETF_B), which were reduced to the red (ETF_R) and blue semiquinone (ETF_B), respectively (11). Analysis of the isolated cofactors demonstrated the presence of a flavin species with absorption maxima at 463 and 352 nm, which are in fact very similar to the spectral features observed for the 8f-FAD spectrum after denaturation of wildtype hETF purified at pH 8.5 (Figure 2B, *red solid line*). Furthermore, Lehman and Thorpe (11)

reported the occurrence of a pink species upon reduction featuring an absorption maximum at 520 nm. Again, this is reminiscent of the absorption spectrum obtained when the α N259A hETF variant is photoreduced (Figure 6B, *dashed black line*). Similarly, Yorita *et al.* (13) reported the same species upon reduction of 8-formyl FMN bound to lactate oxidase. Therefore, we assume that Lehman and Thorpe (11) have also isolated the 8f-FAD cofactor from pig liver ETF; however, neither the chemical nature of the flavin nor the mode of its generation was further investigated.

Because the amino acid residues in the FAD binding pocket of mammalian and bacterial ETFs are highly conserved (Figure 8), it was tempting to assume that the generation of 8f-FAD is a common feature in this protein family.

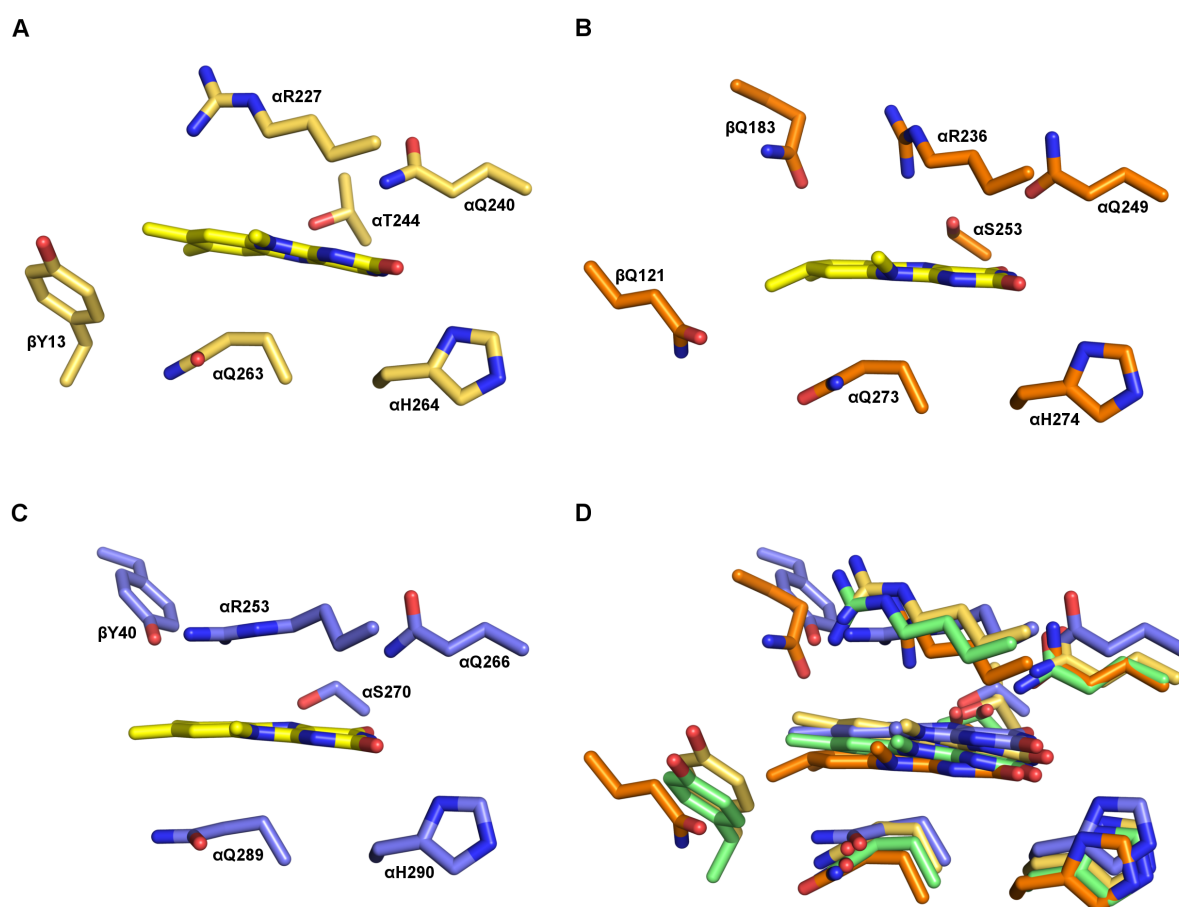


Figure 8: Composition of FAD-binding site of additional ETF structures. The crystal structures of bacterial ETFs from *P. denitrificans* (A, *gold*; PDB code 1EFP), *M. methylotrophus* (B, *orange*; PDB code 1O96), and *A. fermentans* (C, *blue*; PDB code 4KPU) were aligned with the structure of hETF (D, *green*; PDB code 1EFV). The alignment shows that all four structures have a very conserved active site composition.

Thus, we have analyzed the crystal structures of previously published ETF structures, hETF (PDB code 1EFV), the ETF from *Methylophilus methylotrophus* (PDB code 1O96), *Paracoccus denitrificans* (PDB code 1EFP), and *Acidaminococcus fermentans* (PDB code 4KPU). Closer

inspection of the electron densities obtained for the 8α -position showed obvious deviations from the expected electron density of a methyl group for some reported crystal structures (Figure 9).

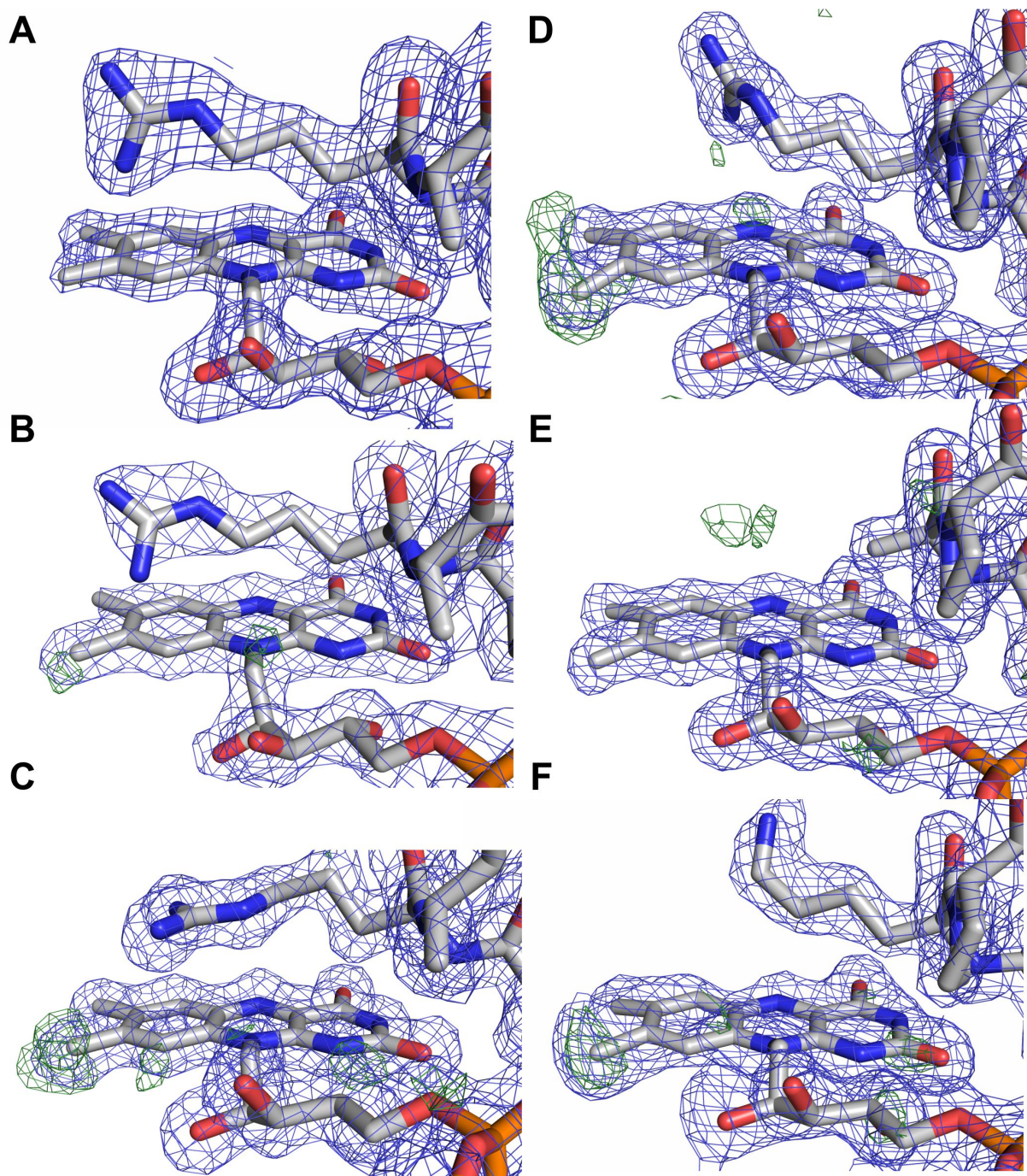


Figure 9: Electron densities of the FAD region of selected ETF proteins. **A**, Human ETF (PDB code 1EFV); **B**, human ETF β E165A variant (PDB code 2A1U); **C**, *A. fermentans* ETF (PDB code 4KPU); **D**, *M. methylotrophus* ETF (PDB code 1O96); **E**, *M. methylotrophus* ETF α R236A variant (PDB code 3CLR); and **F**, *M. methylotrophus* ETF α R236K variant (PDB code 3CLU). In all panels, the $2F_o-F_c$ electron density map contoured at 1σ is shown as *light blue mesh* around the cofactor and residues of an important loop region on the *re* side of the flavin. The *green* density map corresponds to the F_o-F_c map contoured at 3σ .

In fact, in those cases the additional electron density is indicative of a covalent modification of the 8 α -methyl group and is in line with the presence of (partially) formylated FAD (Figure 9). With the exception of hETF, this was also found in cases where crystallization was carried out at or near pH 7, *i.e.* under conditions where oxidation of the 8 α -methyl to the formyl group is very slow. The structurally very similar bacterial ETFs from *A. fermentans* and *M. methylotrophus* show clear indications of FAD modification even for wild type forms and a variant with a conserved positive charge on the *re* side of the flavin (Figure 9, C, D, and F), whereas no indication of 8f-FAD formation is observed for the modification incompetent α R236A variant of *M. methylotrophus* ETF (Figure 9E). With regard to ETF from *M. methylotrophus* it is also noteworthy that Byron *et al.* (15) clearly have observed the 8f-flavin radical species (cf. Figure 4) but did not further elucidate the cause of the drastic change in the absorption spectrum. The occurrence of the 8f-FAD in *M. methylotrophus* ETF is potentially relevant as this could (partially) explain the unusually positive redox potential of the protein (+196 mV for the ETF_{ox}/ETF redox pair) (15), which is in accordance with previous reports that the redox potential of free 8f-FAD is ca. 130-160 mV more positive than that of free FAD (8, 12).

Proposed reaction mechanism for the formation of 8f-FAD

We propose that the oxidation of the 8 α -methyl group is initiated by proton abstraction, as proposed previously (16–18), leading to the formation of a negative charge at the N(1)-C(2)=O locus of the isoalloxazine ring. After addition of water, the reduced intermediate is oxidized to yield the 8 α -hydroxymethylene intermediate, which is again subject to proton abstraction at the 8 α -group with the resulting enol tautomerizing to the reduced 8f-FAD. Taking the results of our mutagenesis study into account, it is conceivable that the phenolate side chain of β Tyr-16 may act as a base (instead of hydroxide). Such an involvement would be reminiscent of the formation of a covalent linkage established in 8 α -tyrosyl-modified flavoenzymes (19–22). The side chains of α Arg-249, α Thr-266 and α His-286 support the reaction by hydrogen bonding to the N(1)-C(2)=O locus (α His-286), N(5) (α Thr-266) and by π -cation interaction (α Arg-249), respectively. Interestingly, variants favoring the open conformation of hETF, *i.e.* β E165A and α N259A (see under “Discussion”), also promote the oxidation of the 8 α -methyl group, probably due to greater solvent exposure of the relevant part of the isoalloxazine ring in line with the proposed role of hydroxide and water in the putative reaction mechanism. Because our experiments have shown that the generated 8f-FAD is preferentially present as the semiquinone, we propose that the 8f-FAD is rapidly reduced, *e.g. in vitro* by light and *in vivo* by one of the client dehydrogenases, to the very stable radical species.

Effect of cofactor oxidation to the 8f-FAD on electron transfer

The oxidation of FAD to 8f-FAD clearly affected the interaction with hDMGDH, which is one of the confirmed client dehydrogenases of hETF. The most striking effect was observed on the apparent K_M value defined here as the concentration of hETF at which the rate of electron transfer proceeds at half maximal velocity. A 5-fold lower K_M value was observed not only in the case of wildtype hETF but also for the β E165A and α N259A variants when 8f-FAD was present as the main cofactor moiety (Table 2). A smaller effect was also seen on the maximal rate of electron transfer from reduced hDMGDH to hETF as well as the β E165A and α N259A variants, which was ~50-60% lower in the proteins containing 8f-FAD instead of FAD (Table 2). Thus, it is apparent that oxidation of the FAD cofactor in hETF significantly affects the interaction with hDMGDH. In fact, Toogood *et al* (9) have reported that hETF variant β E165A has a higher affinity to hMCAD and rat DMGDH compared with the wildtype protein. Because the side chains of amino acid residues β Glu-165 and α Asn-259 stabilize a non-productive, closed hETF conformation (Scheme 1), the replacement by alanine populates the open conformation, which is conducive to complex formation with an electron delivering dehydrogenase and enabled the crystallization of a protein complex comprising hETF and hMCAD (9). As a consequence of this perturbation of the conformational equilibrium of the closed and open conformation, the protein complex of hETF with its client enzymes exhibits higher affinity and thus rationalizes the observed kinetic effects on K_M value and the rate of electron transfer under steady-state conditions (Figure 7 and Table 2).

Interestingly, formation of 8f-FAD appears to exhibit a similar effect on the interaction with client dehydrogenases as seen in the β E165A and α N259A variants. Therefore, we hypothesize that the presence of 8f-FAD in hETF leads to a significant shift of the conformational equilibrium toward the open (productive) conformation, which in turn increases the affinity to client enzymes. Currently, we are conducting hydrogen/deuterium exchange mass spectrometric experiments to test this hypothesis.

Potential physiological role of 8f-FAD in health and disease

Considering the apparent impact of the formylation of the FAD cofactor, the central question that emerges here concerns the physiological relevance of the cofactor modification. As the pH of the mitochondrial matrix was found to be close to 8.0 (23, 24), formylation of wildtype hETF would clearly occur in this environment, albeit at a slow rate; thus, the overall lifetime of the protein will ultimately determine the fraction of hETF containing 8f-FAD. Although, this lifetime is currently not known for hETF, mitochondrial matrix proteins were shown to exhibit half-lives in the range of 17 to more than 100 h (25). In the case that hETF belongs to the long-lived proteins, a significant fraction of the protein will in fact harbor the 8f-FAD cofactor. Moreover, it is conceivable that other proteins, such as the electron delivering dehydrogenases, promote the formation of 8f-FAD by stabilizing the open conformation of hETF as seen in the α N259A and β E165A variants.

In this context, it is very intriguing that several inborn mutations in the gene encoding human ETF are known to cause glutaric aciduria type II (GAI), also called multiple acyl-CoA dehydrogenase deficiency (OMIM entry no. 231680), a disease characterized by severe non-ketotic hypoglycemia, metabolic acidosis, and excretion of large amounts of fatty acid and amino acid-derived metabolites (26, 27). Strikingly, two of the hETF variants generated in our mutagenesis study, namely α R249C and α T266M, were reported as the cause of GAI, with the latter being the most abundant variant found in affected patients (28, 29). Because both of these variants were severely impaired in the formation of the 8f-FAD derivative in their active sites, it is tempting to speculate that the inability to catalyze the oxidation of the 8 α -methyl to the formyl group contributes to the disease causing effect of the underlying genetic mutation. In a previous study, Dwyer *et al.* (30) concluded that α Arg-249 plays a crucial role in stabilizing the flavin semiquinone state; however, at that time the occurrence of 8f-FAD and its mode of generation had not been recognized.

The remarkable stability of the 8f-FAD radical may alter the operational basis of the electron transfer reactions of hETF with the serviced dehydrogenases and the terminal electron acceptor hETF-QO. In hETF with FAD as cofactor, it is assumed that the oxidized FAD receives one electron from a client dehydrogenase generating the FAD semiquinone, which spontaneously disproportionates and subsequently reduces hETF-QO by two single electron transfer processes (29). Only the fully reduced hETF is then able to transfer two electrons to the hETF-QO. Thus, it will be interesting to see how formylation affects the electron transfer process between the hETF and the hETF-QO. In addition, 8f-FAD also possesses a much more positive redox potential, *i.e.* around -90 mV (15), and therefore formylation may also affect the rate of electron transfer between the client dehydrogenases, hETF and hETF-QO.

Conclusions

Our study has conclusively shown that hETF catalyzes the oxidation of FAD to 8f-FAD, an unusual cofactor modification that has not been reported for hETF or any other electron transferring flavoprotein. Furthermore, we have demonstrated that the generation of 8f-FAD strongly depends on the pH, is catalyzed by amino acid residues in the FAD binding pocket, and is favored in variants that preferentially adopt an open conformation. Depending on the lifetime of hETF in the mitochondrial matrix, formation of 8f-FAD will be physiologically relevant in particular because the 8f-FAD alters the interaction with electron-delivering dehydrogenases and the electron acceptor hETF-QO in the inner mitochondrial membrane. It also remains to be seen whether additional factors, such as the interaction with client dehydrogenases or the hETF-QO, affect the formation of 8f-FAD. In any case, it is apparent that our discovery of the spontaneous cofactor oxidation in a central protein of mitochondrial electron handling raises important biochemical and physiological questions with implications for human health and disease.

Experimental procedures

Enzymes and reagents

Restriction enzymes and Phusion DNA polymerase were from Thermo Fisher Scientific (Waltham, MA), purification columns from GE Healthcare (Chalfont St. Giles, UK). Salt free purified oligonucleotides for site directed mutagenesis were synthesized by VBC-Biotech (Vienna, Austria) or Sigma. All other chemicals and media were from Carl Roth GmbH (Karlsruhe, Germany) or Sigma and were of the highest grade available.

hETF-WT and hETF variants gene expression design

The hETF sequence for expression of the mature hETF consisting of α - and β -subunit was designed following a similar strategy as described by Bross *et al.* (31) and was optimized for expression in *E. coli* using GeneOptimizer[®] (Thermo Fisher Scientific). The operon starts with a ribosomal binding site (AAGGAG), followed by a TATA box in front of the ATG start codon of the gene sequence of the β -subunit. After the stop codon of the β -subunit, a 69 bp spacer region between the β and α gene sequence was introduced, which again comprises the same ribosomal binding site and a TATA box in front of the ATG start codon of the α -subunit. The designed gene sequence was flanked by an *Xba*I and an *Xho*I restriction site and cloned for expression into a pET-28a+ vector (Thermo Fisher Scientific). In agreement with Herrick *et al.* (5), the α -subunit starts with the first amino acid of the mature α ETF (α Gln-20). For protein purification, a hexa-histidine tag was added to the N-terminus of the β -subunit. The recombinant plasmid was transformed into *E. coli* BL21 (DE3) cells. Positive clones were selected by kanamycin resistance. Correct cloning and potent expression colonies were verified by automated sequencing. All investigated variants of hETF-WT (α R249C, α N259A, α T266M, α H286A, β Y16F and β E165A) were constructed by two-step site directed mutagenesis with Phusion DNA polymerase and the mutation primers shown in Table 3 (the altered codons are highlighted in bold).

Table 3: Primer sequences used for site-directed mutagenesis.

Primer	DNA Sequence 5' – 3'	T _m
α R249C_fw	GCAGTTGGTGCAAGCT GC GCAGCAGTTGATGC	67.3 °C
α R249C_rev	GCATCAACTGCT GC GCAGCTTGCACCAACTGC	67.3 °C
α N259A_fw	GCAGGTTTTGTTCC GG CTGATATGCAGGTTGG	64.0 °C
α N259A_rev	CCAACCTGCATAT CA GCCGGAACAAAACCTGC	64.0 °C
α T266M_fw	GATATGCAGGTTGGTCAG AT GGGCAAAATTGTTGCAC	64.8 °C
α T266M_rev	GTGCAACAATTTT GC CC AT CTGACCAACCTGCATATC	64.8 °C

α H286A_fw	CAATTCGGCACTGGCAGGCATG	69.3 °C
α H286A_rev	CCTGCCAGTGCCTGAATTGCACC	70.5 °C
β Y16F_fw	GTTAAACGTGTTATTGATTTTGCCGTGAAAATTCGTG	60.0 °C
β Y16F_rev	CACGAATTTTCACGGCAAAATCAATAACACGTTTAA	60.0 °C
β E165A_fw	CTGAAAGTTGAACGTGCGATTGATGGTGGTCTG	63.6 °C
β E165A_rev	CAGACCACCATCAATCGCACGTTCAACTTTCAG	63.6 °C

First, two separate PCRs using either forward or reverse primer with 10 ng hETF-WT template DNA, 1x Phusion HF buffer, 200 μ M dNTPs, 3% DMSO, 1 unit of Phusion DNA polymerase and 0.5 μ M of each primer were run in 50 μ L volumes with (98 °C (2 min) – [98 °C (50 sec) – 60 °C (20 sec) – 68 °C (16.5 min)] x 5 – 4 °C ∞). Afterward, the separated PCRs were combined, and the same PCR program was further employed for another 20 cycles. The PCR was followed by a 2-h *DpnI* digestion step; the plasmid was then transformed into *E. coli* BL21 (DE3) cells, and the strain selection was done as above using the pET28a+ kanamycin resistance.

hETF production

hETF expression was carried out in shake flasks in an HT Multitron Standard shaking system (Infors AG, Basel, Switzerland) at 150 rpm. Briefly, overnight LB medium cultures of *E. coli* BL21 (DE3) cells with the desired hETF variant were used to inoculate 1 liter of main culture in a baffled shake flask to an A_{600} of 0.1. After reaching an A_{600} of 0.6-0.8, the protein production was started by induction with 0.1 mM isopropyl-thio- β -D-galactopyranoside and expression took place overnight at 25 °C. The cell pellet was collected by centrifugation (2 704 g, 15 min, room temperature) and stored at -20 °C.

hETF purification

In general, enzyme purification was carried out according to the following protocol. Cell lysates were prepared by four 3-min sonications (3-min cooling steps) using a Labsonic[®] L sonication probe (B. Braun Biotech, Berlin, Germany) in a Sonopuls[®] rosett cell RZ (Bandelin, Berlin, Germany). The wet cell pellet was suspended in lysis buffer (3 ml of 50 mM HEPES/NaOH, 15 mM imidazole, pH 7.0, 7.8 or 8.5 per g), and a spatula tip of FAD was added before sonication. The lysates were cleared by centrifugation (38,720 x g, 45 min, 4 °C) and filtration through a paper filter. Nickel ion affinity chromatography was performed by applying the cell lysates onto 5-mL HisTrap HP columns (GE Healthcare). Afterward, the columns were washed with at least 10 column volumes lysis buffer, and

the enzyme was stripped off with elution buffer (50 mM HEPES/NaOH, 200 mM imidazole, pH 7.0, 7.8 or 8.5). The purification was monitored by SDS-PAGE, and fractions containing hETF were concentrated using Amicon[®] ultracentrifugal filter units (10 kDa cut-off, Merck-Millipore, Darmstadt, Germany) and rebuffered to storage buffer (50 mM HEPES/NaOH, pH 7.0, 7.8 or 8.5) using Sephadex G-25 PD10 desalting columns (GE Healthcare). After rebuffering, the enzyme solution was incubated at 37 °C for 30 min and afterward cleared by centrifugation in order to remove aggregated protein and excessive hETF β -subunits. The obtained enzyme purity was sufficient for all kinetic and spectrophotometric studies.

hDMGDH production and purification

hDMGDH expression and purification for use in interaction studies for steady-state kinetic analyses was performed as previously reported by Augustin *et al.* (32).

SDS-PAGE

Enzyme samples were separated by SDS-PAGE with 12.5% separation and 5% stacking gels under reducing conditions (100 mM DTT in the sample buffer) as described by Laemmli (33). Gels were stained with Coomassie Brilliant Blue R-250 for purification control, and a PageRuler[®] Prestained protein ladder (Thermo Fisher Scientific) was employed as protein standard.

UV-visible absorption spectroscopy

UV-visible absorption spectra to assess protein concentration, activity, purity, and quality as well as for steady-state kinetic measurements and photoreduction were recorded with a Specord 210 spectrophotometer (Analytik Jena, Jena, Germany).

Protein quantification and calculation of the extinction coefficient

Protein concentrations of purified hETF wild-type and variants were determined using the characteristic absorption of protein bound FAD at 469 nm (isosbestic point of FAD and 8f-FAD). A molar extinction coefficient (ϵ) of $9900 \pm 700 \text{ M}^{-1} \text{ cm}^{-1}$ for hETF was determined using the method described by Macheroux (34) based on an ϵ of free FAD at 469 nm of $9910 \text{ M}^{-1} \text{ cm}^{-1}$.

Extraction and purification of 8f-FAD

Wild-type hETF or the variant α N259A were purified in 50 mM HEPES/NaOH buffer at pH 8.5 and concentrated to about 300-400 μ M using Amicon[®] ultracentrifugal filter units (10 kDa cut-off). After complete denaturation, which was achieved by two times treatment at 70 °C for 10 min and subsequent centrifugation at 18,500 x g for 10 min, the supernatants were transferred to HPLC vials for purification. HPLC purification was done on a Dionex UltiMate 3 000 HPLC (Thermo Fisher Scientific) equipped with an Atlantis[®] dC18 column (5 μ m, 4.6 x 250 mm, Waters, Milford, MA) equilibrated with H₂O/0.1% TFA, 7% acetonitrile and a diode array detector for UV-visible monitoring (λ = 280, 370, 450, 460 nm). An injection volume of 40 μ L, a temperature of 25 °C and a flow rate of 1 mL min⁻¹ were used. 8f-FAD was separated from residual free FAD and other impurities for subsequent UV-visible absorption and NMR-spectroscopy as well as HPLC/MS analyses using the following program: 0-25 min: 7-12% acetonitrile, 25-30 min: 95% acetonitrile, 30-35 min: 7% acetonitrile. 200- μ L fractions were collected between 12.0 and 18.0 min, and fractions with a pure and typical 8f-FAD UV-visible absorption spectrum were combined. The combined fractions were dried using an ISS110 Savant SpeedVac System at 45 °C, < 10 mbar vacuum and an RH64-11 rotor (Thermo Fisher Scientific), and afterward stored at -20 °C until further use. Purity of the cofactor was controlled by HPLC measurements using the same conditions as above.

Analysis of 8f-FAD by HPLC/ESI-MS

For HPLC/MS measurements, an Agilent Technologies 1200 Series (Santa Clara, CA) equipped with a G1379B degasser, G1312B binary pump SL, G1367C HiP-ALS SL autosampler, a G1314C VWD SL UV detector, G1316B TCC SL column oven, and a G1956B MSD mass selective detector was used. The mass spectrometer was operated in positive electro spray ionization mode. The analytes were separated on an Atlantis[®] dC18 column (5 μ m, 4.6 x 250 mm, Waters) at 25 °C by using aqueous eluent (0.1% formic acid) and acetonitrile at a flow rate of 1.0 mL min⁻¹. The column was equilibrated with 7% acetonitrile in water (0.1% formic acid), and the following gradient was used for analysis: 0-2 min: 7% acetonitrile, 2-10 min: 7-100% acetonitrile, 10-12 min: 100% acetonitrile, 12-14 min: 7% acetonitrile. 10 μ L of 300 μ M HPLC purified 8f-FAD or 300 μ M FAD solution for control, dissolved in water, were injected for each run.

¹H-NMR-spectroscopy

4 mM solutions of purified 8f-FAD or FAD dissolved in 20% D₂O in water (v/v) were subjected to ¹H-NMR analysis using a Varian INOVA 500 (499.82 MHz, Agilent) spectrometer. ¹H-NMR spectra were recorded at 500 MHz at 30 °C. The signal of water protons (δ _H 4.75 ppm) was used as the reference for the observed chemical shifts.

EPR-spectroscopy

Electron paramagnetic resonance experiments were performed with 150 μM hETF- αN259A and hETF- βY16F purified in 50 mM HEPES/NaOH, pH 8.5 and with 150 μM hETF-WT purified in 50 mM HEPES/NaOH, pH 7.0 with an X-band ECS 106 spectrometer (Bruker, Billerica, MA) with 9.45 GHz microwave frequency. A microwave power of 2 milliwatts was used, with a modulation amplitude of 2.0 G at a modulation frequency of 50 kHz. Samples were run at 295 K in 100- μL capillaries and 10 scans with a conversion time of 5.12 ms, a time constant of 10.24 ms, and a sweep time of 20.97 s. The magnetic field was scanned for 100 G from 3340 to 3440 G. The magnetic phase and field modulation amplitude of the signal channel of the EPR machine was calibrated with solid DPPH according to the manual to a g factor of 2.0036.

HPLC-analysis of 8f-FAD formation

Protein purified at pH 7.0 was diluted to a final concentration of 40 μM to adjust the pH to 8.5 and then incubated at 25 $^{\circ}\text{C}$. Samples were taken after 0, (1), 2, 4, 6, 8 and 24 h, and the cofactor was isolated according to the protocol described above. After HPLC analysis, areas of the peaks corresponding to FAD and 8f-FAD were determined, and the ratio between the two chromophores was calculated.

Steady-state kinetics

Steady-state kinetic parameters were determined spectrophotometrically according to Okamura-Ikeda *et al.* (35) using DCPIP (2,6-dichlorophenolindophenol) as terminal electron acceptor. For the assays, 125 μM DCPIP, 100 nM hDMGDH, and 0-100 μM hETF in 50 mM HEPES/NaOH pH 7.0, were incubated at 25 $^{\circ}\text{C}$ for 10 min before the reaction was started by addition of 25 mM dimethylglycine, and the change of absorption was monitored at 600 nm for 3 min. For each concentration, at least a triplicate measurement was performed. From these data the initial velocities were determined and K_M and k_{cat} values were assessed using a non-linear hyperbolic fit in Origin 8.6 (OriginLab Corp., Northampton, MA).

Anaerobic photoreduction

Photoreduction of flavoproteins was done according to the method reported by Massey *et al.* (36). The experimental procedure of photoreduction and reoxidation was performed as described by Augustin *et al.* (32). Approximately 20 μM purified enzyme in 50 mM HEPES/NaOH, pH 7.0, was reduced at

15 °C. Further reduction of hETF-WT was achieved by adding a 10-fold excess of sodium dithionite to the solution.

Thermo FAD thermal stability

The temperature stability of the proteins was determined by monitoring the change in the intrinsic protein fluorescence of FAD in a ThermoFluor[®] assay (37). Thermo FAD measurements were carried out with an FX Connect real-time PCR system (Bio-Rad) in 25 µL of 50 mM HEPES/NaOH, pH 7.0, and 30 µM enzyme. The samples were pre-heated to 25 °C, and then the temperature was increased in 0.5 °C/min steps to 95 °C. Fluorescence data were collected using the FRET channel. Melting temperatures (T_m) were determined using the CFX Manager 3.0 software (Bio-Rad).

Author contributions

PA, MT, KF and ECG expressed, purified and characterized wild-type hETF and variants; RP conducted and interpreted EPR data. PA, MT, AW and PM designed biochemical experiments and interpreted the data; PA, MT, AW and PM wrote the manuscript.

Conflict of interest

The authors declare no conflict of interest.

Acknowledgements

We would like to thank Dr. Hansjörg Weber for performing NMR spectroscopy and Thorsten Bachler to set up the HPLC/MS method. We are also grateful to Prof. J.-J. Kim, Medical College of Wisconsin, for providing the electron density map of the human ETF structure (PDB code 1EFV). This work was supported by a grant from the Austrian Science Foundation (FWF) to PM (Doctoral program “Molecular Enzymology” W901).

References

1. Crane, F. L., Mii, S., Hauge, J. G., Green, D. E., and Beinert, H. (1956) On the mechanism of dehydrogenation of fatty acyl derivatives of coenzyme A. I. The general fatty acyl coenzyme A dehydrogenase. *J. Biol. Chem.* **218**, 701–706
2. Toogood, H. S., Leys, D., and Scrutton, N. S. (2007) Dynamics driving function - New insights from electron transferring flavoproteins and partner complexes. *FEBS J.* **274**, 5481–5504
3. Ghisla, S., and Thorpe, C. (2004) Acyl-CoA dehydrogenases: A mechanistic overview. *Eur. J. Biochem.* **271**, 494–508
4. Toogood, H. S., Van Thiel, A., Basran, J., Sutcliffe, M. J., Scrutton, N. S., and Leys, D. (2004) Extensive domain motion and electron transfer in the human electron transferring flavoprotein-medium chain acyl-CoA dehydrogenase complex. *J. Biol. Chem.* **279**, 32904–32912
5. Herrick, K. R., Salazar, D., Goodman, S. I., Finocchiaro, G., Bedzyk, L. A., and Frerman, F. E. (1994) Expression and characterization of human and chimeric human-*Paracoccus denitrificans* electron transfer flavoproteins. *J. Biol. Chem.* **269**, 32239–32245
6. Husain, M., and Steenkamp, D. J. (1983) Electron transfer flavoprotein from pig liver mitochondria. A simple purification and re-evaluation of some of the molecular properties. *Biochem. J.* **209**, 541–545
7. Horai, H., Arita, M., Kanaya, S., Nihei, Y., Ikeda, T., Suwa, K., Ojima, Y., Tanaka, K., Tanaka, S., Aoshima, K., Oda, Y., Kakazu, Y., Kusano, M., Tohge, T., Matsuda, F., Sawada, Y., Hirai, M. Y., Nakanishi, H., Ikeda, K., Akimoto, N., Maoka, T., Takahashi, H., Ara, T., Sakurai, N., Suzuki, H., Shibata, D., Neumann, S., Iida, T., Tanaka, K., Funatsu, K., Matsuura, F., Soga, T., Taguchi, R., Saito, K., and Nishioka, T. (2010) MassBank: A public repository for sharing mass spectral data for life sciences. *J. Mass Spectrom.* **45**, 703–714
8. Doubayashi, D., Ootake, T., Maeda, Y., Oki, M., Tokunaga, Y., Sakurai, A., Nagaosa, Y., Mikami, B., and Uchida, H. (2011) Formate oxidase, an enzyme of the glucose-methanol-choline oxidoreductase family, has a His-Arg pair and 8-formyl-FAD at the catalytic site. *Biosci. Biotechnol. Biochem.* **75**, 1662–1667
9. Toogood, H. S., Van Thiel, A., Scrutton, N. S., and Leys, D. (2005) Stabilization of non-productive conformations underpins rapid electron transfer to electron-transferring flavoprotein. *J. Biol. Chem.* **280**, 30361–30366
10. Schleicher, E., Bittl, R., and Weber, S. (2009) New roles of flavoproteins in molecular cell biology: Blue-light active flavoproteins studied by electron paramagnetic resonance. *FEBS J.* **276**, 4290–4303
11. Lehman, T. C., and Thorpe, C. (1992) A new form of mammalian electron-transferring flavoprotein. *Arch. Biochem. Biophys.* **292**, 594–599

12. Edmondson, D. E. (1974) Intramolecular hemiacetal formation in 8-formylriboflavine. *Biochemistry*. **13**, 2817–21
13. Yorita, K., Matsuoka, T., Misaki, H., and Massey, V. (2000) Interaction of two arginine residues in lactate oxidase with the enzyme flavin: Conversion of FMN to 8-formyl-FMN. *Proc. Natl. Acad. Sci.* **97**, 13039–13044
14. Maeda, Y., Doubayashi, D., Oki, M., Nose, H., Sakurai, A., Isa, K., Fujii, Y., and Uchida, H. (2009) Expression in *Escherichia coli* of an unnamed protein gene from *Aspergillus oryzae* RIB40 and cofactor analyses of the gene product as formate oxidase. *Biosci. Biotechnol. Biochem.* **73**, 2645–9
15. Byron, C. M., Stankovich, M. T., Husain, M., and Davidson, V. L. (1989) Unusual Redox Properties of electron-transfer flavoprotein from *Methylophilus methylotrophus*. *Biochemistry*. **28**, 8582–8587
16. Jhulki, I., Chanani, P. K., Abdelwahed, S. H., and Begley, T. P. (2016) A remarkable oxidative cascade that replaces the riboflavin C8 methyl with an amino group during roseoflavin biosynthesis. *J. Am. Chem. Soc.* **138**, 8324–8327
17. Robbins, J. M., Souffrant, M. G., Hamelberg, D., Gadda, G., and Bommarius, A. S. (2017) Enzyme-mediated conversion of flavin adenine dinucleotide (FAD) to 8-formyl FAD in formate oxidase results in a modified cofactor with enhanced catalytic properties. *Biochemistry*. **56**, 3800–3807
18. Konjik, V., Brünle, S., Demmer, U., Vanselow, A., Sandhoff, R., Ermler, U., and Mack, M. (2017) The crystal structure of RosB: Insights into the reaction mechanism of the first member of a family of flavodoxin-like enzymes. *Angew. Chemie - Int. Ed.* **56**, 1146–1151
19. Mewies, M., McIntire, W. S., and Scrutton, N. S. (1998) Covalent attachment of flavin adenine dinucleotide (FAD) and flavin mononucleotide (FMN) to enzymes: The current state of affairs. *Protein Sci.* **7**, 7–21
20. McIntire, W., Edmondson, D. E., Singer, T. P., and Hopper, D. J. (1981) 8 α -(O-tyrosyl)flavin adenine dinucleotide, the prosthetic group of bacterial *p*-cresol methylhydroxylase. *Biochemistry*. **20**, 3068–3075
21. Kim, J., Fuller, J. H., Cecchini, G., and McIntire, W. S. (1994) Cloning, sequencing, and expression of the structural genes for the cytochrome and flavoprotein subunits of *p*-cresol methylhydroxylase from two strains of *Pseudomonas putida*. *J. Bacteriol.* **176**, 6349–61
22. Reeve, C. D., Carver, M. A., and Hopper, D. J. (1989) The purification and characterization of 4-ethylphenol methylenehydroxylase, a flavocytochrome from *Pseudomonas putida* JD1. *Biochem J.* **263**, 431–437
23. Porcelli, A. M., Ghelli, A., Zanna, C., Pinton, P., Rizzuto, R., and Rugolo, M. (2005) pH difference across the outer mitochondrial membrane measured with a green fluorescent protein mutant. *Biochem. Biophys. Res. Commun.* **326**, 799–804

24. Llopis, J., McCaffery, J. M., Miyawaki, A., Farquhar, M. G., Tsien, R. Y., and Biology, C. (1998) Measurement of cytosolic, mitochondrial, and Golgi pH in single living cells with green fluorescent proteins. *Proc. Natl. Acad. Sci.* **95**, 6803–6808
25. Hare, J. F., and Hodges, R. (1982) Turnover of mitochondrial matrix polypeptides in hepatoma monolayer cultures. *J. Biol. Chem.* **257**, 12950–12953
26. Christensen, E., Kølvråa, S., and Gregersen, N. (1984) Glutaric aciduria type II: Evidence for a defect related to the electron transfer flavoprotein or its dehydrogenase. *Pediatr. Res.* **18**, 663–667
27. Frerman, F. E., and Goodman, S. I. (2001) Defects of electron transfer flavoprotein and electron transfer flavoprotein-ubiquinone oxidoreductase: glutaric acidemia type II. in *The Metabolic and Molecular Bases of Inherited Disease. (8th ed.)*, 8th editio (Scriver, C. R., Beaudet, A. L., Sly, W. S., and Valle, D. eds), pp. 2357–2365, McGraw-Hill, New York
28. Schiff, M., Froissart, R., Olsen, R. K. J., Acquaviva, C., and Vianey-Saban, C. (2006) Electron transfer flavoprotein deficiency: Functional and molecular aspects. *Mol. Genet. Metab.* **88**, 153–158
29. Salazar, D., Zhang, L., DeGala, G. D., and Frerman, F. E. (1997) Expression and characterization of two pathogenic mutations in human electron transfer flavoprotein. *J. Biol. Chem.* **272**, 26425–26433
30. Dwyer, T. M., Zhang, L., Muller, M., Marrugo, F., and Frerman, F. (1999) The functions of the flavin contact residues, α Arg249 and β Tyr16, in human electron transfer flavoprotein. *Biochim. Biophys. Acta - Protein Struct. Mol. Enzymol.* **1433**, 139–152
31. Bross, P., Pedersen, P., Winter, V., Nyholm, M., Johansen, B. N., Olsen, R. K. J., Corydon, M. J., Andresen, B. S., Eiberg, H., Kølvråa, S., and Gregersen, N. (1999) A polymorphic variant in the human electron transfer flavoprotein α -chain (α -T171) displays decreased thermal stability and is overrepresented in very-long-chain acyl-CoA dehydrogenase-deficient patients with mild childhood presentation. *Mol. Genet. Metab.* **67**, 138–147
32. Augustin, P., Hromic, A., Pavkov-Keller, T., Gruber, K., and Macheroux, P. (2016) Structure and biochemical properties of recombinant human dimethylglycine dehydrogenase and comparison to the disease-related H109R variant. *FEBS J.* 10.1111/febs.13828
33. Laemmli, U. K. (1970) Cleavage of structural proteins during the assembly of the head of bacteriophage T4. *Nature.* **227**, 680–685
34. Macheroux, P. (1999) UV-visible spectroscopy as a tool to study flavoproteins. *Methods Mol. Biol.* **131**, 1–7
35. Okamura-Ikeda, K., Ikeda, Y., and Tanaka, K. (1985) An essential cysteine residue located in the vicinity of the FAD-binding site in short-chain, medium-chain, and long-chain acyl-CoA dehydrogenases from rat liver mitochondria. *J. Biol. Chem.* **260**, 1338–1345

36. Massey, V., Hemmerich, P., Knappe, W. R., Duchstein, H. J., and Fenner, H. (1978) Photoreduction of flavoproteins and other biological compounds catalyzed by deazaflavins. Appendix: photochemical formation of deazaflavin dimers. *Biochemistry*. **17**, 9–17
37. Forneris, F., Orru, R., Bonivento, D., Chiarelli, L. R., and Mattevi, A. (2009) Thermo FAD, a ThermoFluor[®]-adapted flavin *ad hoc* detection system for protein folding and ligand binding. *FEBS J.* **276**, 2833–2840

Chapter 4

Mechanism of 8f-FAD formation in hETF

Toward understanding the mechanism of 8-formyl FAD formation in human electron transferring flavoprotein

Marina Toplak, Katharina Fuchs, Julia Brunner and Peter Macheroux

Institute of Biochemistry, Graz University of Technology, Petersgasse 12/II, 8010 Graz, Austria

Running title: Mechanism of 8-formyl-FAD formation in hETF

Keywords: 8-formyl-FAD, electron transfer, flavin semiquinone, reduction potential.

Abbreviations

8f-FAD, 8-formyl-FAD; (h)DMGDH, (human) dimethylglycine dehydrogenase; (h)ETF, (human) electron transferring flavoprotein; (h)ETF-QO, (human) ETF-ubiquinone oxidoreductase; FAD, flavin adenine dinucleotide.

Introduction

In a recent publication, we could show that the flavin cofactor bound to hETF is undergoing spontaneous oxidation to its 8-formyl derivative, leading to strongly altered electron transfer properties of the protein (Chapter 3; (1)). We have found that the process is strongly influenced by the pH and that several amino acids in the active site appear to be involved in flavin oxidation (1). However, the results obtained thus far, were not sufficient to postulate a detailed reaction mechanism for the process of 8-formyl formation.

Therefore, I extended the mutagenesis study and analyzed the role of (α Q262), which had not been considered in our previous investigation. According to the crystal structure of hETF (PDB: 1efv (2)), α Q262 is in hydrogen bonding distance to several atoms of the pyrimidine part of the isoalloxazine ring (in particular to the N3-C4=O locus) as well as to the side-chain amide function of α N259, and thereby may function as a linker between the flavin cofactor and the well-studied salt bridge at the surface of the protein (Figure 1) (3).

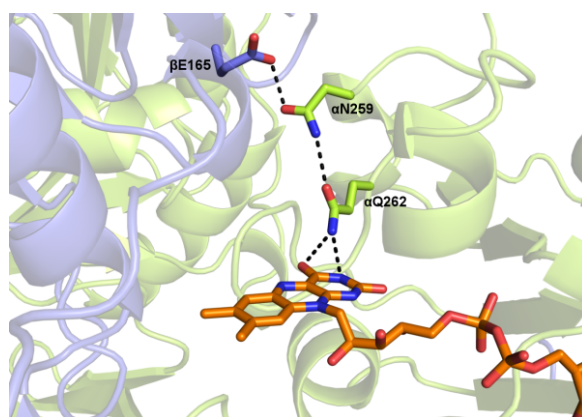
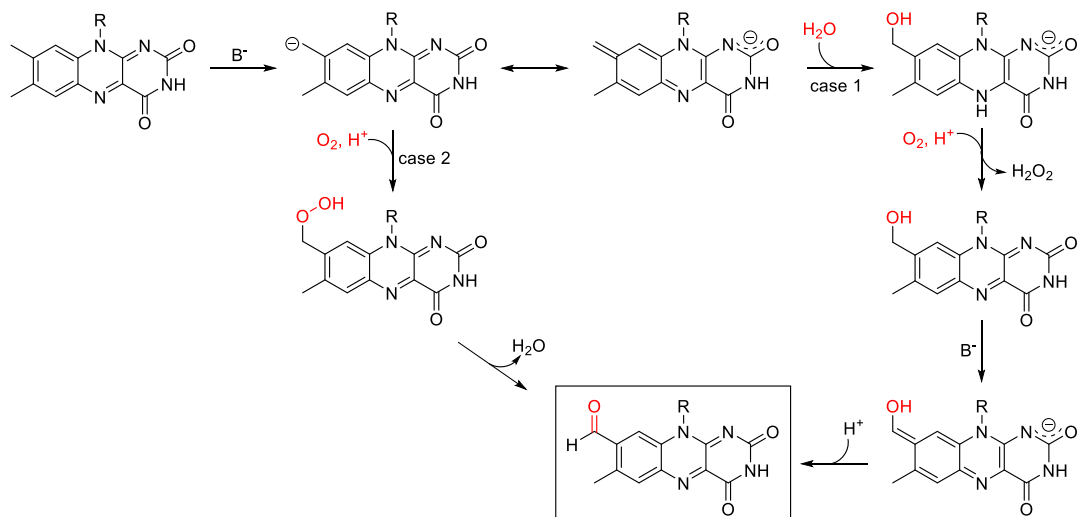


Figure 1: Hydrogen bonding network formed between β Glu165, α Asn259, α Gln262, and the FAD cofactor. According to the crystal structure of hETF (PDB: 1efv (2)), the active site residue (α Q262) investigated in the present study is in H-bonding distance to the side-chain amide function of α N259 as well as to the N3-C4=O locus of the flavin cofactor.

While hETF- α Q262A exhibited similar catalytic properties and showed an almost equal tendency toward 8-formyl-FAD formation like hETF wild type, the spectral properties of hETF- α Q262A were significantly different to those of hETF wild type and the previously investigated protein variants (Chapter 3; (1)).

Earlier studies on 8-formyl formation in other flavin dependent enzymes have suggested that flavin oxidation requires an initial deprotonation of the 8 α methyl group, followed either by the attack of a hydroxylate or by the binding of oxygen/superoxide to the 8 α -position of the isoalloxazine ring (4–6). In the first case, oxygen dependent oxidation, deprotonation, and tautomerization are then needed to yield 8-formylated flavin (Scheme 1, *case 1*), whereas “simple” protonation and release of water will lead to the oxidized flavin species in the second case (Scheme 1, *case 2*) (4–6).

Scheme 1: Proposed mechanisms for 8-formyl formation. So far, studies on the mechanism 8-formyl formation have suggested that flavin oxidation requires an initial deprotonation of the 8 α methyl group, followed either by the attack of a hydroxylate or by the binding of oxygen/superoxide to the 8 α -position of the isoalloxazine ring (4–6). In the first case (*case 1*), oxygen dependent oxidation, deprotonation, and tautomerization are then needed to yield 8-formylated flavin, whereas “simple” protonation and release of water will lead to the oxidized flavin species in the second case (*case 2*) (4–6).



Therefore, we expected that incubation of freshly purified hETF- β E165A (wild type is too slow and precipitates in the course of the assay) under anoxic conditions could help discriminate between the two mechanisms. In the first case, 8 α -hydroxy-FAD should be detected as an intermediate, whereas non-modified FAD should be found in the second case. Interestingly, hETF-bound FAD was not at all modified in oxygen-free atmosphere; however, changes in the absorption characteristics indicated conversion of oxidized FAD to its semiquinone state.

This finding prompted us to investigate the electrochemical properties of hETF-variants that showed no or slow conversion to the oxidized flavin derivative in more detail (1). Surprisingly, but in line with the 8-formyl formation assay, both the β Y16F and the α R249C variant were no longer able to efficiently stabilize the anionic flavin semiquinone and, in contrast to the wild type protein, even full reduction to the hydroquinone form could be achieved upon light illumination.

As mentioned above, our studies have also shown that flavin oxidation in hETF strongly influences the electron transfer properties of the protein. Interaction studies with hDMGDH as electron donor revealed tighter binding to hETF with formylated FAD, though, the overall rate of electron transfer was found to be significantly reduced (Chapter 3; (1)). This, of course, raised the question whether electron delivery to the ETF-ubiquinone oxidoreductase (ETF-QO) was affected in a similar way. In lack of the natural electron acceptor and because efficiency of electron transfer is mainly controlled by the redox properties of the protein-bound flavin moieties, we also determined the catalytically relevant reduction potential of the semiquinone-hydroquinone couple of formylated hETF. We could show that the reduction potential of 8-formylated hETF- α N259A (semiquinone-reduced) is more positive than the one-electron reduction potentials of non-formylated hETF (7) and also more positive than the

reduction potential of the iron-sulfur cluster accepting the electrons in ETF-QO (8), which suggests an impaired transfer of electrons to its final electron acceptor.

Altogether, our results provide deeper insights into the process of 8f-FAD formation and they help to better understand the influence of the cofactor modification on mitochondrial electron transport.

Results

Characterization of the hETF- α Q262A variant

Recombinant production of hETF- α Q262A in *E. coli* and subsequent purification of the protein via Ni-NTA chromatography yielded about 3 mg of pure protein per g cell wet weight. Interestingly, the spectral properties of hETF- α Q262A strongly diverged from hETF-wild type and the previously characterized variants (Figure 2). Protein purified at pH 7 and stored at 4 °C for 72 h, showed a slightly increased longer wavelength absorption (525 to 750 nm) and a bathochromic shift of the 375 nm peak (Figure 2; wild type: *black*, α Q262A: *red*), suggesting the presence of a small amount of a mixture between neutral and anionic flavin semiquinone species. In contrast, the spectral changes observed for the protein purified at pH 8.5 and stored at the same pH for 72 h, indicated the formylation of the FAD chromophore, though the absorption characteristics of this variant were significantly different as compared with formylated hETF- α N259A and hETF- β E165A variant (Figure 2; panel A and B, *black* lines).

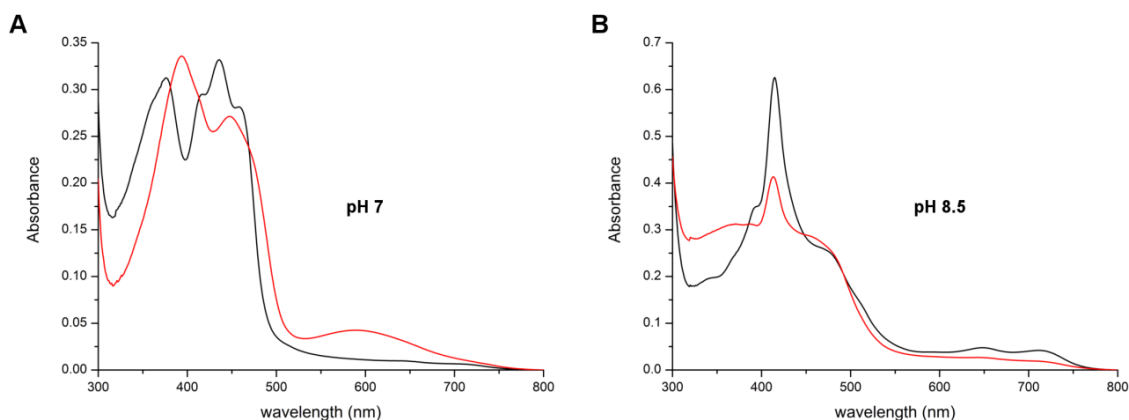


Figure 2: Spectral properties of hETF- α Q262A purified and stored at pH 7 and pH 8.5 (4°C) for 72 h in comparison with hETF wild type and hETF- α N259A, respectively. **A**, hETF wild type (*black* line) and hETF- α Q262A (*red* line) purified at pH 7 were diluted to a final concentration of \sim 25 μ M using 50 mM HEPES pH 7 and UV-visible absorption spectra were recorded between 300 and 800 nm. Comparing the spectra of the two proteins, a bathochromic shift of the 375 nm peak is observed in the variant, which is accompanied by a significantly reduced absorbance in the 450 nm region (wild type: *black* line; α Q262A: *red* line). At the same time, also an increase in the longer wavelength absorbance between 525 and 750 nm is seen. **B**, UV-visible absorption spectra (300-800 nm) of hETF- α N259A (*black* line) and hETF- α Q262A (*red* line) diluted to a final concentration of 25 μ M using 50 mM HEPES pH 8.5, indicating a partial formylation of the cofactor bound to hETF- α Q262A.

To study the ability of the hETF- α Q262A variant to stabilize radical species, photoreduction experiments were carried out with the protein purified at pH 7 and pH 8.5. At pH 7, illumination of the purified protein sample first caused a hypsochromic shift of the 390 nm peak, which was accompanied by a strong decrease in absorption in the 450 nm region (Figure 3; *black* line (start) to *pink* line (20 min)), indicating the formation of an anionic flavin semiquinone. After several minutes, also a slight decrease in absorbance around 375 nm was observed, suggesting the reduction of a minor fraction of the flavin semiquinone species to the hydroquinone form (Figure 3; *dark blue* line).

At pH 7, in the course of the photoreduction of hETF- α Q262A a slight increase in absorption around 415 nm was detected, indicating the conversion of oxidized 8f-FAD to the anionic semiquinone form (Figure 3; *black* and *red* line). After this quick one electron reduction, transfer of the second electron was observed, in the end yielding a pink colored protein solution with absorption characteristics typical for reduced 8f-FAD species (Figure 3; *orange* line).

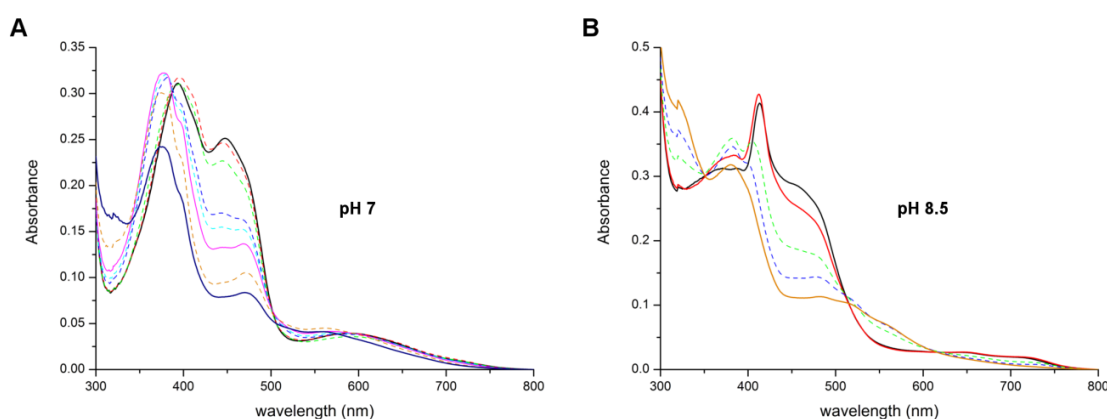


Figure 3: Photoreduction of hETF- α Q262A purified at pH 7 (A) and pH 8.5 (B) and stored at the respective pH (4°C) for 72 h. Spectral changes monitored in the course of the anoxic photoreduction of hETF- α Q262A purified at pH 7 (A) and pH 8.5 (B) and diluted to a final concentration of $\sim 20 \mu\text{M}$ with 50 mM HEPES pH 7 and pH 8.5, respectively. **A**, Within the first 20 minutes, a hypsochromic shift of the 390 nm peak accompanied by a strong decrease in absorbance around 450 nm was observed (start: *black line*; 20 min: *pink line*), indicating the formation of an anionic flavin semiquinone. Upon continuous illumination, the peak around 375 nm then also started to decline, finally yielding the spectrum shown in *dark blue*, which indicated the presence of a mixture of semiquinone and reduced flavin species in the solution. **B**, Illumination of the pH 8.5 purified sample initially caused a slight increase of the peak at 415 nm, indicating the conversion of oxidized 8f-FAD to the flavin semiquinone state (*black* and *red* line), before complete conversion to the hydroquinone form is observed (*orange* line).

To study the kinetics of 8f-FAD formation, hETF- α Q262A purified at pH 7 and stored at the same pH for 72 h, was transferred to 50 mM HEPES pH 8.5 and incubated at this pH for 24 h. Samples were taken after 0, 2, 4, 6, 8, and 24 h and the nature of the flavin chromophore was analyzed on HPLC-DAD. Already at time point “0 h”, about 3 % of the protein was found to contain 8f-FAD as cofactor

and the degree of formylation gradually increased with similar half-times as compared with hETF wild type, reaching ~50% formylation after 24 h of incubation.

8f-FAD formation under anoxic conditions

To better understand of the mechanism of 8f-FAD formation in hETF, we analyzed 8f-FAD formation under anoxic conditions. Freshly purified hETF- β E165A variant (pH 7) was rendered anoxic by incubating a concentrated protein sample in an anaerobic glove box for two hours. Then, the protein was diluted with 50 mM HEPES pH 8.5 (oxygen free) to generate alkaline conditions that are known to speed up the oxidation process (1). At time point 0 h and after 15 h, UV-visible absorption spectra were recorded and protein samples were taken to analyze the nature of the protein-bound cofactors on HPLC-DAD. Interestingly, no 8-formylated cofactor was found in the HPLC analysis and the absorption characteristics of the protein resembled those of oxidized and strongly stabilized anionic flavin semiquinone species. (Figure 4, 0 h: *solid black line* and 15 h: *red dashed line*). To see, whether the presence of molecular oxygen was required to initiate 8f-FAD formation, the protein solution was then exposed to air and further UV-visible absorption spectra were recorded. After 1 h, it seemed as if the protein-bound FAD had returned to its oxidized state, however, the small peak in the longer wavelength region visible in the *red* spectrum was still observed (Figure 4, *green line*). Right at that time, also a shoulder around 415 nm became visible, for the first time indicating the presence of small amounts of formylated cofactor (Figure 4, *green line*) (1). This 415 nm peak then further increased within the following 24 h, until formylation of the majority of the flavin moiety could be detected on HPLC-DAD. 100 % formylation, however, could not be achieved, which can be explained by the fact that significant amounts of protein precipitated in the course of the experiment.

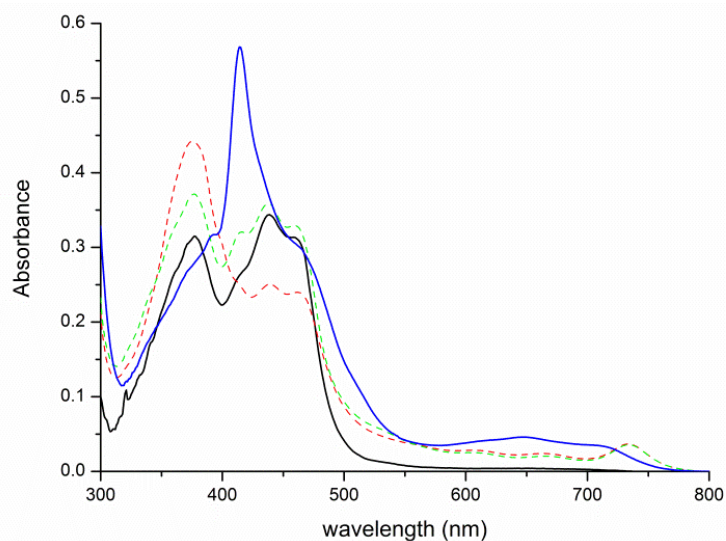


Figure 4: Influence of oxygen availability on 8-formyl formation in hETF. Freshly purified hETF- β E165A variant (pH 7; normalized spectrum: *black* line) was rendered anoxic by incubating the protein solution in an anoxic glove box for 2 h. Then, the protein solution was diluted to a final concentration of $\sim 30 \mu\text{M}$ using 50 mM HEPES pH 8.5 and incubated in the glove box overnight. The next day, a UV-visible absorption spectrum was recorded (*red* line), indicating the formation of an anionic flavin semiquinone species rather than the formation of any modified flavin derivative. To assay the importance of oxygen supply on 8f-FAD formation, the protein solution was then exposed to air and spectral changes were monitored spectrophotometrically. After 1 h of exposure to oxygen, the *green* spectrum was recorded, which in contrast to the black spectrum exhibits a small shoulder at 415 nm, indicating the presence of low amounts of 8f-FAD. This 415 nm peak was observed to further increase, until after 24 h the final *blue* spectrum corresponding almost exclusively to 8-formylated FAD (hETF-bound), was obtained.

Photoreduction of non- and weakly 8-formyl forming variants

The fact that incubation of the hETF- β E165A variant under anoxic conditions did not lead to the formation of any modified flavin species, but caused the conversion of oxidized protein to its semiquinone state, prompted us to investigate the ability of the non- or weaker 8-formyl forming hETF variants to stabilize the radical flavin intermediate by photoreduction.

Interestingly, upon illumination, both the β Y16F and the α R249C variant could be reduced to the hydroquinone form, which is very much in contrast to the wild type protein that undergoes single electron reduction to the semiquinone state (Figure 5A and B and Chapter 3; (1)). While radical formation was still observed in the course of the reduction of the β Y16F variant (Figure 5A), the α R249C variant was hardly able to stabilize the semiquinone intermediate (Figure 5B), which very well correlates with their ability/inability to form the 8-formyl flavin derivative (1). In contrast, the α T266M variant still could only be reduced to the semiquinone state (Figure 5C), though showing significant impairment in 8-formylation activity.

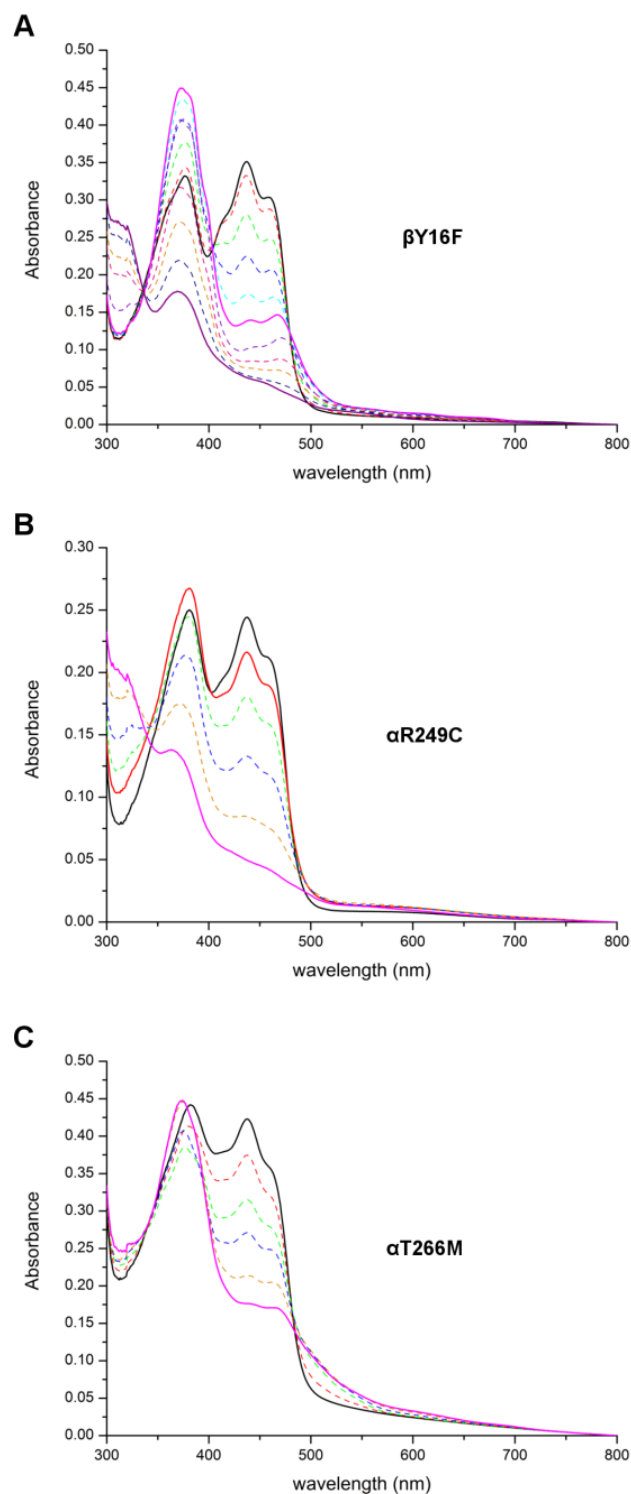


Figure 5: Photoreduction of three hETF-variants: $\beta Y16F$ (A), $\alpha R249C$ (B), and $\alpha T266M$ (C). UV-visible absorption spectra of three hETF-variants ($\beta Y16F$, $\alpha R249C$, and $\alpha T266M$), diluted to a final concentration of $\sim 20\text{-}30\ \mu\text{M}$ using 50 mM HEPES pH 7, recorded in the course of the photoreduction experiment. In each case, the *black* line indicates the starting spectrum, whereas the *purple* ($\beta Y16F$) and *pink* lines ($\alpha R249C$ and $\alpha T266M$) correspond to the final spectra recorded, respectively. All spectra shown with *dashed* lines indicate intermediate states observed in the course of the reduction reaction.

Kinetic characterization of hETF- α Q262A

To study the influence of the single amino acid replacement in hETF- α Q262A as well as the effect of 8-formylation on the electron transfer from hDMGDH to hETF, a coupled assay with DCPIP as final electron acceptor was used (Figure 6). While higher rates of electron transfer were determined with non-formylated hETF- α Q262A (k_{catapp} : $121 \pm 12 \text{ min}^{-1}$ vs $34 \pm 1 \text{ min}^{-1}$), higher affinity of the electron donor to the hETF-variant was observed with the formylated protein (K_{Mapp} : $97 \pm 16 \mu\text{M}$ vs $27 \pm 3 \mu\text{M}$), which is in agreement with the results obtained with hETF wild type and previously studied variants (Chapter 3;(1)).

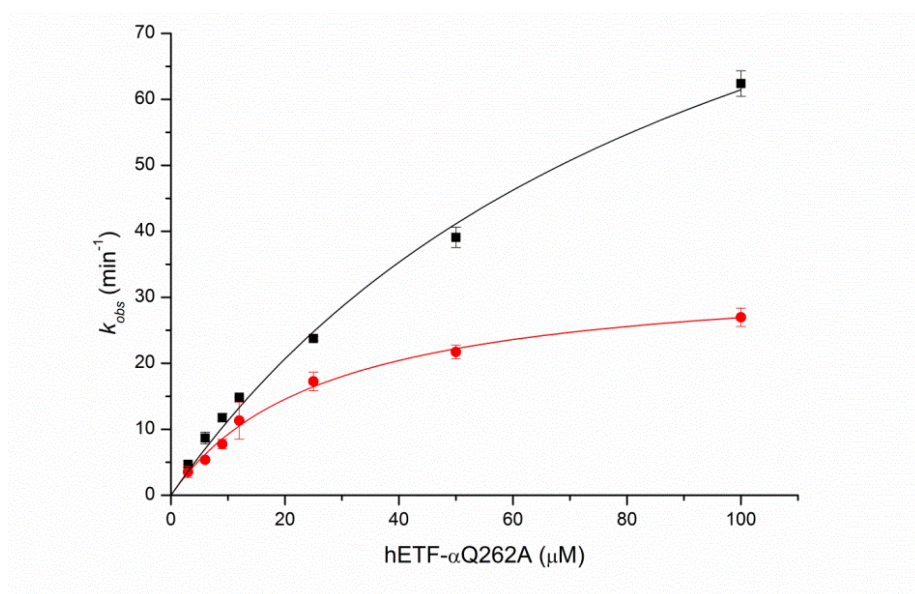


Figure 6: Kinetic characterization of the interaction between hDMGDH and the hETF- α Q262A variant. The kinetic properties of hETF- α Q262A purified at pH 7 and pH 8.5 were studied in a coupled assay with hDMGDH, DMG, and DCPIP as final electron acceptor. hDMGDH (100 nM), DCPIP (125 μM), and different amounts of hETF- α Q262A (3-100 μM) were mixed in 50 mM HEPES pH 7 and incubated at 25°C for 10 min. Then, DMG (25 mM) was added and absorbance changes at 600 nm were recorded for 120 s. By plotting the extracted initial rates as a function of the respective hETF- α Q262A concentrations, hyperbolic curves were obtained (pH 7 (non-formylated), *black squares*; pH 8.5 (formylated), *red spheres*), which enabled the determination of k_{catapp} and K_{Mapp} values for the electron transfer from hDMGDH to hETF- α Q262A.

Redox potential hETF- α N259A (8f-FAD)

Since efficiency of mitochondrial electron transfer is strongly affected by the redox potential of the flavin moieties bound to the various proteins, the redox potential of 8-formylated hETF was determined. To make sure that 100% of the protein in the investigated sample was binding the oxidized cofactor, the experiment was performed with hETF- α N259A. Using the xanthine/xanthine oxidase method, synchronous reduction of the protein-bound 8f-FAD cofactor and the reporting dye thionine acetate (E° : +64 mV) could be observed, enabling the generation of a Nernst plot (Figure 7).

The intercept obtained by plotting the $\log([\text{ox}]/[\text{red}])$ of the protein *versus* the $\log([\text{ox}]/[\text{red}])$ of the dye and fitting the data point with a linear regression function was then used to calculate the redox potential of 8f-FAD bound to hETF- α N259A. The determined reduction potential of $+77 \pm 3$ mV was significantly more positive as compared with the one-electron reduction potentials of hETF wild type with bound FAD (oxidized-semiquinone: +22 mV and semiquinone-reduced: -42 mV; (7)) and still more positive than the reduction potential of the iron-sulfur cluster bound to ETF-QO (+47 mV; (8))

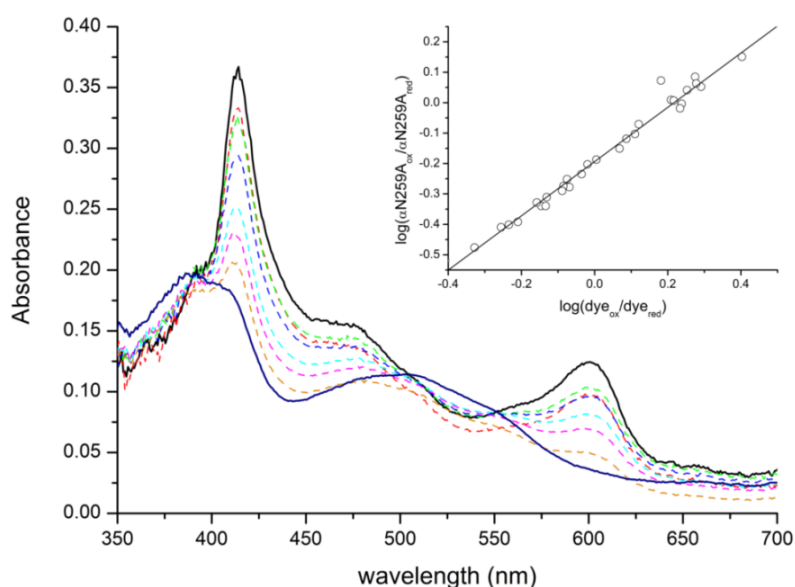


Figure 7: Determination of the redox potential of formylated hETF- α N259A according to the xanthine/xanthine oxidase method (9). hETF- α N259A (~ 15 μ M), xanthine (2.5 mM), methylviologen (2.5 μ M), xanthine oxidase (2.5 nM), and thionine acetate (~ 10 μ M; E° : +64 mV) diluted in 50 mM HEPES, 150 mM NaCl pH7, were mixed in a stopped flow device and changes in the UV-visible absorption spectrum (350-700 nm) were monitored for 25-50 min. The *black* line corresponds to the starting spectrum and the *blue* line indicates the final spectrum recorded after full reduction of the protein-bound flavin and the dye; all spectra shown as dashed lines represent intermediate states. *Inset*, Nernst plot generated based on the absorbance changes at 415 nm (protein) and 600 nm (dye), by plotting the $\log([\text{ox}]/[\text{red}])$ of the protein-bound flavin *versus* the $\log([\text{ox}]/[\text{red}])$ of the dye. The resulting intercept was then used to calculate the redox potential of the 8f-FAD bound to hETF- α N259A ($+77 \pm 3$ mV; from four determinations).

Discussion

Characterization of the hETF- α Q262A variant

The active site residues of electron transferring flavoproteins from a broad range of species are very well-conserved in order to fine-tune the electron transfer properties of the proteins. It could already be shown that α T266 and α R249 are involved in modulating the redox potential of the protein-bound

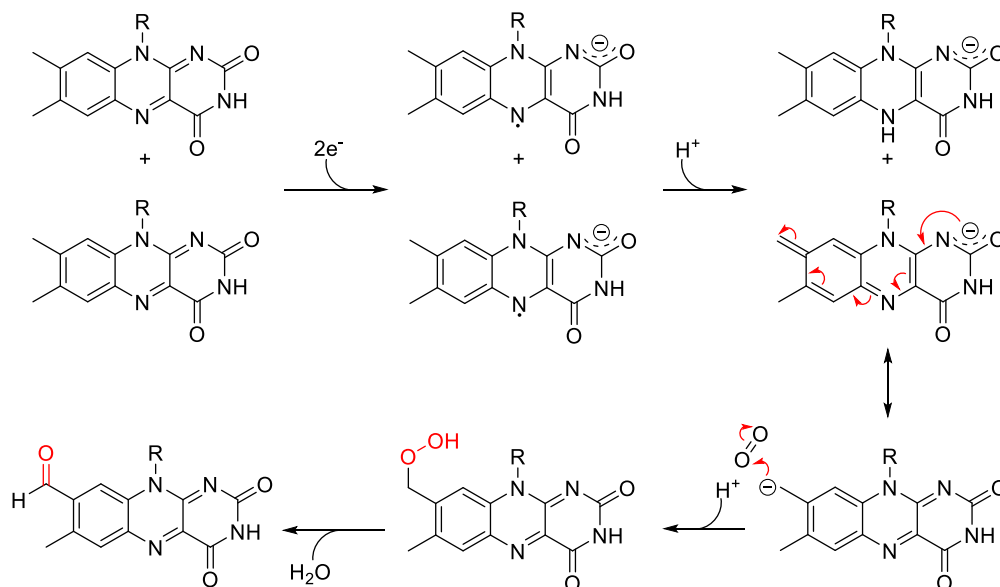
flavin to guarantee efficient electron transfer (7, 10), but information on the importance of other active site residues such as α Q262 was still missing.

In the present study, we could clearly show that the replacement of α Q262 by an alanine does not significantly affect the electron transfer properties of hETF. Similar to the wild type protein, K_{Mapp} values of $97 \pm 16 \mu\text{M}$ vs $27 \pm 3 \mu\text{M}$ and limiting rates of $121 \pm 12 \text{ min}^{-1}$ and $34 \pm 1 \text{ min}^{-1}$ were obtained for non- and predominantly formylated hETF- α Q262, respectively (Figure 6) (1). Therefore, it can be concluded that α Q262 does not play an important role in the electron transfer process from hDMGDH to hETF, which is in line with its localization near the N3-C4=O locus of the isoalloxazine ring (Figure 1). This finding also indicates that despite acting as a linker between the flavin chromophore and the well-studied salt-bridge at the surface of the protein, α Q262 is not involved in controlling the protein motions required for the interconversion between the closed and open state. The latter assumption is even further supported by the observation that hETF- α Q262A, in contrast to hETF- α N259A and hETF- β E165A, is not getting formylated more rapidly than the wild type protein. Despite the very similar biochemical properties of hETF- α Q262A compared with hETF wild type, we still observed very distinct spectral properties for the variant protein. Both, for the protein purified at pH 7 and pH 8.5 the UV-visible absorption spectra indicated the presence of a mixture between neutral and anionic flavin semiquinone (Figure 2 and 3), suggesting an influence of the latter residue on the protonation state of (several) atoms of the pyrimidine ring.

Mechanism of 8-formyl formation

In our previous studies we could show that several amino acid residues in close vicinity of the flavin cofactor may play a role in 8-formyl formation (1), however, we were unable to predict a detailed reaction mechanism. Based on the results obtained from the in-depth characterization of the hETF active-site variants that show strongly impaired 8-formyl formation and from the 8-formyl formation assay performed under anoxic conditions, we can conclude that being able to efficiently form and stabilize the anionic flavin semiquinone coincides with an increased rate of 8-formylation. In addition, 8-formyl formation fully depends on the availability of oxygen, as no modified flavin species could be detected when performing the 8-formylation assay in oxygen free atmosphere (Figure 4). Therefore, it is likely that the mechanism of 8-formyl formation in hETF is similar to the mechanism proposed for the oxidation of riboflavin to 8-formyl riboflavin catalyzed by RosB in roseoflavin biosynthesis (4, 6). However, it is possible that the spontaneous formation of the anionic flavin semiquinone is required to initiate the oxidation process, suggesting an 8-formyl formation mechanism as shown in Scheme 2. The radical flavin species generated in the first step, subsequently, may disproportionate, leading to the formation of reduced cofactor and oxidized deprotonated FAD, and allowing the nucleophilic attack of molecular oxygen. The 8 α -hydroperoxy FAD formed however is not stable, resulting in the release of water and finally yielding 8-formyl FAD as product.

Scheme 2: Proposed mechanism of 8-formyl FAD formation in hETF. Based on our observations we hypothesize that in a first step the FAD cofactor in hETF is undergoing spontaneous one-electron reduction to the anionic flavin semiquinone. Upon disproportionation, reduced cofactor and oxidized, deprotonated FAD are formed, with the latter being strongly resonance stabilized and being able to nucleophilically attack molecular oxygen. The 8 α -hydroperoxy FAD formed in this step however is not stable, leading to the release of water and finally yielding 8-formyl FAD as product.



Based on these assumptions, it is, however, difficult to explain, why 8-formyl formation in hETF- α T266M is so strongly impaired (1). Nevertheless, it is conceivable that the sterically much more demanding methionine residue prevents efficient oxygen binding to the 8 α -position, finally resulting in lower amounts of modified flavin. At the same time, it is also possible that compared to the wild type protein and the two salt-bridge variants (α N259A and β E165A), spontaneous semiquinone formation in hETF- α T266M happens to take place less frequently, which would be in agreement with the much lower one-electron reduction potential (oxidized-semiquinone) of hETF- α T266M as compared to hETF wild type (-27 mV vs +22 mV, respectively (10)).

Influence of 8-formylation of electron transfer

Since electron transport is strongly controlled by the redox potentials of the cofactors bound to the proteins involved in the process, it is rather obvious that already small changes in the nature (*e.g.* formylation of the FAD in hETF) or environment of the cofactors may have adverse effects on the whole system. Already in previous studies we could show that oxidation of the flavin cofactor at the 8 α -position affects the interaction of hETF with its client enzyme hDMGDH, resulting in a tighter binding but a lower rate of electron transfer (1). However, the effect of the flavin modification on electron delivery to ETF-QO remained elusive.

The present study now revealed a rather high reduction redox potential of the catalytically relevant semiquinone-reduced couple of 8-formylated hETF ($+77 \pm 3$ mV), which is about 50 mV (oxidized-semiquinone; (7)) and 120 mV (semiquinone-reduced; (7)) higher than the reduction potentials of hETF with non-modified FAD cofactor, and roughly 30 mV higher than the reduction potential of the iron-sulfur cluster bound to ETF-QO (8). Since electrons are always transferred from cofactors with a lower to those with higher reduction potential, it is thus very likely that electron transfer to its natural electron acceptor is impaired as a result of the modification of the flavin chromophore in hETF. However, interaction studies with the natural electron acceptor will be required to confirm this hypothesis.

Considering that 8-formylation of the cofactor in hETF truly impairs electron delivery to ETF-QO, it would be interesting to see whether this cofactor modification is just a result of the *in vitro* preparation of the protein or whether 8-formylation also takes place *in vivo*. In the case that 8f-FAD formation is also observed in the physiological environment, it would then further be important to find out how humans can deal with the altered properties of such an important protein.

Materials and methods

Cloning and expression (α Q262A)

The hETF- α Q262A variant was generated from the pET28a-hETF wild type construct using a PCR-based mutagenesis approach with both the forward and reverse primer carrying the mutations in the desired codon triplet (fwd: 5'-CCGAATGATATGGCAGTTGGTCAGACCGGCAA-3'; rev: 5'-CGGTCTGACCAACTGCCATATCATTCGGAACAAAACC-3'). Having confirmed the proper replacement of the nucleotides of interest by automated sequencing, the plasmid DNA was transformed with *E. coli* BL21* (DE3) cells for subsequent gene expression.

Protein production and purification were carried out as described in Chapter 3 (Experimental procedures; (1)).

Photoreduction

Photoreduction of various hETF-variants was carried out under anoxic conditions following the instructions provided by Massey *et al.* (11). hETF variants diluted to a final concentration of ~ 20 μ M using 50 mM HEPES pH 7, were mixed with 1 mM EDTA, 1 μ M 5-deaza-FMN and 2 μ M methylviologen and transferred to sealable quartz cuvettes. After recording a UV-visible spectrum between 300 and 800 nm, the samples were irradiated (15°C) and additional spectra were recorded until no further spectral changes were observed. Then, the lids of the cuvettes were removed under aerobic conditions and reoxidation of the flavin chromophore was again monitored spectrophotometrically.

8f-FAD formation (α Q262A)

hETF- α Q262A purified at pH 7 was diluted to a final concentration of $\sim 50 \mu\text{M}$ using 50 mM HEPES pH 8.5 and incubated at 25°C for 24 h. After 0, 2, 4, 6, 8, and 24 h samples were taken and the protein was heat-denatured to obtain free cofactor for the subsequent HPLC analysis (see Augustin *et al.* (1); Experimental procedures). To determine the relative amount of 8f-FAD cofactor in the protein sample, the ratios of the peak areas corresponding to the different flavin species (FAD and 8f-FAD) were calculated.

Steady-state kinetics (α Q262A)

The steady-state parameters for the electron transfer from hDMGDH to the hETF- α Q262A variant were studied in a coupled assay with DCPIP as final electron acceptor. Reaction solutions containing hDMGDH (100 nM), DCPIP (125 μM), and hETF- α Q262A (3-100 μM ; purified at pH 7 or pH 8.5) were mixed in 50 mM HEPES pH 7 and incubated at 25°C for 10 min. Then, the electron transfer was initiated by adding DMG (25 mM), the natural substrate of hDMGDH, and absorbance changes at 600 nm were recorded for 120 s. By plotting the initial velocities (normalized with respect to the enzyme concentration) as a function of different hETF concentrations a hyperbolic curve was obtained, which allowed the determination of limiting rates (k_{catapp}) as well as of K_{Mapp} values for the interaction of hDMGDH with hETF- α Q262A.

Determination of the redox potential of 8-formylated hETF (α N259A)

To get some information about the electrochemical properties of 8-formylated hETF, the redox potential of fully formylated hETF- α N259A variant was determined based on the xanthine/xanthine oxidase method (9). A solution containing $\sim 30 \mu\text{M}$ hETF- α N259A, 5 mM xanthine, and 5 μM methylviologen was mixed with a second solution containing $\sim 20 \mu\text{M}$ thionine acetate (E° : +64 mV) and 5 nM xanthine oxidase under anoxic conditions using a stopped-flow apparatus from Hi-Tech (TgK-Scientific, Bradford-on-Avon, UK) installed in an anaerobic glove box (Belle Technology, Cambridge, UK). Then, spectral changes in the UV-visible absorption characteristics of the flavin chromophore and the dye were monitored (350 to 700 nm) with a KinetaScanT diode array detector (TgK-Scientific) for 25-50 min (four determinations). Based on the relative absorbance changes at 415 nm (protein) and 600 nm (dye) a Nernst plot was generated by plotting the $\log([\text{ox}]/[\text{red}])$ of the protein *versus* the $\log([\text{ox}]/[\text{red}])$ of the dye, which later allowed the determination of the redox potential from the resulting intercept (12).

8f-FAD formation under anoxic conditions

Freshly purified hETF- β E165A variant (pH 7; \sim 230 μ M) was rendered anoxic by incubating the protein sample in an anaerobic glove box for two hours. Then, the protein was diluted with 50 mM HEPES pH 8.5 buffer to a final concentration of about 25 μ M and a UV-*visible* absorption spectrum was recorded between 300 and 800 nm (in a sealable quartz cuvette). After overnight incubation in the glove box (\sim 25 $^{\circ}$ C), another spectrum was recorded, before removing the lid of the cuvette and following the spectral changes under aerobic conditions for additional 24 h.

In addition to the spectral analysis, time-dependent cofactor modification was also studied using HPLC-DAD. Therefore, samples were taken after 0 h, overnight incubation in the glove box, as well as after 24 h of exposure to oxygen, and the flavin cofactor was isolated by heat-denaturing hETF at 95 $^{\circ}$ C for 10 min followed by 10 min of centrifugation at 13,300 rpm. Cofactor analysis was then performed as described by Augustin *et al.* (1).

References

1. Augustin, P., Toplak, M., Fuchs, K., Gerstmann, E. C., Prassl, R., Winkler, A., and Macheroux, P. (2018) Oxidation of the FAD cofactor to the 8-formyl-derivative in human electron-transferring flavoprotein. *J. Biol. Chem.* **293**, 2829–2840
2. Roberts, D. L., Frerman, F. E., and Kim, J. J. (1996) Three-dimensional structure of human electron transfer flavoprotein to 2.1-Å resolution. *Proc. Natl. Acad. Sci. U. S. A.* **93**, 14355–60
3. Toogood, H. S., Van Thiel, A., Scrutton, N. S., and Leys, D. (2005) Stabilization of non-productive conformations underpins rapid electron transfer to electron-transferring flavoprotein. *J. Biol. Chem.* **280**, 30361–30366
4. Konjik, V., Brünle, S., Demmer, U., Vanselow, A., Sandhoff, R., Ermler, U., and Mack, M. (2017) The crystal structure of RosB: Insights into the reaction mechanism of the first member of a family of flavodoxin-like enzymes. *Angew. Chemie - Int. Ed.* **56**, 1146–1151
5. Robbins, J. M., Souffrant, M. G., Hamelberg, D., Gadda, G., and Bommarius, A. S. (2017) Enzyme-mediated conversion of flavin adenine dinucleotide (FAD) to 8-formyl FAD in formate oxidase results in a modified cofactor with enhanced catalytic properties. *Biochemistry.* **56**, 3800–3807
6. Jhulki, I., Chanani, P. K., Abdelwahed, S. H., and Begley, T. P. (2016) A remarkable oxidative cascade that replaces the riboflavin C8 methyl with an amino group during roseoflavin biosynthesis. *J. Am. Chem. Soc.* **138**, 8324–8327
7. Dwyer, T. M., Zhang, L., Muller, M., Marrugo, F., and Frerman, F. (1999) The functions of the flavin contact residues, α Arg249 and β Tyr16, in human electron transfer flavoprotein. *Biochim. Biophys. Acta - Protein Struct. Mol. Enzymol.* **1433**, 139–152
8. Paulsen, K. E., Stankovich, M. T., Orville, A. M., Lipscomb, J. D., and Frerman, F. E. (1992) Redox properties of electron-transfer flavoprotein ubiquinone oxidoreductase as determined by EPR-spectroelectrochemistry. *Biochemistry.* **31**, 11755–11761
9. Massey, V. (1991) A simple method for the determination of redox potentials. in *Flavins and Flavoproteins* (Curti, B., Zanetti, G., and Ronchi, S. eds), pp. 59–66, Walter de Gruyter, Como, Italy
10. Salazar, D., Zhang, L., DeGala, G. D., and Frerman, F. E. (1997) Expression and characterization of two pathogenic mutations in human electron transfer flavoprotein. *J. Biol. Chem.* **272**, 26425–26433
11. Massey, V., Hemmerich, P., Knappe, W. R., Duchstein, H. J., and Fenner, H. (1978) Photoreduction of flavoproteins and other biological compounds catalyzed by deazaflavins. Appendix: photochemical formation of deazaflavin dimers. *Biochemistry.* **17**, 9–17
12. Minnaert, K. (1965) Measurement of the equilibrium constant of the reaction between cytochrome c and cytochrome a. *Biochim. Biophys. Acta.* **110**, 42–56

Chapter 5

Dld2 and yETF

Closing the gap: Yeast electron transferring flavoprotein links the oxidation of D-lactate and D- α -hydroxyglutarate to energy production via the respiratory chain

Marina Toplak, Julia Brunner, Chaitanya Tabib and Peter Macheroux*

Institute of Biochemistry, Graz University of Technology, Petersgasse 12/2, A-8010 Graz, Austria

*to whom correspondence should be addressed:

Prof. Dr. Peter Macheroux

Graz University of Technology

Institute of Biochemistry

Petersgasse 12/2

A-8010 Graz, Austria

Tel.: +43-316-873 6450

Fax: +43-316-873 6952

Email: peter.macheroux@tugraz.at

Running title: Electron transferring flavoprotein and D-lactate dehydrogenase 2 from *S. cerevisiae*

Keywords: D- α -hydroxyglutarate, electron transferring flavoprotein, enzyme kinetics, flavin adenine dinucleotide (FAD), *Saccharomyces cerevisiae*.

Abbreviations

DCPIP, 2,6-dichlorophenol indophenol; Dld2, D-lactate dehydrogenase 2 from *Saccharomyces cerevisiae*; ETF, electron transferring flavoprotein; hETF, ETF from *Homo sapiens*; ETF-QO, ETF-ubiquinone oxidoreductase; 2HG, D-2-hydroxyglutarate or D- α -hydroxyglutarate; yETF, ETF from *Saccharomyces cerevisiae*; PCMH, p-cresol methylhydroxylase.

This chapter has been accepted for publication as “Closing the gap: Yeast electron transferring flavoprotein links the oxidation of D-lactate and D- α -hydroxyglutarate to energy production via the respiratory chain” in FEBS Journal 2019.

Abstract

Electron transferring flavoproteins (ETFs) have been found in all kingdoms of life, mostly assisting in shuttling electrons to the respiratory chain for ATP production. While the human (h) ETF has been studied in great detail, very little is known about the biochemical properties of the homologous protein in the model organism *Saccharomyces cerevisiae* (yETF). In view of the absence of client dehydrogenases, *e.g.* the acyl-CoA dehydrogenases involved in β -oxidation of fatty acids, D-lactate dehydrogenase 2 (Dld2) appeared to be the only relevant enzyme that is serviced by yETF for electron transfer to the mitochondrial electron transport chain. However, this hypothesis was never tested experimentally. Here, we report the biochemical properties of yETF and Dld2 as well as the electron transfer reaction between the two proteins. Our study revealed that Dld2 oxidizes D- α -hydroxyglutarate more efficiently than D-lactate exhibiting k_{catapp}/K_{Mapp} values of $1,200 \pm 300 \text{ M}^{-1} \text{ s}^{-1}$ and $11 \pm 2 \text{ M}^{-1} \text{ s}^{-1}$, respectively. As expected, substrate-reduced Dld2 very slowly reacted with oxygen or the artificial electron acceptor 2,6-dichlorophenol indophenol (DCPIP). However, photoreduced Dld2 was rapidly re-oxidized by oxygen, suggesting that the reaction products, *i.e.* α -ketoglutarate and pyruvate, “lock” the reduced enzyme in an unreactive state. Interestingly, however, we could demonstrate that substrate-reduced Dld2 rapidly transfers electrons to yETF. Therefore, we conclude that formation of a product-reduced Dld2 complex suppresses electron transfer to dioxygen but favors the rapid reduction of yETF, thus preventing the loss of electrons and the generation of reactive oxygen species.

Introduction

Since the discovery of the first electron transferring flavoprotein (ETF) by Crane et al. (1) in 1956, a variety of other proteins belonging to the same family have been identified in all kingdoms of life. In prokaryotes as well as eukaryotes most of them function as housekeeping proteins by coupling the degradation of fatty and amino acids (in humans also of choline) with energy production via the respiratory chain (2–4). This feature is based on the ability of ETFs to accept electrons from various dehydrogenases involved in catabolic pathways and the transfer to an integral membrane protein, ETF-ubiquinone oxidoreductase (ETF-QO), which in turn reduces ubiquinone, a key metabolite of the respiratory chain, and thus directly influence the generation of ATP. In some cases, however, ETF is part of a specialized system, for example in *Methylophilus methylotrophus* and *Peptostreptococcus elsdenii*. In these bacteria reduced trimethylamine dehydrogenase and NADH, respectively, serve as the predominant source for electrons, as these organisms lack the metabolic pathways mentioned above and, therefore, rely on other carbon sources (methanol or trimethylamine and D-lactate, respectively) for energy production (5–9). In other cases, reduced ETFs transfer electrons to acyl-CoA dehydrogenases, which subsequently catalyze the reduction of short chain α,β -unsaturated fatty acids

(7). The cellular role of the electron transferring flavoprotein of *Saccharomyces cerevisiae* (yETF) appears to be similar to bacterial homologs because only one enzyme is currently suspected to deliver electrons, *i.e.* D-lactate dehydrogenase (Dld2), whereas, yETF was reported to deliver the electrons to an ETF-QO homolog, named Cir2p, and thus shares this feature with other eukaryotic organisms (10, 11).

The mitochondrial matrix protein Dld2 was first discovered in a yeast-two-hybrid assay, which was used to identify actin interacting proteins (therefore it was initially called Aip2) (12–14). In the course of subsequent *in vivo* characterizations, however, it was shown that the protein catalyzes the oxidation of D-lactate to pyruvate. Interestingly, recent studies by Becker-Kettern *et al.* revealed that Dld2 was also able to oxidize D- α -hydroxyglutarate to α -ketoglutarate (15). In fact, according to steady-state experiments (with truncated Dld2) D- α -hydroxyglutarate was oxidized with a higher efficiency compared to D-lactate (15). In any case, the oxidation of the two substrates results in the reduction of the flavin cofactor, which needs to be regenerated for turnover. Although the natural electron acceptor of reduced Dld2 remains elusive, the presence of a gene encoding an electron transferring flavoprotein suggested this protein to serve as the electron acceptor, which then further transfers the electrons to a quinone-dependent dehydrogenase in the inner mitochondrial membrane (Cir2p).

To study the possible interaction and the electron transfer between Dld2 and yETF, we produced both proteins in *Komagataella phaffii* and *Escherichia coli*, respectively. In a detailed biochemical characterization of yETF, we could show that it exhibits spectral and electrochemical properties strongly diverging from its human counterpart (16), despite high sequence identity (47 %) and structural similarity. Because we identified only a single amino acid residue in the active site of yETF to be different in comparison with the human homolog (β Phe19 vs β Tyr16), we asked the question whether the replacement of this particular phenylalanine by tyrosine could restore the biochemical properties of hETF (16, 17). Therefore, we also generated a β Phe19Tyr variant, as well as two double variants (β Phe19Tyr- α Asn269Ala and β Phe19Tyr- β Glu169Ala), with an additional amino acid exchange targeting the well-studied salt bridge at the surface of the human protein (equivalent to human α Asn259Ala and β Glu165Ala variants, respectively) (18).

To better understand the catalytic properties of full length Dld2, we performed a detailed kinetic characterization of the enzyme involving steady-state and pre steady-state experiments with both substrates, *i.e.* D- α -hydroxyglutarate and D-lactate. As previously reported by Becker-Kettern *et al.* (15), steady-state experiments revealed a higher catalytic efficiency and lower K_{Mapp} with D- α -hydroxyglutarate, but also a lower turnover. In our pre steady-state experiments, however, D- α -hydroxyglutarate was shown to reduce Dld2 about 10-times faster than D-lactate, which indicated that the oxidative half-reaction was rate limiting under steady-state conditions using DCPIP as electron acceptor. Finally, we could show that substrate-reduced Dld2 rapidly transfers electrons to yETF, suggesting that product binding to the reduced Dld2 suppresses reaction with oxygen but not with yETF. Thus, our study revealed that (i) Dld2 is in fact a more efficient D- α -hydroxyglutaric acid

dehydrogenase, (ii) electron transfer is controlled by product binding to reduced Dld2 and (iii) yETF is the natural electron acceptor of Dld2.

Results

Production, purification and biochemical characterization of yETF

Recombinant production of yETF in *Escherichia coli* and subsequent purification using Ni-NTA affinity chromatography yielded about 3-5 mg of pure heterodimeric protein (Figure 1A, lane 6) per g wet cell weight, which allowed its detailed biochemical characterization. Like other flavoproteins yETF exhibits a characteristic UV-visible absorption spectrum with maxima at 377 nm and 441 nm, which are slightly shifted upon denaturation (Figure 1B, *black* and *red* line, respectively). The maxima at 373 nm and 447 nm observed in the absorption spectrum of denatured yETF further indicate the presence of an FAD chromophore, which is also present in all other electron transferring flavoproteins studied so far (6, 17, 19–22).

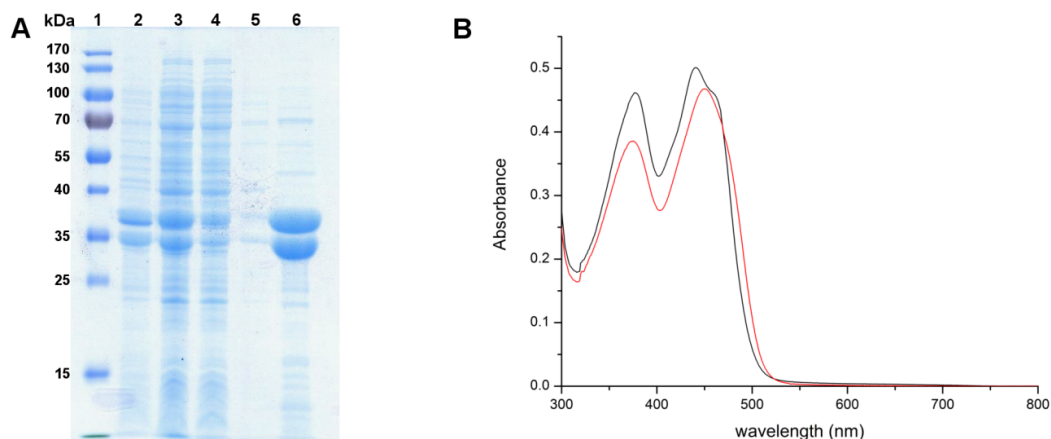


Figure 1: SDS-PAGE analysis of the different steps in yETF purification (A) and UV-visible absorption spectrum of native (*black* line) and denatured (*red* line) yETF (B). A, SDS-PAGE analysis of the different fractions collected during purification of yETF wild type using Ni-NTA affinity chromatography. In lane 1 PageRuler® prestained protein ladder (Thermo Fisher Scientific), in lane 2 the cell pellet after lysis, in lane 3 the cell lysate, in lane 4 the column flow through, in lane 5 the wash fraction and in lane 6 the elution fraction (α -subunit of yETF at 38 kDa; β -subunit at 37 kDa) is shown. B, UV-visible absorption spectra of yETF diluted to a final concentration of 40 μ M with 50 mM HEPES pH 7 + 1 mM DTT (*black* line) and denatured using 2 % SDS (*red* line) were recorded between 300 and 800 nm at 25 °C. Based on the extinction coefficient of free FAD (denatured, *red* line) at 450 nm ($11,300 \text{ M}^{-1} \text{ cm}^{-1}$), the extinction coefficient of yETF wild type at 450 nm ($11,600 \text{ M}^{-1} \text{ cm}^{-1}$) and 469 nm ($9,900 \text{ M}^{-1} \text{ cm}^{-1}$) could be determined.

Though all ETFs share the same cofactor, their electrochemical properties are tuned to the electron transfer pathway they service. Eukaryotic ETFs were found to efficiently stabilize the anionic flavin

semiquinone state and therefore mainly receive single electrons from their donor systems (20), while the protein-bound FAD cofactor in bacterial ETF from *Megasphaera elsdenii* was shown to undergo two-electron reduction when accepting electrons (7). To study the ability of yETF to stabilize the radical intermediate state, photoreduction and redox potential experiments were conducted. Upon illumination of oxidized yETF (Figure 2A, *black* line) under anoxic conditions, a short-lived anionic semiquinone (Figure 2A, *red* line) was observed, which could easily be further reduced to the hydroquinone form (Figure 2A, *blue* line). In the course of the reoxidation, no stable semiquinone intermediate was detected.

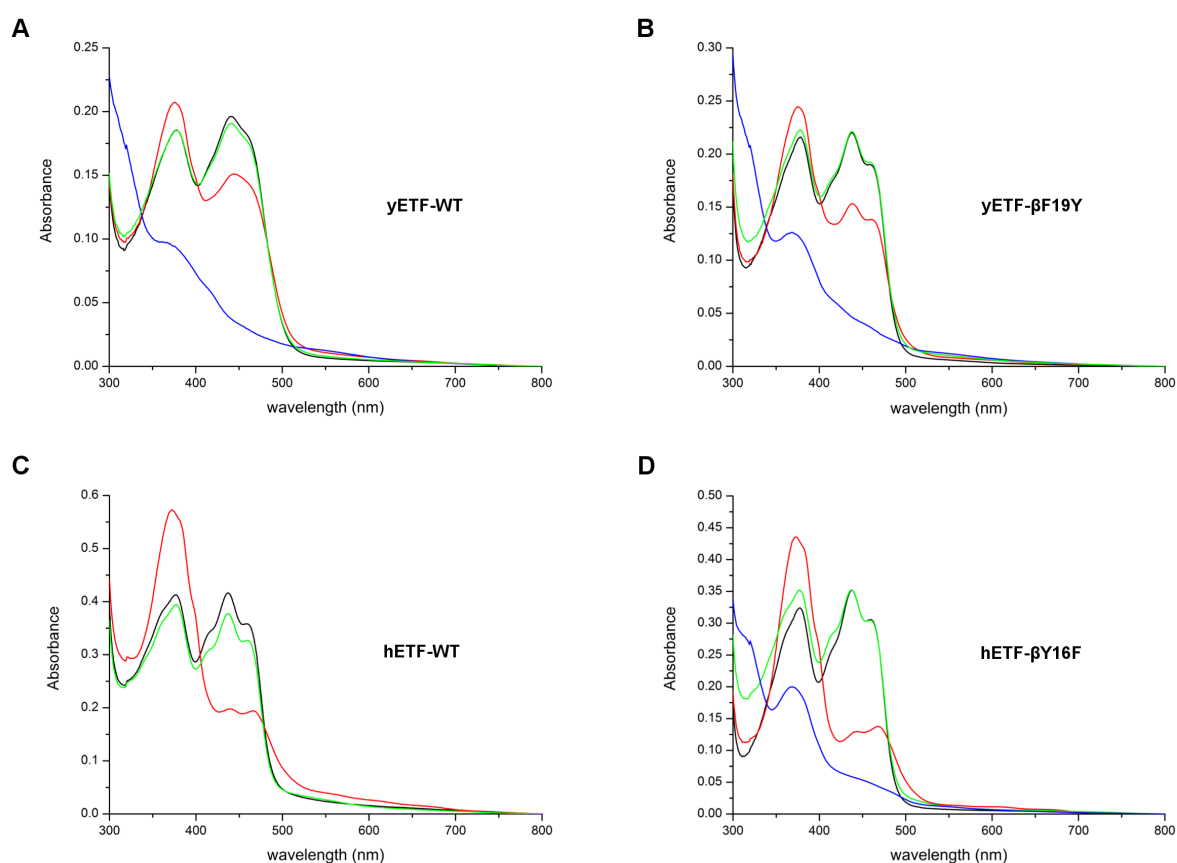


Figure 2: Photoreduction of yETF wild type (A) and yETF-βPhe19Tyr (B) as well as of hETF wild type (C) and hETF-βTyr16Phe (D) under anoxic conditions. UV-visible absorption spectra (300-800 nm) of yETF wild type and yETF-βPhe19Tyr as well as of hETF wild type and hETF-βTyr16Phe, diluted to a final concentration of 30 μM using 50 mM HEPES pH 7 containing 1 mM DTT, recorded during anaerobic photoreduction. The four spectra in each panel correspond to the different flavin redox states observed for yETF wild type (A), yETF-βPhe19Tyr (B), hETF wild type (C) and hETF-βTyr16Phe (D) in the course of the photoreduction: oxidized FAD (start spectrum, *black* line), anionic semiquinone (*red* line), reduced (*blue* line) and reoxidized FAD (*green* line).

When determining the redox potential of yETF, by applying the dye equilibration method (23), no stabilization of the flavin radical was observed, at all. The flavin chromophore and the reporting dye (indigo carmine; E° : -125 mV) were reduced almost synchronously (Figure 3), allowing the generation of a Nernst plot by plotting the $\log(yETF_{ox}/yETF_{red})$ as a function of the $\log(dye_{ox}/dye_{red})$. From the intercept a midpoint potential of -101 ± 2 mV (oxidized to reduced) was calculated, which is more negative compared to eukaryotic ETFs, *i.e.* around -20 mV (24, 25), but more positive than of the prokaryotic ETF from *Megasphaera (Peptostreptococcus) elsdenii* (-259 mV) (26). Therefore, yETF can be considered a better electron acceptor than the ETF from *Megasphaera elsdenii*, but a weaker electron acceptor than the eukaryotic homologs.

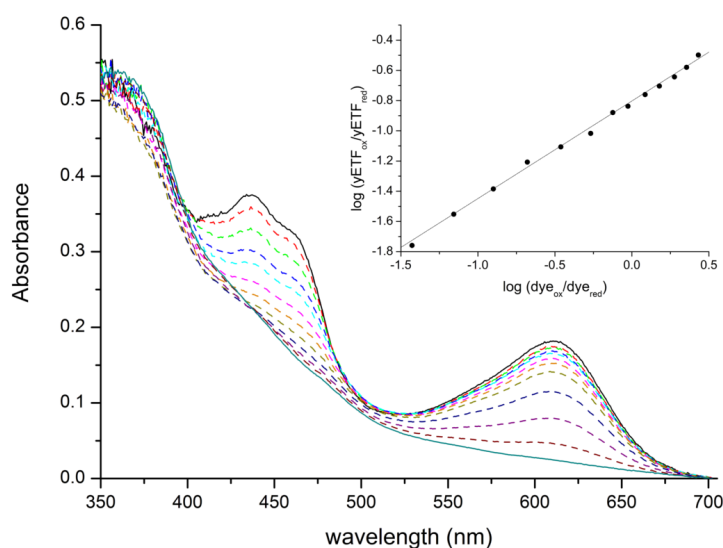


Figure 3: Determination of the redox potential of yETF wild type. Spectral changes of yETF ($\sim 25 \mu\text{M}$) and indigo carmine ($\sim 20 \mu\text{M}$; E° : -125 mV) observed in the course of the reduction reaction (2 h), indicating full reduction of the FAD cofactor and the dye and therefore a 2-electron transfer onto yETF. All measurements were carried out in 50 mM HEPES pH 7 + 1 mM DTT at a constant temperature of 25 °C. *Inset*, Nernst plot obtained from a single measurement by plotting the $\log(yETF_{ox}/yETF_{red})$ as a function of the $\log(dye_{ox}/dye_{red})$ - to determine the $\log(yETF_{ox}/yETF_{red})$ and the $\log(dye_{ox}/dye_{red})$ the relative absorption changes at 460 and 610 nm, respectively, were used. From the intercept a redox potential of -101 ± 2 mV was calculated (from four determinations).

Comparison of the yeast ETF to the human homolog

Based on the X-ray structure of hETF, we have built a homology model of yETF indicating conservation of the overall fold (Figure 4A) and composition of the amino acid residues forming the FAD-binding pocket (Figure 4B). The only obvious difference found in the active site of the model is the change of Tyr16 in hETF to Phe19 in yETF in the β -subunit (Figure 4B).

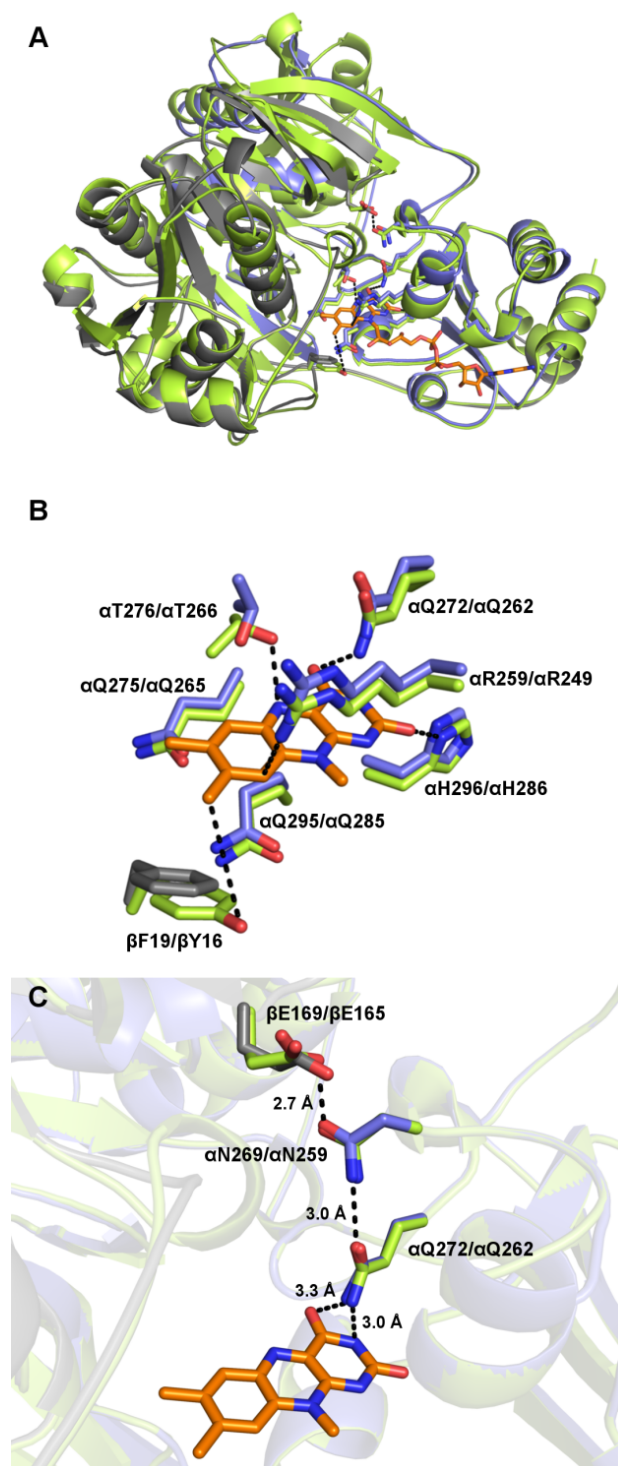


Figure 4: Structural comparison of yETF and hETF. **A**, Overall structure comparison of yETF (*blue*: α -subunit, *grey*: β -subunit; model based on hETF) and hETF (*green*; PDB: 1efv). **B**, Comparison of the active site residues of yETF (*blue*: α -subunit, *grey*: β -subunit) and hETF (*green*). The FAD cofactor (*orange*) and the important amino acid residues are shown as sticks (*blue* and *grey*: yETF; *green*: hETF) and are labeled as follows: yETF/hETF. **C**, Close-up view of the well-studied salt-bridge formed between β Glu169 and α Asn269, which was shown to determine the dynamics of hETF (β Glu165 and α Asn259, respectively). The third residue displayed as sticks is α Gln272, which is in H-bonding distance to both α Asn269 and the N3-C4=O locus of the flavin cofactor.

Recently, we have shown that the FAD cofactor of hETF is oxidized at the 8 α -position to yield 8-formyl FAD upon incubation under slightly alkaline conditions (16). Interestingly, this reaction is promoted by β Tyr16 in hETF (16, 27, 28) and thus we hypothesized that yETF may be resistant toward oxidation of the FAD cofactor. To test our hypothesis, we transferred purified yETF to 50 mM HEPES pH 8.5 containing 1 mM DTT and incubated the sample at 25 °C for 24 h. After denaturation of the protein, the free cofactor was analyzed on HPLC-DAD, which indeed revealed no 8-formyl modification of the flavin cofactor. Instead, a mix of other flavin derivatives, which could not be identified due to their low abundance and insufficient purity, was found (Table 1).

Table 1: Cofactor modification in yETF wild type and variants after 24 h of incubation at pH 8.5: yETF wild type and the variants were diluted to a final concentration of ~50 μ M using 50 mM HEPES pH 8.5 + 1 mM DTT and incubated at 25°C for 24 h. After denaturation of the proteins their cofactor was analyzed with HPLC-DAD. Total cofactor modification (%) refers to the amount of flavin cofactor altered upon incubation under alkaline conditions (column 2). Columns 3 and 4 provide a more detailed analysis of the obtained results - the fraction of flavin species that could be clearly identified as 8-formyl FAD (based on retention time and flavin spectrum) is given in column three, whereas the amount of unknown flavin species is summarized in column 4.

protein	total cofactor modification [%]	8f-FAD [%]	unknown modification [%]
WT	12	0	12
β F19Y	13	0	13
α N269A	26	26	0
β F19Y- α N269A	42	31	11
β E169A	36	0	0
β F19Y- β E169A	n.d.*	yes*	n.d.*

* as this variant is very unstable, cofactor modification cannot be assessed/quantified reliably

In order to determine whether the tyrosine to phenylalanine replacement in yETF renders the 8 α -methyl group stable toward oxidation, we generated the hETF-like variant yETF- β Phe19Tyr. In the modification assay, however, this variant behaved rather similarly compared with wild-type yETF by exhibiting an equal amount of overall flavin modification and not being able to form 8f-FAD (Table 1). This finding, of course, raised the question which other factors are important for the oxidation reaction at this position. Since the cleavage of the salt bridge (between α Asn259 and β Glu165), which was shown to strongly influence the flexibility of the human protein (18), resulted in a much higher degree of formylation (16), we also generated two single variants (α Asn269Ala and β Glu169Ala) and two double variants (β Phe19Tyr- α Asn269Ala and β Phe19Tyr- β Glu169Ala) targeting this interaction (Figure 4C). Although these variants exhibited a slightly higher degree of overall cofactor modification (Table 1), neither one of the variants showed 8 α -oxidation comparable with hETF.

Similarly, also the spectral properties remained almost unaffected by the amino acid replacements. Photoreduction of the single and the double variants, like for the wild type protein first yielded a short lived anionic semiquinone, which was further reduced to the flavin hydroquinone (Figure 2B). This finding is in contrast to the homologous human proteins (wild type, α Asn259Ala and β Glu165Ala variant), which strongly stabilize the flavin semiquinone and, therefore, do not allow full reduction of their FAD cofactor in the photoreduction experiment (Figure 2C and (16)).

Biochemical characterization of Dld2

To obtain satisfactory amounts of full length Dld2 from *Saccharomyces cerevisiae*, recombinant expression was carried out in *Komagataella phaffii*. Despite the presence of an α -factor (secretion signal), the protein was not secreted to the culture medium, which required its purification from the cell pellet and yielded about 2-3 mg of pure enzyme per kg of wet cell weight. In its pure form, Dld2 exhibits absorption maxima at 383 nm and 454 nm, which are shifted to 375 and 450 nm, respectively, when the protein is denatured using 2% SDS, confirming the presence of an FAD cofactor (Figure 5A).

To obtain information about the electrochemical properties of Dld2, we performed a photoreduction and determined the redox potential of the enzyme. Photochemical reduction of Dld2 required the use of high amounts of the redox mediators 5-deaza FMN (2.5 μ M) and methylviologen (6 μ M) and yielded fully reduced enzyme after about half an hour of irradiation. Neither in the course of the reduction, nor upon reoxidation was a flavin radical observed (Figure 5B), however, we found that under aerobic conditions Dld2 was reoxidized within a few seconds, which is in contrast to what one would expect from a dehydrogenase.

Like for yETF, the redox potential of Dld2 was determined by applying the xanthine/xanthine oxidase method first reported by Massey (23). The redox dye phenosafranine (E° : -252 mV) and the enzyme were reduced almost synchronously without the appearance of any radical intermediate species, indicating a two electron transfer onto Dld2 and the dye (Figure 5C). This finding is in line with the photoreduction experiment and the slope near unity obtained when plotting the log of the relative absorption changes of Dld2 (450 nm) as a function of the log of the relative absorption changes of phenosafranine (520 nm). From the intercept a redox potential of -246 ± 2 mV was calculated, which is clearly much more negative than that of yETF (midpoint potential: -101 mV) and thus in line with electron transfer from Dld2 to yETF.

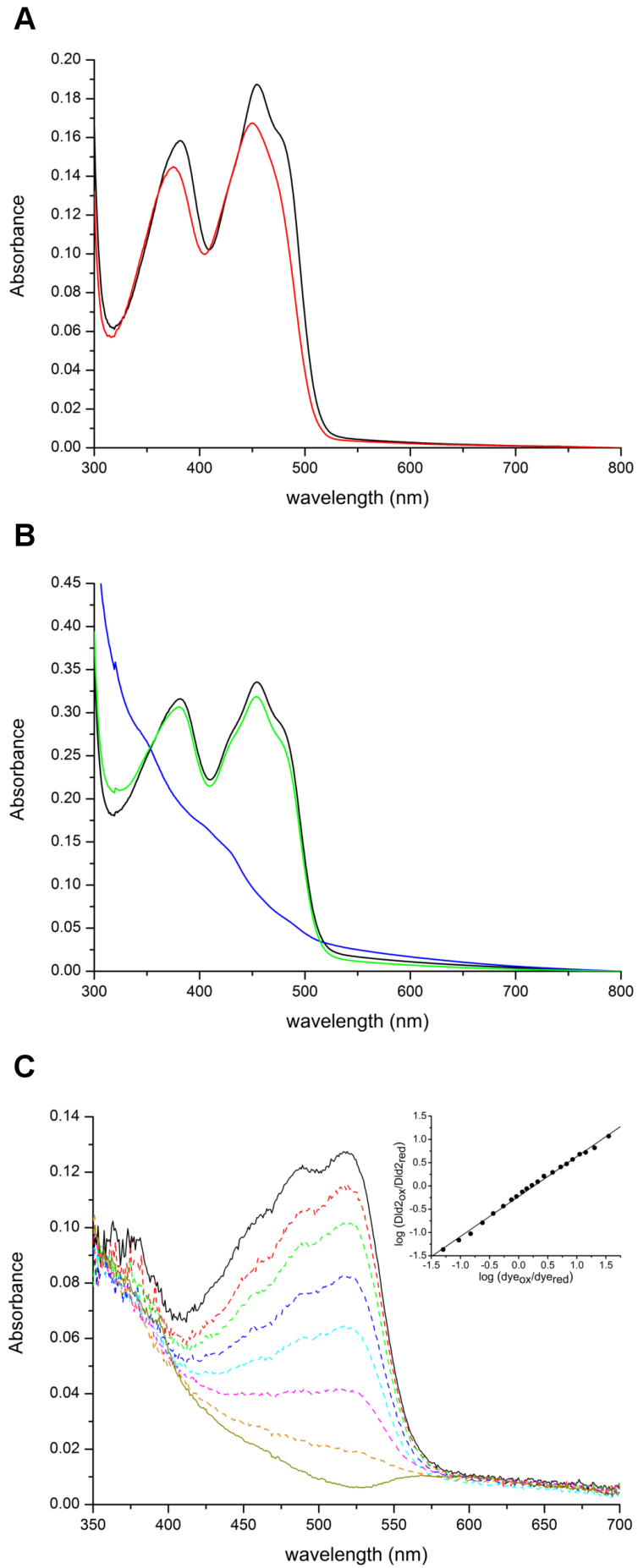


Figure 5: UV-visible absorption spectrum (A), photoreduction (B) and determination of the redox potential (C) of Dld2. **A**, UV-visible absorption spectra of Dld2 diluted to a final concentration of 10 μM with 50 mM HEPES, 150 mM NaCl pH 7 (*black* line) and denatured using 2 % SDS (*red* line) were recorded between 300 and 800 nm at 25 °C. Based on the extinction coefficient of free FAD (denatured, *red* line) at 450 nm ($11,300 \text{ M}^{-1} \text{ cm}^{-1}$), the extinction coefficient of Dld2 at 450 nm ($12,700 \text{ M}^{-1} \text{ cm}^{-1}$) could be determined. **B**, UV-visible absorption spectra (300-800 nm) of oxidized (*black* line), fully reduced (*blue* line) and reoxidized (*green* line) Dld2 (diluted to a final concentration of 30 μM using 50 mM HEPES, 150 mM NaCl pH 7) recorded during anaerobic photoreduction. **C**, Time dependent spectral changes of Dld2 ($\sim 10 \mu\text{M}$) and phenosafranine ($\sim 10 \mu\text{M}$; E° : -252 mV) observed in the course of the reduction reaction (25 min), indicating full reduction of the FAD cofactor and the dye and therefore a 2-electron transfer onto Dld2. All measurements were carried out in 50 mM HEPES, 150 mM NaCl pH 7 at a constant temperature of 25 °C. **Inset**, Nernst plot obtained from a single measurement by plotting the $\log(\text{Dld2}_{\text{ox}}/\text{Dld2}_{\text{red}})$ as a function of the $\log(\text{dye}_{\text{ox}}/\text{dye}_{\text{red}})$ - to determine the $\log(\text{Dld2}_{\text{ox}}/\text{Dld2}_{\text{red}})$ and the $\log(\text{dye}_{\text{ox}}/\text{dye}_{\text{red}})$ the relative absorption changes at 450 and 520 nm, respectively, were used. From the intercept a redox potential of $-246 \pm 2 \text{ mV}$ was calculated (from seven determinations).

Kinetic properties of Dld2 and electron transfer to yETF

To learn more about the kinetic properties of full length Dld2 from *S. cerevisiae*, we conducted pre steady-state experiments in a stopped-flow apparatus. By studying the rate of flavin reduction in the presence of different substrate concentrations (50-1500 μM D- α -hydroxyglutarate; 1 to 100 mM D-lactate), observed rates were measured and plotted as a function of substrate concentration. Using a hyperbolic fit, limiting rate constants (k_{red}) and dissociation constants (K_D) for both substrates were determined (Figure 6A and B, Table 2).

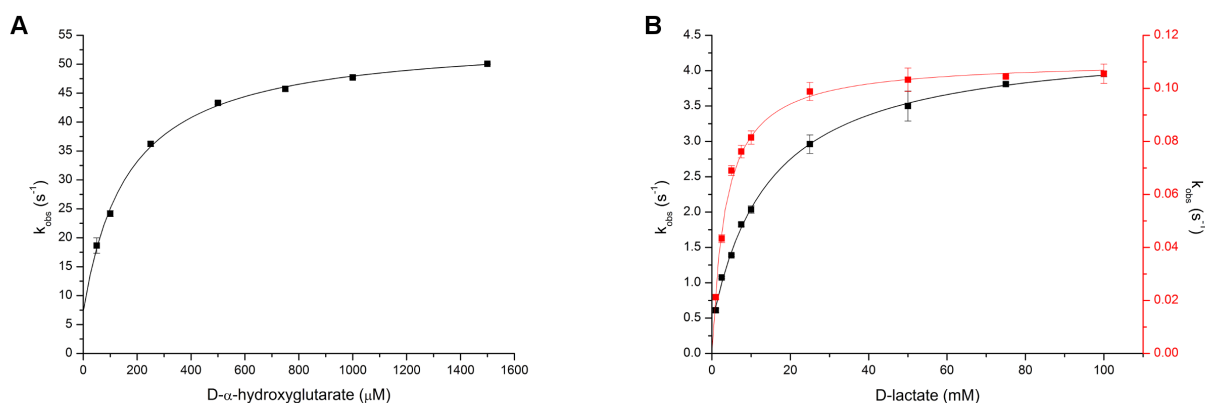


Figure 6: Rapid reaction kinetics of Dld2 using D- α -hydroxyglutarate (A) and D-lactate (B) as substrate.

The reductive half reaction of Dld2 was studied by mixing Dld2 ($\sim 10 \mu\text{M}$ final concentration) with varying concentrations of D- α -hydroxyglutarate (final concentrations: 50 to 1,500 μM) and D-lactate (final concentrations: 1 - 100 mM) in 50 mM HEPES, 150 mM NaCl pH 7 at 25 °C. The observed rate constants (k_{obs}) were plotted as a function of the substrate concentration to give a hyperbolic curve that allowed the determination of the reductive rate (k_{red}) and the dissociation constant (K_D) of Dld2 with D- α -hydroxyglutarate ($K_D = 170 \pm 20 \mu\text{M}$, $k_{red} = 47 \pm 1 \text{ s}^{-1}$, observed rate constants at each substrate concentration were determined in triplicate; standard deviations are indicated by error bars) and D-lactate ($K_D = 15 \pm 1 \text{ mM}$, $k_{red} = 4.1 \pm 0.1 \text{ s}^{-1}$, observed rate constants at each substrate concentration were determined in triplicate), respectively. In the course of the reduction of Dld2 with D-lactate a second slower phase was observed, which was analyzed in the same way to yield a $K_D = 3.5 \pm 0.2 \text{ mM}$ and a $k_{red} = 0.11 \pm 0.00 \text{ s}^{-1}$ (panel B, red line).

Table 2: Kinetic parameters of Dld2 determined with D- α -hydroxyglutarate and D-lactate under pre steady-state and steady state conditions. In the course of the pre steady-state experiment 10 μM Dld2 (in reaction) were mixed with varying concentrations of D- α -hydroxyglutarate (final concentrations: 50 – 1,500 μM) and D-lactate (final concentrations: 1 -100 mM) in 50 mM HEPES, 150 mM NaCl pH 7 and spectral changes were monitored for 1.5-150 s. From the absorbance changes at 450 nm observed rate constants were extracted and plotted as function of the corresponding substrate concentrations to obtain reductive rates (k_{red}) as well as dissociation constants (K_D) for the interaction of Dld2 with both substrates.

Kinetic characterization of Dld2 under steady-state conditions was performed using DCPIP as final electron acceptor. Dld2 (100 nM), DCPIP (125 μM) and varying final concentrations of D- α -hydroxyglutarate (25 μM to 1,000 μM) or D-lactate (1 mM to 250 mM) were mixed in 50 mM HEPES, 150 mM NaCl pH 7 and absorbance changes at 600 nm were recorded for 120 s. By plotting the initial rates as function of the substrate concentrations, additionally k_{catapp} and K_{Mapp} values for the interaction of Dld2 with both accepted substrates were obtained.

kinetic parameters	D- α -hydroxyglutarate	D-lactate
$k_{red} [\text{s}^{-1}]$	47 ± 1	4.1 ± 0.1
$k_{-1} [\text{s}^{-1}]$	7.3 ± 1.7	0.4 ± 0.1
$K_D [\text{mM}]$	0.17 ± 0.02	15 ± 1
$k_{catapp} [\text{s}^{-1}]$	0.42 ± 0.02	1.2 ± 0.1
$K_{Mapp} [\text{mM}]$	0.35 ± 0.05	110 ± 10
$k_{catapp}/K_{Mapp} [\text{M}^{-1} \text{ s}^{-1}]$	$1,200 \pm 300$	11 ± 2

The rate of reduction was $47 \pm 1 \text{ s}^{-1}$ and $4.1 \pm 0.1 \text{ s}^{-1}$ for D- α -hydroxyglutarate and D-lactate with dissociation constants of $0.17 \pm 0.02 \text{ mM}$ and $15 \pm 1 \text{ mM}$, respectively. Thus, D- α -hydroxyglutarate is oxidized more efficiently by the enzyme than D-lactate. The graphs in Figure 6A and B also indicate reversibility of the electron transfer reaction because the hyperbolic fit to the data yielded y-axis

intercepts of $k_{-1} = 7.3 \pm 1.7 \text{ s}^{-1}$ and $0.4 \pm 0.1 \text{ s}^{-1}$ ($\sim 6\%$ of k_{red}) for D- α -hydroxyglutarate ($\sim 10\%$ of k_{red}) and D-lactate, respectively.

Interestingly, detailed analysis of the reduction reaction further revealed that flavin reduction proceeded in two distinct phases (Figure 6B and Figure 7A and B).

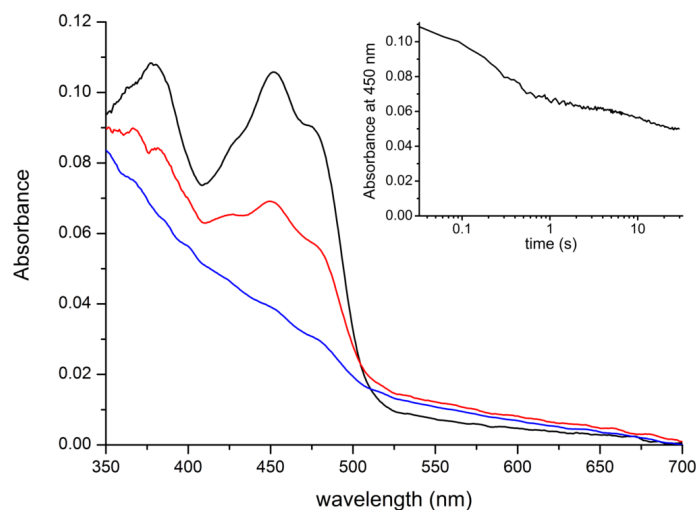


Figure 7: Spectral changes monitored in the course of the rapid reaction kinetics of Dld2 with D-lactate.

A, Spectral changes recorded within 3 s, when mixing Dld2 (final concentration: 10 μM) with D-lactate (final concentration: 100 mM) in 50 mM HEPES, 150 mM NaCl pH7. In a first, fast phase, oxidized Dld2 (*black* line) is partially reduced to yield the spectrum shown in *red*, before undergoing full reduction (*blue* line) in a second much slower phase. **Inset**, Two distinct phases of flavin reduction observed in the course of the rapid reaction kinetics experiment involving Dld2 (final concentration: 10 μM) and D-lactate (final concentration: 100 mM). Absorbance changes at 450 nm were plotted as a function of time (logarithmic time scale) to determine the rate of flavin reduction in both phases.

In the case of D- α -hydroxyglutarate the second phase was about 200-times slower than the first and thus exact quantification of the rate was not possible. In the case of D-lactate, the second phase was determined to $0.11 \pm 0.00 \text{ s}^{-1}$ and exhibited a dissociation constant of $3.5 \pm 0.2 \text{ mM}$. Next, we determined kinetic parameters for steady-state conditions using DCPIP as an artificial electron acceptor under aerobic conditions. The turnover rates with D- α -hydroxyglutarate and D-lactate were $0.42 \pm 0.02 \text{ s}^{-1}$ and $1.2 \pm 0.1 \text{ s}^{-1}$, respectively. However, the observed K_{Mapp} was much lower for D- α -hydroxyglutarate ($350 \pm 50 \mu\text{M}$) than for D-lactate ($110 \pm 10 \text{ mM}$) resulting in a higher catalytic efficiency for D- α -hydroxyglutarate ($1,200 \pm 300 \text{ M}^{-1} \text{ s}^{-1}$ vs $11 \pm 2 \text{ M}^{-1} \text{ s}^{-1}$). A summary of kinetic parameters is provided in Table 2. The large difference between the rate of reduction and the turnover rate suggested that the oxidative rate is rate limiting, which prompted us to analyze the rate of reoxidation of photoreduced and substrate-reduced Dld2 using molecular oxygen as electron acceptor. Interestingly, photoreduced Dld2 was reoxidized about 5000-times faster than the enzyme reduced with D- α -hydroxyglutarate ($k_{ox} = 3.3 \cdot 10^4 \pm 0.2 \cdot 10^4 \text{ M}^{-1} \text{ s}^{-1}$ vs $7 \pm 1 \text{ M}^{-1} \text{ s}^{-1}$). This result suggested

that the reaction product (*i.e.* α -ketoglutarate or pyruvate) tightly binds to the enzyme, thereby inhibiting the reoxidation by molecular oxygen. The addition of α -ketoglutarate (or pyruvate) to photoreduced Dld2, either before or after the photoreduction, however, had no effect on the rate of reoxidation. Equally, titration of α -ketoglutarate (or pyruvate) to oxidized Dld2 did not produce any changes in the UV-visible absorption spectrum of the FAD-cofactor, suggesting that the products only bind to the enzyme when generated in the course of the oxidation reaction. This interesting behavior prompted us to investigate the reoxidation of reduced Dld2 using its putative natural electron acceptor yETF. First, we incubated yETF (10 μ M) with catalytic amounts of Dld2 (10 nM) and an excess of D- α -hydroxyglutarate (1 mM) and monitored the reduction of yETF by UV-visible absorption spectrometry. As shown in Figure 8A, yETF was reduced directly from the oxidized state to the fully reduced (hydroquinone) state within 4 minutes, which is in agreement with earlier experiments that have demonstrated the preferential two-electron reduction of yETF.

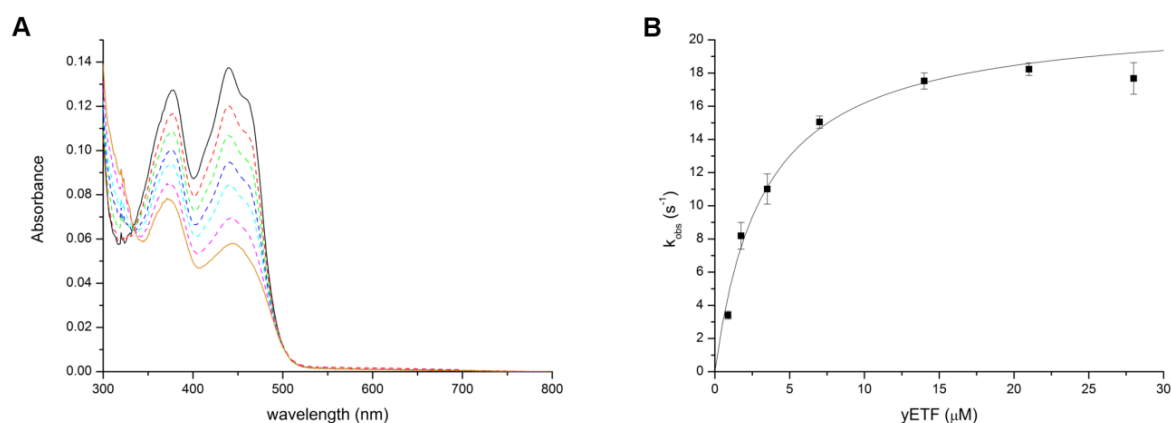


Figure 8: Electron transfer from Dld2 onto yETF. **A**, yETF was diluted to a final concentration of 10 μ M using 50 mM HEPES pH 7 + 1 mM DTT (*black* spectrum) and mixed with 1 mM D- α -hydroxyglutarate and 10 nM Dld2 at 25 $^{\circ}$ C. Then, time-dependent spectral changes were monitored until no further changes were observed. The *black* spectrum corresponds to fully oxidized yETF, while the *orange* line represents the final spectrum recorded after 4 min. All other spectra recorded in the course of the reaction are shown using *dashed* lines. **B**, Steady state turnover assays involving 1 mM D- α -hydroxyglutarate, 10 nM Dld2, yETF (0.875 to 28 μ M) and 125 μ M DCPIP as final electron acceptor were carried out in 50 mM HEPES pH 7 containing 1 mM DTT at 25 $^{\circ}$ C. Initial rates (normalized to enzyme concentration) were extracted from the absorbance changes recorded at 600 nm and plotted as a function of the yETF concentration. By applying a hyperbolic fit, the kinetic parameters K_{Mapp} and k_{catapp} were determined ($K_{Mapp} = 3.3 \pm 0.4 \mu$ M, $k_{catapp} = 21 \pm 1 \text{ s}^{-1}$; initial rates at each yETF concentration were determined in triplicate; standard deviations are indicated by error bars).

For a more detailed kinetic characterization, steady state measurements using DCPIP as final electron acceptor were performed (Figure 8B, Table 3) yielding an apparent k_{catapp} of $21 \pm 1 \text{ s}^{-1}$ and K_{Mapp} of $3.3 \pm 0.4 \mu$ M, which confirm an efficient electron transfer from Dld2 to yETF (catalytic efficiency:

$6 \cdot 10^6 \pm 1 \cdot 10^6 \text{ M}^{-1} \text{ s}^{-1}$). Thus, electron transfer to the cognate electron acceptor, yETF, is several orders of magnitude faster than the reoxidation by either oxygen or DCPIP.

Table 3: Kinetic parameters determined for the electron transfer from Dld2 onto yETF under steady-state conditions.

The steady-state parameters for the electron transfer were determined in a coupled assay involving 1mM D- α -hydroxyglutarate, 10 nM Dld2, 125 μM DCPIP and varying concentrations of yETF in 50 mM HEPES pH 7 containing 1mM DTT (when using D-lactate as substrate for Dld2 its reduction became rate limiting). By monitoring the decolorization of DCPIP at 600 nm for 120 s initial rates could be obtained and plotted as function of the yETF concentrations to yield the kinetic parameters k_{catapp} and K_{Mapp} .

kinetic parameters	D- α -hydroxyglutarate	D-lactate
$k_{catapp} [\text{s}^{-1}]$	21 ± 1	0.8 ± 0.4
$K_{Mapp} [\mu\text{M}]$	3.2 ± 0.4	rate ETF-concentration independent

Discussion

Biochemical characterization of yETF

Successful production of recombinant yETF and full length Dld2 from *S. cerevisiae* in *E. coli* and *K. phaffii*, respectively, enabled us to study their biochemical properties and the presumed electron transfer from Dld2 to yETF. Despite the extensive sequence similarity in the FAD binding pocket, we found that the properties of yETF diverge significantly from the human ortholog. The most salient differences concern the reduction behavior of yETF as evidenced by the absence of the anionic flavin semiquinone and the much more negative redox potential (-101 mV and -20 mV for yETF and hETF, respectively). Thus far, all ETFs characterized showed the preferential one-electron reduction of FAD to yield the anionic semiquinone including mammalian and bacterial proteins (7, 16, 29, 30). In fact, the formation of the anionic semiquinone is thought to be critical for electron transfer from client dehydrogenases (31). Because of the obvious difference in the single active site residue provided by the β -chain (βTyr16 in hETF and βPhe19 in yETF), we hypothesized that this amino acid exchange in yETF may be responsible for the distinct reduction behavior. In order to investigate this possibility, we generated the $\beta\text{Tyr16Phe}$ and $\beta\text{Phe19Tyr}$ variant for hETF and yETF, respectively. While the replacement of βTyr16 by Phe in hETF strongly affected the stabilization of the anionic semiquinone, enabling full reduction of the protein in the course of the photoreduction experiment, the $\beta\text{Phe19Tyr}$ variant of yETF did not behave like hETF (Figure 2, panels A-D). Similarly, we have recently reported that replacement of βTyr16 by Phe impedes the oxidation of the 8 α -methyl to the 8-formyl-group and, therefore, we have also tested the propensity of wild-type yETF and the $\beta\text{Phe19Tyr}$ variant

to form 8-formyl-FAD. Surprisingly, we have found that neither the wild-type yETF nor the β Phe19Tyr variant formed 8-formyl-FAD. Even the introduction of further amino acid replacements (*i.e.* in the variants β Phe19Tyr- α Asn269Ala and β Phe19Tyr- β Glu169Ala) that significantly enhanced the rate of oxidation at the 8α -methyl group in hETF wild-type (16) did not result in increased formation of the 8-formyl group. Thus, it appears that the redox properties of the FAD cofactor as well as the reactivity of the 8α -methyl group is not simply governed by amino acid residues in the direct vicinity of the isoalloxazine ring but also by other factors such as amino acids in the second shell and the overall dynamics of the protein, which for example may influence the accessibility of the FAD cofactor. This view is in accordance with observations by Salazar *et al.* (1997), who reported that the redox properties of ETFs are not solely affected by the amino acids found in the vicinity of the flavin moiety (17).

Kinetic characterization of Dld2

Recently, the determination of steady-state kinetic parameters by Becker-Kettern *et al.* revealed very slow turnover numbers for the oxidation of D-lactate (1.3 s^{-1}) and D- α -hydroxyglutarate (0.18 s^{-1}) using N-terminally truncated Dld2 (15). Thus, we decided to reinvestigate the steady-state kinetics of Dld2 using full-length Dld2 recombinantly produced in *K. phaffii* (see Experimental Procedures). However, we virtually obtained very similar values for k_{catapp} for D-lactate and D- α -hydroxyglutarate of 1.2 and 0.42 s^{-1} , respectively, suggesting that the truncation at the N-terminus does not compromise the catalytic properties of the enzyme. In order to identify the rate-limiting step during turnover, we then investigated pre steady-state kinetics using stopped-flow absorption spectrophotometry. This clearly showed that the reductive half reaction with D-lactate and D- α -hydroxyglutarate proceeds at a limiting rate of $4.1 \pm 0.1 \text{ s}^{-1}$ and $47 \pm 1 \text{ s}^{-1}$, respectively (Table 2). In the case of D- α -hydroxyglutarate, the reductive rate is thus three orders of magnitude faster than the observed turnover. This result indicated that the oxidative half reaction is rate limiting. Surprisingly, when photoreduced Dld2 was reacted with dioxygen, we also found a rapid rate of reoxidation of $3.3 \cdot 10^4 \pm 0.2 \cdot 10^4 \text{ M}^{-1} \text{ s}^{-1}$. However, substrate-reduced Dld2 reacted much slower with dioxygen. In the case of D- α -hydroxyglutarate, the rate of reoxidation was only $7 \text{ M}^{-1} \text{ s}^{-1}$, *i.e.* 5,000-times slower as observed for the photoreduced enzyme. This suggested that the reaction product, pyruvate or α -ketoglutarate, forms a complex with the reduced enzyme and thereby impedes re-oxidation by dioxygen. Interestingly, addition of either pyruvate or α -ketoglutarate to photoreduced enzyme exhibited no effect on the rate of re-oxidation with dioxygen. Thus, we conclude that during the oxidation of the substrate the formed product stabilizes a conformation of the enzyme in which access to the reduced FAD is denied. A similar behavior has been observed for other client enzymes of electron transferring flavoproteins. In the case of acyl-CoA dehydrogenases, reduced either by dithionite or by light irradiation, a very fast reoxidation was observed. If, however, the reaction product or a substrate/product mimic is bound to

the protein, oxygen reactivity was reduced by a factor of 3,000-4,000 (32–34). Wang *et al.* hypothesized that this effect is caused by the tight binding of enoyl-CoA (and derivatives), which results in a significantly more hydrophobic active site and, therefore, prohibits the stabilization of superoxide radical species required for flavin reoxidation (33). Since α -ketoglutarate and pyruvate are far less hydrophobic, it is difficult to imagine that oxygen reactivity is controlled by the same mechanism. Therefore, we suggest that product binding to Dld2 reduces the accessibility for oxygen to the active site and thereby impedes the reaction with the reduced FAD cofactor.

The occurrence of a product-reduced enzyme complex is also supported by an increase in the long-wavelength absorption (~510-625 nm) during the reductive half-reaction (Figure 7), indicating the formation of a charge-transfer complex between α -ketoglutarate or pyruvate and reduced Dld2. In keeping with this interpretation, we also observed that the long wavelength absorption disappeared during re-oxidation of substrate-reduced Dld2 with dioxygen. The formation of the charge-transfer complex is apparently connected to the fast phase of reduction, which was also previously observed for acyl-CoA dehydrogenases. It was postulated for the latter enzymes that formation of a charge transfer complex is indicative of tight product binding, which is used to shift the reaction equilibrium toward enoyl-CoA formation (34, 35). Tight binding of the enoyl-CoA product was argued to be necessary because the acyl-CoA substrates have a very similar or even more positive redox potential than the FAD cofactor bound to the acyl-CoA dehydrogenases, making acyl-CoA oxidation rather unfavorable (35). Because the redox potential of the D-lactate/pyruvate couple (-190 mV) is more positive than the midpoint potential of Dld2, it is plausible that charge-transfer formation and tight product binding play a similar role in the yeast enzyme. In addition, the rather high k_{-1} -rates observed in the rapid reaction kinetics are in line with this hypothesis.

The slow re-oxidation of substrate-reduced Dld2 by oxygen and DCPIP prompted us to investigate re-oxidation using the cognate electron acceptor, yETF. Initial experiments clearly demonstrated that yETF is rapidly reduced by catalytic amounts of Dld2 utilizing D- α -hydroxyglutarate as the substrate (Figure 8A). Further steady-state experiments established that the rate of electron transfer increased hyperbolically with the concentration of yETF, reaching a limiting value of 21 s⁻¹ and thus approaching the rate of reduction of Dld2 with D- α -hydroxyglutarate. In other words, electron transfer from the product-reduced enzyme complex to yETF is fast in contrast to reoxidation with oxygen or DCPIP and, therefore, product binding suppresses the undesired transfer of electrons to oxygen. The exact mechanism by which yETF obtains the electrons from the reduced enzyme are not clear yet but two scenarios are possible: (i) binding of yETF to the product-reduced enzyme complex leads to the rapid release of the product and subsequently to electron transfer to yETF or (ii) binding of yETF directly leads to electron transfer and to product dissociation from the re-oxidized enzyme. As Dld2 very much behaves like acyl-CoA dehydrogenases, it is tempting to speculate that also the mechanism of electron transfer to ETF is similar. In acyl-CoA dehydrogenases the rapid reoxidation of the enzyme by hETF (32) was assumed to be promoted by a lower pK_a-value of the reduced FAD cofactor in the

product complex (36–38). In addition, tight product binding, as discussed above, shifts the equilibrium toward the reduced FAD cofactor and therefore electron transfer to ETF is more likely to occur prior to product release (36–38). Since Dld2 and the acyl-CoA dehydrogenases are structurally very distinct, *p*-cresol methylhydroxylase- (PCMH-) fold vs acyl-CoA dehydrogenase fold, and the chemical properties of their respective reaction products are rather different, further studies will be required to clearly resolve the exact mechanism of electron transfer from substrate-reduced Dld2 to yETF.

Two-electron transfer from Dld2 to yETF

It should also be noted that reduction of yETF by Dld2 apparently involves the transfer of two electrons (Figure 8A), which is in agreement with the large difference in redox potential of the two proteins ($E^\circ = -101$ and -246 mV for yETF and Dld2, respectively). This finding is in line with our observations that yETF only weakly stabilizes the anionic semiquinone during photoreduction, and the reduction of Dld2, either by light irradiation or substrate, directly leads to the hydroquinone without the occurrence of a stable flavin semiquinone. This observation was rather surprising because all eukaryotic ETFs investigated so far were reported to operate through single electron transfer from the client dehydrogenase to the ETF (3, 7, 32, 39, 40). Furthermore, it was demonstrated that disproportionation of the flavin semiquinone to the oxidized and hydroquinone state occurs upon interaction with ETF-QO, which is required for successful electron transfer (17, 39). Presently, the mechanism of electron transfer between yETF and its *in vivo* electron acceptor, Cir2p, is unknown. Previous studies involving various ETFs and their corresponding electron acceptors have indicated that electron transfer requires the transfer of single electrons and therefore relies on the stabilization of the flavin semiquinone (41–43). Owing to the electrochemical properties of yETF, it is thus conceivable that the mechanism of electron transfer to Cir2p is also different compared to the previously investigated electron transfer systems in eukaryotic cells.

Experimental procedures

Materials

All chemicals and media ingredients were purchased from Sigma-Aldrich (St. Louis, MO, USA), Roth (Karlsruhe, Germany), Merck (Darmstadt, Germany), Fluka (Buchs, Switzerland) or Becton, Dickinson and Company (Franklin, Lakes, NJ, USA) and were of the highest grade commercially available.

All restriction enzymes used were ordered from Thermo Scientific/Fermentas (St. Leon-Rot, Germany) or New England Biolabs (Ipswich, MA, USA) and Ni-sepharose column material was obtained from GE Healthcare (Chalfont St. Giles, UK).

Cloning and recombinant production of yETF (E. coli)

To produce yETF in *Escherichia coli* the respective gene was purchased from Thermo Scientific, codon optimized for the *E. coli* organism. The received gene was subcloned to the *E. coli* pJET vector and then, digested with *NcoI* and *NotI* to produce sticky ends on the DNA string. For gene expression the *yETF* gene subsequently was inserted into the vector pETM11-His TEV Appa, which added nucleotides coding for an N-terminal hexahistidine tag to the gene sequence. Proper insertion of the gene was confirmed by sequencing, before transforming the recombinant plasmid with *E. coli* Rosetta (DE3)-pLysS cells for gene expression.

For expression, LB medium containing 50 µg/mL kanamycin as well as 20 µg/mL chloramphenicol for selection was inoculated with an overnight culture to an optical density at 600 nm (OD₆₀₀) of approximately 0.1. Then, cultures were left to grow to an OD₆₀₀ of about 0.7 at 37°C and 140 rpm, before adding 100 µM IPTG to induce gene expression. To maximize the protein yield, the cultures were incubated at 20 °C and 140 rpm overnight.

Harvested cells were resuspended and lysed in binding buffer (50 mM HEPES, 15 mM imidazole, pH 7 + 1 mM DTT) by sonication with a Labsonic L sonication probe (B. Braun Biotech, Berlin, Germany) for 2 x 5 min. After centrifugation at 38,500 g for 1 h (4 °C), the cleared cell lysate was loaded onto a Ni-NTA column equilibrated with binding buffer. After removing unspecifically bound protein with wash buffer (50 mM HEPES, 15 mM imidazole, pH 7 containing 1 mM DTT), yETF was eluted with elution buffer (50 mM HEPES, 500 mM imidazole, pH 7 containing 1 mM DTT). To confirm the presence of the desired protein in the fractions as well as to determine the quality of the purification SDS-PAGE analysis was used. Fractions containing yETF were pooled and dialyzed against 50 mM HEPES pH 7 + 1mM DTT for three hours. Then, the protein was concentrated to approximately 100 µM using Centripreps® 30 kDa MWCO (Merck Millipore, Burlington, MA, USA), flash frozen with liquid nitrogen and stored at -80 °C until further use.

Cloning and recombinant production of Dld2 (K. phaffii)

For recombinant expression of Dld2 in *Komagataella phaffii*, the respective gene was purchased from Thermo Scientific. On ordering, the sequence, flanked with the restriction sites *XhoI* (5') and *NotI* (3'), was optimized for *Komagataella phaffii*. Additionally, a nucleotide sequence coding for an octahistidine tag was added to the 3'-end of the gene, to allow purification by Ni-NTA affinity chromatography.

The received DNA string was cloned into the *Komagataella phaffii* vector pPICZα, using the *XhoI* and *NotI* restriction sites and successful insertion was confirmed by sequencing. Having linearized the plasmid DNA using *SacI*, electroporation was carried out, according to the instructions provided by the EasySelect™ ExpressionKit (Invitrogen), to transform KM71H cells with our construct of interest.

Additionally, the cells were transformed with pPICK-PDI plasmid DNA to allow co-expression of the protein disulfide isomerase of *Saccharomyces cerevisiae*.

Small-scale expression in 96 well plates was performed as described by Weis et al. (44) in order to identify stably and well-expressing clones. Clones, which displayed the high signal intensity when analyzing the expression supernatants with dot blot, were later used in large-scale expression.

Large-scale expression was performed in a BBI CT5-2 fermenter (Sartorius, Göttingen, Germany) as described in (45). After an induction time of 24 h (a total of 250 g MeOH were added), the pH was set to 8 and cells and medium were separated by centrifugation at 3,500 g for 30 min. As Dld2 was, despite the presence of an α -factor, not properly secreted, the protein had to be purified from the cell pellets. Therefore, the pellets (cell wet weight: about 1.2-1.5 kg per fermenter) were suspended in an equal volume of lysis buffer (50 mM HEPES, 150 mM NaCl, 10 mM imidazole pH 8 + 2 mM DTT and 2 mM PMSF) and lysed using zirconium oxide beads in a Merckenschlager (Braun Biotech International, Melsungen, Germany).

After centrifugation of the suspension (38,500 g for 1 h), the cleared lysate was incubated with 15 mL of equilibrated Ni-Sepharose™ (GE Healthcare) Fast Flow column material at 4°C for approximately 1.5 h. Then, the supernatant was decanted and the column material was packed into an empty column and washed with approximately 150 mL wash buffer (50 mM HEPES, 150 mM NaCl, 20 mM imidazole, pH 8), before eluting Dld2 with elution buffer (50 mM HEPES, 150 mM NaCl, 300 mM imidazole, pH 8). SDS-PAGE was used to identify fractions containing the protein, which, subsequently were pooled and concentrated.

To obtain Dld2 of satisfactory purity a second purification step was needed, which required the buffer to be exchanged to 50 mM HEPES, 150 mM NaCl, pH 8 using a Sephadex G-25 PD10 desalting column (GE Healthcare). Then, the protein solution was applied to a MonoQ™ 5/50 GL column (GE Healthcare), attached to an ÄKTA system (GE Healthcare) and equilibrated with buffer A (50 mM HEPES, 150 mM NaCl, pH 8). After a short wash with buffer A, the protein was eluted using a linear gradient of buffer A and buffer B (50 mM HEPES, 1 M NaCl, pH 8) (flow: 1 mL/min, linear gradient: 0 → 100 % buffer B in 40 minutes). Fractions containing pure Dld2 (the protein eluted at approximately 40 to 55 % buffer B) were pooled and concentrated using Centripreps® 30 kDa MWCO (Merck Millipore). The concentrated protein was flash frozen using liquid nitrogen and stored at -80 °C until further use.

Protein denaturation and determination of the extinction coefficient of yETF and Dld2

To determine the extinction coefficient of yETF, a spectrum of native as well as of denatured yETF was recorded as suggested by Macheroux (46). Assuming that the spectrum of the denatured protein equals the one of free FAD, the extinction coefficient of free FAD ($11,300 \text{ M}^{-1} \text{ cm}^{-1}$ at 450 nm) could

be used to calculate the extinction coefficient of yETF at 450 nm ($11,600 \text{ M}^{-1} \text{ cm}^{-1}$) and 469 nm ($9,900 \text{ M}^{-1} \text{ cm}^{-1}$; independent of flavin modification), respectively.

The extinction coefficient of Dld2 was determined as described for yETF. From the absorbance at 450 nm recorded for native and denatured enzyme, an extinction coefficient of $12,700 \text{ M}^{-1} \text{ cm}^{-1}$ at 450 nm was calculated for Dld2.

Photoreduction of yETF and Dld2

Photoreduction was performed under anoxic conditions as described by Massey *et al.* (1978) (47). For yETF, a solution containing 30 μM protein, 1 mM EDTA, 2 μM methylviologen and 1 μM 5-deaza-FMN was rendered anaerobic and transferred to a sealable quartz cuvette. After recording a UV-visible absorption spectrum from 300 to 800 nm, the sample was irradiated and additional spectra were recorded at a constant temperature of 15 °C, until no further spectral changes were observed. Then, the lid was removed under aerobic conditions to initiate reoxidation of the protein, which again was monitored spectrophotometrically.

Photoreduction of Dld2 was performed as described for yETF, just the amount of EDTA (2.5 mM), 5-deaza-FMN (2.5 μM) and methylviologen (6 μM) was adapted, as the sample turned out to be difficult to reduce.

Expression, purification and photoreduction of hETF- βY16F

Cloning and expression of the hETF-variant βY16F was carried out as described previously (16). Photoreduction was carried out as described for yETF (see above).

Determination of the redox potential of yETF and Dld2

The redox potential of yETF was studied under anoxic conditions using a stopped flow device from Hi-Tech (SF-61DX2; TgK-Scientific, Bradford-on-Avon, UK) placed in an anaerobic glove box (Belle Technology, Cambridge, UK) by applying the dye equilibrium method based on the xanthine/xanthine oxidase system, as reported by Massey (23). Two solutions, one containing $\sim 50 \mu\text{M}$ yETF, 500 μM xanthine and 5 μM methyl viologen and a second one with $\sim 40 \mu\text{M}$ indigo carmine (A_{610} : ~ 0.5 ; E° : -125 mV) and $\sim 200 \text{ nM}$ xanthine oxidase, were prepared in 50 mM HEPES pH 7 + 1 mM DTT and mixed using the stopped flow device. Then, reduction of the flavin and the dye was monitored by recording 500 absorption spectra (350 to 700 nm) with a KinetaScan T diode array detector (MG-6560) within 2 h (four measurements). From these data a Nernst plot was generated by plotting the log ([ox]/[red]) of the protein as a function of the log ([ox]/[red]) of the dye - to determine the

$\log(\text{yETF}_{\text{ox}}/\text{yETF}_{\text{red}})$ and the $\log(\text{dye}_{\text{ox}}/\text{dye}_{\text{red}})$ the relative absorption changes at 460 nm and 610 nm, respectively, were used. Using the resulting intercept the redox potential of yETF could be determined as described by Minnaert (48).

To determine the redox potential of Dld2, two solutions, one containing $\sim 20 \mu\text{M}$ Dld2, $500 \mu\text{M}$ xanthine and $5 \mu\text{M}$ methyl viologen and a second one with $\sim 20 \mu\text{M}$ phenosafranin (A_{520} : ~ 0.2 ; E° : -252 mV) and $\sim 200 \text{ nM}$ xanthine oxidase, were prepared in 50 mM HEPES, 150 mM NaCl pH 7 and mixed using the stopped flow device. Then, reduction of the flavin and the dye was monitored by recording 500 absorption spectra (350 to 700 nm) with a KinetaScan T diode array detector (MG-6560) within 25 min (seven measurements). From these data a Nernst plot was generated by plotting the $\log([\text{ox}]/[\text{red}])$ of the enzyme as a function of the $\log([\text{ox}]/[\text{red}])$ of the dye - to determine the $\log(\text{Dld2}_{\text{ox}}/\text{Dld2}_{\text{red}})$ and the $\log(\text{dye}_{\text{ox}}/\text{dye}_{\text{red}})$ the relative absorption changes at 450 nm and 520 nm, respectively, were used. Using the resulting intercept the redox potential of yETF could again be determined as described by Minnaert (48).

Analysis of time-dependent modification in yETF by HPLC

To analyze the degree and type of modification of the flavin bound to yETF, the protein was diluted to a concentration of approximately $50 \mu\text{M}$ at pH 8.5 and incubated at $25 \text{ }^\circ\text{C}$ for 24 h. Samples were taken after 0 and 24 h and inactivated by heat denaturation (10 min at $80\text{--}90 \text{ }^\circ\text{C}$). After 10 min of centrifugation at 13,300 rpm, the supernatant was transferred to HPLC-vials for following HPLC-DAD analysis with a Dionex Ultimate 3000 HPLC instrument (Thermo Fisher Scientific) equipped with an Atlantis® dC18 column ($5 \mu\text{m}$, $4.6 \times 250 \text{ mm}$, Waters, Milford, MA, USA) equilibrated with $\text{H}_2\text{O}/0.1 \text{ } \%$ TFA, $7 \text{ } \%$ acetonitrile. For all measurements, $100 \mu\text{L}$ of sample was injected and separation was carried out at a constant temperature of $25 \text{ }^\circ\text{C}$ and a flow rate of 1 mL min^{-1} by applying the following gradient: 0 - 10 min, $7 - 9 \text{ } \%$ acetonitrile; 10 - 25 min, $10 \text{ } \%$ acetonitrile; 25 - 30 min, $12 \text{ } \%$ acetonitrile; 30 -32 min, $95 \text{ } \%$ acetonitrile; 32 - 40 min, $7 \text{ } \%$ acetonitrile. Elution of the different flavin species was monitored with a diode array detector (DAD; $\lambda = 280, 370, 450, 460 \text{ nm}$, full spectrum).

Homology modeling of yETF

A homology model of yETF was generated using the SWISS-MODEL server (49–51). Since yETF was found to share the highest sequence coverage and identity with hETF (PDB: 1efv (4)) the crystal structure of the latter protein was chosen as template. Additionally, the flavin cofactor was modeled into the predicted structure of yETF by aligning the two proteins and copying the flavin moiety from hETF to the active site of the yeast homolog.

Site directed mutagenesis

To get more information about the role of various active site residues found in yETF, variants were generated from the pETM11-yETF wild type construct, using PCR based mutagenesis. All required nucleotide exchanges were introduced using forward and reverse primers carrying the desired mutations (for primers see Table 4). Constructs confirmed by sequencing were transformed with *E. coli* Rosetta (DE3)-pLysS cells, to allow expression and purification as described for yETF wild type.

Table 4: Mutagenesis primers used for the generation of the various yETF-variants, with the codon triplets carrying the desired mutations shown in bold.

Variant	Type	Primer Sequence
βF19Y	fwd.	5'– GCGTATTCTGGTTCCGGTTAAACGTGTTGTTGATTATCAGATTAAACCG – 3'
	rev.	5'– CGGTCAGGGTTTTATTACACGCGGTTAATCTGATAATCAACAACACG – 3'
αN269A	fwd.	5'– CGTGCAAGCGTTGATAATGGCCTGTGTGATGCTAGCCTGCAGATTGG – 3'
	rev.	5'– GCAACAACCTTACC GG TCTGACCAATCTGCAGGCTAGCATCACACAGG – 3'
βE169A	fwd.	5'– CTGGATAATGGTCGTGTTTCAGGTTACCCGTGCAATCGATGATGGTG – 3'
	rev.	5'– GGCTTGCTTCAATAACTTCTTCACCATCATCGATTGCACGGGTAACC – 3'

Reductive and oxidative half reaction (Dld2)

To study the pre steady-state kinetics of Dld2, time dependent spectral changes of the flavin absorption were recorded under anoxic conditions using a stopped flow device (Hi-Tech, TgK Scientific), placed in a glove box (Belle Technology), and monitored with a KinetikaScan T diode array detector (MG-6560). The following analysis was performed by fitting the data points recorded at 450 nm with the Kinetic Studio Software (TgK Scientific).

For the determination of the reductive rate of Dld2, its flavin reduction was studied in the presence of seven different D-α-hydroxyglutarate (final concentration: 50 μM to 1500 μM) and nine D-lactate (final concentration: 1 mM to 100 mM) concentrations. A 20 μM enzyme solution and the substrate solutions were prepared in 50 mM HEPES, 150 mM NaCl pH 7, before mixing them in the stopped flow device and recording the spectral changes between 350 and 700 nm (measurements were performed 4-times at each substrate concentration). The extracted observed rate constants were plotted as a function of the respective substrate concentrations to obtain a hyperbolic curve, which allowed determination of the reduction rates (k_{red}) as well as of the dissociation constants (K_D).

To study the effect of product binding on the rate or reoxidation, one sample of reduced Dld2 (20 μM) was generated using photoreduction (see above) and a second one by adding about 1.5 eq of D-α-hydroxyglutarate. Then, both samples were mixed with air saturated buffer (20 °C) in a stopped flow

device and spectral changes between 350 nm and 700 nm were monitored for 1.5 - 3 s and 25 - 50 min, respectively. To obtain bimolecular reoxidation rates, the observed rate constants were divided by the final oxygen concentration in the reaction mixture (final concentration: 140 μM).

Qualitative analysis of the electron transfer from Dld2 to yETF

To analyze the possible electron transfer from Dld2 to yETF, yETF was diluted to a final concentration of $\sim 10 \mu\text{M}$ using 50 mM HEPES pH 7 + 1 mM DTT and mixed with 1 mM of D- α -hydroxyglutarate. After recording an initial UV-visible absorption spectrum between 300 and 800 nm, Dld2 was added to a final concentration of 10 nM and changes in the absorption characteristics of yETF were monitored over time.

Steady state kinetics (Dld2)

To study the kinetic parameters of Dld2 under steady state conditions, a coupled assay with DCPIP as final electron acceptor was used. Solutions containing varying final concentrations of D- α -hydroxyglutarate (25 μM to 1000 μM) or D-lactate (1 mM to 250 mM) were prepared in 50 mM HEPES, 150 mM NaCl pH 7 and mixed with 125 μM DCPIP. After 10 minutes of incubation at 25 $^{\circ}\text{C}$, Dld2 was added to a final concentration of 100 nM and absorbance changes at 600 nm were recorded for 120 s. By plotting the extracted initial rates as a function of the corresponding substrate concentrations the kinetic parameters K_{Mapp} and k_{catapp} could be determined.

Steady state analysis of the electron transfer from Dld2 onto yETF

Steady state parameters for the electron transfer of Dld2 onto wild type yETF were determined by performing a coupled assay with DCPIP as final electron acceptor. Therefore, buffer (50 mM HEPES pH 7 containing 1 mM DTT), Dld2 (10 nM), yETF (0.875 to 28 μM) and DCPIP (125 μM) were mixed and incubated at 25 $^{\circ}\text{C}$ for 10 minutes. Then, the reaction was started by adding 1 mM D- α -hydroxyglutarate, the substrate of Dld2, and the decrease in absorption at 600 nm was monitored at 25 $^{\circ}\text{C}$ for 120 s (measurements at each yETF concentration were performed in triplicate). To determine the kinetic parameters K_{Mapp} and k_{catapp} the extracted initial velocities (normalized to enzyme concentration) were plotted as a function of the respective yETF concentrations yielding a hyperbolic curve, which was fitted using the program Origin 7 (OriginLab, Northampton, MA, USA).

Titration of yETF and Dld2 with α -ketoglutarate

To study the binding of α -ketoglutarate to yETF and Dld2, 800 μ L of protein diluted to a final concentration of about 10 μ M using 50 mM HEPES pH 7 + 1 mM DTT and 50 mM HEPES, 150 mM NaCl pH 7, respectively, were transferred to a quartz cuvette (reference just 800 μ L of buffer) and a UV-visible absorption spectrum between 300 and 800 nm was recorded. Then, 10 μ L aliquots of 2.5 mM α -ketoglutarate were added to both the reference and the measurement cuvette and further spectra were recorded after an incubation time of 1 min following the addition of the metabolite.

Author contributions

MT, JB and CT prepared the constructs for heterologous gene expression; MT and JB expressed the genes, purified the produced proteins and performed biochemical experiments; MT, JB and PM designed the biochemical and kinetic experiments and interpreted the data; MT, JB and PM wrote the manuscript.

Conflict of interest

The authors declare no conflict of interest.

Acknowledgements

We are grateful to Dr. Majd Lahham for his support during the initial phase of the project. This work was supported by the Austrian Science Fund (FWF) through grant W901 (Doctoral Program “Molecular Enzymology”). The authors are also grateful for the support by the interuniversity program in natural sciences (NAWI Graz).

References

1. Crane, F. L., Mii, S., Hauge, J. G., Green, D. E., and Beinert, H. (1956) On the mechanism of dehydrogenation of fatty acyl derivatives of coenzyme A. I. The general fatty acyl coenzyme A dehydrogenase. *J. Biol. Chem.* **218**, 701–706
2. Weidenhaupt, M., Rossi, P., Beck, C., Fischer, H. M., and Hennecke, H. (1996) *Bradyrhizobium japonicum* possesses two discrete sets of electron transfer flavoprotein genes: FixA, fixB and etfS, etfL. *Arch. Microbiol.* **165**, 169–178
3. Steenkamp, D. J., and Husain, M. (1982) The effect of tetrahydrofolate on the reduction of electron transfer flavoprotein by sarcosine and dimethylglycine dehydrogenases. *Biochem. J.* **203**, 707–715
4. Roberts, D. L., Frerman, F. E., and Kim, J. J. (1996) Three-dimensional structure of human electron transfer flavoprotein to 2.1-Å resolution. *Proc. Natl. Acad. Sci. U. S. A.* **93**, 14355–60
5. Jang, M. H., Scrutton, N. S., and Hille, R. (2000) Formation of W3A1 electron-transferring flavoprotein (ETF) hydroquinone in the trimethylamine dehydrogenase-ETF protein complex. *J. Biol. Chem.* **275**, 12546–12552
6. Talfournier, F., Munro, A. W., Basran, J., Sutcliffe, M. J., Daff, S., Chapman, S. K., and Scrutton, N. S. (2001) α Arg-237 in *Methylophilus methylotrophus* (sp. W3A1) electron-transferring flavoprotein affords ~200-millivolt stabilization of the FAD anionic semiquinone and a kinetic block on full reduction to the dihydroquinone. *J. Biol. Chem.* **276**, 20190–20196
7. Whitfield, C. D., and Mayhew, S. G. (1974) Purification and properties of electron-transferring flavoprotein from *Peptostreptococcus elsdenii*. *J. Biol. Chem.* **249**, 2801–2810
8. Elsdén, S. R., Gilchrist, F. M., Lewis, D., and Volcani, B. E. (1956) Properties of a fatty acid forming organism isolated from the rumen of sheep. *J. Bacteriol.* **72**, 681–689
9. Jenkins, O., Byrom, D., and Jones, D. (1987) *Methylophilus*: a new genus of methanol-utilizing bacteria. *Int. J. Syst. Bacteriol.* **37**, 446–448
10. Gudipati, V., Koch, K., Lienhart, W.-D., and Macheroux, P. (2014) The flavoproteome of the yeast *Saccharomyces cerevisiae*. *Biochim. Biophys. Acta - Proteins Proteomics.* **1844**, 535–544
11. Lopes, J., Pinto, M. J., Rodrigues, A., Vasconcelos, F., and Oliveira, R. (2010) The *Saccharomyces cerevisiae* genes, AIM45, YGR207c/CIR1 and YOR356w/CIR2, are involved in cellular redox state under stress conditions. *Open Microbiol. J.* **4**, 75–82
12. Amberg, D. C., Basart, E., and Botstein, D. (1995) Defining protein interactions with yeast actin in vivo. *Nat. Struct. Biol.* **2**, 28–35
13. Hachiya, N. S., Sakasegawa, Y., Jozuka, A., Tsukita, S., and Kaneko, K. (2004) Interaction of D-lactate dehydrogenase protein 2 (Dld2p) with F-actin: Implication for an alternative function of Dld2p. *Biochem. Biophys. Res. Commun.* **319**, 78–82

14. Hachiya, N. S., Sakasegawa, Y., Sasaki, H., Jozuka, A., Tsukita, S., and Kaneko, K. (2004) Oligomeric Aip2p/Dld2p forms a novel grapple-like structure and has an ATP-dependent F-actin conformation modifying activity in vitro. *Biochem. Biophys. Res. Commun.* **320**, 1271–1276
15. Becker-Ketterer, J., Paczia, N., Conrotte, J. F., Kay, D. P., Guignard, C., Jung, P. P., and Linster, C. L. (2016) *Saccharomyces cerevisiae* forms D-2-hydroxyglutarate and couples its degradation to D-lactate formation via a cytosolic transhydrogenase. *J. Biol. Chem.* **291**, 6036–6058
16. Augustin, P., Toplak, M., Fuchs, K., Gerstmann, E. C., Prassl, R., Winkler, A., and Macheroux, P. (2018) Oxidation of the FAD cofactor to the 8-formyl-derivative in human electron-transferring flavoprotein. *J. Biol. Chem.* **293**, 2829–2840
17. Salazar, D., Zhang, L., DeGala, G. D., and Frerman, F. E. (1997) Expression and characterization of two pathogenic mutations in human electron transfer flavoprotein. *J. Biol. Chem.* **272**, 26425–26433
18. Toogood, H. S., Van Thiel, A., Scrutton, N. S., and Leys, D. (2005) Stabilization of non-productive conformations underpins rapid electron transfer to electron-transferring flavoprotein. *J. Biol. Chem.* **280**, 30361–30366
19. Mayhew, S. G., Whitfield, C. D., Ghisla, S., and Schuman-Jörns, M. (1974) Identification and properties of new flavins in electron-transferring flavoprotein from *Peptostreptococcus elsdenii* and pig-liver glycolate oxidase. *Eur. J. Biochem.* **44**, 579–591
20. Lehman, T. C., and Thorpe, C. (1992) A new form of mammalian electron-transferring flavoprotein. *Arch. Biochem. Biophys.* **292**, 594–599
21. Komuniecki, R., McCrury, J., Thissen, J., and Rubin, N. (1989) Electron-transfer flavoprotein from anaerobic *Ascaris suum* mitochondria and its role in NADH-dependent 2-methyl branched-chain enoyl-CoA reduction. *BBA - Bioenerg.* **975**, 127–131
22. Demmer, J. K., Pal Chowdhury, N., Selmer, T., Ermler, U., and Buckel, W. (2017) The semiquinone swing in the bifurcating electron transferring flavoprotein/butyryl-CoA dehydrogenase complex from *Clostridium difficile*. *Nat. Commun.* 10.1038/s41467-017-01746-3
23. Massey, V. (1991) A simple method for the determination of redox potentials. in *Flavins and Flavoproteins* (Curti, B., Zanetti, G., and Ronchi, S. eds), pp. 59–66, Walter de Gruyter, Como, Italy
24. Husain, M., Stankovich, M. T., and Fox, B. G. (1984) Measurement of the oxidation-reduction potentials for one-electron and two-electron reduction of electron-transfer flavoprotein from pig liver. *Biochem. J.* **219**, 1043–1047

25. Dwyer, T. M., Zhang, L., Muller, M., Marrugo, F., and Frerman, F. (1999) The functions of the flavin contact residues, α Arg249 and β Tyr16, in human electron transfer flavoprotein. *Biochim. Biophys. Acta - Protein Struct. Mol. Enzymol.* **1433**, 139–152
26. Pace, C. P., and Stankovich, M. T. (1987) Redox properties of electron-transferring flavoprotein from *Megasphaera elsdenii*. *Biochim. Biophys. Acta (BBA)/Protein Struct. Mol.* **911**, 267–276
27. Konjik, V., Brünle, S., Demmer, U., Vanselow, A., Sandhoff, R., Ermler, U., and Mack, M. (2017) The crystal structure of RosB: Insights into the reaction mechanism of the first member of a family of flavodoxin-like enzymes. *Angew. Chemie - Int. Ed.* **56**, 1146–1151
28. Robbins, J. M., Souffrant, M. G., Hamelberg, D., Gadda, G., and Bommarius, A. S. (2017) Enzyme-mediated conversion of flavin adenine dinucleotide (FAD) to 8-formyl FAD in formate oxidase results in a modified cofactor with enhanced catalytic properties. *Biochemistry.* **56**, 3800–3807
29. Husain, M., and Steenkamp, D. J. (1983) Electron transfer flavoprotein from pig liver mitochondria. A simple purification and re-evaluation of some of the molecular properties. *Biochem. J.* **209**, 541–545
30. Watmough, N. J., Kiss, J., and Frerman, F. E. (1992) Structural and redox relationships between *Paracoccus denitrificans*, porcine and human electron-transferring flavoproteins. *Eur. J. Biochem.* **205**, 1089–1097
31. Gorelick, R. J., and Thorpe, C. (1986) Electron-transferring flavoprotein from pig kidney: Flavin analogue studies. *Biochemistry.* **25**, 7092–7098
32. Gorelick, R. J., Schopfer, L. M., Ballou, D. P., Massey, V., and Thorpe, C. (1985) Interflavin oxidation-reduction reactions between pig kidney general acyl-CoA dehydrogenase and electron-transferring flavoprotein. *Biochemistry.* **24**, 6830–6839
33. Wang, R., and Thorpe, C. (1991) Reactivity of medium-chain acyl-CoA dehydrogenase toward molecular oxygen. *Biochemistry.* **30**, 7895–7901
34. DuPlessis, E. R., Pellett, J., Stankovich, M. T., and Thorpe, C. (1998) Oxidase activity of the acyl-CoA dehydrogenases. *Biochemistry.* **37**, 10469–10477
35. Lenn, N. D., Stankovich, M. T., and Liu, H. W. (1990) Regulation of the redox potential of general acyl-CoA dehydrogenase by substrate binding. *Biochemistry.* **29**, 3709–3715
36. Lehman, T. C., and Thorpe, C. (1990) Alternate electron acceptors for medium-chain acyl-CoA dehydrogenase: Use of ferricenium salts. *Biochemistry.* **29**, 10594–10602
37. Toogood, H. S., Leys, D., and Scrutton, N. S. (2007) Dynamics driving function - New insights from electron transferring flavoproteins and partner complexes. *FEBS J.* **274**, 5481–5504
38. Ghisla, S., and Thorpe, C. (2004) Acyl-CoA dehydrogenases: A mechanistic overview. *Eur. J. Biochem.* **271**, 494–508

39. Ramsay, R. R., Steenkamp, D. J., and Husain, M. (1987) Reactions of electron-transfer flavoprotein and electron-transfer flavoprotein: ubiquinone oxidoreductase. *Biochem. J.* **241**, 883–892
40. Byron, C. M., Stankovich, M. T., Husain, M., and Davidson, V. L. (1989) Unusual redox properties of electron-transfer flavoprotein from *Methylophilus methylotrophus*. *Biochemistry.* **28**, 8582–8587
41. Watmough, N. J., and Frerman, F. E. (2010) The electron transfer flavoprotein: Ubiquinone oxidoreductases. *Biochim. Biophys. Acta - Bioenerg.* **1797**, 1910–1916
42. Swanson, M. A., Usselman, R. J., Frerman, F. E., Eaton, G. R., and Eaton, S. S. (2008) The iron-sulfur cluster of electron transfer flavoprotein-ubiquinone oxidoreductase is the electron acceptor for electron transfer flavoprotein. *Biochemistry.* **47**, 8894–8901
43. Usselman, R. J., Fielding, A. J., Frerman, F. E., Watmough, N. J., Eaton, G. R., and Eaton, S. S. (2008) Impact of mutations on the midpoint potential of the [4Fe-4S] +1,+2 cluster and on catalytic activity in electron transfer flavoprotein-ubiquinone oxidoreductase (ETF-QO). *Biochemistry.* **47**, 92–100
44. Weis, R., Luiten, R., Skranc, W., Schwab, H., Wubbolts, M., and Glieder, A. (2004) Reliable high-throughput screening with *Pichia pastoris* by limiting yeast cell death phenomena. *FEMS Yeast Res.* **5**, 179–189
45. Schrittwieser, J. H., Resch, V., Wallner, S., Lienhart, W. D., Sattler, J. H., Resch, J., Macheroux, P., and Kroutil, W. (2011) Biocatalytic organic synthesis of optically pure (S)-scoulerine and berbine and benzyloisoquinoline alkaloids. *J. Org. Chem.* **76**, 6703–6714
46. Macheroux, P. (1999) UV-visible spectroscopy as a tool to study flavoproteins. *Methods Mol. Biol.* **131**, 1–7
47. Massey, V., Hemmerich, P., Knappe, W. R., Duchstein, H. J., and Fenner, H. (1978) Photoreduction of flavoproteins and other biological compounds catalyzed by deazaflavins. Appendix: photochemical formation of deazaflavin dimers. *Biochemistry.* **17**, 9–17
48. Minnaert, K. (1965) Measurement of the equilibrium constant of the reaction between cytochrome c and cytochrome a. *Biochim. Biophys. Acta.* **110**, 42–56
49. Biasini, M., Bienert, S., Waterhouse, A., Arnold, K., Studer, G., Schmidt, T., Kiefer, F., Cassarino, T. G., Bertoni, M., Bordoli, L., and Schwede, T. (2014) SWISS-MODEL: Modelling protein tertiary and quaternary structure using evolutionary information. *Nucleic Acids Res.* 10.1093/nar/gku340
50. Arnold, K., Bordoli, L., Kopp, J., and Schwede, T. (2006) The SWISS-MODEL workspace: A web-based environment for protein structure homology modelling. *Bioinformatics.* **22**, 195–201
51. Benkert, P., Biasini, M., and Schwede, T. (2011) Toward the estimation of the absolute quality of individual protein structure models. *Bioinformatics.* **27**, 343–350

Chapter 6

human D-2-hydroxyglutarate dehydrogenase

Biochemical characterization of human D-2-hydroxyglutarate dehydrogenase and two disease-related variants reveal the molecular cause of D-2-hydroxyglutaric aciduria

Marina Toplak, Julia Brunner, Julia Schmidt and Peter Macheroux*

Institute of Biochemistry, Graz University of Technology, Petersgasse 12/2, A-8010 Graz, Austria

*to whom correspondence should be addressed:

Prof. Dr. Peter Macheroux

Graz University of Technology

Institute of Biochemistry

Petersgasse 12/2

A-8010 Graz, Austria

Tel.: +43-316-873 6450

Fax: +43-316-873 6952

Email: peter.macheroux@tugraz.at

Keywords: D-2-hydroxyglutaric aciduria, D-lactate, D-2-hydroxyglutarate, electron transferring flavoprotein

Abbreviations

CD, circular dichroism; ETF, electron transferring flavoprotein; ETF-QO, ETF-ubiquinone oxidoreductase; FAD, flavin adenine dinucleotide; GHB; 4-hydroxybutyrate; hD2HGDH, human D-2-hydroxyglutarate dehydrogenase; hDMGDH, human dimethylglycine dehydrogenase; hMCAD, human medium chain acyl-CoA dehydrogenase; HOT, hydroxyacid-oxoacid transhydrogenase; MADD, multiple acyl-CoA dehydrogenase deficiency

Abstract

D-2-hydroxyglutaric aciduria is a neurometabolic disorder, characterized by the accumulation of D-2-hydroxyglutarate (D-2HG) in human mitochondria. Recent studies have shown that patients suffering from this disease exhibited point mutations in the *d2hgdh* gene, leading to single amino acid replacements in the mature protein (Ile147Ser and Val444Ala) affecting the catalytic activity of the enzyme. However, the molecular basis of this loss of enzymatic function could not be delineated in detail.

We recombinantly produced wild type hD2HGDH as well as two disease-related protein variants and performed their detailed biochemical characterization. We could show that hD2HGDH is an FAD-dependent protein, which is able to catalyze the oxidation of both D-2HG and D-lactate to α -ketoglutarate and pyruvate, respectively. The two variants were obtained as apo-proteins and were thus catalytically inactive. The addition of FAD failed to restore enzymatic activity indicating that the cofactor binding site is severely compromised by the single amino acid replacements. Further analyses revealed that both variants form aggregates that are apparently unable to bind the FAD cofactor.

Interestingly, D-2-hydroxyglutaric aciduria may also result from a loss of function of either the electron transferring flavoprotein (ETF) or its downstream electron acceptor ETF-ubiquinone oxidoreductase, which suggests that ETF may serve as the cognate electron acceptor of reduced hD2HGDH. Here, we show that hD2HGDH directly reduces recombinant human ETF, thus establishing a metabolic link between the oxidation of D-2-hydroxyglutaric acid and the mitochondrial electron transport chain.

Introduction

D-2-hydroxyglutaric aciduria (D-2HGA) is a neurometabolic disorder, characterized by a strong accumulation of D-2HG in affected patients (1). The phenotypes associated with increased levels of D-2HG are rather inhomogeneous, with some of the patients suffering from severe disorders such as early-infantile-onset epileptic encephalopathy and cardiomyopathy, as well as from developmental delay and dysmorphic features, while others exhibit much weaker clinical symptoms (1, 2). To date, very little is known about the metabolic processes that lead to the formation and degradation of D-2HG. It was speculated that the main enzyme responsible for the synthesis of D-2HG in humans is the so called hydroxyacid-oxoacid-transhydrogenase (HOT), which catalyzes the α -ketoglutarate dependent oxidation of 4-hydroxybutyrate (GHB) to succinic semialdehyde in the mitochondrial matrix, yielding D-2HG as side product (2). Therefore, patients suffering from D-2HGA were tested for the hyperactivity of HOT, but none of them showed higher activity of the enzyme as compared to healthy individuals suggesting that enzymes involved in the break-down of D-2HG might be responsible for D-2HGA (3). This observation brought the only enzyme known to specifically act on

D-2HG, i.e. D-2-hydroxyglutarate dehydrogenase (D2HGDH) into the spotlight of research (4, 5). D2HGDH is localized in the mitochondrial matrix and shares high sequence identity with the yeast enzyme D-lactate dehydrogenase 2 (Dld2; Uniprot ID: P46681; 53% identity on amino acid sequence level) and its plant homolog (*Arabidopsis thaliana*- (*At*-) D2HGDH; Uniprot ID: O23240; 56% identity on amino acid sequence level). Both of these homologs are serviced by an electron transferring flavoprotein (ETF) (6, 7) (+Chapter 5) and therefore it appears likely that the human enzyme also delivers electrons directly to ETF, although this was not shown experimentally thus far.

In addition to the uncertainty revolving around the electron pathway from D-2HG to the mitochondrial electron transport chain, the molecular cause(s) of hD2HGDH deficiency are still unknown. Genetic studies by Struys *et al.* (2005) and Kranendijk *et al.* (2009) revealed several pathogenic mutations in the *d2hgdh* gene of patients with severe phenotypes (1, 8), two of which have been investigated in more detail (1). Struys *et al.* (2005) have shown that two single point mutations at nucleotide position 440 (T→G) and at position 1331 (T→C) lead to missense mutations, causing the replacement of an isoleucine by a serine (Ile147Ser variant) and a valine by an alanine (Val444Ala variant), respectively. In order to analyze the pathogenicity of the two amino acid replacements, they also determined the enzyme activity of both variants in a radiochemical cell-line based assay, which revealed residual activities of 25% (Val444Ala) and 0% (Ile147Ser) as compared to the wild type protein (1). Based on their studies, however, they could not explain the reason for the dramatic loss of enzymatic function.

In order to better understand the effect of the two amino acid replacements on the overall activity of hD2HGDH, as well as to find the natural electron acceptor of the protein, we produced recombinant wild type hD2HGDH as well as the Ile147Ser and the Val444Ala variants in *Escherichia coli*. The purified recombinant wild type hD2HGDH possessed a flavin cofactor and exhibited oxidase activity toward D-lactate and D-2HG, but showed a clear preference for the oxidation of D-2HG. In contrast, the two variants were isolated as apo-proteins and were devoid of enzymatic activity. Further analyses revealed that both disease-related variants were unable to bind the FAD cofactor and showed higher tendency toward aggregation. Here, we also demonstrate that reduced hD2HGDH rapidly donates electrons to recombinant human ETF, linking D-2HG oxidation directly to the mitochondrial electron transport chain.

Taken together, our study has provided a more detailed understanding of the molecular cause of disease related variants of hD2HGDH and we have firmly established human ETF as the natural electron acceptor of the enzyme. Our findings also provide the bases to rationalize the occurrence of D-2HGA in cases where either hETF or hETF-ubiquinone oxidoreductase (hETF-QO) deficiency was observed.

Results

Production, purification and biochemical characterization of hD2HGDH

Since recombinant production of full-length hD2HGDH and of a truncated version of the protein lacking the putative mitochondrial targeting sequence (hD2HGDH₅₄) was unsuccessful in *E. coli* and in *Komagataella phaffii*, a fusion construct with the solubility tag GB1 (B1 domain of *Streptococcal* protein G) was generated. This approach produced soluble fusion protein (GB1-hD2HGDH₅₄) in *E. coli* and subsequent purification using affinity chromatography (Ni-NTA) and gel filtration yielded about 3 mg of pure protein from 120 g cell (wet weight). After purification, the *N*-terminal fusion-tag could be removed by means of the tobacco etch virus protease. Although removal of GB1 had no adverse effect on the solubility and stability of hD2HGDH, this procedure incurred a severe loss of total protein resulting in a final yield of 0.5 mg. Therefore, the “free” hD2HGDH was only prepared for select experiments such as steady-state turnover and interaction studies with human ETF (see below).

The purified protein (with and without GB1) exhibited absorption maxima at 378 nm and 453 nm, indicating the presence of a flavin chromophore. The spectral changes observed upon denaturation of the protein are consistent with FAD being the cofactor (Figure 1A), which is in accordance with previous reports on homologs of hD2HGDH (7) (+Chapter 5).

In order to obtain information about the electrochemical properties of hD2HGDH, the enzyme was photoreduced and the redox potential was determined using the xanthine/xanthine oxidase method reported by Massey (9). Photoreduction of hD2HGDH required the use of significant amounts of the redox mediators 5-deaza-FMN (2.5 μ M) and methylviologen (7 μ M) yielding fully reduced enzyme (Figure 1B, oxidized: *black*; reduced: *blue*) after 45 min of irradiation. In the course of the reduction, as well as upon reoxidation (Figure 1B, reoxidized: *green*) no radical intermediate was observed, indicating that radical flavin species are not stabilized. Similarly, hD2HGDH was directly reduced to the hydroquinone form in the redox potential experiment. Using roseoFMN as the reporting dye, the flavin chromophore and the dye were fully reduced almost synchronously (Figure 1C), which allowed the determination of the redox potential by plotting the $\log(\text{hD2HGDH}_{\text{ox}}/\text{hD2HGDH}_{\text{red}})$ as a function of the $\log(\text{roseoFMN}_{\text{ox}}/\text{roseoFMN}_{\text{red}})$. This yielded a redox potential of -196 ± 1 mV, which is significantly more negative than determined for other dehydrogenases (*e.g.* hMCAD: -87 mV (10)).

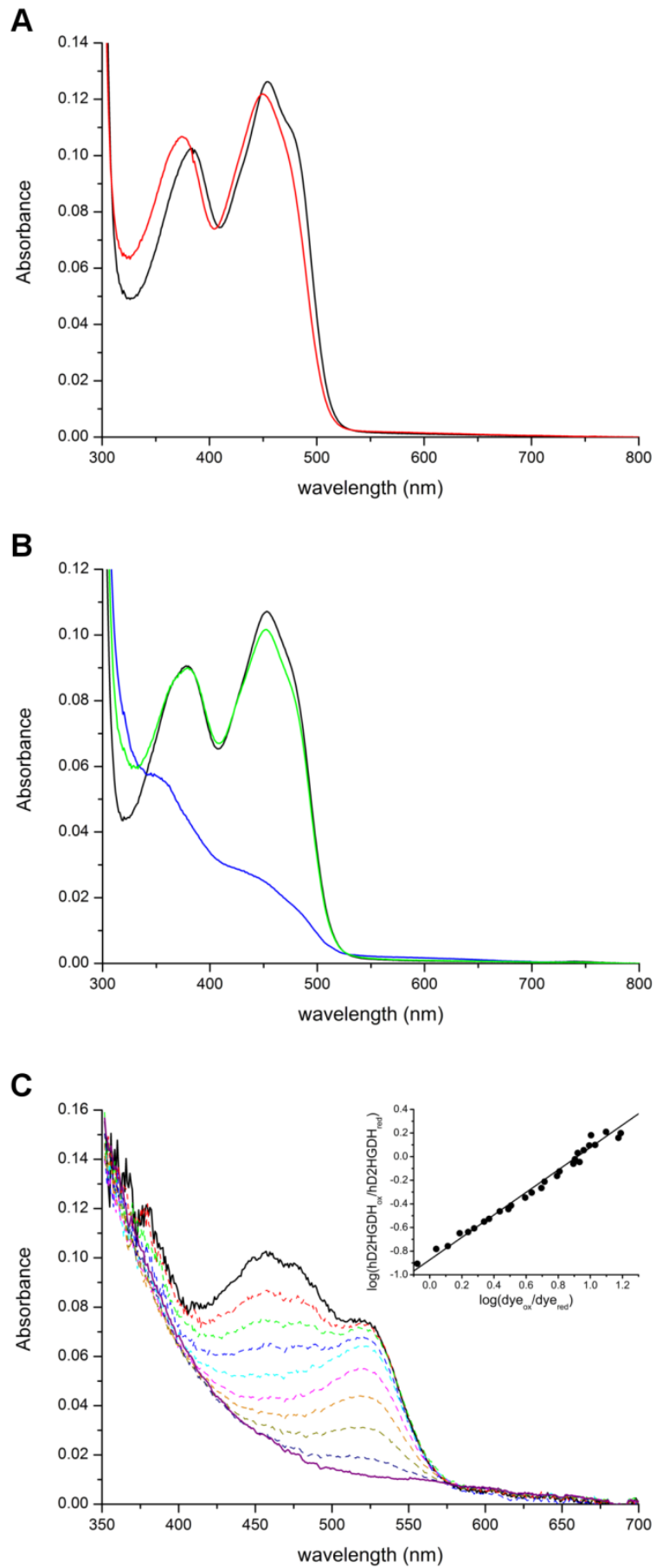


Figure 1: Spectral and electrochemical characterization of (GB1-)hD2HGDH. **A**, To determine the molar extinction coefficient of hD2HGDH at 450 nm, UV-visible absorption spectra of native (*black line*) and denatured (2% SDS; *red line*) hD2HGDH, diluted to a final concentration of 10 μM with 50 mM HEPES, 150 mM NaCl pH 7, were recorded between 300 and 800 nm (25°C). Assuming that the spectrum of denatured hD2HGDH corresponds to the spectrum of free FAD (ϵ_{450} : 11,300 $\text{M}^{-1} \text{cm}^{-1}$), the molar extinction coefficient of hD2HGDH was calculated (ϵ_{450} : 11,600 \pm 300 $\text{M}^{-1} \text{cm}^{-1}$). **B**, UV-visible absorption spectra (300-800 nm) corresponding to the different flavin redox states observed in the course of the anoxic photoreduction of hD2HGDH (diluted to a final concentration of 10 μM using 50 mM HEPES, 150 mM NaCl pH 7): oxidized (*black line*), fully reduced (*blue line*) and reoxidized (*green line*). **C**, Time-dependent spectral changes of hD2HGDH (\sim 10 μM) and roseoFMN (\sim 10 μM ; E° : -222 mV) monitored in the course of the reduction reaction (25 min), indicating a two-electron reduction of both the FAD cofactor and the dye. All measurements were carried out in 50 mM HEPES, 150 mM NaCl pH 7 at a constant temperature of 25°C. *Inset*, Based on the relative absorbance changes at 450 and 525 nm, respectively, a Nernst plot was generated by plotting the $\log(\text{hD2HGDH}_{\text{ox}}/\text{hD2HGDH}_{\text{red}})$ as a function of the $\log(\text{dye}_{\text{ox}}/\text{dye}_{\text{red}})$. From the resulting intercept a redox potential of -196 ± 2 mV was calculated (from four determinations).

Kinetic characterization of hD2HGDH

Detailed kinetic characterization of both GB1-tagged and “free” hD2HGDH revealed that the *N*-terminal fusion tag does not influence the kinetic properties of the protein. hD2HGDH is efficiently reduced by D-2HG as well as by D-lactate, reaching limiting rates with 1 mM D-2HG (k_{red} : $1.9 \pm 0.1 \text{ s}^{-1}$; K_D : $83 \pm 14 \mu\text{M}$; Figure 2B) and 75 mM D-lactate (k_{red} : $0.30 \pm 0.01 \text{ s}^{-1}$; K_D : $2500 \pm 200 \mu\text{M}$), respectively (Table 1). However, it should be noted that substrate-induced flavin reduction proceeds in two distinct phases, with the second phase being \sim 200-fold (2-HG) and \sim 20-fold (D-lactate) slower than the first phase (Figure 2A). A difference between the two phases is also observed in the spectral changes monitored in the course of the reduction. While a significant increase in longer-wavelength absorption is detected in the first phase (Figure 2A, *black* and *red line*), the decrease in intensity of the flavin absorption is visible in the second phase (Figure 2A, *black* and *red line*). Interestingly, it was also observed that the amplitude of the two phases strongly depended on the substrate concentration; the more substrate was used, the greater was the amplitude of the first phase.

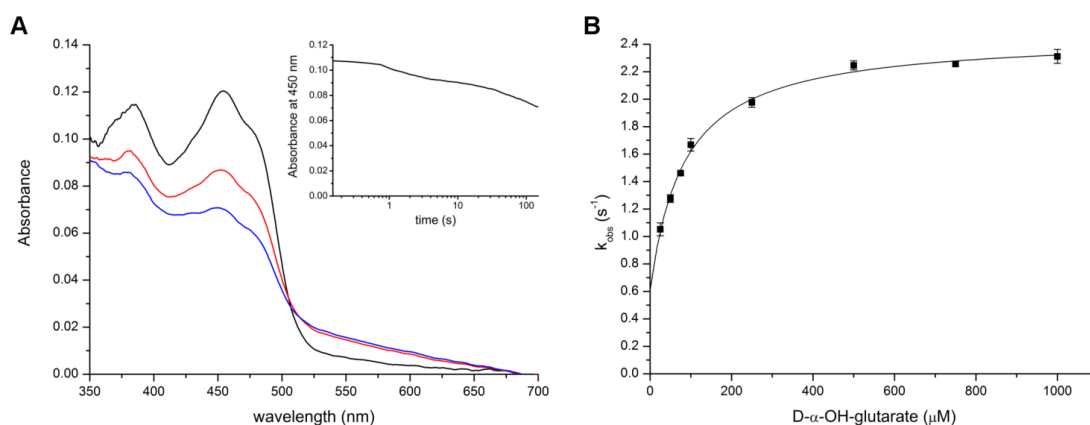


Figure 2: Determination of the reductive rate of hD2HGDH with D-2HG. **A**, UV-visible absorption spectra recorded after mixing $\sim 10 \mu\text{M}$ hD2HGDH with 1 mM of D2HG in 50 mM HEPES, 150 mM NaCl pH 7 in a stopped-flow device. The *black* line indicates the starting spectrum, while the *blue* line reflects the final spectrum monitored after 150 s (at this substrate concentration full reduction of the protein-bound flavin cofactor could not be achieved). Interestingly, reduction of hD2HGDH proceeds in two distinct phases as indicated by the *red* spectrum and the *inset*. In the first phase, the decrease in absorbance at 450 nm is accompanied by a significant increase in longer wavelength absorbance, which is not observed in the second, much slower phase. **B**, To determine the limiting rate (k_{red}) as well as the dissociation constant (K_D) of D2HG with hD2HGDH, observed rate constants (k_{obs}) for the flavin reduction were extracted and plotted as a function of the corresponding D2HG concentrations.

Next, we also performed steady-state kinetics to better understand the overall turnover process. In a steady-state assay using DCPIP as the final electron acceptor, a higher catalytic efficiency of hD2HGDH with D-2HG was observed than with D-lactate ($1.3 \cdot 10^4 \pm 0.2 \cdot 10^4 \text{ M}^{-1} \text{ s}^{-1}$ vs $300 \pm 30 \text{ M}^{-1} \text{ s}^{-1}$). However, the turnover numbers obtained with D-2HG were ~ 5 -times lower than the reduction rates (Table 1), indicating that the oxidative half-reaction is the rate-limiting process under steady-state conditions.

Table 1: Kinetic parameters of hD2HGDH determined with D-2-hydroxyglutarate and D-lactate under pre steady-state and steady-state conditions (25°C). Reductive rates (k_{red}) and dissociation constants (K_D -values) were determined under pre steady-state conditions by mixing hD2HGDH (10 μM final concentration) with varying concentrations of D-2-hydroxyglutarate (final concentrations: 25 – 1000 μM) as well as of D-lactate (final concentrations: 0.25 - 75 mM). Both, enzyme and substrate solutions were prepared in 50 mM HEPES, 150 mM NaCl pH 7 and flavin reduction was monitored between 350 and 700 nm for 1.5 to 150 s. Absorbance changes at 450 nm were used to extract observed rate constants (k_{obs}), which were then plotted as a function of the respective substrate concentrations to obtain limiting rates (k_{red}) as well as dissociation constants (K_D) for the interaction of hD2HGDH with the two substrates.

Under steady-state conditions, kinetic characterization of the enzyme was carried out by using DCPIP as final electron acceptor. Buffer (50 mM HEPES, 150 mM NaCl pH 7), hD2HGDH (100 nM) and DCPIP (125 μM) were mixed and incubated at 25°C for 10 min. Then, varying amounts of D-2-hydroxyglutarate (final concentrations: 6.25 μM to 1000 μM) or D-lactate (final concentrations: 0.25 mM to 25 mM) were added and absorbance changes at 600 nm were recorded for 120 s. By plotting the initial rates as function of the substrate concentrations, k_{catapp} and K_{Mapp} values for the interaction of hD2HGDH with both accepted substrates could be determined.

kinetic parameters	D-2-hydroxyglutarate	D-lactate
$k_{red} [\text{s}^{-1}]$	1.9 ± 0.1	0.30 ± 0.01
$k_{-1} [\text{s}^{-1}]$	0.6 ± 0.1	0.08 ± 0.01
$K_D [\mu\text{M}]$	83 ± 14	2500 ± 200
$k_{catapp} [\text{s}^{-1}]$	0.51 ± 0.01	0.39 ± 0.01
$K_{Mapp} [\mu\text{M}]$	38 ± 3	1300 ± 100
$k_{catapp} / K_{Mapp} (\text{M}^{-1} \text{ s}^{-1})$	$1.3 \cdot 10^4 \pm 0.2 \cdot 10^4$	300 ± 30

Therefore, we also analyzed the reoxidation of photoreduced- and substrate-reduced protein by molecular oxygen in a stopped-flow apparatus. While photoreduced hD2HGDH was reoxidized within a couple of seconds (k_{ox} : $2.1 \cdot 10^4 \pm 0.1 \cdot 10^4 \text{ M}^{-1} \text{ s}^{-1}$), the rate of reoxidation observed for the substrate-reduced enzyme was about 1500-fold lower (k_{ox} : $14 \pm 1 \text{ M}^{-1} \text{ s}^{-1}$), suggesting that the reaction products, *i.e.* α -ketoglutarate or pyruvate, remain bound to the enzyme and suppress oxygen reactivity. Interestingly, however, the addition of α -ketoglutarate to photoreduced hD2HGDH did not affect the rate of reoxidation, indicating that the protein undergoes conformational changes during substrate oxidation, creating a binding pocket for the product.

Electron transfer from hD2HGDH to hETF

It was previously assumed that reduced hD2HGDH may transfer electrons to hETF, which is known to service several dehydrogenases in the mitochondrial matrix and thus serves as a central electron acceptor. In order to substantiate this assumption experimentally, we investigated the putative transfer of electrons from reduced hD2HGDH to hETF under steady-state conditions. Briefly, hETF (10 μM) was mixed with 1 μM of hD2HGDH and 1 mM of D2HG in a stopped-flow device and the changes in the UV-visible absorption spectrum of hETF were monitored for 150 s. Within the first 10 s, a strong absorbance increase at 375 nm and a strong decrease at 450 nm were observed (Figure 3A, *black line to cyan line*), indicating the formation of an anionic flavin semiquinone species and confirming the successful electron transfer from hD2HGDH to hETF. The radical flavin species, however, was not stable over time and was further reduced to the hydroquinone form within the next 100 s (Figure 3A, *cyan line to purple line*). Therefore, it can be concluded that hETF can accept two electrons from hD2HGDH, with the transfer of the second electron being about 10-fold slower than of the first.

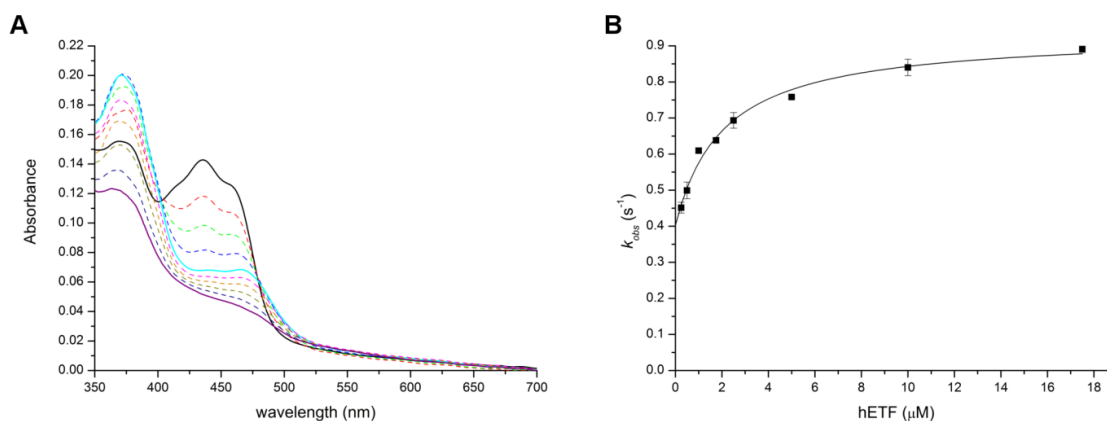


Figure 3: Electron transfer from hD2HGDH to hETF. **A**, Electron transfer from reduced hD2HGDH to hETF was studied under anoxic conditions in 50 mM HEPES, 150 mM NaCl pH 7. 10 μM hETF and 1 μM substrate-reduced hD2HGDH (excess of substrate \rightarrow 1 mM D-2HG) were mixed in a stopped-flow device and changes in the absorption characteristics of hETF were monitored between 350 and 700 nm for 150 s. Within the first 10 s, formation of an anionic flavin semiquinone species was observed (*black to light blue* line), indicating the transfer of single electrons from hD2HGDH to hETF. However, the radical species was not stable over time and full reduction to the hydroquinone form was observed after 150 s (*light blue* line to *purple* line). **B**, The rate of electron transfer from hD2HGDH to hETF was studied using a coupled assay with DCPIP as final electron acceptor. hD2HGDH (100 nM), DCPIP (125 μM) and varying concentrations of hETF (0.25 to 17.5 μM) were mixed in 50 mM HEPES pH 7 and incubated at 25°C for 10 min. Then, D-2HG (1 mM) was added and changes in the absorbance at 600 nm were recorded for 120 s. By plotting the extracted initial velocities as a function of the hETF concentrations, a hyperbolic curve was obtained, which allowed the determination of the limiting rate (k_{catapp}) as well as of the K_{Mapp} -value for the electron transfer from hD2HGDH to hETF (k_{catapp} : $0.53 \pm 0.03 \text{ s}^{-1}$; K_{Mapp} : $2.1 \pm 0.5 \mu\text{M}$).

For a more detailed characterization of the electron transfer process, we then performed a coupled assay with DCPIP as terminal electron acceptor. By studying the rates of electron transfer in the presence of different hETF concentrations, a limiting rate (k_{cat}) as well as a K_M value for the interaction between reduced hD2HGDH and hETF could be obtained (Figure 3B, Table 2).

Table 2: Kinetic parameters determined for the electron transfer from D2HGDH to hETF under steady-state conditions. The steady-state parameters for the electron transfer were determined in a coupled assay involving 1 mM D-2-hydroxyglutarate, 100 nM hD2HGDH, 125 μM DCPIP and varying concentrations of hETF (0.25 to 17.5 μM) in 50 mM HEPES, 150 mM NaCl pH 7. By monitoring the decrease in absorbance of DCPIP at 600 nm for 120 s, initial rates could be obtained and plotted as function of the hETF concentrations to yield the kinetic parameters k_{catapp} and K_{Mapp} .

kinetic parameters	D- α -hydroxyglutarate
$k_{catapp} [\text{s}^{-1}]$	0.53 ± 0.03
$K_{Mapp} [\mu\text{M}]$	2.1 ± 0.5

The rather low K_M value of $2.1 \pm 0.5 \mu\text{M}$ indicates a relatively high affinity of the reduced donor enzyme to hETF, however, electron transfer looks to be less efficient as compared with other client enzymes (k_{cat} : $0.53 \pm 0.03 \text{ s}^{-1}$ vs. $\sim 2 \text{ s}^{-1}$ for hDMGDH, hMCAD) under the same assay conditions (11, 12).

Production, purification and characterization of two pathogenic variants of hD2HGDH

Recent studies aiming to understand the molecular causes of D-2-hydroxyglutaric aciduria revealed two pathogenic single nucleotide replacements in the respective gene (c.440T→G and c.1331T→C), leading to single amino acid exchanges in the mature protein (Ile147Ser and Val444Ala; Figure 4A and B).

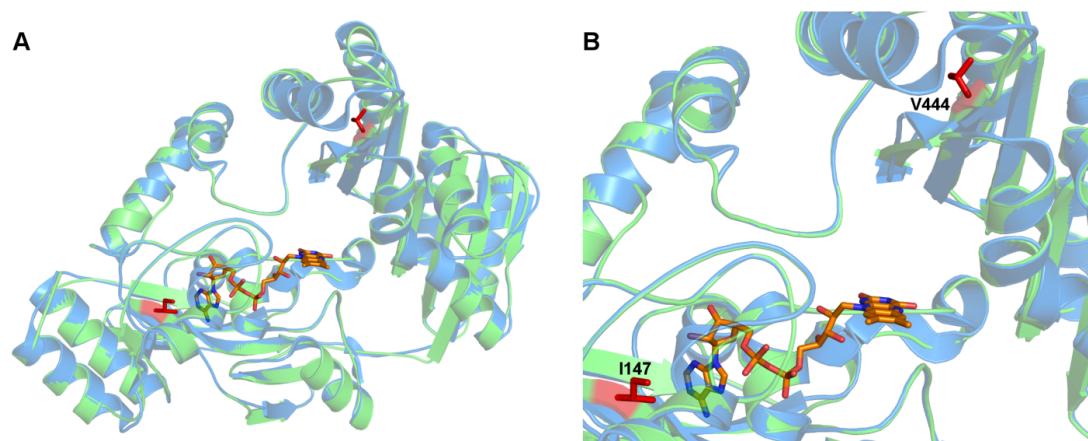


Figure 4: Structural model of hD2HGDH. **A**, Overall structural model of hD2HGDH (green) generated based on the crystal structure of a putative dehydrogenase (RPA1076) from *Rhodospseudomonas palustris* CGA009 (PDB code, 3pm9; blue). Several patients diagnosed with D-2-hydroxyglutaric aciduria were found to suffer from deficiencies of hD2HGDH, resulting from single pathogenic amino acid replacements of either one of the two amino acid residues displayed as red sticks (Ile147 and Val444); Ile147 and Val444 were found to be replaced by a serine (Ile147Ser) or an alanine (Val444Ala), respectively. **B**, Close-up view of the active site with the two important amino acid residues altered in patients suffering from D-2-hydroxyglutarate dehydrogenase deficiency shown as red sticks (Ile147 and Val444).

It was shown that both protein variants exhibit much lower activity (Ile147Ser: 0% and Val444Ala: 25%) as compared with the wild type in a cell-line based assay. However, the reasons for the dramatic loss in catalytic activity remained elusive (1). In order to address this question, we recombinantly produced both variants with an *N*-terminal GB1-tag in *E. coli*. In contrast to the wild type protein, both variants were obtained as apo-proteins, indicating that they exhibited severely impaired flavin binding properties. Since hD2HGDH requires the flavin cofactor for proper enzymatic function, this fact explains the loss in catalytic activity found in a radiochemical assay performed by Struys *et al.* (2005) (1). The presence of an excess of FAD, *i.e.* 50 and 500 μ M FAD failed to restore the catalytic activity of the variant proteins. For both variants residual activities in the range of 0.1% of the wild type enzyme were obtained indicating that flavin binding was seriously compromised by the single amino acid replacements.

To further assess the structural properties of the variant proteins the CD-spectrum of the wild type and the two protein variants were recorded. This analysis revealed no significant difference in secondary structure elements between the wild-type and the two variant proteins (Figure 5A and Table 3),

indicating some other factor to be responsible for the reduced FAD binding affinity and enzymatic activity. Therefore, we decided to also investigate the proteolytic stability of the variants compared to wild type hD2HGDH. Interestingly, both of them showed a strongly reduced susceptibility for proteolytic degradation as compared to the wild type (Figure 5B), which is a strong indication for the variants to be aggregated. This supposition was further tested by subjecting purified samples of wild type and variant proteins to analytical size-exclusion chromatography. As shown in Figure 5C, this clearly demonstrated that the two variants form aggregates, whereas the wild type protein is a dimer in solution.

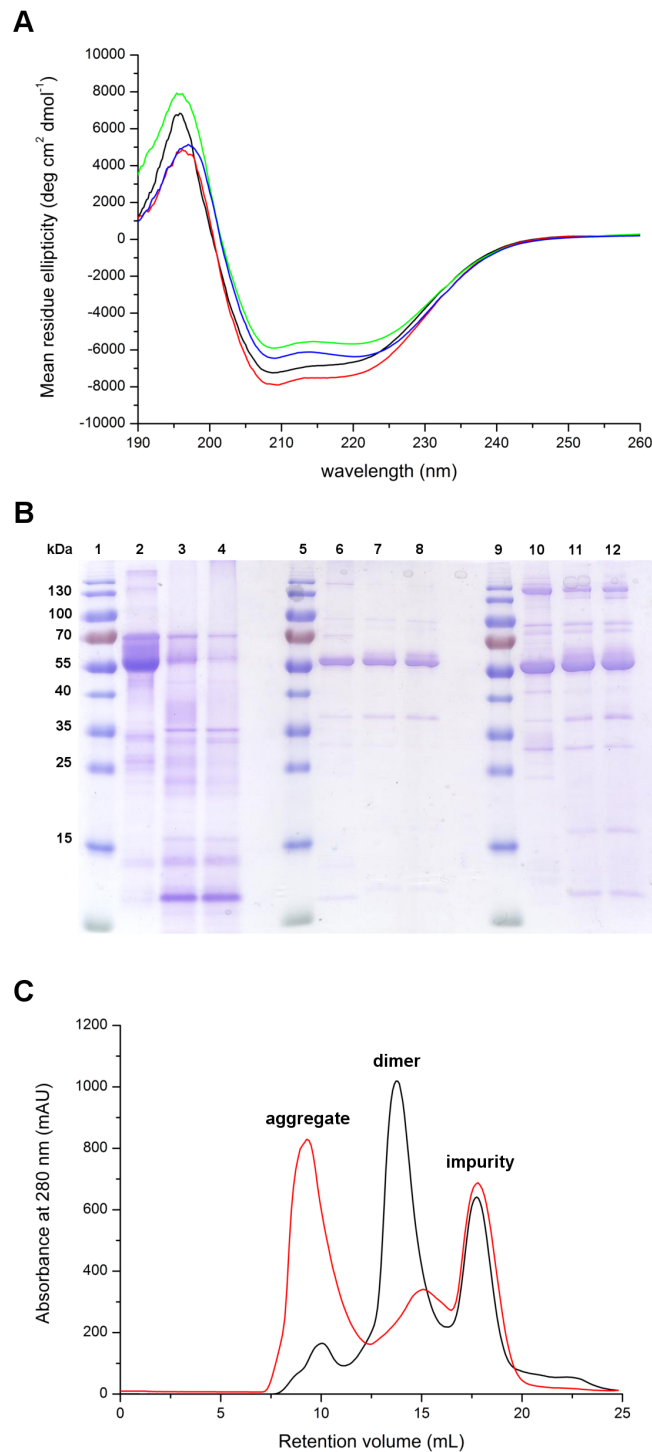


Figure 5: Biochemical and biophysical characterization of hD2HGDH wild type, GB1-hD2HGDH wild type, GB1-hD2HGDH-I147S and GB1-hD2HGDH-V444A. **A**, CD-spectra obtained with hD2HGDH wild type (*black* line), GB1-hD2HGDH wild type (*red* line), GB1-hD2HGDH-I147S (*green* line), and GB1-hD2HGDH-V444A (*blue* line). The proteins were rebuffered to 50 mM NaH₂PO₄ pH 7 and diluted to a final concentration of 11, 11, 16, and 19 μM, respectively. Then, the solutions were transferred to cuvettes (d, 0.1 cm) and CD-spectra were recorded at 20 °C between 260 and 190 nm and averaged over three scans. **B**, SDS-PAGE analysis of the limited proteolysis experiment performed with GB1-hD2HGDH wild type, GB1-hD2HGDH-I147S, and GB1-hD2HGDH-V444A. In lanes 1, 5, and 9 PageRuler® prestained protein ladder (Thermo Fisher Scientific) is depicted, whereas in the remaining lanes the fragmentation pattern of GB1-hD2HGDH wild type (lane 2-4), GB1-hD2HGDH-I147S (lane 6-8), and GB1-hD2HGDH-V444A (lane 10-12) after 0, 90, and 180 min is shown. **C**, Chromatogram obtained in the course of the gel filtration of GB1-hD2HGDH wild type (*black* line) and GB1-hD2HGDH-I147S (*red* line) using a Superdex200 increase column (10/300 GL) equilibrated with 50 mM HEPES, 150 mM NaCl pH 7. The elution pattern indicates the wild type protein to be a dimer in solution, whereas the variants seem to form aggregates.

Table 3: Secondary structure prediction for hD2HGDH wildtype, GB1-hD2HGDH wild type, and the two protein variants GB1-hD2HGDH-I147S and GB1-hD2HGDH-V444A. Wild type and variant proteins were diluted to a final concentration of 11 and 16/19 μM, respectively, using 50 mM NaH₂PO₄ pH 7. Then, CD-spectra were recorded between 260 and 190 nm, which allowed subsequent secondary structure prediction using the online program DichroWeb (38–40).

Secondary structure	hD2HGDH wild type	GB1-hD2HGDH wild type	GB1-hD2HGDH-I147S	GB1-hD2HGDH-V444A
α-helix (%)	21	24	19	20
β-sheet (%)	26	24	30	28
turn (%)	14	14	13	13
random (%)	39	39	37	38

* the CD-spectra were analyzed using the program CDSSTR (42, 43) and the SP175 reference dataset (44) between 190 and 240 nm.

Discussion

Kinetic characterization of hD2HGDH

The successful recombinant production of hD2HGDH as fusion construct with the solubility enhancer GB1 in *E. coli* enabled the detailed biochemical characterization of hD2HGDH and allowed to establish its suspected interaction with the human electron transferring flavoprotein (hETF). Kinetic characterization revealed that hD2HGDH is able to efficiently catalyze the oxidation of D-2HG as well as of D-lactate, though the reduction rates determined with the latter substrate were almost a factor of 5 lower as compared with D-2HG (k_{red} : $1.9 \pm 0.1 \text{ s}^{-1}$; $0.39 \pm 0.05 \text{ s}^{-1}$, respectively). Also, the dissociation constants obtained for D-lactate were much higher than with D-2HG indicating that D-

2HG is more efficiently oxidized by the enzyme. Steady-state experiments showed that k_{catapp} was 4-5-times lower with D-2HG than the limiting rate of reduction (Table 1) suggesting that the oxidative half-reaction was rate-limiting under these conditions. Nevertheless, this is in agreement with the low reoxidation rates obtained with substrate-reduced hD2HGDH as compared with photoreduced enzyme, indicating that the reaction products form a complex with reduced enzyme and thereby influence oxygen reactivity. The formation of such a product-reduced enzyme complex is also in line with the increase in longer wavelength absorbance observed in our rapid-reactions studies (Figure 2A), which indicates the presence of a charge-transfer complex. However, the effect was more pronounced when the enzyme was reduced by D-2HG, which is in agreement with the fact that α -ketoglutarate is probably bound more tightly to hD2HGDH than pyruvate.

How flavoenzymes exert control over the reactivity of the reduced cofactor with dioxygen is a longstanding topic in this research field (13–15). Mostly, oxygen reactivity is an intrinsic feature of the proteins (13, 16, 17), however, in the case of classical client dehydrogenases, *e.g.* the family of acyl-CoA dehydrogenases, a similar concept of product-controlled oxygen reactivity has already been described (18–20). In these enzymes, product binding is required to shift the equilibrium of acyl-CoA oxidation toward flavin reduction, in the first place. This was shown to be necessary, since the redox potentials of the substrates are similar or even more positive than the reduction potential of the protein-bound flavin, thus making substrate conversion rather unfavorable (18–20). At the same time, product binding is used to increase the hydrophobicity in the active site, thereby impeding the stabilization of superoxide species required for the reoxidation of reduced flavin cofactors by molecular oxygen (21). Just recently it could be shown that also Dld2 from *Saccharomyces cerevisiae* controls oxygen reactivity by product binding (+Chapter 5). However, in contrast to acyl-CoA dehydrogenases the reduced activity toward dioxygen appears to be the result of conformational changes that take place in the course of substrate binding and conversion to the oxidized product (+Chapter 5). Since only the presence of α -ketoglutarate was not sufficient to prohibit reoxidation of reduced hD2HGDH by molecular oxygen and considering that the enzyme is an ortholog of Dld2, it is very likely that hD2HGDH controls oxygen reactivity in a similar way as the yeast counterpart.

Electron transfer to hETF

The hETF services at least thirteen different dehydrogenases in the mitochondrial matrix, including the acyl-CoA dehydrogenases required for fatty acid and amino acid degradation (12). Based on the observation that D-2HG accumulates as a result of defects in either the hETF or its final electron acceptor ETF-QO (22), hD2HGDH was also proposed to be a client enzyme of hETF, however, the interaction was not tested experimentally so far. In the present study, we could clearly demonstrate that reduced hD2HGDH is indeed capable of donating electrons to hETF and thus this enzyme can be safely added to the list of hETF clients. While oxygen reactivity is strongly suppressed in substrate-

reduced hD2HGDH (see above), electron transfer to hETF readily occurs as could be shown by mixing hETF with catalytic amounts of hD2HGDH and an excess of D-2HG in a stopped-flow device (Figure 3A). Spectral analysis of the reduction of hETF by hD2HGDH revealed a fast transfer of single electrons, resulting in the generation of an anionic flavin semiquinone, which was subsequently further reduced to the hydroquinone, albeit at a 10-times slower rate. This behavior is quite similar to the interaction of hETF with other clients such as the acyl-CoA dehydrogenases (20, 23–25). Like hD2HGDH, substrate reduced acyl-CoA dehydrogenases exhibit rather poor reactivity toward molecular oxygen, but undergo rapid one-electron transfer reactions with hETF (19, 23). Whether the mechanisms used to guarantee successful electron delivery to hETF are the same in both enzymes is presently unclear. Given the differences in the three-dimensional structure of the family of acyl-CoA dehydrogenases (acyl-CoA dehydrogenase-fold) and of D-lactate/D-2-hydroxyglutarate dehydrogenase (*p*-cresol methylhydroxylase-fold), it is conceivable that the molecular mechanisms enabling successful electron transfer are also distinct. In any case, being able to control oxygen reactivity is important to ensure the delivery of electrons to the mitochondrial electron transport chain and at the same time limits the production of undesired reactive oxygen species, such as hydrogen peroxide.

Interestingly, the overall turnover rates determined for the electron transfer from hD2HGDH to hETF are in a similar range, but slightly lower as compared with other client dehydrogenases ($0.53 \pm 0.03 \text{ s}^{-1}$ vs $\sim 2 \text{ s}^{-1}$ of hDMGDH and hMCAD). However, it should be noted that the interaction of hETF with hD2HGDH is tighter as compared with other donor dehydrogenases ($K_M = 2.1 \pm 0.5 \text{ }\mu\text{M}$ vs $\sim 70 \text{ }\mu\text{M}$ and $\sim 8 \text{ }\mu\text{M}$ for hDMGDH and MCAD, respectively) (11, 12), which requires the use of very low hETF concentrations (lowest hETF concentration: 250 nM vs 100 nM hD2HGDH) in the turnover assay. Therefore, it is possible that reduced hD2HGDH to some extent directly transfers electrons to DCPIP, thereby seemingly lowering the turnover rates for the electron transfer from hD2HGDH to hETF. This interpretation is also in line with the fact that by applying a hyperbolic fit to the data points, a y-axis intercept at a k_{obs} of $\sim 0.4 \text{ s}^{-1}$ was obtained, which is in the same range as the limiting rate (k_{catapp}) determined for the oxidation of D-2HG by hD2HGDH in the DCPIP assay (see above).

Disease related variants

Recently, two disease-causing mutations in the *hg2hgdh* gene have been identified in patients suffering from D-2HGA (1). Although it was shown that the enzymatic activity of the resulting protein variants (hD2HGDH-Ile147Ser and hD2HGDH-Val444Ala) was severely reduced, the reason for the loss in protein function remained elusive, in particular because the position(s) of the amino acid replacement(s) as well as the conservative nature of the exchange(s) did not provide a straight forward explanation (1). Thus, we produced the two variants in *E. coli* to investigate the loss of activity in more detail. Both variants were isolated as apo-proteins and the addition of FAD could not reconstitute

the holo-protein. This finding was surprising because neither one of the positions where the amino acid replacements have occurred appears to be involved in FAD binding (Figure 4). In order to better understand the lack of FAD binding, we performed CD-spectroscopy and limited proteolysis experiments as well as size-exclusion chromatography. We could clearly show that while the secondary structure elements largely remained unaffected by the single amino acid replacements (Figure 5A and Table 3), their quaternary structures were strongly impaired (Figure 5B and C). Size exclusion chromatography, for example, revealed that both variants exhibit an increased tendency toward aggregate formation, whereas the wild type enzyme is a dimer in solution. This fact is also in agreement with the results obtained from the limited proteolysis experiment, which revealed a reduced susceptibility of the variants to proteolytic degradation, and may explain the decreased binding affinity of the FAD cofactor as compared to the wild type enzyme.

The findings are also very well in line with the observation of Struys *et al.* (2005) that the replacement of Ile147 by a serine results in a complete loss in enzymatic activity, but they do not explain the residual activity of 25% determined for the Val444Ala variant (1). However, there are several reasons, why different results could have been obtained in our study, as compared to Struys *et al.* (1). Firstly, the completely diminished oxidase activity observed in our studies might result from the recombinant production of the protein in *E. coli*. While humans employ a set of chaperones in order to ensure properly-folded proteins, the latter are absent in the bacterial expression system. On the other hand, co-production of the chaperonin complex GroES/GroEL in *E. coli* failed to reduce the amount of catalytically inactive aggregate. Apart from the presence of molecular chaperones, also the availability of free FAD was reported to affect protein folding and activity (26, 27). Studies by Saijo *et al.* (26) and Cornelius *et al.* (27), for example, have shown that increasing the levels of riboflavin in the culture media reduced the aggregation of defective MCAD and ETF-QO variants, resulting in a higher activity of these proteins. However, in the case of the two hD2HGDH variants the amount of aggregate could not substantially be reduced by riboflavin supplementation in the culture medium. Nevertheless, since vitamin B₂ supplementation has been successfully used for the treatment of milder forms of multiple acyl-CoA dehydrogenase deficiency (MADD) and glutaric aciduria type I and II (28–30), it is conceivable that increased riboflavin levels may have a beneficial effect on the activity of the variant proteins *in vivo*.

Conclusions

In the present study, we have established the kinetic parameters for the oxidation of D-lactate and D-2HG by hD2HGDH, which have clearly identified D-2HG as the preferred substrate. We have also shown that product binding to the reduced enzyme suppresses the reactivity with oxygen and turns the enzyme into a dehydrogenase. Moreover, we have provided experimental evidence that substrate-reduced enzyme transfers electrons to hETF and thus oxidation of D-2HG is coupled to the

mitochondrial electron transport chain. Finally, our results also explain the lack of enzymatic activity in two disease-related variants discovered in patients suffering from D-2HGA.

Experimental procedures

Materials

All chemicals and media ingredients were purchased from Sigma-Aldrich (St. Louis, MO, USA), Roth (Karlsruhe, Germany), Merck (Darmstadt, Germany) or Fluka (Buchs, Switzerland) and were of the highest grade commercially available.

All restriction enzymes used were ordered from Thermo Scientific/Fermentas (Waltham, MA, USA) or New England Biolabs (Ipswich, MA, USA) and Ni-NTA columns were obtained from GE Healthcare (Chalfont St. Giles, UK).

Cloning and recombinant production of hD2HGDH

With the initial plan of expressing full-length hD2HGDH (just without the *N*-terminal signal peptide predicted by Signal P (31)) in *Komagataella phaffii*, the gene was purchased from Thermo Fisher Scientific (Waltham, MA, USA), codon optimized for expression in the yeast organism. On ordering, additionally, a nucleotide sequence coding for an octahistidine-tag was fused to the 3' end of the gene. Since expression in *Komagataella phaffii* was not successful, a truncated version of the gene lacking the coding sequence of the first 53 amino acid residues at the *N*-terminus and the *C*-terminal histidine-tag was generated using PCR (fwd. primer: 5'-TAATCCATGGTCCAGAGATTGCCATTCTCCACTGTTTCC-3' and rev. primer: 5'-ATATGCGGCCGCCTAAGCCTGAGATGGCAAGGTCTTG-3'). After restriction digestion with *NcoI* and *NotI*, the DNA string was inserted into the vector pETM11-His-GB1 TEV Appa, which added nucleotides coding for an additional *N*-terminal hexahistidine-tag, as well as for the fusion protein GB1 (B1 domain of *Streptococcal* protein G). Having confirmed the construct by sequencing, the recombinant plasmid was transformed with *E. coli* Rosetta (DE3)-pLysS cells for subsequent gene expression.

For production, LB medium containing 50 µg/mL kanamycin as well as 20 µg/mL chloramphenicol for selection was inoculated with an overnight culture to an optical density of approximately 0.1. Then, cultures were left to grow to an optical density at 600 nm (OD₆₀₀) of about 0.8-0.9 at 37°C and 140 rpm, before adding 100 µM IPTG to induce gene expression. To maximize the protein yield, the cultures were incubated at 20 °C and 140 rpm overnight (about 16 h).

Harvested cells were resuspended in binding buffer (50 mM HEPES, 150 mM NaCl, 10 mM imidazole, pH 7 or 8 + 1 mM DTT) and lysed by sonication with a Labsonic L sonication probe (B. Braun Biotech, Berlin, Germany) for 2 x 5 min. After centrifugation at 38,500 g for 1 h (4 °C), the

cleared cell lysate was loaded onto a Ni-NTA column equilibrated with binding buffer (without DTT). Unspecifically bound protein was washed off with wash buffer (50 mM HEPES, 150 mM NaCl, 20 mM imidazole, pH 7 or 8 + 1 mM DTT) and GB1-hD2HGDH was eluted with elution buffer (50 mM HEPES, 500 mM imidazole, pH 7 or 8 + 1 mM DTT). To confirm the presence of the desired protein in the fractions as well as to determine the quality of the purification, SDS-PAGE analysis was used. Fractions containing GB1-hD2HGDH were pooled and buffer was exchanged to 50 mM HEPES, 150 mM NaCl pH 7 or 8 by repeated concentration and dilution using Centripreps® 30 kDa MWCO (Merck Millipore, Burlington, MA, USA).

Because substantial amounts of impurities were detected on the SDS-PAGE right after purification via Ni-NTA chromatography, an additional gel filtration step was introduced, if no TEV-digestion (see below) was performed. The protein was applied to a Superdex200 increase (10/300 GL) column equilibrated with 50 mM HEPES, 150 mM NaCl pH 7 and elution of the protein was followed by monitoring the spectral changes at 280, 375 and 450 nm using a DAD. Presence of GB1-hD2HGDH in the fractions was again confirmed by SDS-PAGE analysis. Fractions containing pure GB1-hD2HGDH were pooled and buffer was exchanged to 50 mM HEPES, 150 mM NaCl pH 7. Concentrated protein (about 100 μ M) was flash frozen with liquid nitrogen and stored at -80 °C until further use.

To remove the solubility enhancer (GB1) from hD2HGDH, tobacco etch virus (TEV)-digestion was performed overnight. The protein solution containing the fusion construct was mixed with the protease in a 10:1 (m/m) ratio and incubated at 4°C for 16 h. Then, another affinity-chromatography purification was performed (as described above), yielding hD2HGDH in the flow-through fraction (and wash fraction with 50 mM imidazole). GB1 and not digested GB1-hD2HGDH, in contrast, remained bound to the column and could only be stripped off with elution buffer. To confirm the presence of the desired protein in the fractions as well as to determine the quality of the purification, again, SDS-PAGE analysis was used. Fractions containing pure hD2HGDH were pooled and buffer was exchanged to 50 mM HEPES, 150 mM NaCl pH 7. Concentrated protein (about 100 μ M) was flash frozen with liquid nitrogen and stored at -80 °C until further use.

Protein denaturation and determination of the extinction coefficient of hD2HGDH

To determine the extinction coefficient of hD2HGDH, a spectrum of native as well as of denatured hD2HGDH was recorded as suggested by Macheroux (32). Assuming that the spectrum of the denatured protein equals the one of free FAD, the extinction coefficient of free FAD (11,300 $M^{-1} cm^{-1}$ at 450 nm) could be used to calculate the extinction coefficient of hD2HGDH at 450 nm (11,600 \pm 300 $M^{-1} cm^{-1}$).

Photoreduction of hD2HGDH

Photoreduction was performed under anoxic conditions as described by Massey (1978) (33). A protein solution containing 10 μM hD2HGDH, 2.5 mM EDTA, 7.5 μM methylviologen, and 1 μM 5-deaza-FMN was rendered anaerobic and transferred to a sealable quartz cuvette. After recording a UV-visible spectrum between 300 and 800 nm, the sample was irradiated and additional spectra were recorded at a constant temperature of 15 °C, until no further spectral changes were observed. Then, the lid was removed under aerobic conditions to initiate reoxidation of the protein, which again was monitored spectrophotometrically.

Determination of the redox potential of hD2HGDH

The redox potential of hD2HGDH was studied under anoxic conditions using a stopped flow device from Hi-Tech (SF-61DX2) placed in an anaerobic glove box (Belle Technology, Cambridge, UK) by applying the dye equilibrium method based on the xanthine/xanthine oxidase system, as reported by Massey (9). Two solutions, one containing ~ 25 μM hD2HGDH, 500 μM xanthine, and 5 μM methylviologen and a second one with ~ 20 μM roseoFMN (A_{525} : ~ 0.2 ; E° : -252 mV) and ~ 200 nM xanthine oxidase, were prepared in 50 mM HEPES, 150 mM NaCl pH 7 and mixed using the stopped flow device. Then, reduction of the flavin and the dye was monitored by recording 500 absorption spectra (350 to 700 nm) with a KinetaScanT diode array detector (MG-6560) within 25 min (four measurements). From these data a Nernst plot was generated by plotting the log ($[\text{ox}]/[\text{red}]$) of the enzyme as a function of the log ($[\text{ox}]/[\text{red}]$) of the dye - to determine the log($\text{hD2HGDH}_{\text{ox}}/\text{hD2HGDH}_{\text{red}}$) and the log($\text{dye}_{\text{ox}}/\text{dye}_{\text{red}}$) the relative absorption changes at 450 nm and 525 nm, respectively, were used. Using the resulting intercept the redox potential of hD2HGDH could be determined as described by Minnaert (34).

Homology model of hD2HGDH

A homology model of hD2HGDH was generated with the SWISS-MODEL server (35–37) using the crystal structure of a putative dehydrogenase (RPA1076) from *Rhodospseudomonas palustris* CGA009 as template (pdb: 3pm9). The flavin cofactor depicted in the figure was modeled into the predicted structure of hD2HGDH by aligning the two proteins and copying the flavin moiety from the putative dehydrogenase from *Rhodospseudomonas palustris* to the active site of the human D-2-hydroxyglutarate dehydrogenase.

Reductive and oxidative half-reaction

To study the reductive and oxidative half-reaction (of hD2HGDH), time dependent spectral changes of the flavin absorption were recorded under anoxic conditions using a stopped flow device (Hi-Tech, TgK Scientific, Bradford-on-Avon, UK), placed in a glove box (Belle Technology, Cambridge, UK), and monitored with a KinetikaScanT diode array detector (MG-6560). The following analysis was performed by fitting the data points recorded at 450 nm with the Kinetic Studio Software (TgK Scientific).

For the determination of the reduction rate of hD2HGDH, its flavin reduction was studied in the presence of eight different D-2-hydroxyglutarate (final concentration: 25 μ M to 1000 μ M) and nine D-lactate (final concentration: 0.5 mM to 75 mM) concentrations. A 20 μ M enzyme solution and the substrate solutions were prepared in 50 mM HEPES, 150 mM NaCl pH 7, before mixing them in the stopped flow device and recording the spectral changes between 350 and 700 nm (measurements were performed 4-times at each substrate concentration). The extracted observed rate constants (k_{obs}) were plotted as a function of the respective substrate concentrations to obtain a hyperbolic curve, which allowed determination of the limiting reduction rates (k_{red}) as well as of the dissociation constants (K_d). To study the effect of product binding on the rate or reoxidation, one sample of reduced hD2HGDH (10 μ M) was generated using photoreduction (see above) and a second one by adding about 1.5 eq of D- α -hydroxyglutarate. Then, both samples were mixed with air saturated buffer (20°C) in a stopped flow device and spectral changes between 350 nm and 700 nm were monitored for 1.5 - 3 s and 25 - 50 min, respectively. To obtain bimolecular reoxidation rates, the observed rate constants were divided by the final oxygen concentration in the reaction mixture (final concentration: 140 μ M).

Electron transfer from hD2HGDH to hETF

To study the electron transfer from hD2HGDH to hETF, hETF was diluted to a final concentration of 20 μ M using 50 mM HEPES, 150 mM NaCl pH 7 and mixed with 2 μ M hD2HGDH (in the presence of 1 mM of D-2HG) in a stopped-flow device (Hi-Tech, TgK Scientific, Bradford-on-Avon), placed in an anaerobic glove box (Belle Technology, Cambridge, UK). The resulting time dependent spectral changes were monitored between 350 and 700 nm using a KinetikaScanT diode array detector (MG-6560) for 150 s.

Steady-state kinetics (hD2HGDH)

To determine the kinetic parameters of hD2HGDH under steady-state conditions, a coupled assay with DCPIP as final electron acceptor was used. Solutions containing 100 nM hD2HGDH and 125 μ M DCPIP were prepared in 50 mM HEPES, 150 mM NaCl pH 7 and incubated at 25 °C for 10 min.

Then, the reactions were started by adding varying final concentrations of D-2HG (6.25 μM to 1000 μM) or D-lactate (0.25 mM to 25 mM) and absorbance changes at 600 nm were recorded for 120 s. By plotting the extracted initial rates as a function of the corresponding substrate concentrations the kinetic parameters K_{Mapp} and k_{catapp} could be determined.

Steady-state analysis of the electron transfer from hD2HGDH to hETF

Steady-state parameters for the electron transfer of hD2HGDH to wild type hETF were determined in a coupled assay with DCPIP as final electron acceptor. Buffer (50 mM HEPES, 150 mM NaCl pH 7), hD2HGDH (100 nM), hETF (0.25 to 17.5 μM), and DCPIP (125 μM) were mixed and incubated at 25 °C for 10 minutes. Then, the reaction was started by adding 1 mM D- α -hydroxyglutarate, and the decrease in absorbance at 600 nm was monitored at 25°C for 120 s (measurements at each hETF concentration were performed in triplicate). To determine the kinetic parameters K_{Mapp} and k_{catapp} the extracted initial velocities (normalized to enzyme concentration) were plotted as a function of the respective hETF concentration yielding a hyperbolic curve, which was fitted using the program Origin 7 (OriginLab, Northampton, MA, USA).

Site-directed mutagenesis

The two hD2HGDH-variants were generated from the wild type construct pETM11-GB1-hD2HGDH using PCR-based mutagenesis (for primers see Table 4). Having confirmed the variation in the nucleotide sequence by automated sequencing, the plasmids were transformed with *E. coli* Rosetta (DE3)-pLysS cells for subsequent gene expression. Protein production and purification were then performed as described for the wild type protein (*Cloning and recombinant production of hD2HGDH*).

Table 4: Mutagenesis primers required for the generation of the hD2HGDH-variants in a PCR-based approach (the codon triplets carrying the desired mutations in the nucleotide sequence are shown in bold).

Primer name	Primer sequence
I147S fwd.	5'-CAGTTTTCGACGAGAT TCT CTTTGTCCACCGC-3'
I147S rev.	5'-CTGGCGGTGGACAAAGAG AT CTCGTCG-3'
V444A fwd.	5'-GGTAACTTGC ACT TGAACGCTACTGCTGAGGC-3'
V444A rev.	5'-GGAGAAAGCCTCAGCAG TAG CGTTCAAGTGC-3'

Co-production of GB1-hD2HGDH variants and the groES-groEL complex

For co-production of GB1-hD2HGDH and the groES/groEL-complex, pET-M11-GB1-hD2HGDH-I147S and -V444A plasmid DNA was transformed with *E. coli* BL21 (DE3) cells already harboring the pGro7-plasmid.

For protein production, LB medium containing 50 µg/mL kanamycin as well as 20 µg/mL chloramphenicol for selection and 0.5 mg/mL of L-arabinose to initiate chaperone expression was inoculated with an overnight culture to an optical density of approximately 0.1. Then, cultures were left to grow to an optical density at 600 nm (OD₆₀₀) of about 0.8-0.9 at 37°C and 140 rpm, before adding 100 µM IPTG to induce gene expression. To maximize the protein yield, the cultures were incubated at 20 °C and 140 rpm overnight (about 16 h). Purification was carried out as described above (*Cloning and recombinant production of hD2HGDH*).

Production of GB1-hD2HGDH variants in the presence of increased riboflavin levels in the culture medium

To study the effect of increased riboflavin levels on protein folding, GB1-hD2HGDH-Ile147S and GB1-hD2HGDH-Val444Ala were again produced as described previously. However, the culture medium was supplemented with 0.1 mM of riboflavin. Additionally, FAD (100 µM) was added to all buffers used in the course of the affinity purification of the proteins.

CD-spectroscopy

In order to study the influence of the two pathogenic amino acid replacements (Ile147Ser and Val444Ala) on protein folding, CD-spectroscopy experiments were performed. hD2HGDH wild type, GB1-hD2HGDH wild type, GB1-hD2HGDH-Ile147Ser, and GB1-hD2HGDH-Val444Ala were rebuffed to 50 mM NaH₂PO₄ pH 7 and diluted to final concentrations of 11, 11, 16 and 19 µM, respectively. Then, the protein solutions were transferred to cuvettes (d, 0.1 cm) and CD spectra were recorded between 260 and 190 nm in a JASCO J-1500 spectrophotometer (JASCO Inc., Tokyo, Japan) equipped with a PM-593 detector (Scan speed, 50 nm/min; Interval, 0.2 nm; CD-scale, 200 mdeg/1.0 dOD) and averaged over three scans.

Subsequent data analysis was performed using the program Spectral Manager (JASCO Inc., Tokyo, Japan), which also allowed prediction of the secondary structure elements using the online program DichroWeb (38–40).

Limited proteolysis

In order to investigate the proteolytic stability of GB1-hD2HGDH wild type and the two variants, the proteins were diluted to a final concentration of ~15 μ M using 50 mM HEPES, 150 mM NaCl pH 7 and incubated at 37°C for 5 min. Then, trypsin (Promega, Madison, WI, USA) was added (2 μ g/mL) and samples were taken after 0, 30, 60, 90, 120, 150, and 180 min, mixed with Laemmli sample buffer (41), and inactivated at 95°C for 10 min. Finally, SDS-PAGE analysis was performed to determine the fragmentation pattern of the different proteins.

Author contributions

MT, JB and JS cloned the genes, produced the proteins and performed the biochemical characterization of hD2HGDH wild type and the variants; MT, JB and PM designed the biochemical experiments and interpreted the data; MT and PM wrote the manuscript.

Conflict of interest

The authors declare no conflict of interest.

Acknowledgements

We would like to thank Eva Frießer for her help with the production as well as with the purification of GB1-hD2HGDH wild type and the variants and Dr. Gustav Oberdorfer for his assistance with the CD-spectroscopy experiments. This work was supported by a grant from the Austrian Science Fund (FWF) through grant W901 (Doctoral Program “Molecular Enzymology”). The authors are also grateful for the support by the interuniversity program in natural sciences (NAWI Graz).

References

1. Struys, E. A. (2005) Mutations in the D-2-hydroxyglutarate dehydrogenase gene cause D-2-hydroxyglutaric aciduria. *Am J Hum Genet.* **76**, 358–360
2. Kaufman, E. E., Nelson, T., Fales, H. M., and Levin, D. M. (1988) Isolation and characterization of a hydroxyacid-oxoacid transhydrogenase from rat kidney mitochondria. *J. Biol. Chem.* **263**, 16872–16879
3. Struys, E. A., Verhoeven, N. M., Brink, H. J., Wickenhagen, W. V., Gibson, K. M., and Jakobs, C. (2005) Kinetic characterization of human hydroxyacid-oxoacid transhydrogenase: Relevance to D-2-hydroxyglutaric and γ -hydroxybutyric acidurias. *J. Inherit. Metab. Dis.* **28**, 921–930
4. Achouri, Y., Noël, G., Vertommen, D., Rider, M. H., Veiga-da-Cunha, M., and van Schaftingen, E. (2004) Identification of a dehydrogenase acting on D-2-hydroxyglutarate. *Biochem. J.* **381**, 35–42
5. Engqvist, M. K. M., Eßer, C., Maier, A., Lercher, M. J., and Maurino, V. G. (2014) Mitochondrial 2-hydroxyglutarate metabolism. *Mitochondrion.* **19**, 275–281
6. Becker-Kettern, J., Paczia, N., Conrotte, J. F., Kay, D. P., Guignard, C., Jung, P. P., and Linster, C. L. (2016) *Saccharomyces cerevisiae* forms D-2-hydroxyglutarate and couples its degradation to D-lactate formation via a cytosolic transhydrogenase. *J. Biol. Chem.* **291**, 6036–6058
7. Engqvist, M., Drincovich, M. F., Flügge, U. I., and Maurino, V. G. (2009) Two D-2-hydroxyacid dehydrogenases in *Arabidopsis thaliana* with catalytic capacities to participate in the last reactions of the methylglyoxal and β -oxidation pathways. *J. Biol. Chem.* **284**, 25026–25037
8. Kranendijk, M., Struys, E. A., Gibson, K. M., Wickenhagen, W. V., Abdenur, J. E., Buechner, J., Christensen, E., De Kremer, R. D., Errami, A., Gissen, P., Gradowska, W., Hobson, E., Islam, L., Korman, S. H., Kurczynski, T., Maranda, B., Meli, C., Rizzo, C., Sansaricq, C., Trefz, F. K., Webster, R., Jakobs, C., and Salomons, G. S. (2010) Evidence for genetic heterogeneity in D-2-hydroxyglutaric aciduria. *Hum. Mutat.* **31**, 279–283
9. Massey, V. (1991) A simple method for the determination of redox potentials. in *Flavins and Flavoproteins* (Curti, B., Zanetti, G., and Ronchi, S. eds), pp. 59–66, Walter de Gruyter, Como, Italy
10. Mancini-Samuelson, G. J., Kieweg, V., Sabaj, K. M., Ghisla, S., and Stankovich, M. T. (1998) Redox properties of human medium-chain Acyl-CoA dehydrogenase, modulation by charged active-site amino acid residues. *Biochemistry.* **37**, 14605–14612
11. Toogood, H. S., Van Thiel, A., Scrutton, N. S., and Leys, D. (2005) Stabilization of non-productive conformations underpins rapid electron transfer to electron-transferring flavoprotein. *J. Biol. Chem.* **280**, 30361–30366

12. Augustin, P., Toplak, M., Fuchs, K., Gerstmann, E. C., Prassl, R., Winkler, A., and Macheroux, P. (2018) Oxidation of the FAD cofactor to the 8-formyl-derivative in human electron-transferring flavoprotein. *J. Biol. Chem.* **293**, 2829–2840
13. Massey, V., and Ghisla, S. (1983) The mechanism of action of flavoprotein - catalyzed reactions. in *Biological Oxidations* (Sund, H., and Ullrich, V. eds), pp. 114–139, Springer, Berlin, **34**, 114–139
14. Mattevi, A. (2006) To be or not to be an oxidase: challenging the oxygen reactivity of flavoenzymes. *Trends Biochem. Sci.* **31**, 276–283
15. Chaiyen, P., Fraaije, M. W., and Mattevi, A. (2012) The enigmatic reaction of flavins with oxygen. *Trends Biochem. Sci.* **37**, 373–380
16. Lindqvist, Y., Branden, C. I., Mathews, F. S., and Lederer, F. (1991) Spinach glycolate oxidase and yeast flavocytochrome b₂ are structurally homologous and evolutionarily related enzymes with distinctly different function and flavin mononucleotide binding. *J. Biol. Chem.* **266**, 3198–3207
17. Zafred, D., Steiner, B., Teufelberger, A. R., Hromic, A., Karplus, P. A., Schofield, C. J., Wallner, S., and Macheroux, P. (2015) Rationally engineered flavin-dependent oxidase reveals steric control of dioxygen reduction. *FEBS J.* **282**, 3060–3074
18. Johnson, B. D., and Stankovich, M. T. (1993) Influence of two substrate analogues on thermodynamic properties of medium-chain acyl-CoA dehydrogenase. *Biochemistry.* **32**, 10779–10785
19. Ghisla, S., and Thorpe, C. (2004) Acyl-CoA dehydrogenases: A mechanistic overview. *Eur. J. Biochem.* **271**, 494–508
20. Toogood, H. S., Leys, D., and Scrutton, N. S. (2007) Dynamics driving function - New insights from electron transferring flavoproteins and partner complexes. *FEBS J.* **274**, 5481–5504
21. Thorpe, C., and Kim, J.-J. (1995) Structure and mechanism of action of the acyl-CoA dehydrogenases. *FASEB J.* **9**, 718–725
22. Watanabe, H., Yamaguchi, S., Saiki, K., Shimizu, N., Fukao, T., Kondo, N., and Orii, T. (1995) Identification of the D-enantiomer of 2-hydroxyglutaric acid in glutaric aciduria type II. *Clin. Chim. Acta.* **238**, 115–124
23. Gorelick, R. J., Schopfer, L. M., Ballou, D. P., Massey, V., and Thorpe, C. (1985) Interflavin oxidation-reduction reactions between pig kidney general acyl-CoA dehydrogenase and electron-transferring flavoprotein. *Biochemistry.* **24**, 6830–6839
24. Reinsch, J., Katz, A., Wean, J., Aprahamian, G., and McFarland, J. T. (1980) The deuterium isotope effect upon the reaction of fatty acyl-CoA dehydrogenase and butyryl-CoA. *J. Biol. Chem.* **255**, 9093–9097
25. Hall, C. L., and Lambeth, J. D. (1980) Studies on electron transfer from general acyl-CoA dehydrogenase to electron transfer flavoprotein. *J. Biol. Chem.* **255**, 3591–3595

26. Saijo, T., Kim, J. J. P., Kuroda, Y., and Tanaka, K. (1998) The roles of threonine-136 and glutamate-137 of human medium chain Acyl- CoA dehydrogenase in FAD binding and peptide folding using site-directed mutagenesis: Creation of an FAD-dependent mutant, T136D. *Arch. Biochem. Biophys.* **358**, 49–57
27. Cornelius, N., Freyman, F. E., Corydon, T. J., Palmfeldt, J., Bross, P., Gregersen, N., and Olsen, R. K. J. (2012) Molecular mechanisms of riboflavin responsiveness in patients with ETF-QO variations and multiple acyl-CoA dehydrogenation deficiency. *Hum. Mol. Genet.* **21**, 3435–3448
28. Chalmers, R. A., Bain, M. D., and Zschocke, J. (2006) Riboflavin-responsive glutaryl CoA dehydrogenase deficiency. *Mol. Genet. Metab.* **88**, 29–37
29. Henriques, B. J., Olsen, R. K., Bross, P., and Gomes, C. M. (2010) Emerging roles for riboflavin in functional rescue of mitochondrial β -oxidation flavoenzymes. *Curr. Med. Chem.* **17**, 3842–3854
30. Missaglia, S., Taviani, D., Moro, L., and Angelini, C. (2018) Characterization of two ETFDH mutations in a novel case of riboflavin-responsive multiple acyl-CoA dehydrogenase deficiency. *Lipids Health Dis.* **17**, 254
31. Petersen, T. N., Brunak, S., von Heijne, G., and Nielsen, H. (2011) SignalP 4.0: discriminating signal peptides from transmembrane regions. *Nat. Methods.* **8**, 785–786
32. Macheroux, P. (1999) UV-visible spectroscopy as a tool to study flavoproteins. *Methods Mol. Biol.* **131**, 1–7
33. Massey, V., Hemmerich, P., Knappe, W. R., Duchstein, H. J., and Fenner, H. (1978) Photoreduction of flavoproteins and other biological compounds catalyzed by deazaflavins. Appendix: photochemical formation of deazaflavin dimers. *Biochemistry.* **17**, 9–17
34. Minnaert, K. (1965) Measurement of the equilibrium constant of the reaction between cytochrome c and cytochrome a. *Biochim. Biophys. Acta.* **110**, 42–56
35. Biasini, M., Bienert, S., Waterhouse, A., Arnold, K., Studer, G., Schmidt, T., Kiefer, F., Cassarino, T. G., Bertoni, M., Bordoli, L., and Schwede, T. (2014) SWISS-MODEL: Modelling protein tertiary and quaternary structure using evolutionary information. *Nucleic Acids Res.* 10.1093/nar/gku340
36. Arnold, K., Bordoli, L., Kopp, J., and Schwede, T. (2006) The SWISS-MODEL workspace: A web-based environment for protein structure homology modelling. *Bioinformatics.* **22**, 195–201
37. Benkert, P., Biasini, M., and Schwede, T. (2011) Toward the estimation of the absolute quality of individual protein structure models. *Bioinformatics.* **27**, 343–350
38. Lobley, A., Whitmore, L., and Wallace, B. A. (2002) DICHROWEB: An interactive website for the analysis of protein secondary structure from circular dichroism spectra. *Bioinformatics.* **18**, 211–212

39. Whitmore, L., and Wallace, B. A. (2004) DICHROWEB, an online server for protein secondary structure analyses from circular dichroism spectroscopic data. *Nucleic Acids Res.* 10.1093/nar/gkh371
40. Whitmore, L., and Wallace, B. A. (2008) Protein secondary structure analyses from circular dichroism spectroscopy: Methods and reference databases. *Biopolymers.* **89**, 392–400
41. Laemmli, U. K. (1970) Cleavage of structural proteins during the assembly of the head of bacteriophage T4. *Nature.* **227**, 680–685
42. Compton, L. A., and Johnson, W. C. (1986) Analysis of protein circular dichroism spectra for secondary structure using a simple matrix multiplication. *Anal. Biochem.* **155**, 155–167
43. Sreerama, N., and Woody, R. W. (2000) Estimation of protein secondary structure from circular dichroism spectra: Comparison of CONTIN, SELCON, and CDSSTR methods with an expanded reference set. *Anal. Biochem.* **287**, 252–260
44. Lees, J. G., Miles, A. J., Wien, F., and Wallace, B. A. (2006) A reference database for circular dichroism spectroscopy covering fold and secondary structure space. *Bioinformatics.* **22**, 1955–1962

Appendix A

Inhibition of *PbCS* by CP1

Promising new antifungal treatment targeting chorismate synthase from *Paracoccidioides brasiliensis*

Franciele Abigail Vilugron Rodrigues-Vendramini^a, Cidnei Marschalk^b, Marina Toplak^c,
Peter Macheroux^c, Patricia de Souza Bonfim-Mendonça^a, Terezinha Inez Estivalet Svidzinski^a,
Flavio Augusto Vicente Seixas^b, Erika Seki Kioshima^{a#}

^a Department of Clinical Analysis and Biomedicine, Universidade Estadual de Maringá, Av. Colombo
5790, 87020-900 Maringá, PR, Brazil

^b Department of Technology, Universidade Estadual de Maringá, Av. Ângelo Moreira da Fonseca, 1800,
87506-370 Umuarama, PR, Brazil

^c Institute for Biochemistry, Graz University of Technology, Petersgasse 12/2, 8010 Graz, Austria

#Corresponding author

E-mail: eskioshima@gmail.com. Phone: +55 44 30114810

Keywords: chorismate synthase, molecular modeling, new antifungal, paracoccidioidomycosis, virtual screening

Abbreviations

CP1, (1*S*,2*S*,3*aS*,4*S*,9*bR*)-1-chloro-6-nitro-2-[(2-nitrophenyl)sulfanyl]-2,3,3*a*,4,5,9*b*-hexahydro-1*H*-cyclopenta[*c*]quinoline-4-carboxylic acid; *PbCS*, chorismate synthase from *Paracoccidioides brasiliensis*

This chapter was published as “Promising new antifungal treatment targeting chorismate synthase from *Paracoccidioides brasiliensis*” in *Antimicrobial Agents and Chemotherapy* 2019, Vol. 63(1):e01097-18. <https://doi.org/10.1128/AAC.01097-18>.

Abstract

Paracoccidioidomycosis (PCM), caused by the *Paracoccidioides* species, is a systemic mycosis with granulomatous character and a restricted therapeutic arsenal. The aim of this work was to search for new alternatives to treat largely neglected tropical mycosis, such as PCM. In this context, the enzymes of the shikimate pathway constitute excellent drug targets for conferring selective toxicity because this pathway is absent in humans but essential for the fungus. In this work, we have used a homology model of the chorismate synthase (EC 4.2.3.5) from *Paracoccidioides brasiliensis* (PbCS) and performed a combination of virtual screening and molecular dynamics to identify new potential inhibitors. The best hit, CP1, successfully adhered to pharmacologic criteria (adsorption, distribution, metabolism, excretion, and toxicity) and was therefore used in *in vitro* experiments. Here, we demonstrate that CP1 binds with a dissociation constant of $64 \pm 1 \mu\text{M}$ to recombinant chorismate synthase from *P. brasiliensis* and inhibits enzymatic activity, with a 50% inhibitory concentration (IC_{50}) of $47 \pm 5 \mu\text{M}$. As expected, CP1 showed no toxicity in three cell lines. On the other hand, CP1 reduced the fungal burden in lungs from treated mice, similar to itraconazole. In addition, histopathological analysis showed that animals treated with CP1 displayed less lung tissue infiltration, fewer yeast cells, and large areas with preserved architecture. Therefore, CP1 was able to control PCM in mice with less inflammatory response and is thus a promising candidate and lead structure for the development of drugs useful in PCM treatment.

Introduction

Paracoccidioidomycosis (PCM) is a systemic granulomatous disease caused by thermally dimorphic fungi of the genus *Paracoccidioides* (1, 2). PCM is endemic in Latin America, mainly southern Brazil, and features one of the highest mortality rates among chronic fungal diseases. With an average of 2.7 new cases per 100.000 habitants per year, this mycosis is among the 10 largest causes of death in predominantly chronic diseases and has high mortality rates among systemic mycoses (3, 4). Recent studies have shown that PCM is responsible for approximately 51.2% of deaths caused by systemic mycoses in Brazil (5). In addition, PCM has a high social and economic cost since it may leave important sequelae in individuals during their productive age. Despite these social problems, the prevalence of this mycosis is underestimated since it is based on reported cases or hospitalization and mortality data (5).

PCM presents two principal clinical forms, acute/subacute and chronic. The acute or subacute form, also known as juvenile form, predominantly affects young adults of both sexes. The infection rapidly evolves and disseminates to multiple organs, with many severe symptoms, such as lymphadenomegaly, hepatosplenomegaly, fever, weight loss, and anorexia (5, 6). This form is responsible for up to 25% of PCM cases. The chronic form represents the majority of PCM cases (74 to 96%), affecting mainly male adults. The chronic form of PCM is characterized by slow progression, frequently with pulmonary

involvement, and the mucocutaneous tissue may be affected (6). Therefore, PCM could result in serious sequelae or lead to death if not detected early. Thus, this disease fits into the neglected endemic mycoses and requires epidemiological data and surveillance to fully comprehend the magnitude of the problem (7).

In clinical practice, the following three medications are commonly used for the treatment of PCM: azole derivatives (itraconazole) [ITZ], sulfanilamide compounds (trimethoprim-sulfamethoxazole), and polyenes (amphotericin B [AmB]). Unlike for other pathogenic fungi, there is no solid evidence to indicate that *P. brasiliensis* develops resistance to antifungal agents (6). However, treatment may range from several months to a year depending on the patient's condition. Thus, the limitations for the treatment of PCM are linked to few therapeutic options, drug interactions, infusion-related events, nephrotoxicity, and prolonged antifungal treatment (5). The eukaryotic nature shared by fungi and the host is the major challenge for treatment of infectious diseases (8).

A promising strategy for selective antimicrobial therapy has been to exploit the inhibition of unique targets essential to the pathogen but absent in humans (9). In this sense, the shikimate pathway is an attractive target since it is present in bacteria, fungi, plants, and apicomplexan parasites, but absent from mammals (10-12). Equally important, this pathway is essential for the survival of these organisms, and therefore, the enzymes are promising targets for drug development (13). Notably, the broad-spectrum herbicide glyphosate, one of the most successful herbicides currently used worldwide, inhibits the sixth enzyme of the pathway, 5-enolpyruvylshikimate-3-phosphate synthase (14).

The enzyme chorismate synthase (EC: 4.2.3.5) is the seventh enzyme in the shikimate pathway and is responsible for the synthesis of chorismate, the branch point in the biosynthesis of several important aromatic molecules, including aromatic amino acids, folate, naphthoquinones, and menaquinones. This enzyme catalyzes the conversion of 5-enolpyruvylshikimate-3-phosphate (EPSP) to chorismate in the presence of reduced flavin mononucleotide (FMNH₂), which is not consumed in the reaction (15). Although the three-dimensional structure of chorismate synthase (CS) from *Paracoccidioides brasiliensis* (*PbCS*) has not been solved yet, its amino acid sequence shares 67.9% identity with that of the homologous enzyme from *Saccharomyces cerevisiae* (16).

Therefore, the aim of this study was to identify potential inhibitors of CS from *Paracoccidioides brasiliensis* by *in silico* methodologies and to validate potential candidates for their usefulness as compounds or lead structures for the development of new antifungals. In this work, we describe the identification and (partial) characterization of a new compound possessing promising antifungal activity against *Paracoccidioides* species. Most importantly, we demonstrate that this compound significantly reduces the fungal burden in the lung of infected mice, resulting in diminished tissue damage.

Results

Protein modeling and evaluation

The high sequence identity of *PbCS* to the main template from *Saccharomyces cerevisiae*, 63.9%, enabled homology modeling of the three-dimensional structure (17, 18). The short insertions and deletions observed in the multiple alignments did not affect the active site with regard to substrate and cofactor binding. The Psipred server suggested that the two segments in *PbCS* did not have the secondary-structure element compatible with the template. Thus, no restriction was added to these segments during the modeling process. The high degree of freedom regarding protein movement in the protomer could compromise the active-site configuration, essentially structured by random segments of structure (loops and turns). For this reason, the protein was modeled as a homotetramer (Figure 1). Therefore, symmetry restraints were imposed on alpha-carbons of the subunits to generate symmetry and to decrease possible model inconsistencies for virtual screening (VS). Once modeled, only the A subunit was used in the docking studies. The final model of *PbCS* (Figure 1) exhibited excellent stereochemical quality, with 91.4% of residues in the most favorable regions and 8.6% in additional allowed regions of the Ramachandran plot.

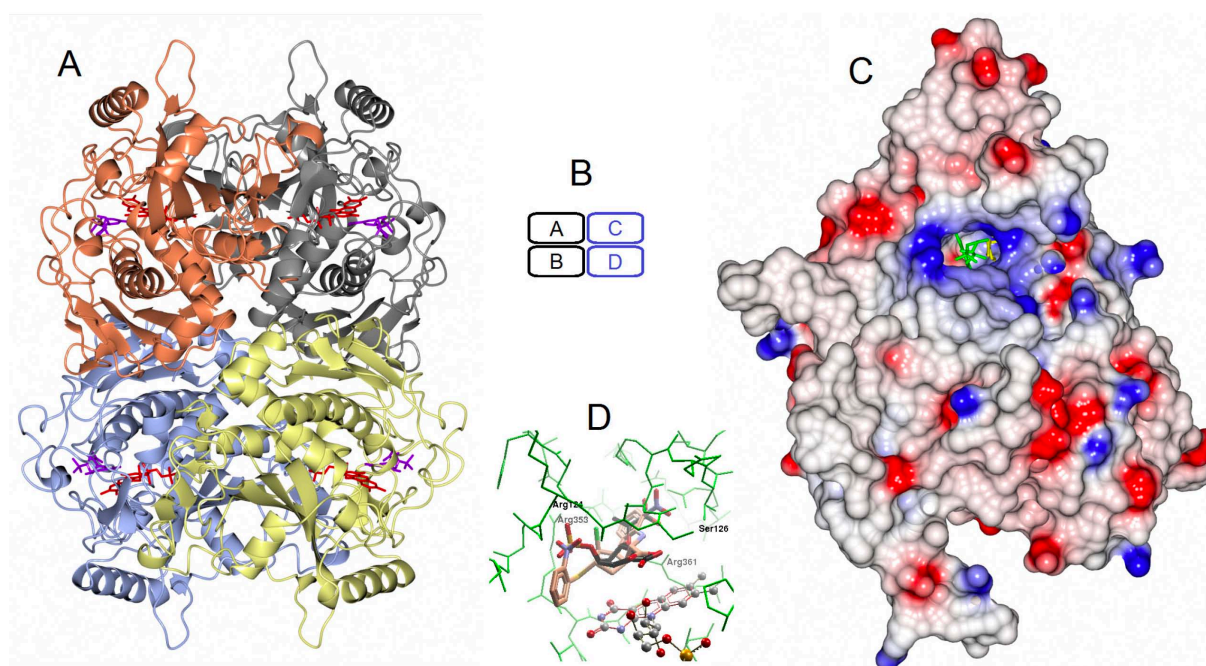


Figure 1. **A**, Ribbon model of biological unity of *PbCS* bonded to FMNH₂ (red) and EPSP (purple). **B**, Homotetramer protein chains. **C**, Monomeric structure colored by electrostatic potential, highlighting the sites of FMNH₂ and EPSP with electropositive potential (blue). **D**, Close view of EPSP binding site. The most important residues in the docking of both CP1 (brown) and EPSP (black), as presented in *Table S1*, are labeled. The FMNH₂ is represented by a ball & stick.

Virtual screening

The application of the validated docking protocols shows the substrate EPSP overlay almost perfectly to the minimized pose, exhibiting an average root mean square deviation (RMSD) of $0.57 \pm 0.13 \text{ \AA}$ and a mean ranking of $-12.7 \pm 1.06 \text{ kcal mol}^{-1}$. At the end of the virtual screening, 53 compounds were selected and were used in an additional 5 screening repetitions using AutoDock and 5 screenings using Molegro, totaling 10 repetitions. The compounds Zinc13370291 (CP3), Zinc06445857 {CP1; (1*S*,2*S*,3*aS*,4*S*,9*bR*)-1-chloro-6-nitro-2-[(2-nitrophenyl)sulfonyl]-2,3,3*a*,4,5,9*b*-hexahydro-1*H*-cyclopenta[*c*]quinoline-4-carboxylic acid}, and Zinc06445743 (CP2) were always ranked among the best 5 in all 10 repetitions, exhibiting mean $\Delta G_{\text{binding}}$ values of -14.2 ± 0.13 , -13.3 ± 0.17 , and $-13.1 \pm 0.19 \text{ kcal mol}^{-1}$, respectively (Figure 2).

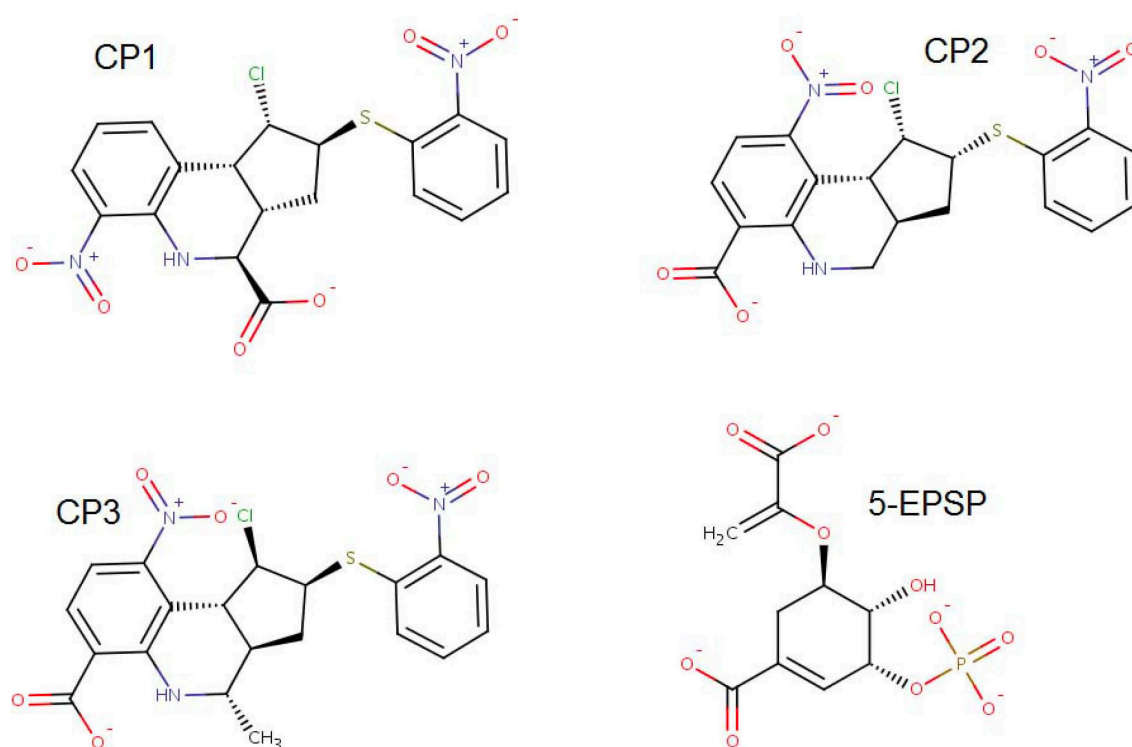


Figure 2. Chemical structure of the 3 molecules selected by virtual screening and the reference ligand EPSP.

These 3 molecules were subjected to ADMETox (adsorption, distribution, metabolism, excretion, and toxicity) evaluation, which includes Lipinski's rule of 5 by means of the server FAF-Drugs (19). After passing these criteria, the molecules were purchased for *in vitro* evaluations. Statistically, when different programs select a common molecule using different search and ranking algorithms, the chances of getting a false-positive result significantly decreases and the chances of the selected molecule exhibiting *in vitro* or *in vivo* activity increases.

MD simulations

In order to investigate the structural stability and folding of *PbCS*, as well as to obtain information about the residues involved in stabilizing ligands, molecular dynamics (MD) simulations were carried out for 20 ns with the protein in the apo- and holo-forms. In these simulations, the final model of *PbCS* with bound FMNH₂ and EPSP, or the best pose of potential inhibitors, was minimized and then equilibrated as described in Materials and Methods. The thermodynamic equilibrium was reached when the RMSD of the main chain atoms of the protein as a function of time had stabilized on a constant level for at least 5 ns. The results showed that the evaluated structures reached an equilibrium after 6 ns of simulation (Figure 3A). The radius of gyration (R_{gyr}) from the protein-ligand complexes was constant during the simulations for all structures evaluated (Figure 3B), indicating that the structures were stable and the presence of the ligands did not lead to protein unfolding. Furthermore, the oscillations of R_{gyr} were lower in the tetrameric structures (biological units) than in the monomeric form, which indicates greater structural stability in this form.

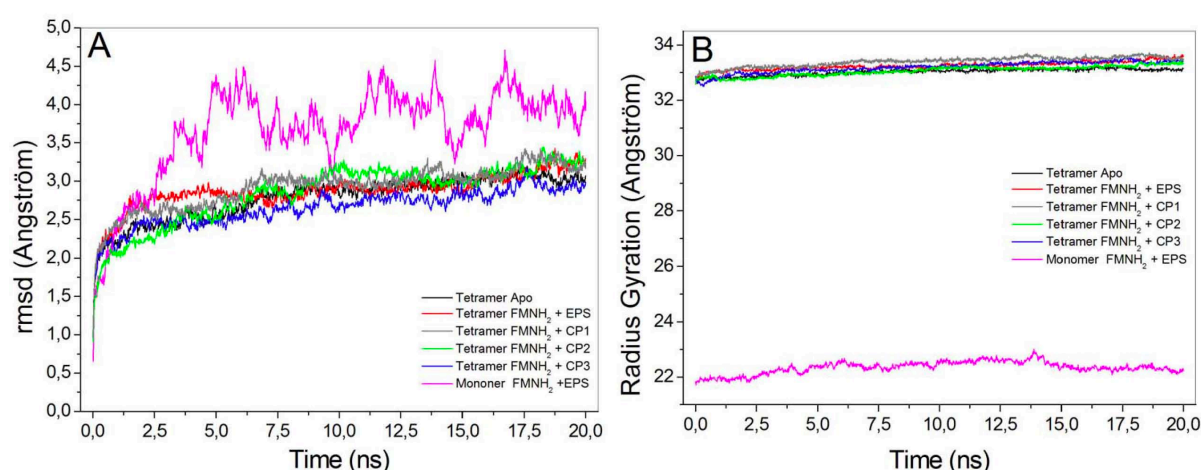


Figure 3. Analysis of the molecular dynamics trajectory for *PbCS* structures. Shown are the A-chain in the complex with FMNH₂ plus EPSP (pink), tetramer apo (black), tetramer with FMNH₂ plus EPSP bound (red), tetramer with bound FMNH₂ plus CP 1 (gray), tetramer with bound FMNH₂ plus CP2 (green), and tetramer with bound FMNH₂ plus CP3 (blue). The RMSD (A) and radius of gyration (B) were obtained from the oscillation of the protein main chain atoms relative to the fully minimized structure.

The protein regions with increased flexibility were evidenced by the root mean square fluctuation (RMSF) of each residue. The RMSF was calculated from C α -atoms from the last 5 ns of the simulation, *i.e.*, during the thermodynamic equilibrium. The residues with greater flexibility were in the N-terminal regions of the 4 chains, a fact that is common to most proteins, and in the case of *PbCS*, refers to a helix with a high degree of freedom of rotation due to a turn that connects it to the remainder of the protein (Figure S2). Because of this, the last 10 residues were disregarded in the calculation of RMSD and R_{gyr} . The RMSF plot also showed that residues making contact with EPSP are located in the most stable regions of the protein with smaller RMSF values (Figure S2).

Residues 290 to 298 constitute a very flexible loop placed on the surface of the protein. Since there are no intramolecular interactions to stabilize this region, it becomes quite flexible in all protein chains. The pronounced increase in this flexibility, as observed in the protein-inhibitor complexes, is not related to the presence of the ligands because this loop is located in a place far away from the ligand binding site, suggesting that this is solely a random variation in the simulation. The great flexibility of these residues is also reflected by the lack of electron density in homologous regions of the crystallographic templates.

Active site and EPSP docking

There is some flexibility in the EPSP binding site, which is structured mainly by loop elements. This prompted us to take special care in modeling this region because this site showed substantial flexibility in the templates (20). Thus, we opted for an interactive model, prioritizing the templates in which the flexible area is in contact with EPSP, *i.e.*, in a closed conformation.

In this work, the binding site was delimited from the residues that had a frequency of contact with the EPSP greater than 70% over the course of the simulation (*Table S1*). This is because each ligand has a specific geometry and composition, making them interact differently with the protein and thus structuring distinct sites.

Ligand CP1

From the 3 potential inhibitors identified by virtual screening, CP1 was the most promising to present fungicidal activity *in vitro*. Thus far, no application of this compound has been reported. In comparison with EPSP, CP1 binds to *PbCS* with fewer hydrogen bonds than does EPSP (*Figure S2*); however, the salt bridges with Arg45, Arg124, Arg353, and Arg361 are still preserved. Several other interactions occur between CP1 and *PbCS*, such as hydrogen bonds and van der Waals contacts, which were reflected in a better ranking than for EPSP.

To support our findings from virtual screening and molecular docking simulations, we produced and purified recombinant CS from *P. brasiliensis* and analyzed the binding of CP1 to the protein. As shown in Figure 4A, the UV-visible (UV-Vis) absorption spectrum of CP1 changes as a function of the *PbCS* concentration, allowing for the calculation of a dissociation constant of $64 \pm 1 \mu\text{M}$ from the hyperbolic plot (Figure 4, *inset*). Next, the influence of CP1 on the enzymatic activity of *PbCS* was analyzed using an enzyme-coupled assay. As shown in Figure 4B, CP1 also affects the activity, yielding a 50% inhibitory concentration (IC_{50}) value of $47 \pm 5 \mu\text{M}$, which fits nicely with the observed dissociation constant. Thus, our biochemical results clearly indicate that CP1 specifically binds and inhibits the target enzyme of our screening approach.

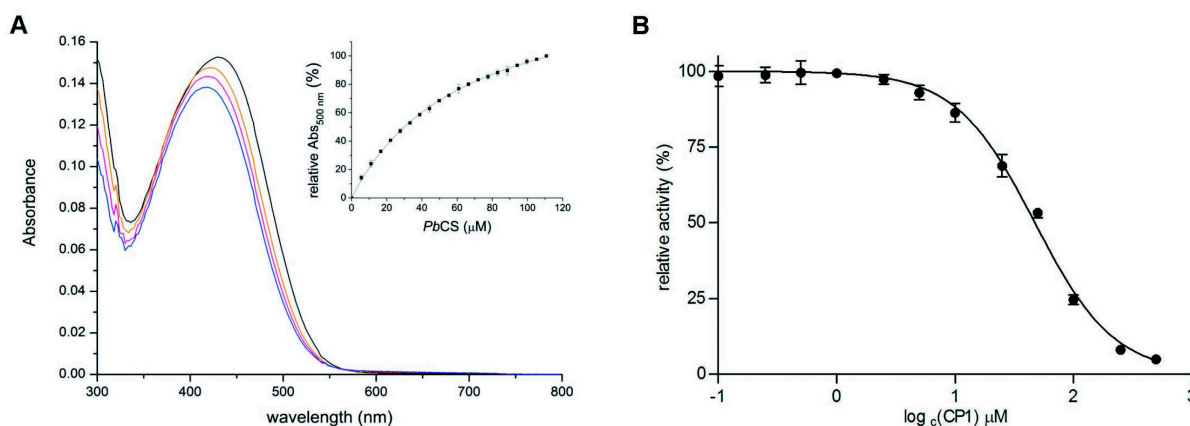


Figure 4. Binding of CP1 to *PbCS* (A) and the effect of CP1 on *PbCS* activity (B). A, CP1 was dissolved in 50 mM MOPS (pH 7.5, $\sim 20 \mu\text{M}$, *black* spectrum) and titrated with *PbCS* ($\sim 443 \mu\text{M}$) using 10 μL aliquots (see *inset*). Spectral changes were monitored at 300 to 800 nm. The *orange* and *pink* traces represent the intermediate spectra at $\sim 39 \mu\text{M}$ *PbCS* and $\sim 72 \mu\text{M}$ *PbCS*, respectively. The *blue* trace corresponds to the final spectrum recorded at $\sim 111 \mu\text{M}$ *PbCS*. The *inset* shows the mean absorption changes at 500 nm (from 3 determinations) as a function of the protein concentration, yielding a dissociation constant of $64 \pm 1 \mu\text{M}$ (the SD at each *PbCS* concentration is shown by an error bar). B, The influence of CP1 on the activity of *PbCS* was tested in an assay involving 80 μM EPSP, 4 μM *PbCS*, and 20 μM anthranilate synthase at 37°C. By forward coupling, the chorismate synthase reaction and *PbCS* activity could be studied spectrofluorometrically by following the increase in fluorescence intensity at 390 nm ($\lambda_{\text{ex}} = 340 \text{ nm}$) for 5 min, which correlates with the amount of anthranilate formed during the course of the reaction. The slopes of the initial velocities were determined and plotted as a function of the log of the corresponding CP1 concentration. Using a non-linear curve fit based on the Hill function, an IC₅₀ value of $47 \pm 5 \mu\text{M}$ was determined (rates were determined in triplicates, with the SDs shown as error bars).

***In vitro* CP1 antifungal activity against *Paracoccidioides* spp**

CP1 inhibited the growth of *Paracoccidioides* spp., with MICs of 2 to 16 mg/liter using *P. brasiliensis* isolates and 16 to 32 mg/liter using *P. lutzii* isolates (Table 1). The minimal fungicidal concentrations (MFCs) were 4 mg/liter for *P. brasiliensis* (Pb18) and 32 to 128 mg/liter for *P. lutzii* isolates (Table 1). All isolates tested showed itraconazole (ITZ) susceptibility (MIC of 1 mg/liter). Although the CP1 MICs were higher than for azole, CP1 showed potent antifungal activity, suggesting a fungicidal effect against several *Paracoccidioides* isolates (Table 1). However, there was no synergistic action between CP1 and the conventional drugs tested (data not shown).

Table 1. MICs and MFCs of CP1 and itraconazole (ITZ) for *Paracoccidioides* species isolates.

Isolate	Species	MIC CP1 (mg/liter)	MFC CP1 (mg/liter)	MIC ITZ (mg/liter)
Pb18	<i>P. brasiliensis</i>	2	4	1
Mg14	<i>P. brasiliensis</i>	16	-*	1
Pb01	<i>P. lutzii</i>	16	128	1
ROSC	<i>P. lutzii</i>	32	32	1
8334	<i>P. lutzii</i>	16	64	1

* there was no fungal growth on the MFC plate.

CP1 had no cytotoxic effect on human cell lines

Initially, J774 macrophages were used because these cells are the first to come into contact with pathogens. In addition, 2 human cell lines, HUVEC and HeLa, were also evaluated. As shown in Figure 5, all cell lines tested showed high viability after exposure to various CP1 concentrations. Even at concentrations of 3 x MIC (128 mg/liter), cell viability was higher than 80% for all cell lines tested, and the differences ($P > 0.05$) were not statistically significant (Figure 5).

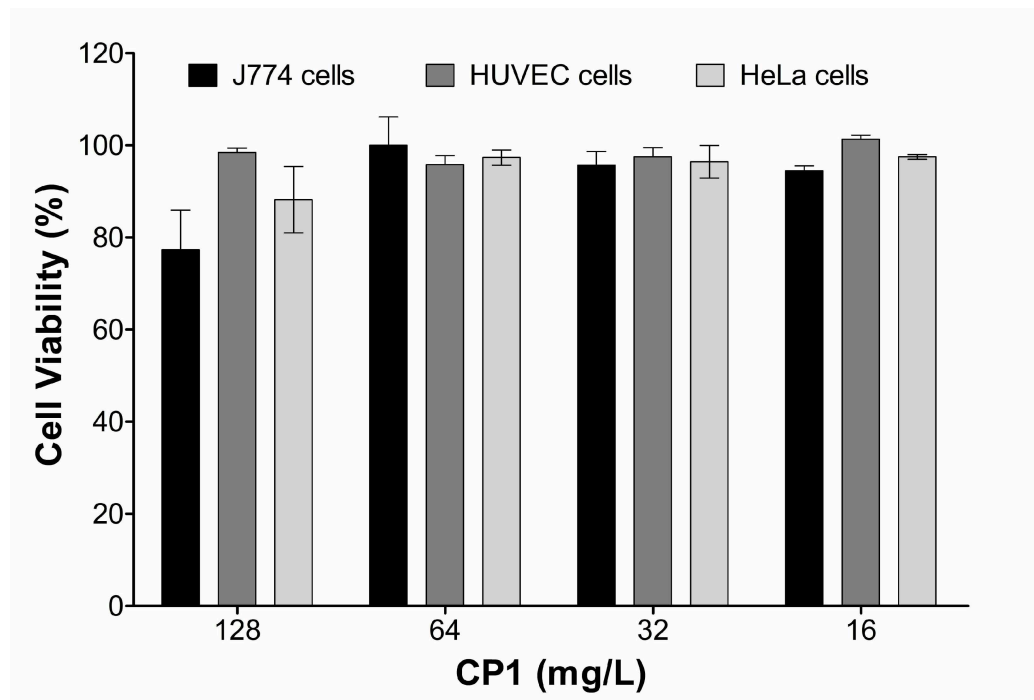


Figure 5. CP1 *in vitro* cytotoxicity assessment. Three cell lines were subjected to cytotoxicity by MTS assay. Various CP1 concentrations were tested (0.0 to 128 mg/liter) without showing significant toxicity. The 3 cell lines evaluated showed high viability after 24 h in contact with CP1, even at concentrations of 2 x MIC (64 mg/liter). The results are representative of those from 3 independent experiments. Bars indicate SDs.

Morphological alteration in P. brasiliensis caused by CP1 treatment

CP1 at 2 x MIC (64 mg/liter) was able to kill all clinical isolates tested, and this CP1 concentration was chosen for further experiments. Electron micrographs revealed deformations in the *P. brasiliensis* cells, including depression and rough surfaces (Figure 6C). Irregularly shaped cells, as well as aggregating cells, were also observed (Figure 6D). These hallmark changes were seen in approximately 80% of the population after treatment. In the control, the typical morphology of *P. brasiliensis* cells was observed (Figure 6A and B).

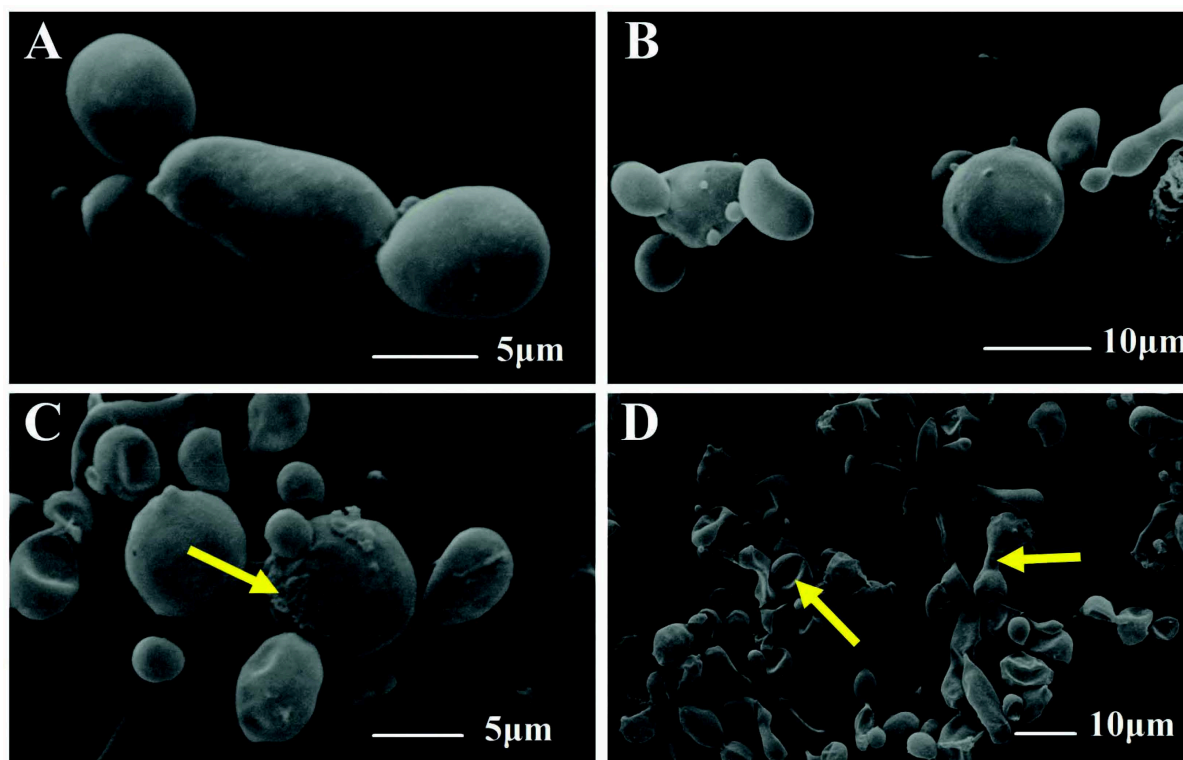


Figure 6. Scanning electron microscopy (SEM) of *Paracoccidioides brasiliensis* (Pb18). Cells of the isolated Pb18 strain were grown at a CP1 concentration of 64 mg/liter. **A** and **B**, Control consisting of *P. brasiliensis* cells without treatment. **C** and **D**, Cells treated with compound CP1 (64 mg/liter). Control cells feature preserved cell surfaces and multibudding. Note the leakage of cellular content and cell surface squashing and depression (*arrows*). In addition, aggregation of cells was observed (**D**). Samples were observed at magnifications of x 3,000 and x 1,000.

Effective in vivo antifungal activity

Intraperitoneal treatment with CP1 (5 mg/kg of body weight) was able to significantly reduce the fungal burden in the lung of infected animals with *P. brasiliensis*. The group treated with ITZ (5 mg/kg) showed a similar efficacy ($P > 0.05$) (Figure 7). Both CP1 and ITZ treatment were able to reduce approximately 90% of CFU recovered from the lungs as compared to the control.

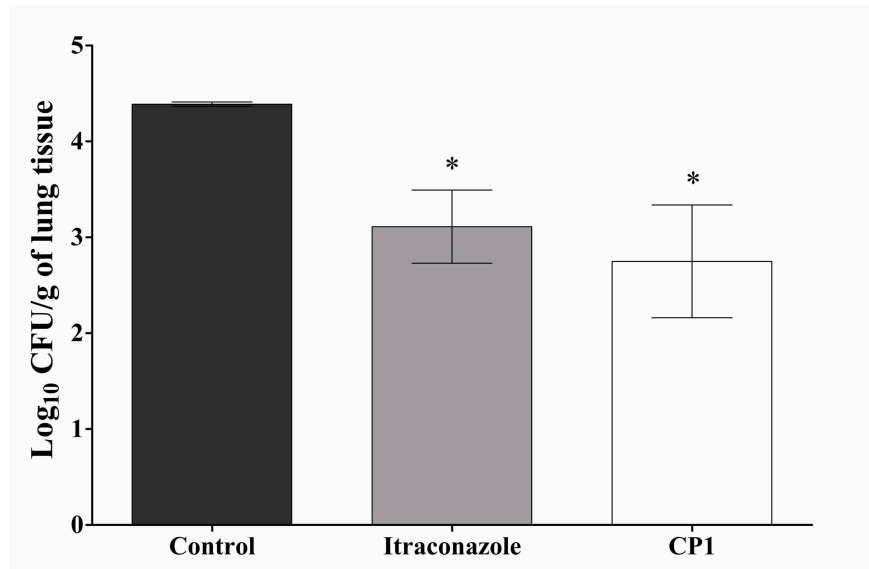


Figure 7. Antifungal activity of CP1 in the treatment of PCM. CFU for lung tissue infected with *P. brasiliensis* are shown. The control group consisted of animals treated with a vehicle. All treatments were performed for 14 days. The experiments were performed in triplicate, and the bars indicate the SDs. *, $P < 0.05$, (statistically significant compared to the control).

The semiquantitative histopathological analysis indicates that the CP1 performance is superior to the treatment with ITZ, considering the tissue damage. The CP1 compound was able to significantly reduce the pulmonary fibrosis and inflammatory infiltrate caused by infection with *P. brasiliensis* (Figure 8). Figure 8A shows a significant reduction in pulmonary fibrosis sequelae compared with the control and ITZ groups. The level of inflammation was lower in the animals treated with CP1, presenting a significant reduction compared with the control group (Figure 8B). Fungal cells were visualized in all treatment groups, with the largest amount of the *P. brasiliensis* cells in the control group. Otherwise, the animals treated with CP1 showed lower scores in the fungal-cell parameter, corroborating the results of the determination of pulmonary fungal burden by CFU counting (Figure 8C).

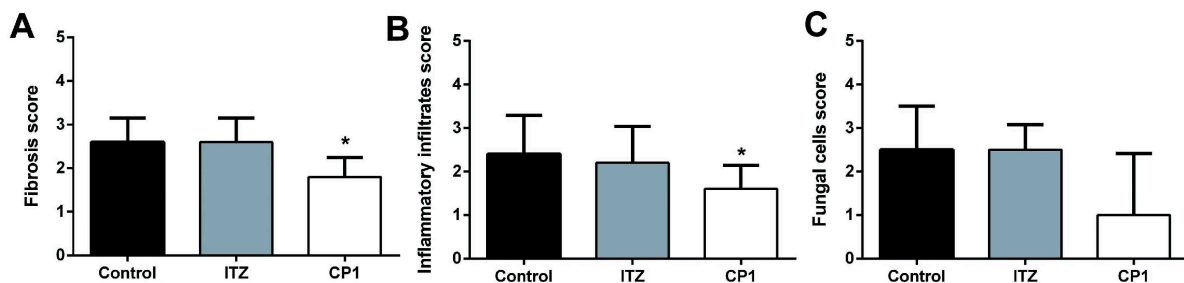


Figure 8. Histopathological score of three factors indicative of lung tissue impairment of animals infected with *Paracoccidioides brasiliensis* (Pb18) after 14 days treatment of ITZ, CP1, and control groups. **A**, Pulmonary fibrotic profile. **B**, Recruitment of inflammatory infiltrates in the lung. **C**, Concentration of fungal cells of the Pb18 in the lung. *, $P < 0.05$, (statistically significant compared to the control).

The histopathological analysis results are represented in Figure 9. The group treated with CPI showed large areas of lung tissue with the preserved structure (Figure 9C), less inflammatory infiltration (Figure 9F), and fewer fungal cells (Figure 9I). The ITZ was less effective in reducing tissue damage caused by *P. brasiliensis* infection, since this group presented poorly preserved lung tissue (Figure 9B) with large areas containing inflammatory infiltration (Figure 9E) and fungal cells (Figure 9H). As expected, the control group presented damage throughout the lung tissue, exhibiting multiple pulmonary foci of epithelioid inflammation with early pulmonary fibrosis (Figure 9B). Therefore, CPI treatment was shown to be more efficient in protecting lung tissue against pulmonary sequelae than the conventional treatment with ITZ in an experimental murine PCM model.

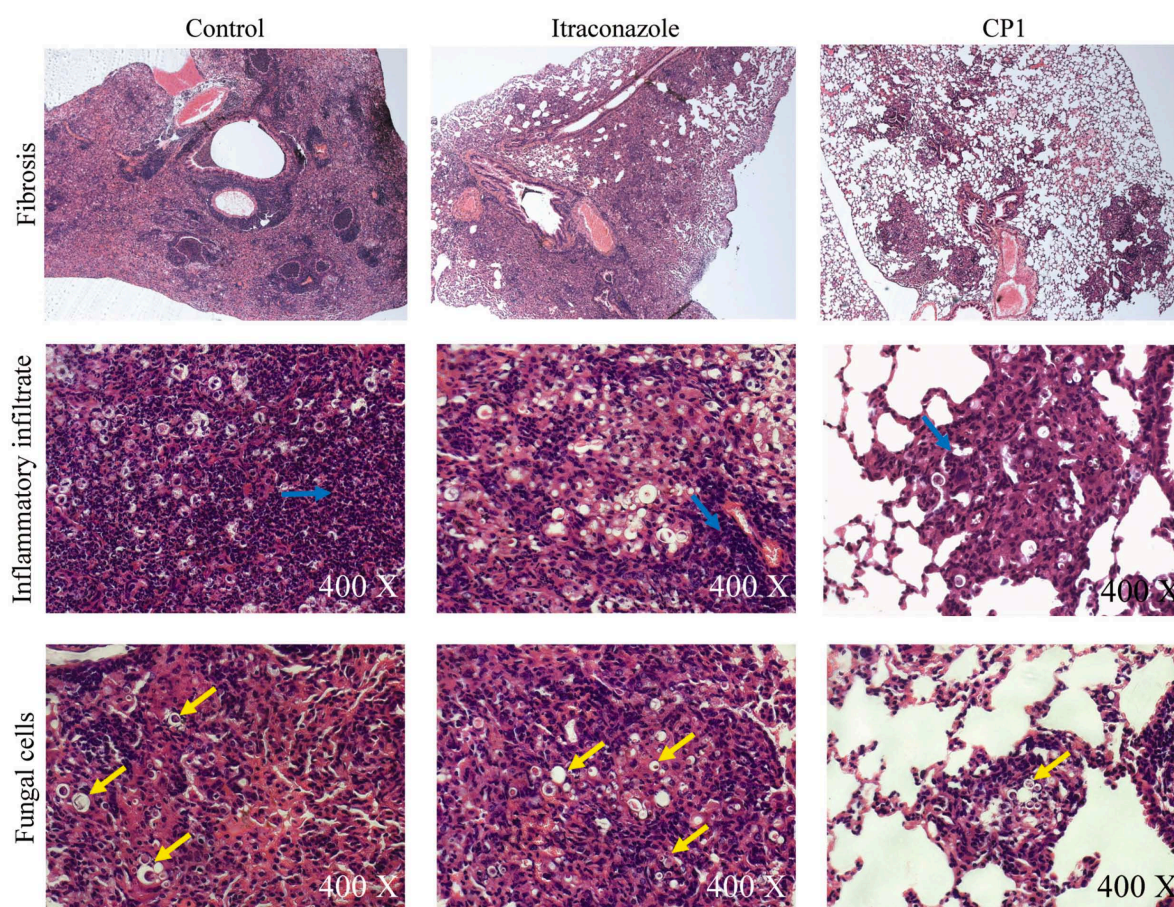


Figure 9. Photomicrographs of the lungs of mice infected with 1×10^6 *P. brasiliensis* (Pb18) cells following treatment and haematoxylin-eosin staining. Representative images of each treatment group are given. Infected mice and mice given vehicle treatment (1% DMSO and 0.2% Pluronic) are the controls (A, D, and G). Images for infected mice and mice treated with 5 mg/kg ITZ (B, E, and H) and 5 mg/kg CPI (C, F, and I) are shown. A, The lung structure was not preserved, showing large fibrotic masses (magnification, x 100). B, The lung structure was severely damaged, showing confluent fibrotic masses (magnification, x 100). C, Preserved lung tissue with single fibrotic masses (magnification, x 100). D and E, Lung tissue with high agglomeration inflammatory infiltrate in the parenchyma (blue arrows; magnification, x 400). F, Moderate inflammatory infiltrate (magnification, x 400). G and H, Accumulation of a large amount of fungal cells (arrows, magnification, x 400). I, Scarce presence of fungal cells in the lung tissue (magnification, x 400).

Discussion

PCM constitutes a substantial public health problem with high mortality rates in Latin America. Several antifungal drugs have been shown to be effective in treating different clinical forms of PCM, including amphotericin B (AmB; formulations in deoxycholate, lipid, and liposomal complex), sulfonamide derivatives (trimethoprim-sulfamethoxazole), and azole derivatives (ITZ and voriconazole or posaconazole). However, the main challenge of systemic mycosis is the requirement for long periods of treatment with antifungal medications that present several limitations (21).

Amphotericin B has been a polyene recommended for severe cases of PCM since 1958, mainly in the initial phase (5, 6). However, it should be noted that this drug has many important limitations, such as intravenous administration and problems related to infusion and high nephrotoxicity. Although there are current liposomal forms of amphotericin B, these are costly and still have several adverse effects (22). In the maintenance phase of treatment, trimethoprim-sulfamethoxazole has been frequently used (23, 24). However, therapeutic failure was described for 5% of patients, and the main disadvantage is the need for long-term treatments (over 12 months), in addition to adverse effects such as hypersensitivity reactions, leukopenia, megaloblastic anemia, and thrombocytopenia (24). For the azole derivatives, ITZ is the best option for PCM treatment in patients not hospitalized (5, 6). The new azoles, such as voriconazole and posaconazole, present high costs and lack of clinical studies demonstrating advantages for their use in clinical practice (24). The main limitations of the azoles are adverse reactions, such as abnormal vision, chromatopsia, rash, headache, and an increase in hepatic transaminases (6). Unfortunately, over the last 30 years only one new antifungal class has been discovered (echinocandins), reinforcing the need to use truly innovative antifungal discovery approaches (25).

The rational design and development of new drugs that specifically act on targets of the pathogenic fungi without producing collateral damage to mammalian cells constitute a great pharmacological challenge. In this study, we identified a new potential antifungal compound against *Paracoccidioides* spp., selected by virtual screening using CS as the target. Our study clearly demonstrates that CP1 binds and inhibits recombinant CS from *P. brasiliensis* (*PbCS*). CS is the seventh enzyme of the common shikimate pathway and occurs only in the fungus and not in humans and thus may help to minimize side effects of the compound on human cells. Since CP1 showed promising activity *in vitro* and *in vivo*, our study identified CS and the shikimate pathway as a new target for the development of antifungal compounds.

Although the most efficient drug in PCM treatment, amphotericin B, is considered a fungicidal agent (2, 26) its administration is limited by toxicity and occasionally discontinuation of the therapy is required owing to its high nephrotoxicity (27). In contrast to AmB, our *in vitro* and *in vivo* study did not indicate any toxicity of CP1 to human cells and thus supports the concept that CP1 has selective activity against fungus, proving to be promising for the new antifungal development.

Although the need for new therapies for PCM (and other diseases caused by pathogenic fungi) is obvious, only a few studies have been reported recently. Recently, 3 thioredoxin reductase inhibitors

were selected by virtual screening with antifungal activity against *Paracoccidioides* spp., with MICs of 8 to 32 mg/liter (28). Furthermore, two compounds (HS1 and HS2) have been identified as homoserine dehydrogenase inhibitors showing antifungal activity (32 to 64 mg/liter) against *P. brasiliensis* (29). A Brazilian medicinal plant called *Schinus terebinthifolius* presented inhibitory activity against isolates Pb18 and Pb01, with MICs of 62.5 to 250 mg/liter (30). Finally, the antifungal activity of a synthetic compound derived from chalcones was analyzed. This 6-quinolinyl *N*-oxide could inhibit the growth of many *Paracoccidioides* isolates, with a MIC of 5.9 mg/liter against Pb18 (31). In comparison with these recent reports, the MIC determined for CP1 (2 mg/liter) against *P. brasiliensis* isolate Pb18 indicates superior antifungal activity, encouraging future efforts to target CS.

Yet another aspect of the usability and efficacy of a drug revolves around synergistic and/or antagonistic effects that are related to the drug target(s) and potential interactions with other drugs. Synergistic relationships can occur in series, in parallel, and in combination, while antagonistic interactions involve positive-feedback interactions (32). In the case of CP1, neither synergistic nor antagonistic effects with ITZ or AmB were observed. This may be rationalized by the fact that CP1, ITZ, and AmB target different pathways, *i.e.*, possess entirely different modes of action. Scanning electron microscopy showed a defect in the budding of yeast cells, suggesting that CP1 interfered with the cell cycle. This effect can be explained by the inhibition of the shikimate pathway, which provides essential metabolites such as aromatic amino acids.

CP1 treatment of animals infected by *P. brasiliensis* was highly effective. This compound was able to reduce pulmonary fibrosis, inflammatory infiltration, and yeast cells at a dosage of 5 mg/kg over 14 days. The efficiency of CP1 in reducing the lung fungal burden was very similar to that of treatment with ITZ, but the host inflammatory response was better controlled in the animals treated with CP1. Similar results were found with treatment with chalcone (compound 4c), which presented pulmonary parenchyma preserved with mild areas of inflammation (31). Although ITZ is an oral drug with good activity against *P. brasiliensis*, it leads to important adverse reactions (33). During treatment with ITZ, patients suffer from irreversible changes in the hepatobiliary system that indicate hepatotoxicity and, consequently, result in the discontinuation of treatment (34).

Another limitation for treatment with ITZ is the development of fibrotic sequelae that was observed in approximately 60% of patients even after prolonged treatment (35, 36). It is important to note that despite the morbidity and mortality associated with pulmonary fibrosis in patients with PCM, there is no effective therapy for this condition (6). Thus, the ability of CP1 to reduce the fungal burden and inflammatory response in the lungs of mice infected with *P. brasiliensis* appears to be very promising for controlling pulmonary sequelae in PCM. It is noteworthy that a similar effect was achieved by a combination of antifungal treatment and immunomodulatory components. The immunization with P10 in association with conventional drugs resulted in the absence of granulomas and areas with very few or undetectable yeast cells (37). Similarly, Naranjo and collaborators combined itraconazole-pentoxifylline treatment to reduce lung fibrosis in the murine model of PCM (36), and Puerta-Arias and

collaborators were able to reduce the infection and pulmonary fibrosis with a combination of ITZ and monoclonal antibody against neutrophils (38).

Conclusions

In conclusion, we have successfully demonstrated the identification of a new antifungal lead structure by a combination of virtual screening and molecular dynamics simulations. Furthermore, we have shown that the identified compound, CP1, was bound to the putative target enzyme, CS, and inhibited its activity. This new compound combines a potent antifungal activity *in vivo* with a significant reduction in lung inflammation that may contribute to the reduction of pulmonary fibrosis, a serious complication frequently occurring in PCM patients. In addition, CP1 could be used as a lead structure to further develop this new class of antifungal compounds, targeting chorismate synthase of the respective pathogenic fungus. Therefore, we are confident that our results provide a promising new direction for the treatment of PCM.

Materials and methods

Sequence analysis and protein modeling

The amino acid sequence of *PbCS* (39) (Uniprot number: C1GBW5) was evaluated by InterProScan server (40) for identification of structural motifs. This sequence was also used to search for structural templates in two ways, via BLASTp (41) and through structural alignment by means of fold recognition using pGenThreader (42), which also provides the prediction of secondary structure. The crystallographic structures of homotetrameric forms of CS from *Saccharomyces cerevisiae* (15) (PDB codes 1R53 and 1R52), from *Streptococcus pneumoniae* (43) (PDB code 1QXO), and from *Helicobacter pylori* (44) (PDB code 1UM0) were used as the main protein templates. Figure S1 in the Supplemental material shows the alignment of the amino acid sequences from templates with *PbCS*. The structure with PDB code 1UM0 was also used as the template for the cofactor FMNH₂, while the structure with PDB code 1QXO was used as the template for the substrate 5-EPSP. The Modeller-v9.11 program (45) generated 1,000 models using a symmetry restraint applied on the alpha- carbons of all four chains. The best five models were selected by the modeler Dope score, where the best one was chosen based on the stereochemical quality evaluated by the program Procheck (CCP4 1994). An additional 1,500 models were generated for correction of eventual residues placed in regions not allowed in the Ramachandran plot, and the best one was chosen according the criterion described above.

Partial charge calculations

The force field Charmm C35b2-C36a2 (46) was used in the protein molecular dynamics (MD) simulations. The files containing spatial coordinates of the ligands 5-EPSP (zinc4095612), CP1 (zinc6445857), CP2 (zinc6445743), CP3 (zinc13370291), and FMNH₂ (zinc31976681) were obtained from the Zinc Database (47), adjusted to its protonation state at pH 7.0, and then submitted to the SwissParam server (48) to generate their force field parameters. The Mülliken charges for each atom of the ligands were calculated using the B3LYP/6-311G* level of theory by means of the program Orca (49).

MD simulations

The MD simulation were done through the program NAMD2 (50). Initially, the modeled homotetramer structure was solvated in a periodic box with TIP3 water, where the limits were at least from 10 Å away from the outer surface of the protein. A sufficient amount of sodium counterions was added to neutralize the system charges. The MD simulation was carried out in four steps. In the first step, all system atoms were minimized by 60,000 steps of conjugate gradient. In the second step, the atoms of protein and ligands were fixed in space and water and ions were equilibrated for 60 ps. In the third step, all atoms of the system were minimized again for 60,000 steps, where the resulting structure (minimized 3) was used in redocking and virtual screening simulations. In the fourth and final step, the entire system was equilibrated for 20 ns. All simulations were performed at 300 K, 1 atm, and pH 7.0. All other simulation parameters were adjusted according to the protocol previously described (51). The simulations were evaluated in terms of root mean square deviation (RMSD) using the full minimized structure (minimized 3) as the reference. The radius of gyration (R_{gyr}) of the protein-ligand complexes, the protein residues in contact with inhibitors until a distance of 4.0 Å, the root mean square fluctuation (RMSF) of alpha-carbons of each protein residue, and the number of hydrogen bonds between protein and ligands were extracted from the trajectory file. The simulations were carried out in four nodes of an SGI Altix ICE 8400 LX running parallel and using two processors, Intel Six Core 5680 of 3.33 GHz in each node (48 cores) and 36GB RAM, at CENAPAD/Unicamp, Brazil.

VS simulations

The docking protocol was established from redocking evaluations of 5-EPSP on the full minimized structure of the protein-cofactor complex by means of two programs, the Autodock v.4.2.3 (52) implemented in the Pyrx-0.9 graphical interface (53), and the program Molegro Virtual Docker v.6 (54). The Autodock program uses the default search and rank algorithms and a default box size centered on 5-EPSP. The search and rank protocols for Molegro were Moldock Simplex Evolution and Moldock Score (Grid), respectively. The 10-Å radius of the search sphere was centered on 5-EPSP. Both

protocols were validated by five repetitions, providing an average docking RMSD of 0.57 ± 0.130 Å, which was applied in virtual screening (VS). The library used in the VS was built through a literature search and by searching in the Binding Database (55) and Brenda enzymes (56) by molecules with known inhibitory activities on CS. For each identified molecule, a new search was made in the Zinc database for molecules with 80% structural similarity and commercial availability (2,555 molecules). The Natural Products library from Zinc (204,400 molecules) was added to the first, totaling 206,955 structures, plus the structure of 5-EPSP, so that at the end of the simulation only the best ranked substrates were considered.

Compound CPI

The CPI compound {(1*S*,2*S*,3*aS*,4*S*,9*bR*)-1-chloro-6-nitro-2-[(2-nitrophenyl)sulfanyl]-2,3,3*a*,4,5,9*b*-hexahydro-1*H*-cyclopenta[*c*]quinoline-4-carboxylic acid} was purchased from Specs, Netherlands. The stock solution was prepared in dimethyl sulfoxide (DMSO) at a concentration of 100 mg/mL. For the assay, this solution was diluted in a culture medium or phosphate-buffered saline (PBS, 0.1 M, pH 7) and complete solubilization was achieved with Pluronic (0.2%; Sigma-Aldrich, St. Louis, MO).

Plasmid construction

The CS gene of the Pb18 isolate from *P. brasiliensis* (GenBank accession no. XM_010761971.1; 1218 bp) was commercially synthesized with the preferred codons of *Escherichia coli* (Epoch Biolabs, Missouri City, TX) and cloned into a pET21a vector using the *NdeI* and *XhoI* restriction sites at the 5' and 3' ends, respectively. Thereby, a nucleotide sequence coding for a C-terminal hexahistidine-tag was fused to the gene of interest to allow for purification of the recombinant protein by affinity chromatography. Clones containing the correct insert were transformed with *E. coli* BL21 (λ DE3) cells (Novagen, San Diego, CA) for gene expression.

Production and purification of recombinant PbCS

For expression of *PbCS*, Luria-Bertani (LB) medium containing 100 µg/mL ampicillin was inoculated with an overnight culture to an optical density at 600 nm (OD_{600}) of 0.1, and cultures were grown to an OD_{600} of 0.7 at 37°C and 140 rpm. Then, expression was induced by adding isopropyl β -D-1-thiogalactopyranoside (IPTG) to a final concentration of 0.1 mM, and cultures were further incubated at 20°C and 140 rpm overnight (16 h). Cells were harvested by centrifugation (5,500 x g for 15 min) and the resulting cell pellets were stored at -20°C until further use.

To obtain pure *PbCS*, cell pellets (approximately 15 g cell [wet weight]) were resuspended in about 40 mL of binding buffer (50 mM NaH_2PO_4 , 150 mM NaCl, 10 mM imidazole [pH 8]) and lysed by

sonication (2 x 5 min) using a Labsonic L sonication probe (B. Braun Biotech, Berlin, Germany). The lysate was cleared by centrifugation (38,500 x g for 45 min) and loaded onto a nickel-nitriloacetic acid (Ni-NTA) column (5 mL) equilibrated with binding buffer. After extensive washing (10 column volumes) with wash buffer (50 mM NaH₂PO₄, 150 mM NaCl, 20 mM imidazole, [pH 8]) to remove all unspecifically bound proteins, *PbCS* was eluted with elution buffer (50 mM NaH₂PO₄, 150 mM NaCl, 300 mM imidazole, [pH 8]) and SDS-PAGE analysis was used to identify the fractions containing *PbCS* (> 98% purity). The latter were pooled and dialyzed against 50 mM C₇H₁₅NO₄S (MOPS; pH 7.5), overnight before concentrating the protein to about 400 μM using centrprep (30 kDa cut-off, Merck-Millipore, Darmstadt, Germany). The protein was flash frozen using liquid nitrogen and stored at -80°C until further use.

Determination of the dissociation constant of CP1

To assay the binding of CP1 to *PbCS*, changes in the UV-Vis absorption spectrum of CP1 were studied as a function of the concentration of CS. To this end, 800 μL of CP1 diluted to a final concentration of 20 μM using 50 mM MOPS (pH 7.5, A₄₃₉ = ~0.2) was transferred to a quartz cuvette and an absorption spectrum was recorded between 300 and 800 nm. Then, 10-μL aliquots of *PbCS* (400 μM) were added to both the measurement and reference cuvette, and the absorption spectrum was recorded after each addition. To quantify the binding affinity of CP1 to *PbCS*, absorption changes at 500 nm were plotted as a function of the enzyme concentration in the cuvette, with the standard deviation (SD; from three titrations) represented by error bars. Using a hyperbolic fit, a dissociation constant (K_d) could be determined.

Effect of CP1 on chorismate synthase activity

To test the inhibitory effect of CP1 on *PbCS*, a coupled assay involving EPSP, CS, and anthranilate synthase was used (57, 58). This special assay set-up allowed forward coupling of the CS reaction, leading to the formation of anthranilate, a stable product that exhibits a fluorescence emission maximum at 390 nm and can thus be detected spectrofluorometrically.

Reaction mixtures containing 3 mM MgSO₄, 7.5 mM L-Gln, 22.5 mM (NH₄)₂SO₄, 1 mM dithiothreitol (DTT), 10 μM FMN, 80 μM EPSP, 4 μM *PbCS*, ~20 μM anthranilate synthase, and varying concentrations of CP1 (0.1 to 500 μM) were prepared in 100 mM potassium phosphate (pH 7.6) and pipetted into a 96-well plate (triplicate determinations). After the addition of 500 μM NADPH, the plate was incubated at 37°C for 60 s before recording the fluorescence emission changes at 390 nm (λ_{ex} = 340 nm) using a Spectramax Gemini XS Microplate Spectrofluorometer (Molecular Devices, San Jose, CA) for 5 min (data points every 12 s). Initial velocities were extracted from the first 15 data points, and relative rates were plotted as a function of the log (CP1 micromolar concentration), with the standard

deviations shown as error bars (triplicate determinations). Using the program GraphPad Prism 5 (GraphPad Software, Inc., San Diego, CA), the data were fitted applying the non-linear curve fit “log(inhibitor) versus normalized response - variable slope”, which allowed for the determination of IC₅₀s.

Fungal growth conditions

In this study, five isolates from *Paracoccidioides* spp were used, two from *P. brasiliensis* (Mg14 and Pb18) and three from *P. lutzii* (Pb01, 8334 and ROSC). These isolates belong to the Medical Mycology Laboratory Collection of Universidade Estadual de Maringá. Fungal yeast cells were maintained by weekly subcultivation in semisolid Fava Netto culture medium containing 4% glucose at 35°C and were used on the seventh day of culture (59).

Animals

Six-week-old male Balb/c mice bred under specific-pathogen-free conditions at the animal facilities of the Universidade Estadual de Maringá, Brazil, were used. All the procedures were performed according to the regulations of the institutional Ethical Committee for animal experimentation, State University of Maringá, Brazil (approval no. CEP 053/2014). The animals were handled according to guideline for the care and use of laboratory animals of CONCEA (67).

MICs

The antifungal activity assays were performed by the broth microdilution method according to guidelines of the Clinical and Laboratory Standards Institute (CLSI; document M27-A3) (60), with modifications. The CP1 concentration ranged from 0.2 to 128 mg/liter, and only RPMI 1640 medium was used as a negative control. Briefly, yeast cell suspensions (0.5×10^5 to 2.5×10^5 CFU/mL) were prepared in RPMI 1640 and diluted 1:2 at the well plate. The MIC plates were incubated at 35°C for 7 days (61). The minimal fungicidal concentrations (MFCs) were determined by subculture from each well onto brain heart infusion (BHI) agar plates incubated at 35°C for 7 days. The MFC was the lowest drug concentration that showed no growth (30). The synergistic interaction between CP1 and itraconazole or amphotericin B was evaluated by microdilution checkerboard (62).

Cytotoxicity evaluation

The CP1 cytotoxicity evaluation was performed in HeLa, J774, and HUVEC cells using the CellTiter 96 assay (Promega, Madison, WI) based on the reduction of MTS [3-(4,5-dimethylthiazol-2-yl)-5-(3-carboxymethoxyphenyl)-2-(4-sulfophenyl)-2H-tetrazolium] (63).

Scanning electron microscopy (SEM)

Yeast (Pb18 isolate) was incubated for 72 h at 35°C with CP1 (64 mg/liter). The cells were prepared as previously described (64). Samples were then observed with a Shimadzu SS-550 Super Scan (Shimadzu, Tokyo, Japan) at magnifications of x 1,000 and x 3,000.

Experimental paracoccidioidomycosis and treatment

The mice were infected through an intra-tracheal (i.t.) route (1×10^6 viable yeast cells, by trypan blue). After 48 h of infection, the animals were treated intraperitoneally daily with CP1 (5 mg/kg), ITZ (5 mg/kg), or the control for 14 days. The control group was treated with a vehicle (PBS, DMSO [1%], and Pluronic [0.2%]) used for diluting the CP1 compound. Then, the mice were euthanized, and organs were aseptically removed for fungal burden determination (CFU per gram) (65). Briefly, the organs were weighed and macerated in PBS. CFU were recovered in supplemented BHI agar and incubated at 37°C for 7 days or until there was no growth. The CFU was determined, and the results were presented as \log_{10} of the average value \pm standard error. These experiments were repeated three independent times.

Histopathological analysis

Parts of the organs were fixed in PBS-10% formalin, dehydrated, and embedded in paraffin. Five-micrometer sections were stained with hematoxylin and eosin (H&E), and the severity and size of the tissue lesion were examined by microscope. Pathological changes were analyzed based on the size, morphology, and cell composition of granulomatous lesions and the presence of fungi and inflammatory infiltrates. Morphometric analysis was performed using a Nikon DXM 1200c digital camera (magnifications of x 50 and x 400) and Nikon NIS Elements AR 2.30 software (66). Histo-pathological analysis was performed on the lungs of all animals. The following three parameters were analyzed: fibrosis, inflammatory infiltrate, and fungal cells. In the semiquantitative analysis, each one of the parameters was assigned a score that ranged from 1 to 3, increasing and depending on the degree of tissue damage. When the quantifier was not observed, the score was assigned as 0. The obtained scores were plotted and subjected to statistical analysis.

Statistical analysis

Data are expressed as the mean \pm standard deviations (SDs) from at least three independent experiments. Significant differences among means of the variables before and after treatment with CPI were identified using Student's *t* distribution. The data was analyzed using Prism 6.0 software (GraphPad, San Diego, CA). *P* values of ≤ 0.05 were considered statistically significant.

Acknowledgements

We thank the financial support of the Brazilian agencies CAPES, CNPq, and Fundação Araucária (147/14 and 40/16) and CENAPAD/SP and LNCC for computational facilities. PM wishes to express his gratitude to the Austrian Science Fund for providing financial support through DK Molecular Enzymology (W901).

References

1. da Costa MM, da Silva SHM. 2014. Epidemiology, clinical, and therapeutic aspects of paracoccidioidomycosis. *Trop Mycol Current Trop Med Rep* **1(2)**: 138–144.
2. Bocca AL, Amaral AC, Teixeira MM, Sato PK, Shikanai-Yasuda MA, Felipe MSS. 2013. Paracoccidioidomycosis: eco-epidemiology, taxonomy and clinical and therapeutic issues. *Future Microbiol* **8**:1177–1191.
3. Bellissimo-Rodrigues F, Machado AA, Martinez R. 2011. Paracoccidioidomycosis epidemiological features of a 1,000-cases series from a hyperendemic area on the southeast of Brazil. *Am J Trop Med Hyg* **85**:546–550.
4. Coutinho ZF, Silva D, Lazerda M. 2002. Paracoccidioidomycosis mortality in Brazil (1980–1995). *Cad Saú Púb* **18**:1441–54.
5. Martinez R. 2017. New trends in paracoccidioidomycosis epidemiology. *J Fungi* (Basel) **3(1)**. pii: E1.
6. Shikanai-Yasuda MA, Mendes RP, Colombo AL, Queiroz-Telles F, Kono ASG, Paniago AMM, Nathan A, Valle ACFD, Bagagli E, Benard G, Ferreira MS, Teixeira MM, Silva-Vergara ML, Pereira RM, Cavalcante RS, Hahn R, Durlacher RR, Khoury Z, Camargo ZP, Moretti ML, Martinez R. 2017. Brazilian guidelines for the clinical management of paracoccidioidomycosis. *Rev Soc Bras Med Trop* **50(5)**:715–740.
7. Queiroz-Telles F, Fahal AH, Falci DR, Caceres DH, Chiller T, Pasqualotto AC. 2017. Neglected endemic mycoses. *Lancet Infect Dis* **17(11)**:e367–e377.
8. Haanstra JR, Gerding A, Dolga AM, Sorgdrager FJH, Buist-Homan M, du Toit F, Faber KN, Holzhütter HG, Szöör B, Matthews KR, Snoep JL, Westerhof HV, Bakker BM. 2017. Targeting pathogen metabolism without collateral damage to the host. *Sci Rep* **7**:40406.
9. Abadio AK, Kioshima ES, Teixeira MM, Martins NF, Maigret B, Felipe MS. 2011. Comparative genomics allowed the identification of drug targets against human fungal pathogens. *BMC Genomics*. **27**;12:75.
10. Bentley R. 1990. The shikimate pathway--a metabolic tree with many branches. *Biochem Mol Bio* **25**:307–84.
11. Duke SO, Powles SB. 2008. Glyphosate: a once-in-a-century herbicide. *Pest Manag Sci* **648(1)**:319–325.
12. Herrmann KM, Weaver LM. 1999. The shikimate pathway. *Annu Rev Plant Physiol Plant Mol Biol* **50**:473–503.
13. Dias MV, Ely F, Palma MS, de Azevedo WFJ, Basso LA, Santos DS. 2007. Chorismate synthase: an attractive target for drug development against orphan diseases. *Curr Drug Targets* **8(3)**:437–44.

14. Schönbrunn E, Eschenburg S, Shuttleworth WA, Schloss JV, Amrhein N, Evans JN, Kabsch W. 2001. Interaction of the herbicide glyphosate with its target enzyme 5-enolpyruvylshikimate 3-phosphate synthase in atomic detail. *Proc Natl Acad Sci* **98(4)**:1376–1380.
15. Macheroux P, Schmid J, Amrhein N, Schaller A. 1999. A unique reaction in a common pathway: mechanism and function of chorismate synthase in the shikimate pathway. *Planta* **207(3)**:325–334.
16. Quevillon-Cheruel S, Leulliot N, Meyer P, Graille M, Bremang M, Blondeau K, Sorel I, Poupon A, Janin J, van Tilbeurgh H. 2004. Crystal structure of the bifunctional chorismate synthase from *Saccharomyces cerevisiae*. *J Biol Chem* **279(1)**:619–625.
17. Rost B. 1999. Twilight zone of protein sequence alignments. *Protein Eng* **12(2)**:85–94.
18. Yang AS, Honig B. 2000. An integrated approach to the analysis and modeling of protein sequences and structures. III. A comparative study of sequence conservation in protein structural families using multiple structural alignments. *J Mol Biol* **301(3)**:691–711.
19. Miteva MA, Violas S, Montes M, Gomez D, Tuffery P, Villoutreix BO. 2006. FAF-Drugs: free ADME/tox filtering of compound collections. *Nucleic Acids Res* **34** (Web Server issue):W738–744.
20. Tapas S, Kumar A, Dhindwal S, Preeti, Kumar P. 2011. Structural analysis of chorismate synthase from *Plasmodium falciparum*: a novel target for antimalarial drug discovery. *Int J Biol Macromol* **49(4)**:767–777.
21. Cruz RC, Werneck SMC, Oliveira CS, Santos PC, Soares BM, Santos DA, Cisalpino PS. 2012. Conditions for determining the minimal inhibitory concentration (MIC) of seven antifungal agents against *Paracoccidioides brasiliensis* by microdilution: influence of different media, incubation times and temperatures. *J Clin Microbiol* **02231**.
22. Aguirre JPB, Hamid AMR. 2015. Amphotericin B deoxycholate versus liposomal amphotericin B: effects on kidney function. *Cochrane Database Syst Rev* **23**;(11):CD010481.
23. Borges SR, Silva GM, Chambela MC, Oliveira RV, Costa RL, Wanke B, Valle AC. 2014. Itraconazole vs. trimethoprim-sulfamethoxazole: A comparative cohort study of 200 patients with paracoccidioidomycosis. *Med Mycol.* **52(3)**:303–10.
24. Shikanai-Yasuda MA, Benard G, Higaki Y, Del Negro GM, Hoo S, Vaccari EH, Gryschek RC, Segurado AA, Barone AA, Andrade DR. 2002. Randomized trial with itraconazole, ketoconazole and sulfadiazine in paracoccidioidomycosis. *Med Mycol* **40(4)**:411–7.
25. Roemer T, Krysan DJ. 2014. Antifungal drug development: challenges, unmet clinical needs, and new approaches. *Cold Spring Harb Perspect Med* **4(5)**. pii: a019703.
26. Macedo PM, Almeida-Paes R, Freitas DFS, Brito-Santos F, Figueiredo-Carvalho MHG, Soares JCA, Freitas AD, Zancopé-Oliveira RM, do Valle ACF. 2017. Hepatic disease with portal hypertension and acute juvenile paracoccidioidomycosis: A report of two cases and literature review. *Mycopathologia* **182(9-10)**:915-919

27. Laniado-Laborín R, Cabrales-Vargas MN. 2009. Amphotericin B: side effects and toxicity. *Rev Iberoam Micol* **26**: 223–7.
28. Abadio AKR, Kioshima ES, Leroux V, Martins NF, Maigret B, Felipe MSS. 2015. Identification of new antifungal compounds targeting thioredoxin reductase of *paracoccidioides* genus. *PLoS ONE* **10(11)**, e0142926.
29. Batagin MC, Pimentel AL, Biavatti DC, Basso EA, Kioshima ES, Seixas FAV, Gauze GF. 2017. Targeting homoserine dehydrogenase from *Paracoccidioides* Genus against systemic fungal infections. *Antimicrob Agents Chemother pii*: AAC.00165-17.
30. Johann S, Sá NP, Lima LA, Cisalpino PS, Cota BB, Alves TMA, Siqueira EP, Zani CL. 2010. Antifungal activity of schinol and a new biphenyl compound isolated from *Schinus terebinthifolius* against the pathogenic fungus *Paracoccidioides brasiliensis*. *Ann Clin Microbiol Antimicrob* **9**:30. <https://doi.org/10.1186/1476-0711-9-30>.
31. de Sá NP, Cisalpino PS, Tavares LC, Espíndola L, Pizzolatti MG, Santos PC, de Paula TP, Rosa CA, Souza DG, Santos DA, Johann S. 2015. Antifungal activity of 6-quinolinyl N-oxide chalcones against *Paracoccidioides*. *J Antimicrob Chemother* **70**:841–5.
32. Yin N, Ma W, Pei J, Ouyang Q, Tang C, Lai L. 2014. Synergistic and antagonistic drug combinations depend on network topology. *PLoS ONE* **9(4)**, e93960.
33. Queiroz-Telles F, Goldani LZ, Schlamm HT, Goodrich JM, Espinel-Ingroff A, Shikanai-Yasuda MA. 2007. An open-label comparative pilot study of oral voriconazole and itraconazole for long-term treatment of paracoccidioidomycosis. *Clin Infect Dis* **45**:1462–9.
34. Levorato AD, Moris DV, Cavalcante RS, Sylvestre TF, Azevedo PZ, Carvalho LR, Mendes RP. 2017. Evaluation of the hepatobiliary system in patients with paracoccidioidomycosis treated with cotrimoxazole or itraconazole. *Med Mycol* **9**.
35. Tobón AM, Agudelo CA, Osorio ML, Alvarez DL, Arango M, Cano LE, Restrepo A. 2003. Residual pulmonary abnormalities in adult patients with chronic paracoccidioidomycosis: prolonged follow-up after itraconazole therapy. *Clin Infect Dis* **37(7)**:898–904
36. Naranjo TW, Lopera DE, Diaz-Granados LR, Duque JJ, Restrepo AM, Cano LE. 2011. Combined itraconazole-pentoxifylline treatment promptly reduces lung fibrosis induced by chronic pulmonary paracoccidioidomycosis in mice. *Pulm Pharmacol Ther* **24(1)**:81–91.
37. Marques AF, Silva MB, Juliano MAP, Munhõz JE, Travassos LR, Tabora CP. 2008. Additive effect of P10 immunization and chemotherapy in anergic mice challenged intratracheally with virulent yeasts of *Paracoccidioides brasiliensis*. *Microb Infect* **10**:1251-8.
38. Puerta-Arias JD, Pino-Tamayo PA, Arango JC, Salazar-Peláez LM, González A. 2017. Itraconazole in combination with neutrophil depletion reduces the expression of genes related to pulmonary fibrosis in an experimental model of paracoccidioidomycosis. *Med Mycol* **9**.

39. Desjardins CA, Champion MD, Holder JW, Muszewska A, Goldberg J, Bailao AM, Brigido MM, Ferreira ME, Garcia AM, Grynberg M et al. 2011. Comparative genomic analysis of human fungal pathogens causing paracoccidioidomycosis. *PLoS Genet* **7(10)**:e1002345.
40. Mulder N, Apweiler R. 2007. InterPro and InterProScan: tools for protein sequence classification and comparison. *Methods Mol Biol* **396**:59–70.
41. Mount DW. 2007. Using the Basic Local Alignment Search Tool (BLAST). *CSH Protoc*
42. Lobley A, Sadowski MI, Jones DT. 2009. pGenTHREADER and pDomTHREADER: new methods for improved protein fold recognition and superfamily discrimination. *Bioinformatics* **25(14)**:1761–1767.
43. Maclean J, Ali S. 2003. The structure of chorismate synthase reveals a novel flavin binding site fundamental to a unique chemical reaction. *Structure* **11(12)**:1499–1511.
44. Ahn HJ, Yoon HJ, Lee B Suh SW. 2004. Crystal structure of chorismate synthase: a novel FMN-binding protein fold and functional insights. *J Mol Biol* **336(4)**:903–915.
45. Eswar N, Webb B, Marti-Renom MA, Madhusudhan MS, Eramian D, Shen MY, Pieper U, Sali A. 2006. Comparative protein structure modeling using Modeller. *Curr Protoc Bioinformatics* Chapter 5: Unit 5 6.
46. Mackerell AD, Feig M, Brooks CL. 2004. Extending the treatment of backbone energetics in protein force fields: limitations of gas-phase quantum mechanics in reproducing protein conformational distributions in molecular dynamics simulations. *J Comput Chem* **25(11)**:1400–1415.
47. Irwin JJ, Sterling T, Mysinger MM, Bolstad ES, Coleman RG. 2012. ZINC: A free tool to discover chemistry for biology. *J Chem Inf Model* **52(7)**:1757–68.
48. Zoete V, Cuendet MA, Grosdidier A, Michielin O. 2011. SwissParam: a fast force field generation tool for small organic molecules. *J Comput Chem* **32(11)**:2359–2368.
49. Neese F. 2012. The ORCA program system. *Wiley Interdiscip Rev Comput Mol Sci* **2(1)**:73–78.
50. Phillips JC, Braun R, Wang W, Gumbart J, Tajkhorshid E, Villa E, Chipot C, Skeel RD, Kale L, Schulten K. 2005. Scalable molecular dynamics with NAMD. *J Comput Chem* **26(16)**:1781–1802.
51. Homem DP, Flores R, Tosqui P, Rozada TC, Basso EA, Gasparotto A, Seixas FAV. 2013. Homology modeling of dihydrofolate reductase from *T. gondii* bonded to antagonists: molecular docking and molecular dynamics simulations. *Mol Biosyst* **9(6)**:1308–1315.
52. Morris GM, Huey R, Lindstrom W, Sanner MF, Belew RK, Goodsell DS, Olson AJ. 2009. AutoDock4 and AutoDockTools4: Automated docking with selective receptor flexibility. *J Comput Chem* **30(16)**:2785–2791.
53. Wolf LK. 2009. New software and websites for the chemical enterprise. *Chemical & Engineering News* **87(5)**:32.

54. Thomsen R, Christensen MH. 2006. MolDock: a new technique for high-accuracy molecular docking. *J Med Chem* **49(11)**:3315–3321.
55. Gilson MK, Liu T, Baitaluk M, Nicola G, Hwang L, Chong J. 2016. BindingDB in 2015: A public database for medicinal chemistry, computational chemistry and systems pharmacology. *Nucleic acids research* **44(D1)**:D1045–1053.
56. Schomburg I, Chang A, Placzek S, Sohngen C, Rother M, Lang M, Munaretto C, Ulas S, Stelzer M, Grote A. et al. 2013. BRENDA in 2013: integrated reactions, kinetic data, enzyme function data, improved disease classification: new options and contents in BRENDA. *Nucleic acids research* **41(Database issue)**:D764–772.
57. Schaller A, Windhofer V, Amrhein N. 1990. Purification of chorismate synthase from a cell culture of the higher plant *Corydalis sempervirens* Pers. *Arch Biochem Biophys* **282(2)**:437–442.
58. Fitzpatrick TB, Killer P, Thomas RM, Jelesarov I, Amrhein N, Macheroux P. 2001. Chorismate synthase from the hyperthermophile *Thermotoga maritima* combines thermostability and increased rigidity with catalytic and spectral properties similar to mesophilic counterparts. *J Biol Chem* **276(21)**:18052–18059.
59. Fava-Netto C, Vegas VS, Sciannaméa IM, Guarnieri DB. 1969. The polysaccharidic antigen from *Paracoccidioides brasiliensis*. Study of the time of cultivation necessary for the preparation of the antigen. *Rev Inst Med Trop* **11**:177–181. PMID: 5824780.
60. Clinical and Laboratory Standards Institute (CLSI) (2008) Reference Method for broth dilution antifungal susceptibility testing of yeast, 3rd ed. Approved standard. CLSI M27-A3. Wayne, PA: Clinical and Laboratory Standards Institute.
61. Cruz RC, Werneck SMC, Oliveira CS, Santos PC, Soares BM, Santos DA, Cisalpino PS. 2013. Influence of different media, incubation times, and temperatures for determining the MICs of seven antifungal agents against *Paracoccidioides brasiliensis* by microdilution. *J Clin Microbiol* **51**:436–43.
62. Hemaiswarya S, Kruthiventi AK, Doble M. 2008. Synergism between natural products and antibiotics against infectious diseases. *Phytomedicine* **15(8)**:639–52.
63. Capoci IRG, Bonfim-Mendonça PS, Arita GS, Pereira RRA, Consolaro MEL, Bruschi ML, Negri M, Svidzinski TIE. 2015. Propolis is an efficient fungicide and inhibitor of biofilm production by vaginal *Candida albicans*. *Evid-Bas Compl and Alter Medic* **1**:1–9.
64. Sakita KM, Faria DR, Silva EMD, Tobaldini-Valério FK, Kioshima ES, Svidzinski TI, Bonfim-Mendonça PS. 2017. Healthcare workers' hands as a vehicle for the transmission of virulent strains of *Candida* spp. A virulence factor approach. *Microb Pathog* **113**:225–232.
65. Kioshima ES, Aliperti F, Maricato JT, Mortara RA, Bagagli E, Mariano M, Lopes JD. 2011. A synthetic peptide selectively kills only virulent *Paracoccidioides brasiliensis* yeasts. *Microbes Infect* **13(3)**:251–60.

66. Costa TA, Bazan SB, Feriotti C, Araújo EF, Bassi Ê, Loures FV, Calich VL. 2013. Pulmonary paracoccidioidomycosis IL-10 Deficiency Leads to Increased Immunity and Regressive Infection without Enhancing Tissue Pathology. *PLoS Negl Trop Dis* 7: 2512.
67. Ministério da Ciência, Tecnologia e Inovação, Conselho Nacional de Controle de Experimentação Animal (CONCEA), Brazil. 2016. Guia brasileiro de produção, manutenção ou utilização de animais em atividades de ensino ou pesquisa científica. https://www.mctic.gov.br/mctic/export/sites/institucional/legislacao/Arquivos/Anexo_Res_Normativa_Concea_33_2016.pdf.

Supplementary information

	10	20	30	40	50	60
1R53A	MSTFGKLF	RVTTYGES	HCKSVG	CIVDGVP	PGMSL	TEADIQP
1UM0A	MNTLGR	FLRLTTF	GESHG	DVIGG	VLDGMP	SGIKIDY
1QXOB	-----	MRYLT	AGESHG	PRLTAI	IEGIP	AGLPLT
PbCS	-STFG	EYFRV	TTYGES	HCKSVG	CIVDG	CPGMA
		* * * * *		* * *		**
						** * * *
	70	80	90	100	110	120
1R53A	TEFGK	TLGTP	PIAMMI	KN-----	-----	-----
1UM0A	VFEDF	STGTP	IGFLI	HNQR	ARS-----	-----
1QXOB	VRHGK	TTGAP	ITMDV	INKD	HQK--	WLDIM
PbCS	TEFGI	TLGTP	IGMIV	RNE	DQRPK	D-----
		* * *		*		
	140	150	160	170	180	190
1R53A	-----	RETIG	RVASG	AIAEK	FQAQNS	NVEIV
1UM0A	FR-GG	GRS	SARE	S	AIRVA	AAGAF
1QXOB	LRNS	LE	RS	SARE	TTMR	VAVG
PbCS	ASSG	GRS	SARE	TIGR	VAA	GAIAE
		**		** * * *		*
	210	220	230	240	250	260
1R53A	TITRE	KVDS	MGP	IRCP	DASV	AGLM
1UM0A	-YDF	NHAL	K-SE	I	FALDE	EQE
1QXOB	AEIK	QRA	AQ-SE	V	IVNQ	ERE
PbCS	TIDR	P	VDS	FAP	VRC	PEAS
	280	290	300	310	320	330
1R53A	LEAM	LAH	AMLS	IPAS	KGF	EIGSG
1UM0A	LDAK	IAE	AM	MGL	NGV	KAVE
1QXOB	LDAR	LAQ	AVV	SIN	AFK	GV
PbCS	LEAK	LAH	AMLS	IPAT	KGF	EIGSG
		** * *		* * * *		*
	350	360	370	380	390	400
1R53A	ISNG	E	NIY	F	SV	PF
1UM0A	MSNG	E	II	VR	VH	F
1QXOB	MTNG	Q	PI	V	R	G
PbCS	ISNG	A	S	I	Y	F
		** *		*		
	410	420	430			
1R53A	KAR	D	F	S-----		
1UM0A	-----					
1QXOB	FSSD	N	L	E	E	L
PbCS	NARE	T	A	K	N	L

Figure S1. Alignment of the amino acid sequences from templates with *PbCS*. The green squares highlight residues that compose the 5-EPSP binding site in *P. brasiliensis*. Residues that do not have correspondence in the templates are marked in yellow. Conserved residues are represented by an asterisk and the ligands are represented by the points at the end of alignment.

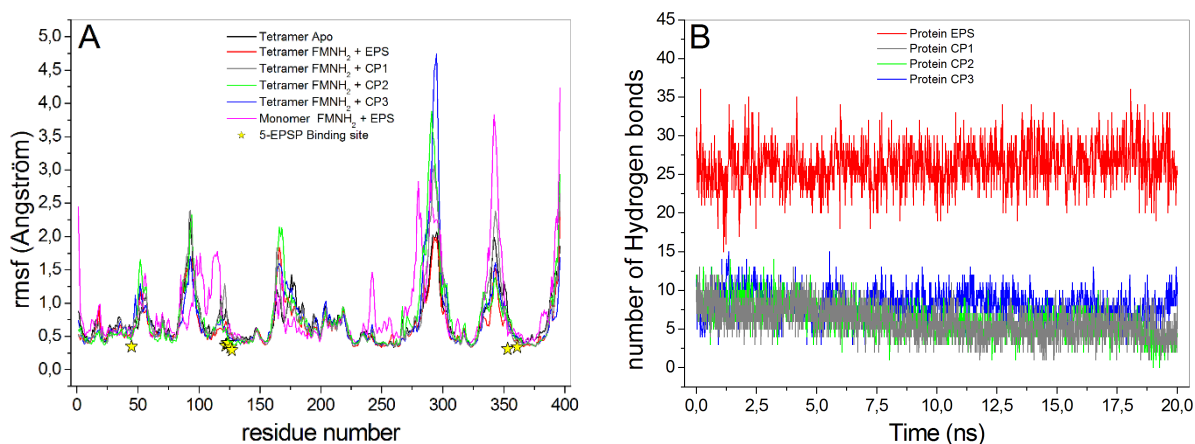


Figure S2. **A**, Root-mean-square fluctuation (RMSF) of Ca atoms from *PbCS* residues. The yellow stars mark the position of the active site residues described in *Table S1*. **B**, Average number of hydrogen bonds formed between the protein and ligand along the simulation. *PbCS* structures: The A chain bonded to FMNH₂ + 5-EPSP (*pink*), tetramer apo (*black*), tetramer bonded to FMNH₂ + 5-EPSP (*red*), tetramer bonded to FMNH₂ + CP 1 (*gray*), tetramer bonded to FMNH₂ + CP2 (*green*), and tetramer bonded to FMNH₂ + CP3 (*blue*). The root-mean-square deviation (**A**) and radius of gyration (**B**) were obtained from the oscillation of the protein main chain atoms relative to the full minimized structure.

Table S1. Contact frequency up to 4 Å between *PbCS* and the evaluated ligands.

Residue	EPSP	CP1	CP2	CP3	Residue	EPSP	CP1	CP2	CP3
Ser-15	–	0.24	–	0.12	Tyr-110	–	0.23	–	–
Arg-45	0.99	0.67	0.73	0.80	Ala-118	–	0.08	–	–
Arg-46	0.21	–	0.29	0.01	Ser-119	–	0.56	–	0.35
Ser-50	–	0.19	–	–	Ser-120	–	0.59	0.17	0.22
Leu-52	–	0.20	0.10	–	Gly-121	0.55	0.23	0.32	0.20
Thr-53	0.32	0.58	0.46	0.26	Gly-122	0.78	0.34	0.74	0.83
Thr-54	0.42	0.43	0.46	0.45	Gly-123	0.97	0.67	0.99	0.90
Pro-55	0.45	0.31	0.26	0.23	Arg-124	0.99	1.00	0.60	0.53
Asn-57	–	–	0.22	0.24	Ser-125	0.52	0.76	–	–
Glu-58	–	0.09	–	0.10	Ser-126	0.97	0.99	0.65	0.49
Asn-84	0.01	0.04	0.11	0.27	Ala-127	0.73	0.61	0.43	0.41
Asp-86	0.22	0.03	0.09	0.38	Thr-128	0.12	–	–	0.24
Gln-87	–	–	0.19	0.28	Thr-130	–	0.36	0.50	0.32
Asp-91	–	–	–	0.10	Ile-131	0.09	0.06	0.02	0.24
Tyr-92	0.10	–	0.05	–	Pro-258	–	0.15	–	–
Gly-93	–	–	–	0.12	Ala-330	–	–	0.06	0.39
Gly-94	–	–	–	0.40	Thr-331	0.08	0.19	0.44	0.48
Ser-95	–	0.20	0.11	0.05	Lys-351	–	–	0.02	0.09
Thr-96	–	–	–	0.06	Gly-352	0.31	0.26	0.28	0.48
Asp-98	–	0.24	–	–	Arg-353	1.00	0.97	0.95	0.99
Arg-102	0.25	0.37	–	0.88	His-354	–	0.27	0.59	0.07
Ser-104	–	–	0.24	–	Asp-355	0.04	0.55	0.52	0.21
His-105	0.25	0.7	0.69	0.64	Val-358	–	–	–	0.05
Ala-106	–	0.27	0.28	–	Arg-361	0.93	0.72	0.95	1.00
Asp-107	–	0.24	–	0.36	FMNH₂	1.00	1.00	1.00	1.00

Obs: only contacts with significant frequently ($p < 0.05$) are presented.

Appendix B

Inhibition of *PbCS* by CaCSO_2

New inhibitors of chorismate synthase present antifungal activity against *P. brasiliensis*

Paulo Sérgio Alves Bueno¹, Franciele Abigail Vilugron Rodrigues-Vendramini²,
Marina Toplak³, Peter Macheroux³, Érika Seki Kioshima Cótica²,
Flavio Augusto Vicente Seixas^{1*}

¹Department of Technology, Universidade Estadual de Maringá, Av. Ângelo Moreira da
Fonseca 1800, 87506-370 Umuarama, PR, Brazil.

²Department of Clinical Analysis and Biomedicine, Universidade Estadual de Maringá,
Av. Colombo 5790, 87020-900 Maringá, PR, Brazil.

³Institute of Biochemistry, Graz University of Technology, Petersgasse 12/2, 8010, Graz, Austria.

*Corresponding author: favseixas@uem.br

Av. Ângelo Moreira da Fonseca, 1800, Jd Universitário

87506-370, Umuarama, PR, Brazil

Fone: (+55) 44 36219337

Fax: (+55) 44 36219326

Keywords: antifungal; chorismate synthase; inhibitor; paracoccidioidomycosis; systemic mycosis.

Abbreviations

AmB, amphotericin B; *Ca*, *Candida albicans*; CG, conjugate gradient; CS, chorismate synthase; EPSP, 5-enolpyruvyl-shikimate-3-phosphate; FF, force field; FIC, fractional inhibitory concentration; FMN, flavin mononucleotide; IC_{50} , 50% inhibitory concentration; MD, molecular dynamics; MIC, minimal inhibitory concentration; MFC, minimal fungicidal concentration; *Pb*, *Paracoccidioides brasiliensis*; PCM, paracoccidioidomycosis; R_{gyr} , radius of gyration; RMSD, root mean square deviation; RMSF, root mean square fluctuation

Abstract

Aim: The structural model of chorismate synthase (CS) from the human pathogenic fungus *Candida albicans* was used for virtual screening simulations. **Methods:** Docking, molecular dynamics, cell growth inhibition and protein binding assays were used for search and validation. **Results:** Two molecules (Zinc6445805 and Zinc4217277, also termed CS8 and CaCS02, respectively) were identified. Further studies of the minimal inhibitory concentration demonstrated fungicidal activity against *Paracoccidioides brasiliensis* with MIC/MFC of 512 and 32 $\mu\text{g}\cdot\text{mL}^{-1}$ for CS8 and CaCS02, respectively. In addition, CaCS02 showed a strong synergistic effect in combination with amphotericin B without cytotoxic effects. *In vitro* studies using recombinant CS from *P. brasiliensis* showed an IC_{50} of 29 μM for CaCS02 supporting our interpretation that inhibition of CS causes the observed fungicidal activity.

Introduction

Invasive fungal infections pose serious threats to human health, resulting in at least 1.5 million deaths worldwide each year (1). Almost half of this number is caused by the *Candida* species (2). It lives commensally in the intestine, urogenital tract and other mucosal surfaces, in the proportion of one of two individuals (3). The immunosuppressed patients such as transplant recipients, patients with cancer, people affected by HIV, among others, are the most affected by these nosocomial infections (4, 5).

The paracoccidioidomycosis (PCM) is another fungal disease, endemic in Latin American countries, which presents a high prevalence in South America and it stands out as the major cause of death among systemic mycoses in Brazil (6, 7). The genus *Paracoccidioides* is composed of thermodynamic fungi *Paracoccidioides brasiliensis* and *Paracoccidioides lutzii*, which are the species most commonly identified as agents of the PCM (8). In Brazil it is estimated that approximately 51.2% of the deaths by systemic mycosis are caused by PCM (9). Among the risk factors for acquiring this infection, we highlight the external activities related to the management of soil contaminated with fungus and geographical exposure in affected regions. In addition, there are other associated factors, such as gender, age, smoking, alcohol consumption and socioeconomic conditions (10).

PCM presents distinct symptoms, and may manifest in the acute/subacute form and chronic form. The chronic form of PCM affects 90% of the patients. In these cases, a pulmonary architectural distortion occurs ranging from 63.8 to 100% of the patients (11–13). The pulmonary damage caused by fungal stimulation remains the same after the treatment, and causes pulmonary fibrosis with loss of respiratory function in 50% of cases (14). The arsenal of drugs against systemic mycoses is limited to antifungal agents such as polyenes (amphotericin B), azoles (itraconazole and fluconazole), and echinocadins (caspofungin, micafungin). However, there are reports in the literature describing strains

resistant to each of these drugs (15), which further limits its use in medicine (16). Therefore, there is an urgent need for the discovery of new antifungal agents, with preference for those that can act on different metabolic targets.

Nowadays, the development of an antifungal agent is a challenge, due to the few potential metabolic targets that are not shared by the fungus and the human species (host). Enzymes of the shikimate pathway are promising targets for the development of new antifungal agents (17), besides antimicrobial agents (18), anti-parasites (19) and herbicides (20), because this pathway is absent in mammals (17). It converts two compounds present in carbohydrate metabolism, phosphoenolpyruvate (PEP) and erythrose-4-phosphate (E4P), into the final chorismate product in a seven-step enzyme-catalyzed pathway. Metabolites such as folic acid, vitamin K, ubiquinone, phenylalanine, tyrosine and tryptophan are produced from chorismate, which are essential for the survival of fungi, bacteria, algae, plants and parasites of the apicomplex phylum (21). Thus, the enzymes that make up this pathway are excellent targets for drug discovery, which remain unexplored in *Candida spp* and *Paracoccidioides spp*.

The enzyme chorismate synthase (CS) (EC.: 4.2.3.5) acts on the last step of the shikimate pathway, catalyzing the conversion of the substrate 5-enolpyruvylshikimate-3-phosphate (EPSP) into chorismate, in the presence of the reduced form of flavin mononucleotide cofactor (FMNH₂) (21, 22). Although the 3D structure of *C. albicans* chorismate synthase (*CaCS*) has not yet been solved by any experimental method, its amino acid sequence has already a confirmed status in the Uniprot database. In addition, there are other CS crystallographic structures deposited in the Protein Data Bank (PDB) as from *Saccharomyces cerevisiae* (23), which shares 76% identity with the homologous enzyme from *C. albicans*.

In this context, the objective of this work was to use bioinformatics tools, such as homology modeling and large-scale virtual screening simulations to discover new molecules with potential antifungal activity. In order to validate the results obtained *in silico*, a set of *in vitro* assays of minimal inhibitory concentration (MIC and MCF) in human pathogenic fungi were performed, as well as kinetic and binding studies using the CS enzyme from *Paracoccidioides brasiliensis* in the presence of the selected ligands.

Results and Discussion

The amino acid sequence of chorismate synthase from *Candida albicans* (*CaCS*) comprises 378 residues giving rise to a molecular mass of 40,895 Da and a pI of 6.14 (24). In fungi, first and seventh enzyme, i.e. CS and phospho-2-dehydro-3-deoxyheptonate aldolase, tyrosine-inhibited, encoded by ARO2 and ARO4, respectively are monofunctional whereas the remainder of the enzymes in the shikimate pathway, catalyzing reactions two through six, form a pentafunctional protein (“arom complex”) encoded by ARO1 (25).

Further analysis of the sequence of *CaCS* by Blastp provided two structural templates: The CS from *Saccharomyces cerevisiae* (PDB ID: 1r53) (23) sharing 76% identity was used as template for the polypeptide chain. Because this structure does not provide the spatial coordinates of the substrate EPSP and the cofactor FMNH₂, we used the structure of CS from *Streptococcus pneumoniae* (PDB ID: 1qxo) (26) sharing 34% identity). The template 1r53 represents the biological unit of the homotetrameric enzyme, however, many residues around the active site are ill-defined due to lack of electron density in this region. Therefore, the B chain of the 1qxo template was used to model these missing regions. CS exhibits two distinct conformations of the active site: in the unliganded apo-form several loops near the active site adopt an open conformation, whereas in the presence of the substrate and FMN, these loops are in a closed conformation basically forming a lid closing access to the active site. The use of the 1qxo template allowed the *CaCS* to be modeled in the closed form and in the presence of the FMNH₂ cofactor plus the substrate, which presumably represents a catalytically active conformation.

The high degree of freedom of movement of the protein in the monomeric form could compromise the configuration of the active site, essentially structured by random segments (loops and turns). Previous MD simulations with the CS of *Mycobacterium tuberculosis* (27), have demonstrated that the homotetrameric form is more stable than the monomeric and dimeric forms. Therefore, we have modeled *CaCS* as a homotetramer, the most likely biological unit. The stereochemical constraints of this conformation diminished possible distortions in the loops, contributing to the active site and thus render this region more amenable to MD simulations. After modeling and minimization, only one of the subunits was effectively used in the docking studies.

The final model of *CaCS* (Figure 1) showed 99.7% of the residues in allowed regions of the Ramachandran plot indicating excellent stereochemical quality.

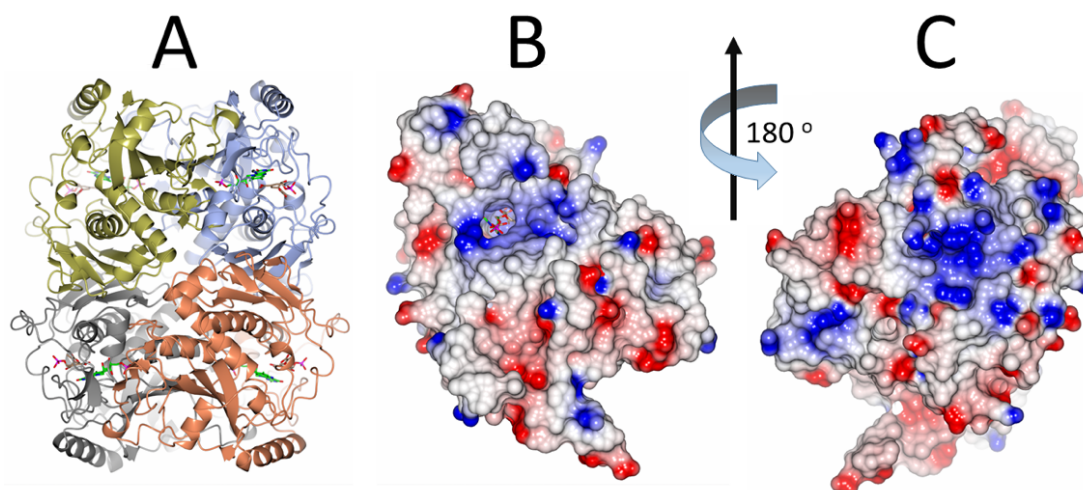


Figure 1: **A**, Ribbon model of the quaternary structure of *CaCS* colored by chain. The molecules bound are EPSP (*brown*) and FMNH₂ (*green*). **B**, Representation of the surface of chain A colored by electrostatic potential seen from the neighboring subunit. The molecules in the cavity are EPSP and FMNH₂. **C**, The same chain after 180° rotation seen from outside. Since the protein was modeled in the “closed conformation” EPSP and FMNH₂ are not visible in this view.

Finally, we have performed a two-step minimization by using the force field of the FMN-cofactor in the reduced form to account for the structural changes that occur upon reduction of the oxidized cofactor as present in the template 1qxo. At the end of the minimization, the isoalloxazine ring showed bending along the N(5)-N(10) axis indicating that the reduced FMN adopts the so-called “butterfly bending” (28).

Validation of docking protocol and large-scale virtual screening

The feasibility of using the *CaCS* in large-scale screening studies as well as the validation of the docking protocol was performed by the redocking method using the Autodock program, which provided an RMSD of 0.762 Å (average of four simulations). Once the results were reproducible (Figure S1, supplementary data), the *CaCS* structure and the docking protocol were validated and were applied in large-scale virtual screening.

The library of compounds similar to the known inhibitors of CS contained 2501 molecules. The library of commercially available natural products from the Zinc database contained 120,435 molecules. The third library was the Sigma-Aldrich catalog containing 73,163 compounds (total 196,099 molecules). The candidates were subdivided into folders with 2,500 molecules each, plus the EPSP structure. The final protocol validated in the redocking was then applied in the virtual screening of the libraries. In the first screening, 941 molecules were better ranked than EPSP (scores better than -11.0 ± 1.45). Of these molecules, 539 presented reproducibility in three new screens to eliminate false-positive results. In all replicates, the molecules Zinc6445805 (CS8) and Zinc4217277 (CaCS02) always appeared among the five best ranked, showing scores of -11.5 ± 0.48 and -11.2 ± 0.51 , respectively. These two molecules were purchased for *in vitro* assays. Figure 3 shows the structures of the molecules CS8, CaCS02 and EPSP. In fact, CS8 is very similar to compound CP1, which was recently demonstrated to exhibit antifungal activity against *P. brasiliensis* and to be a potent inhibitor of *PbCS* (29).

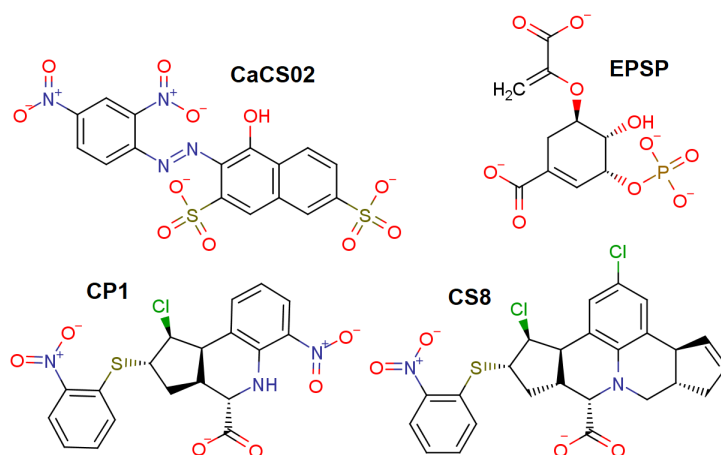


Figure 2: The chemical structure of the molecules selected by the virtual screening, plus the structure of the EPSP substrate and the CP1 molecule, described as a *PbCS* inhibitor

Molecular dynamics simulations

In order to investigate the structural stability of CaCS, as well as to obtain information about the residues involved in the stabilization of the ligands, MD simulations were performed for 50 ns. In these simulations the final model with the cofactor FMNH₂ plus EPSP or the best pose of the CaCS02 or CS8 were minimized and then equilibrated as described in materials and methods. The thermodynamic equilibrium was considered reached when the RMSD of the protein main chain reached a constant plateau by at least 10 ns. As shown in Figure S2A (supplementary data), the structures converged to an equilibrium at 30 ns. For the CaCS-EPSP complex, the RMSD was 3.0 Å ± 0.4. This value is close to those obtained in studies using CS from the bacteria *Mycobacterium tuberculosis* (27) and *Shigella flexneri* (18) as well as for the parasite *Plasmodium falciparum* (19). This result also showed that the enzyme in complex with either CaCS02 or CS8 is more stable as compared to the enzyme-substrate complex. This is probably due to the fact that these ligands are larger and, therefore, interact with a greater number of residues as compared to EPSP (Table S1, supplementary material).

The stability of the structures was also evaluated in terms of the radius of gyration (R_{gyr}), defined as the average quadratic distance of a set of atoms from their common center of gravity. As shown in Figure S2B (supplemental material), the complexes stabilized after 10 ns and protein unfolding was not observed.

From the MD simulations, it was possible to evaluate regions of the protein with greater flexibility by means of the root mean square fluctuation (RMSF) of the C α of each residue in the presence of the ligands. The RMSF was calculated in the last 5 ns of the simulation, when the protein was in its equilibrium state (Figure S3). The residues with greater flexibility were those of the C-terminal regions in all chains, which is common in most proteins, and in the case of CaCS, they refer to a segment without a defined secondary structure. Furthermore, we observed three regions with greater flexibility in the presence of any of the three ligands. These regions 1, 2 and 3 were also verified in previous work (27), indicating that this pattern is a general property of CS in complex with a ligand. However, these regions comprise long loops which, by nature, have a high degree of freedom of movement.

From the trajectory of MD simulations, it was also possible to evaluate the frequency of contacts between amino acid residues of CaCS with the ligands at a distance of up to 4.0 Å. The contact frequency calculation integrated the entire simulation time (50 ns). A frequency greater than 60% was delineated to identify the most important residues in the stabilization of the ligands. Each ligand has specific geometry and composition, which makes them interact differently with the protein and, therefore, structuring different sites. Thus, a complete list of the residues composing the active site for each ligand is shown in Table S1 (Supplementary Material), as probability of binding. It clearly shows that the residues Ser-16, Thr-55, Ser-125, Ala-126, Arg-127, Arg-337, Arg-345 are the most important in the anchoring of the substrate and ligands, which means that amino acid replacements at these

positions may significantly affect the enzymatic activity and/or cause resistance to the presence of the inhibitors. Since our theoretical results strongly indicated that CS8 and CaCS02 bind to CS, we were also interested to evaluate their effect on the growth of fungi, e.g. *C. albicans* and *P. brasiliensis*. Toward this end, we determined the minimum inhibitory concentration (MIC) using fungal strains from *Candida* and *Paracoccidioides*.

Antifungal activity assays

CS8 and CaCS02 were tested with *C. albicans* and *P. brasiliensis* (Pb18). The antifungal activity against *Candida* species was not observed. However, the *in vitro* antifungal activity against *P. brasiliensis* was observed for both compounds with a MIC of 512 $\mu\text{g}\cdot\text{mL}^{-1}$ and 32 $\mu\text{g}\cdot\text{mL}^{-1}$ for CS8 and CaCS02, respectively (Table 1). The minimum fungicidal concentration (MFC) assays showed that the values found for CaCS02 were the same as the MIC, indicating a fungicidal profile (Table 1). However, the most promising result for this compound was the strong synergistic effect observed when combined with amphotericin B. This combination was able to reduce twice the AmpB MIC value and three times that of compound, reducing the CaCS02 MIC value from 32 to 4 $\mu\text{g}\cdot\text{mL}^{-1}$ (Figure S4).

Table 1: MIC effect of CS8 and synergic effect of CaCS02 and AmB for *Paracoccidioides brasiliensis*.

Compound	MIC/MFC ($\mu\text{g}\cdot\text{mL}^{-1}$)			FIC model	
	Alone	Combination	FIC	Σ FIC	Interpretation
CaCS02	32	4	0.125	0.375	Strong synergistic
AmB	0.5	0.125	0.25		
CS8	512	–	–	–	–

Although the development of this study initially focused on *CaCS*, the compounds did not cause any effect on this species. This may be linked to some kind of intrinsic resistance of the fungus *C. albicans* to the compounds (30). In addition, studies have shown that the presence of efflux pumps may further hamper the action of inhibitors (31). However, the most significant difficulty may be related to the reported differences in the cell wall structure and composition of the two species (32).

The Tanimoto index between the CS8 and the recently reported inhibitor CP1 (Figure 1) is 0.75. CP1 was shown to be a potent inhibitor of *PbCS*, which had *in vivo* antifungal activity similar to the reference drug itraconazole. The lower inhibitory activity found in the MIC trials with CS8 is possibly due to the loss of one of the negatively charged groups compared to EPSP, CP1 and CaCS02, indicating that negative charges are very important for the stabilization of the ligand in the active site.

The strongly synergistic effect observed between CaCS02 and AmB (Table 1) is a significant indication that the two ligands act in different metabolic pathways. AmB acts on ergosterol, in order to alter the permeability of the cytoplasmic membrane (33), whereas CaCS02 interferes with the biosynthesis of chorismate and therefore the two compounds exert their influence on different aspects of cellular processes. AmB is the most commonly antifungal agent used in severe forms of the disease, but despite its excellent activity in reducing fungal load, it produces highly toxic adverse effects, such as nephrotoxicity and hepatotoxicity (34). Thus, a molecule capable of enhancing the antifungal activity of AmB may reduce the damage since it could be administered in smaller doses. In order to distinguish that CaCS02 acts a specific inhibitor of *PbCS* and not as pan-assay interference compound (35), we also performed binding and activity assays with recombinant *PbCS*.

Binding assays with *PbCS*

Although ligands CS8 and CaCS02 were identified by virtual screening using modeled *CaCS*, the binding studies were conducted with the enzyme from *P. brasiliensis* (*PbCS*) mainly because the ligands were found to be active against *P. brasiliensis* but not *C. albicans*. Because CS8 showed very poor solubility in aqueous buffers, a detailed analysis was only conducted with CaCS02. As shown in Figure 3A, binding to *PbCS* can be monitored by following the spectral changes occurring upon binding, yielding a dissociation constant of approximately 20 μM . Similarly, CaCS02 inhibited the activity of *PbCS* exhibiting an $\text{IC}_{50} = 29 \pm 3 \mu\text{M}$ (Figure 3B). These results nicely fit to our virtual screening and molecular dynamics simulations.

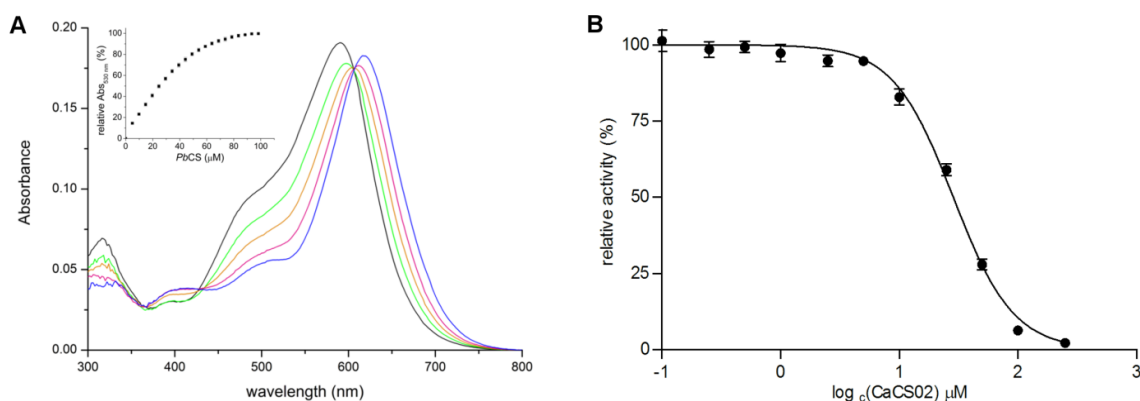


Figure 3: Binding of CaCS02 to *PbCS* (A) and effect of CaCS02 on *PbCS* activity (B): A, CaCS02 was dissolved in 50 mM MOPS, pH 7.5 (~10 μM , black spectrum) and titrated with *PbCS* (~393 μM) using 10 μl aliquots (see inset). Spectral changes were monitored between 300 and 800 nm. The green, the orange and the pink trace represent intermediate spectra at ~15 μM *PbCS*, ~29 μM *PbCS* and ~49 μM *PbCS*, respectively, and the blue trace corresponds to the final spectrum recorded at ~98 μM *PbCS*. The inset shows the mean absorption changes at 530 nm (from three determinations) as a function of the protein concentration indicating binding of CaCS02 to *PbCS* (the standard deviation at each *PbCS* concentration is shown as error bars). B, The influence of CaCS02 on the activity of *PbCS* was tested in an assay involving 80 μM EPSP, 4 μM *PbCS* and 20 μM anthranilate synthase at 37 °C. By forward coupling the chorismate synthase with the anthranilate synthase reaction, *PbCS* activity could be studied spectrofluorometrically by following the increase in fluorescence intensity at 390 nm ($\lambda_{\text{ex}} = 340$ nm) for 5 min, which correlates with the amount of anthranilate formed in the course of the reaction. The slopes of the initial velocities were determined and plotted as a function of the log of the corresponding CaCS02 concentration. Using a non-linear curve fit, based on the Hill-function, an IC_{50} of 29 ± 3 μM was determined (rates were determined in triplicate with the standard deviations shown as error bars).

The CaCS02 ligand has a negative net charge (-2) and partition coefficient (xlogP) of -1.25 at pH 7.0. The presence of these negative charges appears to be crucial for the stabilization of this ligand in the active site, since the simulations predicted binding at the same site as the substrate EPSP, which has several negative charges that interact with the enzyme by means of charge-charge and charge-dipole interactions (Figure 2).

Although CS8 did not lend itself to a more detailed analysis, its similarity to CP1 (29) and its antifungal activity, strongly suggests that it may also bind to *PbCS*. In any case, the high MIC value found does not make it a very promising candidate as a useful drug and thus no further trials were conducted.

Next, we investigated whether CaCS02 has any cytotoxic effects. For this, different concentrations of CaCS02 were incubated in two mammalian cell lines (Figure 4). The results showed that CaCS02 did not present any cytotoxic effects even at the limit of the evaluated concentration, *i.e.* up to 16 times the MIC value.

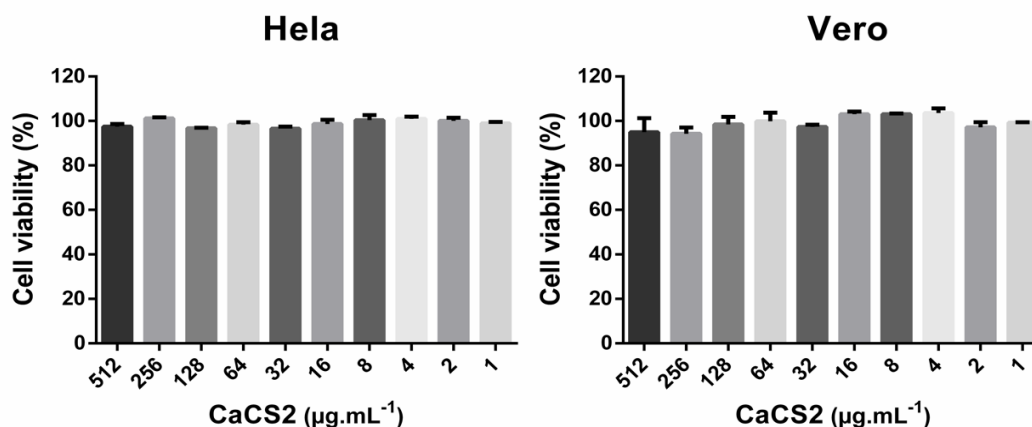


Figure 4: Evaluation of the *in vitro* cytotoxicity of CaCS02 in two cell lines by means of the MTS assay. Several concentrations of CaCS02 were tested (0.0 to 512 $\mu\text{g}\cdot\text{mL}^{-1}$) without showing significant toxicity. The two cell lines evaluated (HeLa and Vero cells) showed high viability after 24 h in contact as CaCS02, even in concentrations 16 \times MIC (32 $\mu\text{g}\cdot\text{mL}^{-1}$). The results represent the mean of three independent trials. Error bars indicate their respective standard deviation.

Although other antifungal candidates against *P. brasiliensis* have already been described with lower MIC values (29, 36, 37), the low cytotoxicity presented by CaCS02, may compensate for the greater dosages required. CaCS02 is a water-soluble azo dye and, to date, this type of molecule has never been described as an inhibitor of CS. Since many azo dyes are commercially available and the fact that isosteric mimetics may be accessible by chemical synthesis, our research group will continue this line of research in the quest to obtain highly specific CS inhibitors. Since CS is also present in bacteria, plants and apicomplexan parasites this research may also contribute to the development of new antibacterials, herbicides and/or antiparasitic (*e.g.* anti-malaria) drugs.

Conclusion

This work presented the modeling, docking and molecular dynamics simulations using the enzyme chorismate synthase from *Candida albicans*. The analysis of the modeled structure demonstrated a good quality of the proposed model, as well as its validation for use in virtual screening simulations. Among the selected molecules, we identified the compound Zinc4217277 (CaCS02) and demonstrated its ability to bind and inhibit the enzyme in *in vitro* studies. Furthermore, CaCS02 showed promising *in vitro* antifungal activity against the most virulent strain of the human pathogenic fungus *P. brasiliensis* (Pb18). Its low cytotoxicity and significant synergistic effect with amphotericin B, which is the reference drug in severe cases of this disease, demonstrated a potential use in a combinatorial drug therapy against paracoccidioidomycosis.

Material and methods

Sequence identification and modeling of the three-dimensional structure

The amino acid sequence of chorismate synthase from *Candida albicans* (CaCS) strain WO-1 was obtained from the Uniprot database (25) (uniprot id: C4YMI5), and was used in the search for structural templates by means of BLASTp (38) in the rcsb PDB (39). The model and template sequences were aligned, and the result was used as the input parameter for the Modeller-9v14 program (40). The structure was modeled in its biological unit (homotetramer) where each subunit was bound to the EPSP substrate and the FMNH₂ cofactor. A symmetry constraint was imposed between the C α

of the four chains and then, 2000 models were generated. The top ten were selected based on Modeller DOPE Score. From these, the best model was selected based on the stereochemical quality evaluated by the program Procheck (41). The residues in forbidden regions of the Ramachandran plot were corrected by means of point modeling.

Energy minimization and molecular dynamics simulations

Energy minimization was performed using the software package NAMD2/VMD (42, 43). The structure of the homotetramer obtained from modeling was solvated with TIP3P water in a periodic box with limits of 10 Å away from the outermost surface of the complex. Na⁺-counter ions were added in sufficient amount to neutralize the system charges. The Charmm force field (FF) c35b2-c36a2 (44) was used for the protein atoms, while the FFs for the substrate, FMNH₂ cofactor, and molecules obtained by the virtual screening were generated in the same format by the Swissparam server (45). To increase the accuracy of the ligand force fields, the Mülliken's charges were calculated at the B3LYP/6-311G level of theory using the Orca program (46), at the protonation state at pH 7.0.

The molecular dynamics (MD) process occurred in five steps. In the first step, the atoms of the ligand and cofactor were fixed in the space, while those of the protein and other atoms of the system were kept free to move. At this point, the system was subjected to 20,000 minimization steps by Conjugate Gradient (CG). In the second step, all the atoms of the system were again minimized by other 10,000 steps of CG. The structure resulting from this step was used in the redocking and docking.

In the third step, the atoms of protein and ligands were kept fixed, while the waters and salts were subjected to 60 ps of equilibrium MD. In the fourth step, all atoms were subjected to a new CG cycle for 20,000 steps. In the fifth and last step, the entire system was subjected to 50 ns of equilibrium MD under NPT conditions (constant: temperature 300K, pressure 1 atm and number of atoms).

The analyzes were performed in terms of root mean square deviation (RMSD) from the reference structure (second step of the MD), as well as the radius of gyration (R_{gyr}) of the protein-ligand complexes, the residues in contact with the inhibitors at a distance of up to 4.0 Å, as well as the root mean square fluctuation (RMSF) of the alpha carbons for each residue were extracted from the trajectory file.

The long time MD simulations required a higher processing power, being performed on 20 nodes of an Intel Xeon E5-2695v2 Ivy Bridge processors, 2.4GHZ (480 cores) from the SDumont supercomputer at LNCC, Brazil.

Docking and virtual screening simulations

The docking protocol was established by redocking simulations of the EPSP substrate in the protein-cofactor complex using the AutoDock-4.2.3 program (47) implemented in the Pyrx-0.9 graphical

interface (48). The parameters used were the standard search algorithm (Lamarckian GA), grid of 0,375 Å, search center on ligand EPSP and box size of 50, 50, 50 on x , y and z . The torsion angles of the enzyme and cofactor were restricted, but flexibility of the binders was allowed. All water molecules and ions were removed from the structure. The protocol was considered validated when the EPSP pose overlapped the pose of the modeled substrate with RMSD less than 0.8 Å.

For the large-scale screening simulations, three libraries were constructed. The first was assembled by searching for purchasable molecules, similar to the known inhibitors of CS, using 70% Tanimoto index at the databases PubChem (49), Zinc (50), DrugBank (51) and Brenda enzymes (52). The second library consisted of the natural products from Zinc database. The third library was the catalog of Sigma-Aldrich. The EPSP structure was included in the libraries so that, at the end of the simulation, only the best ranked molecules relative to the substrate were considered. The selected molecules were downloaded in *.sdf format. Then, the molecules selected in the first screening were subjected to three new screenings (repetitions) to select the ligands with reproducibility, in order to eliminate false positive results.

Microorganisms

The *in vitro* susceptibility assays were performed on the standard strains *C. albicans* ATCC 90028 (American Type Culture Collection) and *P. brasiliensis* (Pb18), both belonging to the library of the State University of Maringá. Prior to testing, the *C. albicans* strain was subcultured on agar sabouraud dextrose (SDA, Difco™, Detroit, MI, USA) and incubated at 35 °C for 24 h. The Pb18 isolate was subcultured on Fava-Netto agar medium (53) at 36 °C for 5 days.

Ligand preparation

The compound CS8 (AG-690/37099007) was from Molport (Latvia) and the compound CaCS02, as well as the control drug, amphotericin B (AmB) were from Sigma-Aldrich (USA). Initially a stock solution of the molecules to be tested was prepared in dimethylsulfoxide (DMSO) at a concentration of 50 mg·mL⁻¹ and stored at -80 °C until further use. For the assays, the molecules were diluted in RPMI [RPMI-1640 without bicarbonate, L-glutamine, supplemented with 2% glucose] and buffered (pH 7.0) with 0.165 M morpholinopropanesulfonic acid (MOPS) (Sigma-Aldrich) plus Pluronic F-127 0.2% (Sigma-Aldrich). The fungi were incubated in the absence and presence of the diluent to confirm that the exposure did not influence the growth of the assayed isolates.

Antifungal activity assays

In order to evaluate the susceptibility profile of the pathogenic fungi to the compounds selected by virtual screening, a test based on the broth microdilution method proposed by CLSI (Clinical and Laboratory Standards Institute, 2008) was performed according to protocol M27-A3 for determination of minimum inhibitory concentration (MIC) and minimum fungicidal concentration (MFC) for *C. albicans*. The method was adapted to the conditions of *P. brasiliensis*, as previously described (29). The tests were performed on sterile flat bottom 96-well microtiter plates (Techno Plastic Products, Switzerland) and the final tested concentrations of the evaluated molecules ranged from 1 to 512 $\mu\text{g}\cdot\text{mL}^{-1}$. The inoculums were suspended in sterile saline buffer (0.85%), to a final concentration of $1\text{-}2\times 10^3$ cells $\cdot\text{mL}^{-1}$ for *C. albicans* and $1\text{-}2\times 10^4$ cells $\cdot\text{mL}^{-1}$ for *P. brasiliensis*. The determination of the end points of the MIC and MFC readings were performed visually and correspond to the concentration of each antifungal capable of inhibiting 100% of the growth of the isolates. The assays were performed in duplicate.

Checkerboard assay

CaCS02 was selected for further trials due to its better antifungal potential. In order to evaluate the synergy between AmB and *CaCS02* microdilution checkerboard was performed. Briefly, concentrations below or above the MIC of the drugs were combined in a 96-well plate, starting at $4\times\text{MIC}$ and vertically distributed, while AmB $2\times\text{MIC}$ was added horizontally (36). After 6 days of incubation at 35 °C, the fungal growth was visualized and 20 μL of Resazurin (Sigma-Aldrich) 0.01% in sterile water were added to each well and incubated for a further 24 h. Past 7th day, the inhibition was confirmed by the abrupt change in color when there was fungal growth. Fractional inhibitory concentration (FIC) was determined by $\Sigma\text{FIC} = \text{FICA} + \text{FICB} = (\text{Comb}_{\text{AmB}}/\text{MIC}_{\text{AmB}}) + (\text{Comb}_{\text{CaCS02}}/\text{MIC}_{\text{CaCS02}})$, revealing a strongly synergistic effect, $\text{FIC}<0.5$; synergistic effect, $\text{FIC}<1$; additive effect, $\text{FIC}=1$; without effect, $1<\text{FIC}<2$; antagonistic effect, $\text{FIC}>2$ (54).

Recombinant production and binding of CaCS02 to PbCS

Recombinant production of chorismate synthase from *Paracoccidioides brasiliensis* (*PbCS*) was performed as described previously (29).

For the binding studies, *CaCS02* was dissolved in 50 mM MOPS, pH 7.5 to a final concentration of ~ 10 μM (A_{590} , ~ 0.2 ; 800 μL) and transferred to a quartz cuvette (in reference cuvette just 800 μL of buffer). After recording an initial UV-visible absorption spectrum between 300 and 800 nm, 10 μL aliquots of *PbCS* (~ 393 μM) were added and spectral changes were monitored after each addition. In order to quantify the binding affinity of *CaCS02* to *PbCS*, the relative absorbance changes at 530 nm

were plotted as a function of the protein concentration in the cuvette, with the standard deviations displayed as error bars (from three titrations).

Inhibitory effect of CaCS02 on recombinant PbCS

To test the inhibitory effect of *CaCS02* on *PbCS*, a coupled assay involving EPSP, CS, and anthranilate synthase was used (55, 56). This special assay setup allowed forward coupling of the CS reaction, leading to the formation of anthranilate, a stable product that exhibits a fluorescence emission maximum at 390 nm and can thus be detected spectrofluorometrically. Reaction mixtures containing 3 mM MgSO_4 , 7.5 mM L-Gln, 22.5 mM $(\text{NH}_4)_2\text{SO}_4$, 1 mM dithiothreitol (DTT), 10 μM FMN, 80 μM EPSP, 4 μM *PbCS*, ~20 μM anthranilate synthase, and various concentrations of *CaCS02* (0.1 to 500 μM) were prepared in 50 mM MOPS (pH 7.5) and pipetted into a 96-well plate (triplicate determinations). After the addition of 500 μM NADPH, the plate was incubated at 37°C for 60s before recording the fluorescence emission changes at 390 nm ($\lambda_{\text{ex}}=340$ nm) using a Spectramax Gemini XS microplate spectrofluorometer (Molecular Devices, San Jose, CA) for 5 min (data points every 12 s). Initial velocities were extracted from the first 15 data points, and relative rates were plotted as a function of the log (*CaCS02* micromolar concentration), with the standard deviations shown as error bars (triplicate determinations). Using the program GraphPad Prism 5 (GraphPad Software, Inc., San Diego, CA), the data were fitted applying the nonlinear curve fit “log (inhibitor) versus normalized response – variable slope,” which allowed for the determination of IC_{50} .

Cytotoxicity assay

The *CaCS02* cytotoxicity evaluation was performed in HeLa and Vero cell lineages, using the CellTiter 96 assay (Promega, Madison, WI) based on the reduction of MTS [*3-(4,5-dimethylthiazol-2-yl)-5-(3-carboxymethoxyphenyl)-2-(4-sulphophenyl)-2H-tetrazolium*]. The cells were incubated in 96-well culture plates maintained in DMEM (Eagle's Modified Dulbecco's Medium) with fetal bovine serum (5%) and treated with different concentrations of the *CaCS02* (0.0 to 512 $\mu\text{g}\cdot\text{mL}^{-1}$). After 24 hours, the MTS solution was added to each well culture and incubated for 180 minutes in a CO_2 oven (5%) at 37 °C for 180 min. Cell viability was determined by optical density in a spectrophotometer at 490 nm. Cytotoxicity was presented as the average of three independent experiments. The percentages of cell viability were calculated relative to controls containing medium only (57).

Acknowledgments

We thank to Fundação Araucária (Process 40/2016), CAPES (cod 001) and CNPq (process 141089/2017-2) for financial support; LNCC for computational facilities; FINEP/COMCAP/UEM for equipment facilities. P.M. thanks the Austrian Science Fund for generous support through the doctoral program “Molecular Enzymology” (W901).

References

1. Pianalto, K., and Alspaugh, J. (2016) New horizons in antifungal therapy. *J. Fungi*. **2**, 26
2. Giacomazzi, J., Baethgen, L., Carneiro, L. C., Millington, M. A., Denning, D. W., Colombo, A. L., and Pasqualotto, A. C. (2016) The burden of serious human fungal infections in Brazil. *Mycoses*. **59**, 145–150
3. da Silva Dantas, A., Lee, K. K., Raziunaite, I., Schaefer, K., Wagener, J., Yadav, B., and Gow, N. A. (2016) Cell biology of *Candida albicans*–host interactions. *Curr. Opin. Microbiol.* **34**, 111–118
4. Kabir, M. A., Hussain, M. A., and Ahmad, Z. (2012) *Candida albicans* : A model organism for studying fungal pathogens. *ISRN Microbiol.* **2012**, 1–15
5. Sheehan, D. J., Hitchcock, C. A., and Sibley, C. M. (1999) Current and emerging azole antifungal agents. *Clin. Microbiol. Rev.* **12**, 40–79
6. Martinez, R. (2015) Epidemiology of paracoccidioidomycosis. *Rev. Inst. Med. Trop. Sao Paulo.* **57**, 11–20
7. Bocca, A. L., Amaral, A. C., Teixeira, M. M., Sato, P., Shikanai-Yasuda, M. A., and Soares Felipe, M. S. (2013) Paracoccidioidomycosis: Eco-epidemiology, taxonomy and clinical and therapeutic issues. *Future Microbiol.* **8**, 1177–1191
8. Teixeira, M. D. M., Theodoro, R. C., Oliveira, F. F. M. De, Machado, G. C., Hahn, R. C., Bagagli, E., San-Blas, G., and Felipe, M. S. S. (2013) *Paracoccidioides lutzii* sp. nov.: biological and clinical implications. *Med. Mycol.* 10.3109/13693786.2013.794311
9. Martinez, R. (2017) New trends in paracoccidioidomycosis epidemiology. *J. Fungi*. **3**, 1
10. da Costa, M. M., and Marques da Silva, S. H. (2014) Epidemiology, clinical, and therapeutic aspects of paracoccidioidomycosis. *Curr. Trop. Med. Reports.* **1**, 138–144
11. Defaveri, J., and Joaquim, A. (2002) Acute form of paracoccidioidomycosis: analysis of thirteen autopsies with emphasis on the pulmonary involvement. *Annu. Rev. Biomed. Sci.*
12. Defaveri, J., and Joaquim, A. (2002) Chronic form of paracoccidioidomycosis: analysis of thirteen autopsies with emphasis on the pulmonary involvement. *Annu. Rev. Biomed. Sci.*
13. Bellissimo-Rodrigues, F., Bollela, V. R., Da Fonseca, B. A. L., and Martinez, R. (2013) Endemic paracoccidioidomycosis: Relationship between clinical presentation and patients' demographic features. *Med. Mycol.* **51**, 313–318
14. Naranjo, T. W., Lopera, D. E., Diaz-Granados, L. R., Duque, J. J., Restrepo M, A., and Cano, L. E. (2011) Combined itraconazole-pentoxifylline treatment promptly reduces lung fibrosis induced by chronic pulmonary paracoccidioidomycosis in mice. *Pulm. Pharmacol. Ther.* **24**, 81–91
15. Spampinato, C., and Leonardi, D. (2013) *Candida* infections, causes, targets, and resistance mechanisms: Traditional and alternative antifungal agents. *Biomed Res. Int.* 10.1155/2013/204237

16. Campoy, S., and Adrio, J. L. (2016) Antifungals. *Biochem. Pharmacol.* 10.1016/j.bcp.2016.11.019.
17. Kaltendorf, M., Srivastava, M., Gupta, S. K., Liang, C., Binder, J., Dietl, A.-M., Meir, Z., Haas, H., Osherov, N., Krappmann, S., and Dandekar, T. (2016) Systematic identification of anti-fungal drug targets by a metabolic network approach. *Front. Mol. Biosci.* 10.3389/fmolb.2016.00022
18. Zhou, H., Singh, N. J., and Kim, K. S. (2006) Homology modeling and molecular dynamics study of chorismate synthase from *Shigella flexneri*. *J. Mol. Graph. Model.* **25**, 434–441
19. Tapas, S., Kumar, A., Dhindwal, S., Preeti, and Kumar, P. (2011) Structural analysis of chorismate synthase from *Plasmodium falciparum*: A novel target for antimalaria drug discovery. *Int. J. Biol. Macromol.* **49**, 767–777
20. Herrmann, K. M., and Weaver, L. M. (1999) The shikimate pathway. *Annu. Rev. Plant Physiol. Plant Mol. Biol.* **50**, 473–503
21. Fernandes, C. L., Breda, A., Santiago Santos, D., Augusto Basso, L., and Osmar Norberto de Souza (2007) A structural model for chorismate synthase from *Mycobacterium tuberculosis* in complex with coenzyme and substrate. *Comput. Biol. Med.* **37**, 149–158
22. Macheroux, P. P., Petersen, J. J., Bornemann, S. S., Lowe, D. J. D. J., and Thorneley, R. N. R. N. (1996) Binding of the oxidized, reduced, and radical flavin species to chorismate synthase. An investigation by spectrophotometry, fluorimetry, and electron paramagnetic resonance and electron nuclear double resonance spectroscopy. *Biochemistry.* **35**, 1643–1652
23. Quevillon-Cheruel, S., Leulliot, N., Meyer, P., Graille, M., Bremang, M., Blondeau, K., Sorel, I., Poupon, A., Janin, J., and Van Tilbeurgh, H. (2004) Crystal structure of the bifunctional chorismate synthase from *Saccharomyces cerevisiae*. *J. Biol. Chem.* **279**, 619–625
24. Wilkins, M. R., Gasteiger, E., Bairoch, A., Sanchez, J. C., Williams, K. L., Appel, R. D., and Hochstrasser, D. F. (1999) Protein identification and analysis tools in the ExPASy server. *Methods Mol. Biol.* **112**, 531–552
25. Magrane, M., and Consortium, U. P. (2011) UniProt Knowledgebase: A hub of integrated protein data. *Database.* 10.1093/database/bar009
26. Maclean, J., and Ali, S. (2003) The structure of chorismate synthase reveals a novel flavin binding site fundamental to a unique chemical reaction. *Structure.* **11**, 1499–1511
27. Rocha, K. B. (2011) Virtual screening e dinâmica molecular para identificação de inibidores da enzima corismato sintase de *Mycobacterium tuberculosis*. *J. Chem. Inf. Model.* 10.1017/CBO9781107415324.004
28. Røhr, Å. K., Hersleth, H. P., and Kristoffer Andersson, K. (2010) Tracking flavin conformations in protein crystal structures with raman spectroscopy and QM/MM calculations. *Angew. Chemie - Int. Ed.* **49**, 2324–2327

29. Rodrigues-Vendramini, F. A. V., Marschalk, C., Toplak, M., Macheroux, P., Bonfim-Mendonça, P. de S., Svidzinski, T. I. E., Seixas, F. A. V., and Kioshima, E. S. (2019) Promising new antifungal treatment targeting chorismate synthase from *Paracoccidioides brasiliensis*. *Antimicrob. Agents Chemother* **63(1)** :e01097-18. [10.1128/AAC.01097-18](https://doi.org/10.1128/AAC.01097-18).
30. Arthington-Skaggs, B. A., and Rex, J. H. (2008) *Resistance to antifungal agents. Antimicrobial resistance and implications for the twenty-first century.*, https://doi.org/10.1007/978-0-387-72418-8_10
31. Ford, C. B., Funt, J. M., Abbey, D., Issi, L., Guiducci, C., Martinez, D. A., Delorey, T., Li, B. Y., White, T., Cuomo, C., Rao, R. P., Berman, J., Thompson, D. A., and Regev, A. (2015) The evolution of drug resistance in clinical isolates of *Candida albicans*. *Elife*. **2015**, 1–27
32. Karkowska-Kuleta, J., and Kozik, A. (2015) Cell wall proteome of pathogenic fungi. *Acta Biochim. Pol.* **62**, 339–351
33. Borba, H. H. L., Steimbach, L. M., Riveros, B. S., Tonin, F. S., Ferreira, V. L., Bagatim, B. A. de Q., Balan, G., Pontarolo, R., and Wiens, A. (2018) Cost-effectiveness of amphotericin B formulations in the treatment of systemic fungal infections. *Mycoses*. **61**, 754–763
34. Linden, P. K. (2003) Amphotericin B lipid complex for the treatment of invasive fungal infections. *Expert Opin. Pharmacother.* **4**, 2099–2110
35. Pouliot, M., and Jeanmart, S. (2016) Pan Assay Interference Compounds (PAINS) and other promiscuous compounds in antifungal research. *J. Med. Chem.* **59**, 497–503
36. Bagatin, M. C., Pimentel, A. L., Biavatti, D. C., Basso, E. A., Kioshima, E. S., Seixas, F. A. V., and Gauze, G. de F. (2017) Targeting the homoserine dehydrogenase of *Paracoccidioides* species for treatment of systemic fungal infections. *Antimicrob. Agents Chemother.* [10.1128/AAC.00165-17](https://doi.org/10.1128/AAC.00165-17)
37. Abadio, A. K. R., Kioshima, E. S., Leroux, V., Martins, N. F., Maigret, B., and Felipe, M. S. S. (2015) Identification of new antifungal compounds targeting thioredoxin reductase of *Paracoccidioides* genus. *PLoS One*. [10.1371/journal.pone.0142926](https://doi.org/10.1371/journal.pone.0142926)
38. Mount, D. W. (2007) Using the Basic Local Alignment Search Tool (BLAST). *Cold Spring Harb. Protoc.* **2007**, pdb.top17
39. Berman, H. M., Battistuz, T., Bhat, T. N., Bluhm, W. F., Bourne, P. E., Burkhardt, K., Feng, Z., Gilliland, G. L., Iype, L., Jain, S., Fagan, P., Marvin, J., Padilla, D., Ravichandran, V., Schneider, B., Thanki, N., Weissig, H., Westbrook, J. D., and Zardecki, C. (2002) The protein data bank. *Acta Crystallogr. Sect. D Biol. Crystallogr.* **58**, 899–907
40. Eswar, N., Webb, B., Marti-Renom, M. a, Madhusudhan, M. S., Eramian, D., Shen, M.-Y., Pieper, U., and Sali, A. (2007) Comparative protein structure modeling using MODELLER. *Curr. Protoc. protein Sci.* **Chapter 2**, Unit 2.9

41. Laskowski, R. A., Rullmann, J. A. C., MacArthur, M. W., Kaptein, R., and Thornton, J. M. (1996) AQUA and PROCHECK-NMR: Programs for checking the quality of protein structures solved by NMR. *J. Biomol. NMR.* **8**, 477–486
42. Humphrey, W., Dalke, A., and Schulten, K. (1996) VMD: Visual molecular dynamics. *J. Mol. Graph.* **14**, 33–38
43. Phillips, J. C., Braun, R., Wang, W., Gumbart, J., Tajkhorshid, E., Villa, E., Chipot, C., Skeel, R. D., Kalé, L., and Schulten, K. (2005) Scalable molecular dynamics with NAMD. *J. Comput. Chem.* **26**, 1781–1802
44. Mackerell, A. D., Feig, M., and Brooks, C. L. (2004) Extending the treatment of backbone energetics in protein force fields: Limitations of gas-phase quantum mechanics in reproducing protein conformational distributions in molecular dynamics simulation. *J. Comput. Chem.* **25**, 1400–1415
45. Zoete, V., Cuendet, M. A., Grosdidier, A., and Michielin, O. (2011) SwissParam: A fast force field generation tool for small organic molecules. *J. Comput. Chem.* **32**, 2359–2368
46. Neese, F. (2012) The ORCA program system. *Wiley Interdiscip. Rev. Comput. Mol. Sci.* **2**, 73–78
47. Morris, G., Huey, R., Lindstrom, W., Sanner, M. F., Belew, R. K., Goodsell, D. S., and Olson, A. J. (2009) AutoDock4 and AutoDockTools4: Automated docking with selective receptor flexibility. *J. Comput. Chem.* **30**, 2785–2791
48. Dallakyan, S., and Olson, A. J. (2015) Small-molecule library screening by docking with PyRx. *Methods Mol. Biol.* **1263**, 243–250
49. Kim, S., Thiessen, P. A., Bolton, E. E., Chen, J., Fu, G., Gindulyte, A., Han, L., He, J., He, S., Shoemaker, B. A., Wang, J., Yu, B., Zhang, J., and Bryant, S. H. (2016) PubChem substance and compound databases. *Nucleic Acids Res.* **44**, D1202–D1213
50. Irwin, J. J., Sterling, T., Mysinger, M. M., Bolstad, E. S., and Coleman, R. G. (2012) ZINC: A free tool to discover chemistry for biology. *J. Chem. Inf. Model.* **52**, 1757–1768
51. Knox, C., Law, V., Jewison, T., Liu, P., Ly, S., Frolkis, A., Pon, A., Banco, K., Mak, C., Neveu, V., Djoumbou, Y., Eisner, R., Guo, A. C., and Wishart, D. S. (2011) DrugBank 3.0: A comprehensive resource for “Omics” research on drugs. *Nucleic Acids Res.* 10.1093/nar/gkq1126
52. Schomburg, I., Chang, A., Placzek, S., Söhngen, C., Rother, M., Lang, M., Munaretto, C., Ulas, S., Stelzer, M., Grote, A., Scheer, M., and Schomburg, D. (2013) BRENDA in 2013: Integrated reactions, kinetic data, enzyme function data, improved disease classification: New options and contents in BRENDA. *Nucleic Acids Res.* 10.1093/nar/gks1049
53. Netto, C. F., Vegas, V., Sciannaméa, I., and Guarnieri, D. (1969) The polysaccharidic antigen from *Paracoccidioides brasiliensis*. Study of the time of cultivation necessary for the preparation of the antigen. *Rev Inst Med Trop Sao Paulo.* **11**, 177

54. Mor, V., Rella, A., Farnou, A. M., Singh, A., Munshi, M., Bryan, A., Naseem, S., Konopka, J. B., Ojima, I., Bullesbach, E., Ashbaugh, A., Linke, M. J., Cushion, M., Collins, M., Ananthula, H. K., Sallans, L., Desai, P. B., Wiederhold, N. P., Fothergill, A. W., Kirkpatrick, W. R., Patterson, T., Wong, L. H., Sinha, S., Giaever, G., Nislow, C., Flaherty, P., Pan, X., Cesar, G. V., Tavares, P. de M., Frases, S., Miranda, K., Rodrigues, M. L., Luberto, C., Nimrichter, L., and Poeta, M. Del (2015) Identification of a new class of antifungals targeting the synthesis of fungal sphingolipids. *MBio*. 10.1128/mBio.00647-15
55. Schaller, A., Windhofer, V., and Amrhein, N. (1990) Purification of chorismate synthase from a cell culture of the higher plant *Corydalis sempervirens* Pers. *Arch. Biochem. Biophys.* **282**, 437–442
56. Fitzpatrick, T. B., Killer, P., Thomas, R. M., Jelesarov, I., Amrhein, N., and Macheroux, P. (2001) Chorismate synthase from the hyperthermophile *Thermotoga maritima* combines thermostability and increased rigidity with catalytic and spectral properties similar to mesophilic counterparts. *J. Biol. Chem.* **276**, 18052–18059
57. Capoci, I. R. G., Bonfim-Mendonça, P. D. S., Arita, G. S., Pereira, R. R. D. A., Consolaro, M. E. L., Bruschi, M. L., Negri, M., and Svidzinski, T. I. E. (2015) Propolis is an efficient fungicide and inhibitor of biofilm production by vaginal *Candida albicans*. *Evidence-based Complement. Altern. Med.* 10.1155/2015/287693

Supplementary information

Figures and Tables

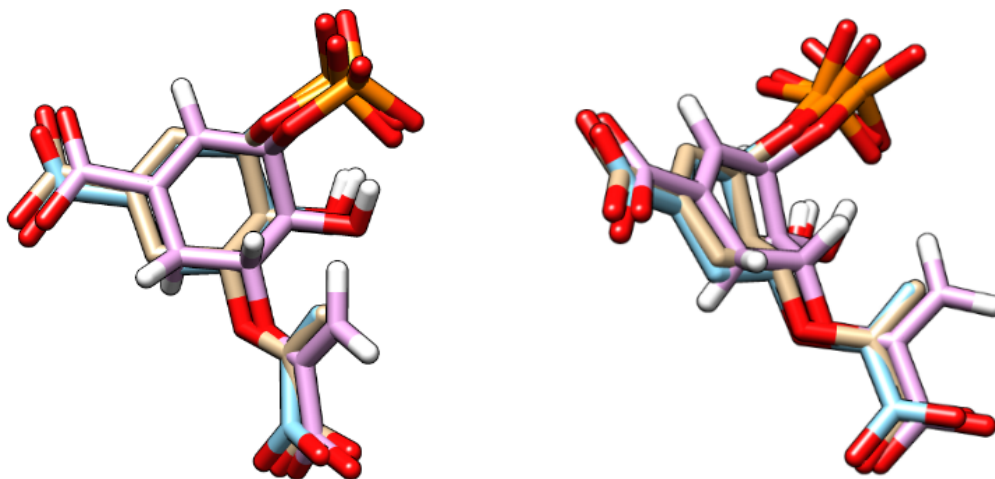


Figure S1. Redocking of the EPSP substrate by the Autodock program. The modeled reference structure is in *coral*; The poses found by redocking are in *blue* and *purple*.

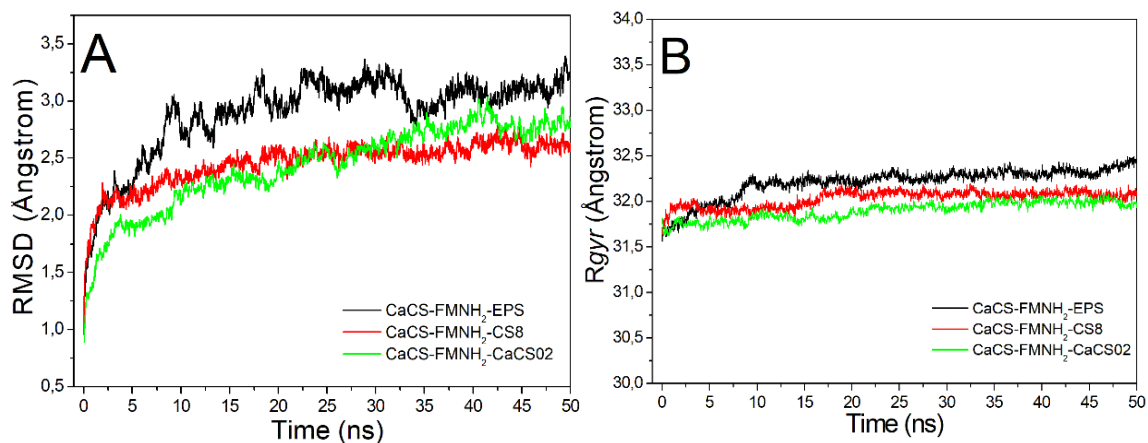


Figure S2: Protein behavior throughout the simulation. The $\text{CaCS-FMNH}_2\text{-EPSP}$ complex (*black*), and the $\text{CaCS-FMNH}_2\text{-CS8}$ complex (*red*) and the $\text{CaCS-FMNH}_2\text{-CaCS02}$ complex (*green*). **A**, RMSD calculated for the protein main chain atoms. **B**, Calculated radius of gyration for protein main chain atoms.

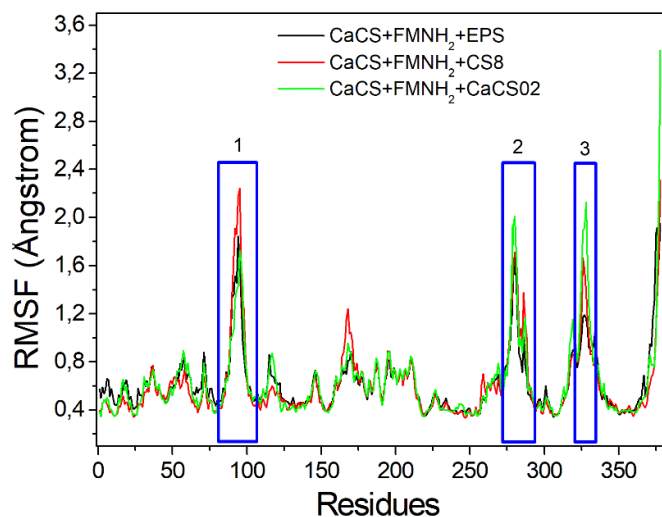


Figure S3. RMSF of the *Ca* atoms of the *CaCS* in the last 5 ns of simulation (equilibrium region). The *blue* boxes highlight the regions with the greatest degree of flexibility.

Table S1: Contact frequency between *CaCS* residues and the evaluated ligands within the range of up to 4 Å.

Residues	EPSP	CS8	CaCS02	Residues	EPSP	CS8	CaCS02
Ser-16	0,71	0,67	0,66	Tyr-99	-	-	0,17
His-17	-	0,53	0,57	Arg-101	0,46	0,96	1,00
Arg-46	0,99	0,31	1,00	His-104	-	-	0,06
Arg-47	0,09	-	0,18	Ser-118	-	-	0,08
Lys-52	0,19	-	-	Gly-121	-	-	0,02
Ser-54	0,62	0,20	0,72	Ser-124	-	0,29	0,01
Thr-55	0,81	0,99	0,77	Ser-125	0,75	0,70	0,70
Pro-56	0,61	0,41	0,38	Ala-126	0,97	0,80	0,89
Asp-58	-	0,10	-	Arg-127	0,96	0,62	0,97
Glu-59	0,08	0,42	0,18	Thr-129	-	0,27	0,31
Lis-86	0,19	-	-	Ile-130	0,06	-	0,02
Asp-87	-	0,26	0,22	Ala-314	-	-	0,02
His-88	0,14	-	0,03	Thr-315	0,12	0,93	0,56
Arg-89	-	0,22	0,03	Ala-334	-	0,19	0,45
Pro-90	-	0,33	0,54	Arg-335	-	0,40	0,17
Tyr-93	0,05	0,31	0,26	Gly-336	-	0,49	0,22
Ser-94	-	-	0,01	Arg-337	0,63	1,00	0,74
Glu-95	-	-	0,14	His-338	-	-	0,19
Thr-96	-	-	0,13	Asp-339	-	-	0,06
Asp-97	-	-	0,35	Arg-345	1,00	0,69	0,99
Leu-98	-	-	0,16	FMN	0,77	1,00	0,99

Residues in bold have a contact frequency with the ligand of greater than 60%.

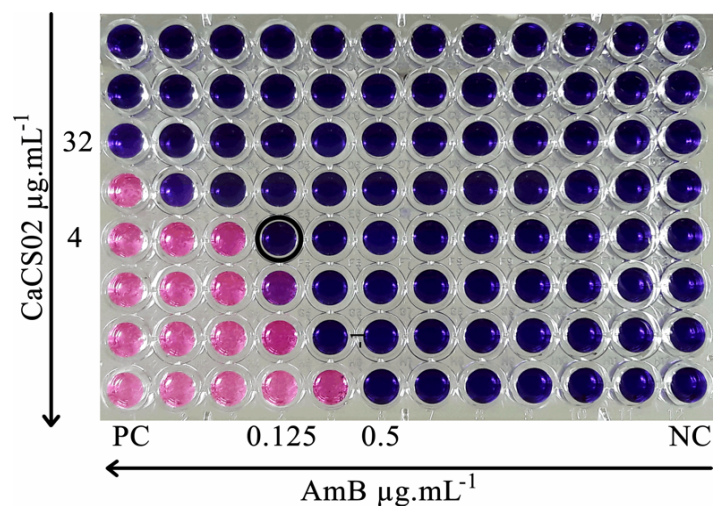


Figure S4. Checkerboard plate of the combination of AmB and CaCS02 assayed in *P. brasiliensis* (Pb18) strains. We found values of $MIC_{AmB} = 0.5 \mu\text{g}\cdot\text{mL}^{-1}$ and $Comb_{AmB} = 0.125 \mu\text{g}\cdot\text{mL}^{-1}$; $MIC_{CaCS02} = 32 \mu\text{g}\cdot\text{mL}^{-1}$ and $Comb_{CaCS02} = 4 \mu\text{g}\cdot\text{mL}^{-1}$. The *black* circle indicates the point of combination between the compounds tested. The 2-fold drop in inhibition concentration for each compound revealed a strong synergistic interaction with $\Sigma\text{FIC} = 0.375$. The plate was incubated at 35 °C for 7 days, on the 6th day resazurin (0.01%) was added to each well. The *blue* color indicates fungal non-viability while the *pink* color indicates viable fungal growth. (PC) Positive control; (CN) negative control.

Appendix C

Ene cyclases

Asymmetric Reductive Carbocyclization Using Engineered Ene Reductases

**Kathrin Heckenbichler,^[a] Anna Schweiger,^[a] Lea Brandner,^[a] Alexandra Binter,^[b,c]
Marina Toplak,^[b] Peter Macheroux,^[b] Karl Gruber,^[c,d] and Rolf Breinbauer^{*[a,c]}**

^[a] Institute of Organic Chemistry, Graz University of Technology, Stremayrgasse 9, A-8010 Graz, Austria

^[b] Institute of Biochemistry, Graz University of Technology, Petersgasse 10-12, A-8010 Graz, Austria

^[c] Austrian Centre of Industrial Biotechnology (ACIB), Petersgasse 14, A-8010 Graz, Austria

^[d] Institute of Molecular Biosciences, University of Graz, Humboldtstrasse 50, A-8010 Graz, Austria

*Corresponding author:

Prof. Dr. Rolf Breinbauer

Institute of Organic Chemistry

Graz University of Technology

Stremayrgasse 9, 8010 Graz

E-mail: breinbauer@tugraz.at

Keywords: asymmetric synthesis • biocatalysis • C-C-bond formation • enoate reductase • protein engineering

This chapter was published as “Asymmetric Reductive Carbocyclization Using Engineered Ene Reductases” in *Angewandte Chemie International Edition* 2018, Vol. 57, p. 7240-7244 (German version: *Angewandte Chemie* 2018, Vol. 130, 7360-7364).

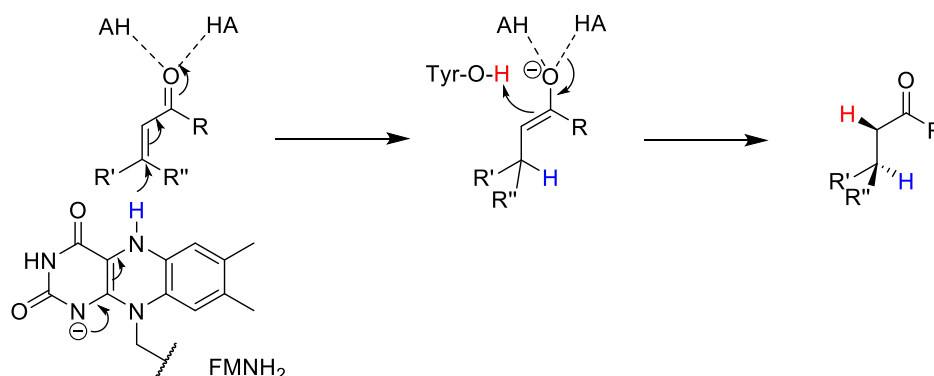
Abstract

Ene reductases from the Old Yellow Enzyme (OYE) family reduce the C=C double bond in α,β -unsaturated compounds bearing an electron-withdrawing group, for example, a carbonyl group. This asymmetric reduction has been exploited for biocatalysis. Going beyond its canonical function, we show that members of this enzyme family can also catalyze the formation of C-C bonds. α,β -Unsaturated aldehydes and ketones containing an additional electrophilic group undergo a reductive cyclization. Mechanistically, the two-electron-reduced enzyme cofactor FMN delivers a hydride generating an enolate intermediate, which reacts with the internal electrophile. Single-site replacement of a crucial Tyr-residue by non-protic Phe or Trp favored the cyclization over the natural reduction reaction. The new transformation allowed the enantioselective synthesis of chiral cyclopropanes in up to >99% ee.

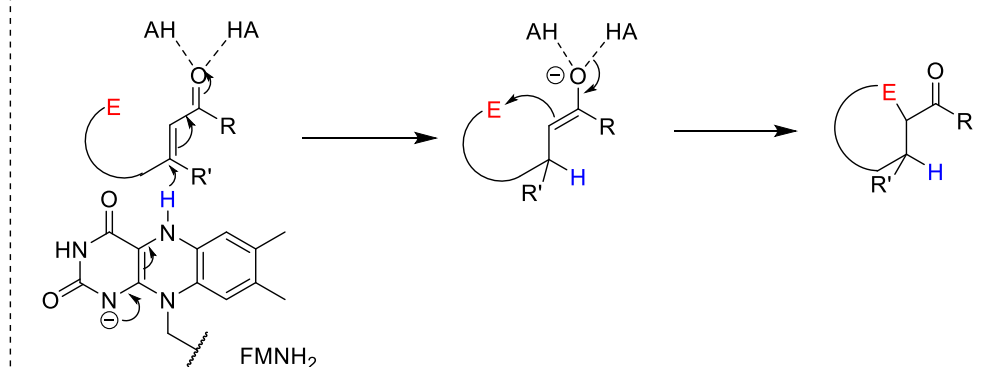
Main article

Over the last decades, the power of enzymatic catalysis has been recognized as an important tool for the stereoselective synthesis of active pharmaceutical ingredients, agrochemicals, and flavor compounds on a laboratory and industrial scale. However, biocatalysis has been largely applied for functional group transformations that follow the natural reactivity of these enzymes, such as hydrolases, reductases, oxidases, or transaminases.^[1] The use of enzymes for C-C bond formations is less established, although notable exceptions exist. Aldolases, hydroxynitrile lyases, thiamine diphosphate dependent enzymes, and terpene cyclases have been used for this type of reactions.^[2] There is a strong desire to expand the biocatalytic tool box with reactions that surpass the established metabolic pathways. Therefore, engineered and artificial metalloenzymes have been developed for biocatalytic C-C bond formations, including olefin cyclopropanation,^[3] Suzuki coupling,^[4] Diels-Alder reaction,^[5] and others.^[6] Herein, we report a new type of enzymatic C-C-bond formation in which a combination of substrate design and protein engineering has enabled the asymmetric reductive cyclization using ene reductases. Ene reductases from the Old Yellow Enzyme (OYE) family are enzymes that reduce electron-deficient alkenes, as present in α,β -unsaturated carbonyl compounds. The synthetic potential of this enzyme family for biocatalytic applications has been recognized in recent years.^[7-8] According to the accepted mechanism, a hydride is delivered from the reduced flavin mononucleotide (FMN) cofactor to the β -carbon to form an enolate, which is subsequently protonated with the assistance of Tyr-OH as a proton source.^[9] We envisioned the use (or modification) of this enzyme family for reductive carbocyclizations by offering substrates that exhibit an additional internal electrophile and thus react intramolecularly with the generated enolate intermediate to produce cyclized products.^[10-11] Toward this goal, carbonyl groups, alkylhalides, or epoxides could be used to serve as the electrophile (Scheme 1).

a) Established Ene-Reductase Scheme:



b) This work: Reductive C-C-Coupling



Scheme 1. **a**, Reduction of an activated C=C bond by ene reductases. Activation of the double bond by hydrogen-bond formation is enabled, for example, by two His residues (shown as “AH”/“HA”). The FMN hydride (shown in *blue*) is transferred to the β -C. The resulting enolate is stabilized by two hydrogen-bonds. Reprotonation at the α -carbon occurs through a conserved tyrosine residue. **b**, Proposed mechanism of reductive C-C coupling. In the absence of the Tyr residue, the enolate attacks the internal electrophilic carbon, thereby enabling the formation of cyclic compounds.

Since the wild-type (WT) enzymes of OPR3 (12-oxophytodienoic acid reductase 3) from tomato (*Solanum lycopersicum*) and YqjM from *Bacillus subtilis* have already shown their value in asymmetric reduction of alkenes in biocatalysis,^[12] we used these enzymes to explore reductive carbocyclization with substrates bearing various electron withdrawing substituents and featuring ω -halo alkyl groups with different chain lengths, which should give rise to different ring sizes (Scheme 2; Table 1). Interestingly, even the wild-type enzymes displayed measurable levels of reductive cyclization when **1a-Br** was offered as a substrate (Table 1, *entries 1 and 2*). However, when (*E*)-4-chlorobut-2-enal (**1a-Cl**) was converted with wild-type OPR3 and YqjM, the natural reduction pathway was dominant over the reductive cyclization reaction (Table 1, *entries 3 and 4*), thus indicating that with a chlorine leaving group, the γ -carbon lacks sufficient electrophilicity. The α,β -unsaturated ketone substrate **1b-Br** was also transformed into a cyclic product though in lower amounts when compared to the more reactive aldehyde substrate **1a-Br** (Table 1, *entries 5 and 6*).

Scheme 2. Reductive C-C bond formations using substrates 1a-Br – 1b-Br. Reaction conditions: 300 μ L stock solution (10 mM substrate, 1 vol% DMF, 1,2 DME as internal standard, and 15 mM NADH in 50 mM sodium phosphate-buffer at pH 7.5 and 150 mM NaCl) and enzyme (5 μ M) in 300 μ L sodium phosphate-buffer (50 mM, pH 7.5, 150 mM NaCl) per tube, 180 min and 25 $^{\circ}$ C at 300 rpm. DMF = *N,N*-dimethylformamide, 1,2 DME = 1,2-dimethoxyethane.

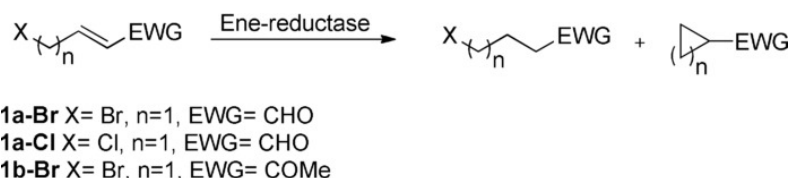


Table 1: Biocatalytic conversions of substrates 1a-Br – 1b-Br.

Entry	Enzyme	Substrate	Conv. [%] ^[a]	Selectivity [red:c]
1	OPR3 WT	1a-Br	74	66:34
2	YqjM WT	1a-Br	>99	59:41
3	WT OPR3	1a-Cl	98	85:15
4	WT YqjM	1a-Cl	>99	83:17
5	WT OPR3	1b-Br	97	72:28
6	WT YqjM	1b-Br	>99	93: 7
7	OPR3 Y190F	1a-Br	93	12:88
8	OPR3 Y190W	1a-Br	45	22:78
9	YqjM Y169F	1a-Br	>99	2:98
10	YqjM Y169W	1a-Br	3	50:50
11	OPR3 Y190F	1a-Cl	99	73:27
12	OPR3 Y190W	1a-Cl	85	82:18
13	YqjM Y169F	1a-Cl	>99	66:34
14	WT OPR3	1b-Br	97	72:28
15	OPR3 Y190F	1b-Br	97	14:86
16	OPR3 Y190W	1b-Br	85	16:84
17	WT YqjM	1b-Br	>99	93: 7
18	YqjM Y169F	1b-Br	>99	2:98
19	YqjM Y169W	1b-Br	28	25:75

^[a] Conversions were determined by GC-FID analysis of the crude reaction mixture by using 1,2-DME as an internal standard; red = reduction product; c = cyclization product; n.d.= not detected.

These initial experiments showed that alkene reduction and enolate trapping are competing pathways. Following our proposal (Scheme 1), we reasoned that the desired enolate alkylation could be favored if protonation of the enolate could be prevented or suppressed by removing proton donors and residual water molecules from the active site. We assumed that exchanging the proton donor (Tyr190 in

OPR3)^[9c] for an aprotic and apolar amino acid (Phe, Trp) should lead to beneficial effects because of an inability to directly reprotonate the intermediate as well as displacement of water from the active site.

Indeed, the OPR3 variants Y190F and Y190W showed a 2-fold improvement in the formation of cyclopropane carbaldehyde from **1a-Br** compared with the wild-type enzyme (Table 1, entries 7 and 8). For engineering YqjM, the critical Tyr residue at position 169^[13] was replaced with Phe or Trp. The Phe variant of YqjM converted (*E*)-4-bromobut-2-enal (**1a-Br**) smoothly in more than 99 % conversion with a high preference for the C-C bond-forming reaction over the natural reduction reaction (Table 1, entry 9).

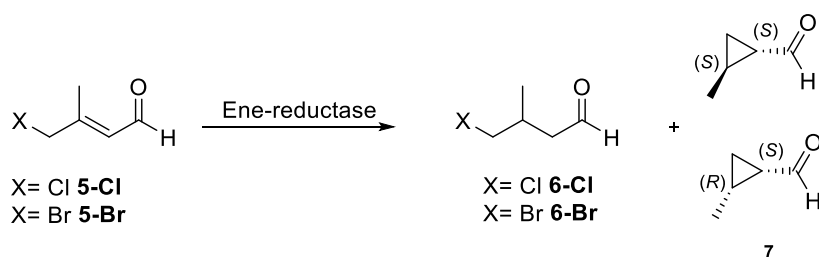
In order to demonstrate the practical value of this transformation, a (*E*)-4-bromobut-2-enal (10 mM) was transformed with YqjM Y169F (0.05 mol%) on a preparative scale. The very volatile cyclopropane carbaldehyde was further converted in a subsequent chemical reaction into the corresponding 2,4-dinitrophenylhydrazone in 79 % yield of isolated product over two steps.

While the WT enzymes showed mainly alkene reduction of α,β -unsaturated ketones (substrate **1b-Br**), YqjM Y169F turned out to be an excellent enzyme for the cyclization, producing acetylcyclopropane in 98 % conversion (Table 1, entry 18).

Ester substrates (**1c-Br** and **1d-Br**) were not converted at all by either the wild-type ene reductase or the variants, and ring formation of 4- or 5-membered rings was not observed (see table S1 in the Supporting information), since the less favorable kinetics of cyclization of such rings in comparison to three-membered rings could not compete with the faster natural reduction reaction.^[14]

For the α -substituted substrate (*E*)-4-Chloro-2-methylbut-2-enal (**4a-Cl**), the Phe variant of YqjM showed highest cyclopropanation activity (up to 76 %; Table S2). In order to test for the possibility of performing asymmetric reductive carbocyclizations, (*E*)-4-chloro-3-methylbut-2-enal (**5-Cl**) and (*E*)-4-bromo-3-methylbut-2-enal (**5-Br**) were used as substrates for wild-type OPR3 and YqjM and the variants thereof (Scheme 3).

Scheme 3: Biocatalytic conversion of substrates 5-Cl and 5-Br. Reaction conditions see Scheme 2.



All of the enzymes converted both substrates equally well in up to >99 % conversion, with the OPR3 and YqjM variants showing a higher preference for cyclopropanation activity (Table 2). With the more

electrophilic substrate **5-Br**, these variants delivered almost exclusively the desired cyclopropanation product (Table 2, *entries 7-8,10*). Interestingly, WT YqjM and its Phe variant showed a reversal in diastereoselectivity when switching from a chlorine to a bromine substrate (Table 2, *entries 4,5 vs. 9,10*).

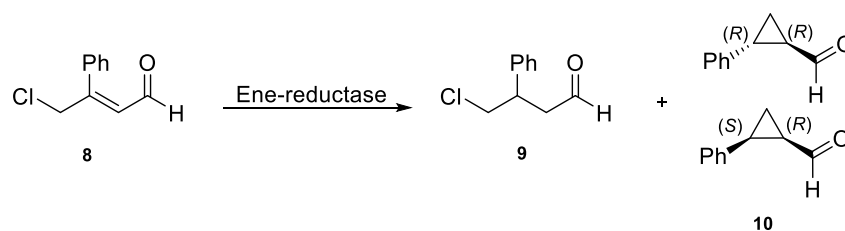
Very good enantioselectivity was observed for WT OPR3, which had a strong preference for the (*R,S*)-**7** enantiomer (>99 % *ee*; Table 2, *entry 1*). The YqjM variant Y169F showed a reversed as well as enhanced enantioselectivity compared to the wild-type enzyme, thus indicating that subtle changes in the binding site might have large consequences for substrate recognition (Table 2, *entry 5*). We were able to rationalize the observed asymmetric reduction through docking studies (Figure S1 in the Supporting information).

Table 2: Biocatalytic conversion of substrates 5-Cl and 5-Br.

Entry	Enzyme	X	Conv. [%] ^[a]	Selectivity [red:c]	<i>de trans/cis</i> [%] ^[b]	<i>ee</i> [%] ^[b] (<i>S,S</i>)- 7	<i>ee</i> [%] ^[b] (<i>R,S</i>)- 7
1	OPR3 WT	Cl	>99	57:43	68	87	>99
2	OPR3 Y190F	Cl	>99	19:81	57	61	54
3	OPR3 Y190W	Cl	>99	22:78	64	31	24
4	YqjM WT	Cl	95	69:31	67	52	56
5	YqjM Y169F	Cl	>99	12:88	72	-80	-55
6	OPR3 WT	Br	>99	13:87	14	92	nd
7	OPR3 Y190F	Br	>99	1:99	58	22	nd
8	OPR3 Y190W	Br	70	1:99	13	39	nd
9	YqjM WT	Br	>99	35:65	-54	81	nd
10	YqjM Y169F	Br	>99	1:99	-30	-67	nd

^[a] Conversions were determined by GC-FID analysis of the crude reaction mixture by using 1,2 DME as an internal standard; nd= not detected. ^[b] For assignment of *de* and *ee* products were analyzed as the corresponding alcohols after reduction of the samples using NaBH₄.

We reasoned that the enantiodiscrimination in the ene reductase enabled carbocyclization could be enhanced by offering a substrate bearing a sterically demanding phenyl substituent at C-β to the wild-type and variant ene reductases (Scheme 4).

Scheme 4. Biocatalytic conversion of substrate 8. Reaction conditions see Scheme 2.

WT OPR3 converted substrate **8-Cl** into cyclopropane **10** with moderate conversion (48 %), whereas OPR3 Y190F and OPR3 Y190W led to good conversion to **10** (75 % and 71 %; Table 3, *entries 1 to 3*). Replacement of Tyr169 by Phe in YqjM is key to achieving a high carbocyclization activity and excellent diastereoselectivity that strongly favors the *trans*-diastereomer (*R,R*-**10**, *de* 94 %; Table 3, *entries 4-5*). Both OPR3 and YqjM (WT and variants) showed a high preference for the (1*R*,2*R*)-2-phenyl-cyclopropyl)methanol (*R,R*-**10**), giving >99 % *ee*.

Table 3: Biocatalytic conversion of substrate 8.

Entry	Enzyme	Conv. [%] ^[a]	Selectivity [red:c]	<i>de trans/cis</i> [%]	<i>ee</i> [%] ^[b] (<i>R,R</i>)- 10	<i>ee</i> [%] ^[b] (<i>S,R</i>)- 10
1	OPR3 WT	>99	52:48	72	>99	54
2	OPR3 Y190F	>99	25:75	71	>99	-43
3	OPR3 Y190W	94	29:71	71	>99	-51
4	YqjM WT	81	28:72	-30	>99	-8
5	YqjM Y169F	89	5:95	94	>99	-29

^[a] Conversions were determined by GC-FID analysis of the crude reaction mixture by using 1,2 DME as an internal standard; nd= not detected. ^[b] For assignment of *ee*, products were analyzed as the corresponding alcohols after reduction of the samples using NaBH₄.

Conclusion

In conclusion, we have presented the first biocatalytic reductive carbocyclization using ene reductases. For our cyclization approach, two strategies proved useful to suppress the natural reduction reaction. First, engineering of the enzymes by replacing the critical proton donor (Tyr190 in OPR3, Tyr169 in YqjM) with Phe or Trp favored the preference for the cyclization reaction. Second, substrate engineering could be used in a synergistic way.

While an increase in the electrophilicity of the γ -carbon favored the cyclization, this approach was often limited by the intrinsic instability of these substrates. Decoration of the scaffold with substituents at the α - and β -position (as present in synthetically more attractive compounds) appeared to be a more universal strategy, leading to improved product selectivity by removing water molecules that could

serve as potential alternative proton donors in the active site. We were able to demonstrate that prochiral substrates can be cyclized to form chiral 1,2-disubstituted cyclopropanes with excellent enantioselectivities. Current efforts in our laboratory aim to expand the scope to larger ring systems by using protein and substrate engineering.

Acknowledgements

We thank Jakob Dohr, Leo Krammer, Christoph Gradwohl, Andrea Walzl and Eva Frießer for skillful assistance in the lab and Stefan Ettl for computational assistance. This research has received funding from NAWI Graz and the Federal Ministry of Science, Research and Economy (BMWFW), the Federal Ministry of Traffic, Innovation and Technology (bmvit), the Styrian Business Promotion Agency SFG, the Standortagentur Tirol, the Government of Lower Austria and ZIT - Technology Agency of the City of Vienna through the COMET-Funding Program managed by the Austrian Research Promotion Agency FFG. Furthermore, the work was supported by the Austrian Science Fund (FWF) to R.B., K.G. and P.M. (DK Molecular Enzymology W901).

Conflict of Interest

The authors declare no conflict of interest.

References

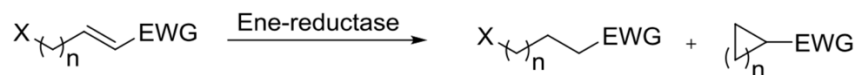
- [1] a) K. Drauz, H. Groeger, O. May (Eds.), *Enzyme Catalysis in Organic Synthesis*, 3rd ed., Wiley-VCH, Weinheim, **2011**; b) K. Faber, *Biotransformations in Organic Chemistry*, 6th ed. Springer, Heidelberg, **2011**.
- [2] Recent reviews: a) N. G. Schmidt, E. Eger, W. Kroutil, *ACS Catal.* **2016**, *6*, 4286-4311; b) K. Fesko, M. Gruber-Khadjawi, *ChemCatChem*, **2013**, *5*, 1248-1272; c) S. C. Hammer, P. O. Syren, M. Seitz, B. M. Nestl, B. Hauer, *Curr. Opin. Chem. Biol.* **2013**, *17*, 293-300; d) M. Brovetto, D. Gamemara, P. S. Méndez, G. A. Seoane, *Chem. Rev.* **2011**, *111*, 4346-4403.
- [3] a) P. S. Coelho, E. M. Brustad, A. Kannan, F. H. Arnold, *Science* **2013**, *339*, 307-310; b) P. S. Coelho, Z. J. Wang, M. E. Ener, S. A. Baril, A. Kannan, F. H. Arnold, E. M. Brustad, *Nat. Chem. Biol.* **2013**, *9*, 485-487; c) Z. J. Wang, H. Renata, N. E. Peck, C. C. Farwell, P. S. Coelho, F. H. Arnold, *Angew. Chem. Int. Ed.* **2014**, *53*, 6810-6813; d) M. Bordeaux, V. Tyagi, R. Fasan, *Angew. Chem. Int. Ed.* **2015**, *54*, 1744-1748; e) P. Srivastava, H. Yang, K. Ellis-Guardiola, J. C. Lewis, *Nat. Commun.* **2015**, *6*, 7789; f) J. G. Gober, A. E. Rydeen, E. J. Gibson-O'Grady, J. B. Leuthaeuser, J. S. Fetrow, E. M. Brustad, *ChemBioChem* **2016**, *17*, 394-397; g) H. M. Key, P. Dydio, Z. Liu, J. Y.- E. Rha, A. Nazarenko, V. Seyedkazemi, D. S. Clark, J. F. Hartwig, *ACS Centr. Sci.* **2017**, *3*, 302-308.
- [4] a) S. Abe, J. Niemeyer, M. Abe, Y. Takezawa, T. Ueno, T. Hikage, G. Erker, Y. Watanabe, *J. Am. Chem. Soc.* **2008**, *130*, 10512-10514; b) A. Chatterjee, H. Mallin, J. Klehr, J. Vallapurackal, A. D. Finke, L. Vera, M. Marsh, T. R. Ward, *Chem. Sci.* **2016**, *7*, 673-677.
- [5] a) D. Coquière, J. Bos, J. Beld, G. Roelfes, *Angew. Chem. Int. Ed.* **2009**, *48*, 5159-5162; b) J. Podtetenieff, A. Taglieber, E. Bill, E. J. Reijerse, M. T. Reetz, *Angew. Chem. Int. Ed.* **2010**, *49*, 5151-5155.
- [6] Friedel-Crafts indole alkylation: a) J. Bos, W. R. Browne, A. J. Driessen, G. Roelfes, *J. Am. Chem. Soc.* **2015**, *137*, 9796-9799; Wittig olefination: b) V. Tyagi, R. Fasan, *Angew. Chem. Int. Ed.* **2016**, *55*, 2512-2516; Olefin metathesis: c) C. Mayer, D. G. Gillingham, T. R. Ward, D. Hilvert, *Chem. Commun.* **2011**, *47*, 12068-12070; d) F. Philippart, M. Arlt, S. Gotzen, S. J. Tenne, M. Bocola, H. H. Chen, L. Zhu, U. Schwaneberg, J. Okuda, *Chem. Eur. J.* **2013**, *19*, 13865-13871; e) M. Basauri-Molina, D. G. A. Verhoeven, A. J. van Schaik, H. Kleijn, R. J. M. K. Gebbink, *Chem. Eur. J.* **2015**, *21*, 15676-15685; Doyle-Kirmse reaction: f) V. Tyagi, G. Sreenilayam, P. Bajaj, A. Tinoco, R. Fasan, *Angew. Chem. Int. Ed.* **2016**, *55*, 13562-13566; Michael reaction: g) X. Garrabou, R. Verez, D. Hilvert, *J. Am. Chem. Soc.* **2017**, *139*, 103-106.
- [7] Reviews: a) K. Faber, M. Hall in *Science of Synthesis: Biocatalysis in Organic Synthesis, Vol. 2* (Eds.: K. Faber, W.-D. Fessner, N. J. Turner), Georg Thieme Verlag, Stuttgart, **2015**, pp. 213-260; b) H. S. Toogood, N. S. Scrutton, *Curr. Opin. Chem. Biol.* **2014**, *19*, 107-115; c) C. K. Winkler, G. Tasnadi, D. Clay, M. Hall, K. Faber, *J. Biotechnol.* **2012**, *162*, 381-389;

- d) H. S. Toogood, J. M. Gardiner, N. S. Scrutton, *ChemCatChem* **2010**, *2*, 892–914; e) R. Stuermer, B. Hauer, M. Hall, K. Faber, *Curr. Opin. Chem. Biol.* **2007**, *11*, 203–213.
- [8] For selected recent contributions, see: a) S. Milker, M. J. Fink, N. Oberleitner, A. K. Ressimann, U. T. Bornscheuer, M. D. Mihovilovic, F. Rudroff, *ChemCatChem* **2017**, *9*, 3420–3427; b) I. Janicki, P. Kielbasinski, N. G. Turrini, K. Faber, M. Hall, *Adv. Synth. Catal.* **2017**, *359*, 4190–4196; c) E. Brenna, M. Crotti, F. G. Gatti, D. Monti, F.; Parmeggiani, S. Santangelo, *ChemCatChem* **2017**, *9*, 2480–2487; d) N. Kress, J. Rapp, B. Hauer, *ChemBioChem* **2017**, *18*, 717–720; e) E. Brenna, M. Crotti, F. G. Gatti, L. Marinoni, D. Monti, S. Quaiato, *J. Org. Chem.* **2017**, *82*, 2114–2122; f) S. H. Lee, D. S. Choi, M. Pesic, Y. W. Lee, C. E. Paul, F. Hollmann, C. B. Park, *Angew. Chem. Int. Ed.* **2017**, *56*, 8681–8685; g) Y. Wang, M. J. Bartlett, C. A. Denard, J. F. Hartwig, H. Zhao, *ACS Catalysis* **2017**, *7*, 2548–2552; h) J. C. Joo, A. N. Khusnutdinova, R. Flick, T. Kim, U. T. Bornscheuer, A. F. Yakunin, R. Mahadevan, *Chem. Sci.* **2017**, *8*, 1406–1413; i) N. G. Turrini, R. C. Cioc, D. J. H. van der Niet, E. Ruijter, R. V. A. Orru, M. Hall, K. Faber, *Green Chem.* **2017**, *19*, 511–518; j) B. R. S. Paula, D. Zampieri, J. A. R. Rodrigues, P. J. S. Moran, *Adv. Synth. Catal.* **2016**, *358*, 3555–3571; k) A. Lygidakis, V. Karuppiah, R. Hoeven, A. N. Cheallaigh, D. Leys, J. M. Gardiner, H. S. Toogood, N. S. Scrutton, *Angew. Chem. Int. Ed.* **2016**, *55*, 9596–9600; l) K. Königer, A. G. Baraibur, C. Mügge, C. E. Paul, F. Hollmann, M. M. Nowaczyk, R. Kourist, *Angew. Chem. Int. Ed.* **2016**, *55*, 5582–5585; m) Y. Okamoto, V. Kohler, C. E. Paul, F. Hollmann, T. R. Ward, *ACS Catalysis* **2016**, *6*, 3553–3557; n) E. Brenna, M. Crotti, F. G. Gatti, D. Monti, F. Parmeggiani, R. W. Powell III, S. Santangelo, J. D. Stewart, *Adv. Synth. Catal.* **2015**, *357*, 1849–1860; o) N. G. Turrini, M. Hall, K. Faber, *Adv. Synth. Catal.* **2015**, *357*, 1861–1871; p) E. Ruethlein, T. Classen, L. Dobnikar, M. Schoelzel, J. Pietruszka, *Adv. Synth. Catal.* **2015**, *357*, 1775–1786; q) T. Ress, W. Hummel, S. P. Hanlon, H. Iding, H. Groeger, *ChemCatChem* **2015**, *7*, 1302–1311; r) G. Steinkellner, C. C. Gruber, T. Pavkov-Keller, A. Binter, K. Steiner, C. Winkler, A. Lyskowski, O. Schwamberger, M. Oberer, H. Schwab, K. Faber, P. Macheroux, K. Gruber, *Nature Commun.* **2014**, *5*, 4150; s) R. Agudo, M. T. Reetz, *Chem. Commun.* **2013**, *49*, 10914–10916, t) A. B. Daugherty, S. Govindarajan, S. Lutz, *J. Am. Chem. Soc.* **2013**, *135*, 14425–14432.
- [9] a) R. Lonsdale, M. T. Reetz, *J. Am. Chem. Soc.* **2015**, *137*, 14733–14742; b) B. J. Brown, Z. Deng, P. A. Karplus, V. Massey, *J. Biol. Chem.* **1998**, *273*, 32753–32762; c) R. M. Kohli, V. Massey, *J. Biol. Chem.* **1998**, *273*, 32763–32770; d) P. A. Karplus, K. M. Fox, V. Massey, *FASEB J.* **1995**, *9*, 1518–1526; e) A. S. Abramovitz, V. Massey, *J. Biol. Chem.* **1976**, *251*, 5327–5336; f) K. M. Fox, P. A. Karplus, *Structure* **1994**, *2*, 1089–1105.
- [10] Reductive cyclizations mediated by enolate formation via hydride delivery to α,β -unsaturated carbonyl compounds has been reported for transition metal catalysis. For a seminal review, see: M.Y. Ngai, J.-R. Kong, M. J. Krische, *J. Org. Chem.* **2007**, *72*, 1063–1071.

- [11] In a mechanistic investigation of the biosynthesis of iridoids, the formation of 5-membered rings via a Michael-type cyclization using a mechanistic probe was observed: S. Lindner, F. Geu-Flores, S. Bräse, N. H. Sherden, S. E. O'Connor, *Chem. Biol.* **2014**, *21*, 1452–1456. For an analysis of cyclopropane formation in polyketide diversification, see: L. Gu, B. Wang, A. Kulkarni, T. W. Geders, R. V. Grindberg, L. Gerwick, K. Hakansson, P. Wipf, J. L. Smith, W. H. Gerwick, D. H. Sherman, *Nature* **2009**, *459*, 731-735.
- [12] a) M. Hall, C. Stueckler, W. Kroutil, P. Macheroux, K. Faber, *Angew. Chem. Int. Ed.* **2007**, *46*, 3934-3937; b) M. Hall, C. Stueckler, H. Ehammer, E. Pointner, G. Oberdorfer, K. Gruber, B. Hauer, R. Stuermer, W. Kroutil, P. Macheroux, K. Faber, *Adv. Synth. Catal.* **2008**, *350*, 411-418; c) C. Stueckler, M. Hall, H. Ehammer, E. Pointner, W. Kroutil, P. Macheroux, K. Faber, *Org. Lett.* **2007**, *9*, 5409-5411; d) M. Hall, C. Stueckler, B. Hauer, R. Stuermer, T. Friedrich, M. Breuer, W. Kroutil, K. Faber, *Eur. J. Org. Chem.* **2008**, 1511-1516; e) H. S. Toogood, A. Fryzkowska, V. Hare, K. Fisher, A. Roujeinikova, D. Leys, J. M. Gardiner, G. M. Stephens, N. S. Scrutton, *Adv. Synth. Catal.* **2008**, *350*, 2789-2803.
- [13] K. Kitzing, T. B. Fitzpatrick, C. Wilken, J. Sawa, G. P. Bourenkov, P. Macheroux, T. Clausen, *J. Biol. Chem.* **2005**, *280*, 27904-27913.
- [14] For seminal studies about the ring closure kinetics of bifunctional chain molecules, see: a) G. Illuminati, L. Mandolini, *Acc. Chem. Res.* **1981**, *14*, 95-102; b) M. A. Casadei, C. Galli, L. Mandolini, *J. Am. Chem. Soc.* **1984**, *106*, 1051–1059.
- [15] While we envisioned to improve the ring formation activity by using a substrate with a bromine at the γ -carbon, we experienced in this and other cases that some of these allylbromide substrates were synthetically not accessible due to their intrinsic instability.
- [16] O. Trott, A. J. Olson, *J. Comput. Chem.* **2010**, *31*, 455-461.
- [17] A. D. Bochevarov, E. Harder, T. F. Hughes, J. R. Greenwood, D. A. Braden, D. M. Philipp, D. Rinaldo, M. D. Halls, J. Zhang, R. A. Friesner, *Int. J. Quantum Chem.* **2013**, *113*, 2110-2142.

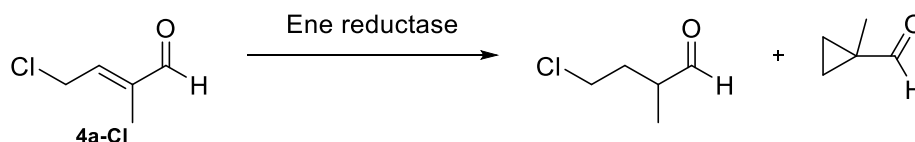
Supporting information (essential for main manuscript)

Tables

Table S1: Biocatalytic conversions of substrates **2a-I**, **2a-Br**, **3a-I**, **3a-Br**, **1d-Br** and **1b-Br**.**1c-Br** X= Br, n=1, EWG= CO₂Me**1d-Br** X= Br, n=1, EWG= CO₂Et**2a-Br** X= Br, n=2, EWG= CHO**2a-I** X= I, n=2, EWG= CHO**3a-Br** X= Br, n=3, EWG= CHO**3a-I** X= I, n=3, EWG= CHO

Entry	Enzyme	Substrate	Conv. [%] ^[a]	Selectivity [red:c]
20	OPR3 Y190F	2a-I	>99	100: 0
21	OPR3 Y190F	2a-Br	>99	100: 0
22	OPR3 Y190F	3a-I	26	100: 0
23	OPR3 Y190F	3a-Br	34	100: 0
24	all enzymes	1d-Br	<1	n.d.
25	all enzymes	1c-Br	<1	n.d.

^[a] Conversions were determined by GC-FID analysis of the crude reaction mixture by using 1,2-DME as an internal standard; red = reduction product; c = cyclization product; n.d.= not detected.

Table S2: Conversion of substrate **4a-Cl**.

Entry	Enzyme	Conversion [%] ^[a]		
1	OPR3 WT	>99	54	46
2	OPR3 Y190F	>99	32	68
3	OPR3 Y190W	>99	35	65
4	YqjM WT	>99	44	56
5	YqjM Y169F	>99	24	76
6	YqjM Y169W	nd	nd	nd

^[a] Conversions were determined by GC-FID analysis of the crude reaction mixture by using 1,2-DME as an internal standard; nd= not detected.

Quantum chemical calculations

Transition states for the reductive cyclization of **5-Cl** were calculated using the program Jaguar employing DFT calculations with the B3LYP functional and the 6-31g*+ basis set¹. Suitable starting structures for the transition state searches were generated using relaxed coordinate scans starting from optimized structures of the respective enolate intermediates resulting from a hydride transfer to the C- β -atom. The nature of the thus identified stationary points were checked by frequency calculations. In all cases a single imaginary frequency was found which corresponded to the supposed reaction coordinate (formation of the C-C bond and cleavage of the C-Cl bond). Transition state structures were calculated for formation of both the *cis*- and the *trans*-cyclopropane derivatives.

Docking

Coordinates for OPR3 and YqjM were obtained from the PDB (entry-codes: 2hsa and 1z41) and were prepared for the docking calculations by the addition of polar hydrogen atoms, the addition of partial charges as well as by assigning the appropriate atom types. The structures of the active site variants (OPR3-Y190F and YqjM-Y169F) were generated with the program PyMOL (<http://www.pymol.org>). Structures of the substrate **5-Cl** were built using the program Maestro (Schrödinger Inc.).

Docking calculations were performed with the program AutoDockVina using the default parameters except for an “exhaustiveness” of 32.² The cubic energy grid was centered on the N5 atom of the FMN cofactor and had an extension of 22.5 Å in each direction. Whereas all ligand structures were treated as flexible to ensure a maximum degree of freedom during the calculations, all protein residues were kept rigid. The resulting docking poses were analyzed using the program PyMOL (<http://www.pymol.org>).

In an attempt to rationalize the enantiodiscrimination observed in the asymmetric cyclization reaction substrate **5-Cl** was docked into the active sites of OPR3 and YqjM using the program AutoDock Vina. In both cases, structures of the wild type enzymes as well as of the Tyr to Phe variants were used. Figure S1 shows the modeled complex of OPR3 WT with **5-Cl**. The binding mode of the compound is typical for OYE substrates with the carbonyl group forming hydrogen bonds to His185 and His188. The C- β -atom is located close to N5 of the flavin cofactor (ideally placed to receive a hydride). The methyl group is oriented toward a small hydrophobic pocket, whereas the chloro-methyl group is exposed to the solvent.

We also calculated ring closure transition state structures starting from the corresponding enolate compound derived from **5-Cl** using the program Jaguar^[17] and again docked these structures into the active sites of OPR3 and YqjM. Figure 1 shows the transition state structure for the formation of the (*R,S*)-**7** bound to OPR3 wild type, which exhibits an ee of >99% in this conversion (Table 2). The modeled binding mode is very similar to the binding mode of **5-Cl** and only small conformational

changes are necessary to reach the transition state after hydride transfer to C- β . The chloride leaving group may interact with the side chains of His244 and/or Tyr370.

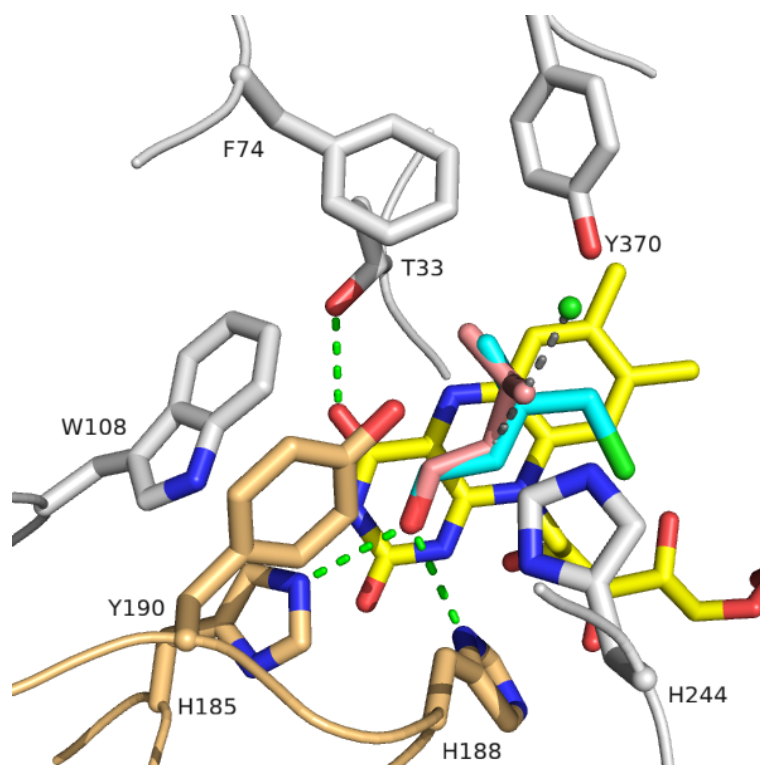


Figure S1: Close-up view of the active site of OPR3 WT in complex with the substrate 5-Cl (*cyan*) and the transition state leading to (*R,S*)-7 (*pink*). Hydrogen bonding interactions are shown as *green dashed lines*, the bonds broken and formed in the transition state are shown as *grey lines*. The figure was prepared using the program PyMOL (<https://www.pymol.org/>).

Additional supporting information and detailed Material and Methods section can be found at:

[anie201802962-sup-0001-misc_information.pdf](https://doi.org/10.1039/c2an201802962-sup-0001-misc_information.pdf)

Author contributions

Chapter 1: The family of berberine bridge enzyme-like enzymes: a treasure-trove of oxidative reactions

This review article was the joint effort of all authors listed, with me generating most of the figures shown in the manuscript and writing the part on “Reactions of BBE-like proteins from bacteria”, which was revised with the input of BD and PM.

Chapter 2: The single berberine bridge enzyme homolog of *Physcomitrella patens* is a cellobiose oxidase

In order to be able to determine the primordial role of BBE-like enzymes in plants, I produced *PpBBE1* wild type and several active-site variants in *Komagataella phaffii* and purified the proteins by means of Ni-NTA affinity chromatography. JU and I used activity assays to find a substrate for the protein and performed the biochemical characterization of *PpBBE1* wild type. The biochemical characterization of the variant proteins was carried out by me. With the help of AW, I also crystallized *PpBBE1* wild type and the D396N variant and determined the 3D-structure of the two proteins. The *in planta* characterization of *PpBBE1* as well as the analysis of a *PpBBE1* knock-out strain was performed by GW, JK, and SNWH, with me performing the molecular cloning of the knock-out gene. I generated Figures 2-8 and wrote the material and methods section describing the biochemical and structural characterization of *PpBBE1*. The results and discussion section were mainly written by PM with input from AW and from my side and with GW and RR providing results and discussion sections covering the *in planta* characterization.

Chapter 3: Oxidation of the FAD cofactor to the 8-formyl-derivative in human electron transferring flavoprotein

The study summarized in this manuscript deals with the identification and characterization of a so far unknown modification of the flavin cofactor bound to hETF. DNA constructs used for the recombinant production of hETF wild type and several active-site variants were generated by PA, KF, ECG, and myself. PA, KF, ECG, and I also recombinantly produced the proteins and purified them by means of Ni-NTA affinity chromatography. PA and I performed the biochemical experiments and interpreted the data with the help of AW and PM. RP performed the EPR-spectroscopy experiments and analyzed the respective data. PA wrote the first draft of the manuscript, which was revised with the inputs from AW, PM, and myself.

Chapter 4: Toward understanding the reaction mechanism of 8-formyl FAD formation in human electron transferring flavoprotein

In this section results helping to get a better understanding of the mechanism of 8-formyl FAD formation in hETF are shown. All experiments presented in this section were performed by me, together with my students KF and JB. Data were analyzed by PM and me. Introduction, results, discussion, as well as the materials and methods section were written by me and revised with the input of PM.

Chapter 5: Closing the gap: Yeast electron transferring flavoprotein links the oxidation of D-lactate and D- α -hydroxyglutarate to energy production via the respiratory chain

This manuscript presents the detailed biochemical characterization of yETF and Dld2 and provides insights into the mechanism of electron transfer from Dld2 to yETF. The constructs used for the recombinant production of Dld2, yETF wild type and several active-site variants were generated by CT, JB, and myself. Production and purification of the recombinant proteins, as well as the biochemical experiments were performed by JB and me. Data were analyzed by JB, PM and myself. JB and I generated the figures presented in the paper. I wrote the first draft of the manuscript, with JB contributing to the material and methods section, and later revised it with the input of PM.

Chapter 6: Biochemical characterization of human D-2-hydroxyglutarate dehydrogenase and two disease-related variants reveal the molecular cause of D-2-hydroxyglutaric aciduria

In this study we analyzed the biochemical properties of hD2HGDH wild type and of two pathogenic variants (I147S and V444A) and performed interaction studies with the putative electron acceptor hETF. Cloning of the DNA constructs and recombinant production and purification of the proteins was performed by my students JB and JS and myself. JB and I performed the biochemical characterization of hD2HGDH wild type and I studied the properties of the two pathogenic variants. I generated all the figures and designed/wrote the first draft of the manuscript, which was revised with the input of PM.

Appendix A: Promising new antifungal treatment targeting chorismate synthase from *Paracoccidioides brasiliensis*

This chapter presents the results of a study aiming to find an inhibitor of a key-enzyme involved in the shikimate pathway, the so-called chorismate synthase. Our collaboration partners from Brazil used virtual screening to identify compounds that could potentially bind to the active-site of CS and could thus possibly serve as inhibitors thereof. In order to prove the results from the *in silico* experiments, I

recombinantly produced *PbCS* in *Escherichia coli*, purified the protein by means of Ni-NTA affinity chromatography and determined the binding affinity of CP1 to *PbCS*. I also analyzed the inhibitory effect of CP1 on the activity of the recombinant protein, generated Figure 4 of the manuscript summarizing our results, and wrote the respective part in the material and methods section.

Appendix B: New inhibitors of chorismate synthase present antifungal activity against *P. brasiliensis*

In addition to CP1, virtual screening performed by our collaboration partners in Brazil revealed a second potential inhibitor of CS, CaCS02. To confirm the *in silico* result, again, I recombinantly produced *PbCS* in *Escherichia coli*, purified the protein by means of Ni-NTA affinity chromatography and determined the binding affinity of CaCS02 to *PbCS*. I also analyzed the inhibitory effect of CaCS02 on the activity of the recombinant protein, generated Figure 3 of the manuscript summarizing our results, and wrote the respective part in the material and methods section.

Appendix C: Asymmetric reductive carbocyclization using engineered ene reductases

This manuscript deals with the use of engineered ene reductases for reductive carbocyclization reactions. I helped with/performed the cloning of the mutant genes as well as with the recombinant production and purification of several protein variants used in the study. I also helped KH with writing of the biochemical part of the materials and methods section.

Curriculum vitae

Personal details

Name: Marina Toplak, BSc MSc
Address: Brucknerstraße 100/1/8, 8010 Graz
Nationality: Austria
Telephone: +43 664 59 45 157
Email: marina.toplak@icloud.com
Date of birth: 11.03.1993



Education

- April 2016 – May 2019: **Member of the Doktoratskolleg (DK) Molecular Enzymology in Graz (NAWI-Graz)**
- October 2015 – May 2019: **Doctoral Program in Natural Sciences**; Branch of study: Biotechnology, Biochemistry und Food Chemistry at the **Graz University of Technology (NAWI-Graz)** –
 PhD thesis on the topic “*Flavin-dependent reactions in carbohydrate metabolism and mitochondrial electron transport*”, under the supervision of Univ.-Prof. Dr. rer. nat. Peter Macheroux
- October 2013 – October 2015: **Master-studies in Biochemistry and Molecular Biomedical Sciences at the Graz University of Technology (NAWI-Graz)** *graduation with distinction* –
 Master thesis in biochemistry on the topic „*Studies on the role of EasC and EasE in ergot alkaloid biosynthesis*“, under the supervision of Univ.-Prof. Dr. rer. nat. Peter Macheroux
- October 2010 – August 2013: **Bachelor-studies in Chemistry at the Graz University of Technology (NAWI-Graz)** –
 Bachelor thesis in organic chemistry on the topic „*Studien zur Synthese eines Dipeptidmimetikums als Teil eines Inhibitors für das Enzym Dipeptidyl Peptidase III*“, under the supervision of Univ.-Prof. Dr. rer. nat. Rolf Breinbauer
- September 2002 – June 2010: **Bundesrealgymnasium Petersgasse, Graz** *graduation from school with distinction*
- September 1999 – July 2002: **Volksschule Waltendorf, Graz**

Laboratory skills

- gene design, molecular cloning, recombinant protein production using *Escherichia coli* and *Komagataella phaffii* as expression hosts
- protein purification using affinity chromatography, gel filtration, anion exchange chromatography, and hydrophobic interaction chromatography, SDS-PAGE electrophoresis, western blot, MALDI-TOF
- UV-visible spectroscopy (including photoreduction of protein-bound flavins), Thermofluor[®], enzyme kinetics (steady-state assays, rapid reaction kinetics using stopped-flow) and inhibition assays, redox potential determination of protein-bound flavins (dye-equilibrium method)
- basic knowledge in crystallization and structure determination, CD-spectroscopy, HPLC-DAD, HPLC-MS, and NMR-analysis

Teaching experience

2015-2019	Teaching assistant in the Biochemistry I lab course (CHE. 154_1)
WS 2016/17	Teaching assistant in the Biochemistry II lab course (CHE. 192)
SS 2017	Teaching assistant in the Immunology lab course (MOL. 401)
2015-2019	Supervision of several project, bachelor and master students
2015-2019	Supervision of pupils in the framework of “Children University”

IT skills

- Microsoft Office (Word, Excel, PowerPoint), Gimp 2
- Origin, GraphPad Prism 5, Chem(Bio)Draw, Kinetic Studio Software, MassLynx[™] Software
- PyMOL, Coot
- Bioinformatic tools (BLAST, Swissmodel etc.), Jalview, Figtree

Languages

Mother tongue:	German
Foreign languages:	English (fluent) French (basic)

Poster and oral presentations at national conferences

- Toplak M, Brunner J and Macheroux P, D-lactate dehydrogenase 2 – the natural electron donor of the electron transferring flavoprotein from *Saccharomyces cerevisiae*? *DK Molecular Enzymology graduate seminar*, Graz, Austria, November 30th 2018, oral presentation (best presentation award)
- Toplak M, Wiedemann G, Ulićević J, Daniel B, Hoernstein S N W, Kothe J, Reski R, Winkler A and Macheroux P, Structural and functional characterization of the berberine bridge enzyme-like protein from *Physcomitrella patens*. *18th Doc Day NAWI Graz Doctoral Schools Molecular Biology and Biochemistry & Molecular Biosciences and Biotechnology*, Graz, Austria, July 10th 2017, oral presentation
- Toplak M, Wiedemann G, Ulićević J, Daniel B, Hoernstein S N W, Kothe J, Reski R, Winkler A and Macheroux P, Structural and functional characterization of the berberine bridge enzyme-like protein from *Physcomitrella patens* giving insight into the evolutionary role of BBE-like enzymes in plants. *DK Molecular Enzymology graduate seminar*, Graz, Austria, June 30th 2017, oral presentation
- Toplak M, Ulićević J, Daniel B, Wallner S and Macheroux P, Studying the role of the only berberine bridge enzyme-like protein in *Physcomitrella patens*. *17th Doc Day NAWI Graz Doctoral Schools Molecular Biology and Biochemistry & Molecular Biosciences and Biotechnology*, Graz, Austria, February 3rd 2017, poster presentation
- Toplak M, Ulićević J, Daniel B, Wallner S and Macheroux P, PpBBE-studying the origin of BBE-like enzymes in plants. *Joint retreat with the DK Biomolecular Technology of Proteins*, Vienna, Semmering, Austria, September 30th 2016, poster presentation
- Toplak M, Daniel B, Wallner S, Wiedemann G, Reski R and Macheroux P, PpBBE – the ancestor of berberine bridge enzyme-like enzymes in plants? *16th Doc Day NAWI Graz Doctoral Schools Molecular Biology and Biochemistry & Molecular Biosciences and Biotechnology*, Graz, Austria, July 7th 2016, poster presentation
- Toplak M, Wallner S and Macheroux P, EasC and EasE – what is their role in chanoclavine I formation? *15th Doc Day NAWI Graz Doctoral Schools Molecular Biology and Biochemistry & Molecular Biosciences and Biotechnology*, Graz, Austria, February 5th 2016 - poster presentation

Poster and oral presentations at international conferences

- Toplak M, Brunner J and Macheroux P, Tight product binding is the key for efficient electron transfer from D-lactate dehydrogenase 2 to the electron transferring flavoprotein of *Saccharomyces cerevisiae*. *Gordon Research Seminar and Conference: Enzymes, Coenzymes and Metabolic Pathways*, Waterville valley, NH, USA, July 2018, poster presentation
- Toplak M, Wiedemann G, Ulićević J, Daniel B, Hoernstein S N W, Kothe J, Niederhauser J, Reski R, Winkler A and Macheroux P, Uncovering the role of the single berberine bridge enzyme homolog of *Physcomitrella patens*. *22nd conference of the Austrian Society of Plant Biology (ATSPB)*, Graz, Austria, April 2018, poster presentation
- Toplak M, Wiedemann G, Ulićević J, Daniel B, Hoernstein S N W, Kothe J, Reski R, Winkler A and Macheroux P, The origin of the berberine bridge enzyme-like protein family in plants. *19th International Symposium on Flavins and Flavoproteins*, Groningen, The Netherlands, July 2017, poster presentation and poster pitch talk
- Toplak M, Daniel B, Wallner S, Wiedemann G, Reski R and Macheroux P, The berberine bridge enzyme-like enzyme from *Physcomitrella patens*. *OxiZymes 2016 (8th European Meeting on Oxizymes)*, Wageningen, The Netherlands, July 2016, poster presentation

Publications (peer-reviewed)

- Daniel B, Konrad B, Toplak M, Lahham M, Messenlehner J, Winkler A and Macheroux P (2017) The family of berberine bridge enzyme-like enzymes: A treasure-trove of oxidative reactions. *Arch. Biochem. Biophys.* **632**, 88-103.
- Augustin P*, Toplak M*, Fuchs K, Gerstmann E, Prassl R and Macheroux P (2018) Oxidation of the FAD cofactor to the 8-formyl-derivative in human electron transferring flavoprotein. *J. Biol. Chem.* **283**, 2829-2840.
* these two authors contributed equally to this work
- Toplak M, Wiedemann G, Ulićević J, Daniel B, Hoernstein S N W, Kothe J, Niederhauser J, Reski R, Winkler A and Macheroux P (2018) The single berberine bridge enzyme homolog of *Physcomitrella patens* is a cellobiose oxidase. *FEBS J* **285**, 1923-1943.
- Heckenbichler K, Schweiger A, Brandner L, Binter A, Toplak M, Macheroux P, Gruber K and Breinbauer R (2018) Asymmetric Reductive Carbocyclization Using Engineered Ene Reductases. *Angew. Chem. Intl. Ed.* **57**, 7240-7244.
- Rodrigues-Vendramini F A V, Marschalk C, Toplak M, Macheroux P, de Souza Bonfim-Mendonça P, Svidzinsk T I E, Seixas F A V and Kioshima E S (2019) Promising new antifungal treatment targeting chorismate synthase from *Paracoccidioides brasiliensis*. *Antimicrob. Agents Chemother.* **63(1)**:e01097-18. <https://doi.org/10.1128/AAC.01097-18>.

- Toplak M, Brunner J, Tabib C R and Macheroux P (2019) Closing the gap: Yeast electron transferring flavoprotein links the oxidation of D-lactate and D- α -hydroxyglutarate to energy production via the respiratory chain. *FEBS J. Accepted*
- Bueno P S A, Rodrigues-Vendramini F A V, Toplak M, Macheroux P, Kioshima Cótica E S and Seixas F A V (2019) New inhibitors of chorismate synthase present antifungal activity against *P. brasiliensis*. *Submitted*
- Toplak M, Brunner J, Schmidt J and Macheroux P (2019) Biochemical characterization of human D-2-hydroxyglutarate dehydrogenase and two disease-related variants reveal the molecular cause of D-2-hydroxyglutaric aciduria. *Submitted*

Awards

- Best presentation prize at the *DK Molecular Enzymology graduate seminar*, Graz, November 2018

“I was taught that the way of progress was neither swift nor easy”
„Ich habe gelernt, dass der Weg des Fortschritts weder kurz noch unbeschwerlich ist.“

Marie Curie (1867 – 1934)